Modern Approaches in Solid Earth Sciences

Yujiro Ogawa
Ryo Anma
Yildirim Dilek *Editors*

Accretionary Prisms and Convergent Margin Tectonics in the Northwest Pacific Basin

Springer

Accretionary Prisms and Convergent Margin Tectonics in the Northwest Pacific Basin

Modern Approaches in Solid Earth Sciences

VOLUME 8

Series Editors

For other titles published in this series, go to
www.springer.com/series/7377

Yujiro Ogawa • Ryo Anma • Yildirim Dilek
Editors

Accretionary Prisms and Convergent Margin Tectonics in the Northwest Pacific Basin

Springer

Editors
Yujiro Ogawa
Century Tsukuba-Miraidaira C-740
Obari, Yokodai 1-127-2
300-2358 Tsukubamirai-shi
Japan
fyogawa45@yahoo.co.jp

Yildirim Dilek
Department of Geology
Miami University
Shideler Hall 114
45056 Oxford Ohio
USA
dileky@muohio.edu

Ryo Anma
Graduate School of Life &
Environmental Sciences
University of Tsukuba
Ten-nodai 1-1-1
305-8572 Tsukuba, Ibaraki
Japan
ranma@sakura.cc.tsukuba.ac.jp

Responsible series editor: Y. Dilek

ISSN 1876-1682 e-ISSN 1876-1690
ISBN 978-90-481-8884-0 e-ISBN 978-90-481-8885-7
DOI 10.1007/978-90-481-8885-7
Springer Dordrecht Heidelberg London New York

Library of Congress Control Number: 2011929049

Credit cover figure: bubaone/istockphoto.com

Printed on acid-free paper

Springer is part of Springer Science+Business Media (www.springer.com)

Preface

The Japanese Islands lie on the Northwestern Pacific rim and have been repeatedly struck by subduction-related earthquakes and associated tsunamis. Until the early 1980s, studies of interplate earthquakes and tsunamigenic processes relied on seismic remote-sensing techniques to attempt to understand the seismogenic processes that take place deep beneath the ocean floor. The challenge of understanding seafloor geological processes associated with subsea earthquakes and tsunamis was addressed when the Japan Agency for Marine-Earth Science and Technology (JAMSTEC) commissioned deep-sea manned submersibles *Shinkai 2000* (1982–2002) and *Shinkai 6500* (1990–) and various remotely operated vehicles (ROVs).

Manned submersibles and ROVs have been valuable tools for investigating abyssal topography, seafloor profiles across intra-oceanic arcs, and geological processes at convergent plate boundaries. Since the 1980s, long-range missions by submersibles have focused on areas in and around deep oceanic trenches near Japan. The French–Japanese KAIKO project was an early milestone that achieved magnificent results, including unraveling the structure of accretionary prisms, mapping the distributions of cold seeps and chemosynthetic bio-communities, and providing detailed geophysical, geological, and topographic data. The project resulted in publication of papers in *Tectonophysics* (1989), *Earth and Planetary Science Letters* (1987, 1992), and *Paleogeography, Paleoceanography and Paleoclimatology* (1989).

Vast amounts of knowledge and experience have now been accumulated from studies involving submersibles. Further knowledge has been gained from several geophysical experiments in the Japan region and from ODP and IODP expeditions. Technological advances in geophysical techniques have provided stunning illustrations of the deep structure of accretionary prisms and decollement surfaces, along-arc and cross-arc structural variations of the Izu–Bonin Arc, and the Moho discontinuity in the Philippine Sea and northwestern Pacific. Recent results from studies combining 3D-seismic and ocean bottom seismograph (OBS) data have been truly amazing. The commissioning in 2005 of JAMSTEC's drilling vessel *Chikyu* extended the limit for offshore scientific drilling to depths of up to 7 km beneath the seafloor. The NantroSEIZE IODP expeditions have not yet drilled to the top of the seismogenic zone, but have already demonstrated an excellent match between borehole data and large-scale structures identified from seismic survey data. Deepening of

holes and detailed analyses of samples may further improve our understanding of seismogenic and tsunamigenic processes. Recent technological developments for autonomous underwater vehicles (AUVs) now allow long-term, continuous subsea observations without labor costs and risk to human life.

However, these technological developments seem to have suppressed research use of manned submersibles. The resolution of seismic survey data is too coarse to identify outcrop-scale structures and their lateral variations. Scientific drilling provides continuous high-resolution data, but it is restricted to one dimension. Techniques of seafloor sampling from AUVs have not yet been perfected. The use of manned submersibles for in situ seafloor observation, sampling, and geological mapping is the only available method to fill these gaps.

Because no compilation of submarine studies of the northwestern Pacific margins has been published for the international science readership since completion of the KAIKO project, we asked the leaders of recent manned dive projects to summarize their results for publication in a single volume of Springer's *Modern Approaches in Solid Earth Sciences* series under the title of *Accretionary Prisms and Convergent Margin Tectonics in the Northwest Pacific Basin*. From many dive projects, thirteen papers were selected.

The topics of the thirteen papers range widely, including a discussion of the bathymetric features of oceanic crust, a technological report on an ocean-bottom observatory, a structural analysis of accretionary prisms, and the petrology of peridotites, to name a few. The opening paper (by Nakanishi) deals with the large-scale bathymetric features of oceanic crust near the subduction zone along the Kuril and northeastern Japan Arcs and discusses the effect of subduction on pre-existing structures in oceanic crust, such as abyssal hills. This broad-scale view is followed by a study by Ogawa that used observations from a submersible vessel to ground-truth the work of Nakanishi.

The most remarkable tectonic feature in the Japan region is the Boso triple junction, where the Pacific and Philippine Sea oceanic plates collide with the Japan Arc. The unique tectonic relationships of this trench–trench–trench-type triple junction and its topographic features are reviewed by Ogawa and Yanagisawa. Their description of the triple junction is followed by Takahashi et al., who provide a large-scale view of the Izu–Ogasawara (Bonin) Arc system obtained from an active seismic experiment using OBSs. Geological and petrological features across the Izu–Ogasawara (Bonin) Arc system are reported from the fore-arc (Ueda et al.) and back-arc regions (Sato and Ishii; Ohara et al.). In the fore-arc region, Ueda et al. attributed serpentinites that accompany eclogitic metamorphic rocks to the existence of a subduction channel. Sato and Ishii report on the petrological characteristics of ultramafic rocks from the southern Mariana Trench. Ohara et al. discuss the formation of an oceanic core complex developed in the Parece Vela Basin, behind the Izu–Ogasawara (Bonin) Arc.

The rest of the volume is devoted to the accretionary complex bordering the Nankai trough. Just as valleys are often favored by field geologists for onshore mapping, the deeply incised profiles along submarine canyons provide an excellent opportunity for three-dimensional seafloor observations and mapping. Using this

approach, Anma et al. and Hayman et al. describe mesoscopic- to macroscopic-scale structures of the accretionary prism along the Shionomisaki and Tenryu submarine canyons, respectively. Kawamura et al. consider the rate of exhumation of foliated low-grade metamorphic rocks exposed in the Tenryu canyon on the basis of depositional age and temperature conditions. Michiguchi and Ogawa extend recent discussions of the importance in the development of accretionary prisms of dark bands in planar quasi-layered structures oblique to bedding planes, which are common in recent submarine and onshore (Boso–Miura) accretionary complexes. Toki et al. demonstrate recent advances in the study of pore-water geochemistry, reporting results from the Nankai Trough. These papers complement the results of deep-sea drilling to the seismogenic zone in the Nankai accretionary prism (the NantroSEIZE project). The volume concludes with a technological paper by Fujimoto et al. who investigated the stability during seismic events of an ocean-bottom observatory deployed from the surface.

All of the papers included in this volume demonstrate the effectiveness of direct observation from manned submersible vessels to produce the outcrop-scale descriptions that are fundamental to the study of geology.

We thank the contributors to this book for their time and effort, and express our gratitude to a large number of scientists who provided valuable reviews of the chapters in it. We are grateful to Japan Agency for Marine–Earth Science and Technology (JAMSTEC) for the invaluable support. The provision of research opportunities and scientifically fruitful and enjoyable cruises are greatly appreciated. Last, but not least, we thank particularly Petra D. van Steenbergen, Senior Publishing Editor at Springer, for her enthusiastic support and motivation throughout the preparation of this book, and Cynthia de Jonge at Springer–Geosciences for her invaluable assistance in formatting and preparing the book for final publication.

14 December 2010

Y. Ogawa
R. Anma
Y. Dilek

Acknowledgements

We wish to thank the following colleagues for their timely and thorough reviews of the manuscripts that greatly improved the content of the book and helped us maintain high scientific standards. We greatly acknowledge their efforts.

Ryo Anma, University of Tsukuba, Japan
Juichiro Ashi, University of Tokyo, Japan
Kurtis C. Burmeister, University of the Pacific, USA
Mark Cloos, University of Texas at Austin, USA
Yildirim Dilek, Miami University, USA
Andrea Festa, University of Torino, Italy
Nicholas W. Hayman, University of Texas at Austin, USA
Keika Horiguchi, Osaka University, Japan
Junichiro Ishibashi, Kyushu University, Japan
Masahiko Ishikawa, Yokohama National University, Japan
Kiichiro Kawamura, Fukada Geological Institute, Japan
Satoru Kojima, Gifu University, Japan
Hidenori Kumagai, JAMSTEC, Japan
Timothy Kusky, China University of Geoscience, Wuhan, China
Katsuyoshi Michibayashi, Shizuoka University, Japan
Gregory F. Moore, University of Hawaii at Manoa, USA
Masao Nakanishi, Chiba University, Japan
Yujiro Ogawa, Tokyo Electric Power Services, Ltd., Japan
Robert J. Stern, University of Texas at Dallas, USA
Tatsuki Tsujimori, Okayama University, Japan
Kohtaro Ujiie, University of Tsukuba, Japan
John Wakabayashi, California State University at Fresno, USA
Yasuhiro Yamada, Kyoto University, Japan

Contents

Contributors

Shunji Akaiwa
Graduate School of Life and Environmental Sciences, University of Tsukuba, Ten-nodai 1-1-1, Tsukuba, Ibaraki 305-8572, Japan
taurushunji@room.ocn.ne.jp

Ryo Anma
Graduate School of Life and Environmental Sciences, University of Tsukuba, Ten-nodai 1-1-1, Tsukuba, Ibaraki 305-8572, Japan
ranma@sakura.cc.tsukuba.ac.jp

Juichiro Ashi
Department of Ocean Floor GeoScience, Atmosphere and Ocean Research Institute, The University of Tokyo, 5-1-5, Kashiwanoha, Kashiwa, Chiba 277-8568, Japan
ashi@aori.u-tokyo.ac.jp

Toyoto Azuma
Hidaka Mountains Museum, 297-12 Honcho-Higashi, Hidaka Town 055-2301, Hokkaido Prefecture, Japan
hmc@town.hidaka.hokkaido.jp

Kurtis C. Burmeister
Department of Earth and Environmental Sciences, University of the Pacific, 3601 Pacific Avenue, Stockton, CA 95211, USA
kburmeister@pacific.edu

Tae Chiba
Graduate School of Life and Environmental Sciences, University of Tsukuba, Tsukuba 305-8572, Japan
icecream.103yen@gmail.com

Shun Chiyonobu
Research Institute of Innovative Technology for the Earth, CO_2 Storage Research Group, 9-2 Kizugawadai, Kizugawa-shi, Kyoto 619-0292, Japan
chiyonob@rite.or.jp

Yildirim Dilek
Department of Geology, Miami University, 114 Shider Hall, Oxford,
OH 45056, USA
dileky@muohio.edu

Ryota Endo
INPEX Corporation, Akasaka Biz Tower 5-3-1 Akasaka,
Minato-ku, Tokyo 107-6332, Japan
rendo@inpex.co.jp

Hiromi Fujimoto
Graduate School of Science, Tohoku University, Aza Aoba 6-6,
Aramaki, Aoba-ku, Sendai 980-8578, Japan
fujimoto@aob.gp.tohoku.ac.jp

Toshitaka Gamo
Marine Inorganic Chemistry Group, Department of Chemical Oceanography,
Atmosphere and Ocean Research Institute, The University of Tokyo, 5-1-5,
Kashiwanoha, Kashiwa, Chiba 277-8564, Japan
gamo@aori.u-tokyo.ac.jp

Hidetoshi Hara
Geological Survey of Japan, AIST Tsukuba Central 7, Tsukuba 305-8567, Japan
hara-hide@aist.co.jp

Nicholas W. Hayman
Institute for Geophysics, Jackson School of Geosciences, University
of Texas at Austin, J.J. Pickle Research Campus, Austin, TX 78758, USA
hayman@ig.utexas.edu

Satoshi Hirano
Marine Works Japan, Showa-machi 3175-25, Kanazawa, Yokohama
236-0001, Japan
hiranos@nwj.co.jp

Ken-ich Hirauchi
Department of Earth and Planetary Systems Science,
Graduate School of Science, Hiroshima University,
1-3-1, Kagamiyama, Higashi-Hiroshima 739-8526, Hiroshima, Japan
k-hirauchi@hiroshima-u.ac.jp

Takeshi Imayama
Center for Chronological Research, Nagoya University,
Furo-cho, Chikusa-ku, Nagoya 464-8602, Japan
imayama@nendai.nagoya-u.ac.jp

Teruaki Ishii
Fukada Geological Institute, 2-13-12 Hon-Komagome, Bunkyo, Tokyo
113-0021, Japan
ishii@fgi.or.jp

Takahiro Izumino
Department of Natural History Sciences, Graduate School of Science, Hokkaido University, N-10, W-8, Sapporo 060-0810, Japan

Yoshiyuki Kaneda
Institute for Research on Earth Evolution (IFREE), Japan Agency for Marine-Earth Science and Technology (JAMSTEC), Showa-machi 3173-25, Kanazawa-ku, Yokohama 236-0001, Japan
kaneday@jamstec.go.jp

Shinsuke Kawagucci
Precambrian Ecosystem Laboratory (PEL), Japan Agency for Marine-Earth Science and Technology (JAMSTEC), 2-15, Natsushima, Yokosuka 237-0061, Japan
kawagucci@jamstec.go.jp

Shunsuke Kawakami
Earth-Appraisal Co. Ltd., Chiyoda, Tokyo 101-0063, Japan
kawakami@earth-app.co.jp

Kiichiro Kawamura
Fukada Geological Institute, 2-13-12 Hon-Komagome, Bunkyo, Tokyo 113-0021, Japan
kichiro@fgi.or.jp

Motoyuki Kido
Graduate School of Science, Tohoku University, Aza Aoba 6-6, Aramaki, Aoba-ku, Sendai 980-8578, Japan
kido@aob.gp.tohoku.ac.jp

Masataka Kinoshita
Institute for Research on Earth Evolution (IFREE), Japan Agency for Marine-Earth Science and Technology (JAMSTEC), 2-15, Natsushima Yokosuka 237-0061, Japan
masa@jamstec.go.jp

Shuichi Kodaira
Institute for Research on Earth Evolution (IFREE), Japan Agency for Marine-Earth Science and Technology (JAMSTEC), Showa-machi 3173-25, Kanazawa-ku, Yokohama 236-0001, Japan
kodaira@jamstec.go.jp

Yoshiyuki Kuramoto
Hokkaido Hiyama-kita Senior High School, 360 Niwa, Kitahiyama-ku, Setana Town 049-4433, Hokkaido Prefecture, Japan
ys.kura@gmail.com

Kozue Kurihara
Japan Marine Enterprise, Ltd., Natsushima-cho 2-15, Yokosuka 237-0061, Japan

Kenji Maegawa
Earth and Planetary System Science, Faculty of Science, Hokkaido University, N10 W8, Kita-ku, Sapporo 060-0810, Japan
maegawa@mail.sci.hokudai.ac.jp

Yoshihiro Matsumoto
Hydrographic and Oceanographic Department, Japan Coast Guard, Tsukiji 5-3-1, Chuo-ku, Tokyo 104-0045, Japan

Martin Meschede
Institute of Geography and Geology, University of Greifswald, Friedrich-Ludwig-Jahn-Str. 17A, Greifswald D-17487, Germany
meschede@uni-greifswald.de

Yoko Michiguchi
Doctoral Program in Earth Evolution Sciences, University of Tsukuba, Tsukuba 305-8572, Japan
Current address:
Japan Nuclear Energy Safety Organization, Toranomon 4-3-20, Tokyo 105-0001, Japan
y-michi@hotmail.co.jp

Ryo Miura
Miarine Science Division, Nippon Marine Enterprises, Ltd., 2-15 Natsushima-cho, Yokosuka 237-0061, Japan
miurar@nme.co.jp

Seiichi Miura
Institute for Research on Earth Evolution (IFREE), Japan Agency for Marine-Earth Science and Technology (JAMSTEC), Showa-machi 3173-25, Kanazawa-ku, Yokohama 236-0001, Japan
miuras@jamstec.go.jp

Yuki Miyajima
Department of Marine Mineral Resources, Faculty of Marine Science and Technology, Tokai University, 3-20-1 Orito, Shimizu-ku, Shizuoka 424-8610, Japan
miyajimay@mwj.co.jp

Gregory F. Moore
School of Ocean and Earth Science and Technology (SOEST), University of Hawaii at Manoa, Honolulu, HI 96822, USA
gmoore@hawaii.edu

Isao Motoyama
Department of Earth and Environmental Sciences, Graduate School of Science Department, Yamagata University, Yamagata 990-8560, Japan
i-motoyama@sci.kj.yamagata-u.ac.jp

Hideki Mukoyoshi
Marine Works Japan, Showa-machi 3175-25, Kanazawa, Yokohama 236-0001, Japan
mukoyoshih@jamstec.go.jp

Masao Nakanishi
Geosystem and Biological Sciences, Graduate School of Science, Chiba University, 1-33 Yayoi-cho, Inage-ku, Chiba 263-8522, Japan
nakanisi@earth.s.chiba-u.ac.jp

Kiyoaki Niida
Department of Natural History Sciences, Graduate School of Science, Hokkaido University, N-10, W-8, Sapporo 060-0810, Japan
kiyo@mail.sci.hokudai.ac.jp

Tetsuo No
Institute for Research on Earth Evolution (IFREE), Japan Agency for Marine-Earth Science and Technology (JAMSTEC), Showa-machi 3173-25, Kanazawa-ku, Yokohama 236-0001, Japan
not@jamstec.go.jp

Yujiro Ogawa
The University of Tsukuba, 1-127-2-C-740 Yokodai, Tsukubamirai 300-2358, Japan (home)
fyogawa45@yahoo.co.jp

Yasuhiko Ohara
Hydrographic and Oceanographic Department of Japan, Tokyo 104-0045, Japan
and
Institute for Research on Earth Evolution, Japan Agency for Marine-Earth Science and Technology, 2-15 Natsushima-cho, Yokosuka 237-0061, Japan
yasuhiko.ohara@gmail.com

Kyoko Okino
Division of Ocean-Earth System Science, Atmosphere and Ocean Research Institute, The University of Tokyo, 5-1-5 Kashiwanoha, Kashiwa-shi, Chiba 277-8564, Japan
okino@aori.u-tokyo.ac.jp

Takashi Okuda
Technical Center of Nagoya University, Furo-cho, Chikusa-ku, Nagoya 464-8602, Japan
okuda@seis.nagoya-u.ac.jp

Yukihito Osada
Graduate School of Science, Tohoku University, Aza Aoba 6-6, Aramaki, Aoba-ku, Sendai 980-8578, Japan
osada@aob.gp.tohoku.ac.jp

Takahiro Saito
Faculty of Education, Hirosaki University, Bunkyocho-1,
Hirosaki 036-8560, Aomori, Japan
qqxp738d@diary.ocn.ne.jp

Izumi Sakamoto
Department of Marine Mineral Resources, Faculty of Marine Science
and Technology, Tokai University, 3-20-1 Orito, Shimizu-ku,
Shizuoka 424-8610, Japan
izumis@scc.u-tokai.ac.jp

Yuji Sano
Atmospheric and Marine Analytical Chemistry Group,
Department of Chemical Oceanography, Atmosphere and Ocean
Research Institute, The University of Tokyo, 5-1-5, Kashiwanoha,
Kashiwa, Chiba 277-8564, Japan
ysano@aori.u-tokyo.ac.jp

Tomoyuki Sasaki
Marine Geology, Department of Ocean Floor Geoscience,
Atmosphere and Ocean Research Institute, The University
of Tokyo, 5-1-5, Kashiwanoha, Kashiwa-shi,
Chiba 277-8564, Japan
tmsasaki@aori.u-tokyo.ac.jp

Hiroshi Sato
Institute of Natural Sciences, Senshu University, 2-1-1 Higashimita, Tama-ku,
Kawasaki, Kanagawa 214-8580, Japan
satohiro@isc.senshu-u.ac.jp

Takeshi Sato
Institute for Research on Earth Evolution (IFREE), Japan Agency
for Marine-Earth Science and Technology (JAMSTEC),
Showa-machi 3173-25, Kanazawa-ku, Yokohama 236-0001, Japan
tsato@jamstec.go.jp

Jonathan E. Snow
Department of Earth and Atmospheric Sciences, University of Houston,
Houston, TX 77204, USA
jesnow@uh.edu

Keiichi Tadokoro
Graduate School of Environmental Studies, Nagoya University,
Furo-cho, Chikusa-ku, Nagoya 464-8602, Japan
tad@seis.nagoya-u.ac.jp

Narumi Takahashi
Institute for Research on Earth Evolution (IFREE), Japan Agency
for Marine-Earth Science and Technology (JAMSTEC),
Showa-machi 3173-25, Kanazawa-ku, Yokohama 236-0001, Japan
narumi@jamstec.go.jp

Naoto Takahata
Atmospheric and Marine Analytical Chemistry Group,
Department of Chemical Oceanography, Atmosphere and Ocean
Research Institute, The University of Tokyo, 5-1-5, Kashiwanoha,
Kashiwa, Chiba 277-8564, Japan
ntaka@aori.u-tokyo.ac.jp

Toru Takeshita
Department of Natural History Sciences, Graduate School of Science,
Hokkaido University, N-10, W-8, Sapporo 060-0810, Japan
torutake@mail.sci.hokudai.ac.jp

Kaoru Takizawa
Institute for Research on Earth Evolution (IFREE), Japan Agency
for Marine-Earth Science and Technology (JAMSTEC),
Showa-machi 3173-25, Kanazawa-ku, Yokohama 236-0001, Japan
and
Nippon Marine Enterprises, Ltd, Showa-machi 3173-25,
Kanazawa-ku, Yokohama 236-0001, Japan
takizawak@jamstec.go.jp

Yoshiyuki Tatsumi
Institute for Research on Earth Evolution (IFREE), Japan Agency
for Marine-Earth Science and Technology (JAMSTEC),
Natsushima-Cho 2-15, Yokosuka 237-0061, Japan
tatsumi@jamstec.go.jp

Tomohiro Toki
Department of Chemistry, Biology and Marine Science, Faculty of Science,
University of the Ryukyus, 1, Senbaru, Nishihara, Okinawa 903-0213, Japan
toki@sci.u-ryukyu.ac.jp

Urumu Tsunogai
Earth and Planetary System Science, Faculty of Science, Hokkaido University,
N10 W8, Kita-ku, Sapporo 060-0810, Japan
urumu@mail.sci.hokudai.ac.jp

Hayato Ueda
Faculty of Education, Hirosaki University, Bunkyocho-1,
Hirosaki 036-8560, Aomori, Japan
ueta@mvf.biglobe.ne.jp

Tadashi Usuki
Institute of Earth Sciences, Academia Sinica, 128 Academia Road
Sec. 2, Nankang, Taipei 11529, Taiwan
usu@earth.sinica.edu.tw

Yasuhiro Yamada
Department of Civil and Earth Resources Engineering, Graduate School
of Engineering, Kyoto University, Kyoto 615-8540, Japan
yamada@earth.kumst.kyoto-u.ac.jp

Mikiya Yamashita
Institute for Research on Earth Evolution (IFREE), Japan Agency for Marine-Earth Science and Technology (JAMSTEC), Showa-machi 3173-25, Kanazawa-ku, Yokohama 236-0001, Japan
mikiya@jamstec.go.jp

Yukio Yanagisawa
Geological Survey of Japan, AIST, Tsukuba 305-8567, Japan
y.yanagisawa@aist.go.jp

Makoto Yuasa
Institute of Geology and Geoinformation, National Institute of Advanced Industrial Science and Technology (AIST), Central 7, 1-1-1 Higashi, Tsukuba, Ibaraki 305-8567, Japan
myuas1764@yahoo.co.jp

Bending-Related Topographic Structures of the Subducting Plate in the Northwestern Pacific Ocean

Masao Nakanishi

Abstract Elongated topographic structures associated with bending of the subducting oceanic plate along the western Kuril, Japan and northern Izu-Ogasawara trenches, were investigated using available multibeam bathymetric data. Magnetic anomaly lineations were also reidentified using available geomagnetic data to reveal controlling factors for strikes of bending-related topographic structures. The new bathymetric map demonstrates that most of bending-related topographic structures exist in the oceanward trench slopes deeper than 5,600 m. The map reveals that bending-related topographic structures are developed parallel to the trench axis or inherited seafloor spreading fabrics. Detailed identification of magnetic anomalies reveals curved lineations and discontinuity of lineations associated with propagation ridges. A trough with elongated escarpments associated with the propagating ridge in mid-Cretaceous Quiet Period was discovered near the trench-trench-trench triple junction. Comparison between the detailed bathymetric and magnetic anomaly lineation maps elucidates that abyssal hill fabrics were reactivated where the angle between abyssal hill fabrics and trench axis is less than about 30°. The topographic expression of bending-related structures are classified into two types according to whether new faults develop parallel to the trench axis or inherited seafloor spreading fabrics reactivate.

Keywords Plate bending • Bending-related topographic structure • Deep-sea trench • Seafloor spreading fabric • Magnetic anomaly lineation

1 Introduction

One of the important properties controlling subduction is the amount of water in the subducting plate. The release of water from the subducting plate controls the fluid pressure along the plate interface (Moore and Saffer 2001) and facilitates the

M. Nakanishi (✉)
Geosystem and Biological Sciences, Graduate School of Science, Chiba University,
1-33 Yayoi-cho, Inage-ku, Chiba 263-8522, Japan
e-mail: nakanisi@earth.s.chiba-u.ac.jp

Y. Ogawa et al. (eds.), *Accretionary Prisms and Convergent Margin Tectonics in the Northwest Pacific Basin*, Modern Approaches in Solid Earth Sciences 8,
DOI 10.1007/978-90-481-8885-7_1,

reactivation of the faults producing earthquakes up to several hundred kilometers deep into the subduction zones. The percolation of water into the overlying asthenosphere reduces the melting temperature of the mantle rock and thus inherently affects arc magmatism (Rüpke et al. 2002). Faults developed by bending the incoming oceanic plate facilitate the infiltration of seawater into the oceanic plate (Ranero et al. 2003). Seismic reflection data support this hypothesis because bending-related faults cut at least 6 km into the uppermost mantle (Grevemeyer et al. 2005). The strike of bending-related faults may give us the useful information about the intermediate-depth seismicity because the seismicity may occur by reactivation of bending-related faults (Ranero et al. 2005). These evidences indicate bending-related faults play an important role in tectonic activity at subduction zones.

Bending-related faults of the oceanward slope are ubiquitous structures of oceanic plates incoming to trenches. In general, the faults are thought to be formed parallel or subparallel to the bending axis of the incoming plate, namely the trench axis, in most trenches. Oceanward slopes of several trenches have bending-related structure with a strike different from the trench axes (Masson 1991; Kobayashi et al. 1995, 1998; Ranero et al. 2003). In these areas, abyssal hill fabrics made parallel to spreading centers by activity of normal faults were reactivated instead of the creation of new faulting parallel to the trench axes.

The Mesozoic Pacific plate is subducting along the Kuril, Japan, Izu-Ogasawara, and Mariana trenches (Nakanishi et al. 1992). Kobayashi et al. (1995, 1998) investigated the bending-related structures of the oceanward trench slope of the western Kuril and northern Japan trenches using the bathymetric data obtained by the multibeam echo-sounder, SeaBeam. They concluded that the abyssal hill fabrics are revalidated when abyssal hill fabrics trend within 30° of trench axes. This conclusion is consistent with the previous work by Masson (1991). Billen et al. (2007) indicated the critical angle for the reactivation of abyssal hill fabrics is 25°, which is smaller than that in the previous works. Renard et al. (1987), Kato (1991), and Seta et al. (1991) described bending-related structures of the oceanward trench slope only near the trench axis of the Izu-Ogasawara Trench. Bending-related structures from the southern Japan and Izu-Ogasawara trenches are not well known.

To examine controlling factors for strikes of bending-related structures, it is indispensable to describe oceanic spreading fabrics and to identify magnetic anomaly lineations. The oceanic spreading fabrics consist of inherited abyssal hill fabrics and other preexisting weak zones related to seafloor spreading process, which are fracture zones, non-transform offsets, and so on. Magnetic anomaly lineations on the Pacific plate incoming to trenches east of Japan were identified by Nakanishi et al. (1989, 1999). The curved lineation was identified at the Japan Trench near 38°N (Nakanishi et al. 1989, 1991), but was not assigned an age. No lineations were identified very near the trench axis of the Izu-Ogasawara Trench (Nakanishi et al. 1989). In these areas, it is difficult to examine controlling factors for strikes of bending-related structures.

In this article, detailed topography of the outer slopes of the trenches near the Japan Islands will be examined based upon an abundance of multibeam bathymetric data (Fig. 1) to analyze the characteristics of tectonic fabrics in the outer slopes of the

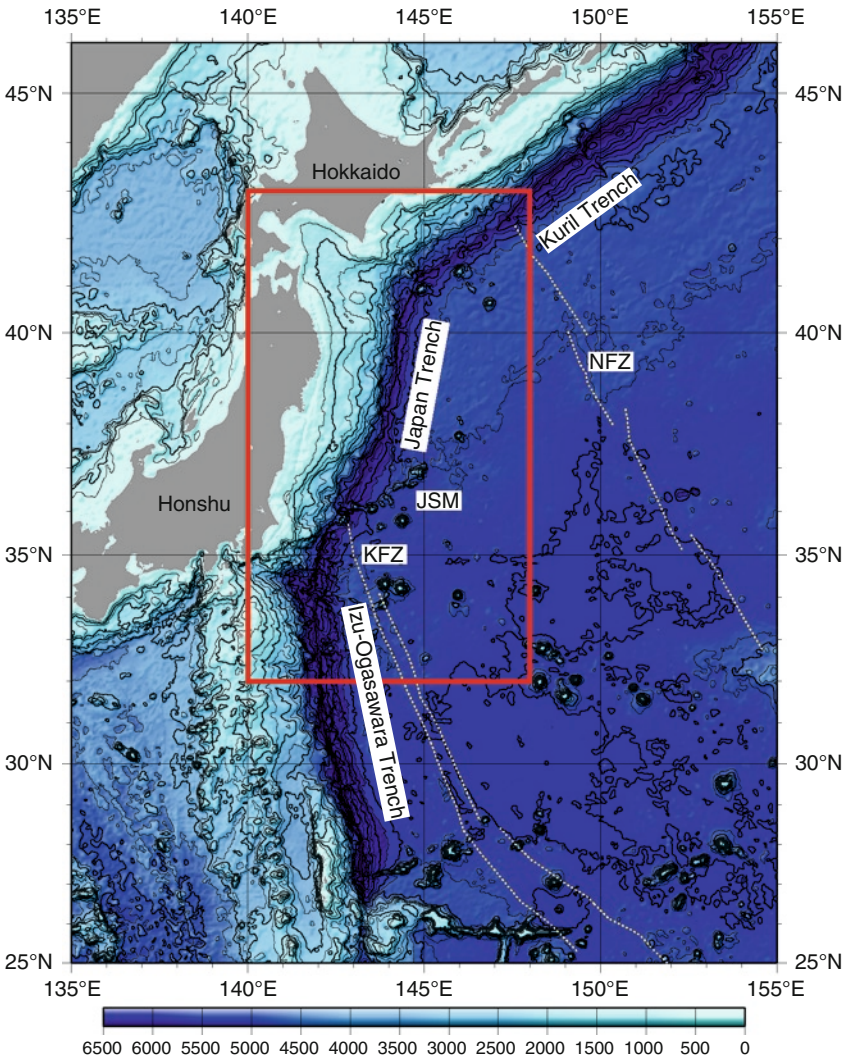

Fig. 1 The bathymetric map around the Japan islands. Bathymetric data are ETOPO1 (Amante and Eakins, 2009). Contour interval is 500 m. A *red rectangle* represents the area of Figs. 2–4. *KFZ* Kashima Fracture Zone, *NFZ* Nosappu Fracture Zone, *JSM* Joban Seamounts

trenches with special attention to patterns of fault structures. A priority of mention is made for the southern portion of the Japan Trench, south of 38°N, which was not elaborated in detail by the previous works of Kobayashi et al. (1998) and Sasaki (2003). Magnetic anomaly lineations are reidentified based on the geomagnetic data newly collected after the previous works (Nakanishi et al. 1989, 1999). Finally, combining the studies of bathymetry and magnetic anomaly lineations, the controlling factors to determine the strike of the bending-related structures are investigated.

2 Data and Methods

To process the multibeam bathymetric data and shipboard geomagnetic data and to make maps of the data, Generic Mapping Tools (GMT; Wessel and Smith 1998), Marine Geophysics Basic Tools (MAGBAT; Tamaki et al. 1992), and MB-System (Caress and Chayes 1996) are used.

2.1 Bathymetric Data

After Kobayashi et al. (1998), seven cruises were conducted by the author in the study area with cruise identifications, KR98-07, KR99-11 (Ogawa 1999), KH-03-1, KR04-08 (Nakanishi et al. 2004), KR06-03 (Nakanishi 2007), KH-06-1 and YK08-09 (Nakanishi and Noguchi 2008). We also obtained multibeam bathymetric data in six cruises by R/V *MIRAI* from 2008 to 2009 for the study of the tectonics of the Pacific plate, MR08-02 (Yoneyama 2008), MR08-03 (Kashino 2008), MR08-04 (Shimada 2008), MR08-05 (Honda 2008), MR08-06, and MR09-03 (Kikuchi and Nishino 2009). Multibeam bathymetric data obtained in the cruises of R/V *KAIREI*, KR08-10 (Yamano 2008), were offered for this study by the shipboard scientists. Multibeam data obtained in the four cruises of R/V *Thomas Washington*, R/V *Melville*, and R/V *Roger Reville*, RNDB10WT, MGLN03MV, MGLN04MV, and ZHNG07RR, were personally supplied by Geological Data Center, Scripps Institution of Oceanography, University of California, San Diego. Other multibeam data were obtained from the databases of Japan Agency for Marine-Earth Science and Technology (JAMSTEC) for research cruises (http://www.godac.jamstec.go.jp/cruisedata/e/index.html) and National Oceanic and Atmospheric Administration/National Geophysical Data Center (NOAA/NGDC; http://www.ngdc.noaa.gov/mgg/bathymetry/multibeam.html). The unpublished bathymetric data collected in eight cruises by R/V *Hakuho-maru* were processed for this study. Finally, bathymetric data compiled for this study are from the 99 cruises listed (Table 1). The bathymetric data made from multibeam data collected by S/V *Takuyo* and S/V *Meiyo* of Hydrographic and Oceanographic Department, Japan Coast Guard (JHOD; e.g., Fujisawa 2009) are additionally used to fill in the data blank areas of the multibeam bathymetric data. Fig. 2 shows ship tracks of cruises that collected multibeam bathymetric data. The areas surveyed by JHOD are shown as shaded areas in Fig. 2.

Most bathymetric data used in this study were well navigated by GPS or other satellite navigation systems. The accuracy of the GPS navigation is generally tens of meters. R/V *KAIREI*, R/V *YOKOSUKA*, and R/V *MIRAI* are better navigated by the differential GPS, whose accuracy is 2–3 m. Kobayashi et al. (1998) and Cadet et al. (1987) used the bathymetric data collected in the KAIKO Project to expose the topographic expression of several portions of the trenches. The bathymetric data from the KAIKO project were excluded for this study because ship positions in the project were determined by Loran-C navigation, whose accuracy is at most several hundred meters. The inaccurate positioning makes artifacts near swath boundaries in bathymetric maps.

Table 1 Sources of multibeam bathymetric data used for this study except for data supplied by JHOD

Research vessel	Institution	Multibeam system	Cruise identification
Hakuho-maru	JAMSTEC (Before 2003, ORI, UT)	SeaBeam (before 1998)	KH-90-1, KH-92-3, KH-93-1, KH-96-3
		SeaBeam 2120	KH-99-2, KH-99-3, KH-00-2, KH-00-3, KH-03-1, KH-05-2, KH-05-3, KH-06-1
KAIREI	JAMSTEC	SeaBeam 2112	KR98-07, KR99-11, KR01-11, KR02-05, KR02-08, KR02-08, KR02-09, KR02-15, KR03-07, KR03-08, KR03-10, KR04-08, KR04-09, KR05-04, KR05-10, KR06-03, KR06-09, KR07-06, KR08-10
MIRAI	JAMSTEC	SeaBeam 2112	MR97-K02, MR97-K04, MR98-K01, MR98-K02, MR99-K01, MR99-K02, MR99-K03, MR99-K04, MR99-K05, MR99-K06, MR00-K01, MR00-K02, MR00-K04, MR00-K05, MR00-K06, MR00-K07, MR00-K08, MR01-K01, MR01-K02, MR01-K03, MR01-K04, MR01-K05, MR02-K01, MR02-K02, MR02-K03, MR02-K04, MR02-K05, MR02-K06, MR03-K01, MR03-K02, MR04-02, MR04-03, MR04-04, MR04-06, MR04-07, MR04-08, MR05-01, MR05-02, MR05-04, MR05-05, MR06-01, MR06-03, MR06-4, MR06-05, MR07-01, MR07-03, MR07-04, MR07-05, MR07-6, MR07-07, MR08-02, MR08-03, MR08-04, MR08-05, MR08-06, MR09-03
YOKOSUKA	JAMSTEC	SeaBeam 2112	YK01-06, YK02-02, YK05-06, YK08-09
Melville	SIO, UCSD	SeaBeam 2000	MGLN03MV, MGLN04MV
Roger Revelle	SIO, UCSD	EM120	ZHNG07RR
Thomas Washington	SIO, UCSD	SeaBeam	RNDB09WT, RNDB10WT
Thomas G. Thompson	University of Washington	Hydrosweep DS	TN168
HEALY	United States Coast Guard Cutter	SeaBeam 2112	HLY-04-Tb, HLY-04-Tc

JAMSTEC Japan Agency for Marine-Earth Science and Technology, *ORI*, *UT* Ocean Research Institution, the University of Tokyo, *SIO*, *UCSD* Scripps Institution of Oceanography, University of California, San Diego

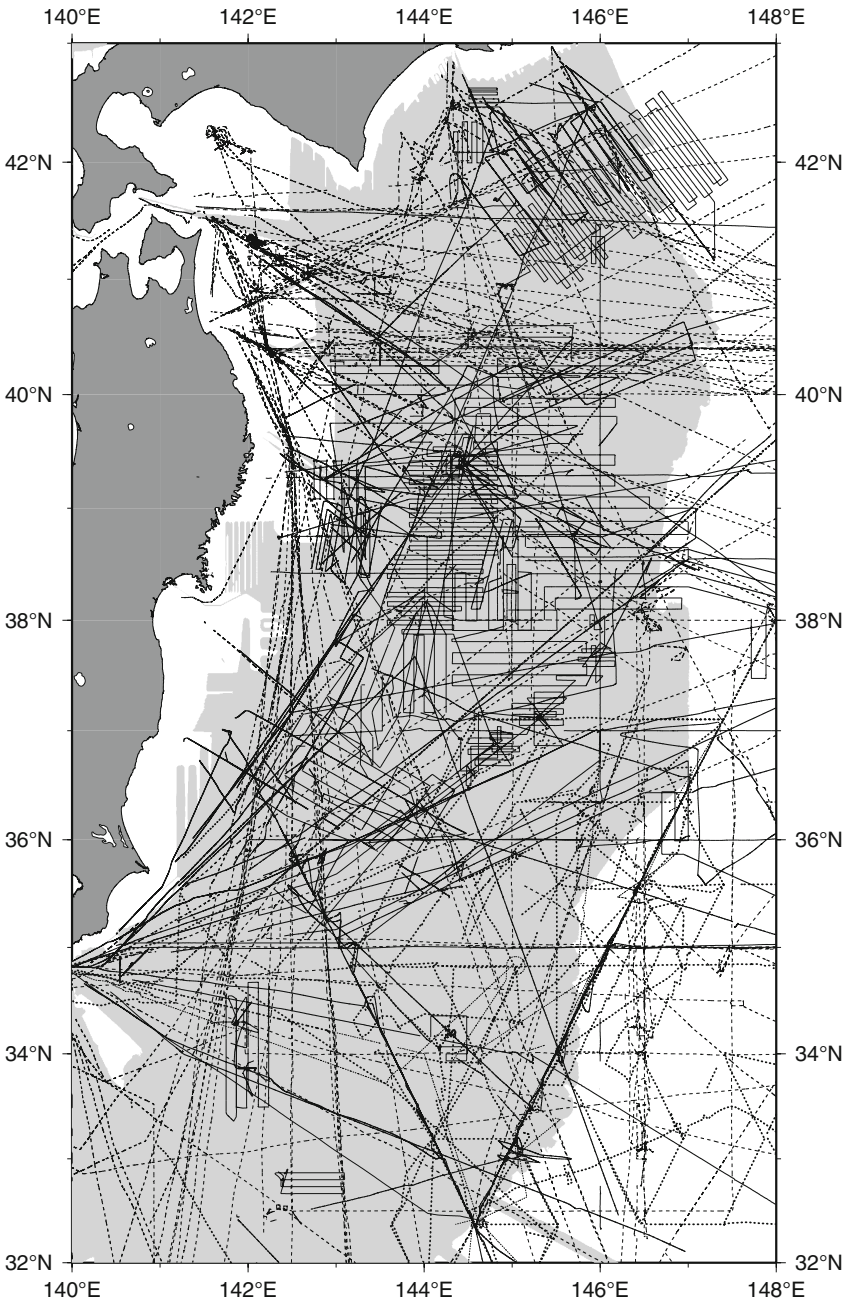

Fig. 2 Cruise tracks of the multibeam bathymetric data for this study. *Gray areas* indicate the survey areas by JHOD. The *solid lines* represent the cruise tracks of R/V *Hakuho-maru*, R/V *KAIREI*, and R/V *YOKOSUKA*. The *broken* and *dotted lines* represent those of R/V *MIRAI* and other research vessels, respectively

Where multibeam bathymetric data are stored in the original vendor format, bathymetry data were manually edited using the interactive graphical utility "mbedit" module of the MB-System to remove bad beams. After identification of bad beams, sound-velocity correlation was done if necessary. The depth recorded by any echo-sounder is strongly dependent on the sound-velocity profile through the water column. We reconstructed bathymetry directly from the travel-time data by full raytracing through an appropriate water sound-velocity profile. If there are available data of expendable bathythermograph or Conductivity-Temperature-Depth casts, sound-velocity profiles in the water column were computed per cruise using the equation of Del Grosso (1974). If not available, temperature and salinity data from the 1982 Climatological Atlas of the World Ocean (Levitus 1982) were used. Finally, a grid file was made, whose interval is 300 m, using the "mbgrid" module of MB-system.

The accuracy of the widely used multibeam echo-sounder system in the cruises for this study, SeaBeam 2112, is approximately 0.5% of water depth. The depth of oceanward slopes has a range from 6,000 to 9,500 m. Thus, the accuracy of the multibeam system is about 3–5 m. The horizontal resolution of the multibeam system is about 2°×2°. This indicates that the horizontal resolution in the study area is about 210–330 m.

2.2 *Geomagnetic Data*

Geomagnetic data incorporated in this study were derived from several different sources (Table 2). We used the same geomagnetic data as Nakanishi et al. (1989) in which magnetic anomaly lineations were identified in the northwestern Pacific Ocean. After 1989, to investigate a pattern of lineations which had been

Table 2 Sources of geomagnetic data used for this study except for data supplied by JHOD that are not included in the database of NOAA/NGDC

Institution	Number of cruises	Cruise identification
ORI, UT	28	KH-67-1, KH-67-5, KH-68-3, KH-68-4A, KH-69-2, KH-70-2, KH-74-2, KH-74-4, KH-75-3, KH-75-4, KH-78-2, KH-78-3, KH-80-3, KH-82-4, KH-82-5, KH-84-1, KH-88-3, KH-89-2, KH-96-3, KH-03-1, KH-06-1, UM6402-A, UM6503-A, UM6402-C, UM6503-B, UM66-A, UM67, DELP86KA
JAMSTEC	10	KR98-07, KR99-1, KR03-07, KR04-08, KR05-10, KR06-03, KR07-06, KR08-10, YK05-06, YK08-09
JHOD	30	HM6703, HM6801, HM6802, HM6804, HM7002, HM7003, HM7103, HM7104, HM7201, HM7807, HM970824, HS000822, HS020810, HS7201, HS7202, HS7502, HS7604, HS7703, HS7802, HS7803, HS980906, HS981012, HS991013, HT881203, HT91T253, HT91T260, HT92T261, HT92T262, HT92T271, HT92T272

(continued)

Table 2 (continued)

Institution	Number of cruises	Cruise identification
GSJ	20	GH7602, GH7703, GH771-C, GH7801, GH7802, GH7901, GH7902, GH7903, GH7904, GH801-A, GH801-B, GH805-A, GH805-B, GH814-A, GH814-B, GH824-A, GH824-B, GH892-C, GH894-A, GH894-B
Kobe University, Japan	6	KUMI, JD04, JD06, JD07, JD08, RF72
Chiba University, Japan	2	DELP87T2, DELP87WA
SIO, UCSD	36	LUSI01AR, SCAN03AR, ZTES2BAR, ZTES03AR, ZTES04AR, ZTES05AR, JPYN02BD, JPYN04BD, DSDP19GC, DSDP20GC, DSDP32GC, DSDP55GC, DSDP56GC, DSDP57GC, DSDP86GC, DSDP87GC, DSDP88GC, DSDP89GC, HUNT01HT, HUNT02HT, HUNT03HT, ANTP03MV, GECS-CMV, GECS-DMV, SILS01BT, SILS02BT, SILS03BT, ARES05WT, ARES06WT, ARES07WT, INDP01WT, INDP02WT, RAMA03WT, RAMA04WT, RNDB10WT, TSDY03WT
LDEO	25	RC1007, RC1008, RC1107, RC1108, RC1205, RC1207, RC1218, RC1219, RC1404, RC1405, RC2004, RC2005, RC2006, V2006, V2007, V2008, V2106, V2815, V2816, V2817, V3212, V3213, V3214, V3311, V3312
Texas A&M University	8	ODP125JR, ODP126JR, ODP127JR, ODP132JR, ODP144JR, ODP145JR, ODP197JR, ODP198JR
U.S. Navy Naval Oceanographic Office	5	SI343608, SI343615, SI932005, SI932009, SI933010
SOEST, Univ. Hawaii	4	77031704, 77031705, 83011604, 84042802
IFREMER, France	3	84002112, 84002113, 84003111
Far East Sci Center, USSR	1	PEGASUS
Mar Geol Geophys, USSR	1	PG30

GSJ Geological Society of Japan, *LDEO* Lamont-Doherty Earth Observatory, *SOEST* School of Ocean and Earth Science and Technology, *IFREMER* Institut Français de Recherche pour l'Exploitation de la Mer

unclear in Nakanishi et al. (1989), geomagnetic measurements were conducted by the author during six cruises by R/V *Hakuho-maru*, KH-90-1 (Nakanishi et al. 1991), KH-92-3 (Nakanishi et al. 1993), KH-93-1 (Nakanishi 1993), KH-96-3, KH-03-1, and KH-06-1, four cruises by R/V *KAIREI*, KR98-07, KR99-11 (Ogawa 1999), KR04-08 (Nakanishi et al. 2004), and KR06-03 (Nakanishi 2007), and one cruise by R/V *YOKOSUKA*, YK08-09 (Nakanishi and Noguchi 2008). We acquired the geomagnetic data collected by JHOD (e.g., Fujisawa 2009). We also obtained the geomagnetic data from the databases of JAMSTEC and

NOAA/NGDC (GEODAS; http://www.ngdc.noaa.gov/mgg/gdas/gd_sys.html). The geomagnetic data obtained in KR08-10 cruise by R/V *KAIREI* was personally obtained from the shipboard scientists of the cruises.

We calculated magnetic anomalies using the 11th Generation International Geomagnetic Reference Field (International Association of Geomagnetism and Aeronomy, Working Group V-MOD 2010). The geomagnetic reversal timescale used in this study is that proposed by Gradstein et al. (2004). Fig. 3 shows magnetic anomaly profiles in the study area.

The magnetic data were analyzed in the usual fashion for magnetic lineation studies: anomalies were plotted as wiggles perpendicular to ship tracks using GMT and MAGBAT and then correlated between tracks by eye. The analysis of geomagnetic data began with the previous magnetic lineation map (Nakanishi et al. 1989) and focused on tracing the lineations. As with any magnetic lineation identification study, the picks were based on a combination of anomaly shape and spacing, extension from better picks, and constraints imposed by geometry and orientation. To help identify individual anomalies, profiles were compared with a synthetic magnetic model based on the Mesozoic geomagnetic reversal timescale of Gradstein et al. (2004).

3 Results

3.1 Overview of the Bathymetric Features

The bathymetric map (Fig. 4) abundantly exposes topography of the seafloor of the Pacific plate. Bathymetric data extend across the trench slope and outer swell to the undeformed oceanic plate. Data coverage spreads more than 200 km from the trench axes and is wider than previous works (e.g., Kobayashi et al. 1998; Sasaki 2003). The wide coverage makes more detailed description of topographic structures of seafloor possible than in previous works.

The crest of the outer swell, Hokkaido Rise, a gently uplifted topographic feature parallel to the trench axis, along the Kuril Trench, has a depth of 5,100 m, which is nearly 1,000 m shallower than the northwestern Pacific basin. The distance between the crest of the outer swell and trench axis is approximately 70 km in the Kuril Trench. The outer swell of the Japan Trench is slightly less clear compared to that of the Kuril Trench. Its crest is deeper than 5,200 m and situated about 80 km east of the Japan Trench axis. The outer swell is distinctly identified north of 37°N in the Japan Trench, north of the Joban Seamounts, but is obscure south of 37°N, near the Joban Seamounts. The outer swell along the Izu-Ogasawara Trench is narrower than those along Kuril and Japan trenches. Kashima Fracture Zone (Nakanishi 1993; Nakanishi et al. 1989) is situated just east of the outer swell. Kashima Fracture Zone prevents the eastern side of the fracture zone from uplifting to make an outer swell.

The remarkable topographic structures on the deep-sea floor, except for deep-sea trenches and outer swells, are Kashima and Nosappu fracture zones, Joban Seamounts and subducting seamounts, Erimo, Daiichi-Kashima, and Mogi. The Kashima

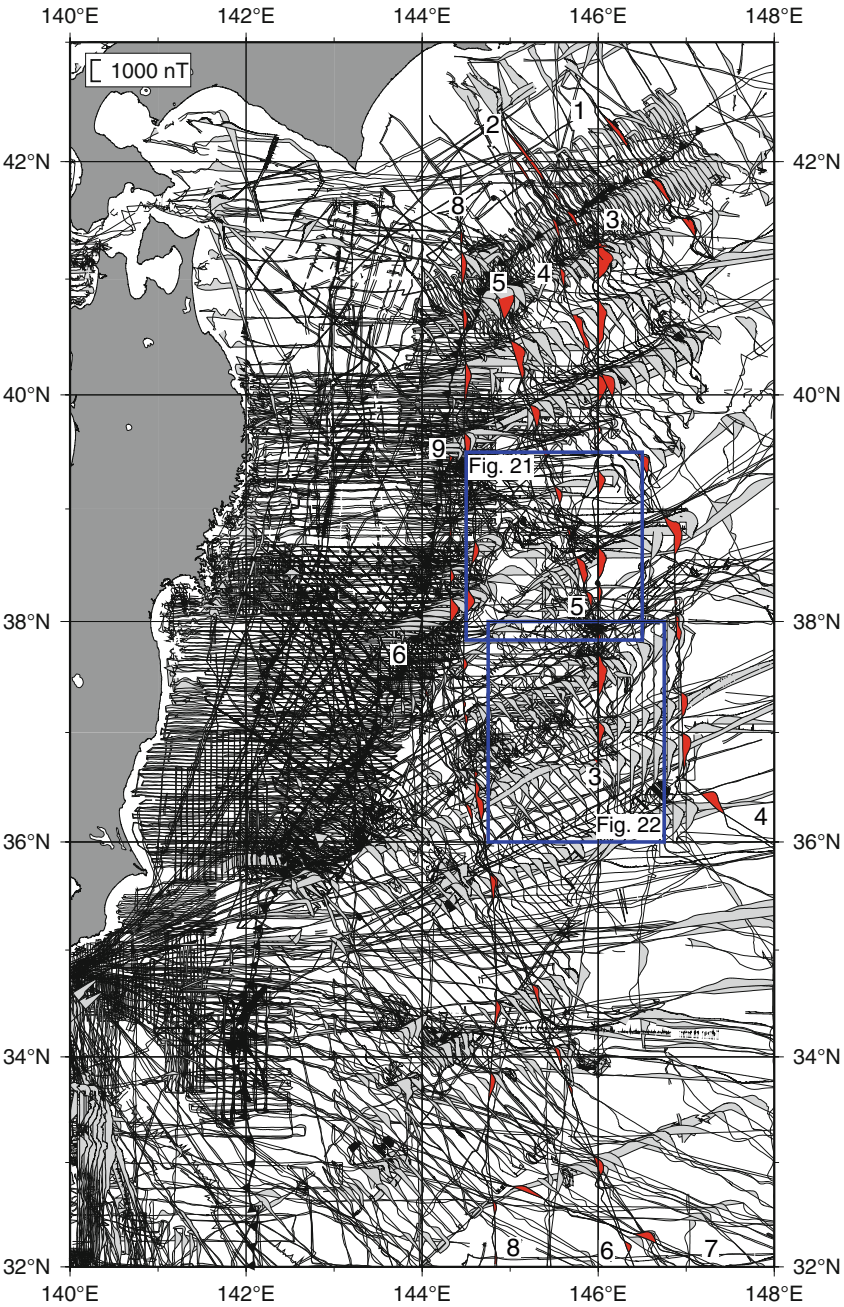

Fig. 3 Along-track magnetic anomaly profiles in the study area. Positive anomalies are shown as *shaded*. The scale bar near the *upper-left corner* is for the amplitude of magnetic anomalies. The profiles shaded in *red* with numbers show the profiles used in Fig. 20. *Blue rectangles* indicate regions of Figs. 21 and 22. *Barbed lines* show the approximate location of trench axes with barbs on the overriding plate

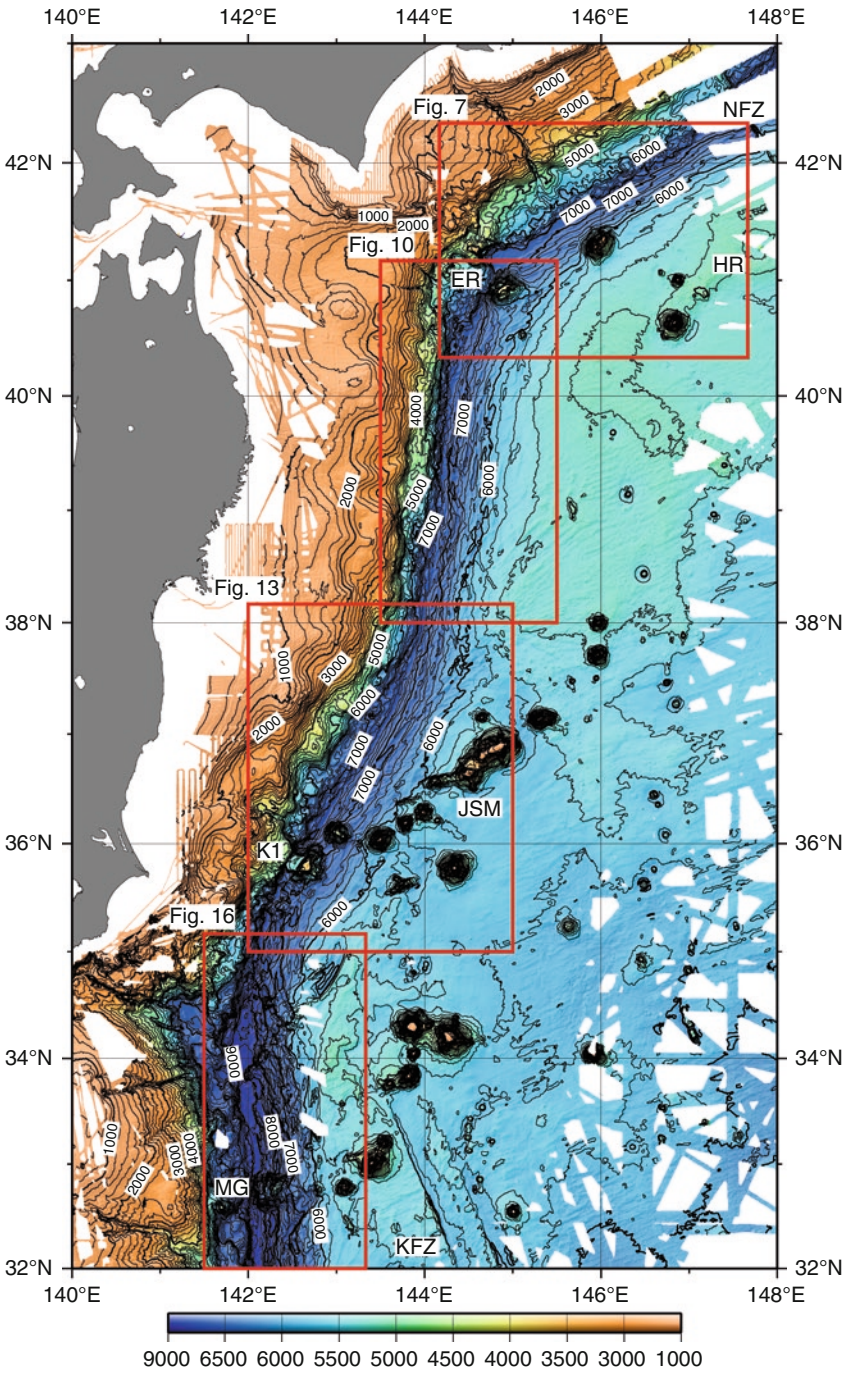

Fig. 4 Bathymetric shaded contour map in the study area. Contour interval is 200 m. *Red rectangles* show regions of Figs. 7, 10, 13, and 16. *HR* Hokkaido Rise, *ER* Erimo Seamount, *K1* Daiichi-Kashima Seamount, *MG* Mogi Seamount. Other conventions are identical to Fig. 1

Fracture Zone, east of the Izu-Ogasawara Trench, is identified by Nakanishi et al. (1989) from magnetic anomaly lineations and examination of single-beam bathymetric data. The Kashima Fracture Zone is characterized by complex trough morphology (Nakanishi 1993). The 30 km-wide trough is bounded by ridges. The expression of the fracture zone is diminished by closing seamounts near 34°N. The western side of the fracture zone is shallower than the eastern side. Vertical relief of the seafloor ranges from 400 to 1,000 m. There is no systematic change of the vertical relief with distance from the axis of the Izu-Ogasawara Trench, implying that the Kashima Fracture Zones has not reactivated by recent subduction-related tectonism of the Izu-Ogasawara Trench.

The bathymetric features of the Joban Seamounts, just east of the Japan Trench, are described in Kobayashi (1991, 1993). The trend of the seamounts is not aligned with any supposed hotspot tracks on the Pacific plate. Daiichi-Kashima and Erimo seamounts are subducting at the Japan and Kuril trenches, respectively. The seamounts were investigated by *Nautile* dives under the KAIKO project (Cadet et al. 1987). Both seamounts are dissected by normal faults. Daiichi-Kashima Seamount is cut by a large normal fault into two blocks, the western half of which is nearly vertically offset from the eastern block by ~1,600 m (Kobayashi et al. 1987). Mogi Seamount, also cut by normal faults, is subducting at the Izu-Ogasawara Trench at 32°50′N.

Bottom topography of the northwestern Pacific basin beyond these outer swells is generally very smooth except for seamounts and knolls. Numerous knolls are situated around 38°N. Hirano et al. (2008) indicated that the knolls are formed by recent volcanism, not related with any plate boundaries.

Abyssal hill fabrics exist on the seafloor east of the Kashima Fracture Zone and Joban Seamounts. Between 38°N and 41°N, there are abyssal hill fabrics east of 145°E. However, the fabrics are not resolvable on the outer swell along the Kuril Trench. Most of the abyssal hill fabrics trend N70°E, parallel to that of magnetic anomaly lineations, with heights of less than 100 m.

3.2 Topographic Expression of the Trenches

The trench axes were determined where direction of trench slopes changes from oceanward to landward. The depth of the trench axis in the Kuril Trench shallows westward from 7,300 to 7,100 m (Fig. 5). The Japan Trench deepens southward from 7,500 to 9,000 m except for the portion of the collision of the Daiichi-Kashima Seamount around 37°N. The trench axis in the Izu-Ogasawara Trench deepens southward from 9,000 to 9,500 m. The seafloor of the trench axis of the western Kuril Trench is smooth at a depth of 7,200 m. The smoothness is due to sediment flow from the Kushiro Submarine Canyon. The seafloor of the trench axis of the northern Izu-Ogasawara Trench around the triple junction between Izu-Ogasawara Trench and Sagami Trough is smooth at a depth of 9,250 m, owing to sediment flow in the Sagami Trough and other deep-sea channels (Ogawa et al. 1989).

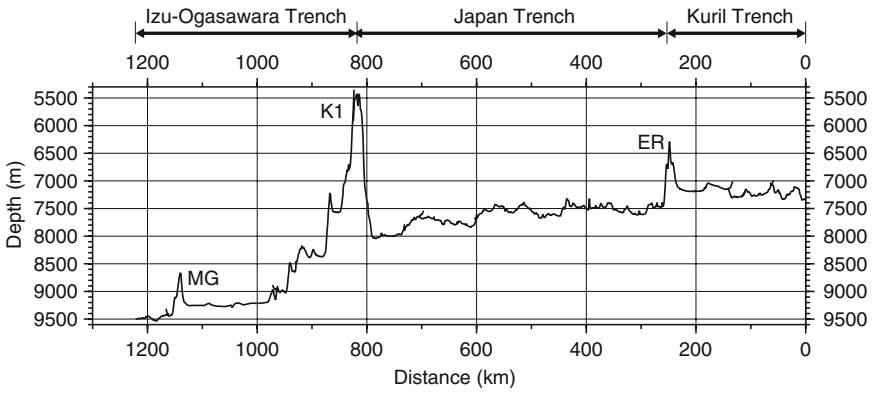

Fig. 5 Depth along the trench axis. *ER* Erimo Seamount, *K1* Daiichi-Kashima Seamount, *MG* Mogi Seamount

3.3 Bending-Related Structures of the Oceanward Trench Slopes

The bathymetric map (Fig. 4) displays pervasive elongated structures, escarpments and ridges, that dissect the oceanward trench slopes (Fig. 6). Increased multibeam bathymetric data made it possible to expose more elongated structures than previous works. Elongate escarpments consist of oceanward- and trenchward-dipping escarpments. Many pairs of oceanward- and trenchward-dipping escarpments form horst and graben structures. Identification of trenchward-dipping escarpments is less certain than that of oceanward-dipping escarpments because of the difficulty in separating these slopes from those made by plate bending and trenchward-dipping escarpments. Moreover, several segments of trenchward dipping escarpments are collapsed owing to subduction of the Pacific plate. Thus, we identified bending-related heights with crests of less than several kilometers width as ridges.

Elongated escarpments and ridges of the oceanward slope of the Japan and Izu-Ogasawara trenches are almost restricted to areas deeper than 5,600 m (Fig. 6) except for around 38°N, where the strike of the Japan Trench changes. The 5,600 m contours are 70 km away from trench axes. The crests of the outer swells along the trenches are situated far away from the trench axes, implying that elongated topographic structures are not formed at the crest of the outer swell.

3.3.1 Kuril Trench

The strike of the Kuril Trench is N65°E. The age of subducting Pacific plate is about 130 Ma (Nakanishi et al. 1989 and see the Sect. 3.4). The bathymetric map (Fig. 7) shows that the distinctive bending-related topographic structures in the oceanward slope are elongated escarpments and ridges. The strike of the bending-related topographic structures range N60–80°E. The length of many escarpments

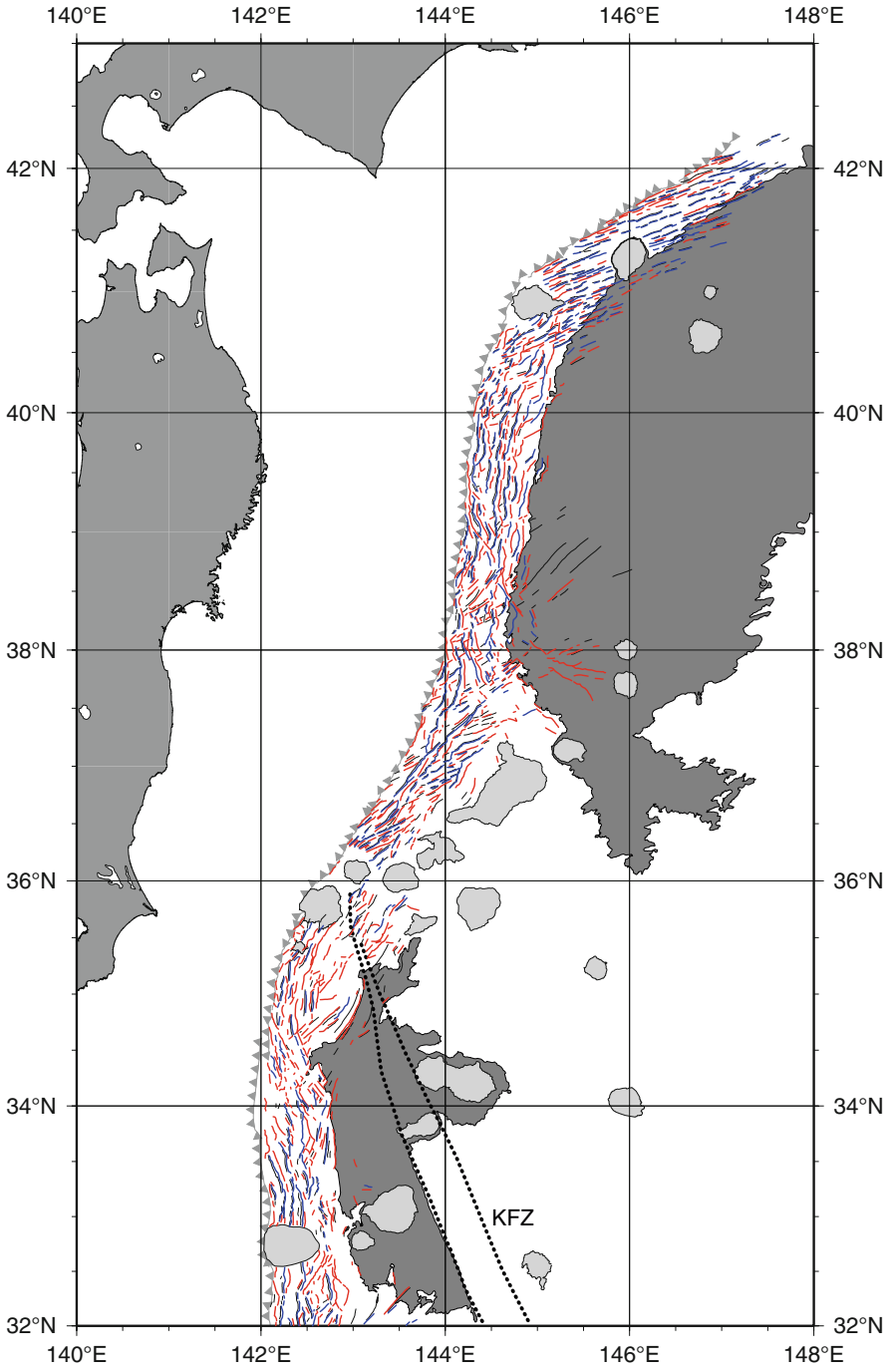

Fig. 6 Distribution of bending-related topographic structures. *Red*, *blue*, and *black solid lines* represent landward- and oceanward-dipping escarpments, and ridges, respectively. *Lightly shaded areas* are topographic heights as seamounts. *Darkly shaded areas* are above 5,600 m depth and outline the outer swells. *Barbed lines* show the approximate location of trench axes with barbs on the overriding plate. *KFZ* Kashima Fracture Zone

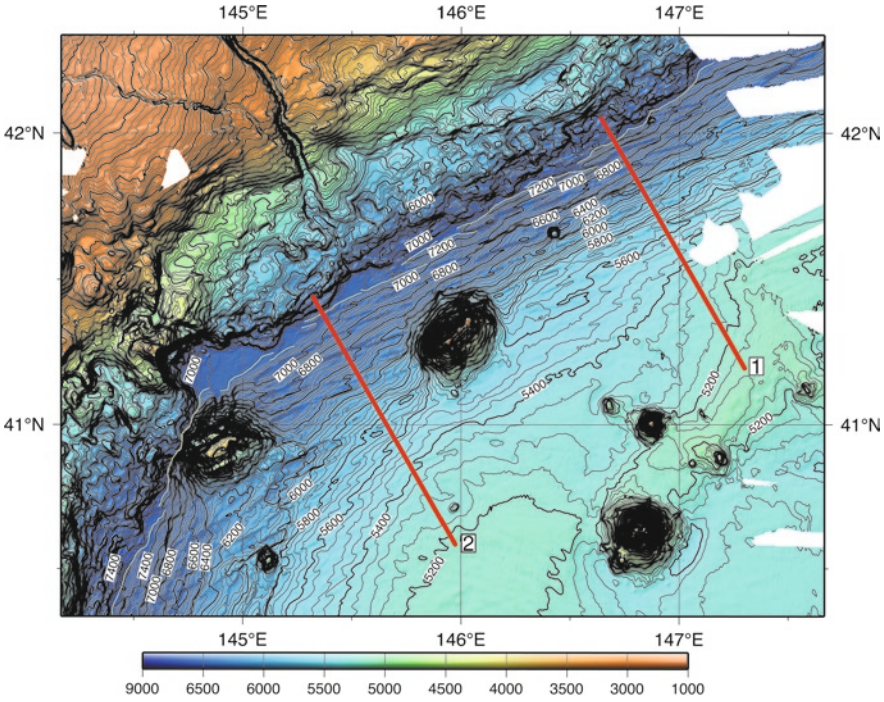

Fig. 7 Shaded bathymetric map of the western Kuril Trench. Contour interval is 50 m. *Red lines* show positions of the profiles in Fig. 8. *Yellow lines* show the approximate location of trench axes

and ridges is less than 20 km. The bending-related topographic structures are limited to areas less than 70 km away from the trench axis (Fig. 8). Ridges and asymmetric grabens, that is half grabens tilted toward the trench, are more prominent than escarpments in the oceanward slope of the western Kuril Trench. The height does not show a gradual change. The height of ridges 20 km away from the trench axis is less than 100 m while those near the trench axis are more than 100 m. The bending-related topographic structures 80 km beyond the trench axis have a height of a few tens of meters, which is comparable to that of abyssal hill fabrics.

Oceanward-dipping escarpments are more common than landward-dipping escarpments east of the Takuyo-Daiichi Seamount (Fig. 9). West of the seamount, landward-dipping escarpments are roughly equal to oceanward-dipping escarpments. Several escarpments with an N-S strike are identified south of the Erimo Seamount at the northern tip of the Japan Trench.

3.3.2 Japan Trench

The strike of the Japan Trench bounded by Daiichi-Kashima and Erimo seamounts changes at around 38°N from about N08°E in the northern part to ~N30°E in the

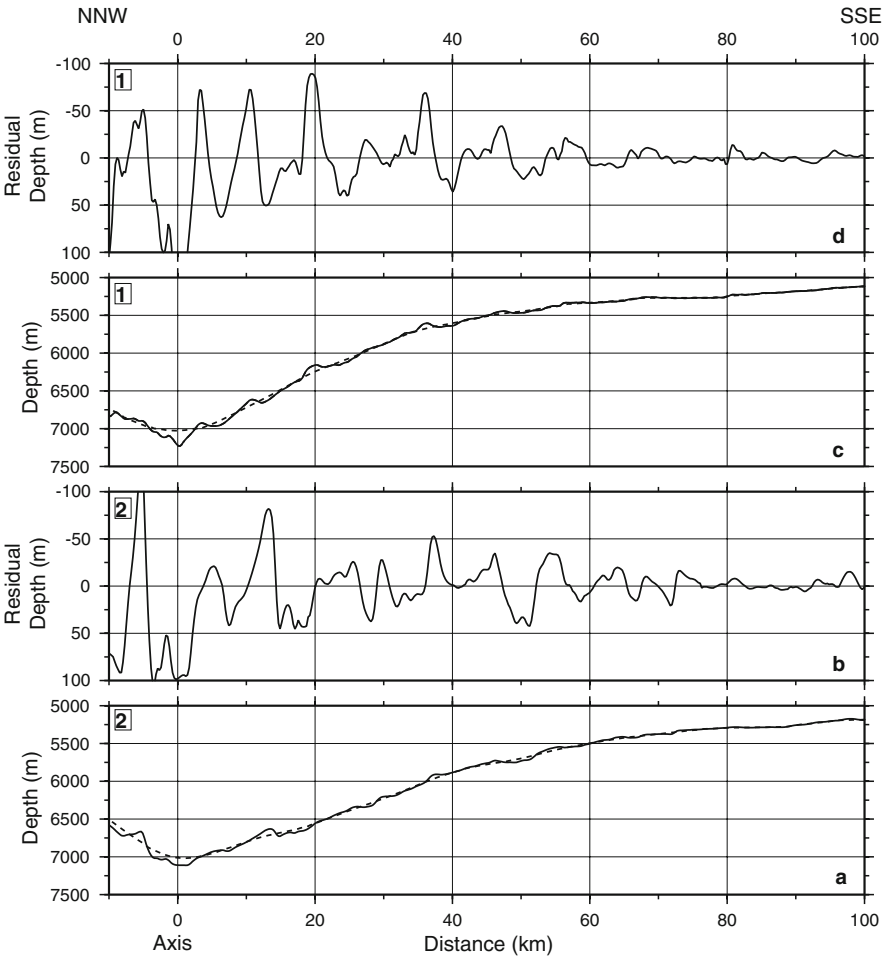

Fig. 8 Selected examples of bathymetric profiles nearly perpendicular to the western Kuril Trench. Positions of the profiles are shown in Fig. 7. (**a**) and (**c**) show the original bathymetric (*solid*) and filtered (*broken*) profiles. (**b**) and (**d**) show the residual profiles calculated by subtracting filtered values from the original water depths

southern part (Fig. 10). Most of bending-related topographic structures in the northern segment of the Japan Trench are subparallel to the trench axis. The bending-related topographic structures are confined to areas less than ~80 km away from the trench axis (Fig. 11). Topographic expressions of these north of 39°40′N are a half graben, an asymmetric graben and ridges, which is similar to that of the western Kuril Trench. The height of bending-related topographic structures does not show any gradual trenchward increase. Some of bending-related topographic structures north of 40°N have the same strike as those of Kuril Trench.

In the middle region of the northern segment between 38°50′N and 39°40′N, bending-related escarpments form symmetric grabens subparallel to the trench axis

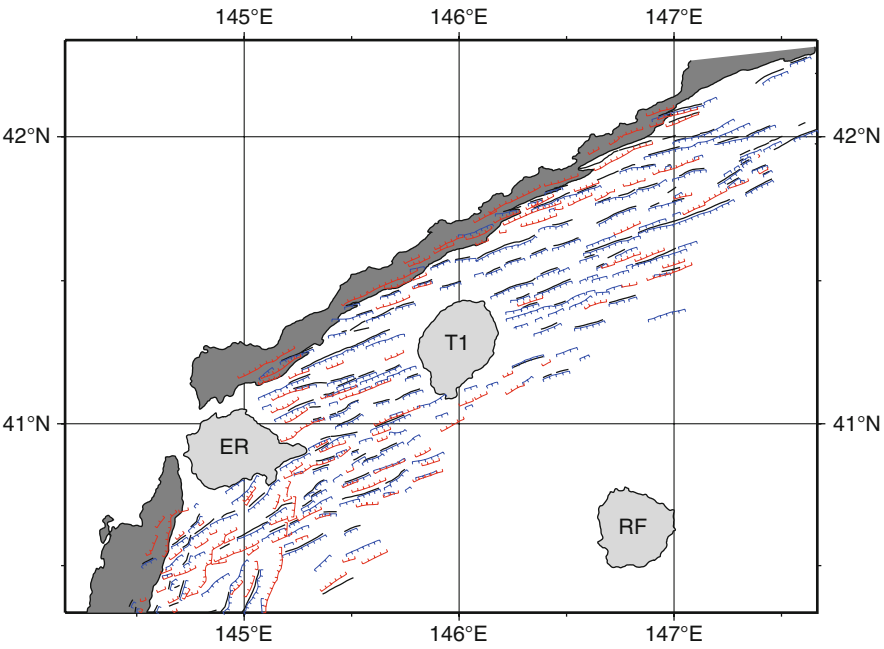

Fig. 9 Distribution of bending-related topographic structures in the western Kuril Trench. *Black lines* represent ridges. *Red* and *blue* lines show landward- and oceanward-dipping elongated escarpments, respectively. *Right* and *dark gray areas* illustrate seamounts and trench bottoms, respectively. *RF* Ryofu Seamount, *T1* Takuyo-Daiichi Seamount, *ER* Erimo Seamount

(Figs. 11 and 12). Gradual growing of the bending-related topographic structures is observed in this area. Trench-subparallel escarpments decrease in relief southward and a dominant set of escarpments become roughly parallel to the seafloor spreading fabrics striking at large angles to the trench axis. Between 38°N and 39°15′N, several elongated escarpments have a strike perpendicular to seafloor spreading fabrics. The abyssal hill fabrics are clear on the outer swell beyond bending-related deformation in the northeastern corner of the Fig. 10.

In the southern segment of the Japan Trench south of around 38°N, the strike of the Japan Trench is N30°E (Fig. 13). The outer swell in this region is obscure around the Joban Seamounts. The bending-related topographic structures are confined to areas less than ~50 km away from the trench axis between the trench and Joban Seamounts (Fig. 13). There are not any bending-related topographic structures seaward of the Joban Seamounts. A topographic expression of bending-related topographic structures is a half graben or ridge, which is similar to that of the western Kuril Trench (Figs. 13 and 14). Most of bending-related topographic structures have an NE-SW strike, N50–70°E, and are not parallel to the trench axis, but subparallel to the trend of the Joban Seamounts (Fig. 15).

Around 36°N, near the Daiichi-Kashima Seamount, near the boundary between Japan and Izu-Ogasawara trenches, the strike of bending-related topographic

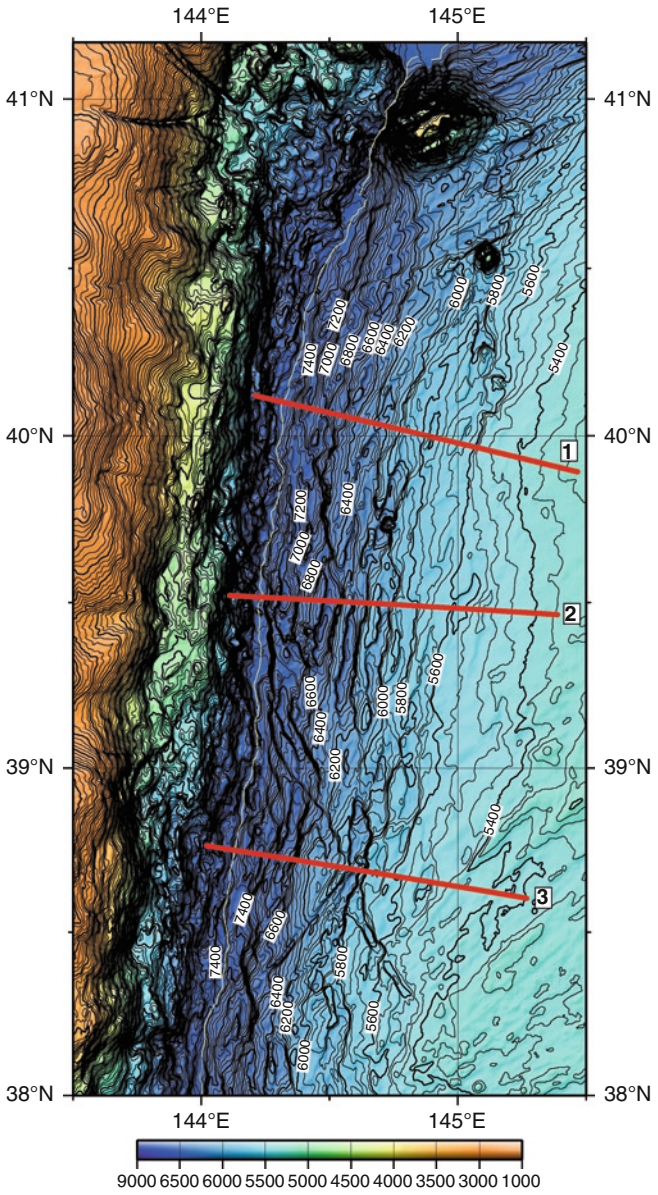

Fig. 10 Shaded bathymetric map of the northern Japan Trench. *Red lines* show the positions of bathymetric profiles in Fig. 11. Other conventions are identical to Fig. 7

structures changes notably to an orientation subparallel to the trench axis, N30°E. The Daiichi-Kashima Seamount is cut by a large normal fault parallel to the trench axis into two blocks, the western half of which is nearly vertically offset from the eastern block by about 1,600 m (Kobayashi et al. 1987).

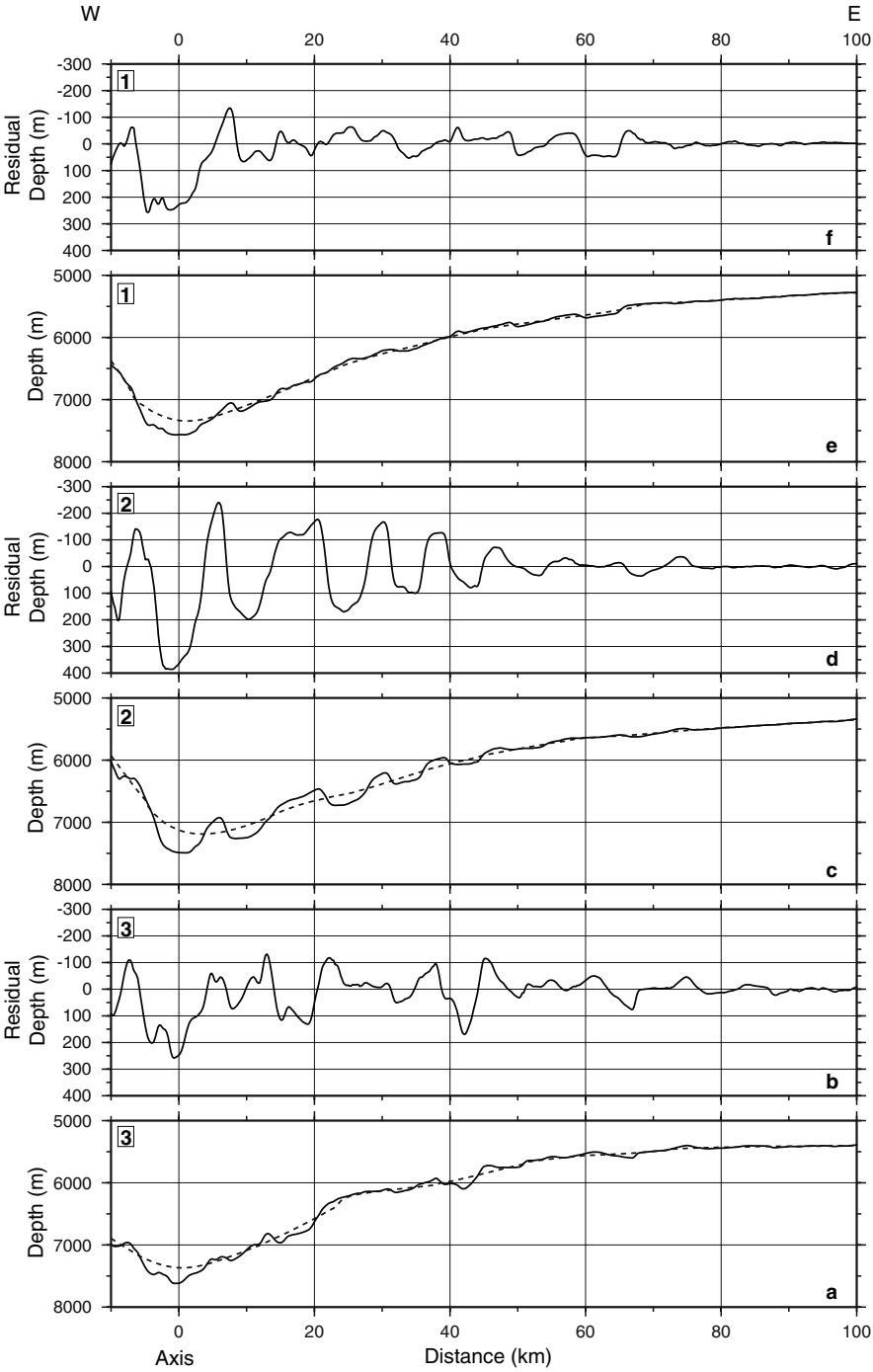

Fig. 11 Bathymetric profiles across the northern Japan Trench. Positions of the profiles are shown in Fig. 10. Other conventions are identical to Fig. 8

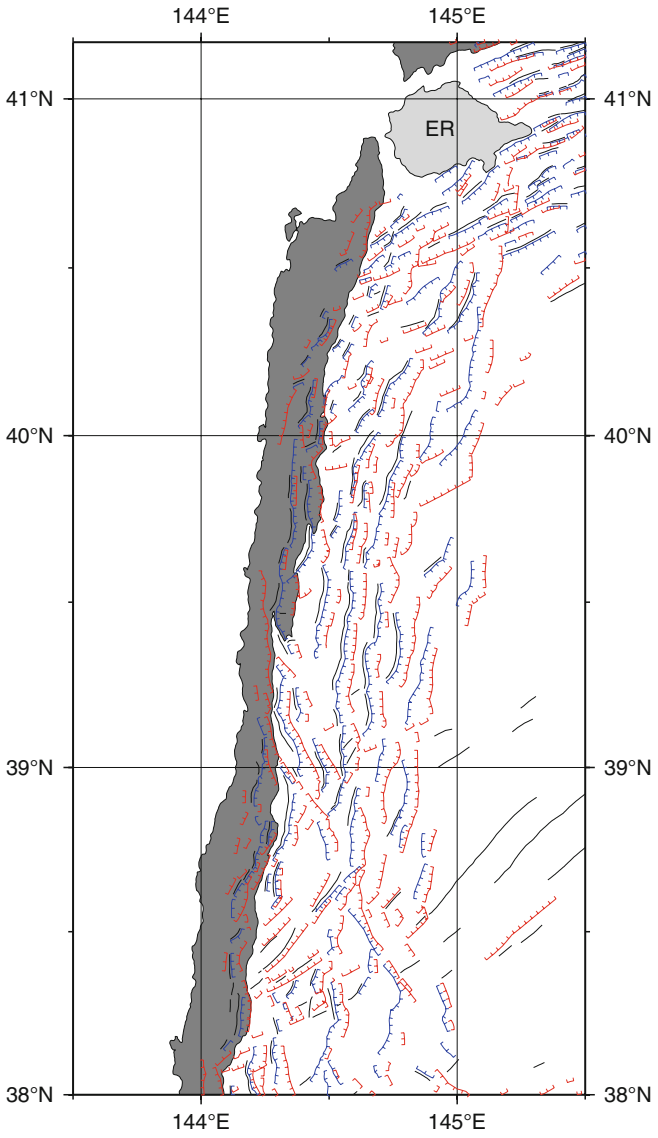

Fig. 12 Distribution of bending-related topographic structures in the northern Japan Trench. Conventions are identical to Fig. 9

3.3.3 Izu-Ogasawara Trench

The Izu-Ogasawara Trench physiographically terminates at the subducting Daiichi-Kashima Seamount. The northernmost portion of the Izu-Ogasawara Trench forms the trench-trench-trench triple junction with Sagami Trough. The seafloor of

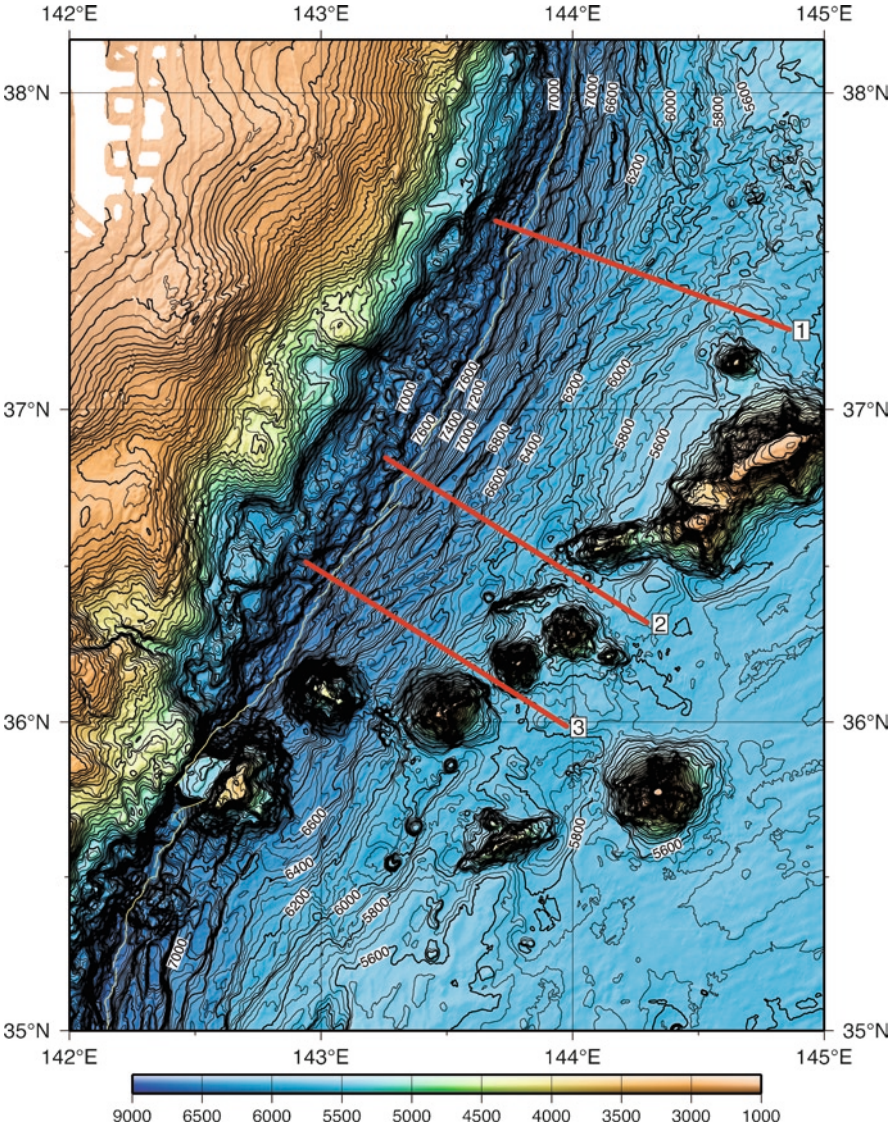

Fig. 13 Shaded bathymetric map of the southern Japan Trench. *Red lines* show positions of the profiles in Fig. 14. Other conventions are identical to Fig. 7

the triple junction, Mogi Fan, is very flat. Previous works indicated thick sediment transported along Sagami Trough there (Ogawa et al. 1989). The strike of the Izu-Ogasawara Trench is almost N-S in the study area except for north of 35°10′N and 33°–33°30′N. Those north of 35°10′N and between 33°N and 33°30′N strike N25°E and N10°W, respectively. The Mogi Seamount is subducting at 32°45′N. The height of the seamount is about 4,200 m, which is larger than that of the

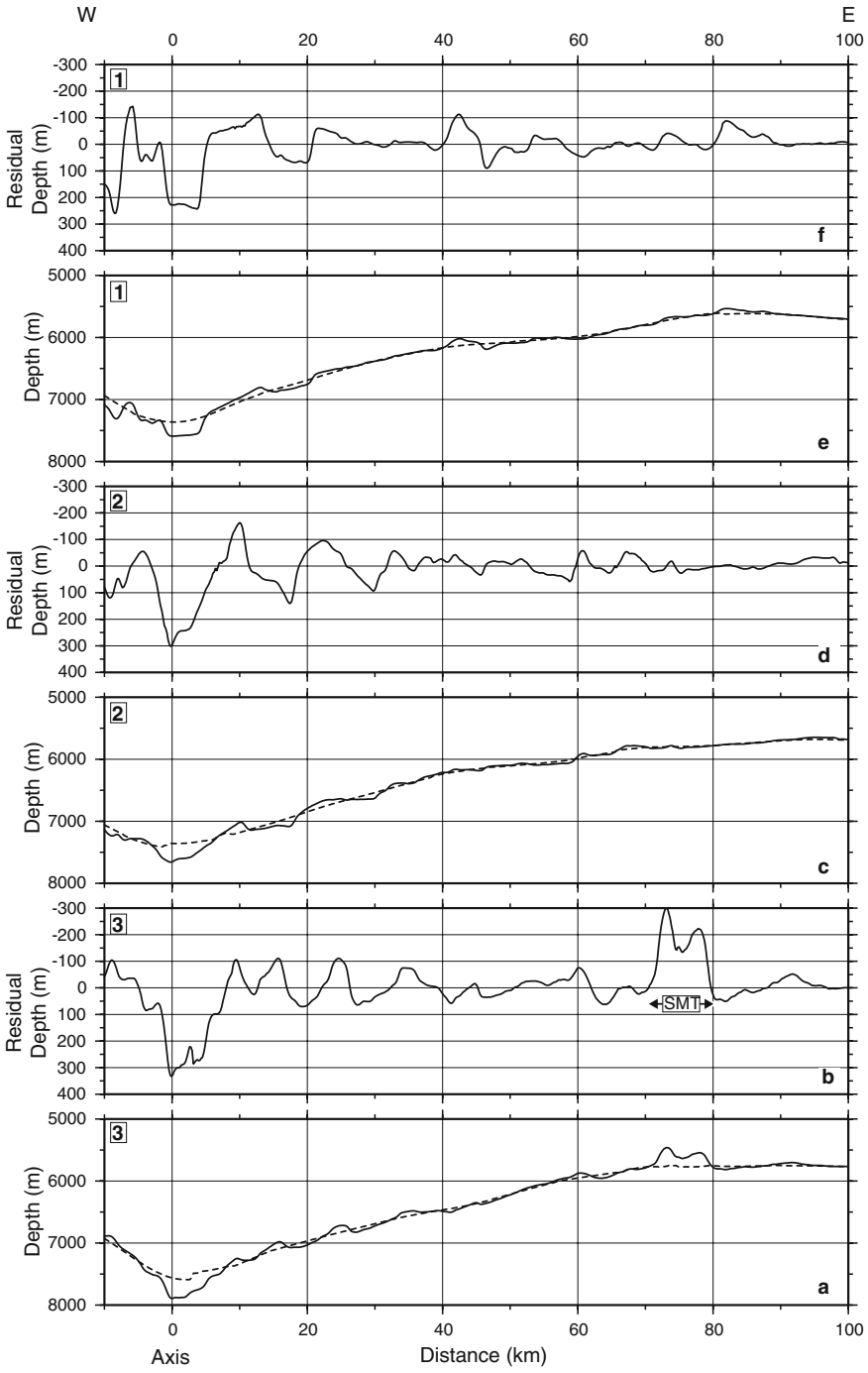

Fig. 14 Bathymetric profiles across the southern Japan Trench. Positions of the profiles are shown in Fig. 13. *SMT* Seamount. Other conventions are identical to Fig. 8

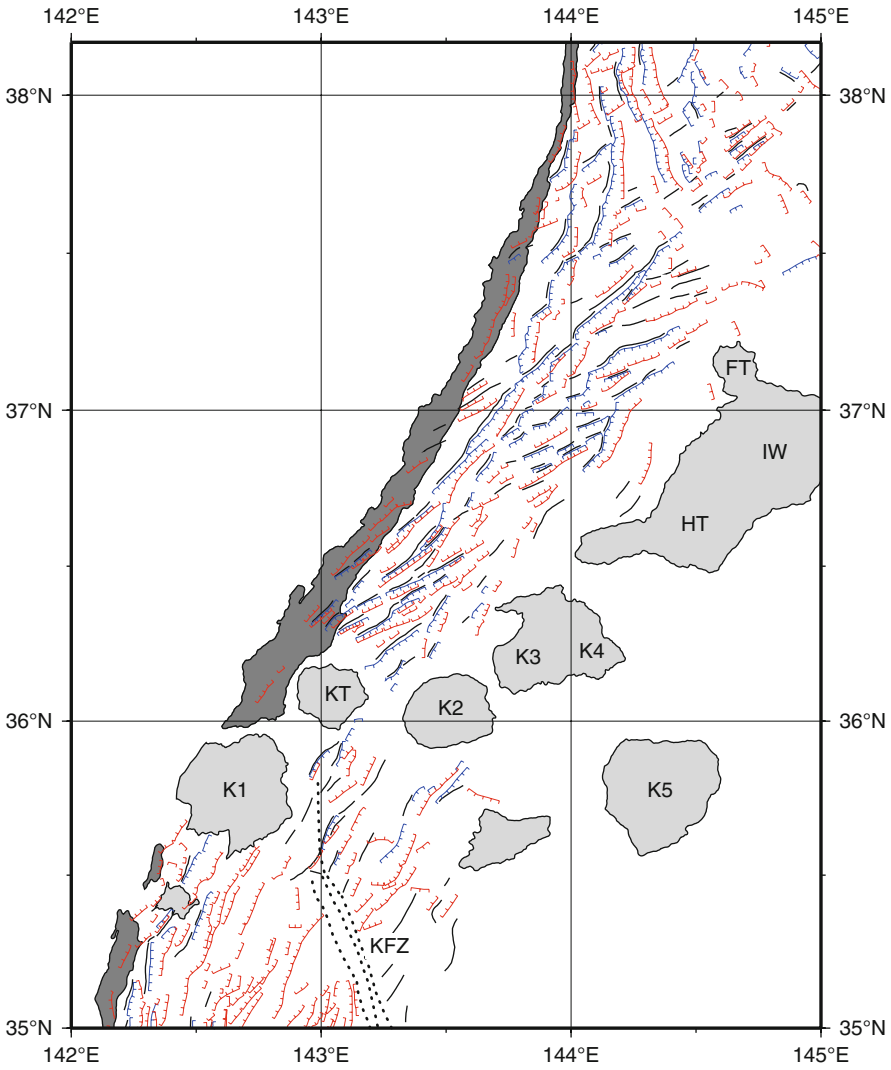

Fig. 15 Distribution of bending-related topographic structures in the southern Japan Trench. *Dotted lines* represent the topographic structures related to the Kashima Fracture Zone. *FT* Futaba Seamount, *IW* Iwaki Seamount, *HT* Hitachi Seamount, *KT* Katori Seamount, *K1* Daiichi-Kashima Seamount, *K2* Daini-Kashima Seamount, *K3* Daisan-Kashima Seamount, *K4* Daiyon-Kashima Seamount, *K5* Daigo-Kashima Seamount. Other conventions are identical to Fig. 9

Daiichi-Kashima Seamount subducting in the Japan Trench at 36°N. The Mogi Seamount is divided into several portions by escarpments.

Seta et al. (1991) and Kato (1991) reported elongated escarpments on the outer slope of the Izu-Ogasawara Trench from bathymetric surveys using the multibeam echo-sounder "classic" SeaBeam system. They indicated that most of escarpments

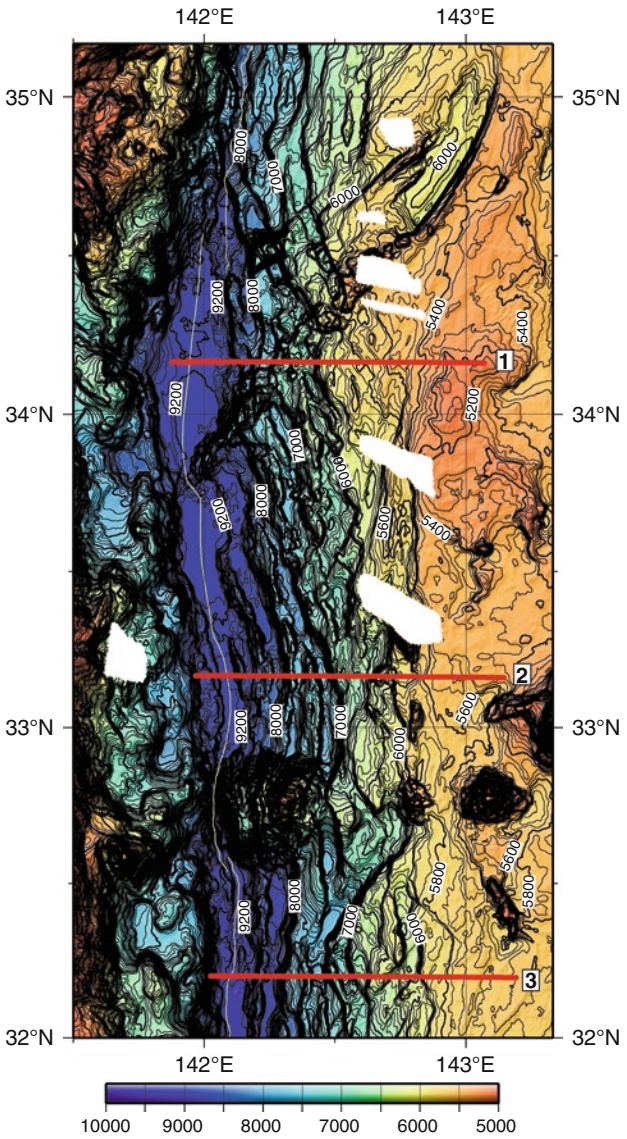

Fig. 16 Shaded bathymetric map of the northern Izu-Ogasawara Trench. *Red lines* show positions of the profiles in Fig. 17. Other conventions are identical to Fig. 7

trend N20–35°W, which is oblique to the strike of trench. Their coverage of bathymetric data is only within 40 km from the trench axis. The bathymetric map made in this study (Fig. 16) displays a number of elongated escarpments and ridges. The coverage of bathymetric data in this study is wider than in previous works (Renard et al. 1987). Bending-related topographic structures related with subduction are limited to within 70 km from the trench axis (Fig. 17). Topographic expression

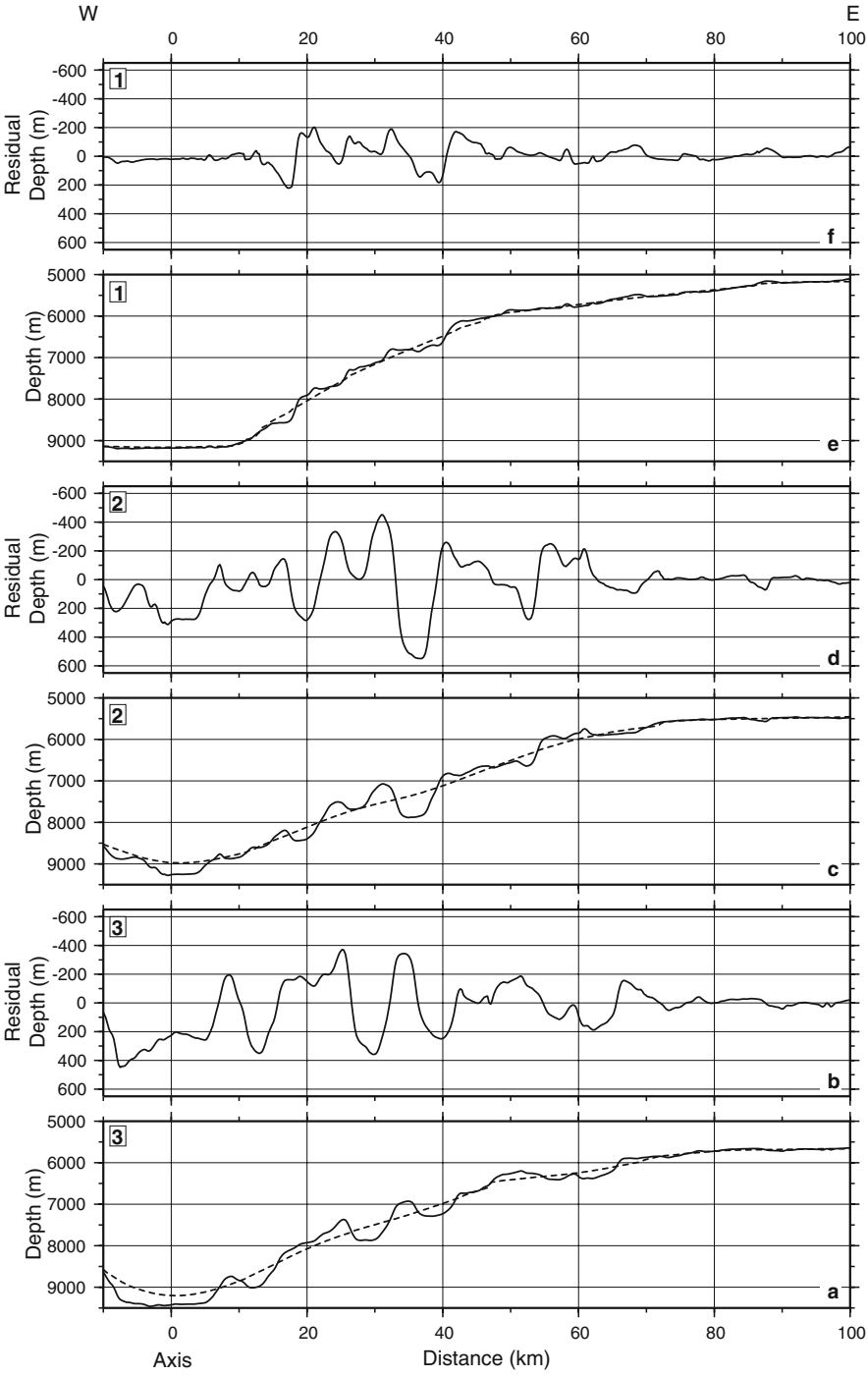

Fig. 17 Bathymetric profiles across the northern Izu-Ogasawara Trench. Positions of the profiles are shown in Fig. 16. Other conventions are identical to Fig. 8

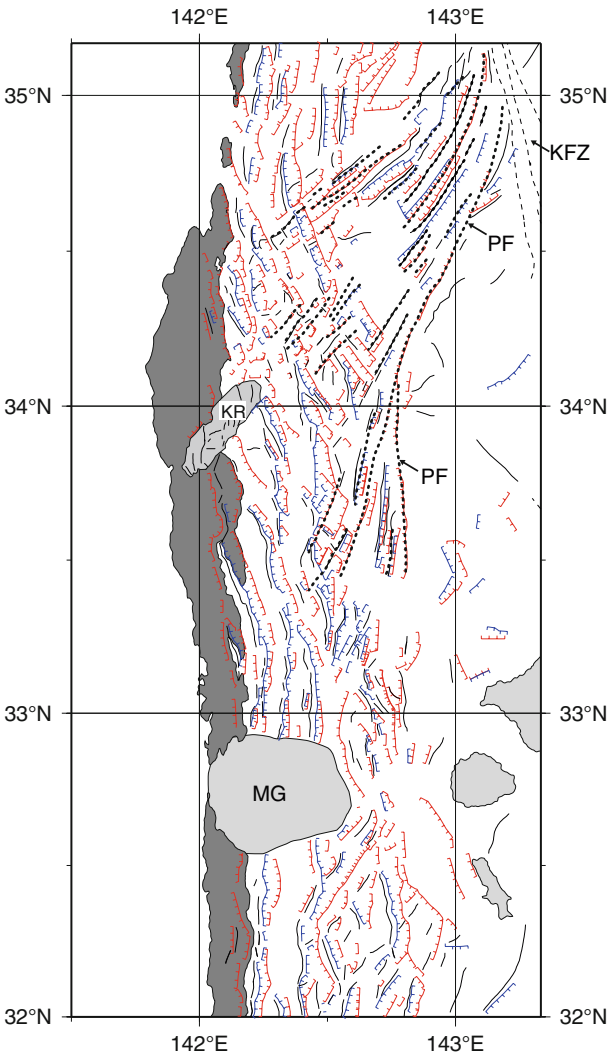

Fig. 18 Distribution of bending-related topographic structures in the northern Izu-Ogasawara Trench. *Dotted lines* represent the topographic structures related to the abandoned propagating spreading ridge. Broken lines illustrate the topographic structures related to Kashima Fracture Zone. *MG* Mogi Seamount, *KR* KAIREI Ridge, *PF* pseudofault, *KFZ* Kashima Fracture Zone. Other conventions are identical to Fig. 9

of most bending-related topographic structures is a symmetric graben. Asymmetric or half grabens are also observed.

Most of bending-related topographic structures identified north of 33°N have an NNW-SSE strike (Fig. 18). The strike is the same as that of trench axis between 33°N and 33°30′N. There are bending-related topographic structures with an N-S strike around the Mogi Seamount. The bending-related topographic structures with an N-S

strike are not so much as those with an NNW-SSE strike. One long escarpment with an N-S strike is situated along 142°50′E between 33°20′N and 34°N (PF in Fig. 18). There are rarely escarpments or ridges east of the PF escarpment. The bending-related topographic structure near the trench axis south of 33°35′N is a ridge about 50 km long. A large escarpment with an NE-SW strike exists between 32°20′N and 32°40′N southeast of the Mogi Seamount. The height of the escarpment is more than 500 m and increases trenchward, which is larger than other escarpments with NE-SW strikes.

There is a curved trough with an NE-SW strike from 33°50′N to 35°10′N near the trench triple junction. The trough is bounded by curved NE-SW trending escarpments of an adjacent elongated ridge. The maximum depth of the trough is 6,000 m. It narrows northeastward. The shape of the trough bears a close resemblance to that of a tip of a propagating spreading ridge observed in Pacific-Antarctic Ridge around 64°S (Briais et al. 2002). The elongated ridge in the trough resembles a neo-volcanic ridge in a propagating spreading ridge (e.g., Kleinrock and Hey 1989; Blais et al. 2002). We conclude that the trough is an extinct propagating spreading ridge and that is not directly related to plate bending. Curved escarpments east of the trough are interpreted as traces of pseudofaults associated with propagation of ridge. The southwest extension of the trough is a fragmented ridge on the outer slope of the Izu-Ogasawara Trough discovered by Kobayashi (1991) and named as the KAIREI Ridge by Ogawa (1999). Basaltic rocks were recovered from the KAIREI Ridge near the trench axis (Ogawa 1999). The continuity between the KAIREI Ridge and the extinct of the propagating spreading ridge indicates that the KAIREI Ridge is a part of the sidewall of the extinct propagating spreading ridge. The KAIREI Ridge is wider than the extinct propagating spreading ridge. The KAIREI Ridge seems to have grown up by off-ridge volcanism along the escarpment.

3.4 Magnetic Anomalies

Amplitudes of magnetic anomalies in the outer side of the trenches are generally more than 300 nT, which are larger than those of other contemporary areas in the western Pacific Ocean (Fig. 3). These have northward increases in amplitude from 300 to 500 nT.

Figure 19 illustrates magnetic anomaly lineations identified in this study. Most of magnetic anomaly lineations younger than M10 are not changed from Nakanishi et al. (1989). Results of the identification in this study is similar to that in previous works (Nakanishi et al. 1989, 1999) except for the areas around the Joban Seamounts, and between the Kashima Fracture Zone and the Izu-Ogasawara Trench.

Figure 20 shows correlations of magnetic anomalies among selected cruise tracks and comparison with a synthetic profile calculated from the geomagnetic reversal timescale of Gradstein et al. (2004). The skewness parameter is −230°, which is the same as those for the Japanese lineation set (Nakanishi et al. 1989, 1999). Resemblance of shapes of magnetic anomaly profiles makes it easy to identify magnetic anomaly lineations.

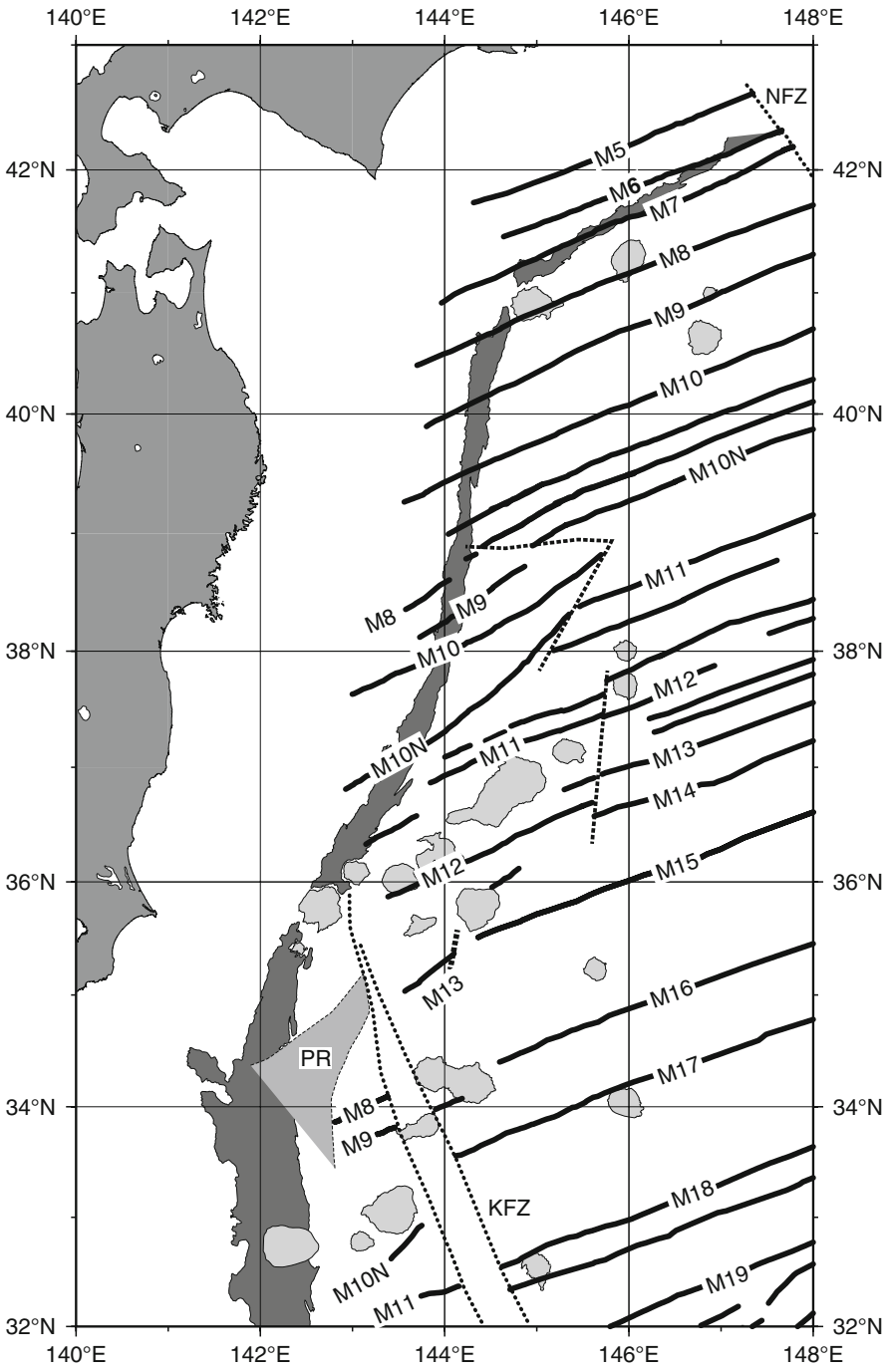

Fig. 19 Magnetic anomaly lineations identified in the study area. Solid lines with M-number and dotted lines denote magnetic anomaly lineations and fracture zones, respectively. *Dashed lines* show possible pseudofaults caused by propagating spreading ridges. *PR* abandoned propagating spreading ridge

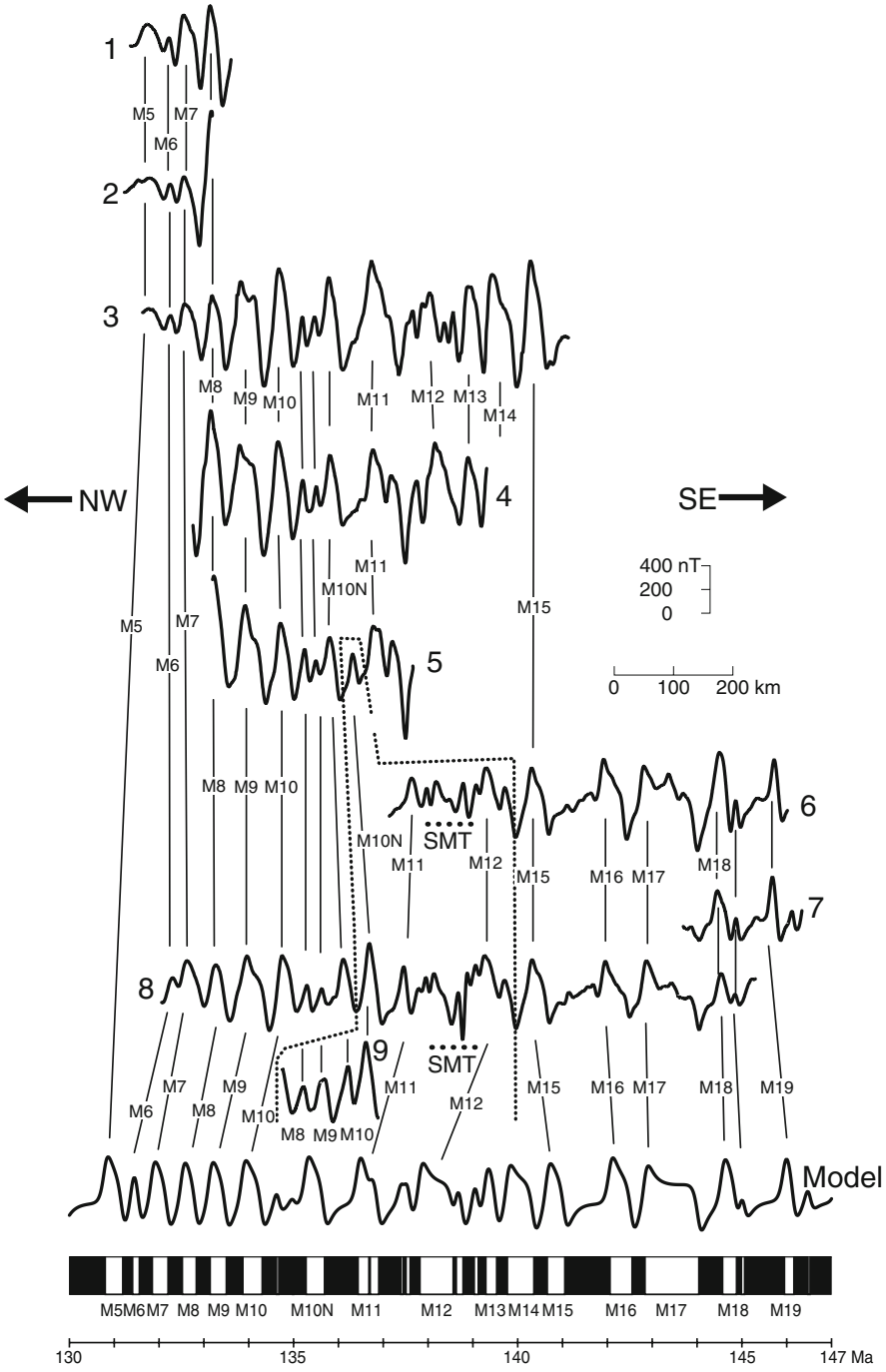

Fig. 20 Identification of selected magnetic anomalies profiles projected approximately normal to the magnetic anomaly lineations. Locations of the profiles are shown in Fig. 3. Magnetic anomaly reversal sequence is from Gradstein et al. (2004). Normally magnetized blocks are solid. *SMT* represents a seamount. *Dashed lines* distinguish possible pseudofaults caused by propagating spreading ridges. The skewness parameter for calculation of the model profile is −230° that is the same as that used in Nakanishi et al. (1989)

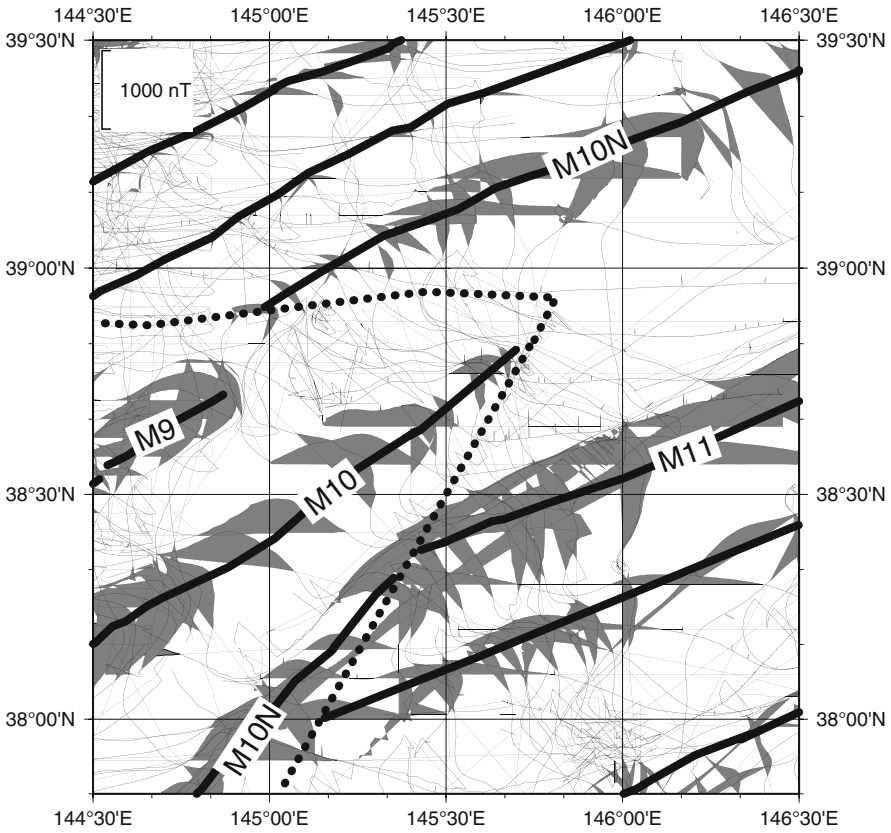

Fig. 21 Along-track magnetic anomaly profiles north of the Joban Seamounts. The area is shown in Fig. 3. Positive anomalies are shown as *shaded*. The scale bar near the *upper-left corner* is for the amplitude of magnetic anomalies. *Bold lines* represent magnetic anomaly lineations. *Dotted lines* distinguish possible pseudofaults caused by a propagating spreading ridge

The most remarkable result about magnetic anomaly lineations in this study is the discovery of magnetic anomaly lineations north the Joban Seamounts with a strike different from that of magnetic anomaly lineations in the other areas (Fig. 21). There are not any remarkable topographic structures near the junction between the regular and irregular lineations which would indicate any post-spreading, off-ridge tectonic event. This implies that these lineations formed during a reorganization of the plate boundaries between the Pacific and Izanagi plates. Nakanishi et al. (1989, 1991) identified similar curved magnetic anomaly lineations and Nakanishi et al. (1991) speculated that the curved lineations are due to a propagating spreading ridge. The identifications in this study support that speculation. The identifications indicate that rift propagation stopped around chron M10 (134 Ma).

The discontinuity of the magnetic anomaly lineations around the Joban Seamounts is also a remarkable result. Increased density of the geomagnetic data

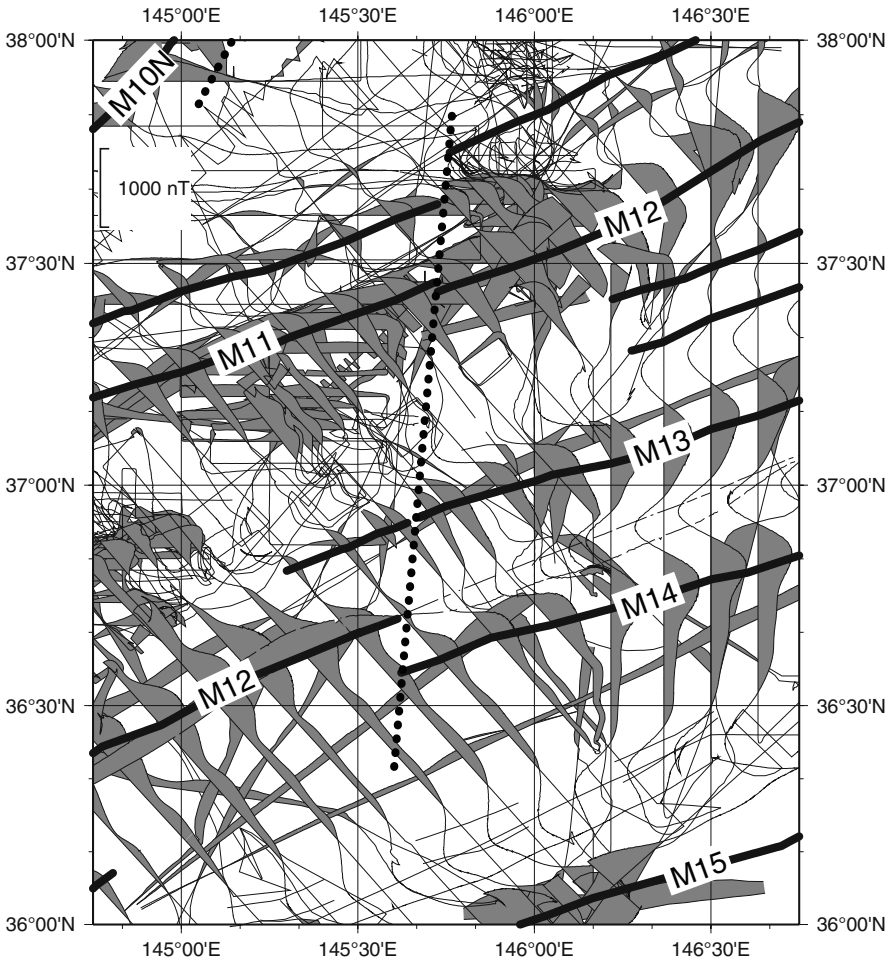

Fig. 22 Along-track magnetic anomaly profiles east of the Joban Seamounts. Conventions are identical to Fig. 21

reveals a discontinuity of lineations between M15 and M12 east of the Kashima Fracture Zone (Fig. 22). The discontinuity can be traced northeastward to lineation M11. The offsets of the magnetic anomaly lineations have a trend different from fracture zones in this study area. This evidence implies that the discontinuity is due to a northeastward propagating spreading ridge.

Nakanishi et al. (1989) identified lineations from M11 to M3 between the Kashima Fracture Zone and the Izu-Ogasawara Trench, which have a strike a little different from those east of the Kashima Fracture Zone. The detailed examination of magnetic anomalies in the study area could not confirm their identification in spite of the increase of cruise data. Magnetic lineations younger than M7 were missed in this area.

4 Discussion

4.1 Strike of Bending-Related Topographic Structures

There is a strong likelihood that the strike of bending-related topographic structures should be parallel to the trench axis. Previous authors (Masson 1991; Kobayashi et al. 1995, 1998; Billen et al 2007) suggested that pre-existing abyssal hill fabrics are also one of the factors controlling the strikes of bending-related topographic structures. Hilde (1983) questioned the occurrence of any consistent control of this process. To examine the relationship between strikes of bending-related topographic structures and oceanic spreading fabrics, rose diagrams were made in reference to the strike of the strike of trench axes (Fig. 23). Most elongated topographic structures are not straight. To determine the dominant orientation of topographic structures, one topographic structure is divided into several straight segments which length is from several to tens kilometers. After the division, strikes of segments were separately calculated per each segment.

Table 3 shows a summary of bending-related topographic structures in oceanward trench slopes and possible controlling factors. It is obvious that strikes of bending-related topographic structures are controlled by strikes of trench axis or by the oceanic spreading fabrics. This result supports the conclusions by Masson (1991) and Kobayashi et al. (1998). Masson (1991) showed that convergence direction and age of the subducting plate have no obvious influences for strikes of bending-related topographic structures like elongated escarpments. The convergence direction of the Pacific plate is almost the same in the study area, N65–67°W (Gripp and Gordon 2002). The Pacific plate in the study area ranges from 130 to 140 Ma in age. The homogeneity of the convergent direction and the narrow age range support the conclusion by Masson (1991).

In the oceanward slope of the western Kuril Trench, bending-related topographic structures have a mode of strikes, N65–70°E, which is the same direction of magnetic anomaly lineations (Fig. 23a). The topographic expression is a half graben or ridge and is similar to that of abyssal hill fabrics. These observations support the conclusion of Kobayashi et al. (1995, 1998) that the bending-related topographic structures of the oceanward slope of the western Kuril Trench is formed by reactivation of abyssal hill fabrics associated with subduction of the Pacific plate.

The graben structure is predominant in the oceanward slope of the Japan Trench north 38°N (Table 3, Fig. 23b, c). Most escarpments have a strike parallel to the trench axis, around north-south. Several escarpments south of 39°30′N have a different strike, N20°W. Kobayashi et al. (1998) suggested that the predominant direction of escarpments is due to reactivation of non-transform offsets. The magnetic anomaly lineations in this area elucidate a northeastward propagating spreading ridge before chron M10 (Fig. 19). The seafloor in this area was formed near the inner pseudofault related with southwestward propagating spreading ridge. The elongated escarpments with an NW-SE strike seem to be developed in the transform zone between propagating doomed ridges.

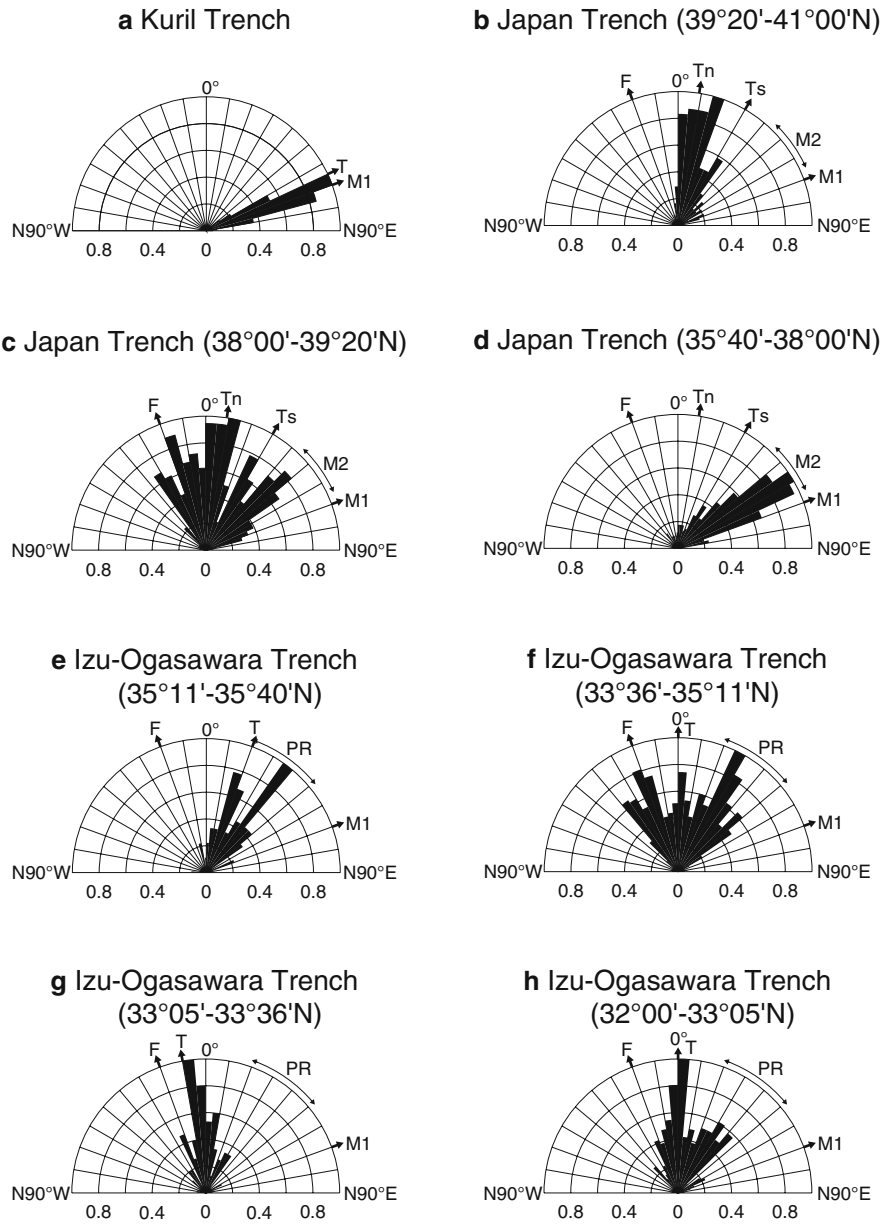

Fig. 23 Rose diagrams showing statistical distribution of bending-related topographic structures in the oceanward slopes of the trenches studied in this study. Rose diagrams are normalized by the number of structures with a mode strike. *F* strike of the fracture zones, *M1* orientation of the magnetic anomaly lineations except for around 38°N near the Japan Trench, *M2* orientation of the magnetic anomaly lineations around 38°N near the Japan Trench, *PR* trend of the abandoned propagating spreading ridge around 34°30′N, *T* general trend of the trench axis, *Tn* general trend of the trench axis of the Japan Trench north of 38°N, *Ts* general trend of the trench axis of the Japan Trench south of 38°N

Table 3 Orientations of bending-related structures, trench axes, and magnetic anomaly lineations and types of graben

Trench	Mode of strike of topographic features	Trench axis	Magnetic anomaly lineation	Types of graben
Kuril	N65–70°E	N65°E	N70°E	A or H
Japan 39°20′–41°00′N	N15–20°E	N10°E	N70°E	A, H, or S
Japan 38°00′–39°20′N	N10–15°E	N00°E	N70°E	A or S
Japan 35°40′–38°00′N	N55–60°E	N20–35°E	N50–65°E	A or H
Izu-Ogasawara 35°11′–35°40′N	N15–20°E	N20°E	N70°E	A, H, or S
Izu-Ogasawara 33°36′–35°11′N	N20–25°W	N-S	N70°E	A, H, or S
Izu-Ogasawara 33°05′–33°36′N	N05–10°W	N10°W	N70°E	A, H, or S
Izu-Ogasawara 32°00′–33°05′N	N00–05°E	N-S	N70°E	A, H, or S

A asymmetric graben, *H* half graben, *S* symmetric graben

Between 38°N and the Joban Seamounts (Fig. 23d), N50–65°E trending structures are predominant. The direction is close to the strike of the magnetic anomaly lineations, which strike is N50–65°E. Ranero et al. (2005) mapped bending-related structures roughly parallel to Juan Fernandez Ridge along the Chile Trench offshore of Valparaiso, Chile. The trend of Joban Seamounts is N50°E, which is not parallel to any hotspot tracks on the Pacific plate. Thus, it is reasonable that the NE-SW trending bending-related topographic structures were form by reactivation of the abyssal hill fabric and that the Joban Seamounts were formed along a crustal structure parallel to the abyssal hill fabrics.

Bending-related structures in the northern Izu-Ogasawara Trench have two distinguishable strikes (Fig. 23e–h). One has the same direction of the trench axis. The other strikes N20°W that is perpendicular to abyssal hill fabrics and dominant between 33°36′N and 35°11′N (Fig. 23f). Seta et al. (1991) mapped the elongated escarpments with the similar strike in the southern Izu-Ogasawara Trench and concluded that the escarpments were formed by reactivation of weak zones, for instance fracture zones, perpendicular to abyssal hill fabrics. This striking also supports the formation of the bending-related structures with an N20°W strike results from reactivation of weak zones perpendicular to abyssal hill fabrics.

Elongated topographic structures with an NE-SW strike are also dominant in the northern Izu-Ogasawara Trench west of Kashima Fracture Zone (Fig. 23e, f). Some of the structures were formed by propagation of a spreading ridge and are not related to plate bending. The abandoned propagating spreading ridge is situated north of Lineation M8 (Fig. 19). No magnetic anomaly lineations younger than

Lineation M7 parallel to the ridge were identified in this area. These evidences imply that the spreading ridge west of the Kashima Fracture Zone propagated in mid-Cretaceous Quiet Period (84–125 Ma).

4.2 Topographic Expression of Bending-Related Structures

The two distinct types of development of bending-related topographic structures were observed in the study area. The bending-related topographic structures resulted from faulting by plate bending are parallel or subparallel to the trench axis and their heights increase progressively trenchward. This type is typically observed from 38°40′N to 40°N in the northern part of the Japan Trench (Figs. 10 and 12). Those originated in reactivation of oceanic spreading fabrics are oblique to the trench axis and not always parallel to trench axis. Their height does not show clearly gradual trenchward growth. This type is typically observed in the western Kuril and southern Japan trenches. The bending-related topographic structures in the Izu-Ogasawara Trench have a combined type.

The dominant topographic expression of the bending-related topographic structures resulted from newly formed faults by plate bending is dominantly a symmetric graben (Table 3). That of the bending-related topographic structures originated in reactivation of oceanic spreading fabrics is an asymmetric graben or a half graben. In the northern Chile Trench, the similar result is obtained by Ranero et al. (2005).

5 Conclusions

The examination of the detailed bathymetrical maps and magnetic anomaly lineations reveal the following evidences.

1. Most of bending-related topographic structures exist in the oceanward trench slopes deeper than 5,600 m.
2. Bending-related topographic structures are developed parallel to the trench axis or inherited seafloor spreading fabrics. Inherited seafloor spreading fabrics are reactivated when they trend within ~30° from the trench axis.
3. The topographic expression of bending-related topographic structures is classified into two types according to whether new faults developed parallel to the trench axis or inherited seafloor spreading fabrics reactivated.
4. Several curved Mesozoic magnetic anomaly lineations exist near the Japan Trench.
5. Discontinuity of magnetic anomaly lineations associated with a propagating spreading ridge is documented around the Joban Seamounts.
6. A trough with elongated escarpments associated with the propagating ridge in mid-Cretaceous Quiet Period was discovered near the trench-trench-trench triple junction.

Acknowledgments The author expresses his deep thanks to Yujiro Ogawa for the opportunity to do this work. The author is grateful to Edward L. Winterer for suggesting a number of improvements to the manuscript. The author is also grateful to the captains, crews, and scientific parties of the cruises for cooperation to collect bathymetric and/or geomagnetic data (KH-90-1, KH-92-3, KH-96-3, KH-03-1, KH-06-1, MR99-K04, KR99-11, KR04-08, KR06-03, YK08-09, MR08-02, MR08-03, MR08-04, MR08-05, MR08-06, and MR09-03). The author acknowledges the staff of JHOD for offering of their bathymetric and magnetic data for this study. The author would like to thank Steve S. Cande, Dru Clark and the staff of the Geological Data Center, Scripps Institution of Oceanography, University of California, San Diego, for providing bathymetric data for three cruises. The author is grateful to Makoto Yamano for permission to use the data collected in the KR08-10 cruise for this study. Acknowledgement is also made to JAMSTEC and NOAA/NGDC for providing bathymetric and magnetic data. The author would like to thank Yujiro Ogawa, Yildirim Dilek, and Tomoyuki Sasaki for helpful comments.

References

Amante C, Eakins BW (2009) ETOPO1 1 arc-minute global relief model: procedures, data sources and analysis. NOAA technical memorandum NESDIS NGDC-24

Billen M, Cowgill E, Buer E (2007) Determination of fault friction from reactivation of abyssal-hill faults in subduction zones. Geology. doi:10.1130/G23847A.1

Blais A, Gente P, Maia M, Naar DF (2002) A history of the Selkirk paleomicroplate. Tectonophysics 359:157–169

Briais A, Aslanian D, Géli L, Ondréas H (2002) Analysis of propagators along the Pacific-Antarctic Ridge: evidence for triggering by kinematic changes. Earth Planet Sci Lett 199:415–428

Cadet J-P, Kobayashi K, Aubouin J, Boulègue J, Dubois J, von Huene R, Jolivet L, Kasahara J, Lallemand S, Nakamura Y, Pautot G, Suyehiro K, Tani S, Tokuyama H, Yamazaki T (1987) The Japan Trench and its juncture with the Kuril Trench; cruise results of the Kaiko project, Leg 3. Earth Planet Sci Lett 83:267–284

Caress D, Chayes DN (1996) Improved procession of hydrosweep DS multibeam data on the R/V Maurice Ewing. Mar Geophys Res 18:631–665

Del Grosso VA (1974) New equation for the speed of sound in natural waters (with comparisons to other equations). J Acoust Soc Am 56:1084–1091

Fujisawa M (2009) Bathymetric surveys under the continental shelf surveys from FY 2003 to FY 2008. Tech Bull Hydrogr Oceanogr 27:135–140

Gradstein FM, Ogg JG, Smith AG (2004) Geologic time scale 2004. Cambridge University Press, Cambridge

Grevemeyer I, Kaul N, Diaz-Naveas JL, Villinger H, Ranero CR, Reichert C (2005) Heat flow and bending-related faulting at subduction trenches: case studies offshore of Nicaragua and Central Chile. Earth Planet Sci Lett 236:238–248

Gripp AE, Gordon RG (2002) Young tracks of hotspots and current plate velocities. Geophys J Int 150:321–361

Hilde TWC (1983) Sediment subduction versus accretion around the Pacific. Tectonophysics 99:381–397

Hirano N, Koppers AAP, Takahashi A, Fujiwara T, Nakanishi M (2008) Seamounts, knolls and petit-spotmonogenetic volcanoes on the subducting Pacific Plate. Basin Res. doi:10.1111/j.1365-2117.2008.00363.x

Honda M (2008) R/V MIRAI cruise report MR08-05. JAMSTEC, Yokosuka

International Association of Geomagnetism and Aeronomy, Working Group V-MOD (2010) International Geomagnetic Reference Field: the eleventh generation. Geophys J Int 83:1216–1230. doi:10.1111/j.1365-246X.2010.04804.x

Kashino Y (2008) R/V MIRAI cruise report MR08-03. JAMSTEC, Yokosuka
Kato S (1991) A geomorphological study of the classification and evolution of trenches around Japan. Rep Hydrogr Res 27:1–57
Kikuchi T, Nishino S (2009) R/V MIRAI cruise report MR09-03. JAMSTEC, Yokosuka
Kleinrock MC, Hey RN (1989) Migrating transform zone and lithospheric transfer at the Galapagos 95.5°W propagator. J Geophys Res 94:13859–13878
Kobayashi K (1991) Preliminary reports of the Hakuho Maru cruise KH-90-1. Ocean Research Institute, the University of Tokyo, Tokyo
Kobayashi K (1993) Preliminary reports of the Hakuho Maru cruise KH-92-3. Ocean Research Institute, the University of Tokyo, Tokyo
Kobayashi K, Cadet J-P, Aubouin J, Boulègue J, Dubois J, von Huene R, Jolivet L, Kasahara J, Lallemand S, Nakamura Y, Pautot G, Suyehiro K, Tani S, Tokuyama H, Yamazaki T (1987) Normal faulting of the Daiichi-Kashima Seamount in the Japan trench revealed by the Kaiko 1 cruise, Leg 3. Earth Planet Sci Lett 83:257–266
Kobayashi K, Tamaki K, Nakanishi M, Ogawa Y (1995) Rejuvenation of 130 m.y.-old fabrics on the outer wall of the western Kuril Trench. Proc Jpn Acad 71B:5–9
Kobayashi K, Nakanishi M, Tamaki K, Ogawa Y (1998) Outer slope faulting associated with western Kuril and Japan trenches. Geophys J Int 134:356–372. doi:10.1046/j.1365-246x.1998.00569.x
Levitus S (1982) Climatological atlas of the world ocean. NOAA Professional Paper 13, U.S. Government Printing Office, Washington, DC
Masson DC (1991) Fault patterns at outer trench walls. Mar Geophys Res 13:209–225
Moore JC, Saffer D (2001) Updip limit of the seismogenic zone beneath the accretionary prism of southwest Japan: an effect of diagenetic to low-grade metamorphic processes and increasing effective stress. Geology 29:183–186
Nakanishi M (1993) Topographic expression of five fracture zones in the northwestern Pacific Ocean. In: Pringle MS, Sagar WW, Sliter WV, Stein S (eds) The Mesozoic Pacific geology, tectonics, and volcanism, Geophys Monogr 77. AGU, Washington, DC, pp 121–136
Nakanishi M (2007) Geomagnetic measurements. In: Nakanishi M (ed) Cruise report R/V KAIREI KR06-03. JAMSTEC, Yokosuka, pp 27–29
Nakanishi M, Noguchi T, (2008) Surface geophysical surveys. In: YOKOSUKA cruise report YK08-09. JAMSTEC, Yokosuka, pp 10–11
Nakanishi M, Tamaki K, Kobayashi K (1989) Mesozoic magnetic anomaly lineations and seafloor spreading history of the northwestern Pacific. J Geophys Res 94:15437–15462
Nakanishi M, Oshida K, Tamaki K (1991) Magnetic anomalies in the Japan Trench. In: Kobayashi K (ed) Preliminary report of the Hakuho Maru cruise KH-90-1. Ocean Research Institute, the University of Tokyo, Tokyo, pp 52–55
Nakanishi M, Tamaki K, Kobayashi K (1992) A new Mesozoic isochron chart of the northwestern Pacific Ocean: paleomagnetic and tectonic implications. Geophys Res Lett 19:693–696
Nakanishi M, Sayanagi K, Tamaki K (1993) Magnetic anomalies near the Kuril Trench. In: Kobayashi K (ed) Preliminary report of the Hakuho Maru cruise KH-92-3. Ocean Research Institute, the University of Tokyo, Tokyo, pp 53–55
Nakanishi M, Sager WW, Klaus A (1999) Magnetic lineations within Shatsky Rise, northwest Pacific Ocean: implications for hot spot-triple junction interaction and oceanic plateau formation. J Geophys Res 104:7539–7556
Nakanishi M, Fujiwara T, Obi A (2004) Magnetic anomalies, In: Hirano N (ed) KR04-08 Cruise: R/V KAIREI onboard report. JAMSTEC, Yokosuka, pp 86
Ogawa Y (1999) Onboard report of Kairei/Kaiko cruise KR99-11 Leg 3. JAMSTEC, Yokosuka
Ogawa Y, Seno T, Tokuyama H, Akiyoshi H, Taniguchi H (1989) Structure and development of the Sagami Trough and off-Boso triple junction. Tectonophysics 160:135–150
Ranero CR, Phipps Morgan J, McIntosh K, Reichert C (2003) Bending-related faulting and mantle serpentinization at the Middle America trench. Nature. doi:10.1038/nature01961
Ranero CR, Villasenor A, Phipps Morgan J, Weinrebe W (2005) Relationship between bending-faulting at trenches and intermediate-depth seismicity. Geochem Geophys Geosyst. doi:10.1029/2005GC000997

Renard V, Nakamura K, Angelier J, Azema J, Bourgois J, Deplus C, Hamano Y, Huchon P, Kinoshita H, Labayme P, Ogawa Y, Seno T, Takeuchi A, Tanahashi M, Uchiyama A, Vigneresse J-L (1987) Trench triple junction off Central Japan-preliminary results of French-Japanese 1984 Kaiko cruise, Leg 2. Earth Planet Sci Lett 83:243–256

Rüpke L, Phipps Morgan J, Hort M, Connolly JAD (2002) Are the regional variations in central America arc lavas due to differing basaltic peridotitic slab sources of fluids? Geology 30: 1035–1038

Sasaki T (2003) Subduction tectonics in the northern Japan Trench based on seafloor swath mapping bathymetry. Doctoral thesis, University of Tokyo (in Japanese with English abstract)

Seta H, Nagaoka S, Kato S (1991) Landforms of the Izu-Ogasawara Trench by the narrow multi beam echo sounder. Rep Hydrogr Res 31:173–180 (in Japanese with English abstract)

Shimada K (2008) R/V MIRAI cruise report MR08-04. JAMSTEC, Yokosuka

Tamaki K, Nakanishi M, Oshida A, Sayanagi K (1992) A universal marine geophysics data processing system, Bulletin of the Ocean Research Institute. Ocean Research Institute, the University of Tokyo, Tokyo

Wessel P, Smith WHF (1998) New, improved version of generic mapping tools released. EOS Trans Am Geophys Union 79:579

Yamano M (2008) KAIREI cruise report KR08-10. JAMSTEC, Yokosuka

Yoneyama K (2008) R/V MIRAI cruise report MR08-02. JAMSTEC, Yokosuka

Erosional Subduction Zone in the Northern Japan Trench: Review of Submersible Dive Reports

Yujiro Ogawa

Abstract Submersible studies of the oceanward and landward slopes of the northern Japan trench are reviewed, and the typical erosional features of this subduction zone are discussed. On the oceanward slope, normal faults with tension cracks have created horst and graben structures, forming a series of steps. On the landward slope, brecciated Miocene sedimentary rocks with calcite veins and cement are exposed on the thrust-controlled slope surfaces, and landsliding of the rocks and sediments of the lower landward slope fills the grabens of the oceanward slope. As a result of this erosion, the trench has advanced, moved landward, at a speed of 5–6 km/m.y. since the middle Miocene.

Keywords Erosional type subduction zone • Normal fault • Thrust fault • Crack • Breccias • Calcite cement

1 Introduction

The Nankai subduction boundary around Japan is now considered an accretion-type margin with typical prism formation (e.g., Moore et al. 2007), although until the late 1960s, the Nankai trough was thought to have a normal faulted boundary (Hilde et al. 1969). The accretionary processes and gravitational collapse along this boundary have been well elucidated by manned submersible studies in Tenryu and Shionomisaki canyons, which incise the prism (Kawamura et al. 2009, 2011; Anma et al. 2011).

The Japan trench, on the other hand, has been considered a type example of subduction erosion with consequent trench advance and trench slope subsidence (von Huene and Lallemand 1990; von Huene and Scholl 1991; von Huene et al. 2004). However, a rather conspicuous thrust-faulted slope with a locally developed accretionary prism at its toe has been observed (Suyehiro and Nishizawa 1994).

Y. Ogawa (✉)
The University of Tsukuba, 1-127-2-C-740 Yokodai, Tsukubamirai 300-2358, Japan (home)
e-mail: fyogawa45@yahoo.co.jp

Y. Ogawa et al. (eds.), *Accretionary Prisms and Convergent Margin Tectonics in the Northwest Pacific Basin*, Modern Approaches in Solid Earth Sciences 8,
DOI 10.1007/978-90-481-8885-7_2,

Moreover, a large-scale submarine landslide has developed elsewhere on the landward slope, the orientation of which is controlled by the lineaments of normal faults in the subducting Pacific slab (Kobayashi 1991; Ogawa and Kobayashi 1994; Sasaki 2004; Nakanishi et al. 2011).

The Nankai trough and the Japan trench margins differ primarily in that the former is characterized by a sediment-supplied trench floor without a normal-faulted slab, and the latter by a sediment-starved trench and a normal-faulted slab. In the Nankai trough, the frontal thrust propagates into trench turbidites, whereas in the Japan trench, the slope rocks slide into grabens in the trench (Taira and Ogawa 1991). Thus, the Japan trench is a typical erosional subduction boundary characterized not by sediment accretion but by erosion. The landward slope of the trench has probably been retreating since at least the Miocene (e.g., DSDP Legs 56, 57, and 87B; von Huene et al. 1980; von Huene and Lallemand 1990; Lallemand and Le Pichon 1987; Clift and Vannucchi 2004).

However, the geology of the Japan trench has not been fully described except in the areas of the French–Japanese KAIKO project, such as its junction with the Kuril trench at its northern end (Erimo area; Cadet et al. 1987) and the Daiichi-Kashima Seamount area at its southern end (Kobayashi et al. 1987, 1998).

Since the KAIKO Project, *Hakuho-Maru* cruises operated by the University of Tokyo have completed mapping the rest of the Japan trench and have identified the Miyako area of the northern trench to be suitable for characterization (Ogawa and Kobayashi 1994; Kobayashi et al. 1998) (Fig. 1). These studies reported the topographical and geological similarities and differences between the oceanward and landward toes and confirmed that erosion of material into the grabens in the subducting slab causes the landward advance of the trench, as suggested by Hilde (1983).

The dive results for the oceanward slope have been described by Ogawa et al. (1991, 1997) and Ogawa (1994), and those for the landward slope by Ogawa et al. (1991, 1996), Iwabuchi et al. (1996), and Kuwano et al. (1997). However, the significance of the trench topography with regard to its tectonic features has not yet been discussed, although the erosional character of the trench may be greatly affected by the geology of the oceanward slope.

2 Oceanward Slope Topography and Geology off Miyako

Ogawa and Kobayashi (1994) briefly described the topography of the toe of the oceanward slope of the northern Japan trench off Miyako, and Kobayashi et al. (1998) discussed its tectonic significance. The slope is characterized by the systematic development of horst and graben structures (Fig. 2), each of which is some kilometers in width with steep walls up to several 100 m in height. The angle of the oceanward slope varies from 10° to 20° (average, 17°), as estimated from a topographic map with a 10-m contour interval. However, direct observation from the submersible showed that the slope is composed of a series of small steps (Fig. 3).

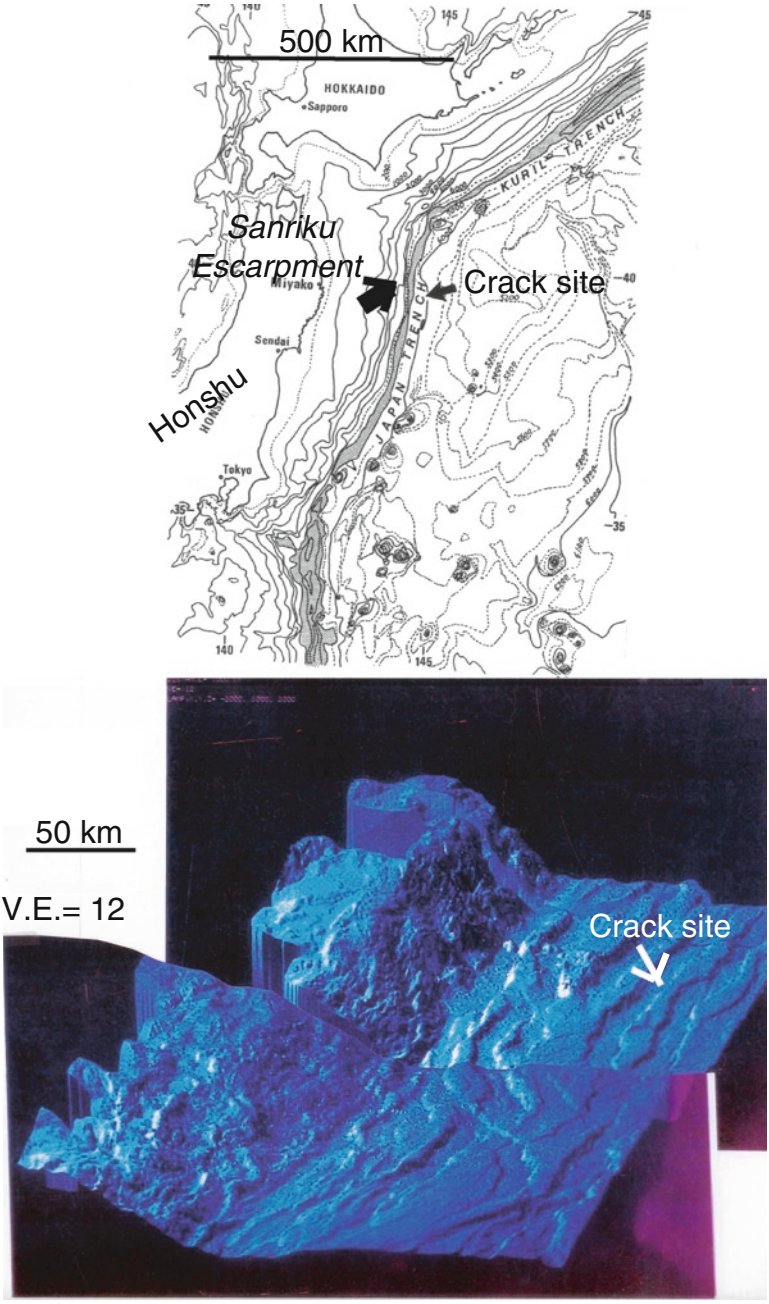

Fig. 1 Index map showing the dive sites, the crack site on the oceanward slope, and the Sanriku escarpment on the landward slope (*top*). Three-dimensional reconstruction (*Whale view*) of the Japan trench off Miyako, around 39°N, prepared by Kensaku Tamaki (*bottom*). Vertical exaggeration ×12

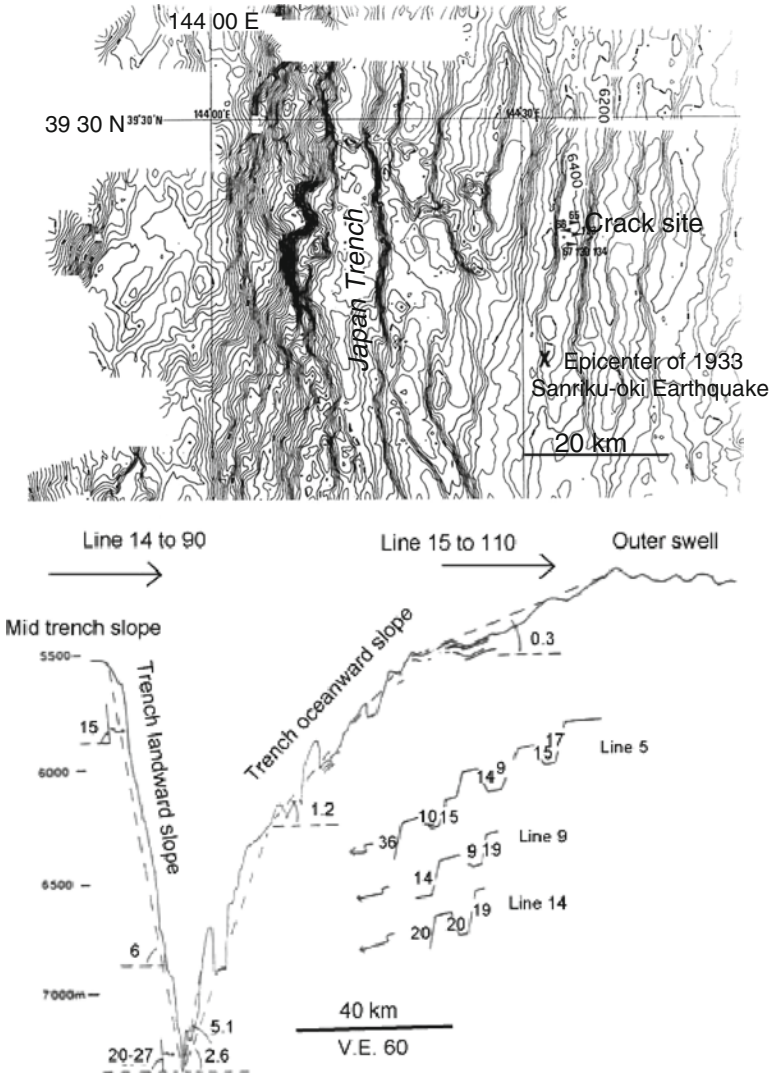

Fig. 2 Multi-narrow-beam swath map around the dive sites at 39°30′N off Miyako (*top*; contour interval, 50 m). Topographic section made by a 3.5-kHz subbottom profiler along 39°30′N (*bottom*). Vertical exaggeration ×60. Notice that the slope angle differs depending on the order. The oceanward slope toe gradients are 2.6°, 5.1°, and around 20°, increasing as the order decreases (Revised from Ogawa and Kobayashi (1994))

Many open cracks could be seen from the submersible windows (Fig. 3) (Ogawa et al. 1997). Ogawa et al. (1997) reported similar cracks in the Mariana trench, and they concluded that the open cracks resulted from shaking caused by large earthquakes occurring beneath the oceanward slope of the trench. This area of the Japan trench includes the epicenter of the 1933 Sanriku-oki earthquake (M = 8.1;

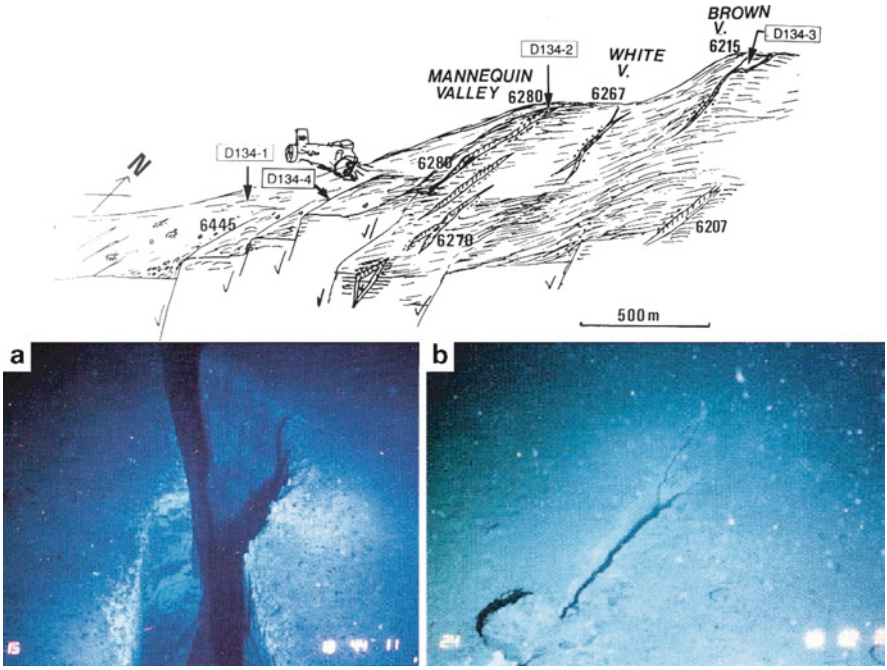

Fig. 3 Whale view sketch of the crack distribution on the shoulder of the normally faulted oceanward slope at dive site 6K#67 (*top*), and views of cracks from the submersible window (*bottom*). (**a**) a sharp crack in the seabed, which consists of diatomaceous mud; view looking southward; (**b**) Y-shaped crack propagation, looking southeastward (From Ogawa 1994; A, dive 6K#67; B, dive 6K#134)

Kanamori 1971), which was caused by normal faulting due to bending of the downgoing Pacific slab (shown by x in Fig. 2). Kanamori (1971) reported that this normal fault cuts almost the entire thickness of the Pacific plate.

The surface of the oceanward slope is composed of diatomaceous mud and mudstone with occasional ash layers. The sediments are not well indurated, nor are they deformed, except by local vein structures (Ogawa 1994). No chemosynthetic biocommunity is present. Repeated observations over 5 years have shown that northward-flowing bottom currents rapidly fill the cracks at the rate of centimeters per year (Hirano et al. 1998).

3 Landward Slope Topography and Geology off Miyako

The landward slope toe of the northern Japan trench off Miyako is also characterized by steep slopes, with a maximum angle of 30°, as estimated from a map with a 10-m contour interval (Fig. 2), and an average angle of 15°. The deepest portion attains a depth of 7,400 m. A steep cliff with a north–south trend at 6,500 m depth,

called the Sanriku Escarpment (Fig. 4), forms the boundary between the lowermost toe and the upper trench wall. This escarpment has been interpreted as the scarp of a large thrust fault (e.g., von Huene and Culotta, 1989). Taira and Ogawa (1991), however, showed that the upper part of the escarpment is characterized by large-scale submarine sliding caused by slope instability, which is later to be known further controlled by thrust faulting (Iwabuchi et al., 1996; Sasaki, 2004) as shown below.

Following Iwabuchi et al. (1996) and Ogawa et al. (1996), Sasaki (2004) summarized the mechanisms generating the topographical features of the Japan trench landward slope, attributing them to erosional subduction zone tectonics. According to Sasaki (2004), the occurrence of many thrust faults within both the upper and lower slope has resulted in the formation of a steep, unstable slope prone to landsliding. The rocks from the slope are fairly old. The traces of most of these thrust faults along the slope are characterized by abundant chemosynthetic biocommunities, dominated by *Calyptogena*, supported by methane-bearing fluids (Ogawa et al. 1996).

The submersible *SHINKAI 6500* (JAMSTEC) made several dives at the foot of the Sanriku Escarpment and further upslope (Fig. 4). The assemblages of fossil diatoms in rock and sediment samples collected by the submersible from the landward slope, identified by Itaru Koizumi, were of middle Miocene to

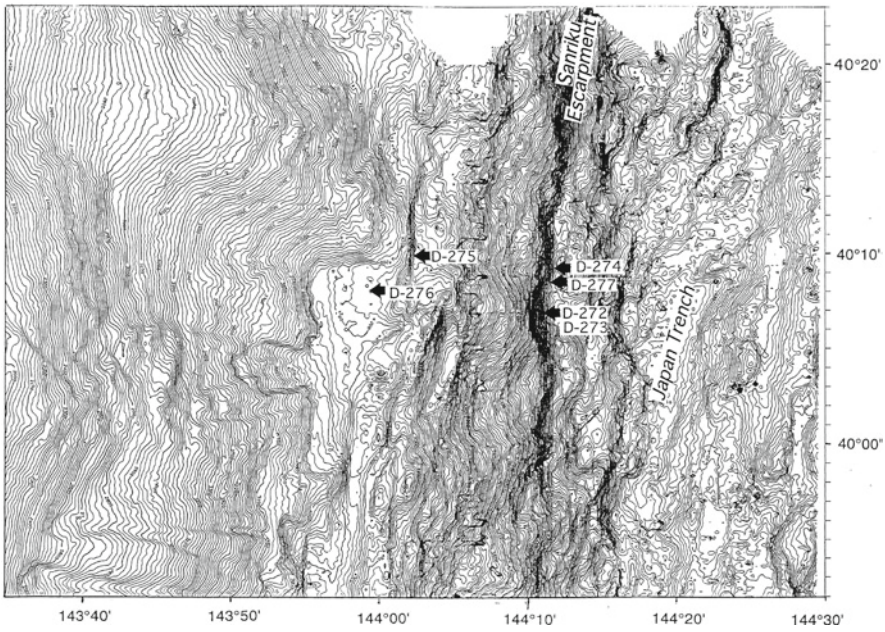

Fig. 4 Multi-narrow-beam swath map of the area around the Sanriku escarpment, off Miyako at 40°N (contour interval 20 m) (Adapted from Ogawa et al. (1996))

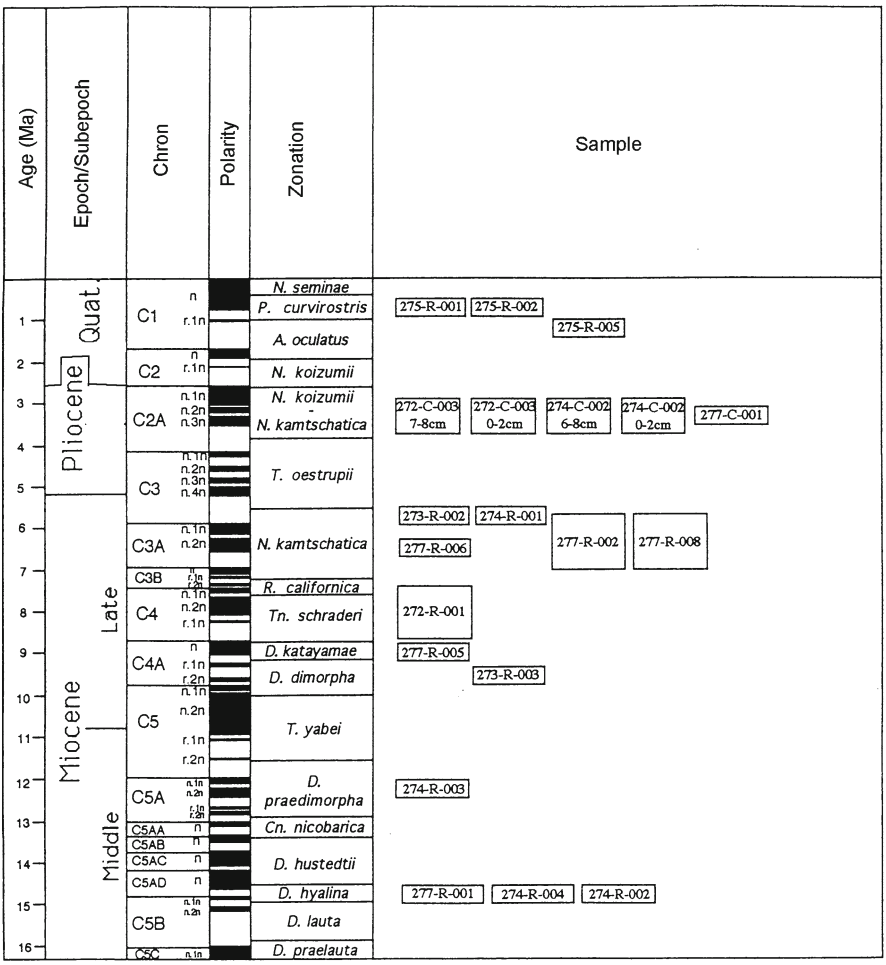

Fig. 5 Sample ages based on diatom biostratigraphic zones determined by Itaru Koizumi (Modified from Kuwano et al. (1997))

Pliocene age (Figs. 5 and 6) (Kuwano et al. 1997), similar to the ages of fossils from Emi Group and Miura Group rocks of the accretionary prisms on the Boso Peninsula (Hirono and Ogawa 1998; Yamamoto and Kawakami 2005). Moreover, some sandstone samples show a web structure, as observed in the Emi Group (Hirono 1996).

Strikingly, the Miocene rocks consist of breccias of diatomaceous mudstone or sandstone with calcareous cement and veins (Fig. 7). The carbon and oxygen isotope ratios of the calcite cement (Fig. 8), measured by Tadamichi Oba (Kuwano et al. 1997), are similar to those in the Oregonian margin (Kulm et al. 1986), the Nankai trough accretionary prism (Sakai et al. 1992), and the Boso Peninsula Miocene

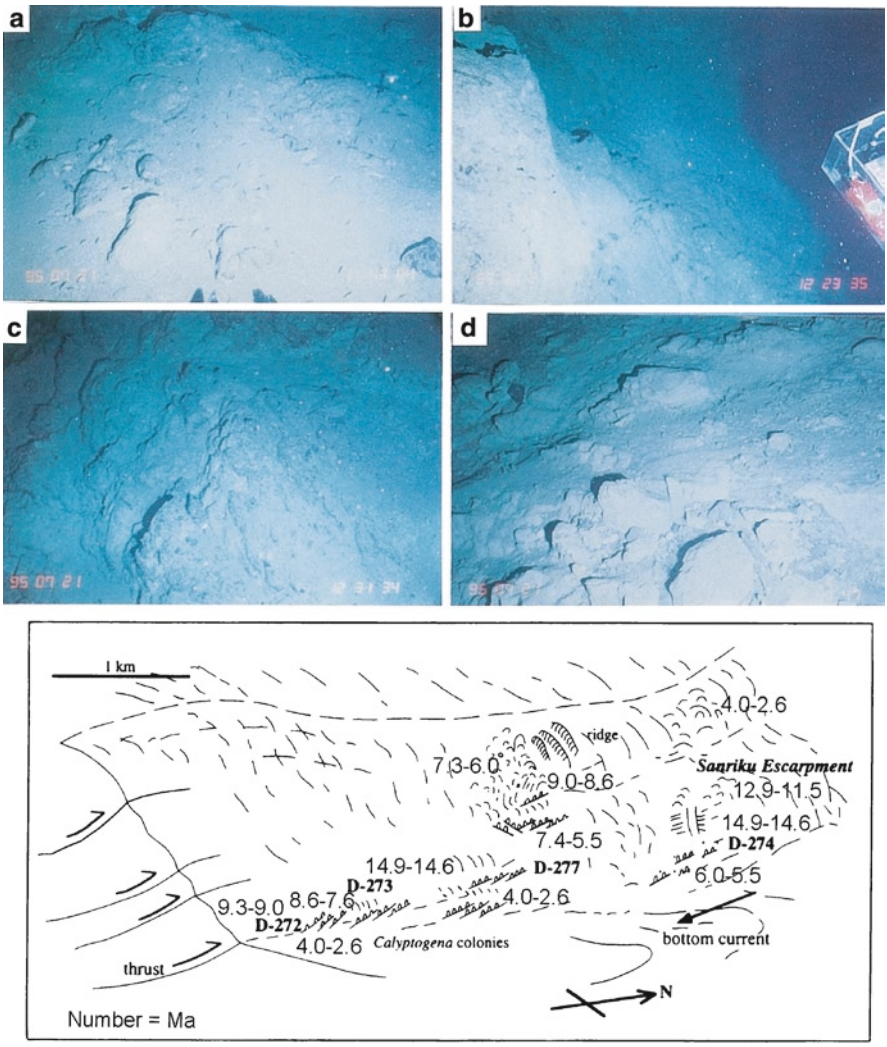

Fig. 6 Slopes and cliffs with cobbles on the landward slope from the video of dive 6K#274 (Adapted from Ogawa et al. 1996) (*top*). Sketch of the Sanriku escarpment. Ages (Ma) of sampled diatom fossils correspond to those in Fig. 5 (Modified from Ogawa et al. 1996) (*bottom*)

to Pliocene sedimentary rocks (Satoshi Hirano, personal communication 2005). It can thus be speculated that methane venting along thrust faults is the original cause of both the brecciation and the calcite cementation. During the Miocene, the Japan trench landward slope may have been part of an accretionary prism zone extending from the south Boso area northward to the area off Miyako. At present, this accretionary prism of Miocene age is being removed by subduction (tectonic) erosion.

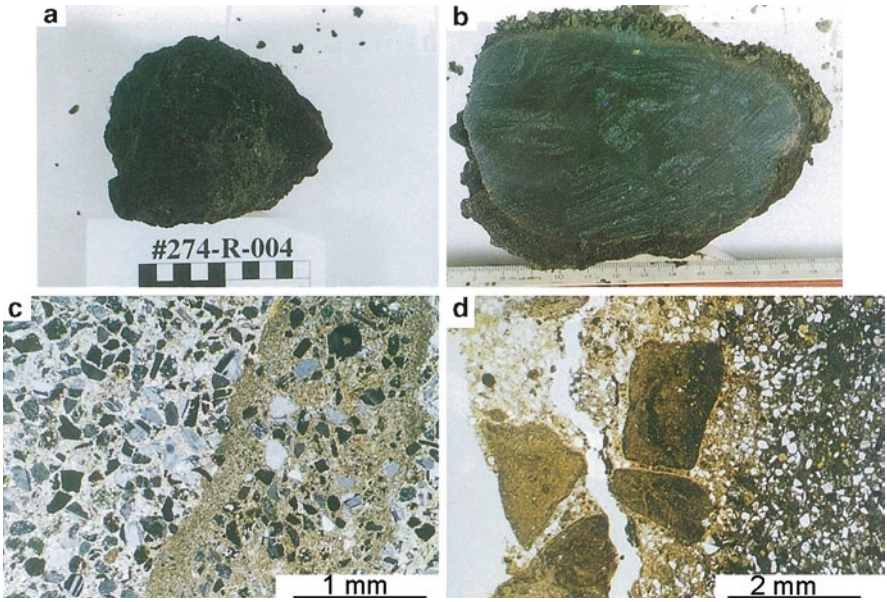

Fig. 7 Photos of representative samples from dives 6 K#274 (**a**, **c**) and #277 (**b**, **d**). Cut surfaces (**a**, **b**) and thin sections (**c**, **d**) showing brecciation and calcite veins and cement. Mudstone breccias can be seen to occur within the calcite cemented part (**b**, **d**) (From Ogawa et al. 1996)

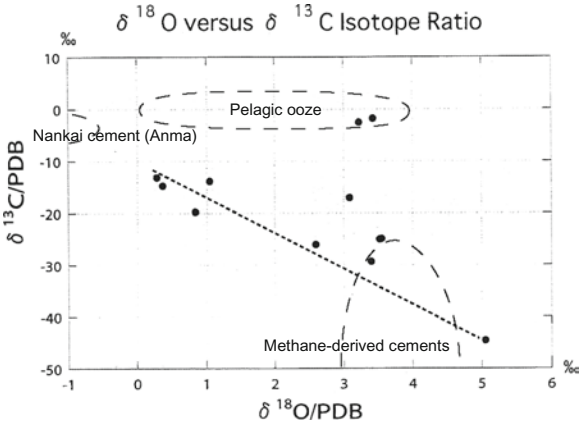

Fig. 8 Oxygen and carbon isotope ratios (*PDB*), analyzed by Tadamichi Oba. The dotted line is a regression line, excluding the upper two data points (from Kuwano et al. 1997). The domains of calcite cements are indicated by dashed ellipses: (*lower right*) methane-derived cements from the Nankai trough (Sakai et al. 1992), and (*top right*) pelagic ooze and (*top left*) Nankai trough cement from Shionomisaki Canyon (From Anma et al. (2011))

4 Lineaments of the Oceanward and Landward Slopes off Miyako

Lineament orientations, based on the 10-m contour interval maps, around the northern Japan trench are very similar between the oceanward and landward slopes (Fig. 9).

Unusually, the two slopes apparently developed differently. As interpreted by Hilde (1983), in the subduction (tectonic) erosion of the Japan trench landward slope, the slope sediments erode into the trench, filling the graben structures of the downgoing Pacific plate. As a result of this erosion, the landward slope is retreating steadily (e.g., von Huene and Lallemand 1990; Clift and Vannucchi 2004). Each of the grabens on the oceanward slope becomes totally filled by the collapse of the landward slope toe. The volume of the retard region suggests that the toe retreats at the rate of 5–6 km per 1 m.y. (Fig. 10). In the 10 m.y. since the middle Miocene, the calculated distance of 50–60 km is a reasonable estimate of trench landward advance caused by erosion of the Honshu arc.

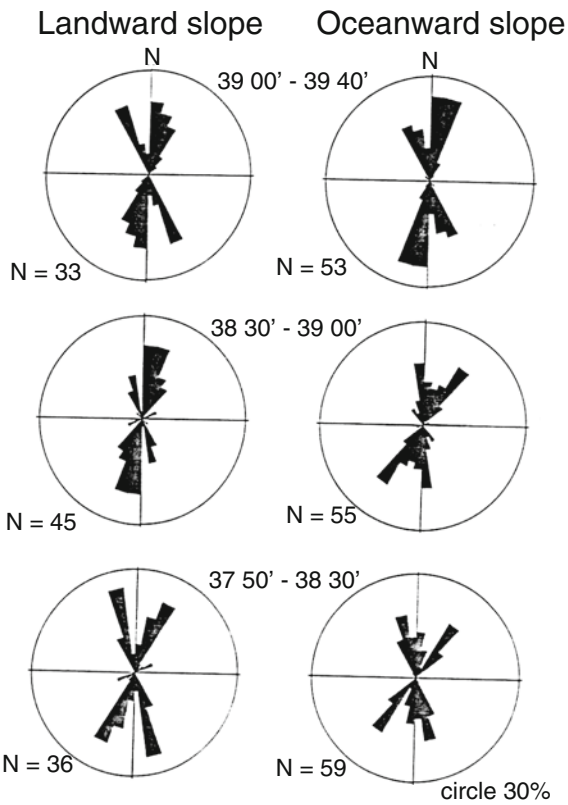

Fig. 9 Rose diagrams of lineaments on the oceanward and landward slopes, taken from the swath maps (From Ogawa and Kobayashi 1994)

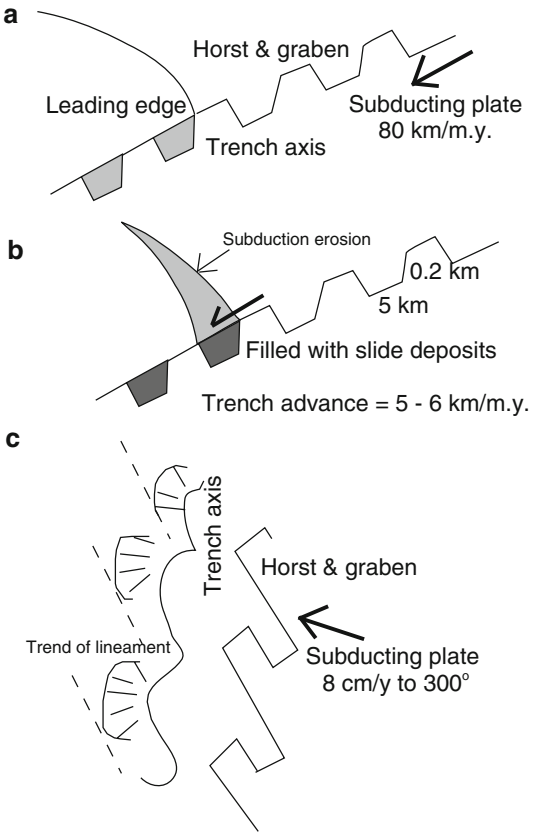

Fig. 10 Model of trench advance to landward caused by landsliding. The graben structures are filled by the collapse of the toe of the landward trench slope. In speed of the advance was calculated to be 5–6 km/m.y.

This first approximation is nearly equal to the value calculated by Lallemand et al. (1994), supporting the idea that the landward slope toe collapses and fills the grabens, and that the trend of the grabens imposes its orientation on the lineaments of the landward slope.

5 Conclusions

1. The oceanward slope of the Japan trench is steep and characterized by horst and graben structures caused by large-scale normal faulting due to downward bending of the subducting Pacific plate.
2. The landward slope toe is also steep, and exhibits conspicuous submarine landsliding. The lineaments on both the oceanward and landward slopes are

approximately parallel, which may be the primary indication that the subduction (tectonic) erosion of the margin is controlled primarily by the trend of the grabens in the subducting Pacific slab.

3. Brecciated rocks of Miocene and Pliocene age, veined and cemented by calcite, on the toe of the landward slope demarcate large-scale thrusting. Methane-bearing fluid seepage along the faults was responsible for the calcite cementation of the fault breccias in an accretionary prism.

Acknowledgments I deeply thank Professor Kazuo Kobayashi, who led the many successful cruises. Rock descriptions, age determinations, and isotope measurements for the landward slope by Drs. Takeshi Kuwano, Itaru Koizumi, and Tadamichi Oba, respectively, are greatly appreciated. Captains, crew, and operation teams of *SHINKAI 6500* of JAMSTEC are gratefully acknowledged. An early version of this manuscript was critically reviewed and revised by Professors Mark Cloos, Satoru Kojima, and Ryo Anma, to whom I am grateful.

References

Anma R, Ogawa Y, Moore G, Kawamura K, Sasaki T, Kawakami S, Dilek Y, Michiguchi Y, Endo R, Akaiwa S, Hirano S, YK99-09, YK00-08, YK05-08, YK06-02 Shipboard Science Parties (2011) Structural profile and development of accretionary complex in the Nankai trough, Southwest Japan: results of submersible studies. In: Ogawa Y, Anma R, Dilek Y (eds) Accretionary prisms and convergent margin tectonics in the Northwest Pacific Basic (Modern approaches in solid earth sciences 8). Springer, Dordrecht, (This volume)

Cadet J-P, Kobayashi K, Aubouin J, Boulègue J, Deplus C, Dubois J, von Huene R, Jolivet J, Kanazawa K, Kasahara J, Koizumi K, Lallemand S, Nakamura Y, Pautot G, Suyehiro K, Tani S, Tokuyama H, Yamazaki T (1987) The Japan Trench and its juncture with the Kurile Trench: cruise results of the Kaiko Project, Leg 3. Earth Planet Sci Lett 83:267–284

Clift P, Vannucchi P (2004) Controls on tectonic accretion versus erosion in subduction zones: implications for the origin and recycling of the continental crust. Rev Geophys 42:RG2001, 1–31. doi:10.1029/2003RG00127

Hilde TWC (1983) Sediment subduction vs. accretion around the Pacific. Tectonophysics 99:381–397

Hilde TWC, Wageman JH, Hammond WT (1969) The structure of Tosa and Nankai trough off southeastern Japan. Deep-Sea Res 16:67–75

Hirano S, Ogawa Y, Fujioka K, Kawamura K (1998) Temporal changes of cracks in the oceanward slope of northern Japan trench of Sanriku: six-year observation by submersible. JAMSTEC Rep 14:445–454

Hirono T (1996) Web structure in Emi Group of the southern Boso Peninsula. J Geol Soc Jpn 102:804–815

Hirono T, Ogawa Y (1998) Duplex arrays and thickening of accretionary prisms – an example from Boso Peninsula, Japan. Geology 26:779–782

Iwabuchi Y, Izumi N, Ogawa Y, Kaiho Y (1996) Topography and geology of landward slope of the Japan trench, off Sanriku. JAMSTEC J Deep Sea Res 12:23–34

Kanamori H (1971) Seismological evidence for a lithospheric normal faulting, the Sanriku earthquake of 1933. Phys Earth Planet Int 4:289–300

Kawamura K, Ogawa Y, Anma R, Yokoyama S, Kawakami S, Dilek Y, Moore GF, Hirano S, Yamaguch A, Sasaki T, YK05-08 Leg 2, YK06-02 Shipboard Scientific Parties (2009) Structural architecture and active deformation of the Nankai Accretionary Prism, Japan:

submersible survey results from the Tenryu Submarine Canyon. Geol Soc Am Bull 121: 1629–1646. doi:10.1130/B26219.1

Kawamura K, Ogawa Y, Hara H, Anma R, Dilek Y, Kawakami S, Chiyonobu S, Mukoyoshi H, Hirano S (2011) Rapid exhumation of subducted sediments due to seamount subduction and out-of-sequence thrust with gravitational collapse in an active eastern Nankai accretionary prism. In: Ogawa Y, Anma R, Dilek Y (eds) Accretionary prisms and convergent margin tectonics in the Northwest Pacific Basic (Modern approaches in solid earth sciences 8). Springer, Dordrecht, (This volume)

Kobayashi K (ed) (1991) Preliminary report of Hakuho Maru cruise KH90-1. Ocean Research Institute, University of Tokyo, Tokyo, 174 pp

Kobayashi K, Cadet J-P, Aubouin J, Boulègue J, Deplus C, Dubois J, von Huene R, Jolivet J, Kanazawa K, Kasahara J, Koizumi K, Lallemand S, Nakamura Y, Pautot G, Suyehiro K, Tani S, Tokuyama H, Yamazaki T (1987) The Japan Trench and its juncture with the Kurile Trench: cruise results of the Kaiko Project, Leg 3. Earth Planet Sci Lett 83:257–266

Kobayashi K, Nakanishi M, Tamaki K, Ogawa Y (1998) Outer slope faulting associated with the western Kuril and Japan trenches. Geophys J Int R Astron Soc Lond 134:356–372

Kulm LD, Suess E, Moore JC, Carson B, Lewis BT, Ritger SD, Kadko DC, Thornburg TM, Embley RW, Rugh WD, Mathos GJ, Langseth MG, Cochrane GR, Scamman RL (1986) Oregon subduction zone: venting, fauna and carbonates. Science 231:561–566

Kuwano K, Ogawa Y, Koizumi I, Oba T (1997) Calcite-cemented Miocene to Pliocene breccia at the Sanriku Escarpment, northern Japan Trench. JAMSTEC J Deep Sea Res 13:573–590

Lallemand S, Le Pichon X (1987) Coulomb wedge model applied to the subduction of seamounts in the Japan Trench. Geology 15:1065–1069

Lallemand SE, Schnurle P, Malavieille J (1994) Coulomb theory applied to accretionary and non-accretionary wedges: possible causes for tectonic erosion and/or frontal accretion. J Geophys Res 99:12,033–12,055

Moore GF, Bangs NL, Taira A, Kuramoto S, Pangborn E, Tobin HJ (2007) Three-dimensional splay fault geometry and implications for tsunami generation. Science 318:1128–1131

Nakanishi M (2011) Bending-related topographic structures of the subducting plate in the northwestern Pacific Ocean. In: Ogawa Y, Anma R, Dilek Y (eds) Accretionary prisms and convergent margin tectonics in the Northwest Pacific Basic (Modern approaches in solid earth sciences 8). Springer, Dordrecht, (This volume)

Ogawa Y (1994) Characteristics and origin of cracks observed by research submersible "Shinkai 6500" in the oceanward slope of the Northern Japan Trench. J Geogr Tokyo Geogr Soc 103:706–718

Ogawa Y, Kobayashi K (1994) Topographic and geologic characteristics of the Japan and Kurile trenches. Earth Mon Spec Issue 9:60–69

Ogawa Y, Kobayashi K, Tamaki K, Fujimoto H, Oshida J, Tanaka T, Matsumoto T, Iino H (1991) Tectonic implications of the topographic features of Japan trench. In: Kobayashi K (ed) Preliminary report of the Hakuho Maru cruise KH 90–1. Ocean Research Institute, University of Tokyo, Japan, pp 11–29

Ogawa Y, Fujioka K, Fujikura K, Iwabuchi Y (1996) En echelon patterns of *Calyptogena* colonies in the Japan Trench. Geology 24:807–810

Ogawa Y, Kobayashi K, Hotta H, Fujioka K (1997) Tension cracks on the oceanward slopes of the northern Japan and Mariana Trenches. Mar Geol 141:111–123

Sakai H, Gamo T, Ogawa Y, Boulegue J (1992) Stable isotopic ratios and origins of the carbonates associated with cold seepage at the eastern Nankai trough. Earth Planet Sci Lett 109:391–404

Sasaki T (2004) Subduction tectonics of the northern Japan trench based on the regional seabeam mapping. PhD Theses, University of Tokyo, 159 pp

Suyehiro K, Nishizawa A (1994) Crustal structure and seismicity beneath the forearc off northern Japan. J Geophys Res 99:22331–22347

Taira A, Ogawa Y (1991) Cretaceous to Holocene forearc evolution in Japan and its implication to crustal dynamics. Episodes 14:205–212

von Huene R, Culotta R (1989) Tectonic erosion at the front of the Japan Trench convergent margin. Tectonophysics 160:75–90
von Huene R, Lallemand S (1990) Tectonic erosion along the Japan and Peru convergent margin. Geol Soc Am Bull 102:704–720
von Huene R, Scholl DW (1991) Observation at convergent margins concerning sediment subduction, subduction erosion, and the growth of continental crust. Rev Geophys 29:279–3116
von Huene R, Langseth MG, Nasu N, Okada H et al. (1980) Summary; Japan Trench transect. Initial Report of DSDP, 56 & 57, Pt. 1, 473–488
von Huene R, Ranero CR, Vannucchi P (2004) Generic model of subduction erosion. Geology 32:913–916
Yamamoto Y, Kawakami S (2005) Rapid tectonics of the Late Miocene Boso accretionary prism related to the Izu–Bonin arc collision. Isl Arc 14:178–198

Boso TTT-Type Triple Junction: Formation of Miocene to Quaternary Accretionary Prisms and Present-Day Gravitational Collapse

Yujiro Ogawa and Yukio Yanagisawa

Abstract The Boso triple junction, the only known trench-trench-trench type triple junction, was surveyed by the ROV *KAIKO-10K* after the French–Japanese KAIKO project and related R/V *Hakuho-Maru* cruises. This paper summarizes the bathymetry and geologic structure, and the types and ages of rocks and sediments observed in the Boso triple junction area during these studies. We used diatom biostratigraphy to elucidate the evolution of Miocene accretionary prism units exposed in the Izu-Bonin forearc and in subaerial exposures on the Boso Peninsula. The instability of the Boso triple junction system since the Miocene is attributed to repeated trench sediment accretion and collapse. We conclude that the Boso triple junction area hosts a sequence of trench-fill sediments that has accumulated between the easternmost margin of the Izu forearc and the easternmost Nankai trough since the Miocene. However, recent instability at the Boso triple junction is characterized by repetitive episodes of development and subsequent collapse of a ponded basin close to the accretionary prism that are intimately associated with the development of the Boso triple junction system.

Keywords Boso triple junction • ROV study • Accretionary prism • Diatom biostratigraphy • Gravitational collapse

Y. Ogawa (✉)
The University of Tsukuba, 1-127-2-C-740 Yokodai, Tsukubamirai 300-2358, Japan (home)
e-mail: fyogawa45@yahoo.co.jp

Y. Yanagisawa
Geological Survey of Japan, AIST, Tsukuba 305-8567, Japan
e-mail: y.yanagisawa@aist.go.jp

Y. Ogawa et al. (eds.), *Accretionary Prisms and Convergent Margin Tectonics in the Northwest Pacific Basin*, Modern Approaches in Solid Earth Sciences 8,
DOI 10.1007/978-90-481-8885-7_3,

1 Introduction

The Boso triple junction is the only known example of a trench-trench-trench type triple junction (Seno et al. 1989; Ogawa et al. 1989) (Fig. 1). At present, three lithospheric plates converge at this junction in a stacked array of subduction systems. The Philippine Sea plate (PHS) forms the southwestern margin of the triple junction system, and is subducting beneath the North America plate (NAM). The motion of the PHS relative to the NAM is thought to be up to 2.7 cm/year toward the northwest, subparallel to the northwest-trending Sagami trough (Seno et al. 1989) (Fig. 1). The Pacific plate (PAC) lies to the east of the triple junction and is subducting westward beneath both the PHS and NAM along the Izu-Bonin (Ogasawara) trench (Fig. 1).

At present, the PHS is not moving parallel to the Izu-Bonin trench, which suggests that the Boso triple junction may be unstable. Indeed, the Boso triple junction may be in transition from a trench-trench-trench junction to a trench-trench-transform junction (Ogawa et al. 1989, 2008; Niitsuma 1996).

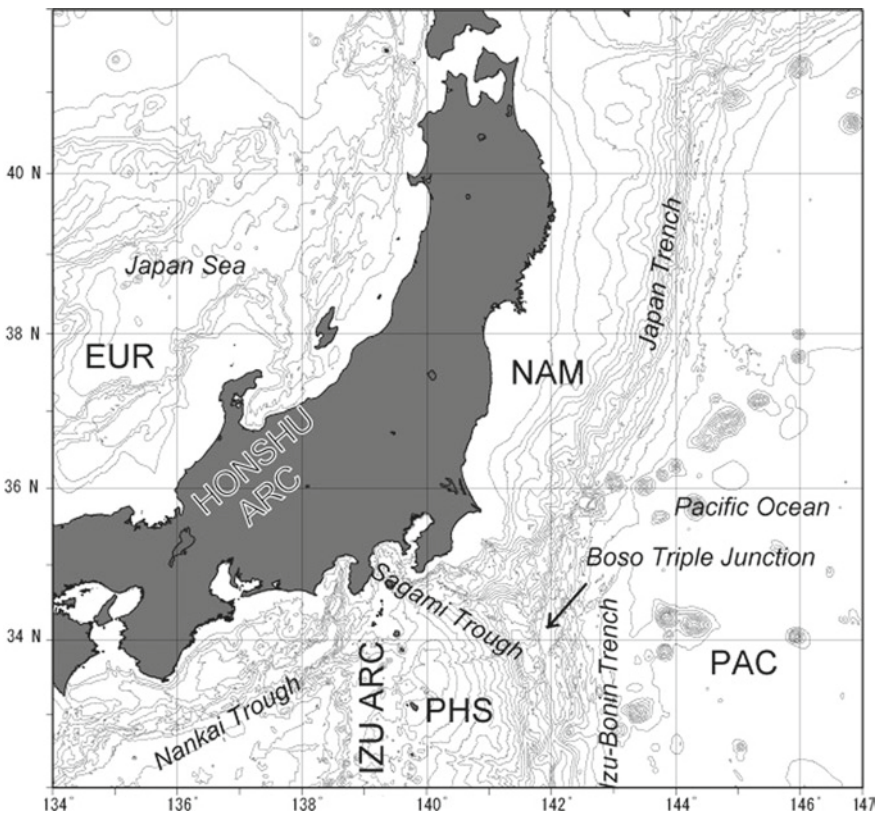

Fig. 1 Map showing the relationships of the Eurasia (*EUR*), North America (*NAM*), Philippine Sea (*PHS*), and Pacific (*PAC*) plates and the associated trenches

Although the geometric (Le Pichon and Huchon 1987; Hamano 1987; Huchon and Labaume 1989), geophysical (Seno et al. 1989), and sedimentologic (Soh et al. 1988, 1990) aspects of the Boso triple junction have been considered, a detailed assessment of its geologic significance has yet to be done. Preliminary reports by Ogawa et al. (1989, 2008) described the unstable topography of the Boso triple junction area from analyses of multibeam echosounder data and single-channel seismic profiles collected during the first phase of the French–Japanese KAIKO project in 1984 (KAIKO I Research Group 1986; Nakamura et al. 1987; Renard et al. 1987; Pautot et al. 1987). However, there remains an abundance of topographic and geologic data collected during the KAIKO project that have not been fully evaluated.

The geology of subaerial exposures of accretionary complexes both on and adjacent to the Honshu and Izu arcs has been well studied (Ogawa and Taniguchi 1988; Geological Survey of Japan 1990). Similarly, correlations among the subaerial and marine exposures of these complexes are well established (Geological Survey of Japan 1990; Ogawa et al. 2008). Together, these geologic relationships suggest that the NW–SE trending geologic units exposed on land on the Miura and Boso peninsulas (Fig. 2) can be extended from the Honshu arc subparallel to the

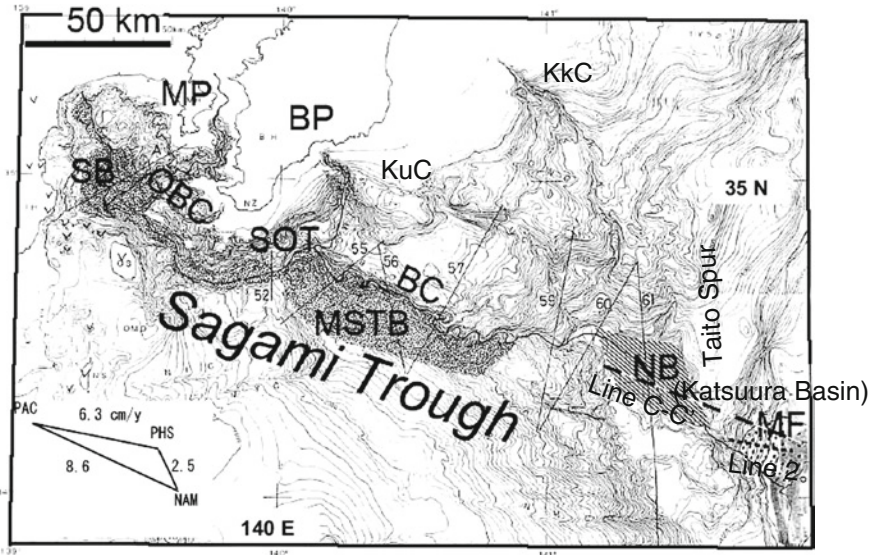

Fig. 2 Bathymetric map of the area around the Sagami trough and Boso triple junction (Hydrographic Department 1988), showing the relation between the North America (*NAM*), Philippine Sea (*PHS*), and Pacific (*PAC*) plates. Shaded and dotted areas indicate the present-day depositional basins: from the northwest, *SB* (Sagami Basin), *MSTB* (Middle Sagami Trough Basin), *NB* (Katsuura Basin), and *MF* (Mogi Fan in the Bando Deepsea Basin). Submarine troughs and canyons are also shown: *SOT* (Soh-Oh Trough), *BC* (Boso Canyon), *KkC* (Katakai Canyon), and *KuC* (Katsuura Canyon). *OBC* is the Okinoyama Bank Chain. *MP* and *BP* are the Miura and Boso peninsulas, respectively (Modified from Ogawa et al. 1989)

Sagami trough trend to the present plate boundary. There is evidence to suggest that this plate boundary has trended WSW–ENE since the Miocene (Taira et al. 1989; Yamamoto and Kawakami 2005; Kanamatsu and Herrero-Berver 2006), but was recently rotated to its current NW–SE trend by collision with the Izu arc on the PHS ca 3 Ma.

The kinematics of the evolution of these trends suggests that the geometry of the Boso triple junction is greatly influenced by regional tectonism. Thus, the geologic relationships shown by subaerial exposures of subduction-related deposits on the Miura and Boso peninsulas suggest that these rocks originated within the Cretaceous–Tertiary Shimanto accretionary prism before the collision of the Izu arc and the development of the Boso triple junction (Ogawa and Taniguchi 1988; Mori and Ogawa 2005; Mori et al. 2011).

In this paper, we first review the depositional and deformational evolution of the area of the Boso triple junction with reference to submarine geologic maps previously published by the Geological Survey of Japan, the results of recent onshore geological surveys, and new diatom age data for subsea samples. We then consider the significance of these results for understanding the Neogene to Quaternary tectonic development of the region. According to the subsea video footage, these strata have undergone complex deformation; there is an alternating sequence of steep and shallow dips that suggests a collisional thrust-and-fold structures and gravitationally collapsed structures.

2 Review of Sedimentation, Topography, and Plate Configuration

2.1 Sedimentation

The present drainage system in the region off the Boso Peninsula transports clastic sediments along the Sagami trough, through the Sagami and Boso submarine canyons, and ultimately into the Boso triple junction, forming the Mogi submarine fan (Nakamura et al. 1987; Renard et al. 1987; Pautot et al. 1987, Ogawa et al. 1989, 2008) (Fig. 2). This sedimentation system includes a series of basins within the Sagami trough (northwestern, central, and southeastern (Katsuura) submarine basins) and the triple junction itself (Bando submarine basin) (Ogawa et al. 1989, 2008; Iwabuchi et al. 1990). Because most of the accretionary prisms on land of Miocene and younger age are composed of volcaniclastic sediments derived from the Izu arc, it is reasonable to consider that they were deposited on the Izu forearc and in the ponded basin along the previous Sagami trough before their accretion at the Honshu margin. These accreted deposits are now subaerially exposed on the Miura and Boso peninsulas as the Emi, Miura, and Chikura accretionary prisms (Hanamura and Ogawa 1993; Hirono and Ogawa 1998; Yamamoto and Kawakami 2005; Michiguchi 2008; Muraoka and Ogawa 2011).

2.2 Topographic Development of the Area from the Eastern Margin of the Sagami Trough to the Boso Triple Junction

Soh et al. (1990) suggested that tectonic instability of the Boso triple junction caused rapid downwarping in the area of the junction in recent times, and that subsidence of the drainage system within the Boso submarine canyon led to significant changes to the meandering drainage system there. Seno et al. (1989) suggested that the tectonic instability of the junction is associated with the 0.5 Ma jump of the NAM plate boundary to the eastern margin of the Japan Sea. Ogawa et al. (1989) and Ogawa et al. (2008) built upon the work of Seno et al. (1989) and suggested that a wide area of the NAM to the immediate northwest of the triple junction has become very unstable due to differential downwarping in response to gravitational instability of the area since the PHS began to move northwestward.

Lallemant et al. (1996) considered the active forearc sliver faults on the Miura and Boso peninsulas and their extensions into the Pacific on the northeast side of the Sagami trough to be a response to oblique subduction with a transform component. They noted that the forearc sliver faults, as exemplified by the presence of the Mineoka belt and a fault along Katsuura Canyon might represent right-lateral dislocation, which may have caused three or more linear NW–SE displacements of the bathymetry off the Boso Peninsula near the Katakai, Katsuura, and Boso canyons (Figs. 2 and 3).

2.3 Katsuura Basin and Mogi Submarine Fan in the Bando Deepsea Basin

The Katsuura and Bando basins are two large, well-defined basins within the Boso triple junction area (Fig. 3). The Katsuura Basin is a lens-shaped depression immediately northwest of the triple junction and bordered by a north–south trending ridge on the landward side of the Izu-Bonin trench (the Taito Spur of Iwabuchi et al. 1990; Fig. 4) (Ogawa et al. 1989; Seno et al. 1989). The Bando Basin (Bando deepsea basin of Iwabuchi et al. 1990) directly overlies the Boso triple junction and hosts the Mogi Fan (Iwabuchi et al. 1990). The North and South Basins of Ogawa et al. (1989) (the northern part of the former coincides with the Katsuura Basin) form a north–south oriented rectangular basin that includes two terraces, one at 6 km water depth and the other at 7 km depth (Fig. 4).

The present axial channel within the Sagami trough cuts through the Katsuura Basin, running through a gorge crossing the Taito Spur between the Katsuura Basin and the trench floor. The channel then crosses the Mogi Fan and flows into the Bando Basin (Ogawa et al. 1989) (Figs. 2–4). Thus, the Katsuura Basin developed as a ponded basin containing a thickness of least 2 km of sediments as a result of damming by the ridge. A small, 20 km-long accretionary prism can be recognized from seismic profiles (Figs. 3 and 4).

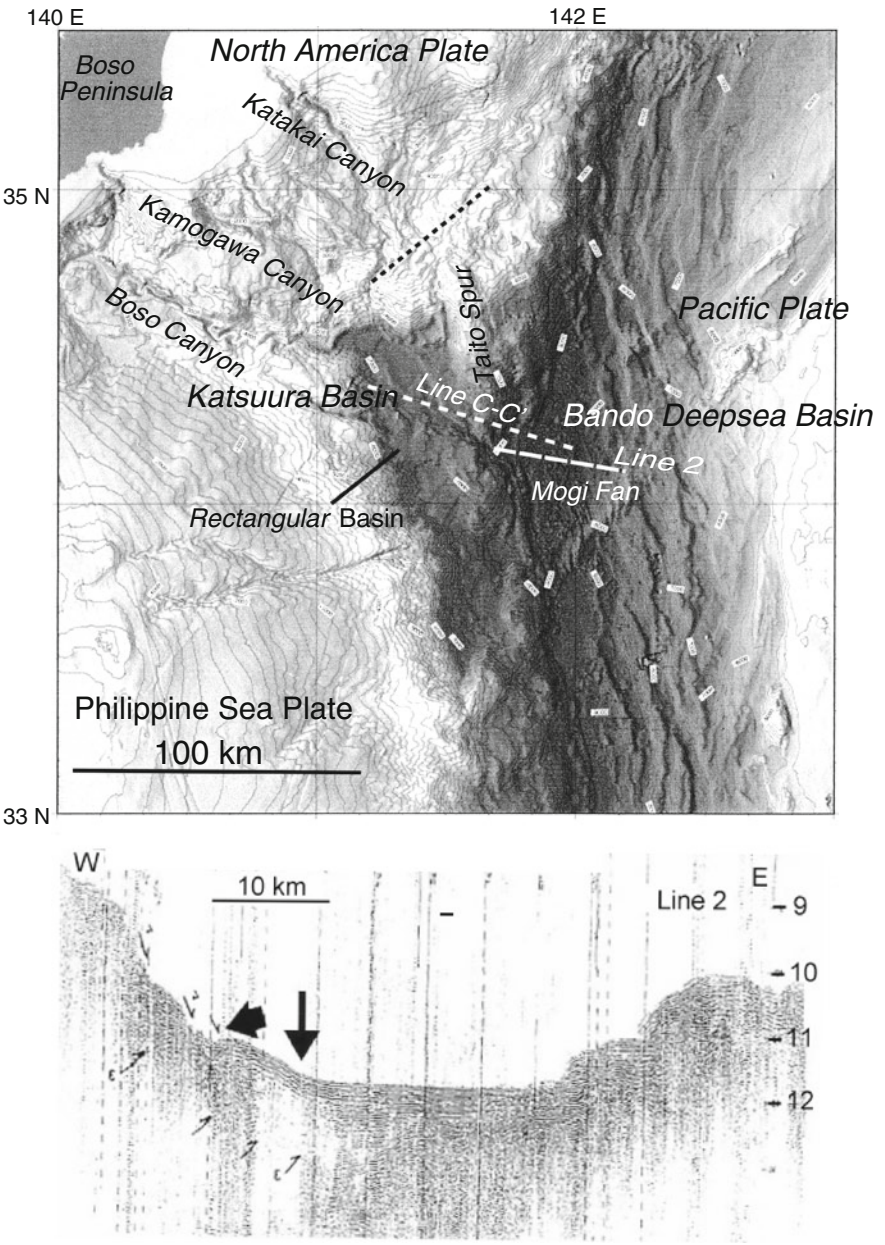

Fig. 3 Bathymetric map of the Boso triple junction area (*top*) (Courtesy M. Nakanishi) and a single-channel seismic profile across the triple junction (*bottom*) (Line 2 of JAMSTEC cruise KH86-5, location shown above). The vertical scale on the profile is two-way travel time. The *narrow arrow* indicates the dive site of the ROV *KAIKO-10K* and the *broad arrow* indicates a submarine landslide (Adapted from Ogawa et al. 1989). The dive area is immediately north of the *Mogi Fan* near the triple junction. The *black dotted line* northwest of the *Katsuura Basin* shows the strike of normal faults identified by Iwabuchi et al. (1990). The *Katsuura Basin* is a ponded basin containing a thickness of at least 7,000 m of sediments dammed by the present-day accretionary prism

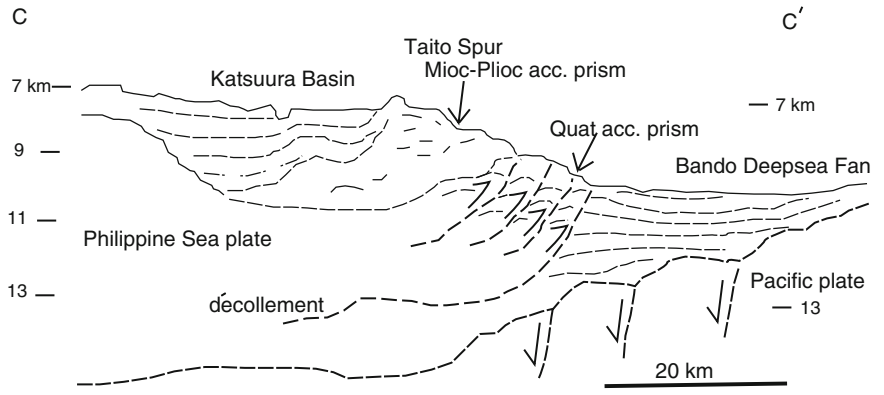

Fig. 4 Our reinterpretation of multichannel seismic profile C–C′ of Iwabuchi et al. (1990). Ridges and slopes between the Katsuura Basin and the Bando Deepsea Fan (Taito Spur) represent Miocene–Pliocene and Quaternary accretionary prisms. *Bold* and *fine dashed lines* are reflectors identified on the seismic profile

According to a submarine geologic map compiled by the Geological Survey of Japan (1990), the area around the Boso triple junction has at least two stratigraphic components: probable Miocene to Pliocene rocks (labeled Paleogene to Miocene on the map), and Quaternary sediments. The latter are sediments scraped from the Mogi Fan deposits in the area of the triple junction (Ogawa et al. 1989) (Figs. 3 and 4).

Thus, damming ridges (including the Taito Spur) have formed repeatedly and are responsible for the sediment collapses that formed the two terraces. At each stage, the formation of an accretionary prism was followed by the development of a ponded basin to the west. When the dams collapsed, the resultant sediment flows formed fan deposits in the area of the triple junction, similar to the present-day Mogi Fan. The collapse of the dams was probably related to faulting at the triple junction.

Transport of sediments from the Izu and Tanzawa areas along the Sagami trough resulted in deposition of thick piles of clastic sediments at some places in the middle of the trough floor (sediments such as those in the present-day Sagami Basin and Middle Sagami Trough Basin), or on the eastern edge of the trough (like those of the present-day Katsuura Basin), and one or more piles of sediment at the triple junction (like those of the present-day Mogi Fan).

Seno et al. (1989) considered several models to explain the instability of the triple-junction area on the basis of gravity data. They suggested that mud filling the trench, or diapiric intrusion of serpentinite into the very base of the Izu-Bonin trench, both of which are common to the south at the toe of the Izu-Bonin-Mariana trench, may have caused the instability. They preferred a thick sedimentary fill in the very deep basin as the source of the considerable negative gravity anomaly. The deepest part of the recent trench-fill sediments attains a maximum thickness of 4 km (based on line C–C′ of Iwabuchi et al. 1990) (Fig. 4). Formation

of such a basin with a negative gravity anomaly indicates that the lens-shaped Katsuura Basin formed as a result of stretching, probably related to westward movement of the PHS.

2.4 Review of 3D Structure Based on Multichannel Seismic Profiles and Multibeam Echosounder Data

Iwabuchi et al. (1990) used multibeam echosounder data and multichannel seismic profiles to interpret the structural relationships of the three tectonic plates in the Boso triple junction area (Fig. 4). They suggested that the PHS lies beneath of the NAM to the north of the triple junction, which indicates that northward subduction of the PHS persisted possibly until the Quaternary. Iwabuchi et al. (1990) also identified a northeast-trending normal fault system approximately 50 km northwest of the triple junction in the southernmost tip of the NAM (northeast-trending dotted line in Fig. 3). The location of this fault system suggests NW–SE extension on the ocean floor in the southernmost part of the NAM.

We have concluded that development of the Boso triple junction was a complicated process controlled by the configuration of the three plates and their interactions. Local horizontal extension in response to the northwestward motion of the PHS is also consistent with formation of the Katsuura Basin in the northeastern corner of the PHS.

If we assume that both the Paleogene–Miocene sequence (as discussed in Sect. 3.4) and part of the PHS remained in the triple junction area, the recent northward movement of the PHS and accretion of the part of the Paleogene–Miocene sequence that is equivalent to the Izu-Bonin forearc strata provide evidence to support the view that the triple junction was stable until recent times. This theory is also supported by new paleontological data presented in Sect. 3.

2.5 Relationship Between the Tectonic and Age Data

To further develop the scenarios for the tectonic development of the Boso triple junction reviewed above, we need to incorporate geochronological data. The water depth of the floor of the depocenter within the Boso triple junction reaches 9.4 km. At such depths, the common methods of marine geological and geophysical exploration cannot generally be used. However, we conducted a successful dive of the unmanned submersible ROV *KAIKO-10K* (Japan Marine Science and Technology Center; now the Japan Agency for Marine-Earth Science and Technology, JAMSTEC) to the deepest part of the basin near the triple junction. Video images of seafloor features were recorded during this dive and rock and sediment samples were collected. The following section describes the age determination of those samples.

3 Diatom Analysis

3.1 Materials, Method, and Results

ROV *KAIKO-10K* dives 10K#148 and #151, during cruise KR99-10 of JAMSTEC's R/V *KAIREI*, investigated the toe of the landward slope of the trench on the Honshu-arc side of the Boso triple junction at depths of about 9,200–8,900 m (Figs. 3 and 5). The ROV dive routes crossed the foot of the accretionary prism, where the seafloor topography is the result of submarine landslides (Figs. 5 and 6). The slopes and cliffs expose soft bedded formations that contain scattered cobbles of harder rocks (Figs. 5 and 6) (Oji et al. 2009). These exposures were sampled using a manipulator arm and push corer installed on ROV *KAIKO-10K*. All samples (except two hard rock samples) broke up in the sample basket.

Diatom analyses of nine samples were performed (Table 1). Samples 10K#148 R1-5 (2, 5, 11, 12), 10K#148 R-2, and 10K#151 R-1 were rock samples. Samples 10K#151 C-1, C-2, and 10K#151 C-1 were core-top samples. Samples 10K#148 R-2 and 10K#151 R-1 were relatively hard, indurated mudstone float clasts taken from the slope and contained ash and diatom fragments. The other samples were soft diatomaceous mud or mudstone that broke up during collection with the manipulator arm and became mixed in the sample box; the sample numbers for these are therefore somewhat arbitrary. The outcrops of steeply dipping or subhorizontal beds shown in Figs. 6 and 7 are probably exposures of such soft sedimentary rocks, which probably represent turbidite deposits.

Unprocessed strewn slides were prepared for each sample following the method described by Akiba (1986). One hundred diatom valves were counted for each slide at 600× magnification. After routine counting, each slide was scanned in its entirety to find diatoms missed during counting. Diatoms found as fragments were also recorded. Resting spores of the genus *Chaetoceros* were counted separately.

Complete diatom valves were found in eight samples; sample 10K#148 R-2 contained only highly fragmented valves (Table 2). Diatom assemblages were a mixture of cold- and warm-water species, except for sample 10K#151 R-1, which was dominated by cold-water diatoms.

3.2 Diatom Biostratigraphy

Because the samples contained cold- and warm-water diatom assemblages, both Neogene North Pacific middle to high latitude diatom zonation (Akiba 1986; Yanagisawa and Akiba 1998) and low-latitude zonation (Barron 1985) can be used for age determination. Table 1 shows the diatom zones and ages for the samples analyzed, and Fig. 8 show the 25 most significant species.

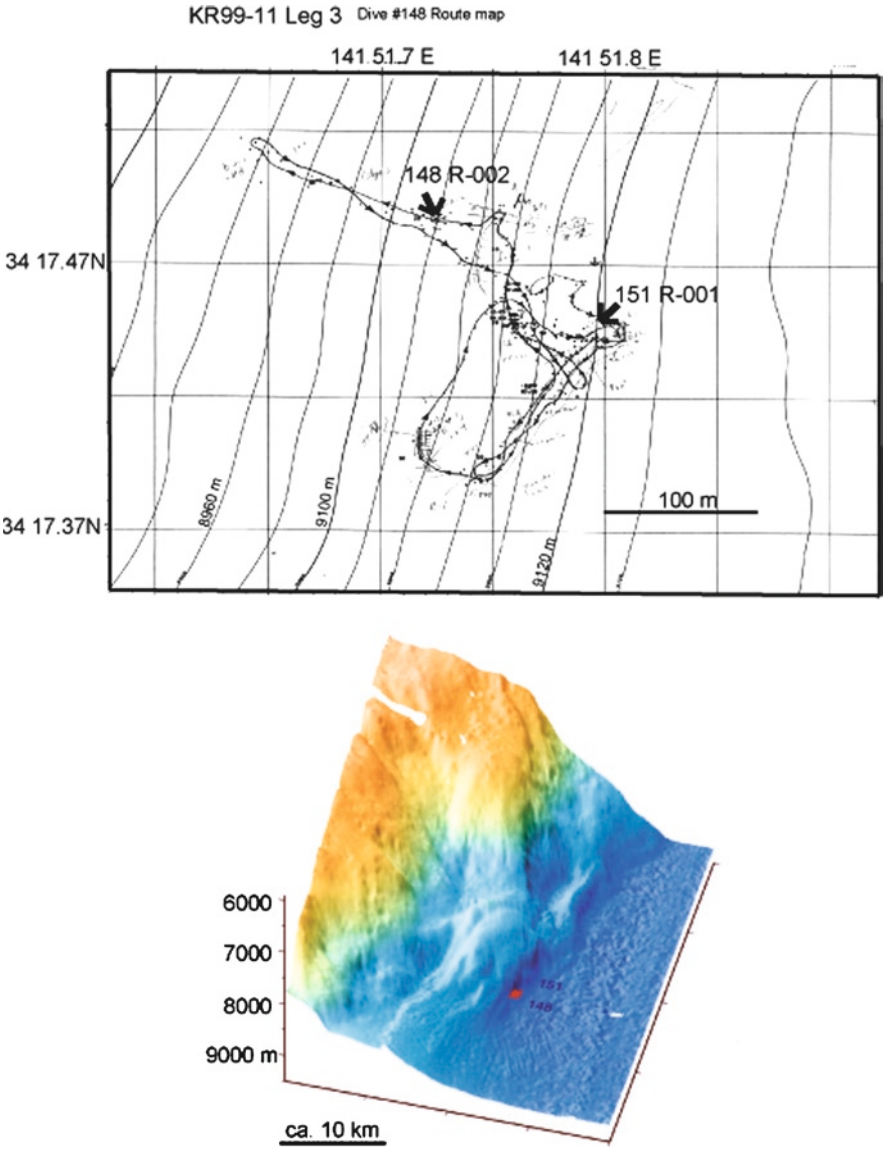

Fig. 5 Map (*top*) showing the route map of dive 10K#148 and locations of sample sites #148 R-002 and #151 R-001 and subsea view (*bottom*) of the dive site (vertical exaggeration ×5)

3.2.1 Pleistocene to Holocene Samples

Samples 10K#148 R1-5 (2, 5, 11, 12), 10K#150 C-1, C-2, and 10K#151 C-1 were assigned to the *Neodenticula seminae* Zone (NPD12, 0–0.3 Ma) of the Neogene

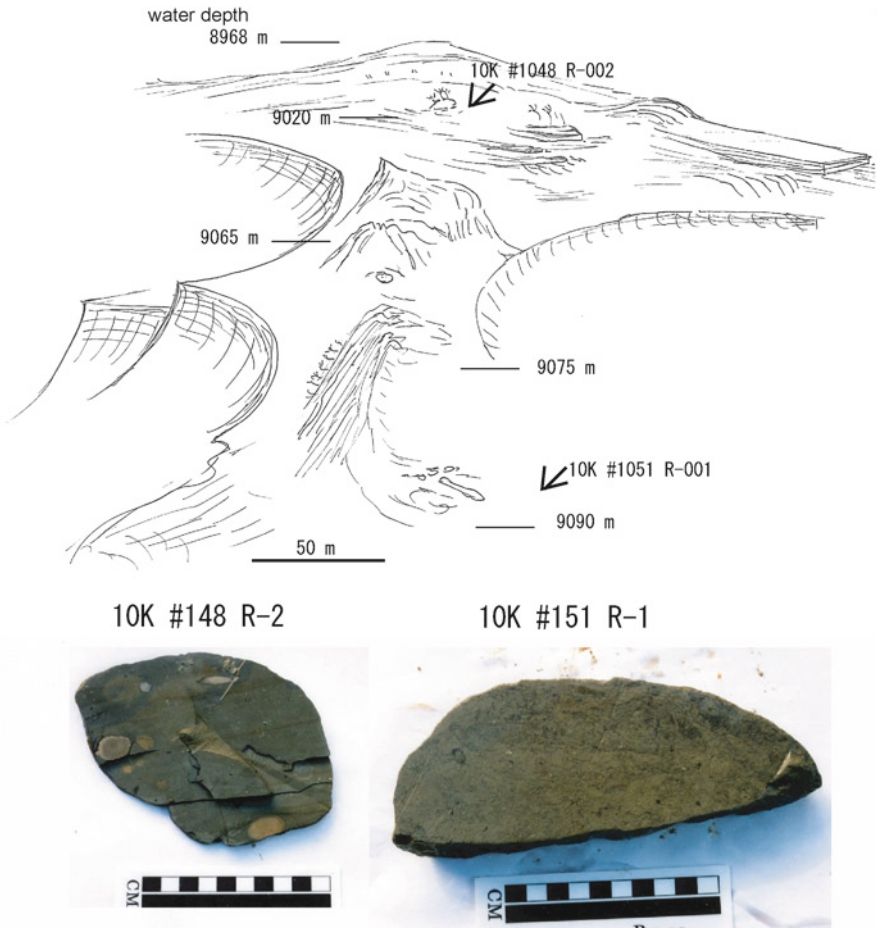

Fig. 6 Topographic sketch (*top*) of the dive area of ROV *KAIKO-10K* dive 148 from videotape, and photos of rock samples (*bottom*). Both rock samples are diatomaceous mudstone. Sample 10K#151 R-001 yielded middle Miocene diatoms. Sample 10K#148 R-002 was barren, but the similar lithologies of the two samples suggest they may correlate

North Pacific diatom zonation (Akiba 1986), on the basis of the presence of *Neodenticula seminae* without *Proboscia curvirostris*. This assignment is supported by the absence of *Thalassiosira jouseae*, for which the last known occurrence was at 0.3 or 0.4 Ma. Four of these samples (10K#148 R1-5 (11, 12), 10K#150 C-2, and 10K#151 C-1) contained warm-water marker diatoms, so we also used the low-latitude diatom biostratigraphy of Barron (1985) for them. The occurrence of *Fragilaropsis doliolus* (=*Pseudoeunotia doliolus*) and the lack of *Nitzschia reinholdii* allowed the assignment of these samples to the *P. doliolus* Zone (NTD17, 0–0.6 Ma) of the low-latitude diatom zonation. These samples contained reworked Miocene and Pliocene diatoms. The Miocene diatoms included *Actinocyclus ingens* f. *ingens*,

Table 1 Diatom zones and estimated ages from subsea samples

Samples	Diatom zones		Estimated age (Ma)	Remarks
	NPD	NTD		
10K#148, R-2	–	–	–	diatom fragments
10K#148, R1-5, 2	NPD12	–	0–0.3	–
10K#148, R1-5, 5	NPD12	–	0–0.3	–
10K#148, R1-5, 11	NPD12	NTD17	0–0.3	–
10K#148, R1-5, 12	NPD12	NTD17	0–0.3	–
10K#150, C-1	NPD12	–	0–0.3	–
10K#150, C-2	NPD12	NTD17	0–0.3	–
10K#151, C-1	NPD12	NTD17	0–0.3	–
10K#151, R-1	NPD4A	–	15.2–15.4	D43–D43.2

NPD Neogene North Pacific diatom zones (Akiba 1986; Yanagisawa and Akiba 1998), *NTD*: Neogene low-latitude diatom zones (Barron, 1985)

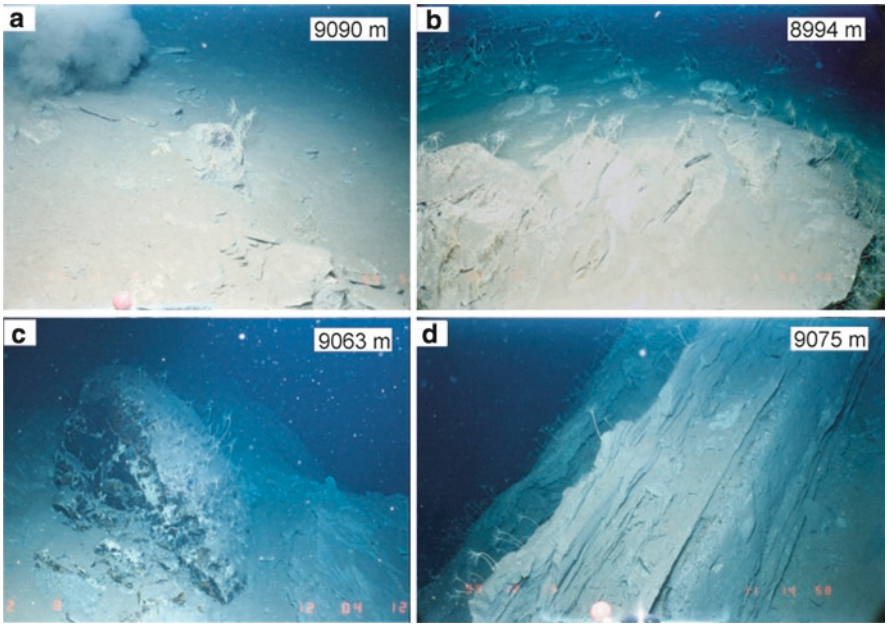

Fig. 7 Outcrop photos taken from ROV *KAIKO-10K*. Depths at which photos were taken are shown. Each view is approximately 3 m wide (Photos courtesy of Tatsuo Oji)

A. ingens f. *nodu*s, *A. ingens* f. *planus*, *Denticulopsis hyalina*, *D. katayamae*, *D. lauta*, *D. praedimorpha*, *D. praehyalina*, *D. simonsenii*, *D. tanimurae*, *D. vulgaris*, *Thalassiosira grunowii*, and others. Reworked species from the Pliocene were *Koizumia tatsunokuchiensis, Neodenticula kamtschatica*, *Thalassiosira antiqua*, and *T. zabelinae*. Fresh-water diatoms such as *Aulacoseira* spp. and *Stephanodiscus* sp. were also recognized in these samples.

Table 2 Diatoms in sediment and rock samples recovered from near the Boso triple junction

	#148	#148	#148	#148	#150	#150	#151	#151
	R1-5	R1-5	R1-5	R1-5	C-1	C-2	C-1	R-1
Sample number 10K	2	5	11	12				
Preservation	P	P	P	P	P	P	P	P
Actinocyclus curvatulus Janisch	1	–	3	+	–	2	2	–
A. ellipticus Grunow	2	–	–	–	–	–	–	–
A. ingens f. *ingens* (Rattray) Whiting et Schrader[a]	6	4	–	–	–	–	1	28
A. ingens f. *nodus* (Baldauf) Whiting et Schrader[a]	1	–	–	–	–	–	–	7
A. ingens f. *planus* Whiting et Schrader[a]	1	–	–	–	–	–	–	2
A. octonarius Ehrenberg	–	–	+	5	3	1	5	5
Actinoptychus senarius (Ehrenberg) Ehrenberg	10	2	1	2	2	9	1	1
A. vulgaris Schmann	–	–	–	–	–	–	+	–
Adoneis pacifica Andrews	–	–	+	–	–	–	–	–
Alveus marinus (Grunow) Kaczmarska et Fryxell	1	+	+	+	5	2	1	–
Asteromphalus sp.	–	–	–	–	1	–	–	–
*Aulacoseira s*pp.[b]	10	1	–	1	–	1	1	–
Azpeitia Africana (Janisch) Fryxell et Watkins	–	–	–	–	–	2	+	–
A. neocrenulata (Van Landingham) Fryxell et Watkins	–	–	–	–	–	–	+	–
A. endoi (Kanaya) Sims et Fryxell[a]	–	–	–	+	–	–	–	–
A. nodulifera (Schmidt) Fryxell et Sims	–	–	–	2	5	4	7	–
A. tabularis (Grunow) Fryxell et Sims	–	–	–	+	1	6	3	–
Bacterosira fragilis (Gran) Gran	–	–	–	4	2	–	2	–
Cavitatus jouseanus (Sheshukova) Williams[a]	+	–	–	–	–	–	–	+
C. lanceolatus Akiba et Hiramatsu[a]	–	–	–	–	–	–	–	+
Cestodiscus sp. (concave)[a]	+	–	–	–	–	–	–	7
Cocconeis costata Gregory	–	–	1	–	–	–	–	–
C. scutellum Ehrenberg	–	1	–	–	–	–	–	–
C. vitrea Brun	–	–	1	1	–	–	–	–
Coscinodiscus lewisianus Greville[a]	–	–	–	–	–	–	–	2
C. marginatus Ehrenberg	1	3	4	–	–	–	–	–
C. radiatus Ehrenberg	–	4	6	6	5	6	9	+
Cyclotella striata (Kützing) Grunow	1	3	2	2	4	3	8	–
Cymatosira debyi Tempére et Brun[a]	–	+	–	–	–	–	–	–
Delphineis miocenica (Schrader) Andrews[a]	–	–	–	–	–	–	–	+
D. surirella (Ehrenberg) Andrews	2	–	+	1	1	–	+	–
Denticulopsis hyaline (Schrader) Simonsen[a]	1	2	1	1	–	1	–	–
D. ichikawae Yanagisawa et Akiba[a]	–	–	–	–	–	–	–	2
D. katayamae Maruyama[a]	–	–	–	–	–	–	1	–

(continued)

Table 2 (continued)

	#148	#148	#148	#148	#150	#150	#151	#151
	R1-5	R1-5	R1-5	R1-5	C-1	C-2	C-1	R-1
Sample number 10K	2	5	11	12				
Preservation	P	P	P	P	P	P	P	P
D. lauta (Bailey) Simonsen[a]	1	–	–	–	–	–	+	+
D. praedimorpha var. *minor* Yanagisawa et Akiba[a]	–	–	–	+	–	–	–	–
D. praedimorpha var. *praedimorpha* Barron ex Akiba[a]	–	–	–	–	–	–	+	–
D. praehyalina Tanimura[a]	1	–	–	–	–	–	–	–
D. simonsenii Yanagisawa et Akiba[a]	–	–	+	–	–	–	1	–
D. tanimurae Yanagisawa et Akiba[a]	1	–	–	1	–	–	–	–
D. vulgaris (Okuno) Yanagisawa et Akiba[a]	1	–	–	+	+	–	+	–
Girdle view of *D. lauta* group[a]	3	–	–	–	–	–	–	–
Diploneis bombus Ehrenberg	–	–	–	–	–	–	–	1
D. smithii (Bébisson) Cleve	–	–	–	–	–	1	–	–
Fragilariopsis doliolus (Wallich) Medlin et Sims	–	–	+	+	–	3	2	–
F. fossilis (Frenguelli) Medlin et Sims[c]	+	–	–	–	–	–	–	–
Hemidiscus cuneiformis Wallich	–	–	–	–	1	1	5	–
Ikebea tenuis (Brun) Akiba[a]	–	+	–	–	–	–	–	–
Koizumia tatsunokuchiensis (Koizumi) Yanagisawa[c]	2	–	–	–	–	–	–	–
Melosira albicans Sheshukova[c]	–	–	–	1	–	–	–	–
Navicula spp.	1	+	–	–	–	–	–	–
Neodenticula kamtschatica (Zabelina) Akiba et Yanagisawa[c]	2	–	1	2	–	+	1	–
N.seminae (Simonsen et Kayana) Akiba et Yanagisawa	+	+	4	1	2	+	1	–
(closed copula of N. seminae)	+	–	1	1	7	8	+	–
Nitzschia interruptestriata Simonsen	–	–	–	+	–	+	–	–
N. koloczeckii Grunow	–	–	–	–	–	1	–	–
N. reinboldii Kanaya ex Barron et Baldauf[c]	+	–	–	–	–	–	+	–
N. rolandii Schrader emend. Koizumi[a]	–	–	+	–	–	–	–	–
N. sicula (Castracane) Hustedt	–	–	–	+	–	2	–	–
Odontella aurita (Lyngobye) Agardh	–	1	+	+	–	1	1	–
Paralia sulcata (Ehrenberg) Cleve	7	8	2	+	15	9	8	7
Planifolia tribranchiata Ernissee[a]	–	–	–	–	–	–	–	2
Proboscia barboi (Brun) Jordan et Priddle[c, a]	1	–	–	1	–	–	–	–
Pseudopodosira elegans Sheshukova[a]	–	–	–	+	–	–	–	–
Pseudotriceratium punctatum (Relfs) Simonsen	–	–	–	–	–	–	1	–
Rhaphoneis scalaris Ehrenberg	1	–	–	–	–	–	–	–
Rhizosolenia hebetate f. *hiemalis* Gran	–	1	2	+	–	4	1	–
R. styliformis Brightwell	–	–	–	–	–	1	–	–

(continued)

Table 2 (continued)

	#148	#148	#148	#148	#150	#150	#151	#151
	R1-5	R1-5	R1-5	R1-5	C-1	C-2	C-1	R-1
Sample number 10K	2	5	11	12				
Preservation	P	P	P	P	P	P	P	P
Stellarima microtrias (Ehrenberg) Hasle et Sims	–	–	–	–	–	–	–	+
Stephanopyxis spp.	9	5	2	2	–	1	+	6
Stephanodiscus sp.[b]	4	–	–	–	–	–	–	–
Thalassionema bacillaris (Heiden) Kolbe	–	–	–	–	3	1	1	–
T. nitzschioides (Grunow) H. et M. Peragallo	22	27	30	32	27	25	13	21
T. nitzschioides var. *parva* Heiden et Kolbe	–	–	2	2	7	–	–	–
T. obtuse (Grunow) Andrews[a]	–	–	–	–	–	–	–	1
Thalassiosira antique (Grunow) Cleve–Euler[c]	1	2	2	–	–	–	–	–
T. convexa Muchina[c]	–	–	–	+	–	1	–	–
T. eccentrica (Ehrenberg) Cleve	–	–	–	4	–	–	–	–
T. gravida f. *fossilis* Jousė	1	15	25	20	–	–	16	–
T. grunowii Akiba et Yanagisawa[a]	–	–	1	–	–	–	–	–
T. leptopus (Grunow) Hasle et Fryxell[a]	–	2	1	–	–	–	2	-
T. oestrupii (Ostenfeld) Proshkina-Labrenko s.1.	–	4	+	2	1	2	1	–
T. praeconxexa Burckle	–	–	2	–	–	–	–	–
T. trifulta Fryxell	–	–	–	–	–	–	+	–
T. zabelinae Jousé[c]	1	–	–	1	–	–	–	–
T. spp.	3	15	7	6	15	10	5	–
Thalassiothrix longissima Cleve et Grunow	1	–	–	+	–	+	+	–
Trochosira spinosa Kitton[a]	–	–	+	–	–	–	–	8
Total number of valves counted	100	100	100	100	100	100	100	100
Resting spore of *Chaetoceros*	11	28	35	45	30	35	17	4

[a] extinct taxa (Miocene)
[b] fresh water taxa
[c] extinct taxa (Pliocene)

3.2.2 Middle Miocene Sample

Sample 10K#151 R-1 yielded *Denticulopsis lauta* and *D. ichikawae*, but not *D. hyalina*, indicating the *D. lauta* Zone (NPD4A) of the Neogene North Pacific diatom zonation (Fig. 8). In addition, the presence of *Cavitatus lanceolatus* and *Actinocyclus ingens* cf. *nodus* without *Denticulopsis okunoi* indicates a depositional age between the last occurrence of *D. okunoi* (D43, 15.4 Ma) and the last occurrence of *C. lanceolatus* (D43.2, 15.2 Ma).

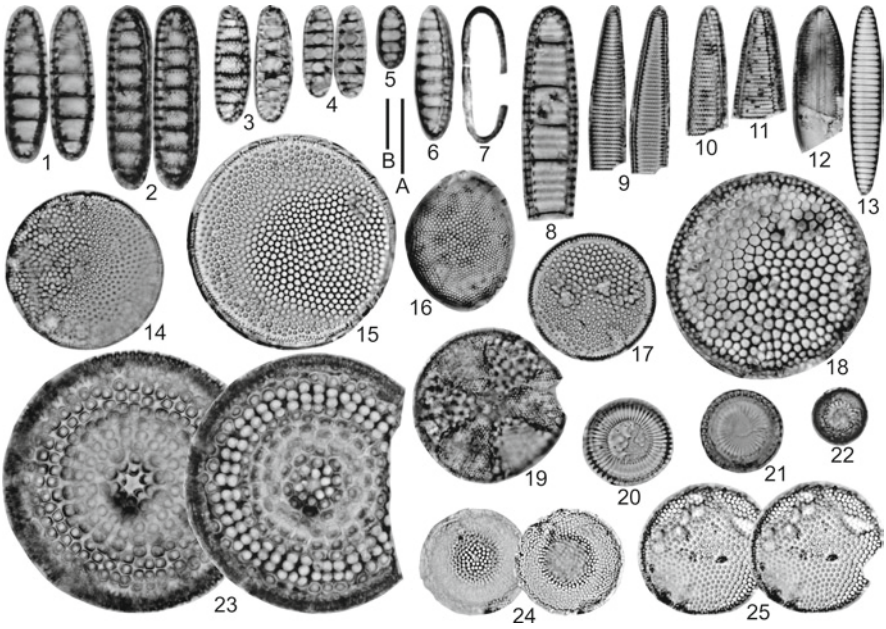

Fig. 8 Photomicrographs of diatoms from sediment and rock samples collected near the Boso triple junction. Scale bars are 10 μm (scale A applies for micrographs 1–8 and scale B applies for micrographs 9–25). *1*, *Denticulopsis hyalina* (Schrader) Simonsen (#148, R1-5, 11); *2*, *Denticulopsis lauta* (Bailey) Simonsen (#148, R1-5, 12); *3*, *Denticulopsis praedimorpha* var. *praedimorpha* Barron ex Akiba (#151, C-1); *4*, *Denticulopsis praedimorpha* var. *minor* Yanagisawa et Akiba (#148, R1-5, 12); *5*, *Neodenticula kamtschatica* (Zabelina) Akiba et Yanagisawa (#148, R1-5, 2); *6*, *Neodenticula kamtschatica* (#148, R1-5, 12); *7*, *Neodenticulina seminae* (Simonsen et Kanaya) Akiba et Yanagisawa (closed copula) (#148, R1-5, 2); *8*, *Neodenticula seminae* (#151, C-1); *9*, *Fragilariopsis doliolus* (Wallich) Medlin et Sims (#148, R1-5, 11); *10*, *Alveus marinus* (Grunow) Kaczmarka et Fryxell (#148, R1-5, 2); *11*, *Nitzschia reinholdii* Kanaya ex Barron et Baldauf (#151, C-1); *12*, *Cavitatus lanceolatus* Akiba et Hiramatsu (#151, R-1); *13*, *Nitzschia sicula* (Castracane) Hustedt (#151, C-2); *14*, *Azpeitia neocrenulata* (Van Landingham) Fryxell et Watkins (#151, C-1); *15*, *Azpeita africana* (Janisch) Fryxell et Watkins (#151, C-1); *16*, *Hemidiscus cuneiformis* Wallich (#150, C-1); *17*, *Azpeitia tabulais* (Grunow) Fryxell et Sims (#148, R1-5, 12); *18*, *Azpeita nodulifera* (Schmidt) Fryxell et Sims (#150, C-1); *19*, *Actinoptychus senarius* (Ehrenberg) Ehrenberg (#150, C-1); *20*, *Cyclotella striata* (Kutzing) Grunow (#148, R1-5, 12); *21*, *Paralia sulcata* (Ehrenberg) Cleve (#151, R-1); *22*, *Trochosira spinosa* Kitton (#148, R1-5, 11); *23*, *Actinocyclus ingens* f. *nodus* (Baldauf) Whiting et Schrader (#151, R-1); *24*, *Bacterosira fragilis* (Gran) Gran (#148, R1-5, 12); *25*, *Thalassiosira antiqua* (Grunow) Cleve-Euler var. 1 (#148, R1-5, 11)

3.3 Summary of Age of Samples

Sample #151 R-1 was assigned to the *Denticulopsis lauta* Zone (NPD4A). According to Watanabe and Takahashi (1997, 2000), this diatom zone corresponds to the lower part of the Kinone Formation of the Miura Group on the Boso Peninsula (Fig. 9).

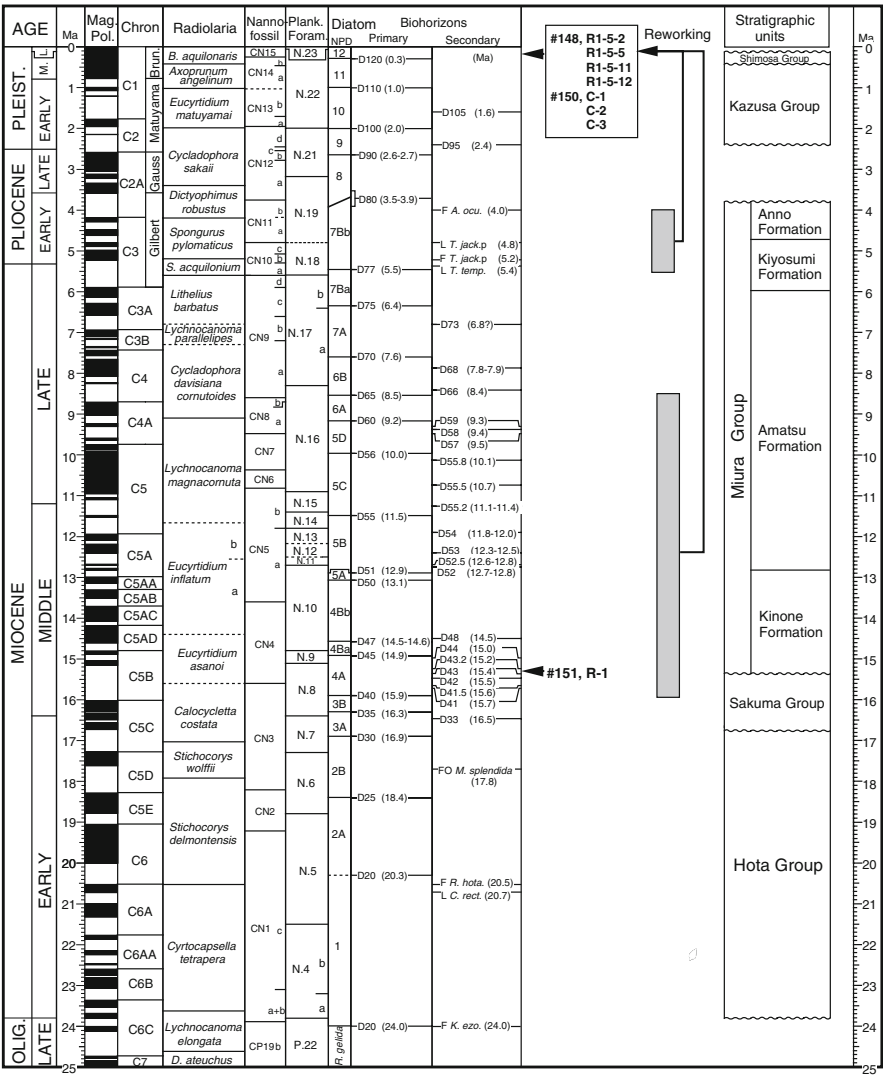

Fig. 9 Chronostratigraphy of the Neogene sequence near the Boso triple junction (Magnetic polarity time scale from Cande and Kent (1995) and Berggren et al. (1995); radiolarian zones from Motoyama (1996) and Riedel and Sanfilippo (1978); *nannofossil* zones from Okada and Bukry (1980); planktonic foraminiferal zonation from Blow (1969); diatom zones from Yanagisawa and Akiba (1998))

The ages of all the other samples analyzed were 0–0.3 Ma, but they also contained reworked Miocene and Pliocene species (Fig. 9). The stratigraphic range of the reworked Miocene diatoms was within the interval from the *D. lauta* Zone (NPD4A) to the *D. katayamae* Zone (NPD 6A); most were in either the *D. lauta* Zone (NPD4A) or the *D. hyalina* Zone (NPD4B). No

reworked species were seen from either the late Miocene *Thalassionema schraderi* Zone (NPD6B) or *Rouxia californica* Zone (NPD7A). The reworked Pliocene species were mostly *Neodenticula kamtschatica,* but not its descendant *N. koizumii,* which is limited to the late Pliocene, suggesting that the reworked Pliocene species were mainly from lower Pliocene sediments. There were no reworked early Pleistocene species.

In summary, all the diatoms in the seven Pleistocene to Holocene samples were from the *Neodenticula seminae* Zone (NPD 12), and four of them correlated to the *Pseudoeunotia doliolus* Zone (NTD 17), which implies an age of 0–0.3 Ma. Sample #151 R-1 was the only markedly older sample; it was assigned to the *Denticulopsis lauta* Zone (NPD 4A), which is of early middle Miocene age (15.2–15.4 Ma).

3.4 Correlation to the Marine Rocks of the Izu Forearc

A submarine geologic map (Fig. 10) published by the Geological Survey of Japan (1990) covers the area of the Boso triple junction, and the accompanying cross section passes through the triple junction. The seafloor ages shown on the map were interpreted from numerous single-channel seismic profiles and dredged samples. The Oligocene to lower Miocene sedimentary rocks (marked Pg) lie on the Taito Spur, which borders the Katsuura Basin on the landward side of the triple junction. The Pg rock unit can be traced from the Bonin Islands in the south to the Boso Peninsula in the north. The map also shows a small area of rocks (marked N and D in Fig. 10) that represent the present-day accretionary prism. This rock assemblage might correlate with the rock sampled during our ROV dives.

4 Tectonic Synthesis: Summary and Conclusion

Diatomaceous mudstone samples of middle Miocene age (15.2–15.4 Ma) were recovered from the toe of the landward slope on the Honshu-arc side of the Boso triple junction. Other samples of slope sediments and rocks were much younger (0–0.3 Ma, Quaternary). The Quaternary sediments and rocks are probably part of the present-day accretionary prism. According to the subsea video footage, these strata have undergone complex deformation; there is an alternating sequence of steep and shallow dips that suggests a collisional thrust-and-fold structure.

The deep-sea rocks of Miocene age that we sampled are diatomaceous mudstones of the same age as the Kinone Formation on Boso Peninsula. The deep-sea sediments may have been deposited over a wide area from the Boso Peninsula to the forearc of the Izu-Bonin trench. The rocks in the latter area may have been incorporated in the triple junction area during formation of an accretionary prism. A Miocene formation such as that we sampled, or its equivalent, may be distributed over a wide area from

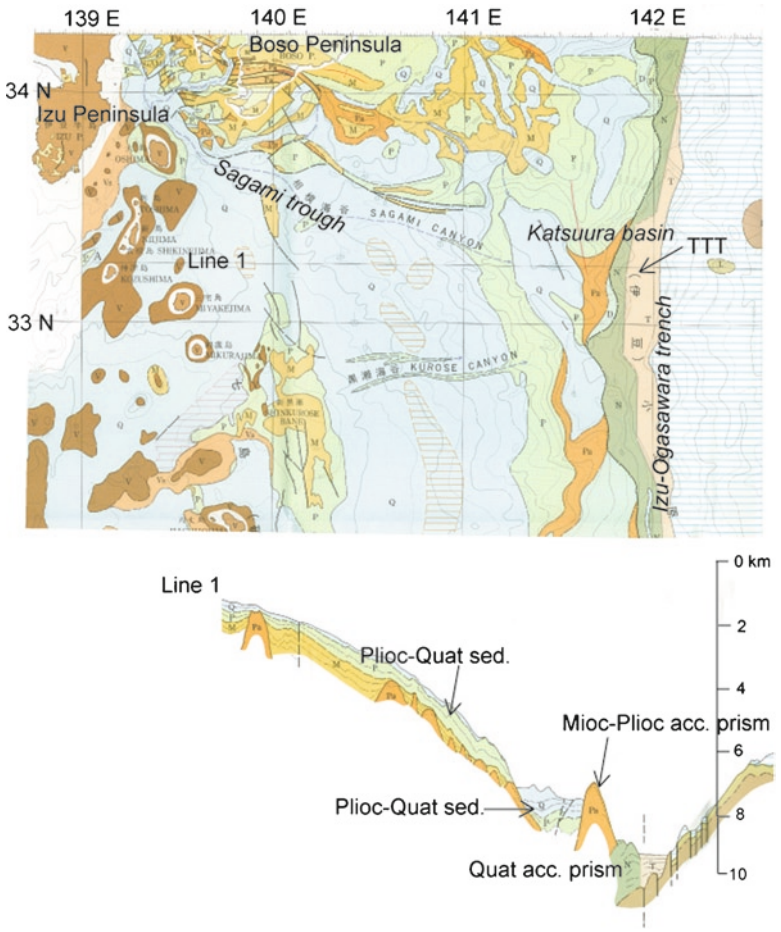

Fig. 10 Geologic map of the subsea area from the Sagami trough to the Boso triple junction (Adapted from Geological Survey of Japan (1990)). The *dark yellow rock* unit Pg may correspond to Paleogene to middle Miocene beds that are partly equivalent to the Kinone Formation on the Boso Peninsula. Yellow units are middle to late Miocene age. The blue unit D, immediately west of the triple junction, represents the present-day accretionary prism and the green unit R corresponds to the Neogene accretionary prism at the landward toe of the Izu-Bonin trench (Copyright permission from Geological Survey of Japan #60635500-A-20110119-002)

the Bonin Islands to the Boso Peninsula, and may be the Oligocene to lower Miocene rock unit (Pg) shown on the submarine geologic map of Fig. 10. We conclude that the Boso triple junction area hosts a sequence of trench-fill sediments that has accumulated between the easternmost margin of the Izu forearc and the easternmost Nankai trough since the Miocene. However, recent instability at the Boso triple junction is characterized by repetitive episodes of development and subsequent collapse of a ponded basin close to the accretionary prism that are intimately associated with the development of the Boso triple junction system.

The data presented and reviewed here are sufficient to put forward a preliminary model to explain the complex tectonic relationships at the Boso triple junction. However, considerably more detailed research is needed to substantiate the broad conclusions presented here.

Acknowledgments We thank the captain and crew of R/V *KAIREI* and the operation team of ROV *KAIKO-10K* during JAMSTEC cruise KR99-11. Thanks are extended to our shipmates, in particular the vice-chief scientist, Prof. Masao Nakanishi. Dive photos were provided courtesy of Prof. Tatsuo Oji. The early manuscript was reviewed and revised by Profs. Kurtis Burmeister, Yasuhiro Yamada, and Ryo Anma, to whom we are grateful.

References

Akiba F (1986) Middle Miocene to Quaternary diatom biostratigraphy in the Nankai Trough and Japan Trench, and modified Lower Miocene through Quaternary diatom zones for middle-to-high latitudes of the North Pacific. In: Kagami H, Karig DE, van Coulbourn WT et al (eds) Initial reports of the deep sea drilling project, vol 87. U. S. Govt. Printing Office, Washington, D C, pp 393–481

Barron JA (1985) Miocene to Holocene planktic diatoms. In: Bolli HM (ed) Plankton stratigraphy. Cambridge University Press, Cambridge, pp 763–809

Berggren WA, Kent DV, Swisher CCIII, Abury M-P (1995) A revised Cenozoic geochronology and chronostratigraphy. SEPM Spec Publ 54:129–212

Blow WH (1969) Late Middle Eocene to Recent planktonic foraminiferal biostratigraphy. In: Brönnimann P, Renz HH (eds) Proceedings of the first international conference on planktonic microfossils (Geneva, 1967), vol 1. EJ Brill, Leiden, pp 199–421

Cande SC, Kent DV (1995) Revised calibration of geomagnetic polarity time scale for the Late Cretaceous and Cenozoic. J Geophys Res 100:6093–6095

Geological Survey of Japan (1990) Marine geological map (1:1,000,000), No.17. Izu-Ogasawara, Geological Survey Japan

Hamano Y (1987) Reliability and stability of TTT triple junctions. Tectonics 6:47–51

Hanamura Y, Ogawa Y (1993) Layer-parallel faults, duplexes, imbricate thrust and vein structures of the Miura Group: key to understanding the Izu fore-arc sediment accretion to the Honshu forearc. Isl Arc 3:126–141

Hirono T, Ogawa Y (1998) Duplex arrays and thickening of accretionary prisms - an example from Boso Peninsula, Japan. Geology 26:779–782

Huchon P, Labaume P (1989) Central Japan triple junction: a three-dimensional compression model. Tectonophysics 160:117–133

Hydrographic Department (1988) Bathymetric chart off Boso. Maritime Safety Agency, Tokyo

Iwabuchi Y, Asada A, Kato Y (1990) Multichannel seismic profiling of the Boso triple junction. J Jpn Soc Mar Surv Technol 2:29–38

KAIKO I Research Group (1986) Topography and structure of Trenches around Japan – Data Atlas of Franco-Japanese Kaiko Project, Phase 1. University of Tokyo Press, Tokyo, p 305

Kanamatsu T, Herrero-Berver E (2006) Anisotropy of magnetic susceptibility and paleomagnetic studies in relation to the tectonic evolution of the Miocene-Pleistocene accretionary sequence in the Boso and Miura Peninsulas, central Japan. Tectonophysics 418:131–144

Lallemant SJ, Le Pichon X, Thoue F, Henry P, Saito S (1996) Shear partitioning near the central Japan triple junction: the 1923 great Kanto earthquake revisited – I. Geophys J Int 126:871–881

Le Pichon X, Huchon P (1987) Central Japan triple junction revisited. Tectonics 6:35–45

Michiguchi Y (2008) Formation process and mechanism of chaotic blocks in the Nisizaki Formation, southern Boso Peninsula. J Geol Soc Japan 114:461–473

Mori R, Ogawa Y (2005) Transpressional tectonics of the Mineoka Ophiolite Belt in a trench-trench-trench-type triple junction, Boso Peninsula, Japan. Isl Arc 14:571–581

Mori R, Ogawa Y, Hirano N, Tsunogae T, Kurosawa M, Chiba T (2011) Role of plutonic and metamorphic block exhumation in a forearc ophiolite mélange belt: An example from the Mineoka belt, Japan. GSA Special Paper 480, Mélange (in press)

Motoyama I (1996) Late Neogene radiolarian biostratigraphy in the subarctic Northwest Pacific. Micropaleontology 42:221–262

Muraoka S, Ogawa Y (2011) Recognition of trench-fill type accretionary prism: Thrust anticlines, duplexes and chaotic deposits of Pliocene-Pleistocene Chikura Group, Boso Peninsula, Japan. GSA Special Paper 480, Melange (in press)

Nakamura K et al (1987) Oblique and near collision subduction, Sagami and Suruga troughs – preliminary results of the French-Japanese Kaiko cruise, Leg 2. Earth Planet Sci Lett 83:229–242

Niitsuma N (1996) The trench-trench-trench triple junction and tectonic evolution of Japan. Geosci Rep Shizuoka Univ 23:1–8

Ogawa Y, Taniguchi H (1988) Geology and tectonics of the Miura-Boso Peninsulas and the adjacent area. Mod Geol 12:147–168

Ogawa Y, Seno T, Tokuyama H, Akiyoshi H, Fujioka K, Taniguchi H (1989) Structure and development of the Sagami trough and off-Boso triple junction. Tectonophysics 160:135–150

Ogawa Y, Takami Y, Takazawa S (2008) Oblique subduction in island arc collision setting: unique sedimentation, accretion and deformation processes in the Boso TTT-type triple junction area, NW Pacific. In: Draut AE, Clift PD, Scholl DW (eds) Formation and applications of the sedimentary record in arc collision zones. Geol Soc Am Spec Pap 436:155–170

Oji T, Ogawa Y, Hunter AW, Kitazawa K (2009) Discovery of dense aggregations of stalked crinoids in Izu-Ogasawara trench, Japan. Zool Sci 26:406–408

Okada H, Bukry D (1980) Supplementary modification and introduction of code numbers to the low-latitude coccolith biostratigraphic zonation (Bukry, 1973, 1975). Mar Micropaleontol 5:321–325

Pautot G et al (1987) Deep-sea submersible survey in the Suruga, Sagami and Japan Trenches: preliminary results of the 1985 Kaiko cruise, Leg 2. Earth Planet Sci Lett 83:300–312

Renard V et al (1987) Trench triple junction off central Japan – preliminary results of French–Japanese 1984 Kaiko cruise, Leg 2. Earth Planet Sci Lett 83:243–256

Riedel WR, Sanfilippo A (1978) Stratigraphy and evolution of tropical radiolarians. Micropaleontogy 23:61–93

Seno T, Ogawa Y, Tokuyama H, Nishiyama E, Taira (1989) Tectonic evolution of the triple junction off central Honshu for the past 1 million years. Tectonophysics 160:91–116

Soh W, Taira A, Tokuyama H (1988) A trench fan in the Izu-Ogasawara Trench on the Boso Trench triple junction, Japan. Mar Geol 82:235–249

Soh W, Tokuyama H, Fujioka K, Kato S, Taira A (1990) Morphology and development of a deep-sea meandering canyon (Boso Canyon) on an active plate margin, Sagami Trough, Japan. Mar Geol 91:227–241

Taira A, Tokuyama H, Soh W (1989) Accretion tectonics and evolution of Japan. In: Ben-Avraham Z (ed) The evolution of the Pacific ocean margins. Oxford University Press, Oxford, pp 100–132

Watanabe M, Takahashi M (1997) Diatom biostratigraphy of the Middle Miocene Kinone and lower Amatsu Formations, Boso Peninsula, central Japan. J Jpn Assoc Petroleum Technol 62:215–225

Watanabe M, Takahashi M (2000) Diatom biostratigraphy of the middle Miocene marine sequence of the Kawadani section in the Kamogawa area, Boso Peninsula, central Japan. J Geol Soc Jpn 106:489–500

Yamamoto Y, Kawakami S (2005) Rapid tectonics of the Late Miocene Boso accretionary prism related to the Izu–Bonin arc collision. Isl Arc 14:178–198

Yanagisawa Y, Akiba F (1998) Revised Neogene diatom biostratigraphy for the northwest Pacific around Japan, with an introduction of code numbers for selected diatom biohorizons. J Geol Soc Jpn 106:395–414

Rifting Structure of Central Izu-Ogasawara (Bonin) Arc Crust: Results of Seismic Crustal Imaging

Narumi Takahashi, Mikiya Yamashita, Shuichi Kodaira, Seiichi Miura, Takeshi Sato, Tetsuo No, Kaoru Takizawa, Yoshiyuki Tatsumi, and Yoshiyuki Kaneda

Abstract We obtained seismic velocity structures for two crustal profiles across the central Izu-Ogasawara (Bonin) intra-oceanic arc using a multichannel reflection system and ocean-bottom seismographs. The crust beneath the volcanic front in this region is less than 20 km thick. A middle crustal layer (P-wave velocity *Vp* ~6 km/s), representing andesitic proto-continental crust, is found beneath the volcanic front, the rear-arc, the fore-arc basin and Ogasawara Ridge. Crust with 15–20 km thick beneath the fore-arc basin may have formed in Paleogene time because it is covered with thick sediments. Crustal thinning by rifting is seen between the volcanic front and the rear-arc, where the crustal thickness is ~15 km, the lower crust has high *Vp* (>7.3 km/s) and there are normal faults in the shallow crust. Rifted crust also occupies a broad area in the eastern Shikoku Basin. The central Izu-Ogasawara arc has been affected by four rifting episodes compared to two for the northern Izu-Ogasawara arc. The volume of the entire arc crust in the central region is ~20% greater than in the northern region, even though the crust

N. Takahashi (✉), M. Yamashita, S. Kodaira, S. Miura, T. Sato, T. No, and Y. Kaneda
Institute for Research on Earth Evolution (IFREE), Japan Agency
for Marine-Earth Science and Technology (JAMSTEC),
Showa-machi 3173-25, Kanazawa-ku, Yokohama 236-0001, Japan
e-mail: narumi@jamstec.go.jp; mikiya@jamstec.go.jp; kodaira@jamstec.go.jp;
miuras@jamstec.go.jp; tsato@jamstec.go.jp; not@jamstec.go.jp; kaneday@jamstec.go.jp

K. Takizawa
Institute for Research on Earth Evolution (IFREE), Japan Agency for Marine-Earth
Science and Technology (JAMSTEC), Showa-machi 3173-25, Kanazawa-ku,
Yokohama 236-0001, Japan
and
Nippon Marine Enterprises, Ltd, Showa-machi 3173-25, Kanazawa-ku,
Yokohama 236-0001, Japan
e-mail: takizawak@jamstec.go.jp

Y. Tatsumi
Institute for Research on Earth Evolution (IFREE), Japan Agency
for Marine-Earth Science and Technology (JAMSTEC),
Natsushima-Cho 2-15, Yokosuka 237-0061, Japan
e-mail: tatsumi@jamstec.go.jp

Y. Ogawa et al. (eds.), *Accretionary Prisms and Convergent Margin Tectonics in the Northwest Pacific Basin*, Modern Approaches in Solid Earth Sciences 8,
DOI 10.1007/978-90-481-8885-7_4,

beneath the volcanic front is the thinnest in the entire Izu-Ogasawara arc, as shown by previous studies. The thinner crust in this region reflects greater extension here relative to the arc to the north.

Keywords Crustal rifting • Crustal production rate • MCS • OBS

1 Introduction

The Izu-Ogasawara (Bonin) arc, the northern part of the Izu-Bonin-Mariana arc (IBM) arc, is an intra-oceanic arc formed by interaction between two oceanic crusts without involvement of continental crust (e.g., Taylor 1992; Stern 2010). It is thus an excellent location to study how juvenile arcs create mature continental crust with an intermediate and andesitic composition (Tatsumi et al. 2008). Because the middle crust in the Izu-Ogasawara arc has a P-wave velocity (*Vp*) of 6 km/s, similar to the average *Vp* of continental crust (Suyehiro et al. 1996; Takahashi et al. 1998), it is commonly inferred that subduction has produced andesitic proto-continental crust, and that this early stage of continental crustal growth can be studied here.

According to Tatsumi et al. (2008), crustal growth in this setting occurs as follows: (1) Subduction causes melting in the mantle wedge, producing basaltic magmas that rise and are underplated at the bottom of the crust beneath the volcanic front. (2) Basaltic melts are repeatedly differentiated and remelted producing dense olivine-rich cumulates, tonalitic middle crust, and complementary restites. (3) The differentiated basalts and restites make up the lower arc crust and uppermost mantle, respectively. (4) Dense materials of crustal origin must be recycled back into the mantle, as shown by comparisons of the petrologic model and volumes of the crustal layers identified from seismic studies (Takahashi et al. 2007a; Tatsumi et al. 2008).

The amount of crustal growth depends on the volume of the underplated basaltic magmas and the heat supply. Kodaira et al. (2007a) showed that rhyolitic magmas are found where the crust is characterized by low average *Vp*, and Tatsumi et al. (2008) suggested that the andesitic middle crust is consumed to produce rhyolitic magmas and complementary restites. However, continuous crustal differentiation to produce continental middle crust requires a continuous input of heat. Production of felsic middle crust likely stops without heat brought by melts of basaltic material.

This simple petrologic scenario should be modified because the Izu-Ogasawara arc has experienced not only underplating of basaltic melts, as shown by many papers, but also crustal rifting and spreading since construction of the Eocene arc at 50 Ma (e.g., Okino et al. 1994; Taylor 1992). It is well known that the Shikoku and Parece Vela Basins were produced by back-arc opening between the current IBM arc and the Kyushu Palau Ridge (Okino et al. 1994, 1998). It is also well known that crustal rifting occurred at the volcanic front and within both rear-arc

and fore-arc regions. Kodaira et al. (2008) showed that the crustal thickness variations beneath the rear-arc side correlate with that beneath the volcanic front, and they concluded that crustal rifting occurred along a NNE–SSW trend between the volcanic front and the rear-arc. Based on their across-arc structural model of the southern Izu-Ogasawara arc, Takahashi et al. (2009) showed that crustal thinning occurred both between the volcanic front and the rear-arc, and between the volcanic front and the fore-arc. They also found that such crustal thinning accompanying the rifting process is associated with lower crust with high *Vp* (>7 km/s).

Kodaira et al. (2007b) showed that the central Izu-Ogasawara arc has thinner crust than the northern part, and that the proportions of upper, middle, and lower crustal layers are similar. Two possible reasons for the thin crust in the central arc are that (1) it has lower magma production rates than the northern arc and that (2) most crustal growth occurred early in the history of both segments, but rifting in the central arc caused thinner crust. To evaluate these possibilities, we carried out seismic studies in the central part of the Izu-Ogasawara arc using ocean-bottom seismographs (OBSs) and modeled the velocity structure across this area. In this paper, we show two *Vp* models of the central Izu-Ogasawara arc and discuss crustal structure from the Izu-Ogasawara Trench on the east to the Shikoku Basin on the west. We also show multichannel seismic (MCS) reflection profiles along these lines. We use these profiles to better understand rifting of the central Izu-Ogasawara arc, and thence to address the question of why the arc crust here is so thin.

2 Data Acquisition

Seismic data to construct crustal structures were collected during cruises of R/V *Kaiyo* and R/V *Kairei* of the Japan Agency for Marine-Earth Science and Technology. Cruise KY06–09 of R/V *Kaiyo* (Aug. 3 to Sept. 1, 2006) deployed 95 OBSs along line IBr9 on Fig. 1 (Takahashi et al. 2007b), and cruise KR07-13 of *Kairei* (Sept. 30 to Oct. 29, 2008) deployed 102 OBSs along line IBr10 (Miura et al. 2008).

Line IBr9 runs from the Izu-Ogasawara Trench to the eastern foot of the Kinan Seamount chain in the Shikoku Basin. It traverses the northern tip of the Ogasawara Trough, the northern foot of Nichiyo Seamount (volcanic front), the northern part of the Sofu Trough, An'ei and Kan'ei Seamounts in the rear-arc region, and the Kinan escarpment. Line IBr10 is parallel to and south of line IBr9 and runs from the Izu-Ogasawara Trench to the Kinan Seamount chain through the northern part of Ogasawara Ridge, the northern part of the Ogasawara Trough, the northern foot of Suiyo Seamount (volcanic front), the northern tip of the Nishinoshima Trough, the northern foot of Kyowa Seamount in the rear-arc region, and the Kinan escarpment. Both lines cross the volcanic front where it has relatively thin crust (Kodaira et al. 2007b).

Both cruises used arrays of eight airguns with total capacity of 12,000 cu. in. (1,500 cu. in. each). Shot intervals were 200 m along both lines. Air pressure sent to the airguns was 2,000 PSI.

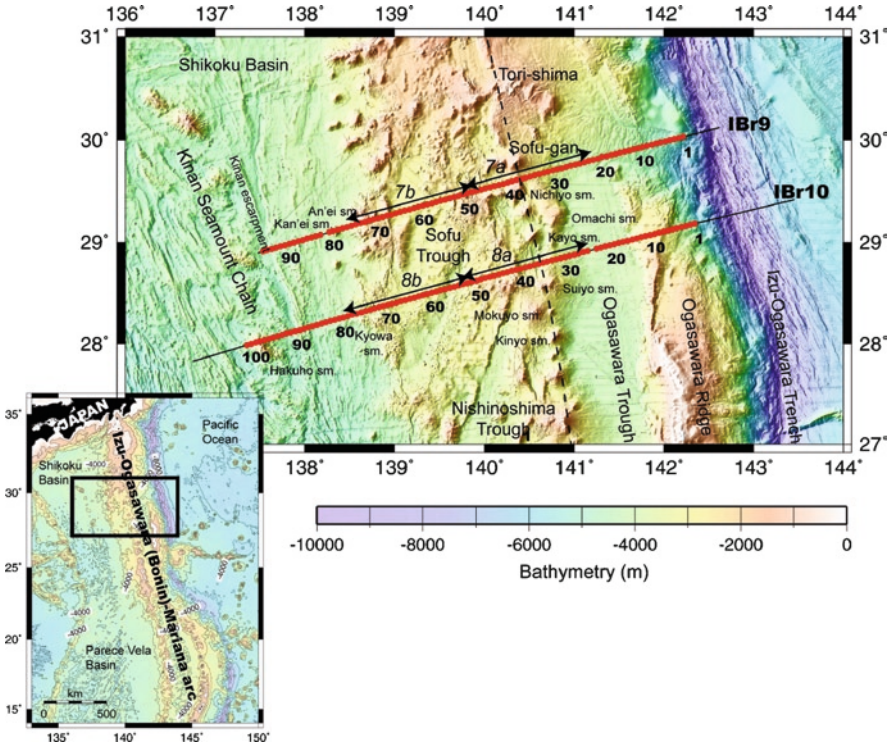

Fig. 1 Location of seismic lines IBr9 and IBr10 across the central Izu-Ogasawara arc. *Black lines* indicate shot positions, *red circles* indicate OBS locations, *dashed line* indicates the current volcanic front, and *numerals* indicate numbers of OBSs. *Lines with arrows* indicate areas shown in Figs. 7 and 8. *Inset* shows bathymetry of IBM arc and a *rectangle* indicating the map area

In addition, we carried out MCS reflection surveys in 2006 and 2007. We used the same airgun source and a 204-channel streamer, with total length of approximately 5 km and with group interval of 25 m, installed on R/V *Kairei* (Kaiho et al. 2007; No et al. 2008). We used conventional procedures for data analysis: amplitude recovery, minimum-phase conversion, predictive deconvolution, common midpoint (CMP) sort, dip moveout, velocity analysis, normal moveout correction, CMP stacking, and Kirchhoff time migration. The reflection sections are of good quality, confirming shallow sedimentary structures and deformation. We traced the shape of the basement bathymetry and incorporated it into the *Vp* models.

All OBSs were equipped with three-component geophones (vertical and two perpendicular horizontal components), using gimbal mechanisms and a hydrophone sensor. Natural frequencies of the geophones were 4.5 Hz. Our OBSs were originally designed by Kanazawa and Shiobara (1994), and the digital recorder with a 16-bit analog-to-digital converter was developed by Shinohara et al. (1993). In this study, the sampling interval was 10 ms.

3 Data and Modeling Procedure

Data quality of the seismic profiles was generally good, and first arrivals could be traced out to a distance of 70–100 km (Fig. 2). To trace refractions and reflections, we applied a 5–15 Hz band-pass filter and a deconvolution filter when necessary. In particular, the deconvolution filter helped in picking reflections, because these were overprinted by reverberations of strong first arrivals. Figure 2 shows examples of OBS record sections for vertical components on the two lines. Most sections display refractions through the crust and upper mantle as well as reflections from the Moho.

For modeling, we applied tomographic inversion using first arrivals (GeoCT-II, Zhang et al. 1998) and diffraction-stack migration for reflections (Fujie et al. 2006). This inversion has the advantage of allowing structural imaging without phase identification, although we have to determine if the phases are refractions or reflections. If reflections are mistakenly picked as refractions, a zone of artificially low *Vp* is imposed on the *Vp* model. In particular, shadow zones without refractions likely broaden in regions having severe structural variations like those of arc crust. We paid special attention to pick first arrivals that corresponded to refraction. In addition, the tomographic inversion easily creates an artificial *Vp* anomaly when an inappropriate initial model is compared with the real structure. The OBS interval of 5 km might be too large to determine shallow structure; therefore, we applied a *Vp* model based on MCS velocity analysis to construct the shallow part of the initial model.

We carried out tomographic inversions with the following steps. We first applied a tomographic inversion using first arrivals out to 20 km from each OBS. We applied a second tomographic inversion using results from the first inversion and first arrivals out to 60 km from each OBS. Then we applied a third inversion using the second result and all first arrivals. We did this to avoid cases with artificial anomalies introduced to satisfy time differences between far-offset first arrivals and synthetics. Using a final model based on the third inversion, we picked and mapped reflections from the Moho (PmPs) and the top of the subducting plate. Ideally, regions having sharp *Vp* gradients should correspond to reflections, which are imaged by mapping picked reflections. However, this situation is rare because of the small number of deep refractions and the variation in ray density. Therefore, we constructed a new initial model using the mapped image of reflections and the final model of the second inversion. At this step, the initial model has a sharp *Vp* gradient matching the distribution of reflection points obtained by the diffraction-stack migration technique. Then the final inversion was performed again using the new initial model and all first arrivals, and a new reflection image was also constructed by the diffraction-stack migration technique.

We applied this procedure to data from both lines. To compare the crustal images for these lines, it is important to use common specifications for *Vp* modeling. Because the images depend on the ray densities, comparing the two images is not always straightforward. To check the resolution of the obtained image, we used a checkerboard test (Fig. 3c) with the following steps. First, we constructed a *Vp* model having perturbations of 5% using the initial model from the last inversion, and

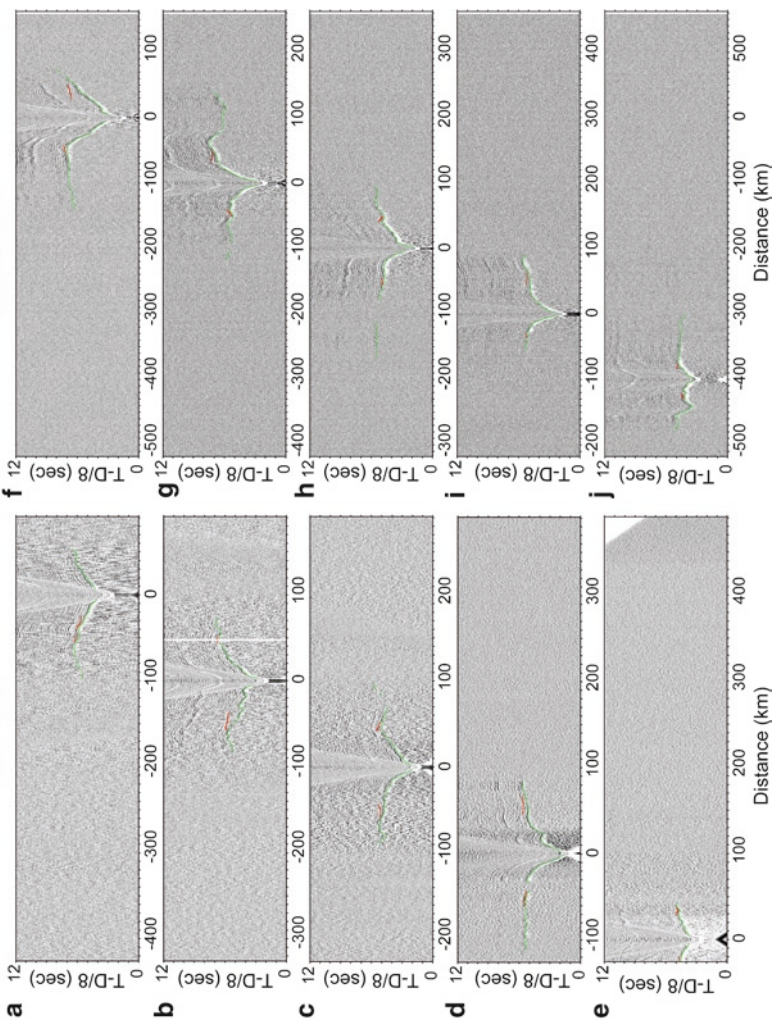

Fig. 2 Examples of OBS records processed with deconvolution and bandpass filters (5–15 Hz). *Green and red lines* indicate picked traveltimes for first arrivals and PmPs, respectively. (**a**) OBS11 on line IBr9. (**b**) OBS31. (**c**) OBS51. (**d**) OBS71. (**e**) OBS91. (**f**) OBS11 on line IBr10. (**g**) OBS31. (**h**) OBS51. (**i**) OBS71. (**j**) OBS91

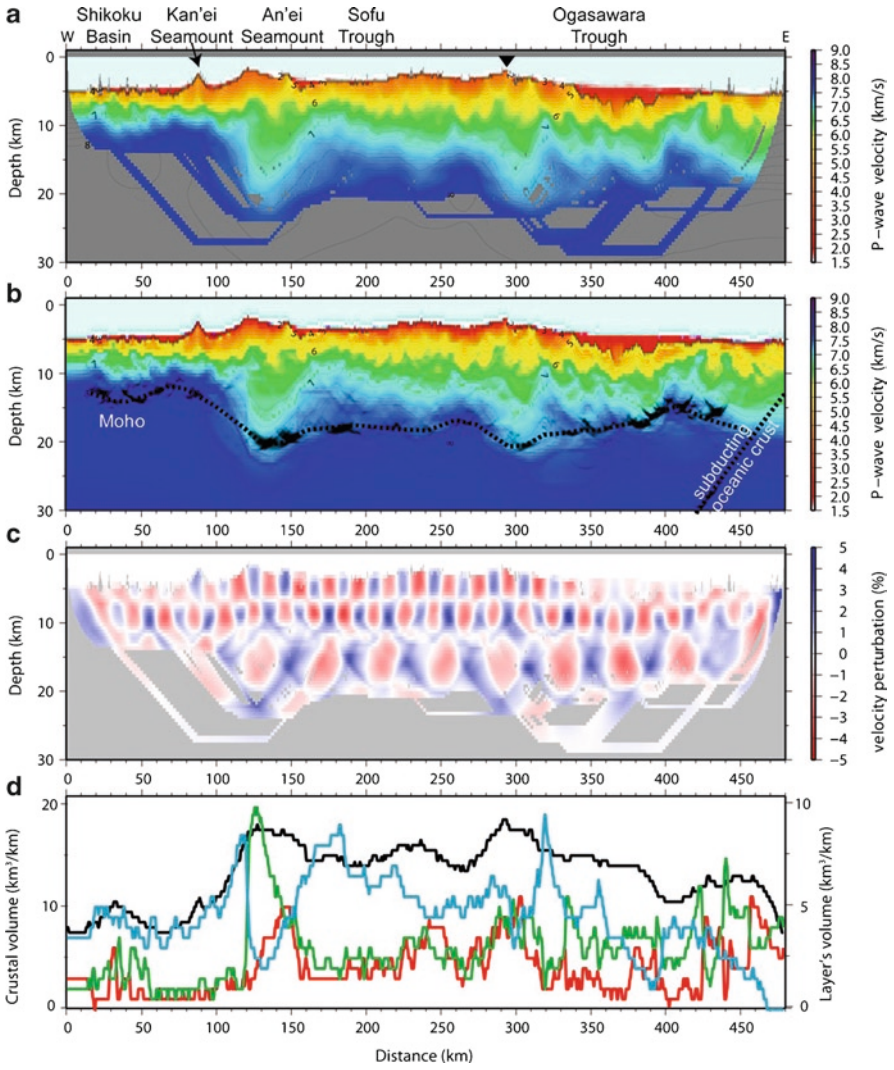

Fig. 3 Results of tomographic inversion for line IBr9. (**a**) Final *Vp* image. *Gray area* has too few ray paths for resolution. *Black triangle* shows the volcanic front. (**b**) Reflective traces of Moho and the *top* of the Pacific plate mapped on the tomographic image. (**c**) Results of checkerboard test. (**d**) 2-dimensional volumes of each crustal layer. *Black line* is profile of entire crust (*scale on left*); *blue, green, and red lines* respectively indicate profiles of the lower part of the lower crust (*Vp* 7.0–7.5 km/s), the upper part of the lower crust (*Vp* 6.5–7.0 km/s) and the middle crust (*Vp* 6.0–6.5 km/s) (*scale on right*)

synthetic traveltimes were calculated with the same offsets as the real ones for the picked first arrivals. Then, we performed a tomographic inversion using the synthetic traveltimes and the initial model from the last inversion. We constructed checkerboard patterns by subtracting velocities for the final model from those on the model having perturbations. Test grids were 10×5 km down to 12 km depth, and 20×10 km for depths below 12 km. This means that the *Vp* variation of the

same scale as that of the checkerboard grid could be derived. We estimated *Vp* accuracy using the differences between a given *Vp* perturbation (5% in this study) and the result of the checkerboard test. If a *Vp* perturbation of 3% was obtained for a *Vp* of 6–7 km/s, the accuracy is 0.10–0.15 km/s.

4 Description of Velocity Images

In this section, we introduce the *Vp* profiles of lines IBr9 and IBr10 and describe the reliability of the *Vp* models. It is important for understanding the crustal characteristics to specify the Moho. The major interfaces along the two profiles are the Moho and the top of the subducting oceanic crust. For the Moho we selected a continuous interface along contours between 7.5 km/s and 8.0 km/s, using a diffraction-stack migrated image of the reflections on the *Vp* image.

4.1 Line IBr9

Line IBr9 runs from the Pacific plate to the Shikoku Basin. The four panels of Fig. 3 show the final *Vp* image (Fig. 3a), Moho reflections mapped onto the *Vp* image (Fig. 3b), the result of the checkerboard test (Fig. 3c), and the 2-dimensional volume of each crustal layer along the line (Fig. 3d). This line crosses the Izu-Ogasawara Trench, off the northern tip of Ogasawara Ridge (east of 390 km in Fig. 3), the northern part of the Ogasawara Trough (310–390 km), the northern foot of Nichiyo Seamount in the volcanic front (295 km), the Sofu Trough (160–210 km), the southern foot of An'ei Seamount in the rear-arc (120–150 km), and Kan'ei Seamount (90 km). This line crosses a volcanic front with relatively thin crust as published by Kodaira et al. (2008).

The crust is thickest (18–19 km) beneath the volcanic front and the southern foot of An'ei Seamount (Fig. 3d). Crustal thickness decreases toward the fore-arc to about 12 km beneath the northern tip of Ogasawara Ridge. Between the volcanic front and the rear-arc, it is 15–17 km thick, with almost constant thickness beneath the Sofu Trough. Beneath the Shikoku Basin, the crust thins to approximately 8 km, similar to that of typical oceanic crust (White et al. 1992).

Upper crust with *Vp* of 5–6 km/s is about 3–4 km thick between the fore-arc and the rear-arc. Middle crust with *Vp* of 6.0–6.5 km/s is thickest beneath the fore-arc basin (380–390 km), the volcanic front (280–310 km), a seamount at the eastern edge of the Sofu Trough (220–260 km), and the southern foot of An'ei Seamount in the rear-arc (120–160 km), as shown by the red line in Fig. 3d. The middle crust is thin beneath the western Ogasawara Trough, the Sofu Trough, and the Shikoku Basin. Lower crust with *Vp* of 6.5–7.5 km/s is thick beneath the rear-arc and the volcanic front. Although the thickness of the lower crust is almost constant from the rear-arc to the volcanic front, *Vp* in this layer varies. In the lower crust beneath the rear-arc (120–160 km) and the volcanic front (280–310 km), areas with *Vp* of 6.5–7.0 km/s (green line in Fig. 3d) are thicker than areas of 7.0–7.5 km/s (blue line in Fig. 3d).

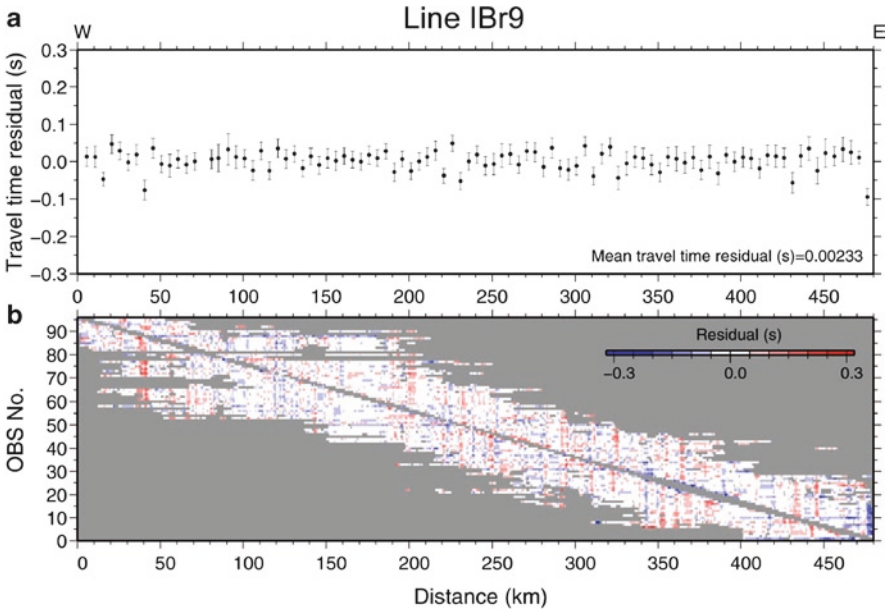

Fig. 4 Comparison between observed and synthetic traveltimes for line IBr9. (**a**) Mean traveltime residuals for each OBS. (**b**) Traveltime residuals for each shot at each OBS

On the other hand, lower crust beneath the western rear-arc (100–120 km), the Sofu Trough and its eastern margin (160–260 km), the western Ogasawara Trough (310–380 km), and off the northern tip of Ogasawara Ridge (400–420 km) has thicker areas with *Vp* of 7.0–7.5 km/s (blue line in Fig. 3d) than areas of 6.5–7.0 km/s (green line in Fig. 3d). Uppermost mantle velocities also vary, being slow (~7.5 km/s) beneath the rear-arc, the volcanic front, and the western Ogasawara Trough. The velocity of the uppermost mantle is also somewhat slow (7.6 km/s) beneath the northern tip of Ogasawara Ridge. The Shikoku Basin has normal mantle *Vp* of 8.0 km/s.

We picked first arrivals for 87,224 traces and used these for the tomographic inversion to model the crustal structure. Final traveltime residuals were approximately 25 ms and were quite small for each OBS (Fig. 4). According to the result of the checkerboard test (Fig. 3c), the resolved maximum depth ranges from 15 km (beneath the Shikoku Basin) to 25 km (beneath the Ogasawara Trough). The resolved area covers the entire region of the crust and uppermost mantle. The recovery of the *Vp* perturbation was maximum 2–4% on the background velocity of 6.0–7.5 km/s, and the *Vp* accuracies were within 0.10–0.25 km/s.

4.2 Line IBr10

Line IBr10 is about 100 km south of line IBr9, running from the Pacific plate to the Shikoku Basin. Figure 5 shows the final *Vp* image (Fig. 5a), mapping of reflections from the Moho on the *Vp* image (Fig. 5b), the result of the checkerboard test (Fig. 5c),

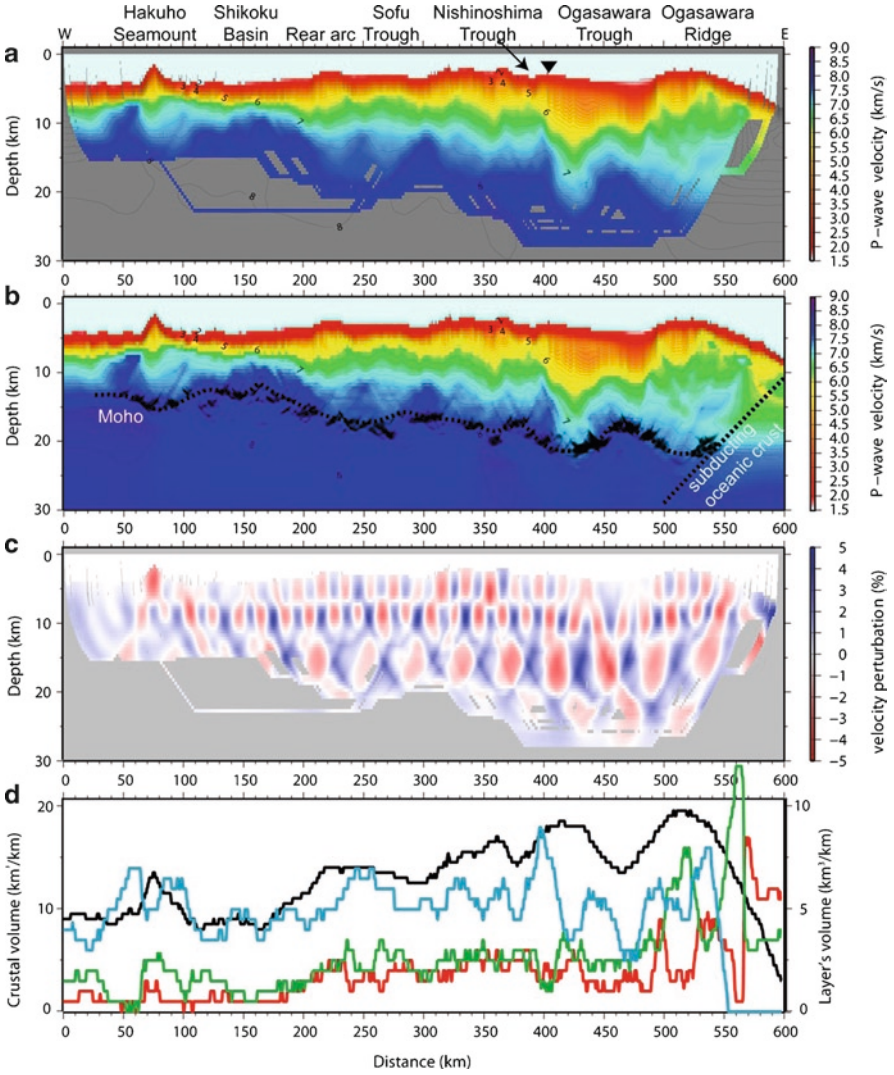

Fig. 5 Results of tomographic inversion for line IBr10. See Fig. 3 for explanation

and the two-dimensional volume of imaged layers. From east to west, this line crosses the northern Ogasawara Ridge (east of 490 km in Fig. 5), the Ogasawara Trough (410–480 km), the northern foot of Suiyo Seamount in the volcanic front (405 km), the northern tip of the Nishinoshima Trough (380–400 km), an unnamed seamount (360–370 km), the Sofu Trough (240–360 km), the southern foot of Kita-Kyowa Seamount in the rear-arc (210–230 km), the eastern Shikoku Basin (100–200 km), and Hakuho Seamount (60–90 km) in the Kinan Seamount Chain. This line also crosses the volcanic front where the crust is thin as shown by Kodaira et al. (2008).

Crustal thickness along line IBr10 varies between 5 and 20 km. The areas of thickest crust, approximately 20 km and 18 km, are beneath the western Ogasawara Trough and Ogasawara Ridge, respectively. Crustal thickness decreases gradually from 18 km to 15 km from the volcanic front toward the rear-arc, except for basins between the Sofu Trough and the Nishinoshima Trough. Beneath the Shikoku Basin, the crust is thin, approximately 8 km. Crustal thickness increases toward Hakuho Seamount.

Upper crust with *Vp* of 5–6 km/s thickens from the unnamed seamount to the Ogasawara Trough, and has a maximum thickness of 5 km. Middle crust with *Vp* of 6.0–6.5 km/s (red line in Fig. 3d) is found from beneath the rear-arc to Ogasawara Ridge, and its thickness does not vary much. Lower crust has a relatively constant thickness of 7 km between the rear-arc and the Ogasawara Trough; however, its velocities change laterally. The western Ogasawara Trough (410–430 km) and Ogasawara Ridge (490–520 km) show relatively low velocities in the lower crust and large areas with *Vp* of 6.5–7.0 km/s (green line in Fig. 5d). The lower crust between the unnamed seamount and the rear-arc has almost constant thickness of 5 km, with *Vp* of 6.5–7.0 km/s. On the other hand, the eastern Ogasawara Trough (440–470 km), the volcanic front (390–400 km), the region between the rear-arc and the Sofu Trough (200–280 km), and the eastern margin of the Shikoku Basin (140–170 km) have large areas with *Vp* of 7.0–7.5 km/s (blue line in Fig. 5d). The uppermost mantle *Vp* is generally 7.8–8.0 km/s.

To construct the *Vp* image, we picked first arrivals for 19,743 traces and used them for the tomographic inversion. Final traveltime residuals were approximately 60 ms and those of each OBS were small (Fig. 6). The checkerboard test (Fig. 5c) shows

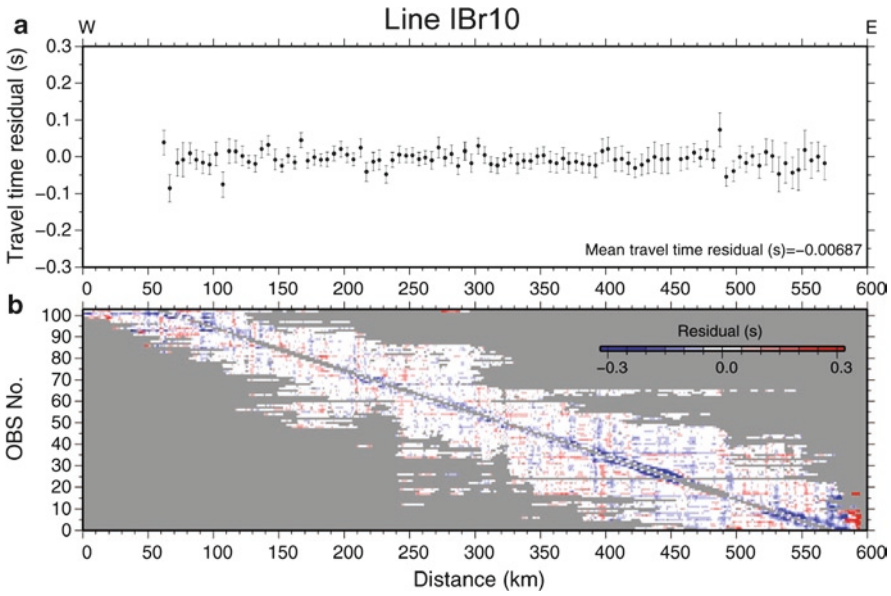

Fig. 6 Comparison between observed and synthetic traveltimes for line IBr10. (**a**) Mean traveltime residuals for each OBS. (**b**) Traveltime residuals for each shot at each OBS

that the resolved depth reaches from 15 km (beneath the Shikoku Basin) to 25 km (beneath the Ogasawara Trough), covering all of the crust and uppermost mantle. The recovery of the *Vp* perturbation was maximum 2–4% on the background *Vp* of 6.0–7.5 km/s, and the *Vp* accuracies were 0.10–0.25 km/s, similar to those for line IBr9.

5 Discussion

In this section, we describe the structural commonalities and differences between lines IBr9 and IBr10 of the central Izu-Ogasawara arc. The most important variations are in the distribution of middle crust with *Vp* of 6.0–6.5 km/s and lower crust with *Vp* > 7.3 km/s, as described in Sect. 4. We also summarize the distribution of rifted lower crust with *Vp* > 7.3 km/s. We confirm from the reflection images that the rifted crust is associated with deformation including normal faults and rotation of crustal blocks. Finally, we construct a tectonic scenario for the central Izu-Ogasawara arc that accounts for its structural differences from the northern Izu-Ogasawara arc.

5.1 Structural Commonalities and Differences

Crustal models for the IBM arc have been constructed by many authors (e.g., Suyehiro et al. 1996; Takahashi et al. 2007a, b, 2008, 2009; Calvert et al. 2008; Kodaira et al. 2007a, 2007b, 2008). Although the Eocene arc is slightly different (Takahashi et al. 2009; Kodaira et al. 2010), these models are similar, including a middle crust with *Vp* of 6.0–6.5 km/s, thick and heterogeneous lower crust, and slow uppermost mantle. The middle crust contributes most to crustal thickening, and thick arc crust always has thick middle crust (Kodaira et al. 2007a).

Our modeling identified common thick arc crust with *Vp* of 6.0–6.5 km/s beneath the western Ogasawara Trough in the fore-arc region, the arc region between the volcanic front and the rear-arc, and the rear-arc. Rifted crust with a high *Vp* lower crust (*Vp* > 7.3 km/s) is found beneath the eastern Ogasawara Trough, the bathymetric low just behind the volcanic front, the Sofu Trough, and the eastern Shikoku Basin. These characteristics are similar to those described by previous studies.

Differences in crustal structure can be seen beneath the volcanic front and the eastern Shikoku Basin. The crustal structure beneath the volcanic front along line IBr9 is similar to those of previous studies. Although the crust here is thin (15–17 km), it has a middle crust with *Vp* of 6.0–6.5 km/s and a proportion of middle crust similar to that seen for the northern Izu-Ogasawara arc. Much of the lower crust here has *Vp* of 7.0–7.3 km/s. However, the volcanic front along line IBr10 overlies lower crust with *Vp* > 7.3 km/s, similar to lower crust found in rifted regions. Because middle crust with *Vp* of 6.0–6.5 km/s exists along line IBr10 and because the crustal thickness is approximately 12 km, the crust has arc rather than oceanic character. This part of line IBr10 is at the northern tip of the Nishinoshima Trough, and we infer that this crust was strongly affected by rifting to form the

trough. We also identified a structural difference in the Shikoku Basin as shown by the two lines. Beneath line IBr9, high-velocity lower crust occupies a narrow region between the rear-arc and the eastern Shikoku Basin, whereas high-velocity lower crust along line IBr10 occupies a relatively broad region.

5.2 Origin of the Arc Crust

Crustal growth in the Izu-Ogasawara arc has occurred since 50 Ma. The first arc crust formed in Eocene time (e.g., Taylor 1992) and included boninites. This ancient arc crust is exposed on Ogasawara Ridge, where the boninitic arc shows a different velocity structure (Takahashi et al. 2009). The arc beneath the current volcanic front is composed of thick middle crust with *Vp* of 6.0–6.5 km/s, heterogeneous lower crust, and low-velocity uppermost mantle. However, the ancient middle crust of Ogasawara Ridge has *Vp* of approximately 6.4–6.5 km/s (e.g., Takahashi et al. 2009). The Aleutian arc also has high-Mg andesite materials (Kelemen et al. 1993), and the 6.0 km/s layer there is thin (Holbrook et al. 1999). In addition, the Ogasawara Ridge has been found to have a narrow (<10 km) region of thin crust (approximately 7 km), similar to the thickness of oceanic crust (Kodaira et al. 2010). This implies that an ophiolite-forming process is one candidate for the formation of boninitic fore-arc crust, as suggested by Pearce et al. (1984).

After Eocene arc construction, crust continued to be constructed in Oligocene time. Magnetic anomaly studies (Yamazaki and Yuasa 1998) suggest that the Oligocene arc lies beneath the fore-arc basin between the current volcanic front and the Eocene arc. Oligocene arc rocks are also found in the rear-arc region (Kodaira et al. 2008). Although arc crustal formation appears to have ceased during opening of the Shikoku and Parece Vela Basins, arc crust formation began again in the Miocene (15 Ma; Straub et al. 2010). The region affected by Miocene arc igneous activity was broad; volcanism moved from the current rear-arc region to the current volcanic front (Ishizuka et al. 2006), where subsequent arc volcanism has occurred.

We interpreted the ages of arc construction according to this history of arc magmatic activity. Crust beneath the fore-arc basin corresponds to the Oligocene arc, which is covered with sediments that have not been intruded by younger magmas. The wide region of arc crust between the rear-arc and the volcanic front provides evidence that arc igneous activity has occurred there since Oligocene time. The arc structure with *Vp* of 6.0–6.5 km/s is consistent with the results of Kodaira et al. (2008), and the rear-arc construction probably occurred in Oligocene time.

5.3 History of the Rifted Crust

Here we discuss the consistency between the time-migrated MCS reflection sections and the distribution of modeled high-velocity lower crust identified beneath the Ogasawara Trough, the bathymetric low immediately behind the volcanic front, the Sofu Trough, and the Shikoku Basin. Despite the NNE–SSW orientation of rifts in

this region, not an optimal direction for the ENE–WSW seismic lines to reveal high-angle faults, evidence for crustal extension should nevertheless be apparent in the *Vp* models and reflection images. In this section, we also discuss our interpretation of the relative timing of rift-related deformation.

Rifted regions of the Izu-Ogasawara arc that are underlain by high-velocity lower crust show clear Moho reflections. High-velocity lower crust may form by underplating mafic materials or it may reflect the presence of serpentinized mantle (White et al. 2003). Mantle rocks undergo serpentinization by reaction with water at low temperatures, and serpentinization is likely to be gradational with depth. If this were the case, the Moho should not be a sharp reflector. In fact, continental margins where serpentinization of the mantle is confirmed by drilling (e.g., ODP Leg 173 Shipboard Scientific Party 1998) have poorly defined Mohos (e.g., Dean et al. 2000). High-velocity lower crust in the Izu-Ogasawara arc is not likely to be serpentinite because it is underlain by a sharp Moho. We conclude that high-velocity lower crust in the Izu-Ogasawara arc has originated from underplating by basaltic magmas.

Crustal rifting often creates normal faults and causes tilting of shallow crustal blocks. We confirmed such deformation in time-migrated reflection images of data from the MCS surveys (Figs. 7 and 8). On line IBr9, we identified deformed areas in front of the volcanic front, immediately behind the volcanic front, and in the Sofu Trough (Fig. 7). The area in front of the volcanic front shows clear normal faults that extend to the seafloor, indicating recent faulting (CDP 33000–34400). The area behind the volcanic front is covered by thin sediments, but some of the normal faults extend to the seafloor (CDP 29500–31700), again showing that the faulting is recent. The Sofu Trough also has normal faults and tilted crustal blocks and is filled by thick sediments. The eastern part has a thickness of ~0.5 s of sediments (~1 km, CDP 23000–26500). However, the western Sofu Trough has thicker sediments than the eastern part (~1 s; CDP 21400–22700); thus, sedimentation may have started in the west first. The oldest sediments in the deepest part of the western Sofu Trough show a convex-upward shape, and the normal faults in the basin do not appear to cut the old sediments. This may indicate that rifting in this region was coeval with deposition of the older sediments. These images suggest that rifting was activated in eastward order from the western Sofu Trough, the eastern Sofu Trough, the bathymetric low area behind the volcanic front, and the fore-arc in front of the volcanic front.

The reflection images along line IBr10 have similar characteristics (Fig. 8). Normal faults are identified just in front of the volcanic front (CDP 22200–22700), the bathymetric low corresponding to the northernmost Nishinoshima Trough immediately behind the volcanic front (CDP 23000–23700; CDP 25000–26300), and the Sofu Trough (CDP 29500–30200; CDP 31600–35100). The Sofu Trough is filled by thick sediments, thickening toward the west. The bathymetric low along the volcanic front is currently active on its eastern side in proximity to the Sofugan tectonic line. These relationships are similar to those seen along line IBr9.

Kodaira et al. (2008) suggested that rifting occurred between the rear-arc and current volcanic front in Oligocene time. In the central Izu-Ogasawara arc, we identified rifting in two places in the Sofu Trough. Another rift we identified behind the volcanic front corresponds to the Sumisu rift to the north. Another rift we identified

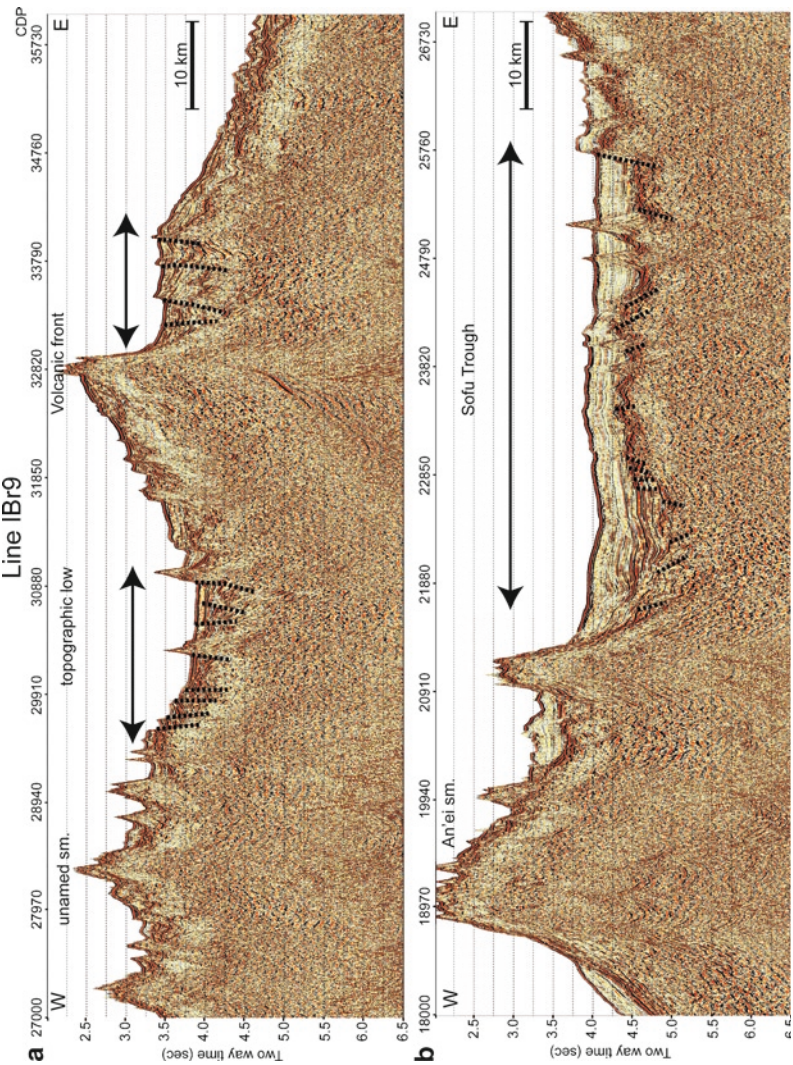

Fig. 7 Time-migrated section obtained from MCS survey data along line IBr9 (location shown on Fig. 1). *Dashed lines* indicate interpretations. *Lines with arrows* indicate regions of rifted crust with normal faults. (**a**) Eastern part of section between the fore-arc basin and the unnamed seamount. (**b**) Western part of section between the Sofu Trough and the rear-arc region

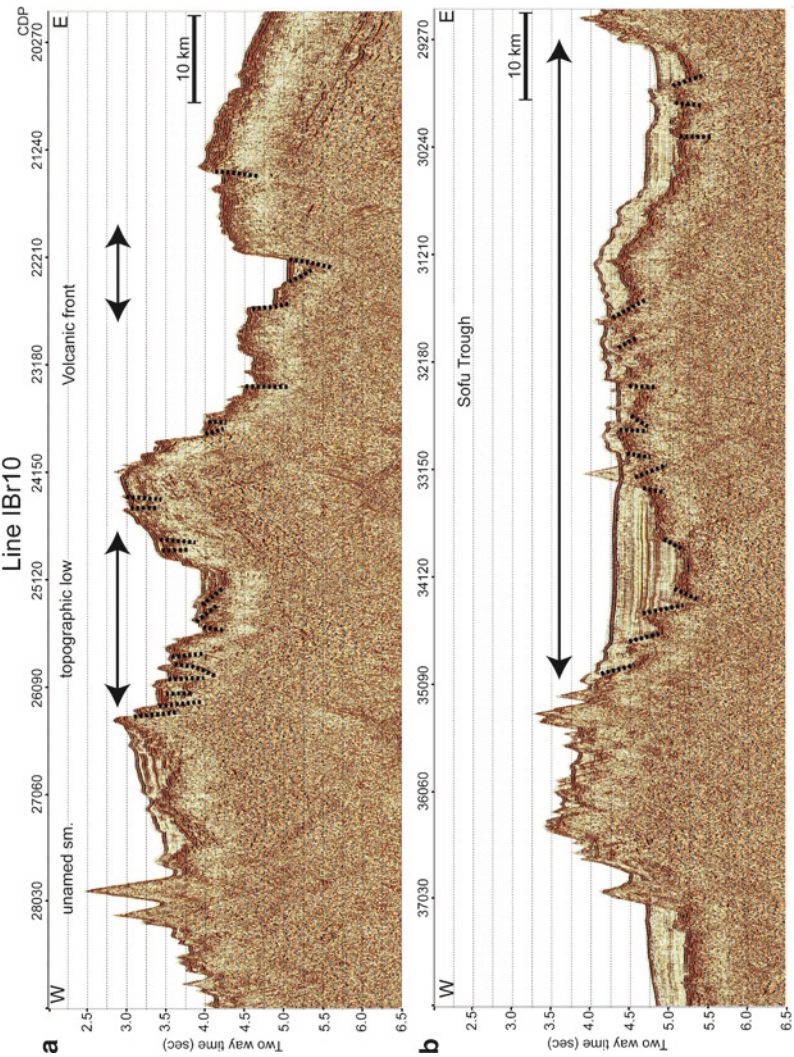

Fig. 8 Time-migrated section obtained from MCS survey data along line IBr10 (location shown on Fig. 1). *Dashed lines* indicate interpretations. *Lines with arrows indicate* regions of rifted crust with normal faults. (**a**) Eastern part of section between the fore-arc basin and the unnamed seamount. (**b**) Western part of section between the Sofu Trough and the rear-arc region

immediately in front of the volcanic front with normal faults exposed on the seafloor is the most recent, and is not identified to the north. Together, our reflection images suggest that rifting occurred four times after Oligocene time, although the details of timing are poorly constrained without drilling data.

5.4 Reason for the Thin Crust in the Central Izu-Ogasawara Arc

Our study has clarified that arc crustal structure extends E–W from the Ogasawara Ridge to the rear-arc region for 390 km and 430 km along lines IBr9 and IBr10, respectively. This is significantly greater than the 300 km width of the northern Izu-Ogasawara arc (Suyehiro et al. 1996). Although it is known that arc materials and high-velocity lower crust are widely distributed underneath the eastern half of the Shikoku Basin (Ishizuka et al. 2006; Takahashi et al. 2010), we calculated the crustal volumes of areas between the rear-arc and trench along both seismic lines by using a procedure similar to that used in the northern Izu-Ogasawara arc by Takahashi et al. (2007a, b). The crustal volumes we estimated along lines IBr9 and IBr10 are 5,563 km^3/km and 6,068 km^3/km, respectively, notably greater than the 4,646 km^3/km estimated for the northern Izu-Ogasawara arc by Takahashi et al. (2007a, b). Thus, the crust is much thinner in the central Izu-Ogasawara arc than it is to the north, but the crustal volume is much larger. These results probably reflect greater extension in the central region. In this study, we identified four episodes of rifting based on seismic-reflection profiles. This contrasts with two known episodes of post-Oligocene rifting in the north and is an indication of more rifting in the central region than in the arc to the north (Fig. 9). Thus the volumetric and seismic-reflection evidence are mutually consistent.

Kodaira et al. (2008) suggested that differences in rear-arc crustal volume between the northern and central Izu-Ogasawara arc segments correlate to that beneath the volcanic front, and they suggested that NNE–SSW rifting occurred between the two segments. Such rifting is consistent with formation of the Sofu and Nishinoshima Troughs. The earliest post-Oligocene rift corresponds to the two-stage rifting identified by this study in the Sofu Trough. There is no evidence for similar early rifting in the northern Izu-Ogasawara arc. Recent rifting in the north, like the Sumisu Rift (post 3 Ma), corresponds to the bathymetric low just behind the volcanic front documented in this study. The latest rifting identified here in front of the volcanic front has no correlative in the northern Izu-Ogasawara arc. Comparing the northern and central Izu-Ogasawara arc segments, the central part exhibits more rifting episodes, which is consistent with the greater width of this arc segment.

We infer from the results of our study that the total volume of crust (~5,000–6,000 km^3/km) and rate of crustal growth (~100–120 km^3/km-m.y.) in the central Izu-Ogasawara arc is ~20% greater than that of the northern part. This estimate is a minimum because it does not take into account arc crust now preserved in the eastern half of the Shikoku Basin and the Kyushu-Palau Ridge. The evidence also

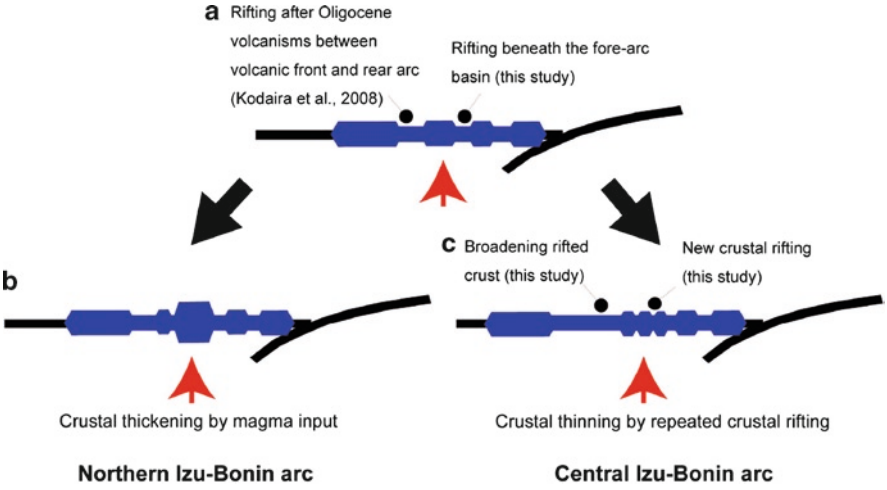

Fig. 9 Schematic diagram of the tectonic history of northern and central segments of the Izu-Ogasawara arc. *Blue regions* show arc crust. *Red arrows* show the volcanic front. In the central arc, the crust beneath the volcanic front has remained thin because of repeated crustal rifting. (**a**) Tectonic situation just after back-arc opening between volcanic front and rear-arc as described by Kodaira et al. (2008). (**b**) Current situation in the northern part. (**c**) Current situation in the central part

shows that there has been more rifting in the central part than in the northern part. Therefore, we suggest that the origin of the thin crust beneath the current volcanic front is repeated crustal rifting.

6 Conclusion

We imaged the crustal structure of the central Izu-Ogasawara arc by tomographic inversion and diffraction-stack migration techniques as well as MCS reflection images processed from 204-channel streamer data. The *Vp* images show that this arc segment has thinner crust (~15 km) than the northern Izu-Ogasawara arc (~25 km). Nevertheless, the volume of arc crust is ~20% greater than that estimated for the northern segment (Kodaira et al. 2007b). Arc crust in the central arc segment lies beneath Ogasawara Ridge, the fore-arc Ogasawara Trough, the volcanic front, the bathymetric high between the volcanic front and the rear-arc region, and the rear-arc region. Thin rifted crust that is approximately 10 km thick and high-velocity lower crust (>7.3 km/s) is found beneath the Ogasawara Trough, a bathymetric low just behind the volcanic front, the Sofu Trough, and the eastern part of the Shikoku Basin.

In reflection images along the two survey lines across the central arc segment, we identified deformation related to extension, including normal faults and rotated crustal blocks. The resulting rift zones occur in front of the volcanic front, in the bathymetric low just behind the volcanic front, and in the Sofu Trough. In addition,

sedimentary thicknesses in the Sofu Trough reveal different rifting histories for the eastern and western parts of the basin. The western part has thicker sediments and structures indicating that rifting is older there than in the eastern part. Evidence for recent rifting is also seen on both sides of the volcanic front. The rift just behind the volcanic front may correspond to the activity of the Sumisu rift in the northern Izu-Ogasawara arc, and the area in front of the volcanic front is the most recent rift.

We suggest that the crust is so thin beneath the central Izu-Ogasawara arc because it has been repeatedly rifted. The crustal volume of the central arc segment is larger than that of the northern segment, which has much thicker crust beneath the volcanic front. This means that the basic scenario of crustal growth is similar for the Izu-Ogasawara arc, but that extension histories vary significantly along strike.

Acknowledgement We greatly thank R. J. Stern and M. Ishikawa for providing us with helpful comments. Their comments significantly improved this paper. We also thank Norio Shimomura for his support in the data analysis and Go Fujie for seismic tools that he developed. We also appreciate support during data acquisition by the captains and crews of R/V "Kairei" and R/V "Kaiyo", and marine technicians of Nippon Marine Enterprises. This study was funded by the Institute for Research on Earth Evolution, Japan Agency for Marine-Earth Science and Technology, and partially supported by Grant-in-Aid for Creative Scientific Research (19GS0211) and Grant-in-Aid for Scientific Research (B) (20340122).

References

Calvert AJ, Klemperer SL, Takahashi N, Kerr BC (2008) Three-dimensional crustal structure of the Mariana island arc from seismic tomography. J Geophys Res 113:B01406. doi:10.1029/2007JB004939

Dean SM, Minshull TA, Whotmarsh RB, Louden KE (2000) Deep structure of the ocean-continent transition in the southern Iberia Abyssal Plain from seismic refraction profiles: the IAM-9 transect at 40°20'N. J Geophys Res 105:5859–5885

Fujie G, Ito A, Kodaira S, Takahashi N, Kaneda Y (2006) Confirming shark bending of the Pacific plate in the northern Japan trench subduction zone by applying a traveltime mapping method. Phys Earth Planet Inter 157:72–85

Holbrook WS, Lizarralde D, McGeary S, Bangs N, Diebold J (1999) Structure and composition of the Aleutian island arc and implications for continental crustal growth. Geology 27(1):31–34

Ishizuka O, Taylor RN, Milton JA, Nesbitt RW, Yuasa M, Sakamoto I (2006) Variation in the mantle sources of the northern Izu arc with time and space: constraints from high-precision Pb isotopes-. J Volcanol Geotherm Res 156:266–290

Kaiho Y, No T, Yamashita M, Takizawa K, Takahashi N, Kodaira S, Kaneda Y (2007) MCS seismic profiling of an oceanic island arc in the southern Izu-Ogasawara arc-backarc area, -KR0607 cruise-. JAMSTEC Rep Res Dev 5:51–60

Kanazawa T, Shiobara H (1994) Newly developed ocean bottom seismometer. Prog Abstr Jpn Earth Planet Sci Joint Meet 2:240

Kelemen PB, Yogodzinski GM, Scholl DW (1993) Along-strike variation in the Aleutian arc: genesis of high Mg# andesite and implications for continental crust, Inside the Subduction Factory, Geophysical Monograph 138, AGU, 10.1029/138GM11

Kodaira S, Sato T, Takahashi N, Ito A, Tamura Y, Tatsumi Y, Kaneda Y (2007a) Seismological evidences for variation of continental growth along the Izu intra-oceanic arc and its implication for arc volcanism. J Geophys Res 112:B05104. doi:10.1029/2006JB004593

Kodaira S, Sato T, Takahashi N, Miura S, Tamura Y, Tatsumi Y, Kaneda Y (2007b) New seismological constraints on growth of continental crust in the Izu-Bonin intra-oceanic arc. Geology 35:11. doi:10.1130/G23901A, 1031-1034

Kodaira S, Sato T, Takahashi N, Yamashita M, No T, Kaneda Y (2008) Seismic imaging of a possible paleoarc in the Izu-Bonin intraoceanic arc and its implications for arc evolution processes. Geochem Geophys Geosyst 9:Q10X01. doi:10.1029/2008GC002073

Kodaira S, Noguchi N, Takahashi N, Ishizuka O, Kaneda Y (2010) Evolution from fore-arc oceanic crust to island arc crust: a seismic study along the Izu-Bonin fore arc. J Geophys Res 115:B09102. doi:10.1029/2009JB006968

Miura S, Yamashita M, Takahashi N, Kodaira S, Kaneda Y (2008) Wide-angle seismic profiling acrooss the middle Izu-Ogasawara arc –KR07-13 crusie-. JAMSTEC Rep Res Dev 7:19–29

No T, Takizawa K, Takahashi N, Kodaira S, Kaneda Y (2008) Multi-channel seismic reflection survey in the northern Izu-Ogasawara island arc –KR07-09 cruise-. JAMSTEC Rep Res Dev 7:31–41

ODP Leg 173 Shipboard Scientific Party (1998) Drilling reveals transition from continental breakup to early magmatic crust. Eos Trans AGU 79:173–181

Okino K, Shimakawa Y, Nagaoka S (1994) Evolution of the Shikoku basin. J Geomagn Geoelectr 46:463–479

Okino K, Kasuga S, Ohara Y (1998) A new scenario of the Parace Vela basin genesis. Mar Geophys Res 20:21–40

Pearce JA, Lippard SJ, Roberts S (1984) Characteristics and tectonic significance of suprasubduction zone ophiolites, in Marginal Basin Geology, edited by Kokelaar BP and Howell MF. Geol Soc Spec Publ 16:77–94

Shinohara M, Suyehiro K, Matsuda S, Ozawa K (1993) Digital recording ocean bottom seismometer using portable digital audio tape recorder. J Jpn Soc Mar Surv Technol 5:21–31

Stern RJ (2010) The anatomy and ontogeny of modern intra-oceanic arc systems. In: Kusky TM, Zhai Mingguo, Wenjiao Xiao (eds) The evolving continents: understanding processes of continental growth. Geological Society of London, London, Spec Publ 338:7–34

Straub SM, Goldstein SL, Class C, Schmidt A, Gomeztuena A (2010) Slab and mantle controls on the Sr-Nd-Pb-Hf isotope evolution of the post-42 Ma Izu Bonin volcanic arc. J Petrol: 51(5):993–1026. doi:10.1093/petrology/egq009

Suyehiro K, Takahashi N, Ariie Y, Yokoi Y, Hino R, Shinohara M, Kanazawa T, Hirata N, Tokuyama H, Taira A (1996) Continental crust, crustal underplating, and low-Q upper mantle beneath an oceanic island arc. Science 272:390–392

Takahashi N, Suyehiro K, Shinohara M (1998) Implications from the seismic crustal structure of the northern Izu-Ogasawara arc. Isl Arc 7:383–394

Takahashi N, Kodaira S, Klemperer SL, Tatsumi Y, Kaneda Y, Suyehiro K (2007a) Crustal structure and evolution of the Mariana intra-oceanic island arc. Geology 35(3):203–206. doi:10.1130/G23212A

Takahashi N, Sato T, Kodaira S, Kaneda Y (2007b) Wide-angle seismic profiling across the middle Izu-Ogasawara arc for understanding boundary structure between the mature and juvenile arcs, -KY0609 cruise-. JAMSTEC Rep Res Dev 5:9–20

Takahashi N, Kodaira S, Tatsumi Y, Kaneda Y, Suyehiro K (2008) Structure and growth of the Izu-Bonin-Mariana arc crust: 1. Seismic constraint on crust and mantle structure of the Mariana arc–back-arc system. J Geophys Res 113:B01104. doi:10.1029/2007JB005120

Takahashi N, Kodaira S, Tatsumi Y, Yamashita M, Sato T, Kaiho Y, Miura S, No T, Takizawa K, Kaneda Y (2009) Structural variations of arc crusts and rifted margins in southern Izu-Ogasawara arc-backarc system. Geochem Geophys Geosyst 10:Q09X08. doi:10.1029/2008GC002146

Takahashi N, Kodaira S, Tatsumi Y, Miura S, Sato T, Yamashita M, No T, Takahashi T, Noguchi N, Takizawa K, Kaiho Y, Kaneda Y (2010) Crustal structure and growth of the Izu-Bonin-Mariana arc. Abstract of Western Pacific Geophysical Meeting, AGU

Tatsumi Y, Tani K, Kogiso T, Takahashi N, Kodaira S (2008) Structure and growth of the Izu-Bonin-Mariana arc crust: II. Arc evolution, continental crust formation. and crust-mantle transformation. J Geophys Res 113:B02203. doi:10.1029/2007JB005121

Taylor B (1992) Rifting and the volcanic-tectonic evolution of the Izu-Bonin-Mariana arc. In: Taylor B et al (eds) Proceedings of the Ocean Drilling Program in scientific results, vol 126. ODP Texas A&M University, College Station, pp 627–650

White RS, McKenzie D, O'Nions RK (1992) Oceanic crustal thickness from seismic measurements and rate earth element inversions. J Geophys Res 97:19683–19715

White N, Thompson M, Barwise T (2003) Understanding the thermal evolution of deep-water continental margins. Nature 426:334–343

Yamazaki T, Yuasa M (1998) Possible Miocene rifting of the Izu-Ogasawara (Bonin) arc deduced from magnetic anomalies. Isl Arc 7:374–382

Zhang J, Ten Brink US, Toksöz MN (1998) Nonlinear refraction and reflection travel time tomography. J Geophys Res 103:29743–29757

Seafloor Geology of the Basement Serpentinite Body in the Ohmachi Seamount (Izu-Bonin Arc) as Exhumed Parts of a Subduction Zone Within the Philippine Sea

Hayato Ueda, Kiyoaki Niida, Tadashi Usuki, Ken-ich Hirauchi, Martin Meschede, Ryo Miura, Yujiro Ogawa, Makoto Yuasa, Izumi Sakamoto, Tae Chiba, Takahiro Izumino, Yoshiyuki Kuramoto, Toyoto Azuma, Toru Takeshita, Takeshi Imayama, Yuki Miyajima, and Takahiro Saito

Abstract The Ohmachi Seamount in the Izu-Bonin frontal arc is one of the very rare localities where rocks from a deep subduction zone are exposed on the modern sea floor. Submersible and dredge results revealed that the basement serpentinite body is accompanied by small amounts of amphibole schist (six float stones less than 20 cm in diameter were collected) with relics of the blueschist to eclogite facies minerals, and is covered by volcanic and sedimentary sequences of Eocene to Miocene ages. In contrast to the occurrences of well-known serpentine mud volcanoes in the Mariana forearc, the Ohmachi Seamount serpentinite body is a coherent mass composed dominantly of massive serpentinite in upper horizons and of schistose serpentinite with amphibole schist in lower horizons. Both types of serpentinites consist mainly of antigorite ± olivine, and suffered greenschist to amphibolite grade metamorphism. Geologic structures are truncated by the base of the Paleogene, and the serpentinite body is interpreted as a basement complex representing a set of the hanging-wall wedge mantle (massive serpentinite) and the subduction channel (schistose serpentinite), which trapped pieces from the foot-wall subducted slab. The complex was exhumed probably along with one of the back-arc spreading in the Philippine Sea plate.

Keywords Subduction channel • Antigorite schist • Eclogite • Wedge mantle Geological map • Submersible clinometer

H. Ueda (✉) and T. Saito
Faculty of Education, Hirosaki University, Bunkyocho-1,
Hirosaki 036-8560, Aomori, Japan
e-mail: ueta@mvf.biglobe.ne.jp; qqxp738d@diary.ocn.ne.jp

K. Niida, T. Izumino, and T. Takeshita
Department of Natural History Sciences, Graduate School of Science,
Hokkaido University, N-10, W-8, Sapporo 060-0810, Japan
e-mail: kiyo@mail.sci.hokudai.ac.jp; torutake@mail.sci.hokudai.ac.jp

Y. Ogawa et al. (eds.), *Accretionary Prisms and Convergent Margin Tectonics in the Northwest Pacific Basin*, Modern Approaches in Solid Earth Sciences 8,
DOI 10.1007/978-90-481-8885-7_5, © Springer Science+Business Media B.V. 2011

T. Usuki
Institute of Earth Sciences, Academia Sinica, 128 Academia Road
Sec. 2, Nankang, Taipei 11529, Taiwan
e-mail: usu@earth.sinica.edu.tw

Ken-ich Hirauchi
Department of Earth and Planetary Systems Science,
Graduate School of Science, Hiroshima University,
1-3-1, Kagamiyama, Higashi-Hiroshima 739-8526, Hiroshima Japan
e-mail: k-hirauchi@hiroshima-u.ac.jp

M. Meschede
Institute of Geography and Geology, University of Greifswald,
Friedrich-Ludwig-Jahn-Str. 17A, Greifswald D-17487, Germany
e-mail: meschede@uni-greifswald.de

R. Miura
Miarine Science Division, Nippon Marine Enterprises, Ltd.,
2-15 Natsushima-cho, Yokosuka 237-0061, Japan
e-mail: miurar@nme.co.jp

Y. Ogawa
The University of Tsukuba, 1-127-2-C-740
Yokodai, Tsukubamirai 300-2358, Japan (home)
e-mail: fyogawa45@yahoo.co.jp

M. Yuasa
Institute of Geology and Geoinformation, National Institute of Advanced Industrial
Science and Technology (AIST), Central 7, 1-1-1 Higashi, Tsukuba,
Ibaraki 305-8567, Japan
e-mail: myuas1764@yahoo.co.jp

I. Sakamoto and Y. Miyajima
Department of Marine Mineral Resources, Faculty of Marine Science
and Technology, Tokai University, 3-20-1 Orito, Shimizu-ku,
Shizuoka 424-8610, Japan
e-mail: izumis@scc.u-tokai.ac.jp; miyajimay@mwj.co.jp

T. Chiba
Graduate School of Life and Environmental Sciences,
University of Tsukuba, Tsukuba 305-8572, Japan
e-mail: icecream.103yen@gmail.com

Y. Kuramoto
Hokkaido Hiyama-kita Senior High School, 360 Niwa, Kitahiyama-ku,
Setana Town 049-4433, Hokkaido Prefecture, Japan
e-mail: ys.kura@gmail.com

T. Azuma
Hidaka Mountains Museum, 297-12 Honcho-Higashi, Hidaka Town 055-2301,
Hokkaido Prefecture, Japan
e-mail: hmc@town.hidaka.hokkaido.jp

T. Imayama
Center for Chronological Research, Nagoya University,
Furo-cho, Chikusa-ku, Nagoya 464-8602, Japan
e-mail: imayama@nendai.nagoya-u.ac.jp

1 Introduction

Serpentinite bodies accompanied by high-pressure (HP) metamorphic rocks are common in orogenic belts exposed on land. They are regarded to have originated from ancient convergent margins in terms of low thermal gradient during the formation of accompanied metamorphic rocks. Based on highly sheared and mixed-up structures with metamorphic pressure of upper mantle depths, they are recently regarded as exhumed parts of subduction channels of mantle depths (Guillot et al. 2001; Gerya et al. 2002; Ganne et al. 2006; Federico et al. 2007) as the interface shear zones of upper and lower plates, where material transports were channelized (Cloos and Shreve 1988). It is considered that the serpentinites and the HP metamorphic rocks were formed and exhumed not only in collision settings but also in subduction settings of oceanic crust as suggested by protoliths of metamorphic rocks (Maruyama et al. 1996). They are occasionally associated with hanging-wall ophiolites of supra-subduction natures, which suggest subduction beneath immature, rather oceanic thin crusts in intraoceanic settings or continental margin forearcs (e.g. Dickinson et al. 1996).

Compared to collision and continental margin settings, it is more difficult to explain the driving forces of exhumation in non-collisional oceanic subduction settings: the buoyancy of the subducted slab or the voluminous subducted sediments is not expected to lift or squeeze deep seated rocks upward. A possible resolution to this problem comes from the properties of serpentinite, which is characterized by much lower densities and shear strength than mantle peridotites (Hermann et al. 2000; Guillot et al. 2001), and its volume expansion during hydration of peridotites (Fryer and Fryer 1987; Shervais et al. 2004). The subduction channel structure, in which serpentinites occur along the interface between peridotites of the hanging wall and foot wall lithosphere, might be common in subduction zones. Therefore, the serpentinite bodies with HP metamorphic rocks can be a geological key target to understand structure and dynamics of deep inside subduction zones, and those formed in intraoceanic settings might represent an end-member condition where material input into the channel is minimal. However, serpentinites with HP metamorphic rocks occurring in orogenic belts on land are structurally modified by subsequent tectonics such as continental collision or sediment accretion etc., and it is somewhat difficult to read primary structures from them.

The Izu-Bonin-Mariana (IBM) arc comprises a typical intraoceanic subduction system (Fig. 1), which generated since the Eocene. The earliest-stage basement rocks of the IBM are ophiolite consisting of serpentinite, gabbro, and dominantly undifferentiated volcanic rocks including boninites (Bloomer 1983; Ishii 1985), and are referred to modern analogue of supra-subduction zone ophiolites (Stern and Bloomer 1991; Bloomer et al. 1995). Serpentinites are occasionally accompanied by HP metamorphic rocks (Maekawa et al. 1993), proving formation and exhumation of HP metamorphic rocks in normal subduction settings of intraoceanic environments. Most of the HP metamorphic rocks occur in forearc seamounts as millimeter- to decimeter-scale clasts enclosed in serpentine mud flows from mud volcanoes (Fryer 1992; Maekawa et al. 1992, 1993). These occurrences have been generally regarded as the typical style of exhumation in modern intraoceanic

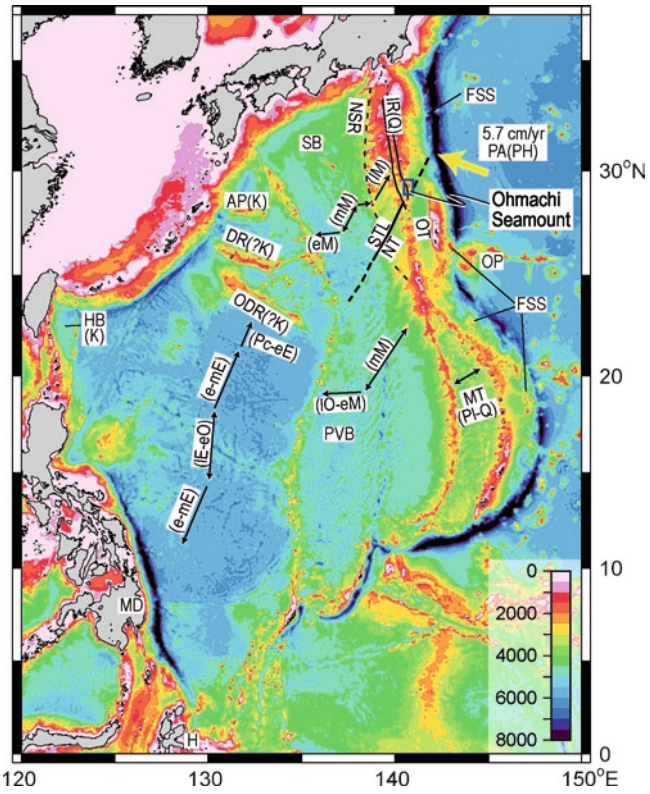

Fig. 1 Tectonic features of the Philippine Sea plate (PH) and the location of the Ohmachi Seamount. Bathymetry based on ETOPO1 (Amante and Eakins 2009). *Yellow arrow* indicates present-day velocity vector of the Pacific plate (PA) relative to PH (After DeMets et al. 1994). *Black arrows* represent the spreading directions of back-arc basins (Hilde and Lee 1984; Okino et al. 1994; Yamazaki and Yuasa 1998) with labels with parentheses showing the timing of the spreading. Age abbreviations: *K* Cretaceous, *Pc* Paleocene, *E* Eocene, *O* Oligocene, *M* Miocene, *Pl* Pliocene, *Q* Quaternary, and *e*, *m*, and *l* correspond to early, middle, and late, respectively. Other abbreviations: *AP* Amami Plateau, *DR* Daito Ridge, *FSS* representative forearc serpentinite seamounts, *H* Halmahera Island, *HB* Huatung Basin, *IR* intra-arc rift basins, *MD* Mindanao Island, *MT* Mariana Trough, *NSR* Nishi-Shichito Ridge, *NT* Nishinoshima Trough, *ODR* Oki-Daito Ridge, *OP* Ogasawara Plateau, *OT* Ogasawara Trough, *PVB* Parece Vela Basin, *SB* Shikoku Basin, and *STL* Sofugan tectonic line

subduction zone. However, scarcity of on-land analogues for serpentine mud volcanoes in orogenic belts remains a gap of understandings between marine and on-land geology on the subduction zone dynamics.

The Ohmachi Seamount in the Izu-Bonin frontal arc (Fig. 1) is one of the localities where serpentinites accompanied by HP metamorphic rocks are exposed on the seafloor. In contrast to mud volcanoes of the forearc serpentinite seamounts, the Ohmachi Seamount serpentinites comprise a coherent body as the basement of overlying strata, and partly occur as crystalline schist. Because such occurrences are common in orogenic belts, the Ohmachi Seamount is expected to more closely

link subduction zone tectonics in the ocean and those recorded in on-land orogenic belts. Serpentinite with HP metamorphic rocks in the Ohmachi Seamount still remains in the intra-oceanic setting, and probably free from extensive structural modification by subsequent accretionary or collision tectonics. They are thus expected to show more primary structural and metamorphic features reflecting the dynamics within a subduction channel. In addition, metamorphic rocks in the Ohmachi Seamount contain relics of the eclogite facies metamorphism, which occurred as deep as 70–80 km (600–700°C, 2.0–2.5 GPa: Ueda et al. 2004, 2005), as the only known locality of eclogite facies rocks of non-collisional subduction setting in the modern ocean. The peak metamorphic depths are much greater than the incipient blueschist facies clasts in the forearc serpentinite seamounts (~20 km: Maekawa et al. 1992, 1993, 1995). The serpentinite body and accompanied HP metamorphic rocks in the Ohmachi Seamount will provide petrologic and structural information of deeper portions of a subduction zone.

This paper aims to describe and summarize results of submersible dives (JAMSTEC YK01-04 and YK08-05 cruises by R/V *Yokosuka* and submersible *Shinkai 6500*) and dredges (ORI/JAMSTEC KT04-28 cruise by R/V *Tansei-maru*) on the serpentinite body of the Ohmachi Seamount, with reviews of earlier researches, focusing on its geological structures. Accumulation of these data enables us to construct an ocean-bottom geologic map, here newly presented, with a resolution approaching to on-land geology. Based on these results, the significance of the geologic structure related to subduction zone dynamics is discussed.

2 Geologic Setting and Bathymetry

The Ohmachi Seamount is located at 29°00-30'N and 140°35-55'E in the middle part of the Izu-Bonin arc of the Philippine Sea plate (Fig. 1) about 20 km east of the Quaternary volcanic front and 180 km west of the trench. The seamount is part of a structural high elongated along north-south direction (Fig. 2) representing the rear-side termination of the forearc basin (Ogasawara Trough) in the east, and the trench-ward bank of the Quaternary intra-arc rift basin (Nishinoshima rift) in the west. Moreover, the seamount is in prolongation of the NNE-SSW-trending Sofugan tectonic line (STL) as the largest fracture zone separating the Miocene back-arc basin into the Shikoku and Parece Vela basins (Fig. 1). The Izu-Bonin arc itself is also separated by the STL (Yuasa 1985, 1992): the arc crust in the north is more matured with 20–30 km thickness as opposed to the south with less than 20 km thickness (Kodaira et al. 2007). The STL comprises more than 200 km-long escarpment facing the southeast with vertical throws of 1,000–1,500 m, on which basaltic lavas, dikes, and hyaloclastites are exposed (Sakamoto et al. 1997, 1998). Both the northwest and southeast blocks bounded by STL tilted northwestward, resulting in the southeast-facing escarpment, and in a narrow depression (Nishinoshima Trough) directly in the neighborhood to the southeast of the STL. The crust in the Nishinoshima Trough, which terminates at the Ohmachi Seamount,

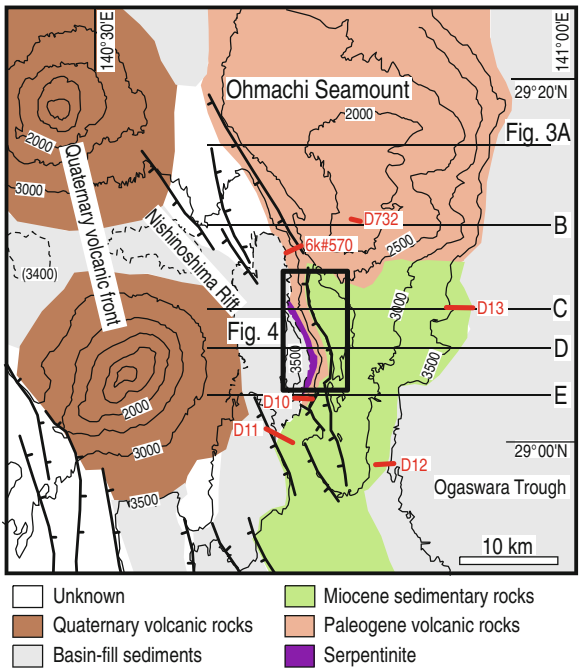

Fig. 2 Bathymetric features and inferable geologic outline of the Ohmachi Seamount (Bathymetry based on Sakamoto et al. 2001). Dive and dredge locations out of the field of Fig. 4 are shown

is the thinnest with about 10 km, and this ocean-like crust splits the northern and southern Izu-Bonin arc crust (Yuasa 1992).

The Ohmachi Seamount has a tadpole-like outline with the main part (body) in the north and the peninsular part (tail) in the south (Fig. 2). The main part comprises a broad and north-trending elliptical high ~20 km in width and ~30 km in length, whose summit is ~1,700 mbsl (meters below sea level). The peninsular part is a N-S-trending ridge with less elevated (~2,300 mbsl at the ridge crest) and asymmetric cross sections (Fig. 3). Its eastern slope is relatively flat and gentle (~6°), whereas the western slope is much steeper with average dips of ~30°. The western slope comprises normal fault scarps of the Nishinoshima Rift basin in the west. Single-channel seismic reflection profiles (Yuasa et al. 1991) displayed that the rift basin-fill deposits abut onto the fault scarp, whereas seemingly dragged by the fault in deeper horizons. The western slope of the peninsular part consists of two alternating domains trending 0–20° and ~340°, probably resulted from a rhombus geometry of the rift normal faults. To the south of 29°08'N, the western slope has a terrace-like gently-dipping band at the level of 3,000–3,200 mbsl. The asymmetric bathymetry is likely to have resulted from tilting and uplifting of initially flat basin floor.

The Ohmachi Seamount shows a broad positive magnetic anomaly (Yamazaki et al. 1991; Yamazaki and Yuasa 1998), inferred as an effect of somewhat deeply-seated magnetized body (Yamazaki et al. 1991).

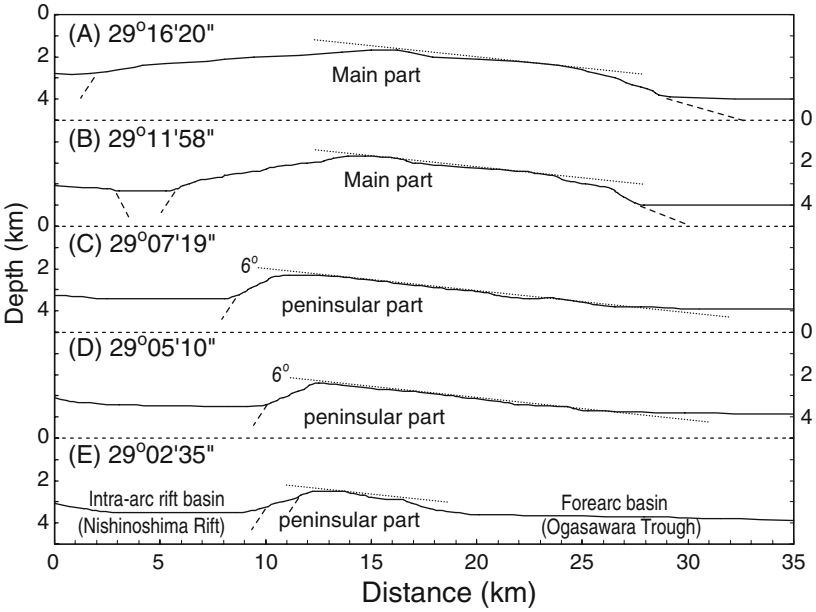

Fig. 3 East-west topographic cross sections of the Ohmachi Seamount. Reference *broken lines* tilting at 6° to the east are drawn for the interpretation of flat surfaces on the eastern slopes of the peninsular part. Also shown are inferable projections of the normal faults by recent intra-arc rifting

3 Lithology

The Ohmachi Seamount is composed mainly of the basement serpentinite with trace amphibole schist, Paleogene volcanic rocks, and Miocene sedimentary rocks (Figs. 2 and 4). Common lithological characteristics are described here, and their occurrences in each dive tracks will be described in the next section.

3.1 Serpentinites

Serpentinites in the Ohmachi Seamount are classified into two major groups: massive and schistose serpentinites (Figs. 5 and 6), in terms of development of mineral foliation. The massive serpentinite occasionally accompanies ultramafic dikes.

3.1.1 Massive Serpentinite

The massive serpentinites are characterized by lacking or very weak mineral foliation (Fig. 5c–d). They are jointed or fractured to varying extent, and

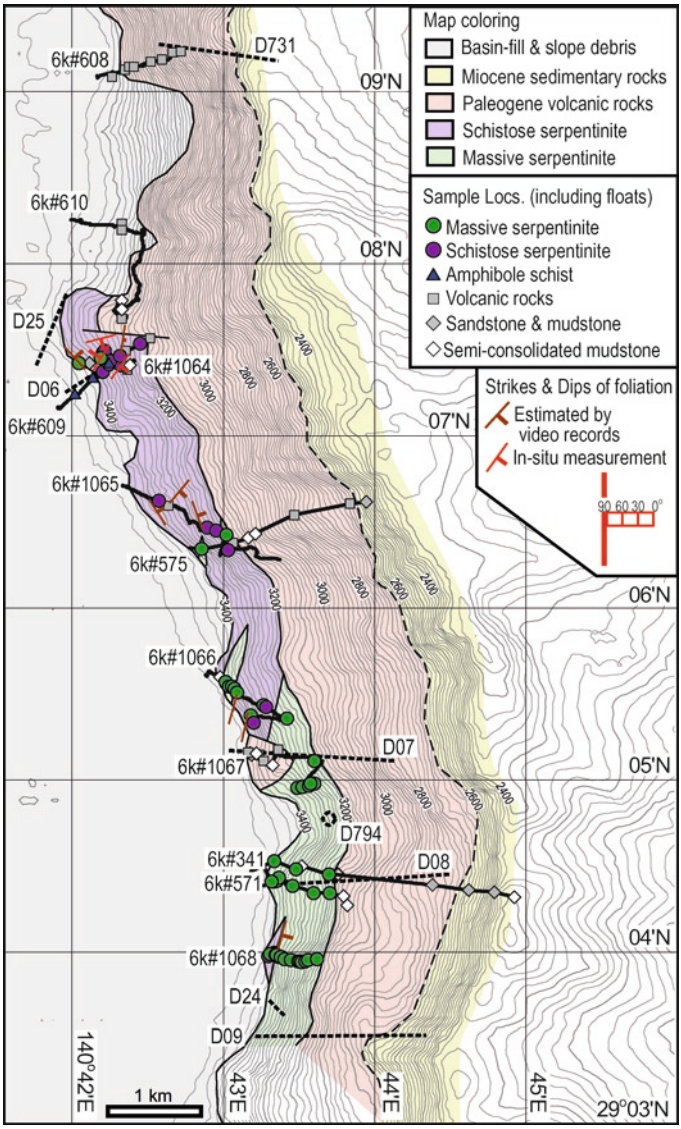

Fig. 4 Sea-floor geological map of the Ohmachi seamount. Dive and dredge trails and localities of rock samples (including floats) by lithotypes are shown

Fig. 5 Representative lithofacies of the Ohmachi Seamount. (**a**) Schistose serpentinite (dive 6K#1064) with foliation gently dipping to the south. (**b**) Schistose serpentinite (6K#1066) with near-vertical foliation. (**c**) Jointed massive serpentinite (6K#1065). (**d**) Locally brecciated serpentinite in contact with unfractured massive serpentinite (transitionally schistose in thin section; 6K#1068). (**e**) Locality of an amphibole schist float (6K#609R002) collected from rock debris (*dark part: arrowed*) covered by recent calcareous mud (*light colored*), both exposed on a landslide scarp in the slope apron. (**f**) Sub-horizontally stratified outcrop near the base of the Paleogene volcanic sequence, consisting of reworked volcanic breccia (*lower*) and felsic tuff (*upper*), observed during the dive 6K#609. (**g**) Scanned thin section of a limestone float (6K#1065R003) of shallow-marine origin showing molds of dissolved colonial corals mostly filled by secondary calcite. (**h**) Cut surface of a float of turbidite (6K#1064R007)

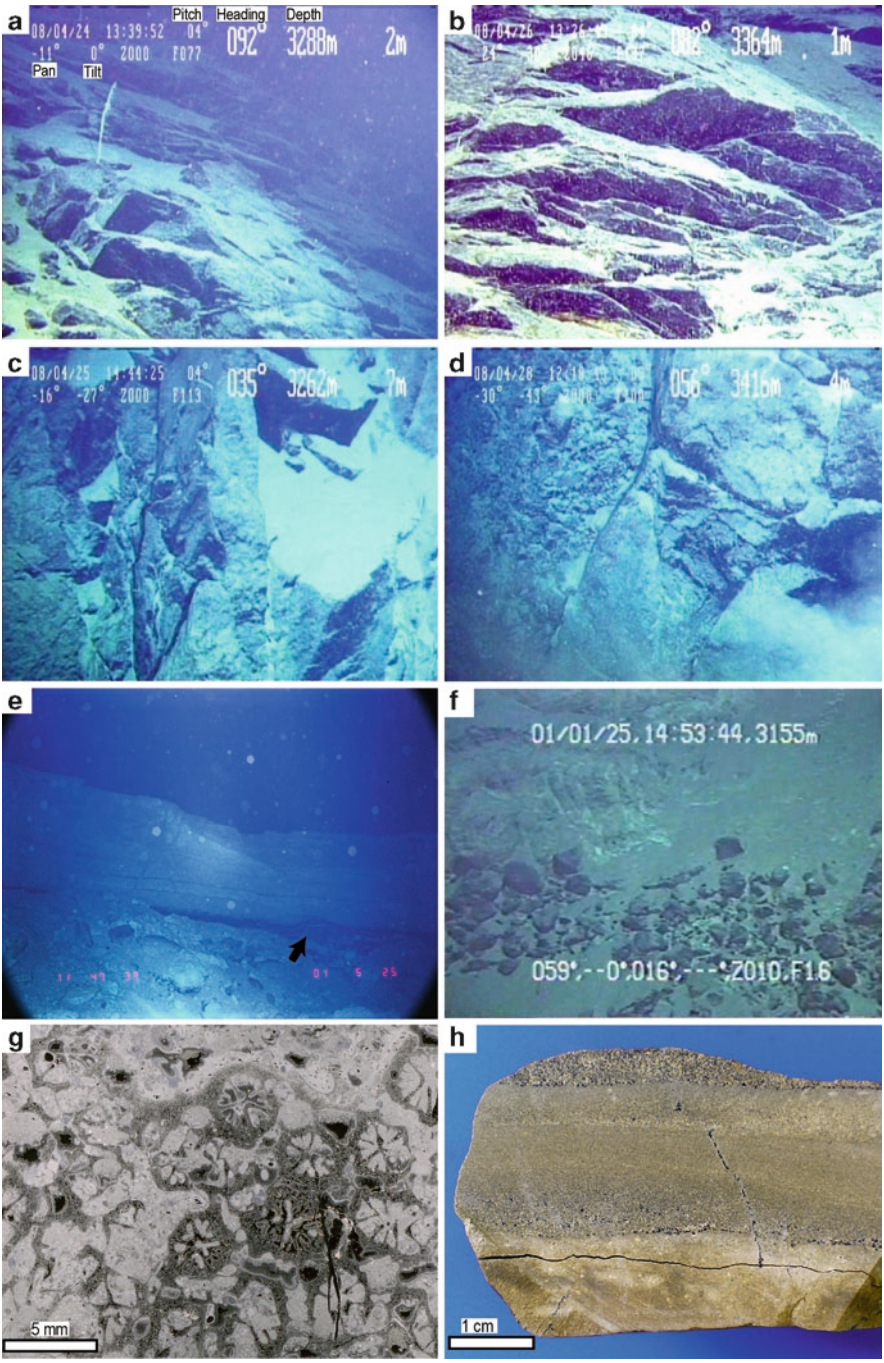
a
Pitch
Heading
Depth
092°
3288m
2m
Pan
Tilt
b
3364m
1m
c
035°
3262m
7m
d
056°
3416m
4m
e
f
01/01/25,14:53:44.3155m
059°,--0°,016°,---°,Z010.F16
g
5 mm
h
1 cm

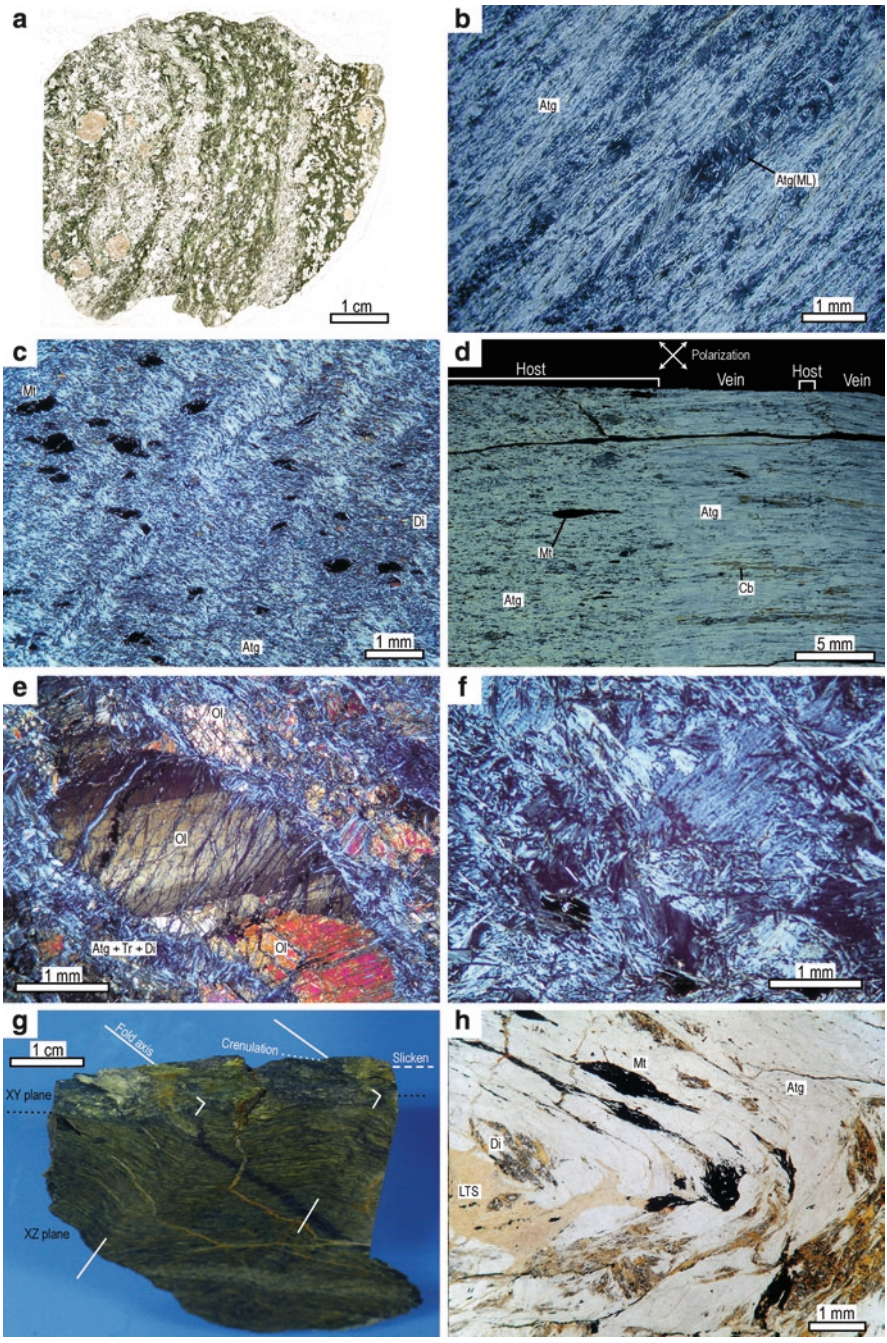
a
1 cm
b
Atg
Atg(ML)
1 mm
c
Mt
Di
Atg
1 mm
d
Host
Polarization
Vein
Host
Vein
Atg
Mt
Cb
Atg
5 mm
e
Ol
Ol
Atg + Tr + Di
Ol
1 mm
f
1 mm
g
1 cm
Fold axis
Crenulation
Slicken
XY plane
XZ plane
h
Mt
Atg
Di
LTS
1 mm

brecciated variations also locally occur (Fig. 5d). Microscopic textures vary from pseudomorphic mesh textures by low-T serpentines to completely recrystallized interpenetrating textures mainly by antigorite ± olivine (Fig. 6e–f). Bastite is common. A few samples preserve relic orthopyroxene, clinopyroxene, Cr-spinel, and pargasite as the primary phases. Most of olivine crystals may have originated from an igneous phase, but were extensively modified to be cleavable with antigorite films along partings, as suggestive of crystallographic reequilibration along with antigorite-forming metamorphism (Uda 1984; Akikawa and Tokonami 1987). Minor secondary growth of olivine with inclusions of serpentine and magnetite also occurred. Low-T serpentines occasionally crosscut antigorite, so that the mesh textures generated after the main metamorphism, where antigorite + olivine assemblage was stable. Degree of serpentinization (antigoritization) in the main metamorphic stage (before generation of low-T serpentines in later stages) are highly variable from nearly zero to 100%, but greater than 90% in the majority .

In addition to olivine and serpentine minerals, they commonly contain chlorite and magnetite, occasionally with diopside and tremolite, as metamorphic products. Typical metamorphic mineral assemblages are Ol + Atg + Di + Chl + Mag and Ol + Atg + Tr ± Di + Chl + Mag (mineral abbreviations after Kretz 1983), representing upper greenschist to lower amphibolite-grade temperatures (Evans 1977; O'Hanley 1996).

Textures and relic and/or metamorphic mineral assemblages suggest that the massive serpentinite originated from residual peridotite (lherzolite and harzburgite) and lesser amounts of dunite. Relic spinels show lesser degrees of partial melting than typical arc peridotite, but edenitic to pargasitic amphibole as a high-temperature hydrous phase is common (Niida et al. 2001, 2003, 2005). These less refractory but hydrous features were interpreted to reflect one of the three candidates of their origins as: (a) relics of sub-continental lithosphere on whose margin the Philippine

Fig. 6 Microscopic and mesoscopic photographs of amphibole schists and serpentinites. (**a**) Micro-folds in garnet-epidote amphibolite (D06-1; unpolarized light) in the YZ section normal both to foliation and to lineation. (**b**) Schistose serpentinite (6K#609R007; cross-polarized light) in a view of XZ section normal to foliation and parallel to lineation. Relics of early massive textures (ML: microlithon) are surrounded by highly schistose neoblasts of antigorite. (**c**) Microfolds with lineation-parallel axes in the YZ section of schistose serpentinite (6K#609R009; cross-polarized light). (**d**) Scanned thin section of schistose serpentinite (6K#609R008; cross-polarized light) in XZ section. Note the highly elongated magnetite porphyroblasts and lineation-normal crack-seal veins of fibrous antigorite. (**e**) Massive serpentinite (6K#1067R013; cross-polarized light) consisting mainly of cleavable olivine and antigorite. (**f**) Massive serpentinite (6K#1065R006; cross-polarized light) with an inter-penetrating texture of antigorite. (**g**) A fold structure in schistose serpentinite (6K#1066R026; oblique view of the slab of XZ section). Fold axes crosscut lineation and crenulation (microfold axes). Slicken sides correspond to foliation-subparallel slip surfaces with low-temperature serpentine. (**h**) Hinge part of a fold (crosscutting lineation) with fractures filled by low-T serpentine in schistose serpentinite (6K#1066R020; open-polarized light). Mineral abbreviations: *Atg* antigorite, *Cb* carbonate, *Di* diopside, *LTS* low-temperature serpentine, *Mt* magnetite, *Ol* olivine, and *Tr* tremolite

Sea Plate initiated, (b) peridotites beneath a slow-spreading back-arc basin, and (c) island-arc upper mantle with secondary enrichment in hydrous basaltic melt components (Niida et al. 2003, 2005).

The ultramafic dikes in massive serpentinites consist of clinopyroxenite-wehrlite and olivine-hornblendite, and show cumulate textures in less deformed and less recrystallized specimens. These ultramafic dikes (except for Ol-poor clinopyroxenite) commonly contain antigorite, and olivine-rich varieties show the same metamorphic mineral assemblages as the host massive serpentinites. They occasionally show weak metamorphic mineral foliation, which suggest their intrusion prior to the main metamorphic and deformation event.

3.1.2 Schistose Serpentinite

The schistose serpentinite is characterized by lepidoblastic textures consisting solely of antigorite, thus comprising antigorite schist (Fig. 6b–d). The rocks also commonly contain minor amounts of magnetite and chlorite, and are occasionally accompanied by carbonate, diopside, and olivine. Acicular crystals of diopside also partly contribute to the schistosity. Modal abundance of olivine and its pseudomorphs are small (approximately less than 10%), and the majority of the schistose serpentinite does not contain olivine. The lowest-variance metamorphic mineral assemblages is Atg + Ol + Di + Chl + Mag, representing upper greenschist- to lower amphibolite-grade temperatures (Evans 1977; O'Hanley 1996) consistent with retrograde (decompression) conditions of amphibole schists as described later.

Magnetite occurs as ellipsoidal porphyroblasts and/or pseudomorphs after spinel (Fig. 6d), whose long axes define a stretching lineation. Development of schistosity is variable and transitional from the massive serpentinite. Hirauchi et al. (2010) showed that alignment of crystallographic axes of antigorite in massive, transitional, and schistose serpentinites progressively increases in ascending order (c-axis parallel to the schistosity, and b-axis to the lineation). The transition from massive to schistose serpentinites is also occasionally visible on cut surfaces of hand specimens, where parts of massive serpentinites are stretched along their margins or shear zones and grade into schistose serpentinite. Here we describe as schistose serpentinite when lepidoblastic antigorite exceeds 50 modal %. Schistosity is occasionally recognizable on some outcrop surfaces, whereas it is not evident and apparently massive on some outcrops. In some cases the foliation surfaces are accompanied by slicken lines, whose orientations are regardless of stretching lineations by magnetite porphyroblasts. Apparent foliation on rock surfaces probably resulted from overprint of later slip and/or weathering parallel to the schistosity. Fold structures are not uncommon (Fig. 6c, g, h). Lineation-orthogonal veins of fibrous to acicular antigorite crystals (picrolite), whose long axes are parallel to stretching lineations, are rarely seen in schistose serpentinite (Fig. 6d).

3.2 Amphibole Schist

Six samples of amphibole schists commonly with relics of high-pressure metamorphism were collected from the Ohmachi Seamount. They consist of three lithotypes: epidote (Ep) – albite (Ab) amphibolite (four samples), garnet (Grt) – zoisite (Zo) amphibolite (one sample), and Grt-Ep amphibolite (one sample: Fig. 6a). Rocks of the former two types contain microinclusions of the eclogite facies minerals such as omphacite as reported by Ueda et al. (2004). For the Grt-Zo amphibolite sample, Ueda et al. (2004, 2005) estimated P-T conditions of the peak metamorphic stage as 600–700°C, 2.0–2.5 GPa, and of decompression stage as 500–600°C, <1.3 GPa. Grt-Ep amphibolite has glaucophane and albite microinclusions in garnet, suggesting early blueschist facies metamorphism. All types of the amphibole schists show nematoblastic textures of amphiboles and epidote or zoisite, with evident mineral lineation. The Grt-Zo amphibolite also show compositional banding of amphibole-rich and zoisite-rich layers.

The collected samples are float stones with diameters of several to ten and several centimeters, whose surfaces commonly have slicken lines. Their localities are limited near the northern end of the schistose serpentinite exposures (at dive site 6K#609 and dredge site D06: see the next section), and their amount is probably quite small relative to that of serpentinites. It is thus assumed that they originated from faulted blocks or clasts sparsely hosted by the schistose serpentinite.

3.3 Paleogene Volcanic Rocks

Volcanic rocks are the main constituent of the Ohmachi Seamount. They consist mainly of hornblende andesite and two-pyroxene andesite of calc-alkaline series (Yuasa and Nohara 1992; Yuasa et al. 1999). They occur as lava and volcanic or tuff breccia (Fig. 5f) accompanied by tuff and volcanic sandstone and conglomerate. Hypabyssal varieties were also observed in the main parts of the seamount. No deformation structures have been found in these rocks. Volcanic glass is preserved in unaltered rocks, whereas altered rocks contain zeolites and clay minerals. From two-pyroxene andesite cobbles dredged at site D731 (Fig. 4), K-Ar ages of 31.9 ± 1.2 Ma and 33.6 ± 1.2 Ma (latest Eocene to Early Oligocene) were reported by Yuasa et al. (1988). Another variety of volcanic rocks from site D794 (Fig. 4) was reported by Yuasa and Nohara (1992) and Yuasa et al. (1992, 1999), mainly comprising sheared volcanic breccia with slicken sides. Clasts consist of basaltic andesite to andesite of calc-alkaline series, and contain pseudomorphs after pyroxene and olivine. Matrix and phenocrysts were extensively recrystallized by prehnite-pumpellyite facies metamorphic minerals. Severely altered olivine basaltic andesites were also collected during dive 6K#610 at 3,230 mbsl. Yuasa et al. (1999) suggested that these metamorphosed volcanic rocks underlie the relatively unaltered andesites.

Minor amounts of limestone and calcareous sandstone were dredged. Nishimura (1992) dated calcareous sandstone containing andesite pebbles (dredged from D731: Fig. 4) as Late Eocene based on larger benthic foraminifera. Nishimura et al. (1997) gave $^{87}Sr/^{86}Sr$ stratigraphic ages for two limestone samples. A limestone dredged at site D732 (Fig. 2) was dated as 34.23 ± 0.78 Ma (Late Eocene to earliest Oligocene). Calcareous matrix of a conglomerate dredged at site D731 was dated as 39.65 ± 0.71 Ma (Late Eocene). These Eocene limestones were dredged from the upper slope of the seamount, and are inferred to be intercalated within or capping the Paleogene volcanic rocks. Floats of foraminiferal limestone were also found in the debris apron near the basin floor. One of them (6K#1065R003) also contained dissolved molds of colonial corals (Fig. 5g).

3.4 Miocene Turbidite

Alternating beds of siltstone, sandstone, and conglomerate were observed on the upper slope (ca. 2,650–2,400 mbsl) of dive track 6K#341. These beds were considered as turbidite in terms of graded beds with parallel and cross laminae (Yuasa et al. 1998, 1999). Siltstone yielded planktonic foraminifers indicating a late Early Miocene age (N8: ~16Ma; Yuasa et al. 1998). Turbidite alternation of sandstone and siltstone were also collected as float stones in debris apron near the basin floor (3,381 mbsl) during dive 6K#1064 (Fig. 5h).

3.5 Soft Mud Beds

On the western slope (fault scarp) of the Ohmachi Seamount, semi-consolidated beds of soft and cohesive mud occasionally occurred in outcrops. They are composed of several meters thick beds parallel to the slope surface, with jointed escarpments at each termination. Their surfaces are coated by thin ferro-manganese oxides. Open burrows are common. The mud contains abundant coccoliths accompanied by vitric tuff, foraminferal and radiolarian remnants, and rock fragments in cases. They are considered as post-rifting slope cover sediments, whose exposure presumably resulted from active erosion by landslide and bottom currents.

4 Dive and Dredge Results

Four scientific cruises (YK96-11, YK00-08, YK01-04, and YK08-05) by JAMSTEC R/V *Yokosuka* with 12 dives in total have been performed on the Ohmachi Seamount using submersible "*Shinkai 6500*". All submersible dive tracks were set on the western slope (fault scarp) of the seamount (Fig. 4).

4.1 Dive 6K#341

This dive was the first research that discovered the occurrence of serpentinites. The route was set at 29°04.33-4.12'N climbing eastward from the Nishinoshima Rift basin floor to the ridge crest of the peninsular part. Dive results have been reported by Yuasa et al. (1998, 1999), as briefly reviewed here. The lower slope between 3,487 mbsl (edge of basin floor) and ~3,180 mbsl was covered by slope debris containing serpentinite blocks and clasts, whose amounts and sizes increased upslope. Between the depths of 3,180 and 3,080 mbsl foliated rocks occurred, which were not sampled. The foliated rocks were first described as presumable metamorphic rocks, however, now they are considered to be schistose serpentinite taking into account results from the following dive investigations. The slopes became gentler between 3,080 and 2,800 mbsl and were covered by mud. Slopes between the depths of 2,800 and 2,600 mbsl were composed mainly of talus consisting of blocks of Miocene turbidite slid from cliffs above. A near-vertical cliff appeared at ~2,500 mbsl, where Miocene conglomerates and turbidites were exposed. Foreign pumice was collected on the ridge crest at 2,393 mbsl.

4.2 Dive 6K#570

This one and the following dives 6K#571 and 6K# 575 were performed during YK00-08 cruise, whose results were reported in JAMSTEC (2000), Fujiwara et al. (2001) and Niida et al. (2001). Dive 6K#570 climbed the western fault scarp on the main part of the seamount at ~29°10.5'N. The lower slope between 3,460 (basin floor) and 2,990 mbsl comprised landslide debris and talus deposits covered by soft muddy sediments. In the upper slopes (2,990–2,670 mbsl) occurred dacite and dioritic porphyrite partly with platy and/or columnar joints. Volcanic breccia occurred between 2,670 and 2,570 mbsl. The uppermost outcrops (2,526–2,483 mbsl) at the edge of a terrace at ~2,500–2,400 mbsl consisted of well stratified volcanic sandstone containing pumiceous layers and foraminifers.

4.3 Dive 6K#571

This dive route roughly tracked the lower section (3,506–3,079 mbsl) of the dive 6K#341. Less fractured massive serpentinite and associated clinopyroxenite appeared from the foot of the fault scarp at 3,480–3,300 mbsl as sporadic outcrops among debris blocks and soft sediment covers. Serpentinites between 3,300 and 3,200 mbsl were massive but highly fractured enclosed in clayey matrices, occurring within slope debris. This fracturing probably resulted from a landslide, on whose bathymetric feature the submersible crossed at these depths. Hornblendite

samples were taken from an outcrop at 3,225 mbsl. Serpentinites and associated ultramafic cumulates were covered by semi-consolidated mud between 3,129 and 3,079 mbsl.

4.4 Dive 6K#575

Above the debris apron containing float stones of limestone and massive serpentinite, outcrops of massive serpentinite occurred between 3,360 and 3,290 mbsl. Foliated rocks, which were not sampled but now inferred as schistose serpentinite, were observed at 3,236 mbsl. The lowermost locality of volcanic rocks lies at 3,212 mbsl, and sporadic occurrences of volcanic rocks and volcanic conglomerate continued until 2,614 mbsl. The uppermost section between 2,600 and 2,460 mbsl consisted of stratified sedimentary rocks, parts of which were confirmed as massive or thin-bedded mudstone samples.

4.5 Dive 6K#608

Gentle debris slope containing blocks of dacite continued between the basin floor at 3,440 and 3,400 mbsl. Between 3,400 and 3,100 mbsl, the slope had many cliffs of andesite lava. Gentler mud-covered slope with sporadic exposures of andesite continued until the off-bottom point at 2,840 mbsl. Andesite lava was generally fractured.

4.6 Dive 6K#609

The lowermost part of the slope comprised a debris apron with local landslide scarps (Fig. 5e). Collected debris was composed of schistose serpentinite and amphibole schist (6K#609R002 and R004-R006: Ep-Ab amphibolite). Outcrops of schistose serpentinite sporadically occurred on generally mud-covered lower slope between 3,350 and 3,240 mbsl. Serpentinite on outcrops were generally intact with scarce joints, and with apparently weak foliations gently dipping east to southeast. Lineations were nearly horizontal in schistose serpentinite samples whose orientation can be restored by video records. A float of amphibole schist (#609R012: Grt-Zo amphibolite) was collected at the foot of a serpentinite outcrop at 3,340 mbsl. The middle terrace between 3,240 and 3,220 mbsl was a mud-covered gentle slope, on which floated blocks of serpentinite and volcanic rocks were scattered. The shallowest occurrence of serpentinite debris was at 3,175 mbsl within the basal talus of the upper slope. At 3,155 mbsl occurred an outcrop of horizontally stratified tuff breccia with polymict andesite clasts (Fig. 5f).

4.7 Dive 6K#610

This dive aimed to confirm the northern limit of serpentinite exposure. The landed point was located on the basin floor along 29°8.22'N, where the middle terrace is not evident, and the submersible first climbed upslope to the east. Debris apron between the basin floor and 3,270 mbsl contained blocks of andesitic tuff breccia and limestone. Outcrop at 3,270 mbsl consisted of hornblende andesite lava. From this point, the dive route was set as iso-contour traverse around 3,270–3,230 mbsl toward the south, along which jointed lava was occasionally exposed on the steep slope covered by volcaniclastic debris and semi-consolidated mud. Floats (?) of altered and amygdaloidal olivine basaltic andesite were collected at 29°7.68'N (3,230 mbsl) at the northern end of the mid-slope terrace.

4.8 Dive 6K#1064

This route was approximately the same site as, and crossing the track of dive 6K#609. The slope deeper than 3,340 mbsl was covered by debris and mud, from which blocks correlative to Miocene turbidite were collected (Fig. 5h). Outcrops of schistose serpentinite, each of which was separated from others by mud-covered talus, occurred between 3,340 and 3,260 mbsl. At 3,238–3,234 mbsl occurred a bed of semi-consolidated mudstone, whose surface was covered by thin Fe-Mn oxide. The bed was parallel to the slope surface. Between 3,234 and 3,228 mbsl, the slope was covered by presumable landslide debris of rectangular blocks and very loose rock masses of basaltic volcanic rocks. The slope between 3,202 m and the off-bottom point (3,176 m) was covered by mud and partly by semi-consolidated mud.

4.9 Dive 6K#1065

This dive route obliquely climbed the slope from the landed point near the base of slope apron at 29°6.7'N (3,453 mbsl) heading ESE, crossing the #575 track, where foliated rocks were not sampled by the previous dive. The first outcrop, which appeared at 3,381 mbsl above a mud-covered rubbly apron, consisted of schistose serpentinite with pronounced foliation moderately dipping to northeast. Schistose serpentinite also occurred at 3,361–3,365 mbsl, where foliation moderately dips to southeast, and at 3,272–3,228 mbsl, where it showed apparently weaker foliation on surfaces. Floats of pumice tuff and coral limestone (Fig. 5g) were collected on the steep and mud-covered talus among these outcrops. Partly fractured massive serpentinite was exposed between 3,218 and 3,204 mbsl. Here the submersible headed south moving to a deeper part of the slope. Apparently massive serpentinite was exposed between 3,267 and 3,236 mbsl. At 3,236 mbsl, a schistose serpentinite was collected from a fractured outcrop. The outcrop of

fractured serpentinite continued until 3,153 mbsl, above which the slopes were covered by mud with sporadic debris until the off-bottom point at 3,078 mbsl.

4.10 Dive 6K#1066

The first (3,443–3,401 mbsl) and second (3,387–3,382 mbsl) outcrops occurred above the mud-covered debris apron. They consisted of massive pseudomorphic serpentinite of dunite origin and highly foliated schistose serpentinite. The third outcrop at 3,365–3,363 mbsl was of platy-jointed schistose serpentinite with foliations steeply (70–80°) dipping ESE. Serpentinite sporadically occurred until 3,351 m. Between 3,350 and 3,205 mbsl, the slope was covered by semi-consolidated mudstone and landslide debris containing rubble and blocks of serpentinite, andesite to dacite, and sandstone. Then the submersible moved downslope to 3,407 mbsl, where serpentinite breccia and schistose serpentinite were exposed.

4.11 Dive 6K#1067

The gentle lowermost slope between 3,452 and 3,436 mbsl was the mud-covered and subsequent rubbly apron, from which a float stone of basaltic breccia was collected. The steep slope with cliffs between 3,375 and 3,273 mbsl consisted of fractured blocky rocks of basaltic breccia (at 3,391 mbsl) and andesite (at 3,376 and 3,306 mbsl), partly covered by semi-consolidated mud (at 3,436 mbsl). These extraordinary deep occurrences of volcanic rocks are interpreted as slid-down blocks either by rift faulting or landslide. After climbing mud-covered slopes, an outcrop of massive serpentinite occurred at 3,175 mbsl. The mud slope continued until 3,135 mbsl, where the submersible turned to the south and downslope.

The new track started at 3,323 mbsl on a mud-covered slope. Outcrops of fractured but massive serpentinite intermittently occurred at 3,322–3,372, 3,245, and 3,225–3,222 mbsl. A schistose serpentinite was also collected at 3,245 mbsl.

4.12 Dive 6K#1068

The submersible landed at 3,453 mbsl and climbed upslope on mud-covered debris apron with sporadic blocks, from which schistose and transitionally massive serpentinite floats were collected. The first outcrop of massive to transitionally schistose serpentinite continued between 3,412 and 3,363 mbsl. Foliations are mostly invisible in the outcrops, with exceptions at 3,389 and 3,363 mbsl, where it gently (presumably <30) dipped to the southeast and northwest, respectively. Above the outcrop, the slope between 3,360 and 3,160 mbsl consisted of rubbly talus containing

clasts and blocks of massive serpentinite. Massive serpentinite sporadically occurred between 3,160 and 3,100 mbsl among rubbly talus. Between 3,100 and 3,080 mbsl (off-bottom point) was a mud-covered gentle slope, on which debris blocks of semi-consolidated mudstone were partly observed.

4.13 Dredges

Rocks were first dredged from three sites on the Ohmachi Seamount (D731, D732, and D794) during R/V "*Hakurei-Maru*" GH85-1 cruise in 1985 and GH86-1 cruise in 1986. From D731 on the western slope of the main part of the seamount (Fig. 4), calcareous sandstone, volcaniclastic conglomerate with calcareous matrices, and andesite cobbles were dredged. Andesites and calcareous conglomerate were dated as Late Eocene to Early Oligocene (see Sec. 3.3). D732 on the southern slope of the main part (Fig. 2) yielded limestone of Late Eocene to earliest Oligocene age (Nishimura et al. 1997). Dredge hauls of D794 on the western scarp of the peninsular part (Fig. 4) were composed of andesite, dolerite, basaltic and andesitic breccia, and sandstone. Two breccia samples contain the prehnite-pumpellyite facies metamorphic minerals (Yuasa et al. 1992, 1999).

Nine dredges (KT04-28 D06~D13, D24 and D25: Figs. 2 and 4) were performed during the cruise KT04-28 by R/V"*Tansei-Maru*" in 2004. Dredge sites D06~D11 are located on the southwestern slope of the Ohmachi Seamount from north to south, and the sites D12 and D13 is on the eastern slope. Location of D25 was nearly identical to D06, and D24 was close to D09. Serpentinites were collected on sites D06, D07, D08, D09, D24, and D25. The other sites (D10~D13) yielded either of dacite-andesite and their volcaniclastic varieties correlative to the Paleogene, sandstone and mudstone to the Miocene, and unaltered basalt and pumice presumably of Quaternary tephra or debris. Dredge hauls at D09 also contained significant amounts of volcanic and sedimentary rocks in addition to serpentinites. Serpentinites collected at D06, D07, and D25 were dominantly schistose, whereas those at D08, D09, and D24 were mostly massive (Fig. 7). Sites D06 was set approximately the same site as lower parts of dives #609 and #1064, and yielded a piece of Grt-Ep amphibolite (D06-1) in addition to dominantly schistose serpentinite clasts.

5 Interpretation of Geologic Structures

A geological map for the fault scarp of the peninsular part of the Ohmachi Seamount was constructed based on the dive and dredge results as shown in Fig. 4. Semi-quantitative orientation data of dips and strikes of foliation (schistosity) read from video images are shown in Figs. 4 and 8, with three quantitative in-situ measurements of foliation; the method is briefly described in the appendix.

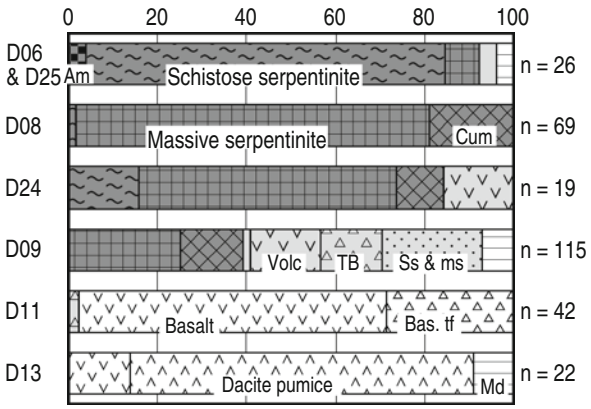

Fig. 7 Number-base proportions of rock species in dredge hauls collected during by the KT04-28 cruise. Dredge sites with poor or no recovery are not shown. For location of the dredge sites, see Figs. 2 and 4. *Am* amphibole schist, *Cum* ultramafic cumulate (clinopyroxenite, wehrlite, and hornblendite) except dunite, *Volc* volcanic rocks mainly of dacite and andesite, *TB* felsic to intermediate volcaniclastic rocks (tuff, lapilli tuff, tuff breccia etc.), *SS and ms* consolidated sandstone and mudstone, *Bas. tf* basaltic tuff and lapilli tuff, and *Md* semi-consolidated mudstone

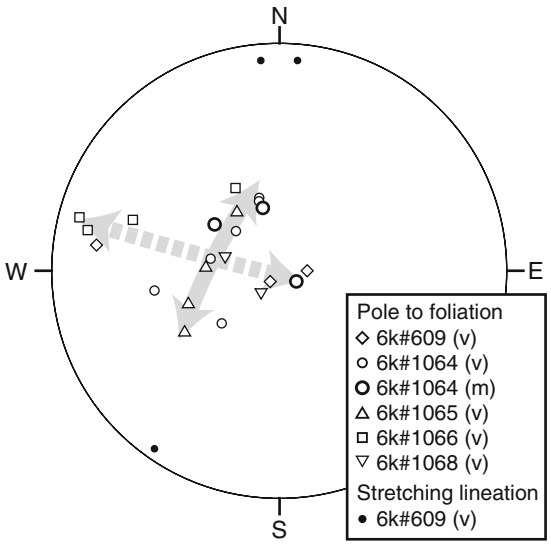

Fig. 8 Stereo net projection of foliation and lineation of schistose serpentinite. (v) Semiquantitative estimation by video image of outcrops and/or semi-oriented samples; and (m): In-situ measurements using the clinometer plate (see Appendix). *Gray arrows* indicate presumable modes of dispersion (*solid line*: by ESE-plunging rotation axis; and *dotted line*: by NNE-trending rotation axis)

5.1 Serpentinite Body

Dive and dredge results show that the northern and southern parts of the serpentinite exposure consist of differing lithotypes. The southern part is dominated by massive serpentinite, accompanied by local and minor schistose serpentinite. In the northern part, however, schistose serpentinite is dominant, with relatively small bodies of massive serpentinite. Foliation (schistosity) of the schistose serpentinite shows scattered orientations generally dipping to the east, southeast, or northeast (Fig. 8), with subhorizontal stretching lineations trending to the north to northeast. Massive serpentinite in the southern part thus structurally overlies dominantly schistose ones in the northern part. The two parts seem transitional without distinct boundary. Localities of amphibole schist floats lie at the structurally lowermost horizons of the serpentinite exposure.

Two kinds of folds are assumed for the varying orientation of foliation planes. One has a southeast-plunging fold axis with variable foliation strikes as typically seen in the variation of the 6K#1065 route (Fig. 8). This type of folds is occasionally found in schistose serpentinite samples (Fig. 6g–h). The fold axes cross the stretching lineations at high angles, and bend both the foliation and the lineation (Fig. 6g). These folds are commonly associated with slip surfaces and fractures filled by low-T serpentinites, carbonates, or magnetite (Fig. 6h). The other type of fold has presumably near-horizontal and north-northeast trending axes, and is mainly responsible for the variation of foliation dips from near-horizontal to near-vertical. The assumed axis is subparallel to the stretching lineation. Fractureless microfolds with lineation-parallel axes are seen in several samples of schistose serpentinite (Fig. 6c) and in an amphibole schist sample (Fig. 6a), and they are regarded as specimen-scale equivalents of the map-scale folds. This type of fold may predate the southeast-trending folds, which bend the lineation.

Comparing the varying orientation of foliation surfaces with specimen-sized fold structures, it is considered that the schistose parts of the serpentinite body are entirely folded (Fig. 9). Foliation dips are dominantly gentle in the northernmost sections (dives 6K#609 and 6K#1064), whereas steeper in the southern section (dive 6K#1066). Therefore, an anticline is assumed in the northernmost part of the serpentinite exposure.

5.2 Overlying Formations

Based on the distribution of rocks and nearly horizontal layering of tuff breccia observed during the dive 6K#609, a nearly flat-lying boundary is assumed between the serpentinite body and the Paleogene volcanic rocks at 3100–3,200 mbsl. Although no outcrop or float stones of the Paleogene volcanic sequence was observed during submersible dives to the south of 29°04.5'N, volcanic rocks and

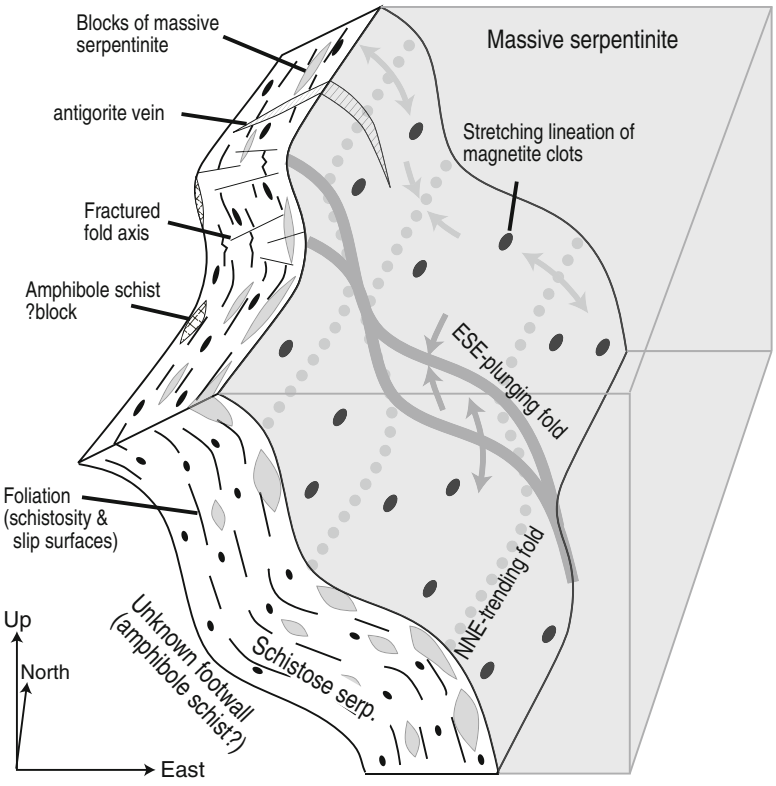

Fig. 9 Schematic block diagram for geologic structures of schistose serpentinite

tuff are not uncommon in dredges from these areas (Fig. 7). Therefore, we infer that the Paleogene continues to the south of the study area decreasing in thickness. The contact relation of the two formations remains uncertain, because no outcrop was found where the boundary could be observed directly. Two solutions are possible for the contact relationship: an unconformity and a flat-lying fault. An unconformable relation is difficult to reconcile with the fact that neither serpentinite xenoliths in volcanic rocks, serpentinite clasts in volcaniclastic rocks, nor volcanic rock dikes crosscutting serpentinite have been found. However, the scarce occurrence of deformed volcanic rocks and the absence of sheared mixture of serpentinite and volcanic materials are inconsistent with a fault contact. Therefore, the nature of the boundary drawn in Fig. 4 is speculative. Anyway, the flat boundary evidently crosscuts the fold structures within the serpentinite body (Fig. 10).

Dives 6K#341 and 6K#575 observed the flat-lying Miocene turbidite formation near the ridge crest with very steep slopes of 200–300 m descent. Common occurrences of debris blocks and dredge hauls of consolidated sandstone and siltstone suggest that the Miocene turbidite formation caps over the peninsular part of the seamount. At 6K#575 route, the base of the Miocene lies at a depth of ~2,500 mbsl, with

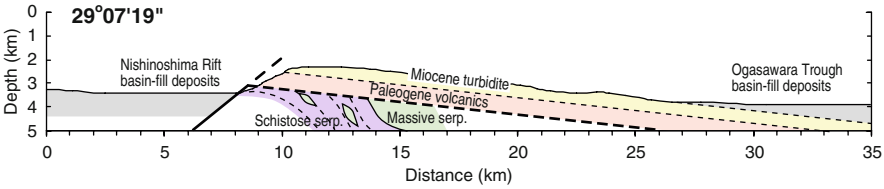

Fig. 10 Geologic cross section schematically projected from the south onto the west-east traverse crossing the localities of float blocks of amphibole schist

a difference in altitude of ca. 200 m from the ridge crest. At 6K#341 route, it is deeper than 2,700 mbsl with a difference in altitude exceeding 300 m from the ridge crest. It is thus inferred that the Miocene (possibly with younger sediments) becomes thicker towards south. On the contrary, the thickness of the Paleogene volcanic sequence is assumed to become thinner towards south, from a thickness of 600–700 m at 6K#575 to less than 400 m at 6K#341. Contrasting lithofacies between shallow-marine (partly reefal) limestone in the Paleogene and the Miocene turbidites imply a disconformable boundary accompanied by significant subsidence, and an abut relation of the Miocene onto a Paleogene volcano is assumed based on the opposite trends of the southward-thinning Paleogene and the southward-thickening Miocene formations.

6 Structural Characteristics of Sub-crustal Origins

Dive and dredge results from the Ohmachi Seamount showed that the mode of occurrences of serpentinites are quite different from those of well-known serpentinite seamounts in the Mariana and Bonin forearcs ("forearc serpentinite seamounts") located much nearer to the trench. The forearc serpentinite seamounts occur in two different modes: mud volcanoes and horsts (Fryer 1992; Fryer et al. 1995). The mud volcanoes are piles of serpentine mud flows, which contain small fragments of serpentinized peridotites, gabbro, volcanic rocks, and high-pressure metamorphic rocks (Maekawa et al. 1992, 1993). Serpentinites consist dominantly of low-T species (chrysotile and lizardite: Saboda et al. 1992), although antigorite-olivine equilibria suggesting greenschist to amphibolite grades are recently found by Murata et al. (2009). Rocks of the horsts are ophiolitic consisting of massive serpentinite accompanied by significant amounts of gabbro and volcanic rocks (Ishii 1985; Ishiwatari et al. 2006). High-pressure metamorphic rocks are rarely associated (Maekawa et al. 2004). Antigorite schist was not found in both types of the forearc serpentinite, and they are either massive or highly fractured enough to be fluidized. These structures obviously crosscut or disturbed the Paleogene volcanic formation including boninite. They are generally considered as diapirs by buoyancy (Ishii et al. 1992) or hydration expansion (Fryer and Fryer 1987; Fryer 1992), and fluidized effusives by over-pressured pore fluids (Fryer 1992).

On the contrary, the serpentinite body of the Ohmachi Seamount lacks crustal rocks which did not suffer high-pressure metamorphism. It consists almost entirely of serpentinite, with trace amounts of amphibole schists with eclogite and blueschist relics. No evidence of mud flow has been observed, and the serpentinite body is likely to occur as a coherent mass except the parts locally fractured by faults and landslides. Antigorite is ubiquitous, although later low-T serpentines after olivine are also common. And most notably, the northern part of the body consists of crystalline schist of antigorite (schistose serpentinite), which has not been found in the forearc serpentinite seamounts. Its folded structure is truncated by the base of the Paleogene. These contrasting occurrences suggest that the serpentinites of the Ohmachi Seamount do not have the same mode of exhumation with the forearc serpentinite seamounts, and might have originated neither from a diapir nor a mud volcano.

Although the extent of the exposed serpentinite body in the Ohmachi Seamount is quite limited, their observed modes of occurrences are rather similar to some of the regional high-pressure metamorphic terranes on land such as Sanbagawa Belt in Japan (Mizukami and Wallis 2005) or the Zermatt-Saas Ophiolite in the Alps (Li et al. 2004). Serpentinites in these terranes are coherent bodies with common occurrences of folded antigorite schist or schistose antigorite peridotite with evident stretching lineation. Accompanied crustal rocks are exclusively high-pressure metamorphic. Therefore, it is probable that the serpentinite exposure in the Ohmachi Seamount is a window of a regional high-pressure metamorphic belt, which formed in the Philippine Sea Plate, although its extent is obscured by cover sequences.

Although there is no direct observation of contact relationship between the schistose serpentinite and the amphibole schists, they share the common structural features such as schistosity, mineral and/or stretching lineation, and folds that deformed the schistosity. These common features suggest that the amphibole schists were incorporated into the schistose serpentinite before or during generation of the schistosity. So far as seen in amphibole schists, the schistosity and the mineral lineation were formed during the decompression stage from the eclogite to the amphibolite facies (Ueda et al. 2004, 2005). Hence, schistosity of serpentinites might also have formed during the same decompression stage as the amphibole schists. Dominantly low-angle foliation and subhorizontal stretching lineation in the schistose serpentinite suggest that the serpentinite body was subvertically flattened and laterally extended during its exhumation. The strain might have been localized in the northern part consisting mainly of schistose serpentinite with amphibole schists, compared to the overlying southern part mostly of massive types. This structural relation implies that the massive serpentinites originated from the hanging-wall of the shear zone which carried up eclogites.

The massive serpentinite occasionally contain edenitic to pargasitic amphiboles which could be stable in primary peridotite stages (Niida et al. 2003, 2005) as hydrous phases, and are intruded by ultramafic cumulate dikes including olivine hornblendite, which suggest pathways of hydrous magma, before the antigorite-forming metamorphism with deformation. Such hydrous natures prefer a wedge mantle origin to subducted oceanic mantle origins as products of less hydrous igneous activity at the mid-oceanic ridge. Although they are much less refractory than the typical forearc

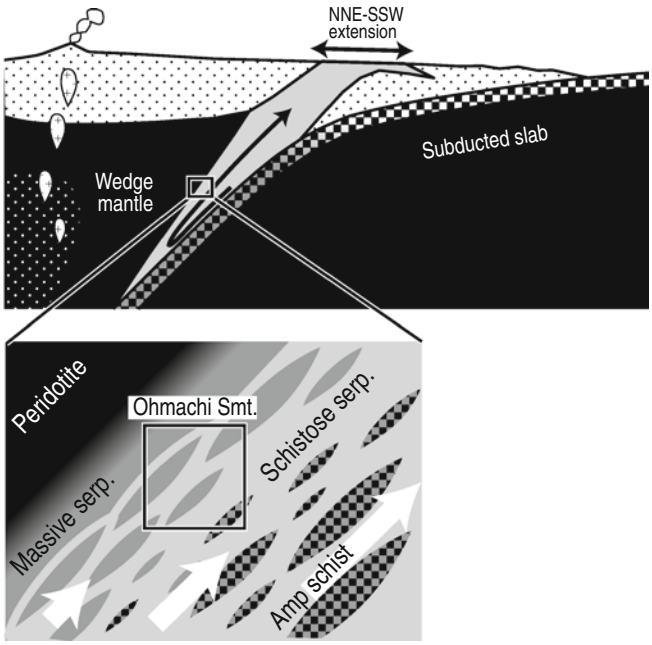

Fig. 11 Model illustrations for the genesis of geologic structure in the Ohmachi Seamount

peridotites as indicated by chemistry of relic spinels (Cr# ~0.15: Yuasa et al. 1999; Niida et al. 2001, 2003), peridotites with similar spinel chemistry and hydrous phases were recently discovered from southern Mariana forearcs (Yanagida et al. 2006; Michibayashi et al. 2009) as well as from back-arc basins in the Philippine Sea Plate (Ohara et al. 2002, 2003). Occurrence of least refractory peridotites in the southern Mariana forearc are attributed to slow and rather amagmatic spreading of a back-arc basin (Mariana Trough) in the upper plate (Michibayashi et al. 2009).

Concerning the structural and petrologic characteristics of serpentinites, the simplest interpretation for the geologic structure is given in Fig. 11, where the fragments of the subducted oceanic crust (blueschists and eclogites) were exhumed along with the shear zone (schistose serpentinite) at the base of the hanging-wall mantle wedge (massive serpentinite).

7 Exhumation to the Surface

Because any geochronological data have not been successfully obtained so far for metamorphic rocks of the Ohmachi Seamount, it is difficult to discuss detailed tectonic processes of their exhumation to the surface. Here we briefly review the tectonic history of the Philippine Sea Plate and several proposed ideas.

The Philippine Sea Plate (PSP) experienced repetitive arc activities and back-arc spreading or rifting in intra-oceanic environments, at youngest since the Early Cretaceous (Fig. 1). Early to Late Cretaceous arc igneous rocks are known to occur in the Amami Plateau (Hickey-Vergas 2005). The plateau, together with the adjacent Daito and Oki-Daito Ridges, is considered as a Cretaceous remnant arc left after back-arc spreading of the West Philippine Basin (WPB) during the Paleocene to the Eocene (Hilde and Lee 1984). The correspondent daughter arcs have been assumed to be Cretaceous ophiolites and arc sequences exposed on the Halmahera and eastern Mindanao islands (Hall et al. 1995; 1988). As WPB spread and the PSP rotated, the proto-Izu-Bonin-Mariana (IBM) arc formed at the present-day Kyushu-Palau Ridge at ~49 Ma (Ishizuka et al. 2006). The IBM arc experienced back-arc rifting and spreading in the late Oligocene to middle Miocene (the Shikoku and Parece Vela Basin: Okino et al. 1994), in the late Miocene (between the Nishi-Shichito Ridge and the present-day IBM arc: Yamazaki and Yuasa 1998; Kodaira et al. 2008), since the Pliocene (West Mariana Basin: Husson and Uyeda 1980), and in the Quaternary (intra-arc rift basins in the Izu-Bonin Arc). Since the Oligocene, the modes and directions of the back-arc spreading separated between the Izu-Bonin and Mariana arcs bounded by the Sofugan Tectonic Line (STL: Yuasa 1985). The Ohmachi Seamount is located at the northeastern termination of the STL and the Nishinoshima Trough, where the IBM arc crust is extremely thin (less than 10 km: Kodaira et al. 2007).

There have been several ideas proposed for the exhumation of the serpentinite body in the Ohmachi Seamount. The earliest model considered it as a diapiric body uprose along with the Quaternary intra-arc rifting (Yuasa et al. 1999). Ohara (2003) also attributed the serpentinite exhumation to the Quaternary rifting, but considered it as an oceanic core complex similar to the other core complexes being discovered in the back-arc spreading systems of the PSP (Ohara et al. 2001, 2003). Ueda et al. (2004) assumed that the timing of the exhumation was older than the overlying volcanic rocks. They first concerned the occurrences of high-pressure metamorphic rocks, and attributed their exhumation to extension by the spreading of the WPB over the subducting Pacific slab in the Eocene. Meschede et al. (2009) proposed that the unroofing resulted from leaky transform displacement (transtension) along the STL based on the difference of spreading directions between the Shikoku and Parece-Vela basins. Most recently, Ota and Kaneko (2010) interpreted the base of the Tertiary as a post-Miocene fault, and attributed the exhumation to squeezing by the shallowing Pacific slab related to subduction of a large buoyant seamount (Ogasawara Plateau: Fig. 1).

Recently accumulated geological and structural observations suggest that the serpentinite body was emplaced earlier than the deposition (or basal faulting) of the overlying Paleogene formation, which is scarcely deformed, and whose base crosscut the foliations of the serpentinite body. The sub-horizontal stretching lineation and subsequent lineation-orthogonal fractures are not consistent with diapiric movements, which prefer dip-slip strain. Hence, diapirism is unlikely to have been the main mode of the exhumation, although buoyancy and volume expansion could have contributed to upward components of the displacement. The NNE-trending stretching lineations are compatible neither with spreading direction of the Quaternary intra-arc rift nor the present-day moving direction of the subducting Pacific plate (Fig. 1).

On the other hand, the lineation trend is sub-parallel to the STL and the spreading direction of the WPB. This implies that the exhumation occurred along with one of the back-arc spreading centers earlier than the Miocene.

In addition to the geochronology of the metamorphic rocks, one of the important points remaining unsolved is the contact relationship between the serpentinite body and the overlying Paleogene volcanic rocks, as previously mentioned. If it is an unconformity, the exhumation exclusively occurred before the Late Eocene, within the WPB or the Cretaceous remnant arcs as a different subduction system from the IBM. If it is a detachment fault, at least the final stage of the exhumation should have occurred after the Early Oligocene, i.e., related to one of the back-arc spreading centers of the IBM system.

Acknowledgments This paper is dedicated to the late Prof. T. Watanabe, who conducted the scientific investigations of the YK01-04 cruise, and guided us to geological and petrological studies on the Ohmachi Seamount. The authors thank Captains O. Yukawa (YK01-04), U. Fujita (KT04-08) and S. Ryono (YK08-05), crews and on-shore staffs of R/V *Yokosuka* and *Tansei-maru*, commanding officers Y. Imai and T. Sakurai and the *Shinkai 6500* operation team for their operation and administrations, and Ms. M. Aoki and M. Imamura for her assistance of onboard works in R/V *Yokosuka*. The *Shinkai 6500* operation team also helped us to develop clinometer plate. Successful dredges of KT04-28 cruise owe greatly to operation and assistance by Prof. T. Ishii, Drs. S. Haraguchi and S. Machida, and other members of KT04-28 scientific party with fruitful discussions. Dr. A. Nishimura helped us to review results of GH84-1 and GH86-1 cruises. Constructive reviews by Drs. J. Wakabayashi and T. Tsujimori greatly helped to improve the manuscript. H. Ueda was financially supported by MEXT grant-in aid for JSPS Fellows 01403900 and 17740329, and for twenty-first Century COE Program "Neo-Science of Natural History" (Hokkaido University).

8 Appendix: In Situ Measurement of Geological Surface Orientation by Submersible

Foliation planes by schistosity were measured by a newly developed clinometer plate at three localities during the dive 6K#1064. Bedding plane of semi-consolidated mudstone was also measured at a locality of the dive 6K#1067 by the same method. Here we describe the outline of the method, and more detailed method, calibration, and evaluation of its reliability will be given in another paper.

The clinometer plate is an acryl disc 24 cm in diameter with a steal vertical bar 12 cm long at the center (Fig. 12). Both the disc and the vertical bar are scaled at 1 cm intervals by painting. The disc is mounted on a steel disc of the same diameter, on which a handle is equipped. At the outcrop, the clinometer plate was laid on, or set parallel to the surface structure of interest, handled by the manipulator of the submersible. And it was photographed by a camera, whose focal length and orientation relative to the submersible were logged. Also logged was orientation of the submersible.

The photographs were analyzed by the following procedures. First, the angle φ of the vertical bar to the line of sight (connecting the lens and disc centers) was calculated by a simple graphical analysis shown in Fig. 13. The lengths b and s in Fig. 13a was determined reading the scale of the point where scales of the disc and

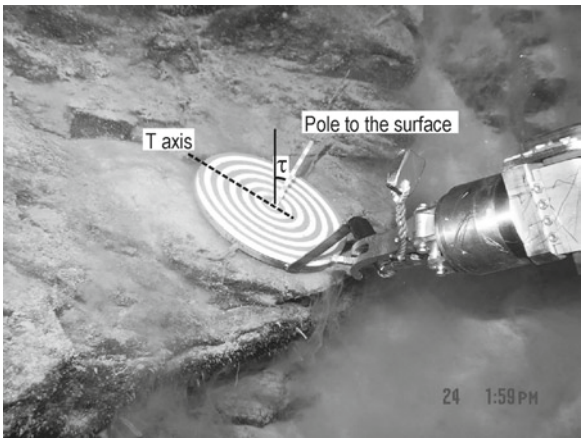

Fig. 12 Photograph of in-situ measurement using the clinometer plate at a sea-floor outcrop (6K#1064 Loc. 5: 3,277 mbsl)

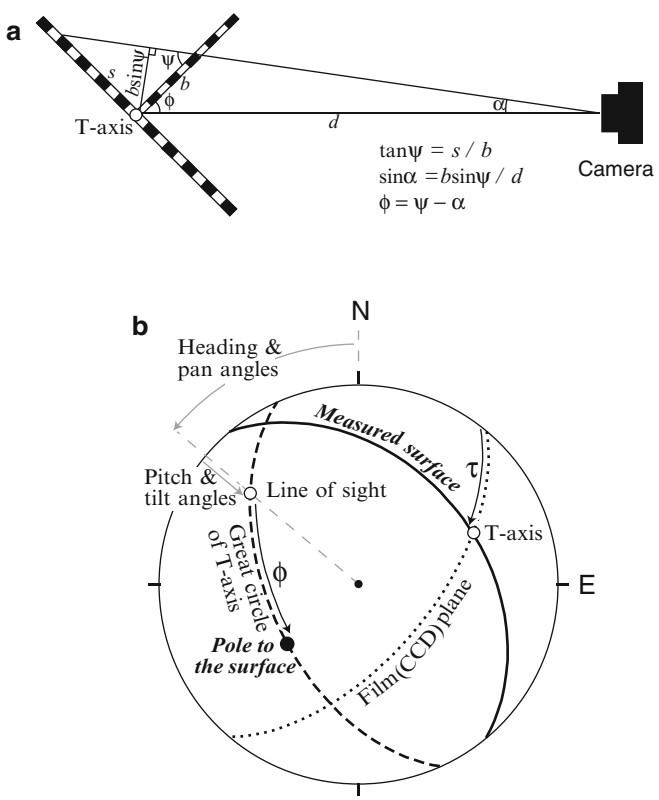

Fig. 13 Theory for the measurement of surface structures by the clinometer plate. (**a**) Measurement of the *bar* angle to the *line* of sight. (**b**) Stereo net projection (*upper hemisphere*) for the relation between graphic analysis and the correspondent surface orientation

the vertical bar were overlapped in the picture. And the distance d was estimated based on the approximate proportional relation between d by the real disc radius and the focal length by the disc radius projected on the imaging device (CCD). Also measured was the projected tilt angle τ of the bar in the picture (Fig. 12). The angles φ and τ give azimuth and dip of the disc plane (i.e. the surface) relative to the line of sight (Fig. 13b). And this apparent orientation was calibrated along with camera centering, pan and tilt angles of the camera, heading, pitch, and roll angles of the submersible, and the installation angles of the rotation axes of the camera to the submersible. Distortion of the picture was not corrected, however, the on-shore tests gave good agreements with measurements by a magnetic clinometer compass within the errors less than several degrees.

References

Akikawa N, Tokonami M (1987) Crystal structure and cation distribution of "cleavable" olivines. Miner J 13:271–279

Amante C, Eakins BW (2009) ETOPO1 1 Arc-minute global relief model: procedures, data sources and analysis. NOAA Tech Memo NESDIS NGDC-24: p 19

Bloomer SH (1983) Distribution and origin of igneous rocks from the landward slopes of the Mariana Trench: implications for its structure and evolution. J Geophys Res 88:7411–7428

Bloomer SH, Taylor B, MacLeod CJ, Stern R, Fryer P, Hawkins JW, Johnson L (1995) Early arc volcanism and the ophiolite problem: a perspective from drilling in the western Pacific. In: Taylor B, Natland J (eds) Active margins and marginal basins of the western Pacific (Geophys Monogr 88). AGU, Washington, DC, pp 1–30

Cloos M, Shreve RL (1988) Subduction-channel model of prism accretion, melange formation, sediment subduction, and subduction erosion at convergent plate margins: 1. Background and description. Pure Appl Geophys 128:455–500

DeMets C, Gordon RG, Argus DF, Stein S (1994) Effect of recent revisions to the geomagnetic reversal time scale on estimates of current plate motions. Geophys Res Lett 21:2191–2194

Dickinson WR, Hopson CA, Saleeby JB (1996) Alternate origins of the coast range ophiolite (California): introduction and implications. GSA Today 6:1–10

Evans BW (1977) Metamorphism of alpine peridotite and serpentinite. Ann Rev Earth Planet Sci 5:397–447

Federico L, Crispini L, Scambelluri M, Capponi G (2007) Ophiolite mélange zone records exhumation in a fossil subduction channel. Geology 35:499–502

Fryer P (1992) A synthesis of Leg 125 drilling of serpentinite seamounts on the Mariana and Izu-Bonin forearcs. Proc ODP Sci Results 125:593–614

Fryer P, Fryer GJ (1987) Origins of nonvolcanic seamounts in a forearc environment. In: Keating BH, Fryer P, Batiza R, Boehlert GW (eds) Seamounts, islands, and atolls (Geophys Monogr 43). Amer Geophysical Union, Washington, DC, pp 61–69

Fryer P, Mottl M, Johnson L, Haggerty J, Phipps S, Maekawa H (1995) Serpentine bodies in the forearcs of western Pacific convergent margins: origin and associated fluids. In: Taylor B, Natland J (eds) Active margins and marginal basins of the western Pacific (Geophys Monogr 88). AGU, Washington, DC, pp 259–279

Fujiwara T, Yuasa M, Watanabe T, Niida K, Nishimura A, Sakamoto I, Ishizuka O, Imamura M, Tsukuda K (2001) Submersible study around the Sofugan Tectonic Line, Izu-Bonin Arc. JAMSTEC Deep Sea Res 18:71–82 (in Japanese with English abstract)

Ganne J, Marquer D, Rosenbaum G, Bertrand JM, Fudral S (2006) Partitioning of deformation within a subduction channel during exhumation of high-pressure rocks: a case study from the Western Alps. J Struct Geol 28:1193–1207

Gerya TV, Stöckhert B, Perchuk A (2002) Exhumation of high-pressure metamorphic rocks in a subduction channel: A numerical simulation. Tectonics 21: p. 1059 doi:10.1029/2002TC001406

Guillot S, Hattori KH, de Sigoyer J, Nägler T, Auzende AL (2001) Evidence of hydration of the mantle wedge and its role in the exhumation of eclogites. Earth Planet Sci Lett 193: 115–127

Hall R, Audley-Charles MG, Banner FT, Hidayat S, Tobing SL (1988) Basement rocks of the Halmahera region, eastern Indonesia: a late cretaceous early tertiary arc and fore-arc. J Geol Soc Lond 145:65–84

Hall R, Fuller M, Ali JR, Anderson CD (1995) The Philippine Sea plate: magnetism and reconstructions. In: Taylor B, Natland J (eds) Active margins and marginal basins of the Western Pacific (Geophys Monogr 88). AGU, Washington, DC, pp 371–404

Hermann J, Münterner O, Scambelluri M (2000) The importance of serpentine mylonites for subduction and exhumation of oceanic crust. Tectonophysics 327:225–238

Hickey-Vergas R (2005) Basalt and tonalite from the Amami Plateau, northern West Philippine Basin: New Early Cretaceous ages and geochemical results, and their petrologic and tectonic implications. I Arc 14:653–665

Hilde TC, Lee CS (1984) Origin and evolution the West Philippine Basin: a new interpretation. Tectonophysics 102:85–104

Hirauchi K, Michibayashi K, Ueda H, Katayama I (2010) Spatial variations in antigorite fabric across a serpentinite subduction channel: insights from the Ohmachi Seamount, Izu-Bonin frontal arc. Earth Planet Sci Lett 299(1–2):196–206

Husson DM, Uyeda S (1980) Tectonic processes and the history of the Mariana arc: a synthesis of the results of Deep Sea Drilling Project Leg 60. Init Rep DSDP 60:909–929

Ishii T (1985) Dredged samples from the Ogasawara fore-arc seamount or "Ogasawara paleoland" – "forearc ophiolite". In: Nasu N, Kobayashi K, Kushiro I, Kagami H (eds) Formation of active ocean margins. Terra Scientific Publishing, Tokyo, pp 307–342

Ishii T, Robinson PT, Maekawa H, Fiske R (1992) Petrological studies of peridotites from diapiric serpentinite seamounts in the Izu-Ogasawara-Mariana forearc, Leg 125. Proc ODP Sci Results 125:445–485

Ishiwatari A, Yanagida Y, Li YB, Ishii T, Haraguchi S, Koizumi K, Ichiyama Y, Umeka M (2006) Dredge petrology of the boninite- and adakite-bearing Hahajima Seamount of the Ogasawara (Bonin) forearc: an ophiolite or a serpentinite seamount? I Arc 15:102–118

Ishizuka O, Kimura JI, Li YB, Stern RJ, Reagan MK, Taylor RN, Ohara Y, Bloomer SH, Ishii T, Hargrove US III, Haraguchi S (2006) Early stages in the volcanism: new age, chemical and isotopic constraints. Earth Planet Sci Lett 250:385–401

JAMSTEC (2000) YK00-08 Leg1 cruise report. Japan Agency for Marine-Earth Science and Technology, p 79

Kodaira S, Sato T, Takahashi N, Miura S, Tamura Y, Tatsumi Y, Kaneda Y (2007) New seismological constraints on growth of continental crust in the Izu-Bonin intra-oceanic arc. Geology 35:1031–1034

Kodaira S, Sato T, Takahashi N, Yamashita M, No T, Kaneda Y (2008) Seismic imaging of a possible paleoarc in the Izu-Bonin intraoceanic arc and its implications for arc evolution processes. Geochem Geophys Geosystems 9: Q10X01, doi:10.1029/2008GC002073

Kretz R (1983) Symbols for rock-forming minerals. Am Mineral 68:277–279

Li XP, Rahn M, Bucher K (2004) Serpentinites of the Zermatt-Saas ophiolite complex and their texture evolution. J Metamorph Geol 22:159–177

Maekawa H, Shozui M, Ishii T, Saboda KL, Ogawa Y (1992) Metamorphic rocks from the serpentinite seamounts in the Mariana and Izu-Ogasawara forearcs. Proc ODP Sci Results 125:415–430

Maekawa H, Shozui M, Ishii T, Fryer P, Pearce J (1993) Blueschist metamorphism in an active subduction zone. Nature 364:520–523

Maekawa H, Fryer P, Ozaki A (1995) Incipient blueschist-facies metamorphism in the active subduction zone beneath the Mariana forearc. In: Taylor B, Natland J (eds) Active margins and marginal basins of the western Pacific (Geophys Monogr 88). AGU, Washington, DC, pp 281–289

Maekawa H, Yamamoto K, Ueno T, Osada Y, Nogami N (2004) Significance of serpentinites and related rocks in the high-pressure metamorphic terranes, circum-Pacific regions. Int Geol Rev 46:426–444

Maruyama S, Liou JG, Terabayashi M (1996) Blueschists and eclogites of the world and their exhumation. Int Geol Rev 38:485–594

Meschede M, Ueda H, Ogawa Y, Shipboard Scientific Party YK08-05 (2009) Serpentinite schists of the Ohmachi seamount and their possible relation to extensional plate movements of the Philippine Sea Plate. Eos Trans AGU 90: Fall Meet Suppl Abstr T21A-1778

Michibayashi K, Ohara Y, Stern RJ, Fryer P, Kimura JI, Tasaka M, Harigane Y, Ishii T (2009) Peridotites from a ductile shear zone within back-arc lithospheric mantle, southern Mariana Trench: Results of a Shinkai 6500 dive. Geochem Geophys Geosystems 10: Q05X06, doi:10.1029/2008GC002197

Mizukami T, Wallis SR (2005) Structural and petrological constraints on the tectonic evolution of the garnet-lherzolite facies Higashi-akaishi peridotite body, Sanbagawa belt, SW Japan. Tectonics 24: TC6012, doi:10.1029/2004TC001733

Murata K, Maekawa H, Yokose H, Yamamoto K, Fujioka K, Ishii T, Chiba H, Wada Y (2009) Significance of serpentinization of wedge mantle peridotites beneath Mariana forearc, western Pacific. Geosphere 5:90–104

Niida K, Yuasa M, Nishimura A, Fujiwara T, Watanabe T (2001) Serpentinites from Ohmachi Seamount: origin of basement lithosphere of the Izu-Ogasawara Arc. JAMSTEC J Deep Sea Res 19:77–86 (in Japanese with English abstract)

Niida K, Izumino T, Yuasa M (2003) The Ohmachi seamount serpentinites derived from the uppermost mantle beneath oceanic island-arc. Chikyu Month Extra-number 43:90–100 (in Japanese)

Niida K, Izumino T, Ishii I, Ishii T (2005) Mineralogical variations of suboceanic peridotites: Unique characteristics of upper mantle peridotites from the Izu-Ogasawara-Mariana arc back-arc basin areas. Chikyu Mon Extra-number 52:165–173 (in Japanese)

Nishimura A (1992) Carbonate bioclasts of shallow-water origin at Site 793. Proc ODP Sci Results 126:231–234

Nishimura A, Nohara M, Usui A (1997) Strontium Isotope stratigraphic ages of limestones taken during the submersible survey using “Shinkai 2000” in the Kyushu-Palau Ridge and the Izu-Bonin Arc. JAMSTEC Deep Sea Res 13:145–153 (in Japanese with English abstract)

O’Hanley DS (1996) Serpentinites. Records of tectonic and petrological history. Oxford University Press, New York, p 277

Ohara Y (2003) Reviews on mantle peridotites from the Philippine Sea back arc spreading systems. Rep Hydrogr Oceanogr Res 39:64–83 (in Japanese with English abstract)

Ohara Y, Yoshida T, Kato T, Kasuga S (2001) Giant megamullion in the Parece Vela backarc basin. Marin Geophys Res 22:47–61

Ohara Y, Stern RJ, Ishii T, Yurimoto H, Yamazaki T (2002) Peridotites from the Mariana Trough: first look at the mantle beneath an active back-arc basin. Contrib Mineral Petrol 143:1–18

Ohara Y, Fujioka K, Ishii T, Yurimoto H (2003) Peridotites and gabbro from the Parece Vela backarc basin: unique tectonic window in an extinct backarc spreading ridge. Geochem Geophys Geosystems 4:8611. doi:10.1029/2002GC000469

Okino K, Shimakawa Y, Nagaoka S (1994) Evolution of the Shikoku Basin. J Geomagn Geoelectr 46:463–479

Ota T, Kaneko Y (2010) Blueschists, eclogites, and subduction zone tectonics: insights from a review of late Miocene blueschists and eclogites, and related young high-pressure metamorphic rocks. Gondwana Res 18:167–188

Saboda KL, Fryer P, Maekawa H (1992) Metamorphism of ultramafic clasts from conical seamount: Sites 778, 779, and 780. Proc ODP Sci Results 125:431–443

Sakamoto I, Sasaki T, Fujioka K (1997) Volcano-stratigraphic characteristics of upper part of oceanic island arc, around the Sofugan Tectonic Line. JAMSTEC Deep Sea Res 13:479–494 (in Japanese with English abstract)

Sakamoto I, Jarvis PA, Okino K, Aoki M, Kanda S, Kashiwase K (1998) Geological and Petrological characteristics of Sofugan Tectonic Line -Report of YK97-04 cruise-. JAMSTEC Deep Sea Res 14:279–229 (in Japanese with English abstract)

Sakamoto I, Fujiwara T, Ishizuka O (2001) Topographical and geological characteristics of Sofugan Tectonic Line (STL) area, Izu-Ogasawara Arc. JAMSTEC Deep Sea Res 18:55–69 (in Japanese with English abstract)

Shervais J, Kolesar P, Andreasen K (2004) A field study of serpentinization – Stonyford, California: chemical flux and mass balance. In: Ernst WG (ed) Serpentinite and serpentinites: mineralogy, petrology, geochemistry, ecology, geophysics, and tectonics. Geological Society America, Boulder, pp 452–474

Stern RJ, Bloomer SH (1991) Subduction zone infancy: examples from the Eocene Izu-Bonin-Mariana and Jurassic California arcs. Geol Surv Am Bull 104:1621–1636

Uda S (1984) The contact metamorphism of the eyama ultrabasic mass and the genesis of the "cleavable olivine". J Geol Soc Jpn 90:393–410

Ueda H, Usuki T, Kuramoto Y (2004) Intra-oceanic unroofing of eclogite-facies rocks in the Omachi Seamount, Izu-Bonin frontal arc. Geology 32:849–852

Ueda H, Usuki T, Kuramoto Y (2005) Eclogite facies metamorphic rocks in the Omachi Seamount, Izu-Bonin arc: exhumation of deeply subducted rocks during intraoceanic subduction infancy(?). Chikyu Mon Extra-number 52:121–128 (in Japanese)

Yamazaki T, Yuasa M (1998) Possible Miocene rifting of the Izu-Ogasawara (Bonin) arc deduced from magnetic anomalies. I Arc 7:374–382

Yamazaki T, Ishihara T, Murakami F (1991) Magnetic anomalies over the Izu-Ogasawara (Bonin) Arc, Mariana Arc and Mariana Trough. Bull Geol Surv Jpn 42:655–686

Yanagida Y, Ishiwatari A, Ishii T (2006) Petrology of ultramafic rocks from the southern part of the Mariana Trench slope. In: Abstract of 133th Annual Meeting of the Geological Soceity of Japan, 238

Yuasa M (1985) Sofugan Tectonic Line, a new tectonic boundary separating northern and southern parts of the Ogasawara (Bonin) arc, northwest Pacific. In: Nasu N, Kobayashi K, Kushiro I, Kagami H (eds) Formation of active ocean margins. Terra Scientific, Tokyo, pp 483–496

Yuasa M (1992) Origin of along-arc geologic variations on the volcanic front of the Izu-Ogasawara (Bonin) Arc. Bull Geol Surv Jpn 43:457–466

Yuasa M, Nohara M (1992) Petrographic and geochemical along-arc variations of volcanic rocks on the volcanic front of the Izu-Ogasawara (Bonin) Arc. Bull Geol Surv Jpn 43:421–456

Yuasa M, Uchiumi S, Nishimura A, Shibata K (1988) K-Ar age of a forearc seamount adjacent to the volcanic front of the Izu-Ogasawara Arc. Bull Volc Soc Jpn 2nd Ser 33: 352–353 (in Japanese)

Yuasa M, Murakami F, Saito E, Watanabe K (1991) Submarine topography of seamounts on the volcanic front of the Izu-Ogasawara (Bonin) Arc. Bull Geol Surv Jpn 42:703–743

Yuasa M, Watanabe T, Kuwajima T, Hirama T, Fujioka K (1992) Prehnite-pumpellyite facies metamorphism in oceanic arc basement from Site 791 in the Sumisu Rift, western Pacific. Proc ODP Sci Results 126:185–193

Yuasa M, Nishimura A, Niida K, Ishizuka O (1998) A serpentinite diapir forming part of the Ohmachi Seamount near the volcanic front of the Izu-Ogasawara Arc (SHINKAI 6500 #341). JAMSTEC Deep Sea Res 14:269–277 (in Japanese with English abstract)

Yuasa M, Nishimura A, Niida K, Ishizuka O (1999) Tertiary system near the volcanic front of central Izu-Ogasawara Arc: geology of the Ohmachi Seamount. Chikyu Mon Extra-number 23:107–115 (in Japanese)

Petrology and Mineralogy of Mantle Peridotites from the Southern Marianas

Hiroshi Sato and Teruaki Ishii

Abstract Plagioclase-bearing mantle peridotites were dredged from two sites along the scarp of a fault (144°E) on the inner wall of the southern Mariana Trench, during cruise KH-98-1 of the R/V *Hakuho-maru*. The peridotites are weakly to moderately serpentinized, with most of the primary minerals retained, at least in part. The spinels have been modified by an impregnating melt, and their compositions indicate that the peridotites represent the residue left over from as much as 15% partial melting. The impregnating melt yielded large amounts of plagioclase and clinopyroxene (up to 7%), and also enriched spinel and pyroxene in TiO_2. The texture of the peridotites, and the degree of melting, suggest that these rocks originated in a back-arc basin. However, the degree of melting and melt impregnation in these peridotites is higher than that in peridotites from the Mariana Trough.

Keywords Mantle peridotite • Impregnation • Back-arc basin • Southern Mariana Trench

1 Introduction

The Izu–Bonin–Mariana (IBM) arc–trench system, along the eastern boundary of the Philippine Sea Plate, is characterized by exposures of serpentinite-dominant seamounts in the fore-arc area (Fryer and Fryer 1987; Fryer et al. 1995). These seamounts are composed of rocks with island-arc affinities and lithologies similar to those of onland ophiolites; therefore, they are classified as "island-arc ophiolites"

H. Sato (✉)
Institute of Natural Sciences, Senshu University, 2-1-1 Higashimita, Tama-ku, Kawasaki, Kanagawa 214-8580, Japan
e-mail: satohiro@isc.senshu-u.ac.jp

T. Ishii
Fukada Geological Institute, 2-13-12 Hon-Komagome, Bunkyo, Tokyo 113-0021, Japan
e-mail: ishii@fgi.or.jp

Y. Ogawa et al. (eds.), *Accretionary Prisms and Convergent Margin Tectonics in the Northwest Pacific Basin*, Modern Approaches in Solid Earth Sciences 8,
DOI 10.1007/978-90-481-8885-7_6,

(Bloomer 1983) or "fore-arc ophiolites" (Ishii 1985). Although mantle peridotites with back-arc basin affinities have been sampled in only a few areas of the Philippine Sea Plate, and information was very limited until the 1990s (Bloomer and Hawkins 1983; Shcheka et al. 1995; Ohara et al. 1996; Stern et al. 1996, 1997), our knowledge of the mantle beneath the various back-arc basins has increased substantially over the past decade. For example, Ohara et al. (2003) provided information on the Parece Vela Rift, which is an extinct Miocene spreading center in the Parece Vela Basin, and Ohara et al. (2002) discussed the Mariana Trough, which is an active spreading center in the southern Philippine Sea Plate.

One of the important localities for exposures of mantle peridotites is the inner wall of the southern Mariana Trench, which has been analyzed in several studies (Bloomer and Hawkins 1983; Fryer 1993; Ohara and Ishii 1998; Michibayashi et al. 2007, 2009). Mantle peridotites are exposed along the southern Mariana Trench, at 143°30′E, 11°30′N, representing the residues following high degrees of melting related to island-arc volcanism (Bloomer 1983; Ohara and Ishii 1998; Michibayashi et al. 2007). East of this site, at 144°10′E, is a large scarp that trends mainly N–S along a fault known either as the Southeastern Mariana Fore-Arc Fault (Fryer 1993) or the West Santa Rosa Bank Fault. Mantle peridotites, together with mafic and intermediate rocks, have been collected from this scarp (Bloomer and Hawkins 1983; Fryer 1993; Michibayashi et al. 2009), with most of them considered to represent residues related to back-arc basin magmatism rather than island-arc activity. Therefore, two distinct types of mantle peridotite are exposed in the southern Mariana area. Bloomer and Hawkins (1983) briefly discussed mantle peridotites dredged from the fault at 144°E, and Michibayashi et al. (2009) provided mineralogical and petrologic data, together with an analysis of olivine crystal preferred orientations, for several mantle peridotites recovered during a submersible dive. In this paper, we document the petrographic, petrologic, and mineralogical characteristics of mantle peridotites from the fault at 144°E in the southern Marianas, and discuss the significance of these rocks.

2 Description of Dredge Sites and Geological Background

Plagioclase-bearing spinel peridotites were recovered from two dredge sites, KH-98-1D1 and KH-98-1D2, during the KH-98-1 cruise of the R/V *Hakuho-maru* (Table 1). These sites are on the scarp of a large fault which trends mainly N–S at about 144°10′E along the Mariana Trench, southwest of Guam.

Prior to this cruise, the same fault scarp had already been investigated during two *Shinkai 6500* dives, 6K#158 and 6K#159 (Fryer 1993), and one dredge haul, D27 (Bloomer and Hawkins 1983) (Fig. 1). During the submersible dives, seven basalts (plagioclase-clinopyroxene basalt) and three microgabbros were recovered (Fryer 1993). Bloomer and Hawkins (1983) recovered serpentinized peridotites, most of which are considered to be lherzolite, and small amounts of mafic rock.

Table 1 Location of the dredge sites of cruise KH-98-1, R/V *Hakuho-maru*

Cruise	KH-98-1 (R/V *Hakuho-maru*)	
Site	D1	D2
Water depth (m)	6,265	5,979
On bottom		
Depth (m)	5,843	4,880
Latitude	12°13.07′N	12°15.83′N
Longitude	144°06.38′N	144°05.19′E

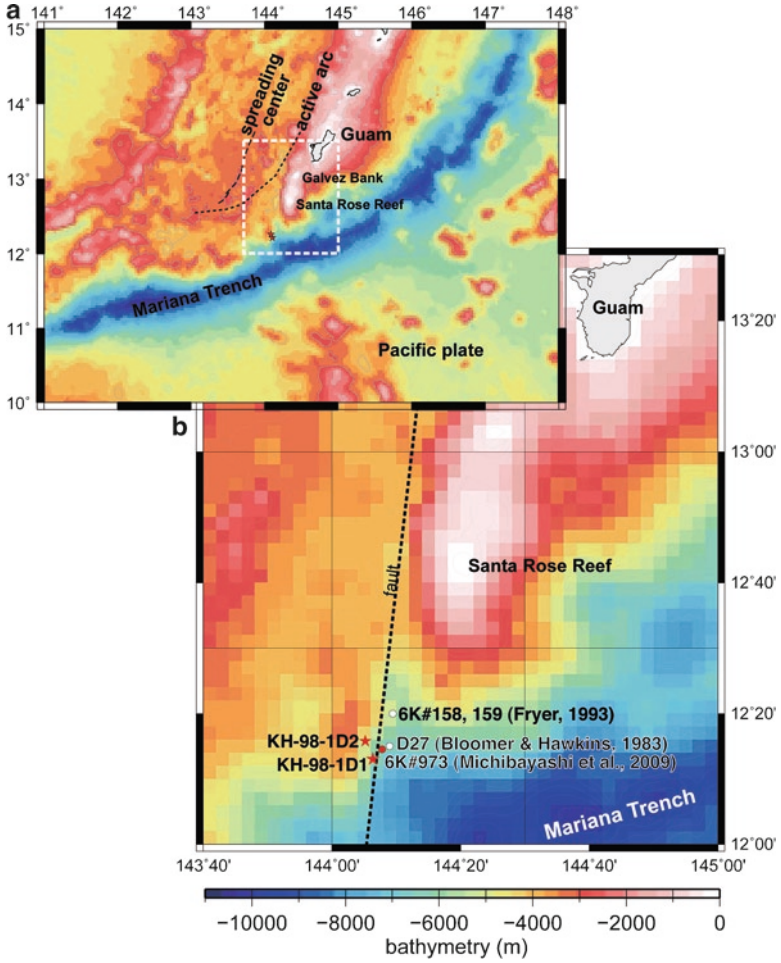

Fig. 1 Location map showing dredge sites KH-98-1D1 and KH-98-1D2. (**a**) Bathymetry of the southern Mariana Trough and satellite altimetry map of the Philippine Sea (Data from Smith and Sandwell 1997). Tectonic features are based on Fryer (1996) and Martinez et al. (2000). (**b**) Bathymetry of the inner wall of the southern Mariana Trench. Also shown are the location of previous survey sites, D27 (Bloomer and Hawkins 1983), and *Shinkai 6500* dives #158 and #159 (Fryer 1993), and #973 (Michibayashi et al. 2009)

Most recently, another *Shinkai 6500* dive (6K#973) has recovered residual peridotites with mylonitic, porphyroclastic, and coarse, moderately deformed secondary textures (Michibayashi et al. 2009). Michibayashi et al. (2009) analyzed the olivine crystal preferred orientations, and concluded that the peridotites represent a ductile shear zone within the lithospheric mantle of the overriding plate (i.e., the Mariana Back-Arc Basin), suggesting that back-arc basin mantle is exposed along the West Santa Rosa Bank Fault, even in its fore-arc setting.

Along the inner wall of the Mariana Trench, southwest of Guam, mantle peridotites have been recovered from several locations (Ohara and Ishii 1998; Michibayashi et al. 2007). Petrologic and mineralogical studies reveal that these peridotites represent the highly refractory residue left behind after extensive mantle melting related to island-arc magmatism (Ohara and Ishii 1998). Therefore, along the Mariana Trench, southwest of Guam, mantle peridotites associated with both back-arc magmatism and island-arc magmatism are exposed.

3 Petrographic Descriptions of the Peridotites

During cruise KH-98-1, along the fault at 144°E in the southern Marianas, serpentinized peridotites weighing approximately 20 and 35 kg were recovered from sites KH-98-1D1 and KH-98-1D2, respectively.

Modal compositions were measured with a point-counter (Table 2). For each specimen, more than 1,000 (usually 2,000) points were counted on a 0.50 × 0.50 mm grid. Computations were then made, fitting mineral compositions (average composition for each thin section) to bulk rock compositions in terms of SiO_2, TiO_2, Al_2O_3, FeO (total Fe as FeO), MnO, MgO, CaO, Na_2O, Cr_2O_3, and NiO contents. For bulk rock compositions, rock samples were initially split and crushed, and then pulverized in an agate ball mill. H_2O and loss on ignition were determined at 110°C and 950°C (over 6 h), respectively. Major elements were determined by X-ray fluorescence (XRF), using a RIGAKU 3270 at the Ocean Research Institute, the University of Tokyo, Japan. The mixture used for major element analysis was ~0.5 g of each powdered sample and 5 g of anhydrous lithium tetraborate ($Li_2B_4O_7$). Bulk rock compositions are listed in Table 2.

Comparing the two methods, point-counting gives higher proportions of olivine and lower proportions of orthopyroxene and clinopyroxene than do the computations, possibly due to: (1) difficulties and errors in identifying small grains of pyroxene and olivine; (2) the problem of dealing with serpentinized minerals where the original mineral could not be identified (our approach was to count such serpentinized grains as olivine); and (3) the inability of our computations to determine the degree of serpentinization. Therefore, in this study, we adopt the figures from point-counting for the degree of serpentinization, and adopt the computations in determining the original lithology.

Based on modes, most of the peridotites from sites KH-98-1D1 and KH-98-1D2 are classified as lherzolite and lherzolitic harzburgite which contain significant

Table 2 Representative results of petrographic and petrologic whole-rock analyses

Sample ID	D1-001	D1-002	D1-003	D1-005	D1-006	D1-007	D2-002	D2-005	D2-007
Major oxides									
SiO_2	44.70	43.90	44.67	44.01	44.41	45.07	44.23	44.54	45.30
TiO_2	0.12	0.09	0.09	0.09	0.08	0.10	0.12	0.10	0.09
Al_2O_3	2.59	2.81	2.56	2.38	1.64	3.04	3.11	2.55	2.67
Fe_2O_3	8.46	8.71	8.87	8.76	9.35	8.58	9.58	9.48	9.26
MnO	0.13	0.13	0.13	0.13	0.13	0.13	0.13	0.14	0.13
MgO	40.79	40.84	41.26	41.78	42.90	40.28	40.83	40.14	40.32
CaO	3.27	2.85	2.83	2.94	1.79	2.91	1.85	3.16	2.60
Na_2O	0.08	0.12	0.06	0.07	0.04	0.12	0.00	0.02	0.13
K_2O	0.01	0.01	0.02	0.01	0.01	0.02	0.02	0.02	0.03
P_2O_5	0.00	0.00	0.00	0.00	0.01	0.00	0.01	0.01	0.01
Total	100.14	99.47	100.49	100.18	100.36	100.24	99.86	100.15	100.53
Trace elements (ppm)									
Co	104	103	99	102	108	98	105	108	104
Cr	2,822	2,756	2,651	2,601	2,547	2,745	3,035	2,267	2,543
Ni	1,988	2,091	2,032	2,139	2,185	1,988	2,155	2,118	2,111
H_2O^-	0.21	0.17	0.12	0.21	0.44	0.37	0.51	0.68	0.54
IGLS	1.62	2.29	2.21	1.58	2.7	2.12	7.07	5.05	5.84
Mg#	0.905	0.903	0.902	0.904	0.901	0.903	0.894	0.893	0.896
Mineral mode (point-counted)									
Total count	1,452	1,277	1,202	1,246	1,624	2,003	1,490	2,284	2,021
Olivine	85.5	86.8	82.1	78.7	90.8	85.1	91.2	85.9	78.7
Orthopyroxene	8.0	8.1	12.4	14.1	4.2	7.8	6.5	9.8	14.0
Clinopyroxene	2.2	2.2	3.1	3.3	3.8	4.0	1.5	3.1	5.0
Plagioclase	3.5	1.6	1.0	2.6	0.6	2.2	0.1	0.9	1.6
Spinel	0.8	1.3	1.4	1.3	0.7	0.9	0.6	0.4	0.7
Degree of serpentinization	24.0	34.4	47.5	31.9	42.7	43.8	74.2	61.1	61.3
Mineral mode (calculated)									
Olivine	63.9	67.1	66.0	68.8	67.2	59.2	61.6	62.4	58.6
Orthopyroxene	20.6	16.8	20.6	16.8	25.1	26.6	28.1	22.6	29.6
Clinopyroxene	10.2	8.7	8.6	9.4	5.3	8.0	2.8	9.7	6.5
Plagioclase	5.0	6.2	4.3	4.3	1.4	5.7	6.1	4.6	4.8
Spinel	0.4	1.2	0.4	0.7	0.9	0.5	1.4	0.7	0.4
Residual sum of squares	0.1	0.7	0.1	0.3	1.0	0.2	1.0	0.3	0.4

amounts (up to 7%) of plagioclase. Although all the peridotites are serpentinized, peridotites from KH-98-1D1 are less serpentinized than those from KH-98-1D2.

Overall, proto-granular to porphyroclastic textures (Mercier and Nicolas 1975) are developed in the peridotites rather than cumulate textures (Fig. 2a, b). Several samples exhibit a mylonitic texture (Fig. 2c). Olivine and orthopyroxene crystals are commonly coarse equidimensional or elongate large crystals with undulatory extinction (Fig. 2a). In places, a porphyroclastic texture is developed, so that fine-grained assemblages (olivine, clinopyroxene, orthopyroxene, amphibole, and

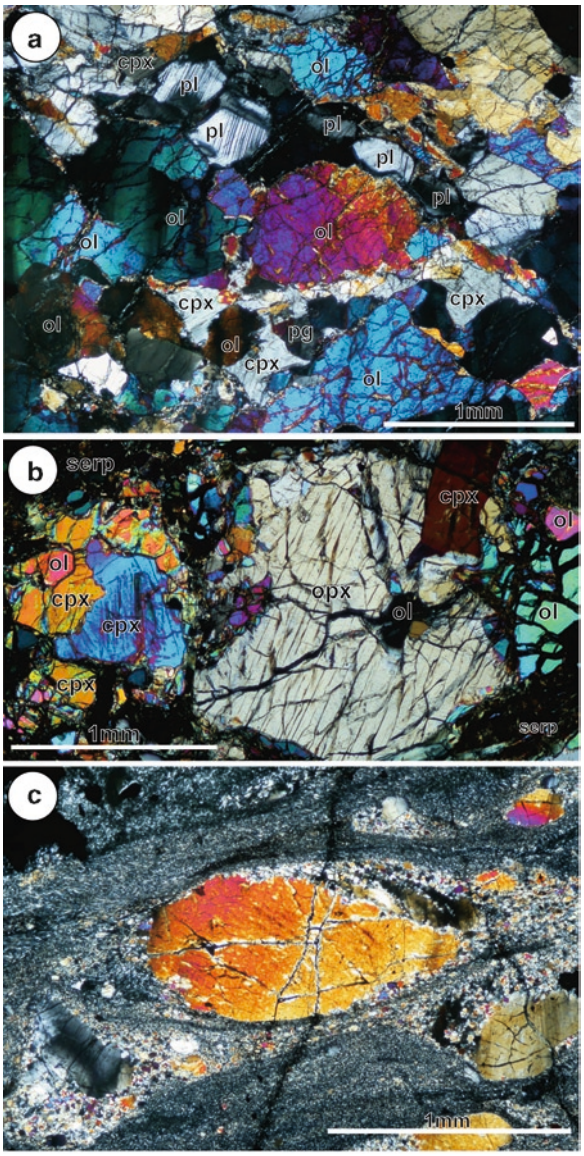

Fig. 2 Photomicrographs of representative structures and modes of occurrence of various minerals. (**a**) Proto-granular to porphyroclastic texture (sample KH98-1D1-001) in crossed polarized light. *ol* olivine, *cpx* clinopyroxene, *pl* plagioclase, *pg* pargasite. (**b**) Porphyroclast of orthopyroxene and clinopyroxene (sample KH98-1D2-007) in crossed polarized light. *opx* orthopyroxene, *serp* serpentine. (**c**) Mylonitized texture (sample KH98-1D1-004) in crossed polarized light

spinel) surround large olivine and/or orthopyroxene crystals. Relatively large clinopyroxene crystals also exhibit undulatory extinction. Plagioclase occurs along the grain boundaries among mafic minerals (Fig. 2a). Small amounts of amphibole occur along the boundaries of major silicates.

4 Chemical Composition of the Minerals

Minerals were analyzed using a JEOL JXA-8900R Superprobe at the Ocean Research Institute of the University of Tokyo. Silicates and oxides were analyzed using a focused beam (~1 μm), an accelerating voltage of 15 kV, and a beam current of 12 nA. Olivines proved to be relatively homogeneous in each thin section, being rich in Mg, with Fo values ranging from 90.0 to 91.5 (Table 3). Orthopyroxene is rich in Mg, with Mg# (= 100 Mg/(Mg + Fe)) ranging from 90 to 92 (Table 4). The orthopyroxenes in the peridotite from KH-98-1D2 have slightly lower Al_2O_3 contents than do those from KH-98-1D1, but otherwise they are similar. Most of the clinopyroxene is diopside (Fig. 3), with Mg# ranging from 91 to 93 (Table 5). Most of grains contain more than 1 wt% Cr_2O_3, indicating chromian diopside.

The Cr# (= Cr/(Cr + Al)) of spinel ranges from 0.40 to 0.51 (Table 6, Fig. 4). Spinel in peridotite from KH-98-1D1 has a lower Cr# than does spinel from KH-98-1D2. The spinel from both the dredge sites is rich in TiO_2, particularly in the peridotites from KH-98-1D2, which show a wide compositional variation among samples.

Plagioclases are calcic with a relatively wide range of compositions from An_{77} to An_{85}. Some grains retain their original compositions and texture, but most plagioclase has been altered to secondary hydrous minerals.

Amphibole is found scattered in the peridotites as a trace mineral. Most of it is pargasite but there are also some tremolites. The pargasite occurs near grain boundaries among other silicate minerals, and is considered to be primary. The tremolite may have resulted from the replacement of pyroxene during late-stage alteration.

5 Discussion

5.1 Origin of the Plagioclase-Bearing Peridotite

The refractory mineral compositions of the peridotites from the fault at 144°E in the southern Marianas, together with the deformed proto-granular to porphyroclastic textures, indicate that they represent the residue left behind after partial melting of mantle peridotite.

Plagioclase peridotite is not a dominant rock type among abyssal peridotites, and typically a plagioclase peridotite contains around 2.5% plagioclase (Dick 1989). Most of the peridotites analyzed in the present study are plagioclase-bearing, containing up to 7% plagioclase. Near to the two dredge sites considered in

Table 3 Chemical compositions of representative olivine grains (average compositions and their 1-sigma statistical variations (s.d.) for each sample)

Sample ID	D1-001		D1-002		D1-003		D1-005		D1-006		D1-007		D2-002		D2-005		D2-007	
Number of analysis	51	s.d.	29	s.d.	18	s.d.	16	s.d.	44	s.d.	12	s.d.	13	s.d.	40	s.d.	14	s.d.
wt%																		
SiO_2	40.20	0.39	40.71	0.45	40.51	0.35	40.31	0.51	40.18	0.26	40.06	0.38	39.74	0.42	39.98	0.43	39.79	0.70
TiO_2	0.07	0.05	0.02	0.03	0.02	0.04	0.03	0.03	0.01	0.01	0.01	0.01	0.02	0.04	0.02	0.03	0.03	0.03
FeO	9.05	0.42	9.47	0.42	9.21	0.28	8.87	0.59	8.52	0.84	9.03	0.42	9.31	0.42	9.92	0.49	9.72	1.12
MnO	0.14	0.03	0.13	0.03	0.15	0.05	0.15	0.04	0.14	0.02	0.14	0.03	0.17	0.04	0.15	0.03	0.14	0.03
MgO	50.30	0.36	50.49	0.55	49.92	0.50	50.34	0.73	49.83	0.66	50.47	0.35	50.06	0.47	49.57	0.34	49.86	0.34
NiO	0.40	0.05	0.41	0.06	0.39	0.05	0.41	0.04	0.44	0.04	0.42	0.05	0.40	0.05	0.38	0.05	0.42	0.06
Total	100.21	0.75	101.31	0.96	100.28	0.80	100.28	1.14	99.20	1.22	100.18	0.37	99.79	0.89	100.13	0.71	100.03	0.54
Cation (O=8)																		
Si	1.97	0.01	1.97	0.01	1.98	0.01	1.97	0.01	1.98	0.01	1.96	0.01	1.96	0.02	1.97	0.01	1.96	0.02
Ti	0.00	0.00	0.00	0.00	0.00	0.00	0.00	0.00	0.00	0.00	0.00	0.00	0.00	0.00	0.00	0.00	0.00	0.00
Fe	0.37	0.02	0.38	0.02	0.38	0.01	0.36	0.03	0.35	0.03	0.37	0.02	0.38	0.02	0.41	0.02	0.40	0.05
Mn	0.01	0.00	0.01	0.00	0.01	0.00	0.01	0.00	0.01	0.00	0.01	0.00	0.01	0.00	0.01	0.00	0.01	0.00
Mg	3.67	0.02	3.64	0.02	3.64	0.02	3.66	0.02	3.66	0.03	3.68	0.03	3.67	0.02	3.63	0.02	3.66	0.03
Ni	0.02	0.00	0.02	0.00	0.02	0.00	0.02	0.00	0.02	0.00	0.02	0.00	0.02	0.00	0.02	0.00	0.02	0.00
Total	6.03	0.01	6.03	0.01	6.02	0.01	6.03	0.01	6.02	0.01	6.04	0.01	6.04	0.01	6.03	0.01	6.04	0.02
Fo	90.83	0.38	90.48	0.38	90.62	0.29	91.00	0.62	91.24	0.79	90.88	0.42	90.55	0.37	80.90	0.46	90.15	1.06

Table 4 Chemical compositions of orthopyroxene grains (average compositions and their 1-sigma statistical variations for each sample)

Sample ID	D1-001		D1-002		D1-003		D1-005		D1-006		D1-007		D2-002		D2-005		D2-007	
Number of analysis	13	s.d.	9	s.d.	5	s.d.	4	s.d.	31	s.d.	4	s.d.	5	s.d.	22	s.d.	16	s.d.
SiO_2	55.42	0.63	56.07	0.59	55.54	0.63	55.68	1.08	55.33	0.60	54.80	0.41	55.02	0.57	55.23	0.45	55.04	0.52
TiO_2	0.19	0.06	0.17	0.07	0.16	0.07	0.18	0.02	0.14	0.04	0.12	0.04	0.17	0.08	0.16	0.06	0.21	0.06
Al_2O_3	2.55	0.57	2.63	0.28	3.21	0.85	2.72	0.81	2.53	0.54	2.71	0.45	2.30	0.54	2.11	0.34	2.41	0.52
FeO	6.21	0.25	6.49	0.21	6.28	0.14	6.33	0.12	5.91	0.56	6.29	0.20	6.07	0.29	6.67	0.31	6.08	0.34
MgO	33.96	0.45	34.02	0.73	33.73	0.54	33.84	0.99	33.82	0.48	34.31	0.48	34.04	0.25	33.87	0.36	33.99	0.65
CaO	0.84	0.19	0.84	0.11	0.68	0.06	0.81	0.20	0.72	0.14	0.58	0.15	0.73	0.14	0.69	0.13	0.91	0.57
Na_2O	0.03	0.02	0.02	0.03	0.00	0.01	0.01	0.01	0.02	0.01	0.02	0.01	0.01	0.02	0.01	0.01	0.02	0.02
Cr_2O_3	0.54	0.15	0.60	0.15	0.63	0.20	0.54	0.19	0.56	0.14	0.62	0.20	0.53	0.18	0.49	0.14	0.62	0.17
Total	99.99	0.76	101.11	0.72	100.51	0.30	100.40	1.17	99.30	0.81	99.72	0.35	99.18	0.63	99.51	0.66	99.59	0.82
Cation (O=6)																		
Si	1.92	0.02	1.92	0.02	1.91	0.02	1.92	0.02	1.93	0.02	1.91	0.01	1.92	0.02	1.93	0.01	1.92	0.01
Ti	0.00	0.00	0.00	0.00	0.00	0.00	0.00	0.00	0.00	0.00	0.00	0.00	0.00	0.00	0.00	0.00	0.01	0.00
Al	0.10	0.02	0.11	0.01	0.13	0.03	0.11	0.03	0.10	0.02	0.11	0.02	0.09	0.02	0.09	0.01	0.10	0.02
Fe	0.18	0.01	0.19	0.01	0.18	0.00	0.18	0.00	0.17	0.02	0.18	0.01	0.18	0.01	0.19	0.01	0.18	0.01
Mg	1.75	0.02	1.74	0.03	1.73	0.02	1.74	0.03	1.75	0.02	1.78	0.03	1.77	0.01	1.76	0.02	1.76	0.04
Ca	0.03	0.01	0.03	0.00	0.03	0.00	0.03	0.01	0.03	0.01	0.02	0.01	0.03	0.01	0.03	0.00	0.03	0.02
Na	0.00	0.00	0.00	0.00	0.00	0.00	0.00	0.00	0.00	0.00	0.00	0.00	0.00	0.00	0.00	0.00	0.00	0.00
Cr	0.01	0.00	0.02	0.00	0.02	0.01	0.01	0.01	0.02	0.00	0.02	0.01	0.01	0.01	0.01	0.00	0.02	0.00
Total	4.02	0.01	4.01	0.02	4.01	0.00	4.01	0.00	4.01	0.01	4.03	0.01	4.02	0.01	4.02	0.01	4.02	0.01
Fs	0.09	0.00	0.10	0.00	0.09	0.00	0.09	0.00	0.09	0.01	0.09	0.00	0.09	0.00	0.10	0.00	0.09	0.01
En	0.89	0.00	0.89	0.00	0.89	0.00	0.89	0.01	0.90	0.01	0.90	0.00	0.90	0.00	0.89	0.00	0.89	0.01
Wo	0.02	0.00	0.02	0.00	0.01	0.00	0.02	0.00	0.01	0.00	0.01	0.00	0.01	0.00	0.01	0.00	0.02	0.01
Mg#	0.91	0.00	0.90	0.00	0.91	0.00	0.90	0.00	0.91	0.01	0.91	0.00	0.91	0.00	0.90	0.00	0.91	0.01

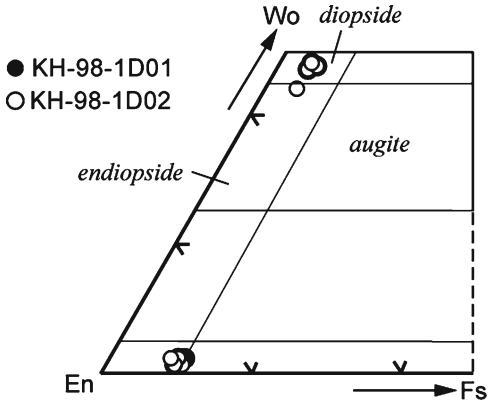

Fig. 3 Classification of Ca-rich and Ca-poor pyroxenes on a Wo–En–Fs ternary plot. Most of the Ca-rich pyroxenes are classified as diopside

the present study, other workers have reported the existence of basalt, gabbro, and plagioclase-free peridotites (Bloomer and Hawkins 1983; Fryer 1993; Michibayashi et al. 2009).

Furthermore, along the inner wall of the southern Mariana Trench, west of the present dredge sites, mantle peridotites are well exposed (Ohara and Ishii 1998). These peridotites are typically plagioclase-free and contain spinel with a high Cr#, indicating that they represent the residue of a relatively high degree of partial melting, probably related to "island-arc" type magmatism.

Therefore, plagioclase peridotites along the southern Mariana Trench are restricted to the area along the fault at 144°E in the southern Marianas, indicating that the magmatic and tectonic developments along the fault zone differ from those along other parts of the southern Mariana Trench.

There are two possible explanations for the existence of plagioclase in residual peridotite: (1) re-equilibration of an ascending mantle as it moves from the spinel-peridotite facies into the plagioclase-peridotite facies by the reaction orthopyroxene + clinopyroxene + Al-spinel = olivine + plagioclase + Cr-spinel (e.g., Hamlyn and Bonatti 1980), or (2) impregnation of residual peridotite by either an in situ or an exotic melt, and reaction between that melt and Al-spinel to give plagioclase and Cr-spinel (Dick and Bullen 1984; Dick 1989).

In the Philippine Sea Plate, plagioclase-bearing peridotites have been reported from the southern Marianas (Bloomer and Hawkins 1983; Michibayashi et al. 2009) and the Parece Vela Rift (Ohara et al. 2003; Ohara 2006). Michibayashi et al. (2009) explained that the occurrence of plagioclase in the peridotites from the southern Marianas can be attributed to the reaction of the peridotite with an impregnating melt, based on the co-existence of both low-Cr# and high-Cr# spinels in a single sample. Ohara et al. (2003) reported the occurrence of plagioclase in peridotites from the Parece Vela Rift, and concluded that the plagioclase was produced by a reaction involving melt, based on the co-existence of fertile peridotite, plagioclase-bearing peridotite, and dunite in a single dredge haul. In the case of the peridotites in our study, the Cr# of spinel has constant value but different from piece to piece, and most of the peridotites from each dredge site are plagioclase-bearing.

Table 5 Chemical compositions of clinopyroxene grains (average compositions and their 1-sigma statistical variations for each sample)

Sample ID	D1-001		D1-002		D1-003		D1-005		D1-006		D1-007		D2-002		D2-004		D2-006		D2-007	
Number of analysis	4	s.d.	4	s.d.	8	s.d.	3	s.d.	60	s.d.	2	s.d.	8	s.d.	13	s.d.	38	s.d.	14	s.d.
SiO_2	52.18	0.57	52.19	0.86	51.37	0.83	52.21	0.55	52.12	0.62	51.46	0.44	51.40	0.90	51.81	0.83	51.52	0.69	51.58	0.75
TiO_2	0.44	0.11	0.61	0.15	0.53	0.11	0.40	0.10	0.42	0.07	0.31	0.02	0.60	0.12	0.45	0.12	0.51	0.11	0.59	0.07
Al_2O_3	3.64	0.87	3.76	0.23	4.05	0.53	3.61	0.61	3.43	0.57	3.62	0.35	3.60	0.58	3.85	0.83	3.71	0.66	3.68	0.44
FeO	2.76	0.12	2.85	0.20	2.74	0.28	2.69	0.37	2.36	0.35	2.51	0.06	2.58	0.29	2.75	0.35	2.77	0.18	2.61	0.13
MgO	16.86	0.41	16.48	0.27	16.34	0.58	16.23	0.48	16.55	0.43	16.57	0.14	16.59	0.72	16.85	1.42	16.46	0.42	16.62	0.35
CaO	22.65	0.59	23.05	0.62	22.96	0.57	22.61	0.45	23.34	0.64	22.81	1.06	22.85	0.55	22.38	1.75	22.82	0.44	23.04	0.31
Na2O	0.50	0.11	0.54	0.05	0.49	0.06	0.39	0.02	0.45	0.05	0.41	0.05	0.48	0.05	0.49	0.05	0.42	0.05	0.45	0.05
Cr_2O_3	1.00	0.25	1.09	0.05	1.16	0.29	1.03	0.24	0.95	0.17	1.22	0.00	1.22	0.22	1.21	0.11	1.09	0.20	1.07	0.15
Total	100.25	0.30	100.75	0.96	99.85	0.62	99.33	0.53	99.83	0.63	99.10	1.85	99.52	1.60	100.01	0.68	99.49	0.57	99.85	0.78
Cation (O=6)																				
Si	1.90	0.02	1.89	0.01	1.88	0.02	1.91	0.02	1.90	0.02	1.89	0.01	1.89	0.02	1.89	0.02	1.89	0.02	1.89	0.02
Ti	0.01	0.00	0.02	0.00	0.01	0.00	0.01	0.00	0.01	0.00	0.01	0.00	0.02	0.00	0.01	0.00	0.01	0.00	0.02	0.00
Al	0.16	0.04	0.16	0.01	0.17	0.02	0.16	0.03	0.15	0.03	0.16	0.01	0.16	0.03	0.17	0.04	0.16	0.03	0.16	0.02
Fe	0.08	0.00	0.09	0.01	0.08	0.01	0.08	0.01	0.07	0.01	0.08	0.00	0.08	0.01	0.08	0.01	0.09	0.01	0.08	0.00
Mg	0.91	0.02	0.89	0.01	0.89	0.03	0.89	0.02	0.90	0.02	0.91	0.02	0.91	0.03	0.91	0.07	0.90	0.02	0.91	0.02
Ca	0.88	0.02	0.89	0.02	0.90	0.03	0.89	0.02	0.91	0.02	0.90	0.03	0.90	0.02	0.87	0.07	0.90	0.02	0.90	0.01
Na	0.04	0.01	0.04	0.00	0.03	0.00	0.03	0.00	0.03	0.00	0.03	0.00	0.03	0.00	0.03	0.00	0.03	0.00	0.03	0.00
Cr	0.03	0.01	0.03	0.00	0.03	0.01	0.03	0.01	0.03	0.00	0.04	0.00	0.04	0.01	0.03	0.00	0.03	0.01	0.03	0.00
Total	4.02	0.01	4.01	0.01	4.02	0.01	4.00	0.00	4.01	0.01	4.01	0.01	4.02	0.01	4.02	0.01	4.01	0.01	4.02	0.01
Fs	0.04	0.00	0.05	0.00	0.04	0.00	0.04	0.01	0.04	0.01	0.04	0.00	0.04	0.00	0.04	0.01	0.05	0.00	0.04	0.00
En	0.49	0.00	0.48	0.01	0.48	0.01	0.48	0.01	0.48	0.01	0.48	0.01	0.48	0.01	0.49	0.04	0.48	0.01	0.48	0.01
Wo	0.47	0.01	0.48	0.01			0.48	0.01	0.48	0.01	0.48	0.01	0.48	0.01	0.47	0.04	0.48	0.01	0.48	0.01
Mg#	0.92	0.00	0.91	0.01	0.91	0.01	0.91	0.01	0.93	0.01	0.92	0.00	0.92	0.01	0.92	0.01	0.91	0.01	0.92	0.00

Table 6 Chemical compositions of spinel grains (average compositions and their 1-sigma statistical variations in each sample)

Sample ID	D1-001		D1-002		D1-003		D1-005		D1-006		D1-007		D2-002		D2-005		D2-007	
Number of analysis	11	s.d.	9	s.d.	10	s.d.	9	s.d.	23	s.d.	7	s.d.	4	s.d.	18	s.d.	12	s.d.
TiO_2	0.31	0.07	0.43	0.09	0.41	0.19	0.31	0.08	0.34	0.11	0.43	0.13	0.67	0.13	0.39	0.14	0.36	0.26
Al_2O_3	30.64	3.38	32.13	3.36	31.14	1.43	31.42	1.79	31.14	2.13	31.12	0.80	28.55	0.91	30.33	3.39	29.75	2.71
FeO	22.14	2.42	21.54	2.38	21.26	1.32	21.68	2.35	18.64	2.77	21.87	2.40	22.09	1.58	22.48	2.16	19.93	1.11
MnO	0.24	0.06	0.23	0.04	0.26	0.04	0.24	0.04	0.26	0.03	0.25	0.04	0.30	0.07	0.28	0.05	0.27	0.05
MgO	13.13	1.04	13.55	1.11	12.95	0.85	13.08	1.25	12.89	1.03	13.22	0.97	12.85	1.37	11.77	1.27	13.32	0.72
Cr_2O_3	32.84	2.76	31.36	2.43	31.87	1.24	32.35	2.04	32.34	1.85	32.51	2.22	35.15	0.81	32.07	2.96	35.49	2.28
V2O3	0.23	0.04	0.24	0.03	0.26	0.05	0.20	0.04	0.24	0.05	0.24	0.03	0.33	0.01	0.31	0.06	0.24	0.06
NiO	0.19	0.05	0.18	0.06	0.20	0.05	0.21	0.06	0.20	0.04	0.20	0.11	0.20	0.08	0.18	0.08	0.15	0.04
Total	99.75	0.89	99.68	1.29	98.38	1.68	99.57	0.68	96.11	2.04	99.90	0.87	100.18	0.30	97.89	1.06	99.56	0.89
Cation (O=32)																		
Ti	0.05	0.01	0.08	0.02	0.07	0.04	0.05	0.01	0.06	0.02	0.08	0.02	0.12	0.02	0.07	0.03	0.07	0.05
Al	8.57	0.79	8.92	0.73	8.82	0.25	8.79	0.38	8.99	0.46	8.69	0.17	8.05	0.16	8.70	0.76	8.37	0.63
Fe^{3+}	1.10	0.32	1.02	0.26	0.93	0.14	0.98	0.29	0.56	0.30	1.03	0.29	1.00	0.07	0.90	0.18	0.75	0.10
Fe^{2+}	3.31	0.29	3.23	0.31	3.35	0.24	3.33	0.36	3.26	0.33	3.31	0.30	3.43	0.44	3.69	0.38	3.24	0.20
Mn	0.05	0.01	0.05	0.01	0.05	0.01	0.05	0.01	0.05	0.01	0.05	0.01	0.06	0.01	0.06	0.01	0.05	0.01
Mg	4.64	0.30	4.76	0.29	4.63	0.24	4.62	0.37	4.70	0.33	4.66	0.31	4.58	0.44	4.27	0.38	4.74	0.19
Cr	6.18	0.60	5.86	0.55	6.05	0.20	6.08	0.43	6.27	0.49	6.09	0.39	6.65	0.22	6.19	0.69	6.71	0.53
V	0.04	0.01	0.05	0.01	0.05	0.01	0.04	0.01	0.05	0.01	0.05	0.01	0.06	0.00	0.06	0.01	0.05	0.01
Ni	0.04	0.01	0.03	0.01	0.04	0.01	0.04	0.01	0.04	0.01	0.04	0.02	0.04	0.01	0.03	0.01	0.03	0.01
Mg#	0.58	0.04	0.60	0.04	0.58	0.03	0.58	0.05	0.59	0.04	0.58	0.04	0.57	0.05	0.54	0.05	0.59	0.02
Cr#	0.42	0.04	0.40	0.04	0.41	0.01	0.41	0.03	0.41	0.03	0.41	0.02	0.45	0.01	0.42	0.05	0.45	0.04

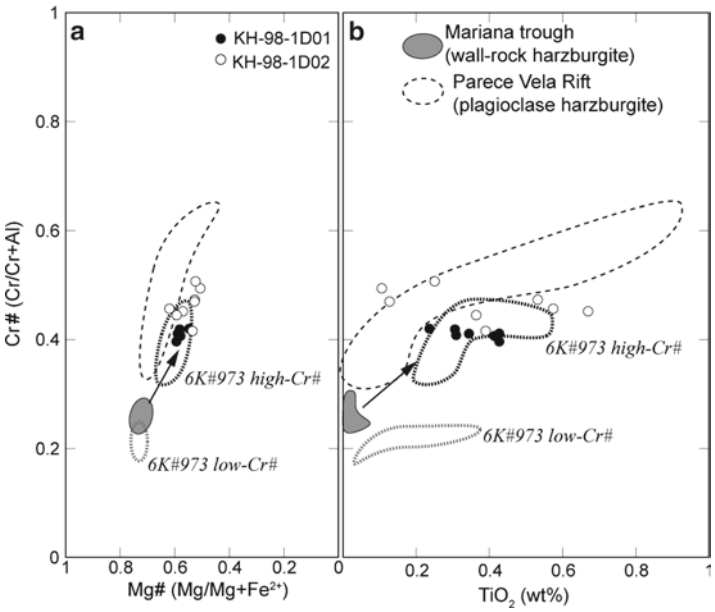

Fig. 4 Chemical compositions of spinel in plagioclase-bearing peridotites from the southern Marianas, with references to those from other areas of the Philippine Sea (Ohara et al. 2002, 2003; Ohara 2006; Michibayashi et al. 2009). The *arrow* indicates the trend for impregnating melts in peridotites from the Mariana Trough. (**a**) Cr# (Cr# = Cr/(Cr + Al)) versus Mg# (Mg# = Mg/(Mg + Fe^{2+})), and (**b**) Cr# versus TiO_2 wt%

These facts make it difficult to evaluate the origin of the plagioclase. However, we propose that impregnating melts influenced the crystallization of plagioclase in peridotites from the fault at 144°E, an idea first mentioned by Bloomer and Hawkins (1983) and more recently by Michibayashi et al. (2009). We base this proposal on the following arguments.

1. Spinel in abyssal peridotites usually contains low or negligible amounts (<0.25 wt%) of TiO_2 (Dick and Bullen 1984). Therefore, it is accepted that Ti-enrichment in spinel results from reactions caused by impregnating melts (e.g., Dick and Bullen 1984; Cannat et al. 1990; Girardeau and Francheteau 1993; Niida 1997; Pearce et al. 2000).
2. The TiO_2 contents of spinel in peridotites from the fault at 144°E are higher than those from the Mariana Trough, and similar or only slightly lower than those in the P (plagioclase)-type peridotites from the Parece Vela Rift (Fig. 4).
3. Spinel in the P-type peridotites from the Parece Vela Rift has compositions that are thought to have been affected by an impregnating melt, and the spinel is richer in TiO_2 than spinel in impregnation-free F (fertile)-type peridotites (Ohara et al. 2002; Ohara 2006). The range of TiO_2 contents in spinel from peridotites along the 144°E fault is similar to that in the P-type peridotites from the Parece Vela Rift (Fig. 4). Michibayashi et al. (2009) found both high- and low-Cr#

spinels in a single peridotite from the southern Marianas during Shinkai 6500 Dive #973. They concluded that the low-Cr# spinel is a relict that survived the process of melt impregnation.

4. Ohara et al. (2002) reported plagioclase-free harzburgites from the Mariana Trough. However, some harzburgites are cut by leucocratic veins and contain altered plagioclase and spinel. This spinel, and its associated pyroxene, is enriched in TiO_2 compared with the same minerals in the host harzburgite. These observations support the idea that Ti-enrichment of spinel and pyroxene provides important evidence for the existing of an impregnating melt.
5. The impregnating melt might yield plagioclase, clinopyroxene, and olivine. Therefore, it is assumed that both the TiO_2 contents of spinel and the modal amount of plagioclase in the peridotite relate to the effects of an impregnating melt. Figure 5 shows the relationships between the calculated modes for each peridotite mineral and the TiO_2 content of the spinels. There is a strong correlation between plagioclase and clinopyroxene modes and TiO_2 in spinel, so that peridotites in which spinels have a higher TiO_2 content contain more plagioclase and clinopyroxene. Assuming that all the plagioclase crystallized from an impregnating melt, any peridotite that was not affected by such a melt should contain spinel with 0.145% TiO_2. This TiO_2 content correlates approximately with a clinopyroxene mode of 1.2%.

   Based on the above observations, we suggest that the peridotites, before impregnation, might have been harzburgites containing olivine, orthopyroxene, clinopyroxene (ca. 1.2%), and spinel, and that plagioclase and clinopyroxene crystallized in these rocks as a result of melt impregnation and reaction.
6. Pyroxenes in peridotites from along the fault at 144°E are also rich in TiO_2. Although these pyroxenes have Mg# values that are similar to those of pyroxenes in peridotites from various back-arc basins in the Philippine Sea Plate (e.g., the Mariana Trough and Parece Vela Rift; Ohara et al. 2002; Ohara 2006), orthopyroxene and clinopyroxene grains in peridotites from along the 144°E fault have higher contents of TiO_2 (Fig. 6), suggesting that impregnating melts had a stronger influence here than in the Mariana Trough and Parece Vela Rift.

5.2 Degree of Partial Melting

It is well known that the Cr# of spinel in residual mantle peridotites is a sensitive indicator of the degree of melting (Dick and Bullen 1984), with a lower Cr# indicating a lower degree of melting, and vice versa. Hellebrand et al. (2001) presented a equation that links the Cr# of spinel to the degree of melting. Adopting this equation, the degree of melting for the peridotites along the fault at 144°E in the southern Marianas is calculated to be around 15%.

However, it must be remembered that the Cr# of spinel from peridotites along the 144°E fault has been modified as a result of melt impregnation, as discussed above. Because spinels become enriched in Cr during interaction with impregnating melts (e.g., Cannat et al. 1990; Niida 1997), the calculated degree of melting

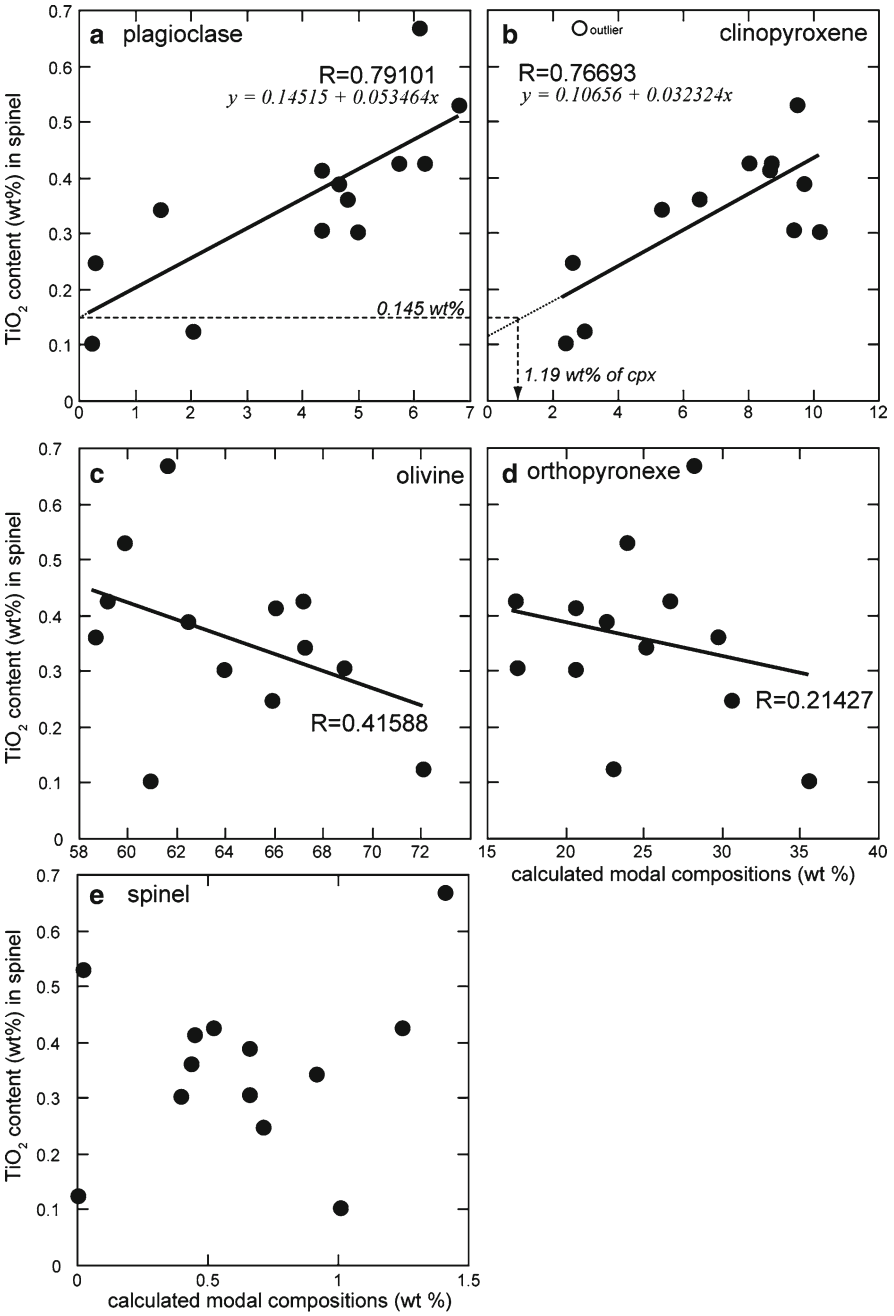

Fig. 5 Relationships between the computed modes for each mineral and TiO_2 content in spinel from mantle peridotites along the fault at 144°E fault in the southern Marianas. Strong positive correlations are observed for plagioclase and clinopyroxene, whereas weak or occasionally negative correlations exist for olivine, orthopyroxene, and spinel

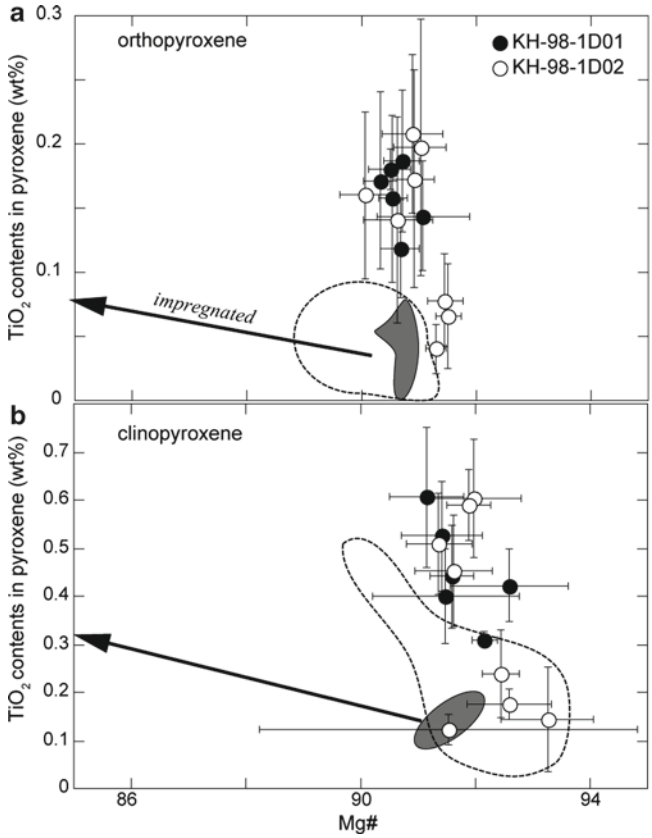

Fig. 6 Relationships between Mg# and TiO_2 in orthopyroxene and clinopyroxene. Error bars indicate variations for each sample (1 standard deviation). The ranges for peridotites from other areas of the Philippine Sea (Ohara et al. 2002, 2003; Ohara 2006) are also shown. *Gray*: wall-rock harzburgites from the Mariana Trough. *Arrow* shows the trend for impregnating melts in peridotites from the southern Marianas. The *dashed line* indicates plagioclase-bearing harzburgite from the Parece Vela Rift

(approximately 15%) is an overestimate; therefore, we suggest that peridotite along the fault at 144°E has undergone less than 15% partial melting, and that melting was accompanied and followed by various reactions.

5.3 Degree of Melt Impregnation

As discussed above, the clinopyroxene and plagioclase in the peridotites along the fault at 144°E in the southern Marianas are thought to have crystallized from impregnating melts. Therefore, the amounts of these minerals reflect the volume

of impregnating melt that interacted with the residual peridotites, and their compositions would be a reflection of melt composition. In the analyzed samples, although the amounts of clinopyroxene and plagioclase vary among the samples, they occupy up to 7% of the peridotite. If Ti-enrichment in spinel and pyroxene is a true indication of the influence of melt impregnation, the peridotites along the fault at 144°E are among the most strongly affected mantle peridotites within the Philippine Sea region.

The Cr# and TiO_2 contents in spinels from the analyzed peridotite samples are among the highest from the Philippine Sea. Similarly, the TiO_2 contents in both orthopyroxene and clinopyroxene are higher than those in any other samples from the Philippine Sea, even though they have similar values of Mg#. Because grains with the lowest TiO_2 contents have similar compositions to those from the Mariana Trough and the Parece Vela Rift (Fig. 4), the differences in Ti content can be ascribed to differences in the degree of melt impregnation. The degrees of impregnation, as estimated from mineral compositions, are similar to those of the P-type peridotites from the Parece Vela Rift, rather than the veined harzburgites from the Mariana Trough.

Ohara (2006) suggested that channeled melt flow under relatively low temperatures is dominant beneath the Mariana Trough, whereas porous melt flow is dominant beneath the Parece Vela Rift. If the differences in degrees of melt impregnation depend on tectonic setting, then the geological setting of the southern Marianas is more similar to the Parece Vela Rift than to the northern Mariana Trough. Geophysical data suggest that the tectonic features of the central Mariana Trough, between 17°N and 18°N, are similar to those of the slow-spreading Mid-Atlantic Ridge, whereas the morphology of the southern Mariana Trough, between 12°30′N and 14°N, has an axial relief similar to that of the East Pacific Rise with fast to superfast spreading rate (Martinez et al. 2000). Therefore, it might be plausible that the peridotites from along the 144°E fault, in the southern Marianas, formed as residues following relatively high degrees of melting and melt impregnation beneath a fast-spreading ridge.

6 Conclusions

Petrographic, petrologic, and mineralogical analyses of mantle peridotites from along the fault at 144°E, in the southern Marianas, revealed that the peridotites are characterized by relatively large amounts of plagioclase, the result of crystallization from an impregnating melt. Reaction with this melt enriched the spinel and pyroxenes in TiO_2, and the spinel compositions indicate that the peridotites represent the residue after as much as 15% partial melting. The degrees of melting and melt impregnation in these peridotites from the southern Marianas are higher than those in peridotites from the Mariana Trough. This might reflect the magma genesis under higher spreading rate in the southern Marianas.

Acknowledgments We owe great thanks to the crew and scientific party on board the R/V *Hakuho-maru* during cruise KH-98-1. An early version of this manuscript was reviewed by and discussed with Drs. Yumul, G.P. Jr., Daniel Curewitz, Hidetsugu Taniguchi and Yasuhiko Ohara, to whom we are grateful. We appropriate Shinji Kanayama for his help with the XRF sample preparation.

References

Bloomer SH (1983) Distribution and origin of igneous rocks from the landward slopes of the Mariana Trench: implications for its structure and evolution. J Geophys Res 88:7411–7428

Bloomer SH, Hawkins JW (1983) Gabbroic and ultramafic rocks from the Mariana trench: an island arc ophiolite. In: Hayes DE (ed.) The tectonic and geologic evolution of Southeast Asian Seas and Islands (Part 2), Geophysical monograph, vol 27. American Geophysical Union, Washington, DC, pp 294–317

Cannat M, Bideau D, Hébert R (1990) Plastic deformation and magmatic impregnation in serpentinized ultramafic rocks from the Garrett transform fault (East Pacific Rise). Earth Planet Sci Lett 101:216–232

Dick HJB (1989) Abyssal peridotites, very slow spreading ridges and ocean ridge magmatism. In: Saunders AD, Norry MJ (eds) Magmatism in the ocean basins, Geological Society Special Publication 42. Geological Society, London, pp 71–105

Dick HJB, Bullen T (1984) Chromian spinel as a petrogenetic indicator in abyssal and alpine-type peridotites and spatially associated lavas. Contrib Mineralog Petrol 86:54–76

Fryer P (1993) The relationship between tectonic deformation, volcanism, and fluid venting in the southeastern Mariana convergent plate margin. Proc JAMSTEC Symp Deep Sea Res 9:161–179

Fryer P (1996) Evolution of the Mariana convergent plate margin system. Rev Geophys 34:89–125

Fryer P, Fryer GJ (1987) Origins of nonvolcanic seamounts in a forearc environment. In: Keating BH, Fryer P, Batiza R, Boehlert GW (eds) Seamounts, islands, and atolls. Geophysical monograph, vol 43. American Geophysical Union, Washington, DC, pp 61–69

Fryer P, Mottl M, Johnson L, Haggerty J, Phipps S, Maekawa H (1995) Serpentine bodies in the forearcs of western Pacific convergent margins: origin and associated fluids. In: Taylor B, Natland J (eds) Active margins and marginal basins of the western Pacific, Geophysical monograph, 88. American Geophysical Union, Washington, DC, pp 259–279

Girardeau J, Francheteau J (1993) Plagioclase-wehrlites and peridotites on the East Pacific Rise (Hess Deep) and the Mid-Atlantic Ridge (DSDP Site 334): evidence for magma percolation in the oceanic upper mantle. Earth Planet Sci Lett 115:137–149

Hamlyn PR, Bonatti E (1980) Petrology of mantle-derived ultramafics from the Owen fracture zone, northwest Indian ocean: implications for the nature of the oceanic upper mantle. Earth Planet Sci Lett 48:65–79

Hellebrand E, Snow JE, Dick HJB, Hofmann AW (2001) Coupled major and trace elements as indicators of extent of melting in mid-ocean-ridge peridotites. Nature 410:677–681

Ishii T (1985) Dredged samples from the Ogasawara fore-arc seamount or "Ogasawara paleoland"-"fore-arc ophiolite". In: Nasu N, Kobayashi K, Kushiro I, Kagami H (eds) Formation of active ocean margins. Terra Scientific Publication, Tokyo, pp 307–342

Martinez F, Fryer P, Becker N (2000) Geophysical characteristics of the southern Mariana Tough, 11°50′N–13°40′N. J Geophys Res 105:16591–16607

Mercier JCC, Nicolas A (1975) Textures and fabrics of upper-mantle peridotites as illustrated by xenoliths from basalts. J Petrol 16:454–487

Michibayashi K, Tasaka M, Ohara Y, Ishii T, Okamoto A, Fryer P (2007) Variable microstructure of peridotite samples from the southern Mariana Trench: evidence of a complex tectonic evolution. Tectonophysics 444:111–118

Michibayashi K, Ohara Y, Stern RJ, Fryer P, Kimura JI, Tasaka M, Harigane Y, Ishii T (2009) Peridoites from a ductile shear zone within back-arc lithospheric mantle, southern Mariana Trench: results of a *Shinkai 6500* dive. Geochem Geophys Geosys. doi:10.1029/2008GC002197

Niida K (1997) Mineralogy of MARK peridotites: replacement through magma channeling examined from Hole 920D, MARK area. In: Karson JA, Cannat M, Miller DJ, Elthon D (eds) Proceedings of the ODP. Scientific results, vol 153. Ocean Drilling Program, College Station, pp 265–275

Ohara Y (2006) Mantle process beneath Philippine Sea back-arc spreading ridges: a synthesis of peridotite petrology and tectonics. Island Arc 15:119–129

Ohara Y, Ishii T (1998) Peridotites from the southern Mariana forearc: heterogeneous fluid supply in mantle wedge. Island Arc 7:541–558

Ohara Y, Kasuga S, Ishii T (1996) Peridotites from the Parece Vela rift in the Philippine Sea – upper mantle material exposed in an extinct back-arc basin. Proc Jpn Acad Ser B 72:118–123

Ohara Y, Stern RJ, Ishii T, Yurimoto H, Yamazaki T (2002) Peridotites from the Mariana Trough: first look at the mantle beneath an active back-arc basin. Contrib Mineralog Petrol. doi:10.1007/s00410-001-0329-2

Ohara Y, Fujioka K, Ishii T, Yurimoto H (2003) Peridotites and gabbros from the Parece Vela backarc basin: unique tectonic window in an extinct backarc spreading ridge. Geochem Geophys Geosys. doi:10.1029/2002GC000469

Pearce JA, Barker PF, Edwards SJ, Parkinson IJ, Leat PT (2000) Geochemistry and tectonic significance of peridotites from the South Sandwich arc-basin system, South Atlantic. Contrib Mineralog Petrol 139:36–53

Shcheka SA, Vysotskiy SV, S'edin VT, Tararin IA (1995) Igneous rocks of the main geological structures of the Philippine Sea floor. In: Tokuyama H, Shcheka SA, Isezaki N et al (eds) Geology and geophysics of the Philippine Sea. Terra Scientific Publication, Tokyo, pp 251–278

Smith WHF, Sandwell DT (1997) Global seafloor topography from satellite altimetry and ship depth soundings. Science 277:1957–1962

Stern RJ, Bloomer SH, Martinez F, Yamazaki T, Harrison TM (1996) The composition of back-arc basin lower crust and upper mantle in the Mariana trough: a first report. Island Arc 5:354–372

Stern RJ, Yamazaki T, Danishwar S, Sun CH (1997) Back-arc basin lower crust and upper mantle in the northern Mariana trough studied with "Shinkai 6500". Proc JAMSTEC Symp Deep Sea Res 13:47–61

Tectonics of Unusual Crustal Accretion in the Parece Vela Basin

Yasuhiko Ohara, Kyoko Okino, and Jonathan E. Snow

Abstract Despite its rapid intermediate-spreading rate, the Parece Vela Basin (PVB) shows unusual characteristics that indicate a depressed magmatic budget, such as the occurrence of numerous oceanic core complexes (OCCs) and rugged terrain, exposing abundant peridotites and gabbros. Based on the geologic interpretations of crust with analogous features on global mid-ocean ridges, we propose three possible mechanisms that can account for these unusual characteristics: (1) presence of a cold and/or refractory mantle domain, (2) declining spreading rate during the later phase of the second-stage spreading of the PVB, and (3) a transform sandwich effect. Recent numerical modeling for formation of OCC suggests that there is a minimum as well as a maximum magmatic supply necessary to produce long-lived detachment fault. In the western PVB, a cold and/or refractory mantle domain inhibited a large amount of mantle melting within an intermediate-spreading ridge, attaining the limited window of the condition of magma supply demonstrated in the numerical model in an otherwise robust magmatic environment. In the central PVB, a transform sandwich effect and/or declining spreading rate inhibited a large amount of mantle melting within an intermediate-spreading ridge, also attaining the limited window of the condition of magma supply demonstrated in the numerical model in an otherwise robust magmatic environment.

Y. Ohara (✉)
Hydrographic and Oceanographic Department of Japan, Tokyo 104-0045, Japan
and
Institute for Research on Earth Evolution, Japan Agency for Marine-Earth Science and Technology, 2-15 Natsushima-cho, Yokosuka 237-0061, Japan
e-mail: yasuhiko.ohara@gmail.com

K. Okino
Division of Ocean-Earth System Science, Atmosphere and Ocean Research Institute, The University of Tokyo, 5-1-5 Kashiwanoha, Kashiwa-shi, Chiba 277-8564, Japan
e-mail: okino@aori.u-tokyo.ac.jp

J.E. Snow
Department of Earth and Atmospheric Sciences, University of Houston, Houston, TX 77204, USA
e-mail: jesnow@uh.edu

Y. Ogawa et al. (eds.), *Accretionary Prisms and Convergent Margin Tectonics in the Northwest Pacific Basin*, Modern Approaches in Solid Earth Sciences 8,
DOI 10.1007/978-90-481-8885-7_7,

Keywords Oceanic core complex • Intermediate-spreading ridge • Parece Vela Basin • Transform sandwich effect

1 Introduction

Backarc basins are diverse geologic settings because they inherently involve both divergent and convergent types of plate boundaries. They show a wide variety of spreading styles and lithospheric compositions (Martinez et al. 2007), making them important areas for studying crustal accretion processes along mid-ocean ridges. The tectonic and magmatic evolution of mid-ocean ridges is governed by a variety of factors, most of which influence the thermal structure of the lithosphere and the melt productivity. These include the spreading rate, potential temperature of the upwelling mantle and mantle composition of ridges, and the presence of large-offset fracture zones, nearby continental crust and hotspots (Parmentier and Morgan 1990; Macdonald et al. 1991; Lin and Morgan 1992; Sinton and Detrick 1992; Niu and Batiza 1993; Niu and Hekinian 1997; Gregg et al. 2007). It is widely accepted that slow- and ultraslow-spreading ridges show characteristics of magma starvation (Cannat et al. 2006; Dick et al. 2003) while intermediate- and fast-spreading ridges are generally magmatically robust.

The Izu-Bonin-Mariana (IBM) arc system in the Northwest Pacific is the classic locality for the study of oceanic convergence. At this plate boundary, the Pacific Plate is actively subducting beneath the Philippine Sea Plate along the Izu-Bonin and Mariana Trenches. Behind this island arc complex, the Philippine Sea is composed of three large basins separated by the Kyushu-Palau and West Mariana Ridges (both are remnant arcs). This region evolved through three stages of arc formation, rifting and backarc spreading (Karig 1971). The Parece Vela Basin (PVB) is the southern portion of the IBM backarc system, exemplifying backarc crustal construction (Fig. 1a). The basin was active during 26–12 Ma at a rapid intermediate-spreading rate of 8.8–7.0 cm/year full-rate (Okino et al. 1998; Ohara et al. 2001, 2003a). After the extinction of the PVB at 12 Ma, backarc spreading resumed in the currently active Mariana Trough, creating the West Mariana Ridge.

Despite its relatively faster spreading rate, the PVB shows distinct characteristics that indicate a depressed magmatic budget, such as the occurrence of numerous oceanic core complexes and rugged terrain, exposing abundant peridotites and gabbros. Many of the peridotites in the PVB are much less depleted than those exposed at comparable spreading rates on other mid-ocean ridge systems (Ohara et al. 2001, 2003a; Ohara 2006).

In this article, we will compare the morphology, tectonics and magmatic history of the PVB to regions on other mid-ocean ridge systems that also display magma-starved characteristics, in order to constrain the mechanisms that explain its unusual crustal accretion processes along a backarc spreading ridge. The aim of this article is to provide the basis for understanding these unusual characteristics to be answered by the ongoing studies that come from a series of recent extensive expeditions to

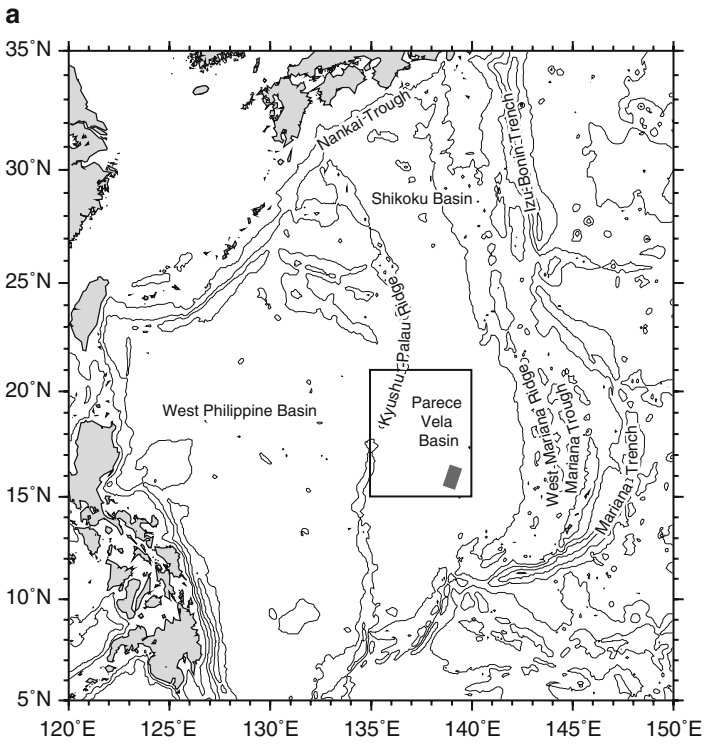

Fig. 1 (**a**) Index map showing the location of the Parece Vela Basin. The *box* indicates the location of (**b**). The *gray rectangular* indicates the location of Godzilla Megamullion. (**b**) Structural image of the Parece Vela Basin illuminated from 90° based on Ohara et al. (2001). *Dashed yellow lines* are the magnetic anomaly isochrons with anomaly number taken from Okino et al. (1998). Chron 7 corresponds to 26 Ma, and Chron 6A corresponds to 21 Ma (Okino et al. 1998). The short, first-order segments of the Parece Vela Rift are labeled as S1–S7 from south to north (Ohara et al. 2001). The Chaotic Terrain is indicated by a *thick dashed line*. Godzilla Megamullion is developed at segment S1. Some pseudofaults (indicated by *dotted lines*) suggest ridge propagation and jump occurred there (Okino et al. 1998)

the area, as well as to provide a better understanding of the convergent margin tectonics in the Northwest Pacific.

2 Oceanic Core Complexes

Oceanic core complexes (OCCs) are domal bathymetric highs, generally characterized by axis-normal corrugations, higher mantle Bouguer anomalies, and peridotite and gabbro exposures. OCCs have been recognized mostly along slow-spreading ridges; these occurrences in intermediate- and ultraslow-spreading ridges are less common (e.g., Tucholke et al. 2008; Blackman et al. 2009). OCCs are interpreted as exhumed

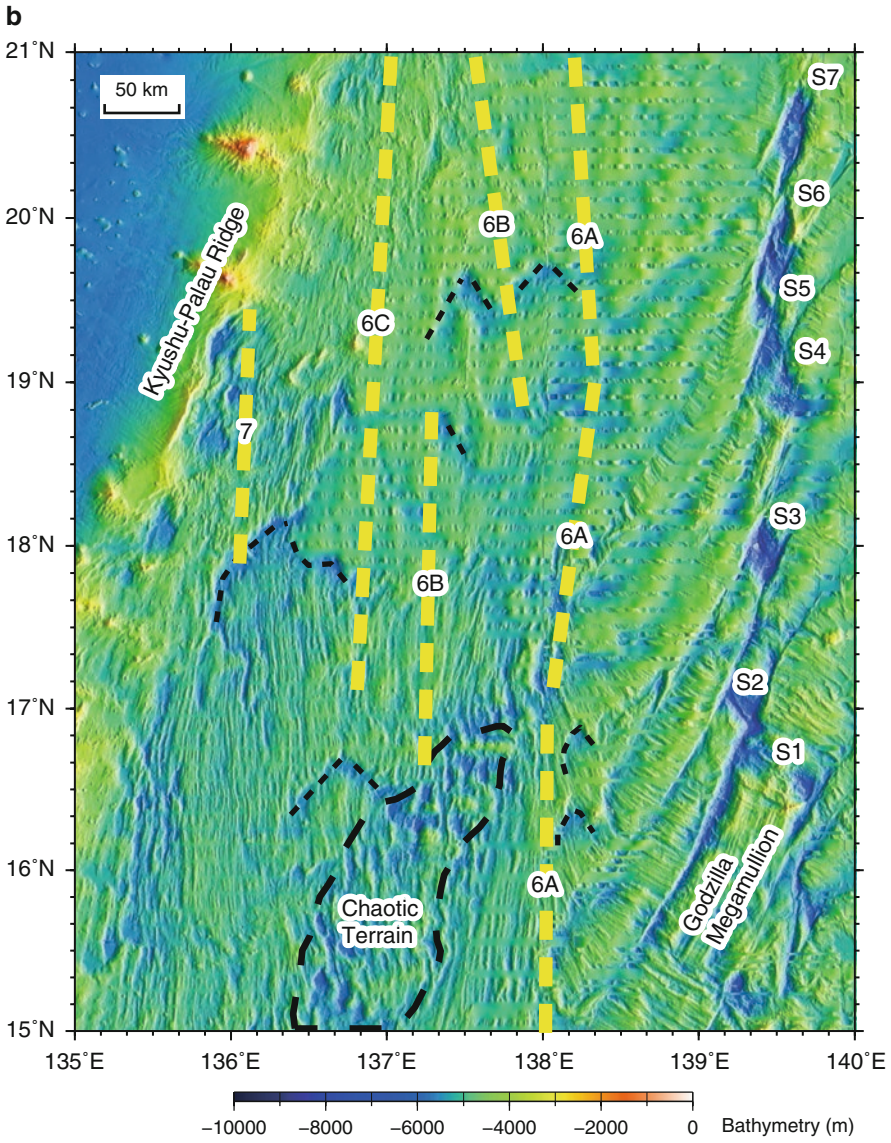

Fig. 1 (continued)

footwalls of low-angle detachment faults (Cann et al. 1997; Blackman et al. 1998; Tucholke et al. 1998; Escartín et al. 2003; MacLeod et al. 2009).

Normal faults are expected to develop increasing offset with increasing tectonic extension. Many earlier models of OCC formation (e.g., Tucholke et al. 1998; Blackman et al. 1998; Escartín et al. 2003) considered that amagmatic extension along a given section of ridge segment was important for long-lived detachment faulting. However, recent studies instead suggest that magmatic supply is the key

to OCC formation (Buck et al. 2005; Ildefonse et al. 2007; Tucholke et al. 2008; MacLeod et al. 2009). These studies suggest that there is a minimum as well as a maximum magmatic supply necessary to produce long-lived detachment fault. Below this minimum, detachment faults do not form or persist for long (Tucholke et al. 2008).

3 Crustal Accretion in the Parece Vela Basin

3.1 Morphology and Spreading of the Parece Vela Basin

The PVB is divided into two parts. The western part, west of about Chron 6A (at 138°E), is dominated by N-S trending well-developed abyssal hills that were produced by E-W orthogonal seafloor spreading (Fig. 1b). Some pseudofaults are identified in the western PVB (Fig. 1b), indicating ridge propagation and jump there (Okino et al. 1998). The "Chaotic Terrain (Ohara et al. 2001, 2007)" is a patchy area within the western PVB, consisting of a series of small OCCs bounded by an otherwise well-ordered abyssal hill floor (Fig. 1b).

The central PVB (east of 138°E) has a stair step morphology of deep rifts (the Parece Vela Rift), as the spreading direction rotated to NE-SW (Fig. 1b). Some pseudofaults are also identified just east of 138°E (Fig. 1b). The geometry of the Parece Vela Rift is composed of a series of short length (~20 to ~55 km) first-order segments (labeled as S1–S7 from south to north) aligned *en-echelon* with closely-spaced fracture zones (Ohara et al. 2001). Each segment becomes shorter and the transform faults closer together as this rotation occurred (Fig. 1b). The Parece Vela Rift is anomalously deep, with an average axial depth of ~6,500 m. The maximum depth (~7,500 m) occurs in the extinct axis of segment S3, corresponding to ~6,200 m zero-age depth after correction of 12 Ma (see below for the age determination) subsidence for a backarc basin setting (Park et al. 1990). The world's largest OCC, Godzilla Megamullion, is developed at segment S1 (Ohara et al. 2001). Other segments, at least S2 and S3, also host smaller OCCs (Figs. 1b and 2).

The spreading history of the PVB consisted of two stages (Fig. 2). The first-stage was E-W rifting and spreading with spreading axes trending N-S, whereas the second-stage involved counter-clockwise rotation of spreading axes from N-S to NW-SE (Okino et al. 1998).

The magnetic lineation pattern of the PVB is very weak, mostly because spreading occurred when the basin was near the magnetic equator (Okino et al. 1998). In order to obtain better magnetic information, Okino et al. (1998) conducted three-dimensional inversion of the magnetic data and successfully identified N-S trending magnetic anomalies 7 to 6A for the western PVB (Fig. 1b). A spreading rate of 4.4 cm/year half-rate was thus reasonably estimated for the first-stage of the basin evolution during the period of 26–21 Ma (Okino et al. 1998). The postulated 8.8 cm/year full-rate is at the highest end of intermediate-spreading rate (4–9 cm/year) based on the

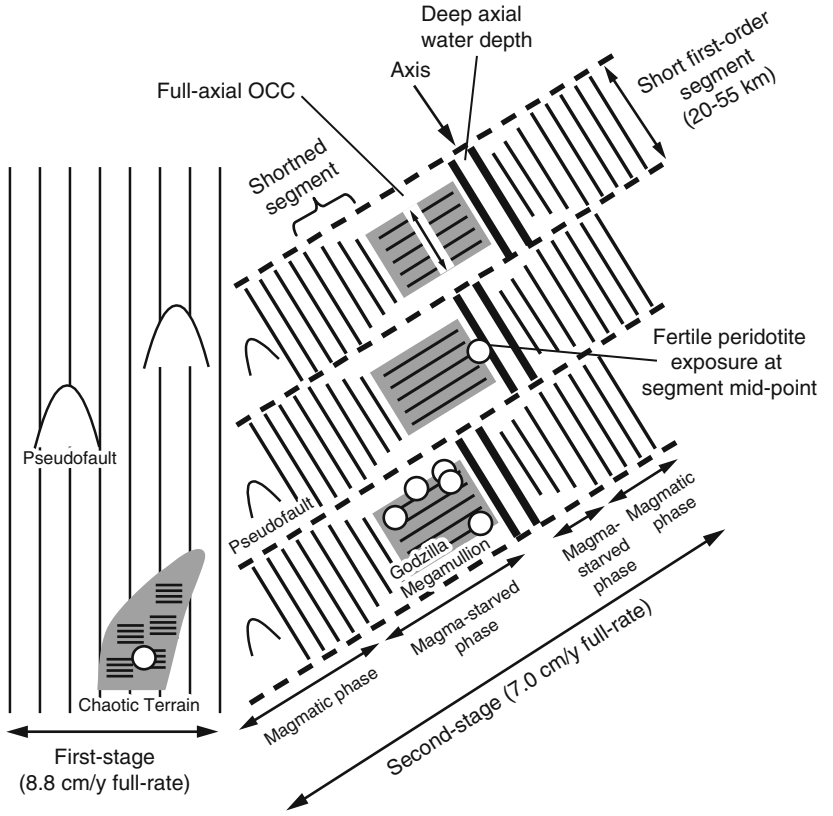

Fig. 2 Schematic cartoon illustrating the bathymetric features of the Parece Vela Basin. *Thick dashed lines* indicate fracture zones, whereas *thin lines* abyssal hills. OCCs are indicated by grey-hatch with axis-normal lineated lines. *White circles* show peridotite exposures (Ohara et al. 2003b)

criterion by Macdonald et al. (1991). In the central PVB, the magnetic lineation pattern is highly segmented and identification of the anomalies was thus impossible.

During the YK00-01 cruise of R/V *Yokosuka*, total geomagnetic intensity was measured with a deep-towed proton magnetometer along a transect across the seafloor of segment S3 in the central PVB (Fujioka et al. 2000). The magnetic anomaly profile from this survey is almost symmetrical about the extinct axis of segment S3. The overall observed anomaly pattern was reasonably explained by spreading with a theoretical half-rate of 3.5 cm/year and cessation of spreading at 12 Ma (Ohara et al. 2003a). The postulated 7.0 cm/year full-rate for the second-stage of the basin evolution is still close to the higher end of intermediate-spreading rates (4–9 cm/year). Ohara et al. (2003a) concluded on this basis that the PVB opened at rapid intermediate-rate 8.8–7.0 cm/year full-rates. The evolution of the spreading rate during the last few million years, as it declined to zero, is presently unknown.

3.2 Oceanic Core Complexes in the Parece Vela Basin

The PVB experienced two major episodes of OCC formation during the basin's spreading history. The first was related to formation of the Chaotic Terrain, and the second was related to the OCCs in the axis of the central PVB just before the ridge went extinct.

The Chaotic Terrain in the western PVB consists of a series of rugged, isolated and elevated domes capped by corrugated axis-normal lineations, and associated deep basins (maximum depth ~6,200 m) (Figs. 1b and 2). This terrain is similar to other areas where OCCs are abundant, like the off-axis regions of the 61°–67°E Southwest Indian Ridge (Cannat et al. 2006) and the 13°N segment of the Mid-Atlantic Ridge (Smith et al. 2008). The axis-normal length of each dome varies from ~3.5 to ~15 km, comparable to the length observed in the OCCs in the Mid-Atlantic Ridge (Ohara et al. 2007). A high mantle Bouguer anomaly (~30 mgal) indicates the presence of relatively thin crust beneath the area (Okino et al. 1998; Ohara et al. 2001). The morphology and gravity signatures of these isolated domes are very similar to global OCCs. Dredging on these domes yielded peridotites and gabbros (Ohara et al. 2003b), also sharing a common characteristic with the global OCCs.

The presence of the Chaotic Terrain indicates the dominance of tectonic over magmatic extension during the time from Chron 6C to 6A (corresponding to 24–21 Ma) of the first-stage spreading of the PVB. This is unusual, since a higher magmatic budget is generally expected for an intermediate-spreading ridge. Among intermediate-spreading ridges, the presence of off-axis OCCs similar to those in the Chaotic Terrain is known in the Australian-Antarctic Discordance (AAD) on the Southeast Indian Ridge (~7.2 cm/year full-rate; Okino et al. 2004).

In the central PVB, Godzilla Megamullion is developed at segment S1 of the Parece Vela Rift (Figs. 1b and 2). It is overall a relatively flat to domal elongated massif with distinct corrugated surface. In detail, it consists of several individual domes. The older edge of the massif is marked sharply by a linear abyssal hill. Well-ordered abyssal hills parallel the strike of the spreading axis further off-axis. The younger edge of the massif consists of an axis-parallel irregular edifice, terminating the corrugations on the massif. Godzilla Megamullion has slightly elevated mantle Bouguer anomalies and yields peridotites and gabbros, also supporting the contention that it is an analogue to global OCCs. Godzilla Megamullion is the largest OCC found to date (Ohara et al. 2001); it extends ~125 km normal to the axis and ~55 km along the axis.

Other segments of the Parece Vela Rift also host rift mountain massifs (Figs. 1b and 2). Although these massifs have no prominent corrugated surfaces, the domal shape and smooth surface of many of these are distinct from the surrounding NW-SE trending well-ordered abyssal hills. The massifs at segments S2 and S3 also yield peridotites (Ohara et al. 2003a, b), supporting the contention that these are analogues to global OCCs. The second-stage spreading of the PVB had an intermediate-spreading rate (postulated 7.0 cm/year full-rate), initially having produced well-ordered abyssal hills. Pronounced tectonic extensions initiated in a later phase

of the second-stage spreading (Fig. 2). This is consistent with a further shortening of segments of the Parece Vela Rift (Figs. 1b and 2) and the collapse of spreading in the system.

An important feature of the OCCs in the central PVB is that many of these are developed along the full length of segments (Ohara et al. 2001) (Figs. 1b and 2). In the Mid-Atlantic Ridge, OCCs normally develop at inside-corners of ridge-transform intersections (e.g., Tucholke et al. 1998). Furthermore, the peridotites from the Parece Vela Rift expose at segment mid-points and include fertile compositions with spinel Cr# (i.e., molar ratio of Cr/(Al+Cr)) ~0.17 (Ohara et al. 2003a; Ohara 2006). This is unusual, because segment mid-points are generally considered to be the most magmatically robust part of a ridge system, with the highest degree of mantle melting (Lin et al. 1990). In addition, fertile peridotites from the Parece Vela Rift are among the least depleted in a global mantle peridotite context (Ohara et al. 2003a; Ohara 2006). This is also unusual, because more depleted peridotites similar to those occur at the Garret Fracture Zone (FZ) in the East Pacific Rise (Constantin 1999) are expected in a relatively fast spreading ridge.

4 Mechanisms That Account for the Unusual Characteristics of the Parece Vela Basin

The unusual tectono-magmatic characteristics of the PVB indicate a relative magma starvation there compared to the crust created at intermediate-spreading ridges (Ohara et al. 2001, 2003a). Based on the geologic interpretations of crust with analogous features on global mid-ocean ridges, we propose three possible mechanisms that can account for these characteristics: (1) presence of a cold and/or refractory mantle domain, (2) declining spreading rate during the later phase of the second-stage spreading of the PVB, and (3) a transform sandwich effect. The first one primarily accounts for the unusual characteristics observed in the western PVB, whereas the last two account for those in the central PVB.

4.1 Presence of a Cold and/or Refractory Mantle Domain

The Chaotic Terrain occupies a part of the well-ordered abyssal hill floor in the western PVB. It abruptly emerged as a patchy area within the well-ordered abyssal hill floor produced under a rapid intermediate-spreading environment when E-W orthogonal spreading occurred, indicating that tectonic extension was occurring in an otherwise magmatic spreading environment.

The presence of persistent transform faults and/or fracture zones is not evident in the western PVB, and therefore the emergence of the Chaotic Terrain was not due to a transform fault effect. The transform fault effect is thought to be a cooling of the axial mantle as a consequence of juxtaposition of a young, hot and thin axial lithosphere against an old, cold and thick lithosphere at a ridge segment end (Fox

and Gallo 1984; Morgan and Forsyth 1988). The abrupt emergence of the Chaotic Terrain may instead require an intrinsic tectonic episode related to the presence of a cold and/or refractory mantle domain.

The cold mantle domain may relate to the emergence of a mantle cold plume beneath the area, and the mantle thus had not undergone significant melting during the certain period of the first-stage spreading of the PVB. A cold mantle domain has been proposed in the Equatorial Mid-Atlantic Ridge (Bonatti et al. 1993) as well as in the Southeast Indian Ridge (at the AAD) (Christie et al. 1998). Numerical modeling by Gerya and Yuen (2003) demonstrated that hydration and partial melting of the mantle along a subducting slab can trigger Rayleigh-Taylor instabilities that evolve into cold plumes that rise through the hot asthenospheric mantle wedge. They demonstrated that these cold plumes are 300–400°C cooler than the ambient mantle.

Heterogeneous mantle containing a refractory domain could also account for the Chaotic Terrain. Long-term preservation of refractory domains in asthenospheric mantle is invoked by Re-Os studies on peridotites from mid-ocean ridges (Harvey et al. 2006; Liu et al. 2008), although there are yet no Re-Os studies on the Chaotic Terrain peridotite to test this hypothesis.

4.2 Declining Spreading Rate During a Later Phase of the Second-Stage Spreading of the Parece Vela Basin

Another mechanism to explain the unusual characteristics of the PVB is related to declining spreading rate during a later phase of the second-stage spreading of the PVB. This mechanism could contribute to the central PVB OCCs.

For the second-stage spreading, a postulated 7.0 cm/year full-rate was obtained by deep-towed proton magnetometer data (Fig. 2; Ohara et al. 2003a). During the second-stage, the full spreading rate varied from 7.0 cm/year to zero (i.e., cessation) at 12 Ma with the ridge jump to the east and the initiation of the Mariana Trough. However, the exact evolution of the decline in spreading rate cannot be constrained from the currently available data. One interpretation of the deep-towed magnetometer data is to assume that the PVB spread at 7.0 cm/year for the entire second-stage and halted abruptly at 12 Ma. However, it is more plausible to suppose a decline in spreading rate during a later phase of the second-stage. If the latter interpretation is valid, then the tectono-magmatic characteristics of the central PVB would have been governed by slower-spreading rate tectonics, which would imply a lower magmatic budget and greater tectonism.

4.3 Transform Sandwich Effect

A further explanation of the unusual characteristics of the central PVB is an extreme transform fault effect (Fox and Gallo 1984; Morgan and Forsyth 1988) beneath the Parece Vela Rift. Ohara et al. (2003a) proposed a “transform sandwich

effect", with which a cooled upper mantle domain is emplaced along an otherwise rapid intermediate-spreading ridge (Fig. 2).

Despite the rapid intermediate-spreading rate, mantle melting beneath each short first-order segment was effectively inhibited due to the "sandwiched" geometry of the two adjacent transform faults, causing primarily tectonic extension in the sandwiched segment. The full-axial OCCs, large axial water depths, peridotite exposures at segment mid-points, and the fertility of the peridotites from the Parece Vela Rift suggest that little mantle melting took place beneath the cooled short first-order segments resulting from an extreme transform fault effect caused by closely-spaced fracture zones (Fig. 2).

The onset of magma-starved rifting did not appear to coincide with the change to short spreading segment geometry within the Parece Vela Rift. Instead, spreading in this segment geometry initially produces well-ordered spreading-normal abyssal hills. Pronounced tectonic extension only initiated during a later phase of the second-stage spreading. We thus infer that the transform sandwich effect on mantle melting gradually increased in the sandwiched segments after the PVB ridge axes started rotating counter-clockwise at ~19 Ma. We further infer that formation of OCCs initiated when mantle upwelling beneath the sandwiched segments was lowered below a critical threshold for melting (Fig. 2).

This mechanism appears to explain the tectonic and magmatic features of the Ascension FZ in the Mid-Atlantic Ridge at ~7°S. The Mid-Atlantic Ridge in this region is unusually magmatically robust given a typical slow-spreading rate of 3.3 cm/year full-rate (Bruguier et al. 2003; based on the global plate motion model NUVEL-1A by DeMets et al. 1994). In spite of the slow-spreading rate, there are an unusually shallow axial depth (~1,200 m) forming a volcanic ridge rather than an axial valley, pseudofaults and overlapping spreading centers, and thickened crust of 10–11 km in this region (Brozena and White 1990; Bruguier et al. 2003). It has therefore been postulated that a mantle plume is responsible for these anomalous characteristics (Brozena and White 1990), although Bruguier et al. (2003) suggested that a small heterogeneity in the mantle is responsible for these. Irrespective of the origin of the anomalies, the Mid-Atlantic Ridge near the Ascension FZ is similar to the Reykjanes Ridge: a ridge with slow-spreading rate showing the robust magmatism typical of a fast-spreading ridge due to the presence of excess melt (in the case of the Reykjanes Ridge caused by the Iceland hotspot; Bell and Buck 1992; Searle et al. 1998). Despite its slow-spreading rate, the Mid-Atlantic Ridge near the Ascension FZ is therefore similar to the magmatically robust portions of the PVB and other intermediate- and fast-spreading ridges in terms of robust magmatic budgets.

The Ascension FZ offsets the Mid-Atlantic Ridge right laterally by ~200 km, and in fact consists of two fracture zones: the North and South Ascension FZs (Fig. 3). A large OCC (here named the Ascension OCC) and a possible fossil OCC are clearly recognizable between the two fracture zones (Fig. 3). The Ascension OCC is relatively large, with the dimension of ~95 km perpendicular to the axis and ~25 km along the axis. Peridotites were recovered at the ridge-transform intersection adjacent to the Ascension OCC by a German expedition (Schulz et al. 1999) (Fig. 3). The Mid-Atlantic Ridge in this region has two distinct characteristics similar

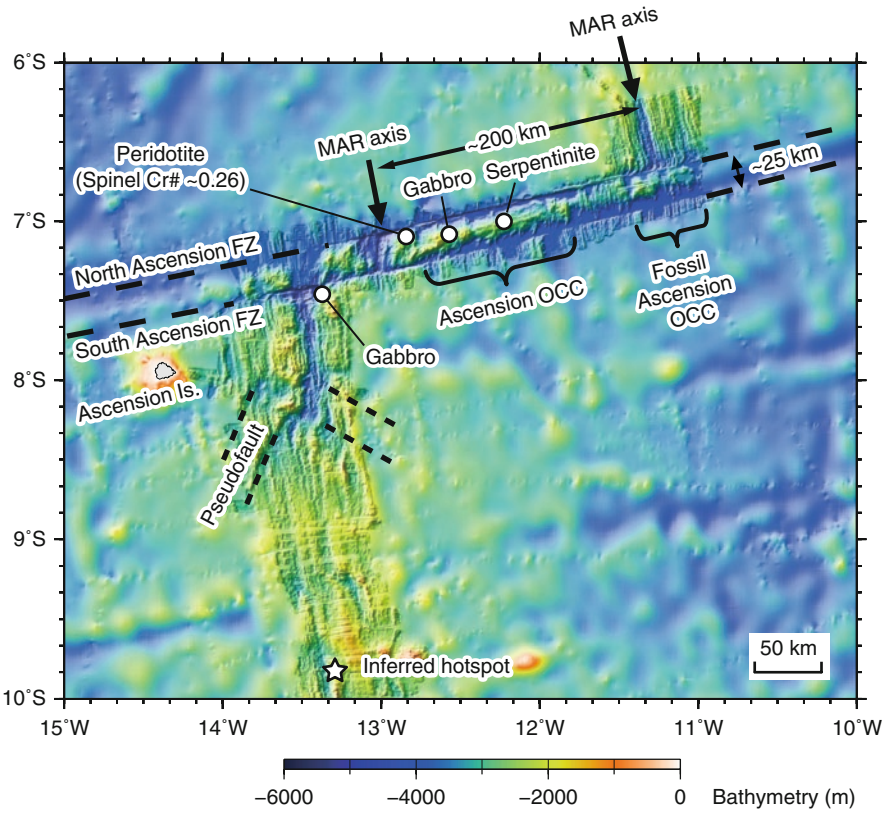

Fig. 3 Structural image of the Ascension Fracture Zone and the adjacent Mid-Atlantic Ridge segments illuminated from 315°. Two-hundred meter grid data from Brozena and White (1990) were utilized (through the Marine Geoscience Data System web site at http://www.marine-geo.org/). Note the corrugated surface and the full axial development (~25 km) of the Ascension OCC. Location of the dredge hauls that recovered peridotites (and serpentinites) and gabbros during the R/V Meteor cruise M41 (Schulz et al. 1999) are shown. The spinel Cr # (~0.26) of peridotite is from E. Hellebrand (personal communication, 2002). Some pseudofaults (indicated by *dotted lines*) suggest ridge propagation and jump occurred at this region of the Mid-Atlantic Ridge (Brozena and White 1990). Location of the inferred hotspot is from Brozena (1986)

to those observed in the central PVB (Fig. 3): (1) the Ascension OCC extends along the full length of the short first-order segment (~25 km) between the closely-spaced North and South Ascension FZs, and (2) the peridotite exposed there is relatively fertile (spinel Cr# ~0.26; E. Hellebrand, personal communication, 2002) compared to the ultra-depleted compositions found at the Bouvet FZ (Johnson et al. 1990) where a melting anomaly influenced by a hotspot is observed.

The Mid-Atlantic Ridge near the Ascension FZ is thus similar to the central PVB in that these distinct characteristics of relative magma starvation are observed in an otherwise robust magmatic budget environment, suggesting a transform sandwich effect is working there.

5 Relationships Between Mantle Thermal Anomaly, Fracture Zone Geometry, Occurrence of Oceanic Core Complexes and Spreading Rate

Although the unusual characteristic of the western PVB is explained by assuming a cold and/or refractory mantle domain, those of the central PVB cannot be explained solely by a single mechanism. We thus examined the literatures to investigate the relationship between mantle thermal anomaly, fracture zone geometry, occurrence of OCCs, and spreading rate in several regions (Table 1). These specific examples are characterized by their unique tectono-magmatic signatures, including the occurrence of cold mantle domains, multiple fracture zones, and OCCs at intermediate-spreading rates.

5.1 St. Paul FZ in the Mid-Atlantic Ridge

In the Equatorial Atlantic, the Mid-Atlantic Ridge is highly segmented and forms *en-echelon* geometry by the left lateral large-offset transform faults (e.g., the St. Paul and Romanche FZs). The ridge axis reaches a maximum depth of 4–5 km at this region, exposing abundant peridotites. Bonatti et al. (1993) and Schilling et al. (1995) suggested that the mantle beneath the Equatorial Mid-Atlantic Ridge is colder than the other region of the Atlantic Ocean based on major element systematics. Recent global mantle tomography model in fact demonstrated the presence of a fossil detached cold subducted slab beneath the Equatorial Atlantic (Sichel et al. 2008).

The Mid-Atlantic Ridge in this region has a typical slow-spreading rate of 3.2 cm/year full-rate (calculation based on NUVEL-1A). The St. Paul FZ offsets the ridge left laterally ~580 km. The fracture zone is made up of four transform faults linked by three short first-order segments (Hékinian et al. 2000). The length of these short first-order segments are ~15 to ~45 km. Presence of OCCs associated with these short first-order segments was not noted by Hékinian et al. (2000), although Sichel et al. (2008) interpreted the ~90 km long massif that host the St. Paul Islet as a large OCC, called "Saint Peter Saint Paul Megamullion". However, they provided no information supporting their contention, and the presence of the OCC is not fully assessed. On the other hand, the bathymetric map shown in Brunelli and Seyler (2010) shows that one of the short first-order segments has a similar morphology to the "smooth seafloor" reported by Cannat et al. (2006). The "smooth seafloor" was first described in the 61°–67°E Southwest Indian Ridge, occurring in the form of broad ridges with a smooth, rounded topography (Cannat et al. 2006). It is considered as a non-volcanic terrain characterized by successive fault surfaces primarily consisted of peridotites. The peridotites from these short first-order segments are relatively fertile with the minimum spinel Cr# 0.22 (Brunelli and Seyler 2010).

The Mid-Atlantic Ridge near the St. Paul FZ is thus similar to the western PVB in that a cold mantle domain is assumed as well as to the central PVB in that a

Table 1 List of mid-ocean ridges showing unusual crustal accretion characteristics

Location name	Spreading full-rate (cm/year)	Robust magmatic region	Cold mantle domain	Multiple FZ	Occurrence of OCC	Degree of mantle melting	Inferred mechanism	References for spreading rate
Parece Vela Basin								
Chaotic Terrain	8.8	Yes	Yes	No	Yes	Moderate	Magmatic + cold mantle	Okino et al. (1998)
Central PVB	7.0	Yes	No	Yes	Yes	Low	Magmatic + TSE	Ohara et al. (2001)
Mid-Atlantic Ridge								
Ascension	3.3	Yes	No	Yes	Yes	Relatively low	Magmatic + TSE	Bruguier et al. (2003)[a]
St. Paul	3.2	No	Yes	Yes	Smooth seafloor	Low	Cold mantle + TSE	DeMets et al. (1994)
Southeast Indian Ridge								
AAD	7.2	Yes	Yes	No	Yes	Relatively low	Magmatic + cold mantle	Okino et al. (2004)[a]
Chile Ridge								
Valdivia	6.2[b]	Yes	No	Yes	Yes	Relatively low	Magmatic + TSE	Tebbens et al. (1997)
East Pacific Rise								
Garret	14.5	Yes	No	Leaky type	No	High	–	Naar and Hey (1989)
Siqueiros	10.7	Yes	No	Leaky type	No	High	–	Pockalny et al. (1997)

TSE transform sandwich effect

[a]Based on NUVEL-1A (DeMets et al. 1994)

[b]Postulated rate; originally appeared as half-rate in the reference

transform sandwich effect may also be working there. The transform sandwich effect in this cold and slow-spreading ridge may be manifesting a similar tectono-magmatic environment to an ultraslow-spreading ridge.

5.2 *Australian-Antarctic Discordance in the Southeast Indian Ridge*

The Australian-Antarctic Discordance (AAD) is a part of the Southeast Indian Ridge. The full-spreading rate is ~7.2 cm/year (Okino et al. 2004; based on NUVEL-1A). The AAD is characterized by unusually deep seafloor compared with the standard age-depth curve (Hayes 1988; Marks et al. 1990) and by its rugged chaotic seafloor morphology (Christie et al. 1998). A cold mantle domain has been proposed beneath the AAD (Christie et al. 1998), being attributed to the presence of a subducted slab (Pacific Plate) beneath the Gondwana Plate (Gurnis et al. 1998).

Within the AAD, the spreading segments are unusually deep for a rapid intermediate-spreading rate ridge with mean water depth ~4,800 m (Okino et al. 2004). OCCs in the AAD appears to develop along the entire second-order segment, which is ~40 km (Okino et al. 2004).

Peridotites were recovered from the AAD (Christie et al. 1998), although no detailed petrological data on these peridotites are published. However, the AAD lavas have higher Na and lower Fe for a given MgO content, than the lavas from the east of AAD (i.e., Pacific-type MORB), indicating low degree of mantle melting and low mean pressure of melting beneath the AAD (Klein et al. 1991).

The Southeast Indian Ridge near the AAD is thus similar to the western PVB in that a cold mantle domain is inferred to occur in an otherwise robust magmatic budget environment.

5.3 *Valdivia FZ in the Chile Ridge*

The Chile Ridge extends from the Juan Fernandez Mircoplate to the Chile margin triple junction. The ridge is offset by 18 transform faults with fossil fracture zones, including two complex fracture zone systems. One of these, the Valdivia FZ system, consists of six parallel fracture zones, separated by first order ridge segments ranging from ~22 to ~27 km (Tebbens et al. 1997). The Valdivia FZ system evolved from a single long left-lateral offset transform fault connecting the Chile Ridge to the Pacific-Antarctic-Nazca triple junction at ~17 Ma when a 10° counterclockwise rotation occurred (Tebbens et al. 1997).

The spreading half-rate of the Chile Ridge varied from ~6.1 cm/year (at ~23 Ma) to ~3.1 cm/year (at ~6 Ma to present) (Tebbens et al. 1997). Since the spreading was generally symmetric (Tebbens et al. 1997), we employ the doubled values as the postulated full-rates for the Chile Ridge (i.e., a fast-spreading rate of ~12.3 cm/year full-rate to an intermediate-spreading rate of ~6.2 cm/year) in this paper

(Table 1). Martinez et al. (1998) noted that the surveyed spreading segments form axial valleys. They also reported OCCs from one area within the Valdivia FZ system (Martinez et al. 1998).

Peridotites were recovered from the Valdivia FZ system, although no detailed petrological data on these peridotites are published (F. Martinez, personal communication, 2009). However, the basalts from the Chile Ridge show higher Na and lower Ca for a given MgO content than the basalts from the East Pacific Rise, indicating low degree of mantle melting and low mantle temperature (Bach et al. 1996). Bach et al. (1996) noted that the mantle beneath the Chile Ridge is characterized by relatively low temperature due to the result of cooling associated with the numerous transform offsets, in fact pointing out a transform sandwich effect.

The Chile Ridge near the Valdivia FZ is thus similar to the central PVB in that these distinct characteristics of relative magma starvation are observed in an otherwise robust magmatic budget environment, suggesting a transform sandwich effect is working there.

6 Tectono-Magmatic Characteristics of Intra-Transform Spreading Centers in Fast-Spreading Ridges

Transform faults along fast-spreading ridges are often segmented by intra-transform spreading centers (ITSCs). The geometry of ITSCs is similar to that of the four specific examples where transform sandwich effect may be working (i.e., the central PVB, and the Ascension, St. Paul and Valdivia FZs). However, the notable characteristic of ITSCs is that magmatic process is dominant there (Hékinian et al. 1992; Perfit et al. 1996). Here we examine two examples from the East Pacific Rise to clarify the tectono-magmatic difference between these two similar features.

The Siqueiros Transform Fault is a left lateral transform fault located on the East Pacific Rise between 8°15′N and 8°30′N. The spreading full-rate of this part of the East Pacific Rise is ~10.7 cm/year (Pockalny et al. 1997; based on NUVEL-1A). Fornari et al. (1989) identified that the transform domain is ~20 km wide and segmented with four ITSCs. Length of each ITSC is ~7 to ~9 km (Pockalny et al. 1997). On the other hand, the Garrett Transform Fault is a right lateral transform fault located on the East Pacific Rise at ~13°28′S. The spreading full-rate of this part of the East Pacific Rise is ~14.5 cm/year (Naar and Hey 1989). The transform domain is ~24 km wide and consists of three ITSCs of ~10 km in length (Hékinian et al. 1995). Magmatic process is dominant along the ITSCs in both the Siqueiros and Garrett Transform Faults (Hékinian et al. 1992; Perfit et al. 1996); occurrence of OCCs is not reported so far from the ITSCs in the East Pacific Rise, although exposure of depleted peridotite is known from the eastern part of the Garrett Transform Fault (Hékinian et al. 1995; Constantin 1999).

It might be expected that the lavas from ITSCs would exhibit chemical characteristics indicative of classic transform fault effect, since the lithosphere within the transform domain would be older and colder than the lithosphere along the adjacent

ridge segments. However, the lavas from the ITSCs in the Siqueiros and Garrett Transform Faults have lower concentrations of incompatible trace elements compared to the lavas from the adjacent ridge segments, showing the opposite signatures expected for a transform fault effect (Perfit et al. 1996; Wendt et al. 1999).

Formation of ITSCs may be the result of a "leaky transform" phenomenon. Segmentation of transform faults is thought to be the result of transtensional forces imposed on the transform domain by plate motion reorganization (Pockalny et al. 1997). The change in spreading direction enables mantle upwelling beneath the transform domain and results in formation of ITSCs (Pockalny et al. 1997). The above geochemical characteristics are explained by the recent numerical modeling that considers brittle weakening of the lithosphere along a transform fault. The model generates a region of enhanced mantle upwelling and elevated temperatures at its center relative to the adjacent ridge segments (Behn et al. 2007). Elevated temperatures near the center of the transform fault may in turn promote the development of ITSCs during changes in plate motion. The leaky-type ITSCs are therefore robustly magmatic and not likely to host OCCs. It should be noted that the peridotites from the Garrett Transform Fault are considered to be exposed at a ridge-transform intersection, not at an ITSC (Constantin 1999). The Garrett peridotite is thus manifesting a classic transform fault effect.

7 Summary

Recent numerical modeling for detachment faulting at spreading ridge (assumed spreading rate = 5 cm/year full-rate) indicates that the right amount of melts is necessary to facilitate long-lived detachment faults and the resultant OCCs (Tucholke et al. 2008). They showed that long-lived detachment faults form when 30–50% of total extension is accommodated by magmatic accretion, and do not form or persist for long when magmatism is extremely limited. This indicates that long-lived detachment faults appear to form only within a limited window of the condition of melt supply where there is neither too much nor too little melt, but instead just right amount of melt. Tucholke et al. (2008) therefore viewed their hypothesis as the "magmatic Goldilocks hypothesis".

We have proposed three possible mechanisms that can explain the unusual tectono-magmatic characteristics of the rapid intermediate-spread PVB. In order to test these ideas, we have examined the global mid-ocean ridges that have the similar features to the PVB in terms of occurrence of assumed cold and/or refractory mantle domain, multiple fracture zones, and OCCs in intermediate-spreading rate. The unusual tectono-magmatic characteristics of the PVB may be manifesting the characteristic features predicted by Tucholke et al.'s model. In the western PVB, a cold and/or refractory mantle domain inhibited a large amount of mantle melting within an intermediate-spreading ridge, attaining the Tucholke et al's limited window of the condition of magma supply in an otherwise robust magmatic environment. In the central PVB, a transform sandwich effect and/or declining spreading

rate inhibited a large amount of mantle melting within an intermediate-spreading ridge, also attaining the Tucholke et al's limited window of the condition of magma supply in an otherwise robust magmatic environment.

Acknowledgments Most of the geophysical data (including bathymetry) for the Parece Vela Basin were obtained through Japan's legal continental shelf survey. We thank our colleagues in Continental Shelf Survey Office of the Hydrographic and Oceanographic Department of Japan for compiling these data. Most of the bottom rock samplings in the Parece Vela Basin were conducted through academic research expeditions with R/Vs *Kairei, Yokosuka* and *Hakuho.* The bathymetric data used for Fig. 3 are from the Marine Geoscience Data System (http://www.marine-geo.org/). We thank Osamu Ishizuka, Kenichiro Tani, Katsutyoshi Michibayahsi, Yumiko Harigane and Teruaki Ishii for discussion. We thank Eric Hellebrand for providing the unpublished Ascension peridotite data. We thank the helpful reviews by Hidenori Kumagai and Yildirim Dilek. We also thank Yujiro Ogawa, Yildirim Dilek, and Ryo Amma for the editorial efforts.

References

Bach W, Erzinger J, Dosso L, Bollinger C, Bougault H, Etoubleau J, Sauerwein J (1996) Unusually large Nb-Ta depletions in North Chile ridge basalts at 36°50′ to 38°56'S: major element, trace element, and isotopic data. Earth Planet Sci Lett 142:223–240

Behn MD, Boettcher MS, Hirth G (2007) Thermal structure of oceanic transform faults. Geology 35:307–310

Bell RE, Buck R (1992) Crustal control of ridge segmentation inferred from observations of the Reykjanes Ridge. Nature 357:583–586

Blackman DK, Cann JR, Janssen B, Smith D (1998) Origin of extensional core complexes: evidence from the Mid-Atlantic Ridge at Atlantis Fracture Zone. J Geophys Res 103(B9):21315–21333

Blackman DK, Canales JP, Harding A (2009) Geophysical signatures of oceanic core complexes. Geophys J Int 178:593–613

Bonatti E, Seyler M, Sushevskaya N (1993) A cold suboceanic mantle belt at the Earth's equator. Science 261:315–320

Brozena JM (1986) Temporal and spatial variability of seafloor spreading processes in the northern South Atlantic. J Geophys Res 91((B1):497–510

Brozena JM, White RS (1990) Ridge jumps and propagations in the South Atlantic Ocean. Nature 348:149–152

Bruguier NJ, Minshull TA, Brozena JM (2003) Morphology and tectonics of the Mid-Atlantic Ridge 7°–12°S. J Geophys Res. doi:10.1029/2001JB001172

Brunelli D, Seyler M (2010) Asthenospheric percolation of alkaline melts beneath the St. Paul region (Central Atlantic Ocean). Earth Planet Sci Lett 289:393–405

Buck WR, Lavier LL, Poliakov ANB (2005) Modes of faulting at mid-ocean ridges. Nature 434:719–723

Cann JR, Blackman DK, Smith DK, McAllister E, Janssen B, Mello S, Avgerinos E, Pascoe AR, Escartín J (1997) Corrugated slip surfaces formed at ridge-transform intersections on the Mid-Atlantic Ridge. Nature 385:329–332

Cannat M, Sauter D, Mendel V, Ruellean E, Okino K, Escartín J, Combier V, Baala M (2006) Modes of seafloor generation at a melt-poor ultraslow-spreading ridge. Geology 34:605–608

Christie DM, West BP, Pyle DG, Hanan BB (1998) Chaotic topography, mantle flow and mantle migration in the Australian-Antarctic discordance. Nature 394:637–644

Constantin M (1999) Gabbroic intrusions and magmatic metasomatism in harzburgites from the Garrett transform fault: implications for the nature of the mantle±crust transition at fast-spreading ridges. Contrib Mineralog Petrol 136:111–130

DeMets C, Gordon RG, Argus DF, Stein S (1994) Effect of recent revisions to the geomagnetic reversal time scale on estimates of current plate motions. Geophys Res Lett 21(20):2191–2194

Dick HJB, Lin J, Schouten H (2003) An ultraslow-spreading class of ocean ridge. Nature 426:405–412

Escartín J, Mével C, MacLeod CJ, McCaig AM (2003) Constraints of deformation conditions and the origin of oceanic detachments: the Mid-Atlantic Ridge core complex at 15°45′N. Geochem Geophys Geosyst. doi:10.1029/2002GC000472

Fornari DJ, Gallo DG, Edwards MH, Madsen JA, Perfit MR, Shor AN (1989) Structure and topography of the Siqueiros transform fault system: evidence for the development of intra-transform spreading centers. Mar Geophys Res 11:263–299

Fox PJ, Gallo DG (1984) A tectonic model for ridge-transform-ridge plate boundary: implications for the structure of oceanic lithosphere. Tectonophysics 104:205–242

Fujioka K, Kanamatsu T, Ohara Y, Fujimoto H, Okino K, Tamura C, Lallemand SE, Deschamps-Boldrini A, Barretto JA, Togashi N, Yamanobe H, So A (2000) Parece Vela Rift and Central Basin Fault revisited: STEPS-IV (structure, tectonics, and evolution of the Philippine Sea) cruise summary report. InterRidge News 9(1):18–22

Gerya TV, Yuen DA (2003) Rayleigh-Taylor instabilities from hydration and melting propel 'cold plumes' at subduction zones. Earth Planet Sci Lett 212:47–62

Gregg PM, Lin J, Behn MD, Montési LGJ (2007) Spreading rate dependence of gravity anomalies along oceanic transform faults. Nature 448:183–187

Gurnis M, Müller RD, Moresi L (1998) Cretaceous vertical motion of Australia and the Australian-Antarctic Discordance. Science 279:1499–1504

Harvey J, Gannoun A, Burton KW, Rogers NW, Alard O, Parkinson IJ (2006) Ancient melt extraction from the oceanic upper mantle revealed by Re-Os isotopes in abyssal peridotites from the Mid-Atlantic ridge. Earth Planet Sci Lett 244:606–621

Hayes DE (1988) Age-depth relationships and depth anomalies in the southeast Indian Ocean and south Atlantic Ocean. J Geophys Res 93(B4):2937–2954

Hékinian R, Bideau D, Cannat M, Francheteau J, Hébert R (1992) Volcanic activity and crust-mantle exposure in the ultrafast Garrett Transform fault near 13°28′S in the Pacific. Earth Planet Sci Lett 108:259–275

Hékinian R, Bideau D, Hébert R, Niu Y (1995) Magmatism in the Garrett transform fault (East Pacific Rise near 13°27′S). J Geophys Res 100(B6):10163–10185

Hékinian R, Juteau T, Gràcia E, Udintsev G, Sichler B, Sichel SE, Appriounal R, Ligi M (2000) Submersible observations of Equatorial Atlantic Mantle: the St. Paul Fracture Zone region. Mar Geophys Res 21:529–560

Ildefonse B, Blackman DK, John BE, Ohara Y, Miller DJ, MacLeod CJ, Integrated Ocean Drilling Program, Expeditions, 304/305 Science Party (2007) Oceanic core complexes and crustal accretion at slow-spreading ridges. Geology 35:623–626

Johnson KTM, Dick HJB, Shimizu N (1990) Melting in the oceanic upper mantle: an ion microprobe study of diopsides in abyssal peridotites. J Geophys Res 95:2661–2678

Karig DE (1971) Origin and development of marginal basins in the Western Pacific. J Geophys Res 76(11):2542–2561

Klein EM, Langmuir CH, Staudigel H (1991) Geochemistry of basalts from the southeast Indian Ridge, 115°E–138°E. J Geophys Res 96(B2):2089–2107

Lin J, Morgan JP (1992) The spreading rate dependence of three-dimensional mid-ocean ridge gravity structure. Geophys Res Lett 19(1):13–16

Lin J, Purdy GM, Schouten H, Sempéré J-C, Zervas C (1990) Evidence from gravity data for focused magmatic accretion along the Mid-Atlantic Ridge. Nature 344:627–632

Liu CZ, Snow JE, Hellebrand E, Brügmann G, von der Handt A, Büchl A, Hofmann AW (2008) Ancient, highly heterogeneous mantle beneath Gakkel ridge, Arctic Ocean. Nature 452:311–316

Macdonald KC, Scheirer DS, Carbotte SM (1991) Mid-ocean ridges: discontinuities, segments and giant cracks. Science 253:986–994

MacLeod CJ, Searle RC, Murton BJ, Casey JF, MallowsC USC, Achenbach KL, Harris M (2009) Life cycle of oceanic core complexes. Earth Planet Sci Lett 287:333–344

Marks KM, Vogt PR, Hall SA (1990) Residual depth anomalies and the origin of the Australian-Antarctic discordance zone. J Geophys Res 95(B11):17325–17337

Martinez F, Karsten J, Klein EM (1998) Recent kinematics and tectonics of the Chile Ridge. EOS Trans AGU 79(45), Fall meeting suppl (Abstract T12C-01)

Martinez F, Okino K, Ohara Y, Reysenbach AL, Goffredi SK (2007) Back-arc basins. Oceanography 20:116–127

Morgan JP, Forsyth DW (1988) Three-dimensional flow and temperature perturbations due to a transform offset: effects on oceanic crustal and upper mantle structure. J Geophys Res 93(B4):2955–2966

Naar DF, Hey RN (1989) Recent Pacific-Easter-Nazca plate motions. In: Sinton JM (ed) Evolution of mid ocean ridges, vol 57, Geophysical monograph series. AGU, Washington, DC, pp 9–30

Niu Y, Batiza R (1993) Chemical variation trends at fast and slow spreading ridges. J Geophys Res 98(B5):7887–7902

Niu Y, Hekinian R (1997) Spreading-rate dependence of the extent of mantle melting beneath ocean ridges. Nature 385:326–329

Ohara Y (2006) Mantle process beneath Philippine Sea back-arc spreading ridges: a synthesis of peridotite petrology and tectonics. Isl Arc 15:119–129

Ohara Y, Yoshida T, Kato Y, Kasuga S (2001) Giant megamullion in the Parece Vela backarc basin. Mar Geophys Res 22:47–61

Ohara Y, Fujioka K, Ishii T, Yurimoto H (2003a) Peridotites and gabbros from the Parece Vela backarc basin: unique tectonic window in an extinct backarc spreading ridge. Geochem Geophys Geosyst. doi:10.1029/2002GC000469

Ohara Y, Okino K, Snow JE, KR03-01 Shipboard Scientific Party (2003b) Preliminary report of Kairei KR03-01 cruise: amagmatic tectonics and lithospheric composition of the Parece Vela Basin. InterRidge News 12(1):27–29

Ohara Y, Okino K, Kasahara J (2007) Seismic study on oceanic core complexes in the Parece Vela backarc basin. Isl Arc 16:348–360

Okino K, Kasuga S, Ohara Y (1998) A new scenario of the Parece Vela Basin genesis. Mar Geophys Res 20:21–40

Okino K, Matsuda K, Christie D, Nogi Y, Koizumi K (2004) Development of oceanic detachment and asymmetric spreading at the Australian-Antarctic discordance. Geochem Geophys Geosyst. doi:10.1029/2004GC000793

Park C, Tamaki K, Kobayashi K (1990) Age-depth correlation of the Philippine Sea back-arc basins and other marginal basins in the world. Tectonophysics 181:351–371

Parmentier EM, Morgan JP (1990) Spreading rate dependence of three-dimensional structure in oceanic spreading centres. Nature 348:25–328

Perfit MR, Fornari DJ, Ridley WI, Kirk PD, Casey J, Kastens KA, Reynolds JR, Edwards M, Desonie D, Shuster R, Paradis S (1996) Recent volcanism in the Siqueiros transform fault: picritic basalts and implications for MORB magma genesis. Earth Planet Sci Lett 141:91–108

Pockalny RA, Fox PJ, Fornari D, Macdonald KC, Perfit MR (1997) Tectonic reconstruction of the Clipperton and Siqueiros Fracture Zones: evidence and consequences of plate motion change for the last 3 Myr. J Geophys Res 102(B2):3167–3181

Schilling JG, Ruppel C, Davis AN, McCully B, Tghe SA, Kingsley RH, Lin J (1995) Thermal structure of the mantle beneath the equatorial Mid-Atlantic Ridge: inference from the spatial variation of dredged basalt glass compositions. J Geophys Res 100(B6):10057–10076

Schulz HD, Devey CW, Pätzold J, Fischer G (1999) Geo Bremen/GPI Kiel South Atlantic 1998, Cruise No. 41. Meteor-Berichte, Universität Hamburg, 13 Feb–13 June 1998

Searle RC, Keeton JA, Owens RB, White RS, Mecklenburghb R, Parsons B, Lee SM (1998) The Reykjanes Ridge: structure and tectonics of a hot-spot-influenced, slow-spreading ridge, from multibeam bathymetry, gravity and magnetic investigations. Earth Planet Sci Lett 160:463–478

Sichel SE, Esperança S, Motoki A, Maia M, Horan MF, Szatmari P, da Costa AE, Mello SLM (2008) Geophysical and geochemical evidence for cold upper mantle beneath the Equatorial Atlantic Ocean. Revista Brasileira de Geofísica 26(1):69–86

Sinton JM, Detrick RS (1992) Mid-ocean ridge magma chambers. J Geophys Res 97(B1):197–216
Smith DK, Escartín J, Schouten H, Cann JR (2008) Fault rotation and core complex formation: significant processes in seafloor formation at slow-spreading mid-ocean ridges (Mid-Atlantic Ridge, 13°–15°N). Geochem Geophys Geosyst. doi:10.1029/2007GC001699
Tebbens SF, Cande SC, Kovacs L, Parra JC, LaBrecque JL, Vergara H (1997) The Chile ridge: a tectonic framework. J Geophys Res 102(B6):12035–12059
Tucholke BE, Lin J, Kleinrock M (1998) Megamullions and mullion structure defining oceanic metamorphic core complexes on the Mid-Atlantic Ridge. J Geophys Res 103(B5):9857–9866
Tucholke BE, Behn MD, Buck WR, Lin J (2008) Role of melt supply in oceanic detachment faulting and formation of megamullions. Geology 36:455–458
Wendt JI, Regelous M, Niu Y, Hékinian R, Collerson KD (1999) Geochemistry of lavas from the Garrett transform fault: insight into mantle heterogeneity beneath the eastern Pacific. Earth Planet Sci Lett 173:271–284

Structural Profile and Development of the Accretionary Complex in the Nankai Trough, Southwest Japan: Results of Submersible Studies

Ryo Anma, Yujiro Ogawa, Gregory F. Moore, Kiichiro Kawamura, Tomoyuki Sasaki, Shunsuke Kawakami, Yildirim Dilek, Yoko Michiguchi, Ryota Endo, Shunji Akaiwa, Satoshi Hirano

Abstract We conducted seafloor geological mapping using the submersible "*SHINKAI 6500*" along the Shionomisaki submarine canyon, off Kii peninsula, Southwest Japan, in order to document the distribution of outcrop-scale structures and strain in the accretionary complex of the Nankai trough. We investigated outcrops in the seaward-most part (frontal thrust zone), the landward-most part (megasplay fault zone) and an intermediate part (imbricate thrust zone) of the

R. Anma (✉)
Graduate School of Life and Environmental Sciences, University of Tsukuba, Ten-nodai 1-1-1, Tsukuba, Ibaraki 305-8572, Japan
e-mail: ranma@sakura.cc.tsukuba.ac.jp

Y. Ogawa
The University of Tsukuba, 1-127-2-C-740 Yokodai, Tsukubamirai 300-2358, Japan (home)
e-mail: fyogawa45@yahoo.co.jp

G.F. Moore
School of Ocean and Earth Science and Technology (SOEST), University of Hawaii at Manoa, Honolulu, HI 96822, USA
e-mail: gmoore@hawaii.edu

K. Kawamura
Fukada Geological Institute, 2-13-12 Hon-Komagome, Bunkyo, Tokyo 113-0021, Japan
e-mail: kichiro@fgi.or.jp

T. Sasaki
Marine Geology, Department of Ocean Floor Geoscience, Atmosphere and Ocean Research Institute, The University of Tokyo, 5-1-5, Kashiwanoha, Kashiwa-shi, Chiba 277-8564, Japan
e-mail: tmsasaki@aori.u-tokyo.ac.jp

S. Kawakami
Earth-Appraisal Co. Ltd., Chiyoda, Tokyo 101-0063, Japan
e-mail: kawakami@earth-app.co.jp

Y. Dilek
Department of Geology, Miami University, 114 Shider Hall, Oxford, OH 45056, USA
e-mail: dileky@muohio.edu

Y. Ogawa et al. (eds.), *Accretionary Prisms and Convergent Margin Tectonics in the Northwest Pacific Basin*, Modern Approaches in Solid Earth Sciences 8,
DOI 10.1007/978-90-481-8885-7_8,

accretionary complex. Turbiditic sediments in the frontal thrust zone have been deformed to form an open anticline. Minor normal faults striking parallel to the trough axis developed in the crest of the anticline. As sediments were transferred into the imbricate thrust zone, both hill-size open anticlines and outcrop-scale open to tight folds developed in the turbiditic sequence. We also observed brittle thrust faults spatially associated with tight folds and development of shear fabrics such as oblique cleavages and en-echelon mineral veins. An out-of-sequence thrust, known as the megasplay fault in this region, then developed in the frontal part of the landward-most ridge composed of thick turbidite sequences. Sandstones just above the megasplay fault are cemented by carbonates. Behind the cemented zone, bifurcations of the megasplay fault are distributed in the sandstone-rich strata dipping steeply to the south. Folds with wavelength of ~200 m developed in mudstone-rich turbidites behind the bifurcating fault zone. The cementation strengthened the frontal part of the megasplay fault zone, which in turn, acted as an indenter for the inner part of the accretionary wedge. The cemented and hardened ridge must have local controls on strain localization and development of the accretionary complex.

Keywords Accretionary complex • Splay fault • Fold • Strain • Cement • Porosity • Strength • Nankai trough

1 Introduction

Our knowledge of the geometry, structure and evolutionary history of accretionary complexes has expanded recently through advancing technologies of geophysical surveys, scientific drilling, and in-situ ocean bottom observations through submersible diving. Amongst modern accretionary wedges of the world, the accretionary complex in the Nankai trough, off Southwest Japan, is the most intensively studied. Here, sediments deposited in the Shikoku Basin were scraped off the downgoing Philippine Sea plate (Aoki et al. 1982; Kato et al. 1983; Leggett et al. 1985; Moore et al. 1990, 2001; Ashi and Taira 1992; Taira et al. 1992; Kuramoto et al. 2000)

Y. Michiguchi
Japan Nuclear Energy Safety Organization, Toranomon 4-3-20, Tokyo 105-0001, Japan
e-mail: y-michi@hotmail.co.jp

R. Endo
INPEX Corporation, Akasaka Biz Tower 5-3-1 Akasaka, Minato-ku, Tokyo 107-6332, Japan
e-mail: rendo@inpex.co.jp

S. Akaiwa
Graduate School of Life and Environmental Sciences, University of Tsukuba, Ten-nodai 1-1-1, Tsukuba, Ibaraki 305-8572, Japan
e-mail: taurushunji@room.ocn.ne.jp

S. Hirano
Marine Works Japan, Showa-machi 3175-25, Kanazawa, Yokohama 236-0001, Japan
e-mail: hiranos@nwj.co.jp

subducting northwestward beneath the Eurasian (or Amurian) plate at a rate of ~4.5 cm/year (Seno et al. 1993), and have been incorporated into an accretionary complex since the late Miocene (Pickering and Taira 1994) (Fig. 1a).

Slip along faults associated with the Nankai trough subduction generated large earthquakes and tsunamis, which repeatedly devastated the Japanese coastal areas (Ando 1975; Baba et al. 2002, 2006; Cummins et al. 2002; Ichinose et al. 2003; Hori et al. 2004). To better understand the geometries and processes in the seismogenic zone and to be better prepared for the anticipated seismic hazard in this region (Le Pichon et al. 1996), several geophysical experiments (Kodaira et al. 2000a, b, 2002; Park et al. 2002a, b; Nakanishi et al. 2002a, b; Takahashi et al. 2003; Kido and Fujiwara 2004) and a complex drilling program (NanTroSEIZE IODP drilling expeditions; Tobin and Kinoshita 2006; Kinoshita et al. 2009) have focused on the accretionary complex in the Nankai trough. Recent 3D seismic data successfully illustrated details of the distribution and amplitude of reflectors (Bangs et al. 2004, 2006, 2009; Moore et al. 2007) and seismic velocity structure (Nakanishi et al. 2008; Park et al. 2010). These observations and surveys then allow the NanTroSEIZE experiment to relate borehole data directly and more effectively to the large-scale seismic structure (Strasser et al. 2009).

However, the resolution of seismic surveys is too coarse to identify outcrop-scale structures and their lateral variations. The observations from scientific drilling provided a continuous high-resolution data set on varying structures of ~1 mm to ~1 m scale (Maltman et al. 1993; Morgan and Karig 1993; Moore et al. 2001; Ujiie et al. 2003, 2004; Morgan and Ask 2004), which are, nevertheless, restricted to one-dimension along the borehole. Direct and in-situ seafloor surveys using submersibles are the only available method that fills the gap in the scale of observation.

Previous submersible studies mainly focused on features exposed on the landward slope of the Nankai trough (Le Pichon et al. 1987a, b, 1992, 1996; Kobayashi 2002; Ashi et al. 2002a). In this study, we focus on a submarine canyon that cuts through the accretionary complex. Submarine canyons, analogous to gorges and valleys favored by field geologists for geological mapping on-land, provide an excellent opportunity for 3-dimensional seafloor observations and mapping along deeply incised profiles (Kawamura et al. 1999, 2009; Anma et al. 2002). Submarine canyons also present an additional advantage in the case of the Nankai trough: the canyons eroded down to the distribution limit of gas hydrates (e.g. Ashi et al. 2002b; Colwell et al. 2004), and hence data undisturbed by hydrates were collected.

We conducted a series of seafloor studies along the Shionomisaki canyon (Fig. 1a), off Kii peninsula, using the submersible *SHINKAI 6500* operated by the Japan Agency for Marine-Earth Science and Technology (JAMSTEC), with an aim to understand the distribution of outcrop-scale structures and physical properties, and their relation to large-scale topographic features of the accretionary complex in the Nankai trough. SeaBeam bathymetric data and side-scan sonar images were used to select exact sites for the submersible study.

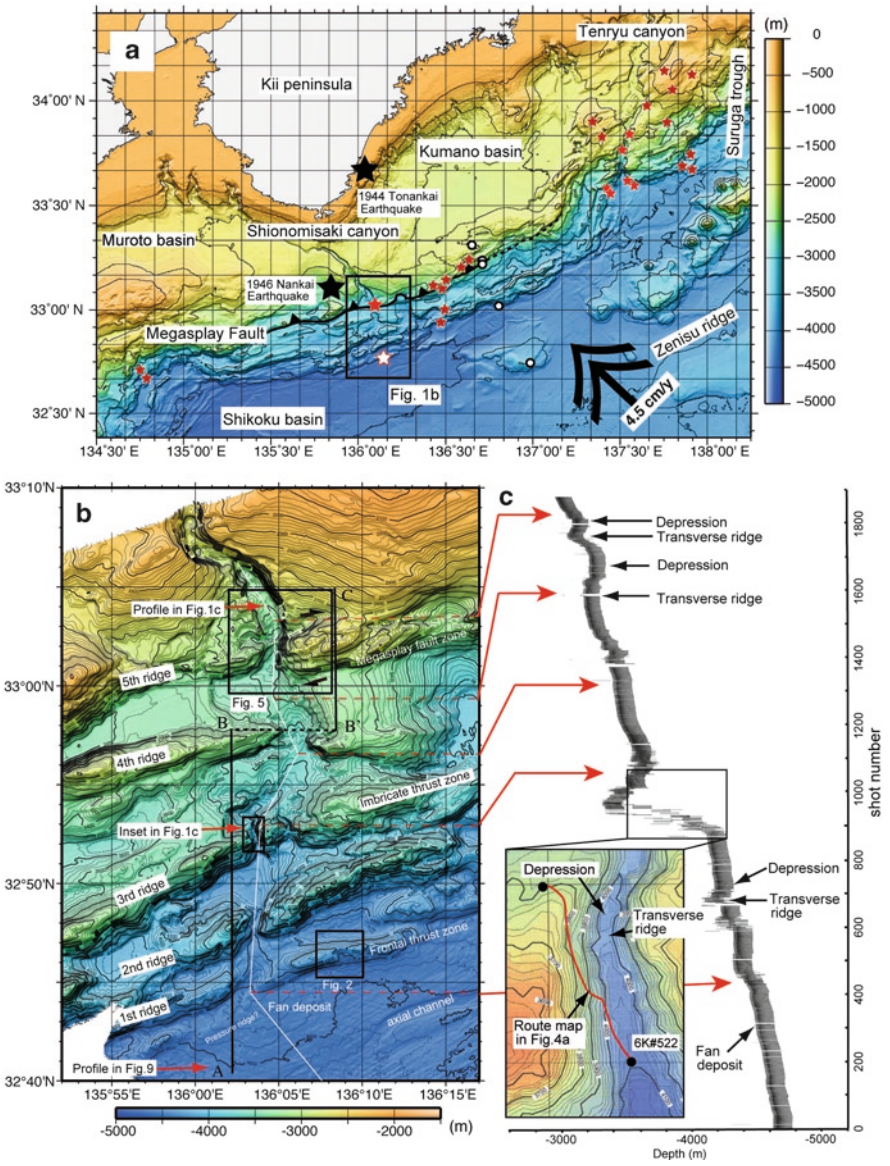

Fig. 1 Bathymetric features in the Nankai trough. (**a**) Bathymetric map of the accretionary complex of the Nankai trough. *Solid line with triangles* indicates megasplay fault deduced form seismic studies (see text). *Solid red star*: location of active cold seep (Modified from Ashi et al. 2002a). *Open star*: fossil cold seep. *Solid black stars*: epicenters of the 1944 Tonankai and 1946 Nankai great earthquakes. *Open circle*: hole drilled by D/V *Chikyu* during IODP Expeditions 314, 315, 316 and 322. (**b**) Detailed bathymetrical map of the Shionomisaki canyon. (**c**) A sub-bottom profile image along the mid-axis of the Shionomisaki canyon (indicated by *white line* in (**b**)). *Inset* in (**c**) indicates distribution of transverse ridge and depression developed upstream from the axis of the 3rd ridge (see text)

2 Framework of the Accretionary Complex in the Nankai Trough and the Shionomisaki Submarine Canyon

The regional bathymetric map of the Nankai trough (Fig. 1a) shows that the accretionary complex is characterized by a series of ENE-WSW-trending culminations (ridges) and depressions stepping up toward the Japanese mainland in the north. Sediments deposited in the forearc basins, namely Kumano and Muroto basins, cover the northern part of the accretionary complex. The Nankai trough itself is characterized by a narrow, WSW-trending axial channel deepening to the west. The upstream (eastern) extension of the axial channel is connected to the Tenryu submarine canyon and the Suruga trough. ENE-WSW-trending knolls that continue through the Zenisu ridge to the Izu arc in the east are distributed south of the axial channel. Crustal-scale faults were seismically observed along the southern and western margins of the knolls (Kodaira et al. 2006).

The Shionomisaki submarine canyon located nearby is the epicenter of the 1944 Tonankai and 1946 Nankai earthquakes (Baba and Cummins 2005) (stars in Fig. 1a). An out-of-sequence thrust, referred to as the 'megasplay fault' hereafter, and numerous in-sequence thrust sheets were imaged by seismic studies (Park et al. 2002a) along transects drilled by D/V *Chikyu* (open circles) during the NanTroSEIZE expeditions. The megasplay fault is likely the up-dip expression of the seismogenic fault that generated large tsunamis (Park et al. 2002a; Nakanishi et al. 2002a; Moore et al. 2007). Cold seepages marked by the distribution of chemosynthetic bio-communities (stars in Fig. 1a) have been reported along the fault (Ashi et al. 2002a).

Shionomisaki canyon is the result of deep erosion of the accretionary complex and crosscuts five EW-trending bathymetric ridges (Fig. 1b). The extension of the megasplay fault is inferred to occur at the landward-most ridge (the 5th ridge in Fig. 1b). We subdivided the accretionary complex in the central Nankai trough into three structural zones based on bathymetric features. The megasplay fault zone marks the seaward limit of the forearc basin, and separates the outer wedge from the inner wedge (Kimura et al. 2007). The frontal thrust zone is the outer margin of the accretionary complex that separates it from the Shikoku basin. The imbricate thrust zone comprises the main body of the accretionary prism and is recognized as a zone of landward-dipping thrust sheets and folds (Kawamura et al. 2009).

Sediments transported through Shionomisaki canyon form a large fan deposit in front of the 1st ridge. The fan deposit buried and deflected the axial channel of the Nankai trough (Fig. 1b). The southward trend of the stream from Shionomisaki canyon is deflected to the WSW after intersecting an ENE-WSW-trending mound developed in the fan deposit (Fig. 1b, also see exaggerated oblique view in Fig. 3). A profile along the mid-axis of the canyon (Fig. 1c) revealed the presence of several transverse ridges that transect the mid-axis of the canyon. In addition, the mid-axis is deflected toward the west south of the 5th ridge (Fig. 1b). SSE-trending gorges in the 3rd ridge and north of the 5th ridge are normal to the general trend of the ridges. The SSE-trend steps westward downstream of the canyon. Such topographic features are likely formed due to tectonic deformation that is still active.

3 Methodology

Shionomisaki canyon exposes a structural profile across the accretionary complex in the Nankai trough along steep, ~500-m-high walls that continue along the length of the canyon. We conducted a total of six dives in *SHINKAI 6500* (6K, hereafter) for this study. Dive 6K#938 (observer: Ogawa) concentrated on structures of the 1st ridge in the frontal thrust zone. Dive 6K#522 (observer: Anma) was conducted at the 3rd ridge in the imbricate thrust zone. Four dives (6K#579: Anma, 6K#889: Anma, 6K#890: Moore, and 6K#891: Ogawa) focused on the megasplay fault zone exposed along the 5th ridge.

During a dive, observations were made through a porthole window and recorded using external video cameras. Apparent dip and strike of planar structures such as bedding plane, cleavage, fault and joint were estimated from video images. The estimated directions were then corrected to true dip and strike using the yaw and pitch of the external video camera and the bearing of the submersible. Precision of the obtained strike and dip was estimated by measuring bedding planes of the same outcrop from several different angles to be approximately ±10° for moderately dipping strata (Anma et al. 2010).

Bedding planes on the video images were defined as continuous planar objects with clear evidence of alternating beds with different components or laminae. Fracture cleavages were recognized as penetrative planar objects oblique to or bifurcating from the bedding planes. Non-penetrative fractures cutting bedding planes and/or cleavages were classified as faults if displacement was obvious, and as joints if not.

Rock samples were collected as often as possible using manipulators of the submersible for offshore description and needle penetration tests to estimate uniaxial compressional strength. We used an SH-70 penetrometer (manufactured by Maruto Co. Ltd.) for the strength measurement. Microscopic observation and porosity measurements were performed in the laboratories at University of Tsukuba and JAMSTEC. Porosity and strength are important physical properties of sediments not only as a measure of consolidation state but also as a mechanical factor controlling deformation behavior.

4 Structural Profile of the Nankai Accretionary Complex

4.1 Frontal Thrust Zone (Dive 6K#938)

Layers of predominantly mudstones alternating with sandstones comprise the southern slope of the 1st ridge (Fig. 2). Bedding planes (Fig. 2c, d) are almost horizontal and folded to form an open anticline about an S80E-trending axis (Fig. 3b). The presence of cross-laminae (Fig. 2d) implies flow from the northwest. Joints trending WNW-ESE and NS are developed in the foot of the ridge (Fig. 2c).

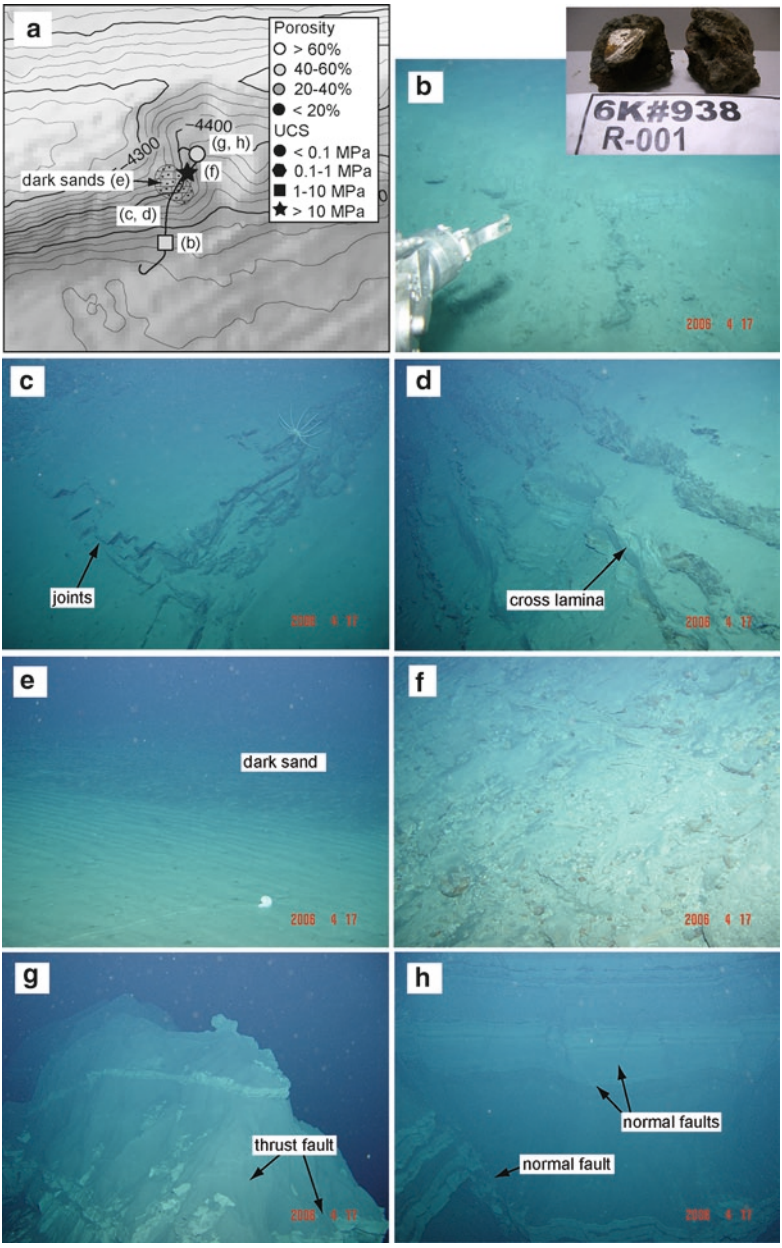

Fig. 2 Geology of the frontal thrust zone. (**a**) Track of Dive 6K#938 in the 1st ridge (map area indicated in Fig. 1b). Localities of photographs (**b**–**h**) and samples with porosity and uniaxial compressional strength (UCS) data are shown. (**b**) Outcrop of fossilized cold seep zone. A fossil of Vesicomyid bivalve (*inset*) was found buried in conglomerate. (**c**) An outcrop with orthogonal joint sets. Field of view (FOV) ~ 3 m. (**d**) Bedding planes with cross laminae. FOV ~ 2 m. (**e**) Ripples and dark sand covering a hump extending southeast from the crest of the 1st ridge (**a**). (**f**) An outcrop of a conglomerate interbedded with sandstone layers and cemented by carbonate minerals. FOV ~ 3 m. (**g**) Thrust fault recognized as oblique plane filled with a thin light film, offsetting bedding planes. FOV ~ 3 m. (**h**) Normal faults offsetting bedding planes. Drags were partly developed. FOV ~ 1 m

Weakly- to moderately-consolidated silty clays (938R-001: Fig. 2b) in an outcrop at the base of the southern slope have strength and porosity of ~7 MPa and ~56% (Fig. 2a), respectively. A buried shell of vesicomyid bivalve was found at the base of the 1st ridge (Fig. 2b).

Light-colored and dark-colored sands with ripple marks of various directions (Fig. 2e) are distributed on a hump extending southeast from the ridge crest (Fig. 2a). Behind the hump, conglomerates and sandstones (Fig. 2f) are cemented by calcite and have a high strength (~10 MPa for silty sandstone) and low porosity (~20%, Fig. 2a).

Near the crest of the 1st ridge, both thrust and normal faults were observed in weak (~0.8 MPa) and porous (~50%) mudstone-dominant beds. The thrust fault in Fig. 2g was recognized as a cohesive fault with thin white fillings and displacing the light-colored bed in the bottom-right. The thrust fault dips ~30° to the north (Fig. 3b). Normal faults (Fig. 2h) were observed near the crest of the 1st ridge, in the hanging wall of the thrust. The normal faults strike parallel to the ridge axis and dip steeply to both directions (Fig. 3b). No crosscutting relations were observed between the thrust and normal faults. No evidence for active cold seepages was observed in this area.

4.2 Imbricate Thrust Zone (Dive 6K#522)

Moderately consolidated (~2–9 MPa) mudstone-dominant beds comprise the western wall of Shionomisaki canyon in the 3rd ridge (Fig. 4). Numerous debris flow deposits were observed in eastward-oriented gullies (Fig. 4a; Anma et al. 2002). Bedding planes dip to the south in the southern part of the 3rd ridge, whereas they dip steeply to the north in the middle part (Fig. 4f, g). The dip angles become gentler (Fig. 4c) in the upper part of the slope in the north (Fig. 4a). Macroscopically, the bedding planes form an open to tight anticline with km-scale (a hill-size) wavelength about an axis plunging gently to ENE (Fig. 3c). Layer-parallel foliations developed in places (Fig. 4h). Both NNE-SSW and EW-trending joints are present.

A 10-m-high outcrop in Fig. 4i exhibits a spectacular view of a brittle thrust and a tight anticline inclined to the south. Bedding planes at the base, dipping moderately to the north, steepened upward and are truncated by the thrust fault just above the hinge of the anticline. The bedding planes become shallower toward the top of the outcrop. Such outcrop-scale folds were observed in several places (e.g., Fig. 4d). The bedding-cleavage relationship in Fig. 4f indicates a top-to-south sense-of-shear. En-echelon mineral veins dipping gently to the northwest (Fig. 4e) also document the development of shear fabrics in the accretionary wedge. The northernmost part of the 3rd ridge was cut by a vertical fault with the north-side down-thrown (Fig. 4b).

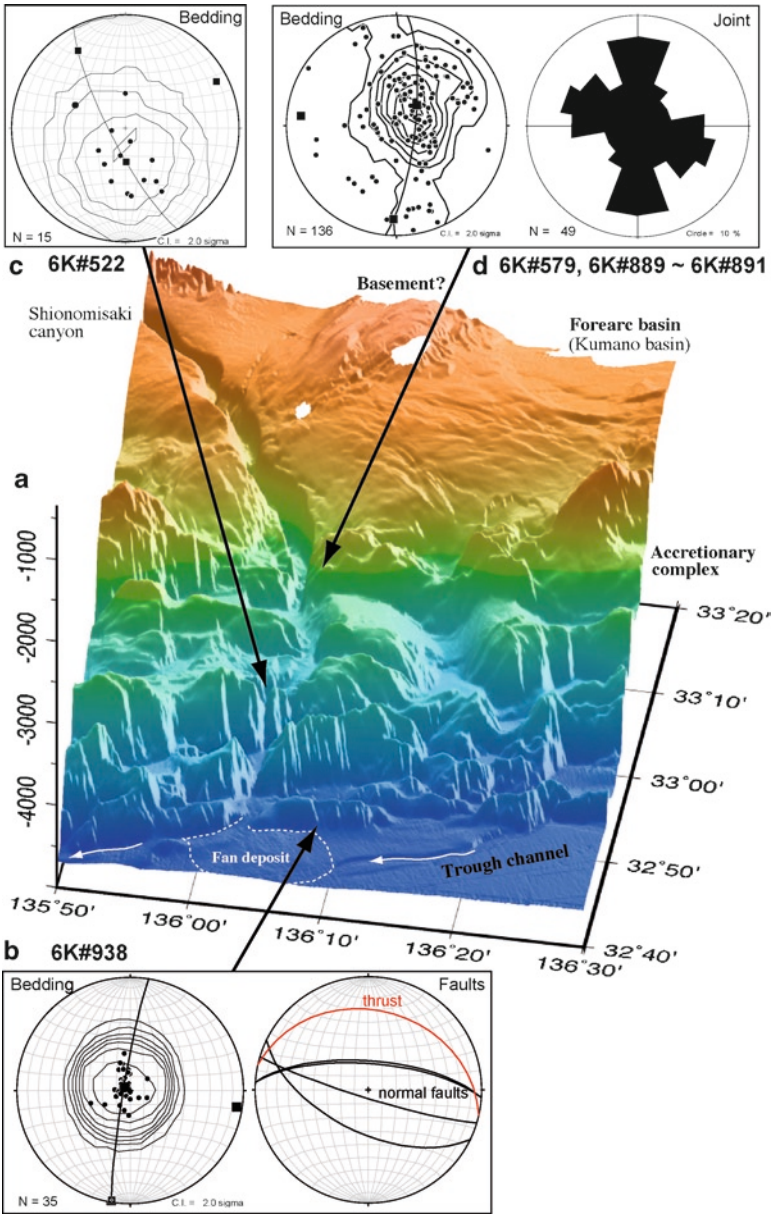

Fig. 3 Structures of the accretionary complex in the Nankai trough. (**a**) Oblique view of Shionomisaki canyon. Vertical scale is exaggerated to show lineament trending NS and trough channel buried by fan deposit at the mouth of Shionomisaki canyon. A WSW-trending ridge is developed in the fan deposit, and the southward trending mid-axis of the canyon swings to a WSW-orientation. *White arrow*: estimated flow direction. (**b**) Stereonet plots of S-poles to bedding planes (*left*) and of faults (*right*) in the 1st ridge (Dive 6K#938). Sub-horizontal strata are open folded about an axis trending S80E. Both thrust and normal faults strike WNW-ESE. (**c**) A plot of S-poles to bedding planes in the 3rd ridge (Dive 6K#522). (**d**) A stereonet plot of S-poles to bedding planes (*left*) and a Rose diagram for joints in the 5th ridge

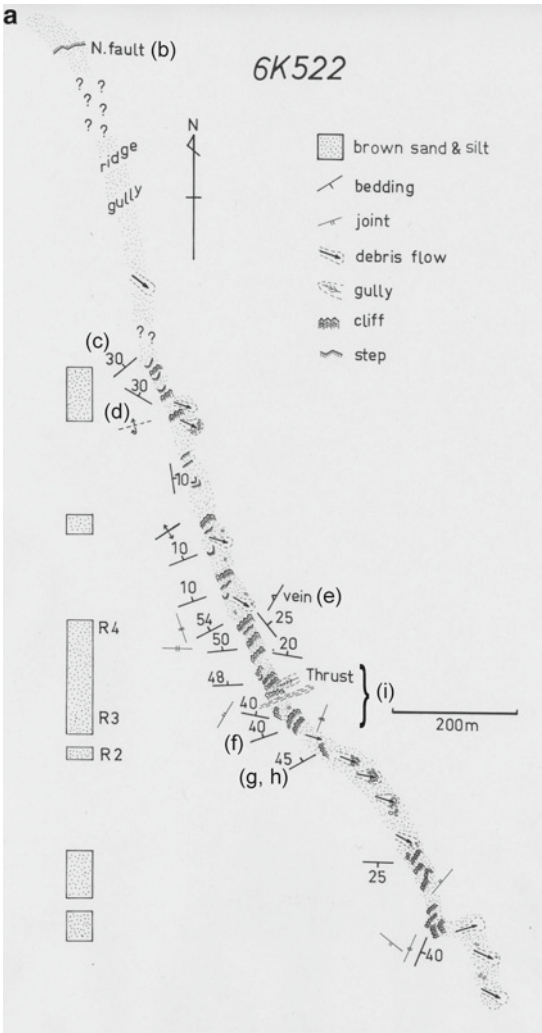

Fig. 4 Geology of the imbricate thrust zone (Reproduced from Anma et al. 2002). (**a**) A route map along the track of the Dive 6K#522 in the 3rd ridge (see *inset* of Fig. 1c for the map area). Locations of outcrops in (**b**)–(**h**) are indicated. (**b**) A fault with north downthrown at the northern margin of the 3rd ridge (FOV ~ 8 m). (**c**) Strata dipping gently to the north (FOV ~ 5 m). (**d**) Folded strata (FOV ~ 2 m). (**e**) Stretched vein (FOV ~ 0.5 m). (**f**) Shear fabric with north upward sense-of-shear. (**g**) Turbidite sequence dipping moderately to the north. (**h**) Development of foliation. (**i**) Anticline and transposed fault. Strata dipping moderately to north at the base of the outcrop steepened upward. An anticlinal structure developed at the middle was transposed by a fault

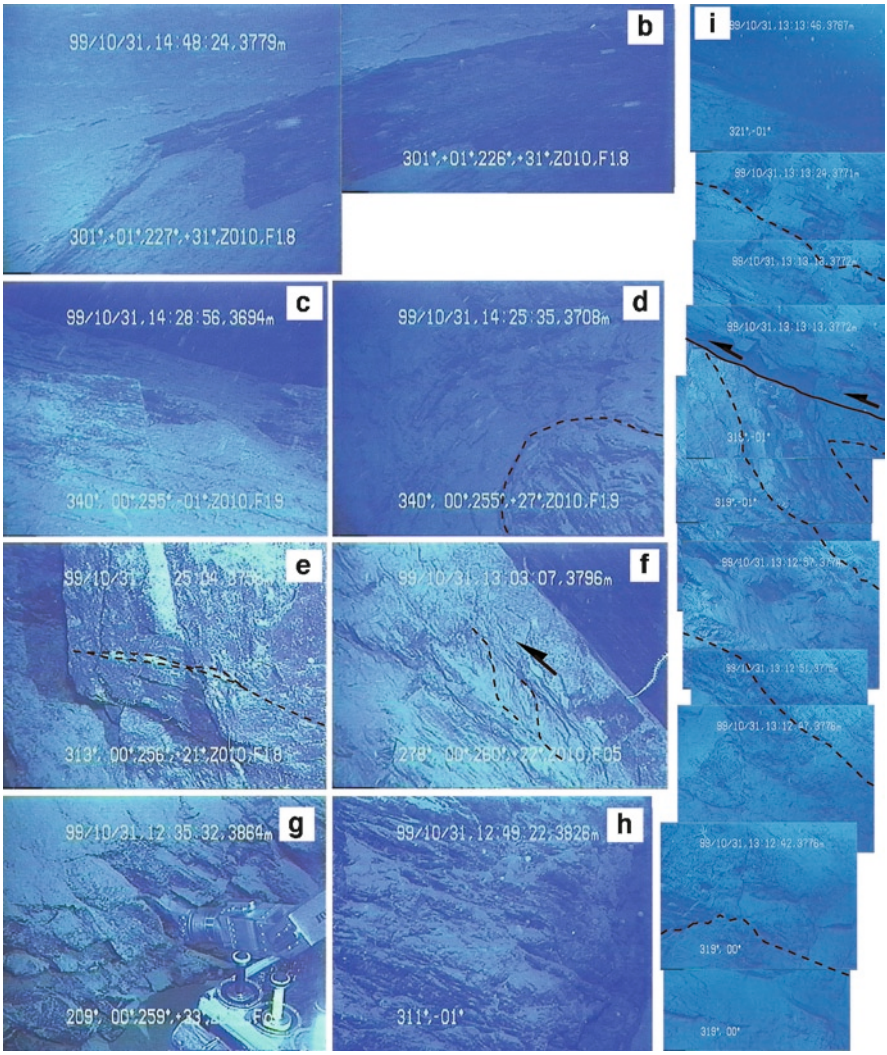

Fig. 4 (continued)

The normal fault in the 3rd ridge (Fig. 4b) occurs in the back-limb of the hill-size anticline and has larger offset than normal faults in the crest of the 1st ridge (Fig. 2h). Thrust faults in the 3rd ridge (Fig. 4i) are more continuous and planar compared to those in the 1st ridge (Fig. 2g). Faults in the 3rd ridge are thus, more brittle and have larger displacement than those of the 1st ridge. The transverse ridge in the 3rd ridge has the largest dip-slip displacement among the Shionomisaki canyon (Fig. 1c). No indication of chemosynthetic bio-communities or other evidence for cold seepage was observed here.

4.3 The Megasplay Fault Zone (6K#579, 6K#889~891): Field Observations

Four dives focused on the structures near the megasplay fault and its bifurcations exposed on the 5th ridge (Fig. 5). Faults on the 5th ridge are associated with active cold seepages. Five fault zones (dashed lines in Fig. 5a) were deduced based on the bathymetric features and distribution of chemosynthetic bio-communities such as vesicomyid bivalves (mainly *Calyptogena nautilei*: Fig. 6e, f) and vestimentiferan tubeworms. Bathymetric features used here are EW-trending depressions along the crest, knicks along the foot of the ridge, and a transverse ridge composed of siltstone (Fig. 5b) and developed across the mid-axis of the canyon. The megasplay fault was inferred to be located along the southern foot of the 5th ridge (fault ① in Fig. 5a). Three bifurcations of the megasplay fault (faults ② to ④) were also recognized, which are continuous with the EW-trending depressions developed in the crest of the ridge. A hump developed between faults ③ and ④ extends westward from the crest of the 5th ridge. The bifurcating faults displaced the surface of the canyon wall. A boundary fault (fault ⑤) was deduced in the north that separates the 5th ridge from its hinterland, and was determined to continue to the northern margin of the transverse ridge developed across the mid-axis of the canyon (Fig. 5a).

Mudstone-dominant turbidites comprise the northern part of the 5th ridge. The sequence becomes rich in sandstones with increasing thickness southward (Fig. 6a). Orientations of the selected bedding planes are shown in Fig. 5a. A plot of S-poles to the bedding planes (Fig. 5c) indicates that the mudstone-dominant strata in the northern part (area of Dive 6K#891) are folded about an axis plunging 17° to the west. The folds have wavelength of few hundred meters. S-pole concentration near the center implies that the majority of the strata are sub-horizontal and/or dip gently to the southwest. The sub-horizontal bedding is steeper near the northern boundary fault ⑤ and fault ④.

Sandstone-dominant turbidite strata dipping steeply to the southwest (Fig. 6a, b) are predominant in the middle part of the 5th ridge (6K#889: Fig. 5). The distribution of S-poles to bedding implies folds with axes plunging 40° to the west (Fig. 5d). Oblique fracture cleavage was observed to have developed in siltstones interbedded with sandstones (Fig. 6b). The fracture cleavages dip steeply to the north. Sub-vertical strata are commonly developed near faults ② to ④ (Fig. 6c). Deformation bands (Ujiie et al. 2004) and web structures (Hirono 2005) are abundant in this area.

The southern part of the 5th ridge (6K#890) consists of sandstone-dominant turbiditic strata dipping gently to the south (Fig. 5e). Sub-horizontal strata in the frontal part are locally deflected and steepened along the megasplay fault (near 890R4 outcrop). The distribution of S-poles implies that bedding is folded about a sub-horizontal axis plunging gently to southeast. The central part of the 5th ridge dips steeply to the south. The sandstone-dominant turbidites are covered by conglomerate with imbricate pebbles (Fig. 6d) that imply transportation from the northwest.

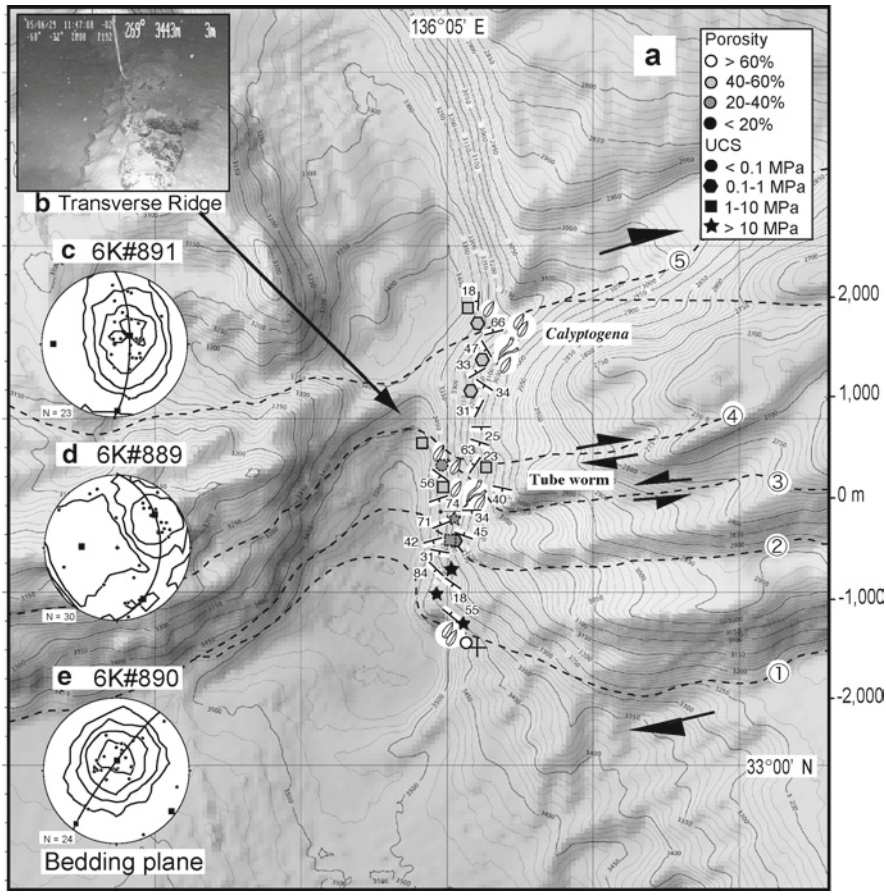

Fig. 5 Geologic structures of the megasplay fault zone (Data source; Anma et al. 2010). (**a**) Map area is indicated in Fig. 1b. Numbers along the NS axis indicate distance (m) from a reference point on 33°01.6′N and are used in Fig. 7. (**b**) Outcrop of siltstone at the site 889R1 (FOV ~ 2 m). This outcrop was observed at the leeward slope of the transverse ridge developed across the mid axis of the canyon. The transverse ridge is considered to be of tectonic origin. (**c**) Stereonet plot of S-poles to bedding planes of the northern domain (6K#891 area) are open-folded about an axis plunging 17° to the west. (**d**) Bedding in the central domain (6K#889 area) folded about an axis plunging 50° to the west. (**e**) Bedding planes of the southern domain (6K#890 area) plot around a sub-horizontal point maximum

Overall structures of this area (Fig. 3d) suggest an anticlinal fold with km-scale wavelength and southward vergence (Fig. 7a). The strata become younger toward the south from the hinge of the anticlinal fold (Fig. 7a). In addition, folds with shorter wavelength (~200 m) are developed in the landward (rear) part of the 5th ridge south of the boundary fault. Two sets of joints are developed in the folded turbidite sequence: one trending NS and the other trending WNW-ESE (Fig. 3d). Fractures are less developed in conglomerates that cover the turbidite sequence.

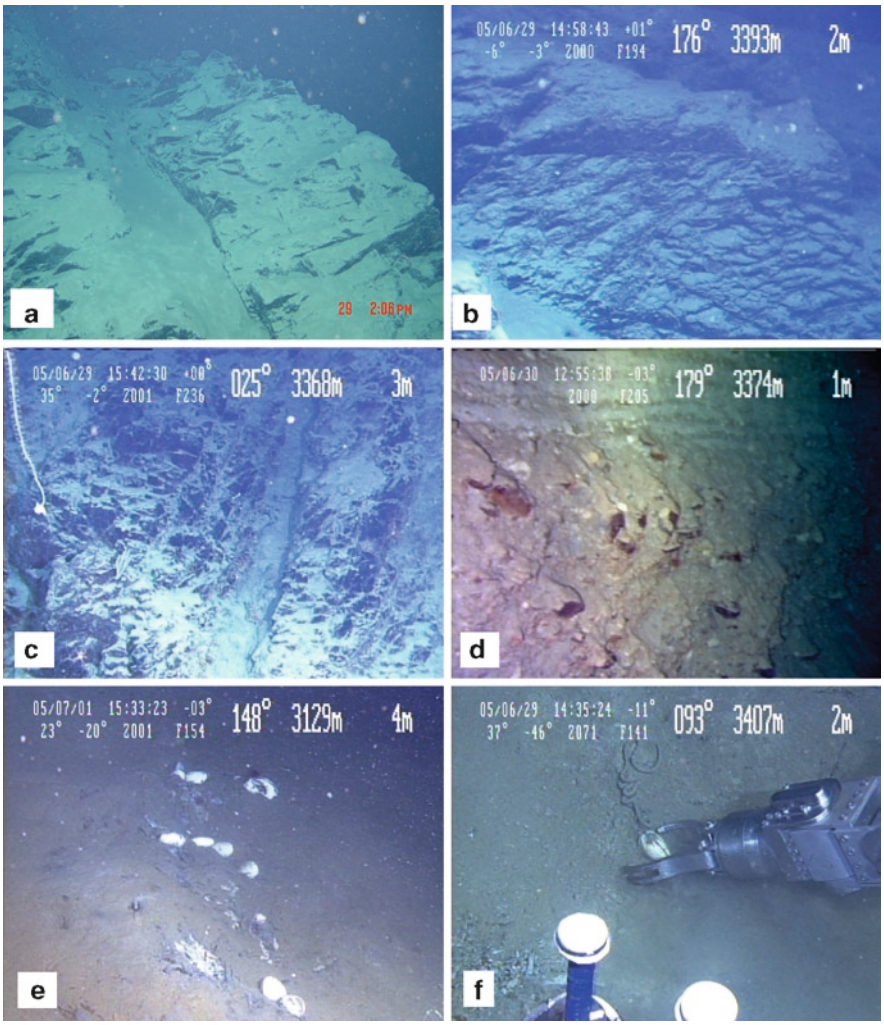

Fig. 6 Outcrops in the megasplay fault zone. (**a**) An outcrop view at site 889R3 in Fig. 7. Southward (seaward) dipping strata are predominant in gently folded, often steeply inclined sandstone-dominant turbidite deposits (FOV~4 m). (**b**) Northward-dipping fracture cleavage developed in mudstones at site 889R6 (Reproduced from Anma et al. 2010; ©Geological Society of Japan). The cleavage developed obliquely to the basal surface of a sandstone layer dipping steeply to south (FOV~4 m). (**c**) Sub-vertical strata at site 889R7. Fracture cleavages are densely developed. (**d**) Subhorizontal deposits of conglomerates interbedded with silty layers (between site 890R2 and 890R3). Imbrication of pebbles indicates southeastward flow (FOV~4 m). (**e**, **f**) Occurrence of *Calyptogena nautilei*. *C. nautilei* shells are half buried in mud exposing the hinge-side into seawater (FOV~1 m). The exposed part of *Calyptogena* shell was dissolved suggesting that the depth at observation (~3, 400m) is located below the carbonate compensation depth of this region. Numbers on top-right in (**b**)–(**f**) indicate heading of the submersible (in degree) and depth (m), respectively

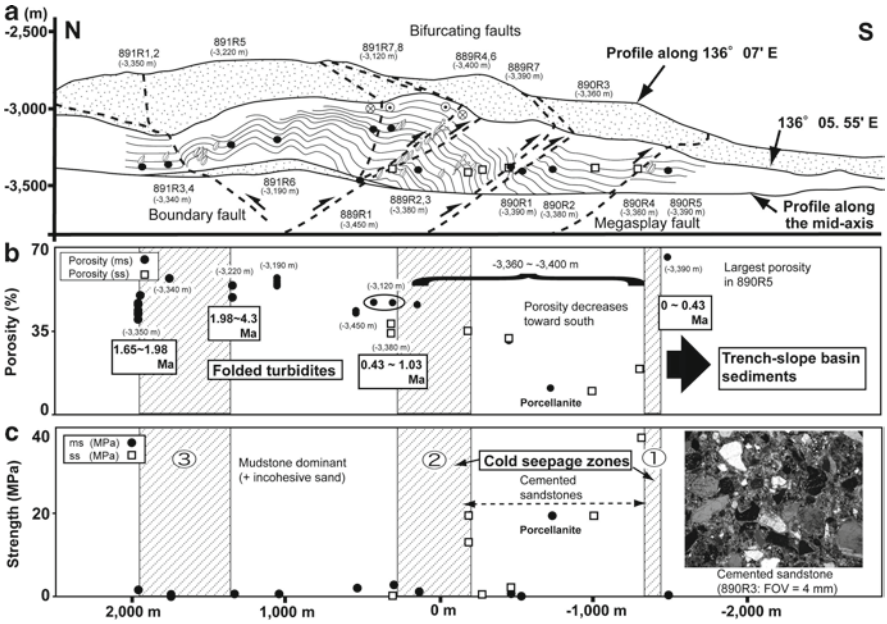

Fig. 7 Geologic cross section of the megasplay fault zone and distributions of material properties (Data source; Anma et al. 2010). (**a**) Pseudo-3D section across the 5th ridge. NS profiles along 136°07′E and 136°05.55′E, and along the mid-axis of the canyon are shown with bedding (*thin lines*), distribution of faults (*dashed lines*), chemosynthetic bio-communities (shells and tube-worms) and sample localities (*solid circle*: mudstone, *open square*: sandstone). Transverse axis presents distance along the NS profile from the reference point on 33°01.6′N. (**b**) Porosity profile. Chemosynthetic biocommunities were observed in shaded area. Depositional ages are based on radiolarian biostratigraphy in Fig. 8. The porosity decrease has an almost negative correlation with the depositional age, except for mudstone from 890R5 site in the southern end. (**c**) Uniaxial compressional strength estimated from a needle penetration test. Sandstones in the south have high strengths due to precipitation of carbonate (*inset* photo-micrograph) in pore space

4.4 The Megasplay Fault Zone: Material Properties, Depositional Ages and Cements

Rock samples were collected from 22 sites to evaluate lateral variations of porosity, strength and sediment textures along a NS profile across the megasplay fault zone. To ensure to sample true horizontal lateral variations, samples were mostly collected from 3,340–3,400 m below sea level (mbsl). Other samples were collected from depths ranging from 3,120–3,450 mbsl (Fig. 7a). Mudstones were mainly collected from the rear part of the 5th ridge, whereas sandstones were mainly from the frontal part.

Lateral variations of porosity and uniaxial compressional strength of the collected samples are shown in Fig.7b, c, respectively. A siltstone sample obtained from a sub-horizontal bed at the 890R5 outcrop in the southernmost part of the transect has

the largest porosity (~65%). The porosity of the mudstone north of the boundary fault (891R1, R2 outcrops) is relatively small (40–50%). The porosity becomes maximum (54–57%) at the 891R4 and 891R6 outcrops in the rear part of the 5th ridge. The porosity decreases southward from the 891R6 outcrop to the position of the megasplay fault in the frontal part.

Uniaxial compressional strength shows good correlation with porosity: sediments with small porosity have high strength (Fig. 7c). Microscopic observations revealed that carbonate cementation (Fig. 7c inset microphotograph) is responsible for a decrease of the porosity and an increase of strength of the sediments. The distribution of such carbonate cementation was constrained between the megasplay fault and the bifurcating faults.

Radiolarian microfossils were separated from mudstones/siltstones collected from the megasplay fault zone (Anma et al. 2010). Reliable depositional ages (Fig. 8) were obtained from sites 891R1 (1.98–1.65 Ma), 891R5 (4.3–1.98 Ma), 579R2 (1.03–0.43 Ma) and 890R5 (<0.43 Ma) from the north to the south. The radiolarian biostratigraphy indicates that sediments with the oldest depositional age (1.98–4.3 Ma) are distributed in the rear part of the 5th ridge (891R5 outcrop), and the ages of deposition become younger in both directions (Fig. 7b).

Sub-horizontal siltstones in the southernmost part of the transect (890R5 outcrop) have the youngest depositional age (<0.43 Ma) and the highest porosity (~65%). Considering the rate of plate motion (Fig. 1) and the young depositional age, we infer that the sub-horizontal siltstone must have been deposited in a trench-slope basin.

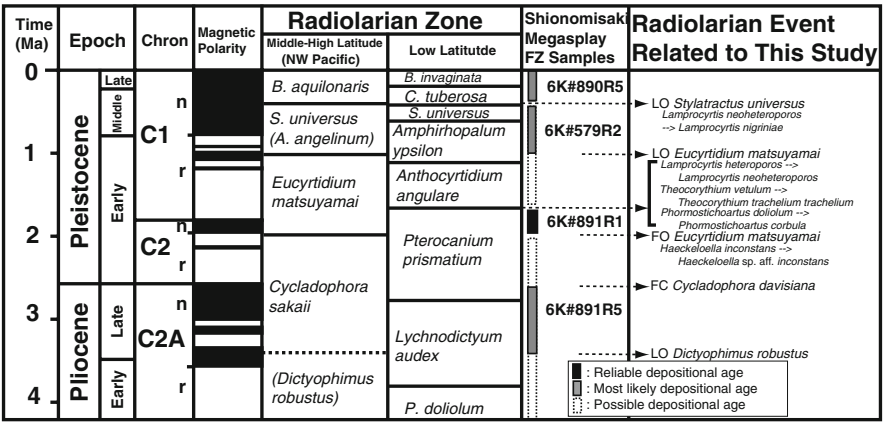

Fig. 8 Radiolarian biostratigraphy of the sediments of Shionomisaki submarine canyon (Reproduced from Anma et al. 2010; ©Geological Society of Japan). Depositional age was determined from mudstones/siltstones at the sites 891R1, 891R5, 579R2 and 890R5. Magnetic polarity: Gradstein et al. (2004), Middle to high latitude radiolarian zone: Motoyama and Maruyama (1998), Motoyama et al. (2004), and Kamikuri et al. (2004), Low latitude radiolarian zone: Sanfilippo and Nigrini (1998). Radiolarian events used for estimation of the likely depositional ages are listed in the *right column*. *FO* first occurrence, *FC* first consistent/common occurrence, *LO* last occurrence, → transition

With exception of the 890R5 outcrop, lateral variations of porosity (Fig. 7b) indicate that the mudstones of the oldest part at the 891R4–891R6 outcrops have the highest porosity (54–57%). The porosity decreases southward toward the megasplay fault in the frontal part. Thus, the porosity decrease has a negative correlation with the age of deposition of the sediments: i.e. older sediments have higher porosity.

Uniaxial compressional strength tests display a similar trend: younger sediments are more consolidated and have high strength (Fig. 7c), except for the 890R5 outcrop. These observations are opposite to the general trend of normal consolidation curve due to simple burial.

Microscopic observation of thin sections revealed that carbonate cementation is responsible for a decrease of porosity and increase of strength of the sediments (inset of Fig. 7c). The carbonate cements have high oxygen and relatively low carbon isotopic ratios (Fig. 9; Anma et al. 2010). The isotopic value is close to that of

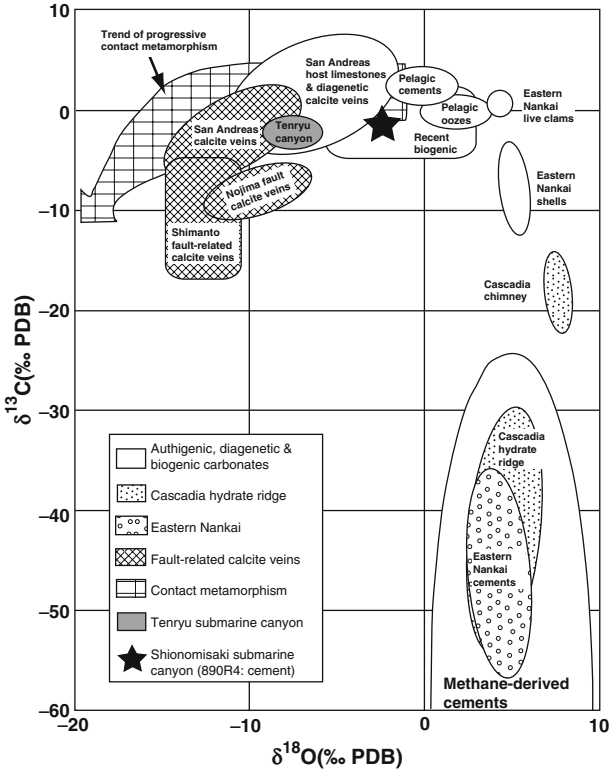

Fig. 9 Carbon and oxygen isotopic ratios of cements from the Shionomisaki submarine canyon (*solid star*) (Reproduced from Anma et al. 2010; ©Geological Society of Japan) (Data source: Nojima faults: Arai et al. (2003), Shimanto fault-related calcite vein: Yamaguchi et al. (2004) and Yamaguchi et al. (2007), San Andreas fault: Pili et al. (2002), Eastern Nankai: Sakai et al. (1992), Cascadia: Kulm and Suess (1990) and Teichert et al. (2005), contact metamorphism: Baumgartner and Valley (2001), veins and cements from the Tenryu submarine canyon: Kawamura et al. (2009), cements from the Shionomisaki submarine canyon: Hirano et al. (2006))

pelagic cements, but plots on a trend of fault-related fluid. Thus, $CaCO_3$ was precipitated near the surface, in the shallow part beneath the sea floor. There was no influence of the hydrate-related fluids.

5 Discussion

5.1 Faults in the Accretionary Complex of the Nankai Trough

The profile along the mid-axis of the canyon (Fig. 1c) indicates the presence of several transverse ridges that involve dip-slip displacement. A NNE-SSW-trending outcrop of siltstone is present at the leeward slope of the transverse ridge (Fig. 5b) at the 5th ridge. This implies that the transverse ridge is not of sedimentary origin (i.e. landslide debris), but of tectonic (faulting or folding) origin. The transverse ridge is located landward compared to the knick along the foot of the 5th ridge. This suggests the presence of a landward-dipping thrust fault. Radiolarian microfossils indicate that the ages of deposition become younger toward both directions from the 891R5 outcrop in the rear part of the 5th ridge (Fig. 7a, b). Therefore, the center of uplift is inferred to be near the 891R5 outcrop. The northern boundary fault must be, therefore, a north-side down-thrown fault, most likely an antithetic thrust fault (Fig. 7a). Offset relationship of the knicks along the northern edges of the 5th ridge and the transverse ridge (Fig. 5a) also support a fault dipping to the south.

The mid-axis of the canyon is deflected westward south of the 5th ridge: this feature indicates that the faults have a right-lateral strike-slip component (Figs. 1b and 5a). The eastern canyon wall of the 5th ridge is displaced along the bifurcating faults and the ridge crest is offset dextrally (Figs. 5a and 7a). Martin et al. (2010) reported the presence of negative flower structures associated with right-lateral displacement above the megasplay fault in the NanTroSEIZE experiment area (around 136°40'E). In contrast, our observations indicate the presence of a positive flower structure along the megasplay fault zone. Variations in the stress-field shifting from transtension to transpression may be expected along the megasplay fault.

The SSE-trending gorges in the 3rd ridge and north of the 5th ridge (Fig. 1a) are normal to the general trend of the ridges. However, this trend is not continuous throughout the length of the canyon, but seems displaced by right-lateral faults parallel to the ridges. Furthermore, the ENE-WSW-trending mound developed in the fan deposit in front of the 1st ridge deflected the stream from the canyon (Figs. 1b and 3). The trend of the mound parallels the general trend of the 1st ridge. This mound could be a hanging wall anticline above the frontal thrust rising in front of the canyon and is still active. The mound may also have developed as a pressure ridge as a result of transpressional tectonic deformation.

Our observations raise a possibility that all these faults may have played a significant role in accommodating the right-lateral strike-slip component caused by

the obliquity of the plate migration (Fig. 1a). Collectively, these findings from the accretionary complex of the Nankai trough point out that strain partitioning did occur, perhaps more pervasively and in a more multi-scale fashion than Fitch (1972) suggested for oblique convergent zones in the Western Pacific. Focal mechanisms of very low frequency earthquakes (Ito and Obara 2006) showed the occurrence of thrust motion with minor oblique slip component along the megasplay thrust zone. However, no focal mechanism that indicate oblique thrust were reported along the frontal thrust zone.

5.2 Tectonic Deformation vs. Creeping

Bedding in the frontal thrust zone is sub-horizontal and gently folded about an EW-trending horizontal axis. Bedding observed on the western canyon wall of the 3rd ridge is folded about an axis plunging to the east, and bedding on the eastern canyon wall of the 5th ridge about an axis plunging to the west (Fig. 3). The fold axes plunging toward the canyon imply an overprinted deformation. There are two possible explanations for the plunging axes: one is tectonic and the other gravitational.

A hump between faults ③ and ④ extends westward from the crest of the 5th ridge, indicating that faults ③ and ④ apparently have opposite sense of shear (Figs. 5a and 7a). The fold axis in this area plunges 40° to west (Fig. 5d). Such local features may be explained in terms of creep deformation enhanced by lateral extrusion. The canyon walls may become unstable as the Shionomisaki canyon deepened and eroded the foot of the canyon walls. Creep of the wall slope must have taken place to tilt the originally horizontal fold axes toward the canyon. Right-lateral transpression may also squeeze materials in the 5th ridge to extrude them westward. NS-trending joints (Fig. 3d) developed in the folded turbidite sequence in the 5th ridge may support the creep model. Fractures trending WNW-ESE, in contrast, may be attributed to tectonic stresses: the NW-SE-trending maximum principal compressional stress deduced from borehole breakout during the NanTroSIEZE experiments (Kinoshita et al. 2009).

Alternatively, a crustal-scale fault that displaces the Philippine Sea plate at the western edge of the Zenisu ridge was reported by Kodaira et al. (2006) to have influence on structures in the accretionary complex along the Shionomisaki canyon. Lateral ramps in the megasplay fault zone (Moore et al. 2007) may also be responsible for the plunging fold axes.

5.3 Development of the Accretionary Complex

Field observations reveal that both normal and thrust faults striking parallel to the Nankai trough were developed in the frontal thrust zone as sediments were accreted

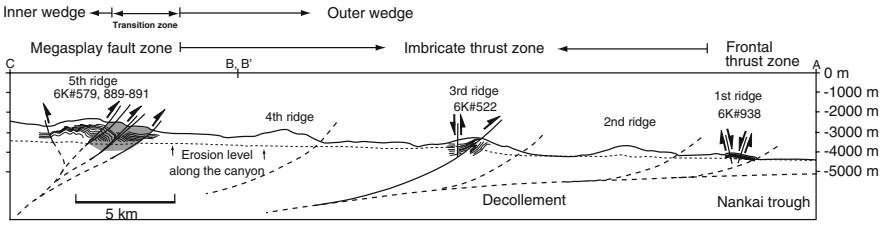

Fig. 10 Geologic cross section along the Shionomisaki canyon. See trace in Fig. 1b. General trend of bedding planes (*thin lines*) and faults (*thick lines*: observed, with *arrows* indicating sense-of-shear, *dashed lines*: deduced) are shown. *Shaded area*: cemented zones

to form a gentle anticline (Fig. 10). The anticline and thrust faults most likely formed synchronously due to north-oriented compressional stress during the inception of accretion. Although no crosscutting relations were observed between thrust and normal faults, or folds and normal faults, we attribute the normal faults to surface extension at the crest of the anticline (Fig. 10). The sediments in the frontal thrust zone were partly cemented by carbonates, and a fossil of a vesicomyid bivalve was recovered. Although it is currently inactive, fluid saturated in $CaCO_3$ must have been circulating and hardened some parts of the ridge. Occurrences of cold seepage were also reported from the eastern extension of the 1st ridge (Fig. 1a).

As sediments transferred into the imbricate thrust zone, both macroscopic and mesoscopic (outcrop-scale) open to tight folds were developed. Thrust faults are more brittle than those developed in the frontal thrust zone and localized shear fabrics have developed in the sedimentary rocks. The transverse ridge in the 3rd ridge has the largest displacement among the Shionomisaki canyon (Fig. 1c), implying a large cumulative dip-slip displacement. No active cold seepage was observed, however, in the 6K#522 dive area.

The megasplay fault zone, in contrast, has several active cold seeps. Vesicomyid bivalves are commonly aligned forming an en-echelon fashion (Fig. 6e), suggesting shear fracture underneath (Ogawa et al. 1996). Nakanishi et al. (2002c, 2008) suggested that the presence of an old (Miocene) accretionary complex coincides with the seaward limit of coseismic slip in the Nankai trough seismogenic zone. Such brittle, coseismic rupturing may control the distribution of cold seeps. Our overall structural interpretation of the megasplay fault zone is illustrated in the schematic profiles in Figs. 7 and 10. Sub-horizontal sandstones just above the megasplay fault were cemented by carbonates. Behind the cemented sandstones, bifurcating faults with cold seeps are present in the sandstone-rich strata dipping steeply to the south in the frontal part of the anticline with a wavelength of ~1 km. The sandstones are partly cemented above the bifurcating faults, hardening the frontal part of the anticline. Folds with wavelengths of ~200 m are developed in mudstone-rich turbidites in the rear part of the 5th ridge behind the bifurcating faults.

5.4 Roles of Carbonate Cementation in Concentration of Fluid and Strain

Carbonate cementation is distributed abruptly along the faults. Observations from the 5th ridge clarified that the distribution of fluid flow is concentrated around the cemented zone. Our observations suggest that cementation and hardening of ridge front or deformation front may play an important role in the concentration of strain, localization of fluid flow and mineral precipitation, thickening of accretionary complex, and development of trench-slope-break. Our scenario is summarized in schematic sketches in Fig. 11.

Initial channels of fluid flow must be formed due to brittle faulting (Fig. 11a). Nakanishi et al. (2008) suggested the presence of a thin low-velocity layer above the megasplay fault with velocities 0.5–1.5 km/s slower than the surrounding rock, implying elevated fluid pressure in the fault zone that resulted in mega-thrust earthquakes earlier. Fault rupturing and subsequent inter-seismic deformation of accretionary complex including very low frequency earthquakes (e.g. Kodaira et al. 2004; Obara and Ito 2005; Ito and Obara 2006) allow $CaCO_3$-saturated fluid to migrate along the fault planes (e.g. Davis et al. 2006). Sandstones with high pore connectivity and permeability nearby the faults were then hardened by the carbonate cementation (Fig. 11b). The cementation decreases the porosity and pore-space connectivity in sandstones, prevents diffusive fluid flow, guides and concentrates flow around the cemented zone (Fig. 11b–d). The distribution of such hardened zones and increased pore pressures around them may also control the position and patterns of fault propagation. A hardened ridge front will form by repeated rupturing, fluid flow and cementation, which in turn act as an indenter for the inner wedge. It is evidenced by the presence of folds with wavelengths of ~200 m developed behind the hardened zone (Fig. 7a), implying that strain was accumulated as the cemented zone was transported landward with the subducting Philippine Sea plate. A new bifurcation fault may be formed behind the hardened zone, whereas slips on the megasplay fault likely took place repeatedly as fluids migrate preferably upward and cement upper part of the fault (Henry et al. 2002; Fig. 11d).

The hardened ridge front may also act as a backstop for the outer wedge and frontal imbrications may propagate forward in the outer wedge. Cemented zones are also present in the 1st ridge, although deformation and strain concentration behind or in front of it was not obvious. This is perhaps due to immaturity of the tectonic deformation in the frontal thrust zone.

Recently, Park et al. (2010) reported detailed seismic velocity structures in the accretionary complex and the presence of a low-velocity zone of maximum of ~2 km thick (Fig. 11e). They attributed the low velocity zone to an underplated, fluid-rich underthrust package, which may supply a significant amount of fluid to the megasplay fault zone, elevate fluid pressure, and eventually foster tsunami generation. It is noteworthy that their velocity structure also indicates the presence of a seaward-dipping high-velocity zone just above the megasplay fault zone (Fig. 11e). Our observations further imply that the presence of such a high-velocity zone may

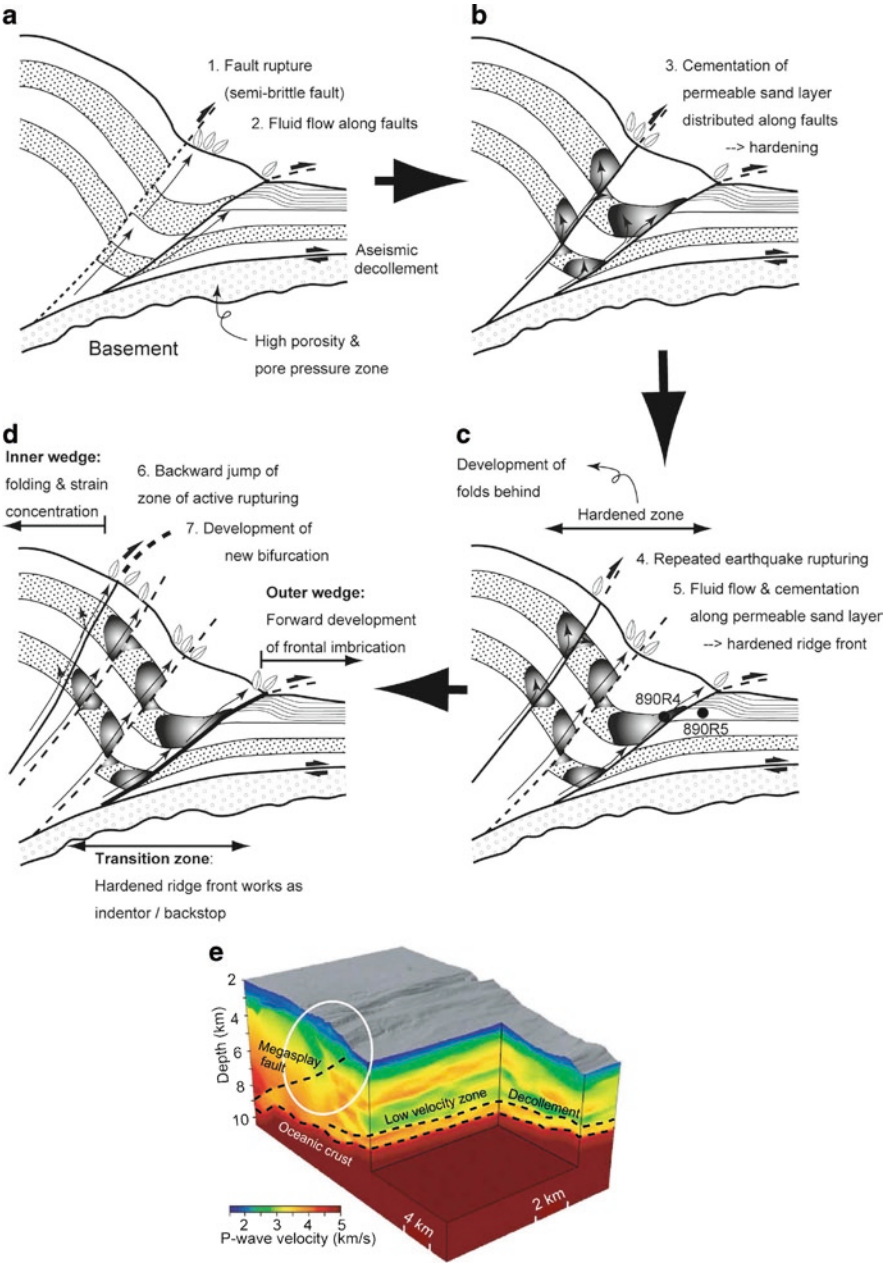

Fig. 11 Schematic sketches of a model that accounts for cementation and migration of active cold seepage zones (Modified based on Anma et al. 2010). Vertical scale is exaggerated and arbitrary. (**a**) Fault rupturing will result in $CaCO_3$-saturated fluid flow migrated along the fault plane and (**b**) precipitated carbonate in nearby sandstones with high pore connectivity and permeability. (**c**) A hardened ridge front will be formed by repeated rupturing and fluid flow, (**d**) which in turn act as an indenter for the inner wedge, and as a backstop for the outer wedge (Fig. 10). A new bifurcation may be formed behind the ridge front, whereas frontal imbrications may propagate forward in the outer wedge. (**e**) Seismic cross section with velocity anomaly (After Park et al. 2010) suggests presence of high velocity zone just above the megasplay fault

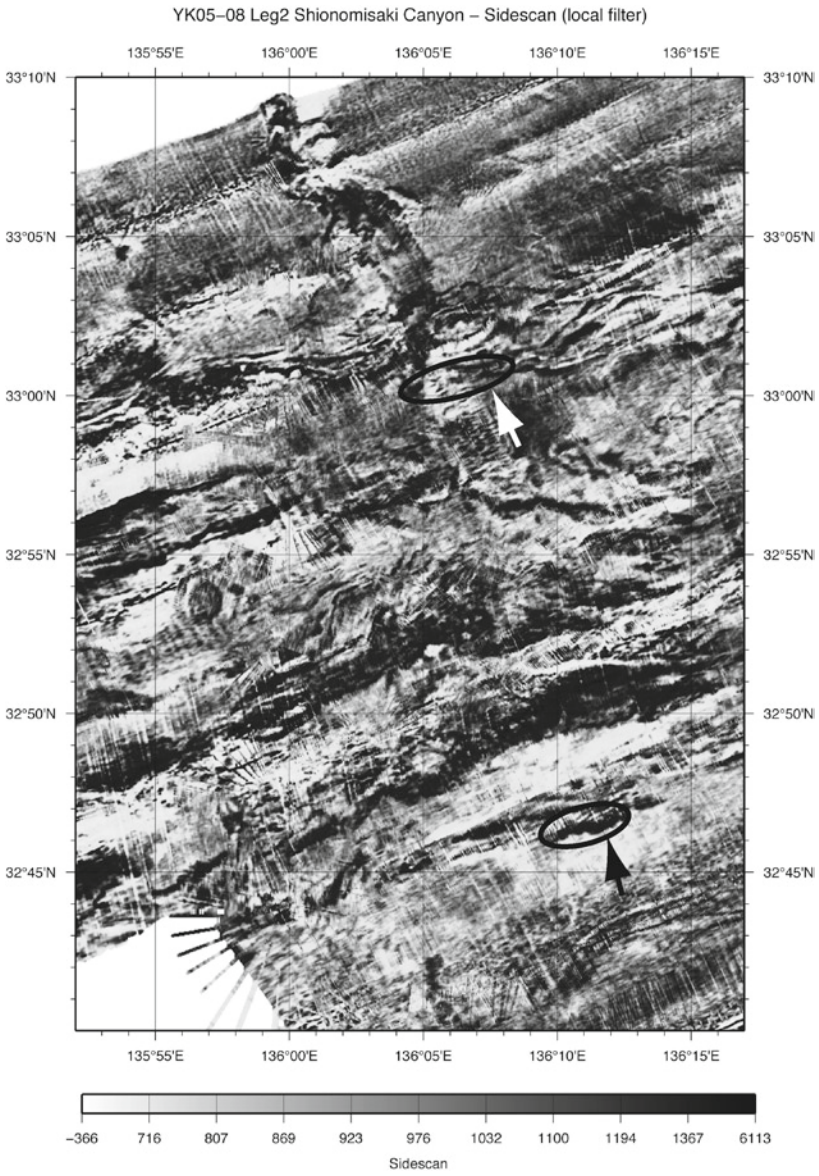

Fig. 12 Side-scan sonar image (local filter) of the area corresponding to Fig. 1b. Observed cemented areas are encircled (also indicated by *arrows*)

be attributed to a cemented zone. The presence of this cemented zone may be detected by side-scan sonar mapping (Fig. 12), if the cemented zone is exposed on the seafloor. Such mapping, in turn, may help to estimate zones of strain localization and hence, zones of potential seismic rupturing.

Accreted strata are, in general, transported landward as subduction proceeds. Sediments deformed at the frontal thrust zone must then be transported to the imbricate thrust zone and eventually undergo deformation in out-of-sequence thrust zones as lateral transportation and sediment compaction continued. Such a uniformitarian view may be modified by the presence of cementation that locally disturbs the regional patterns of strain distribution.

6 Summary

We made field observations using the submersible "*SHINKAI 6500"* in the frontal thrust zone, imbricate thrust zone and megasplay fault zone along the profile of the accretionary complex of the Nankai trough exposed in the Shionomisaki submarine canyon, aiming to understand distribution of outcrop-scale structures and strain, and eventually to understand deformation processes.

Brittle normal faults and cohesive thrust faults striking parallel to the trench axis were developed in the frontal thrust zone during gentle folding as sediments entered into the accretion zone. The sediments in the frontal thrust zone are partly cemented by carbonates. As sediments were transferred to the imbricate thrust zone, both macroscopic and mesoscopic (outcrop-scale) open to tight folds were developed. Thrust faults became brittle and shear fabrics were developed. No active cold seepage was, however, observed in these areas.

The megasplay fault zone, in contrast, contains active cold seeps. Sub-horizontal sandstones just above the megasplay fault were cemented by carbonates. Behind the cemented zone, bifurcations of the megasplay fault, marked by cold seeps, developed in the sandstone-rich turbidite beds that dip steeply to the south. Folds with wavelengths of ~200 m developed in mudstone-rich turbidites behind the bifurcating faults. The cementation strengthened the frontal part of the megasplay fault zone, which in turn, acted as an indenter for the inner wedge. Cementation and hardening of the ridge front have local controls on deformation and development of the accretionary complex. Mapping of hardened zone may help to detect potential zones of seismogenic and tsunamigenic rupturing.

Acknowledgements Our thanks go to the captain and crew of the *R/V Yokosuka*, and the commander and pilots of the "*SHINKAI 6500*" operation team. Our thanks also go to the Shipboard Science Parties of YK99-09, YK00-08, YK05-08 and YK06-02 cruises for their assistance and discussion. We appreciate the support of JAMSTEC during this study. We thank to Prof. Timothy Kusky (China University of Geosciences) and Dr. Andrea Festa (University of Torino) for their critical reviews and constructive comments.

References

Ando M (1975) Source mechanisms and tectonic significance of historical earthquakes along Nankai trough, Japan. Tectonophysics 27:119–140

Anma R, Kawakami S, Yamamoto Y (2002) Structural profile of the Nankai accretionary prism and Calyptogena colonies along the Shionomisaki submarine canyon: results of "*SHINKAI*" 6K#522 and #579 dives. JAMSTEC J Deep Sea Res 20:59–75

Anma R, Ogawa Y, Kawamura K, Moore GF, Sasaki T, Kawakami S, Hirano S, Ohta T, Endo R, Michiguchi Y, YK05-08 Shipboard Science Party (2010) Structures, textures, physical properties of accretionary prism sediments and fluid flow near the Splay Fault zone in the Nankai trough, off Kii peninsula. J Geol Soc Jpn 116:637–660 (in Japanese with English abstract)

Aoki Y, Tamano T, Kato S (1982) Detailed structure of the Nankai trough from migrated seismic sections: studies in continental margin geology. AAPG Mem 34:309–322

Arai T, Tsukahara H, Morikiyo T (2003) Sealing process with calcite in the Nojima active fault zone revealed from isotope analysis of calcite. J Geogr 112:915–925

Ashi J, Taira A (1992) Structures of the Nankai accretionary prism as revealed from IZANAGI sidescan imagery and multichannel seismic reflection profiling. Isl Arc 1:104–115

Ashi J, Kuramoto S, Morita S, Tsunogai U, Goto S, Kojima S, Okamoto T, Ishimura T, Ijiri A, Toki T, Kudo S, Asai S, Utsumi M (2002a) Structure and cold seep of the Nankai accretionary prism off Kumano – outline of the off Kumano survey during YK01-04 Leg 2 Cruise. JAMSTEC J Deep Sea Res 20:1–8

Ashi J, Tokuyama H, Taira A (2002b) Distribution of Methane hydrate BSRs and its implication for the prism growth in the Nankai trough. Mar Geol 187:177–191

Baba T, Cummins PR (2005) Contiguous rupture areas of two Nankai trough earthquakes revealed by high-resolution tsunami waveform inversion. Geophys Res Lett 32:L08305. doi:10.1029/2004GL022320

Baba T, Tanioka Y, Cummins PR, Uhira K (2002) The slip distribution of the 1946 Nankai earthquake estimated from tsunami inversion using a new plate model. Phys Earth Planet Inter 132:59–73

Baba T, Cummins PR, Hori T, Kaneda Y (2006) High precision slip distribution of the 1944 Tonankai earthquake inferred from tsunami waveforms: possible slip on a splay fault. Tectonophysics 426:119–134

Bangs NL, Shipley TH, Gulick SPS, Moore GF, Kuramoto S, Nakamura Y (2004) Evolution of the Nankai trough decollement from the trench into the seismogenic zone: inferences from three-dimensional seismic reflection imaging. Geology 32:273–276

Bangs NL, Gulick SPS, Shipley TH (2006) Seamount subduction erosion in the Nankai trough and its potential impact on the seismogenic zone. Geology 34:701–704

Bangs NLB, Moore GF, Gulick SPS, Pangborn EM, Tobin HJ, Kuramoto S, Taira A (2009) Broad, weak regions of the Nankai Megathrust and implications for shallow coseismic slip. Earth Planet Sci Lett 284:44–49

Baumgartner LP, Valley JW (2001) Stable isotope transport and contact metamorphic fluid flow. Rev Mineral Geochem 43:415–467

Colwell F, Matsumoto R, Reed D (2004) A review of the gas hydrates, geology, and biology of the Nankai trough. Chem Geol 205:391–404

Cummins PR, Baba T, Kodaira S, Kaneda Y (2002) The 1946 Nankai earthquake and segmentation of the Nankai trough. Phys Earth Planet Inter 132:75–87

Davis EE, Becker K, Wang K, Obara K, Ito Y, Kinoshita M (2006) A discrete episode of seismic and aseismic deformation of the Nankai trough subduction zone accretionary prism and incoming Philippine Sea plate. Earth Planet Sci Lett 242:73–84

Fitch TJ (1972) Plate convergence, transcurrent faults, and internal deformation adjacent to Southeast Asia and the Western Pacific. J Geophys Res 77:4432–4460

Gradstein F, Ogg J, Smith A (2004) A geologic time scale. Cambridge University Press, Cambridge, 589 p

Henry P, Lallemant S, Nakamura K, Tsunogai U, Mazzotti S, Kobayashi K (2002) Surface expression of fluid venting at the toe of the Nankai wedge and implications fro flow paths. Mar Geol 187:119–143

Hirano S, Yamaguchi A, Ogawa Y, Anma R, Moore GF, Dilek Y, Kawamura K, YK05-08 Leg2 Shipboard Science Party (2006) Mode of occurrence and stable isotopes of carbonate cements and veins distributed nearby active faults in accretionary prisms (translated from Japanese abstract). JAMSTEC Blue Earth symposium, Abstracts PS82

Hirono T (2005) The role of dewatering in the progressive deformation of a sandy accretionary wedge: constraints from direct imagings of fluid flow and void structure. Tectonophysics 397:261–280

Hori T, Kato N, Hirahara K, Baba T, Kaneda Y (2004) A numerical simulation of earthquake cycles along the Nankai trough in southwest Japan: lateral variation in frictional property due to the slab geometry controls the nucleation position. Earth Planet Sci Lett 228:215–226

Ichinose GA, Thio HK, Somerville PG, Sato T, Ishii T (2003) Rupture process of the 1944 Tonankai earthquake (Ms 8.1) from the inversion of teleseismic and regional seismograms. J Geophys Res 108(B10):ESE 1–ESE 13. doi:10.1029/2003JB002393

Ito Y, Obara K (2006) Dynamic deformation of the accretionary prism excites very low frequency earthquakes. Geophys Res Lett 33:L02311. doi:10.1029/2005GL025270

Kamikuri S, Nishi H, Motoyama I, Saito S (2004) Middle Miocene to Pleistocene radiolarian biostratigraphy in the Northwest Pacific Ocean, ODP Leg 186. Isl Arc 13:191–226

Kato S, Sato T, Sakurai M (1983) Multi-channel seismic reflection survey in the Nankai, Suruga and Sagami troughs. Rep Hydrogr Res 18:1–23

Kawamura K, Ogawa Y, Fujikura K, Hattori M, Machiyama H, Yamamoto T, Iwai M, Hirono T (1999) What did the "KAIKO" watch? – Detail topography and geologic structures at the mouth of Tenryu canyon. JAMSTEC J Deep Sea Res 14:379–388

Kawamura K, Ogawa Y, Anma R, Yokoyama S, Kawakami S, Dilek Y, Moore GF, Hirano S, Yamaguchi A, Sasaki T, YK05–08 Leg 2 and YK06–02 Shipboard Scientific Parties, (2009) Structural architecture and active deformation of the Nankai Accretionary Prism, Japan: submersible survey results from the Tenryu Submarine Canyon. Geol Soc Am Bull 121:1629–1646

Kido Y, Fujiwara T (2004) Regional variation of magnetization of oceanic crust subducting beneath the Nankai trough. Geochem Geophys Geosys 5:Q03002. doi:10.1029/2003GC000649

Kimura G, Kitamura Y, Hashimoto Y, Yamaguchi A, Shibata T, Ujiie K, Okamoto S (2007) Transition of accretionary wedge structures around the up-dip limit of the seismogenic subduction zone. Earth Planet Sci Lett 255:471–484

Kinoshita M, Tobin H, Ashi J, Kimura G, Lallemant S, Screaton EJ, Curewitz D, Masago H, Moe KT, The Expedition 314/315/316 Scientists (2009) Proceedings of the IODP, vol 314/315/316. Integrated Ocean Drilling Program Management International, Washington, DC. doi:10.2204/iodp.proc.314315316.2009

Kobayashi K (2002) Tectonic significance of the cold seepage zones in the eastern Nankai accretionary wedge – an outcome of the 15 year's KAIKO projects. Mar Geol 187:3–30

Kodaira S, Takahashi N, Park JO, Mochizuki K, Shinohara M, Kimura S (2000a) Western Nankai trough seismogenic zone: results from a wide-angle ocean bottom seismic survey. J Geophys Res 105:5887–5905

Kodaira S, Takahashi N, Nakanishi A, Miura S, Kaneda Y (2000b) Subducted seamount images in the rupture zone of the 1946 Nankaido Earthquake. Science 289:104–106

Kodaira S, Kurashimo E, Park JO, Takahashi N, Nakanishi A, Miura S, Iwasaki T, Hirata N, Ito A, Kaneda Y (2002) Structural factors controlling the rupture process of a megathrust earthquake at the Nankai trough seismogenic zone. Geophys J Int 149:815–835

Kodaira S, Iidaka T, Kato A, Park JO, Iwasaki T, Kaneda Y (2004) High pore fluid pressure may cause silent slip in the Nankai trough. Science 304:1295–1298

Kodaira S, Hori T, Ito A, Miura S, Fujie G, Park JO, Baba T, Sakaguchi H, Kaneda Y (2006) A cause of rupture segmentation and synchronization in the Nankai trough revealed by seismic imaging and numerical simulation. J Geophys Res 111:B09301. doi:10.1029/2005JB004030

Kulm LVD, Suess E (1990) Relationship between carbonate deposits and fluid venting: Oregon accretionary prism. J Geophys Res 95:8899–8915

Kuramoto S, Taira A, Bangs NL, Shipley TH, Moore GF, EW99-07, -08 Shipboard Scientific Parties (2000) Seismogenic zone in the Nankai accretionary wedges: general summary of Japan-U.S. collaborative 3-D seismic investigation. J Geogr 109:531–539, in Japanese

Le Pichon X, Iiyama T, Boulegue J, Chavet J, Faure M, Kano K, Lallement S, Okada H, Rangin C, Taira A, Urabe T, Uyeda S (1987a) Nankai trough and Zenisu Ridge: a deep-sea submersible survey. Earth Planet Sci Lett 83:285–299

Le Pichon X, Iiyama T, Chamley H, Charvet J, Faure M, Fujimoto H, Furuta T, Ida Y, Kagami H, Lallemant S, Leggett J, Murata A, Okada H, Rangin C, Renard V, Taira A, Tokuyama H (1987b) The eastern and western ends of Nankai trough: results of box 5 and box 7 Kaiko survey. Earth Planet Sci Lett 83:199–213

Le Pichon X, Kobayashi K, Crew Kaiko-Nankai Scientific (1992) Fluid venting activity within the eastern Nankai trough accretionary wedge: a summary of the 1989 Kaiko-Nankai results. Earth Planet Sci Lett 109:303–318

Le Pichon X, Lallemant S, Tokuyama H, Thoue F, Huchon P, Henry P (1996) Structure and evolution of the backstop in the eastern Nankai trough area (Japan): implications for the soon-to-come Tokai earthquake. Isl Arc 5:440–454

Leggett J, Aoki Y, Toba T (1985) Transition from frontal accretion to underplating in a part of the Nankai trough accretionary complex of Shikoku (SW Japan) and extensional features on the lower trench slope. Mar Petrol Geol 2:131–141

Maltman A, Byrne T, Karig DE, Lallemant S, Knipe R, Prior D (1993) Deformation structures at Site 808, Nankai accretionary prism, Japan. In: Hill IA, Taira A, Firth JV et al (eds) Proceedings of the Ocean Drilling Program, scientific results, vol 131. ODP, College Station, pp 123–133

Martin KM, Gulick SPS, Bangs NLB, Moore GF, Ashi J, Park JO, Kuramoto S, Taira A (2010) Possible strain partitioning structure between the Kumano Forearc Basin and the slope of the Nankai trough accretionary prism. Geochem Geophys Geosyst. doi:10.1029/2009GC002668

Moore GF, Shipley T, Karig D, Taira A, Tokuyama H, Kuramoto S, Suyehiro K (1990) Structural geometry at the toe of the Nankai accretionary prism from MCS and ESP data. J Geophys Res 95:8753–8765

Moore GF, Taira A, Klaus A, Becker L, Boeckel B, Cragg BA, Dean A, Fergusson CL, Henry P, Hirano S, Hisamitsu T, Hunze S, Kastner M, Maltman AJ, Morgan JK, Murakami Y, Saffer DM, Sanchez-Gomez M, Screaton EJ, Smith DC, Spivack AJ, Steurer J, Tobin HJ, Ujiie K, Underwood M, Wilson M (2001) New insights into deformation and fluid flow processes in the Nankai trough accretionary prism: results of Ocean Drilling Program Leg 190. Geochem Geophys Geosyst 2:1058. doi:10.1029/2001GC00166

Moore GF, Bangs NL, Taira A, Kuramoto S, Pangborn E, Tobin HJ (2007) Three-dimensional splay fault geometry and implications for tsunami generation. Science 318:1128–1131

Morgan JK, Ask MVS (2004) Consolidation state and strength of underthrust sediments and evolution of the décollement at the Nankai accretionary margin: Result of uniaxial reconsolidation experiments. J Geophys Res 109. doi:10.1029/2002JB002335

Morgan JK, Karig DE (1993) Ductile strains in clay-rich sediments from hole 808C: preliminary results using X-ray pole figure goniometry. In: Hill IA, Taira A, Firth JV et al (eds) Proceedings of the Ocean Drilling Program, scientific results, vol 131. ODP, College Station, pp 141–155

Motoyama I, Maruyama T (1998) Neogene diatom and radioralian biochronology for the middle-to-high latitudes of the Northwest Pacific region: calibration to the Cande and Kent's geomagnetic polarity time scales (CK92 and CK95). J Geol Soc Jpn 104:171–183

Motoyama I, Niitsuma N, Maruyama T, Hayashi H, Kamikuri S, Shiono M, Kanamatsu T, Aoki K, Morishita C, Hagino K, Nishi H, Oda M (2004) Middle Miocene to Pleistocene magneto-biostratigraphy of ODP Sites 1150 and 1151, northwest Pacific: sedimentation rate and updated regional geological timescale. Isl Arc 13:289–305

Nakanishi A, Shiobara H, Hino R, Kasahara J, Suyehiro K, Shimamura H (2002a) Crustal structure around the eastern end of coseismic rupture zone of the 1944 Tonankai earthquake. Tectonophysics 354:257–275

Nakanishi A, Shiobara H, Hino R, Mochizuki K, Sato T, Kasahara J, Takahashi N, Suyehiro K, Tokuyama H, Segawa J, Shinohara M, Shimamura H (2002b) Deep crustal structure of the eastern Nankai trough and Zenisu Ridge by dense airgun-OBS seismic profiling. Mar Geol 187:47–62

Nakanishi A, Kodaira S, Park JO, Kaneda Y (2002c) Deformable backstop as seaward end of coseismic slip in the Nankai trough seismogenic zone. Earth Planet Sci Lett 203:255–263

Nakanishi A, Kodaira S, Miura S, Ito A, Sato T, Park JO, Kido Y, Kaneda Y (2008) Detailed structural image around splay-fault branching in the Nankai subduction seismogenic zone:

results from a high-density ocean bottom seismic survey. J Geophys Res 113:B03105. doi:10.1029/2007JB004974, 2008

Obara K, Ito Y (2005) Very low frequency earthquakes excited by the 2004 off the Kii peninsula earthquakes: a dynamic deformation process in the large accretionary prism. Earth Planet Space 57:321–326

Ogawa Y, Fujioka K, Fujikura K, Iwabuchi Y (1996) En-echelon patterns of *Calyptogena* colonies in the Japan Trench. Geology 24:807–810

Park JO, Tsuru T, Kodaira S, Cummins PR, Kaneda Y (2002a) Splay fault branching along the Nankai subduction zone. Science 297:1157–1160

Park JO, Tsuru T, Takahashi N, Hori T, Kodaira S, Nakanishi A, Miura S, Kaneda Y (2002b) A deep strong reflector in the Nankai accretionary wedge from multichannel seismic data: implication for underplating and interseismic shear stress release. J Geophys Res 107:2061. doi:10.1029/2001JB000262.2002

Park JO, Fujie G, Wijerathne L, Hori T, Kodaira S, Fukao Y, Moore GF, Bangs NL, Kuramoto S, Taira A (2010) A low-velocity zone with weak reflectivity along the Nankai subduction zone. Geology 38:283–286

Pickering TK, Taira A (1994) Tectonosedimentation: with examples from the tertiary – recent of Southeast Japan. In: Hancock PL (ed) Continental deformation. Pergamon, Oxford, pp 320–354

Pili E, Poitrasson F, Gratier J-P (2002) Carbon-oxygen isotope and trace element constrains on how fluids percolate faulted limestones from the San Andreas Fault system: partitionaing of fluid sources and pathways. Chem Geol 190:231–250

Sakai H, Gamo T, Ogawa Y, Boulegue J (1992) Stable isotopic ratios and origins of the carbonates associated with cold seepage at the eastern Nankai trough. Earth Planet Sci Lett 109:391–404

Sanfilippo A, Nigrini C (1998) Code numbers for Cenozoic low latitude radiolarian biostratigraphic zones and GPTS conversion tables. Mar Micropaleontol 33:109–156

Seno T, Stein S, Gripp AE (1993) A model for the motion of the Philippine Sea Plate consistent with Nuvel I and geological data. J Geophys Res 98:17941–17948

Strasser M, Moore GF, Kimura G, Kitamura Y, Kopf AJ, Lallemant S, Park JO, Screaton EJ, Su X, Underwood MB, Zhao X (2009) Origin and evolution of a splay fault in the Nankai accretionary wedge. Nat Geosci. doi:10.1038/NGEO609

Taira A, Hill I, Firth J, Berner U, Bruckmann W, Byrne T, Chabernaud T, Fisher A, Foucher J-P, Gamo T, Gieskes J, Hyndman R, Karig D, Kastner M, Kato Y, Lallemant S, Lu R, Maltman A, Moore G, Moran K, Olaffson G, Owens W, Pickering K, Siena F, Taylor E, Underwood M, Wilkinson C, Yamano M, Zhang J (1992) Sediment deformation and hydrogeology of the Nankai trough accretionary prism: synthesis of shipboard results of ODP Leg 131. Earth Planet Sci Lett 109:431–450

Takahashi N, Kodaira S, Park JO, Diebold J (2003) Heterogeneous structure of western Nankai seismogenic zone deduced by multichannel reflection data and wide-angle seismic data. Tectonophysics 364:167–190

Teichert BMA, Bohrmann G, Suess E (2005) Chemoherms on hydrate ridge – unique microbially-mediated carbonate build-ups growing into the water column. Paleogeogr Paleoclimatol Paleoecol 227:67–85

Tobin HJ, Kinoshita M (2006) NanTroSEIZE: the IODP Nankai trough seismogenic zone experiment. Sci Drill 2:23–27

Ujiie K, Hisamitsu T, Taira A (2003) Deformation and fluid pressure variation during initiation and evolution of the plate boundary decollement zone in the Nankai accretionary prism. J Geophys Res 108. doi:10.1029/2002JB002314

Ujiie K, Maltman AJ, Sanchez-Gomez M (2004) Origin of deformation bands in argillaceous sediments at the toe of the Nankai accretionary prism, southwest Japan. J Struct Geol 26:221–231

Yamaguchi A, Ujiie K, Kimura G, Matsumoto R (2004) Carbon and oxygen isotopic composition of vein calcite in the Mugi melange, the Shimanto belt, Japan. Japan Geoscience Union Meeting 2004, Abstracts J036-015

Yamaguchi A, Kimura G, Kusaba Y, Sibata T, Yamaguchi H, Okamoto S (2007) Fluid conduit system along the Nobeoka thrust, Shimanto belt: derived from carbon and oxygen isotopic compositions of carbonate veins. 114th Annual Meeting of the Geological Society of Japan, Abstracts O-146

Submarine Outcrop Evidence for Transpressional Deformation Within the Nankai Accretionary Prism, Tenryu Canyon, Japan

Nicholas W. Hayman, Kurtis C. Burmeister, Kiichiro Kawamura, Ryo Anma, and Yasuhiro Yamada

Abstract The Tenryu submarine canyon lies within the eastern edge of the Nankai Trough, Japan, and exposes the internal structure of the Nankai accretionary prism. *SHINKAI 6500* submersible dives within Tenryu Canyon in 2008 collected important new data on the structural geology of well-bedded, Pleistocene turbidite sequences of fine-sand, silt, and mud. These data include estimates of the strike and dip of bedding, and of the joints and faults that cut these strata. Most strata are involved in broad, east-west trending first-order folds (trench parallel) that typify the accretionary prism structure. Aside from the trench-parallel fold hinges and faults, tight outcrop-scale folds and broader <1 km-scale folds have hinge-lines that plunge to the north (trench perpendicular). These trench-perpendicular folds are associated with outcrop-scale evidence for strike-slip faulting and appear to culminate in an oblique imbricate thrust zone near the trace of the Tokai thrust, an approximate equivalent to the 'megasplay' out-of-sequence thrust in the NanTroSEIZE

N.W. Hayman (✉)
Institute for Geophysics, Jackson School of Geosciences, University of Texas at Austin, J.J. Pickle Research Campus, Austin, TX 78758, USA
e-mail: hayman@ig.utexas.edu

K.C. Burmeister
Department of Earth and Environmental Sciences, University of the Pacific, 3601 Pacific Avenue, Stockton, CA 95211, USA
e-mail: kburmeister@pacific.edu

K. Kawamura
Fukada Geological Institute, 2-13-12 Hon-Komagome, Bunkyo, Tokyo 113-0021, Japan
e-mail: kichiro@fgi.or.jp

R. Anma
Graduate School of Life and Environmental Sciences, University of Tsukuba, Ten-nodai 1-1-1, Tsukuba, Ibaraki 305-8572, Japan
e-mail: ranma@sakura.cc.tsukuba.ac.jp

Y. Yamada
Department of Civil and Earth Resources Engineering, Graduate School of Engineering, Kyoto University, Kyoto 615-8540, Japan
e-mail: yamada@earth.kumst.kyoto-u.ac.jp

Y. Ogawa et al. (eds.), *Accretionary Prisms and Convergent Margin Tectonics in the Northwest Pacific Basin*, Modern Approaches in Solid Earth Sciences 8,
DOI 10.1007/978-90-481-8885-7_9,

region to the west. The preferred hypothesis links the transpressional deformation to a subducted seamount or paleo-Zenisu ridge, though it is alternatively possible that transpression accommodates the northward collision of the Izu-Bonin arc and Sagami trough, and oblique subduction of the Philippine Sea plate. The identification of trench-perpendicular fold hinges in Plio-Pleistocene strata illustrates a large component of previously unidentified elastic strain, and faulting that cuts this folded strata may have a strike-slip component. Therefore, these submersible observations are relevant to evaluating seismic hazards confronted by the Tokai region in Japan.

Keywords Accretionary prism • Nankai • Thrust fault • Structural geology • Submersible geology

1 Introduction

The Nankai trough of Japan's (Honshu and Shikoku) southeastern margin is a type locality for studying subduction-zone processes. Here, sediment from the Shikoku basin has been scraped off the subducting Philippine Sea plate into an accretionary prism adjacent to the colliding Izu-Bonin arc since late Miocene-early Pliocene time (Moore and Karig 1976; Seno 1977; Le Pichon et al. 1987a, b; Seno et al. 1996) (Fig. 1). Faults

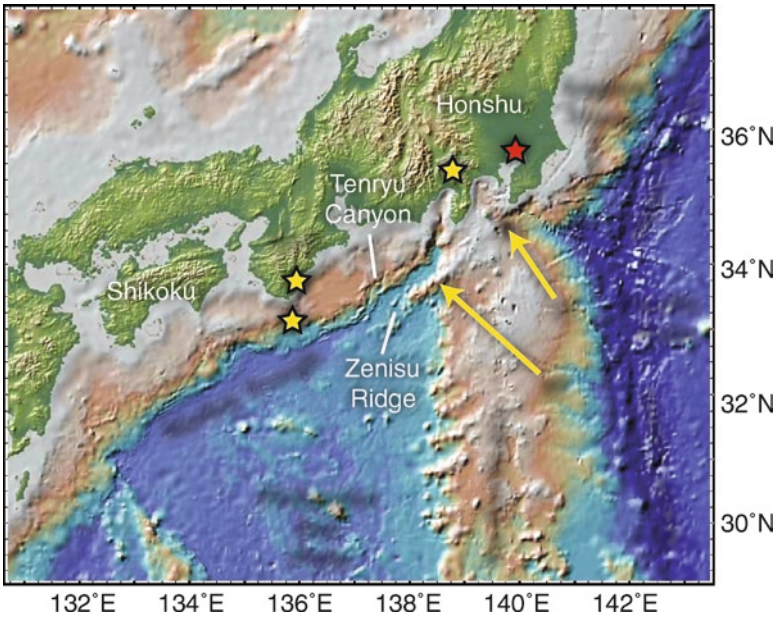

Fig. 1 Plate-tectonic setting of Tenryu Canyon relative to the Nankai trough, Kii Peninsula, and Tokyo Bay (*red star*). Plate convergence vectors compiled by Hirono (2003) (in mm/yr) illustrate local variations in plate convergence in the Tenryu Canyon region; Pacific-Okhotsk plate convergence rate is 70 mm/yr for reference Seno et al. (1996). Zenisu Ridge is one of several basement ridges associated with the Izu-Bonin Arc that collide with the Tenryu canyon section of the Nankai trough. Yellow stars mark the 1944 and 1946 Kii Peninsula epicentral regions and the 1856 Tokai epicentral region (Base image produced with *Geomapapp*)

associated with the Nankai subduction zone have generated large (M > 8) earthquakes and tsunamis, including the 1944 Nankai and 1946 Tonankai earthquakes (Ando 1975; Hyndman et al. 1995; Kodaira et al. 2000; Nakanishi et al. 2002a, b). In response to the combined scientific significance of, and hazards posed by the subduction-zone system, seismic imaging experiments and a complex scientific drilling program (NanTroSEIZE) hsave focused on the Nankai region (Tobin and Kinoshita 2006).

Another area of interest within the Nankai trough is the Tokai region. Located east of the NanTroSEIZE area but just west of the Izu-Bonin arc, the Tokai region was subjected to a M > 8 earthquake during the 1856 Ansei-Tokai event that ruptured across southern Honshu. The Tokai region therefore sits in a "seismic gap" relative to the other Nankai events leading to political-social-economic debate about how best to mitigate seismic hazards in Japan (Mogi 2004). To partially address this debate and to better understand the distribution of strain in the Tokai region, several recent projects used seismic imaging techniques as well as remotely- and human-occupied submersible vehicle surveys to resolve the geologic structure of this eastern part of the Nankai accretionary prism (Le Pichon et al. 1987a, b; Nakanishi et al. 2002a, b; Kawamura et al. 2009). A bi-product of these efforts was the recognition that a deep submarine canyon, Tenryu canyon, provides world-class, cross-sectional exposures of relatively deep structural levels within the Nankai accretionary prism.

Here, we report on observations from three dives in Tenryu canyon conducted during the JAMSTEC R/V Yokosuka YK08-04E cruise in 2008 that bear on both the geological structure of this part of the Nankai accretionary prism and the regional distribution of strain. Strike and dip estimates of bedding determined from *SHINKAI 6500* imaging and navigation systems show that in parts of the accretionary prism Pleistocene strata are folded about northerly plunging axes as a result of shortening parallel to the trench. Such clear evidence for trench-parallel shortening has not, to our knowledge, been reported from active accretionary prisms worldwide. The trench-parallel shortening likely caused the apparent sinuosity of bathymetric features in Tenryu canyon. Moreover, such observations of trench-parallel shortening reinforce suggestions that transpressional deformation in the accretionary prism is accumulating along trench-parallel strike-slip faults that have been interpreted from offset reflectors in seismic reflection data both in the Tenryu canyon and NanTroSEIZE areas (Takahashi et al. 2002; Martin et al. 2010).

The exact cause of transpressional deformation in the Nankai area is unknown, but is likely associated with some combination of: (*i*) changes in the principal stress orientations throughout the prism (Byrne et al. 2009; Lin et al. 2010), (*ii*) lateral ramping in the thrust belt (Moore et al. 2007), (*iii*) accommodation of subducted seamounts (Dominguez et al. 1998; Bangs et al. 2006; Bilek 2007), or (*iv*) strain partitioning to accommodate oblique (~15°) Philippine-Eurasian plate convergence (Martin et al. 2010). A fifth, more specific mechanism for transpression in the Tenryu canyon area is the overall rotation of the compressive axis around the colliding Zenisu and paleo-Zenisu morphological ridges that form along the western margin of the Izu-Bonin arc (Le Pichon et al. 1987a). We consider all of these mechanisms for transpressional deformation in the Tenryu canyon region to be important, especially the collision of the Zenisu ridges. Through this transpressional deformation, the elastic strain in the area is likely increased and favored orientations for fault slip are likely deviated from

areas to the west. Therefore, the geologic structure of the Tenryu canyon area likely influences the seismogenic behavior of the eastern Nankai accretionary prism.

2 Tenryu Canyon

Tenryu canyon cuts deeply into the eastern edge of the Nankai accretionary prism (Fig. 2). Originating as the drainage for the Tenryu river at the coastline, the southern mouth of the canyon opens to the trench roughly 130 km to the south at roughly 3,800 m below sea-level (mbsl). The geomorphology of Tenryu canyon is characterized by steep walls that can be more than 500 m high over similar lateral distances. The morphology of the canyon has been interpreted to signify subsidence of the Nankai trough below the 'antecedent' submarine drainage following subduction of a seamount or an earlier equivalent to the Zenisu ridge (Soh and Tokuyama 2002).

The surface of the accretionary prism in the Tenryu canyon area is cut by several well-mapped, scarp-forming, and seismically imaged faults, including the frontal thrust of the accretionary prism and the Tokai thrust. The Tokai thrust is a prominent out-of-sequence fault that is likely the along-strike structural equivalent to the out-of-sequence 'megasplay' thrust fault in the NanTroSEIZE area. The NanTroSEIZE megasplay fault is likely the up-dip expression of the seismogenic and tsunamigenic fault associated with the Tonankai (1946) earthquake (Park et al. 2002; Nakanishi et al. 2002a, b; Moore et al. 2007). In the Tenryu canyon area the seismogenic history of the Tokai thrust is less certain, and the fault appears to laterally ramp or possibly begin to tip out between two 2D seismic sections (Takahashi et al. 2002).

The Tokai thrust roughly bounds an area where samples of late Pliocene, low-porosity, high-strength phyllite were collected by Kawamura et al. (2009). These relatively consolidated samples contrast with the surrounding <180–480 ka, high porosity and low strength sediments that dominate the area. Kawamura et al. (2009) suggest that the Tokai thrust may therefore have exhumed deeper prism material. We offer an additional hypothesis that the phyllite samples collected by Kawamura et al. (2009) could also represent kinematically independent slivers of material that were deformed and metamorphosed in response to frictional heating and/or enhanced water-rock reactions within the fault zone, though more work is required to test this hypothesis.

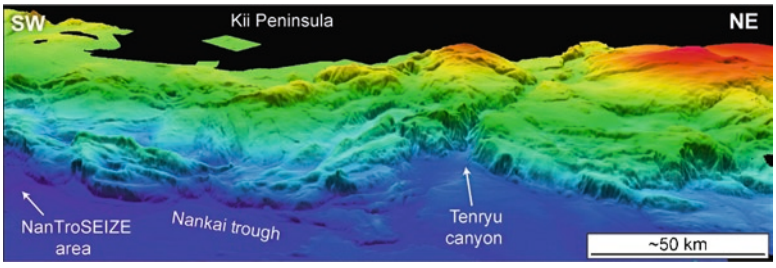

Fig. 2 Oblique, westerly perspective of the Nankai margin and Tenryu canyon area. Note the large bathymetric high (*red*) on the northern edge of Tenryu canyon, and the more northerly striking ridges on the west side

The other faults exposed in Tenryu canyon region have kinematically different histories from the rest of the fold and thrust belt. Some faults, such as the thrust faults in the vicinity of Zenisu ridge, apparently root into the oceanic basement (Le Pichon et al. 1987a; Nakanishi et al. 2002a; Takahashi et al. 2002). Still others, such as the Kodaiba fault apparently do not root in basement and are proposed to have a strong strike-slip component (Takahashi et al. 2002). Similar structural relationships to those among faults in the Tenryu canyon area were observed during the NanTroSEIZE surveys further to the west where thrusts faults may root in basement rocks (Park et al. 2002) and unrooted faults are thought to have a strike-slip component (Martin et al. 2010).

We report here on three *SHINKAI 6500* dives from 2008 that focused on exposures of the footwall, fault zone, and hanging wall of the Tokai thrust in Tenryu canyon (Fig. 3). These three dives were part of a five-dive cruise designed to supplement knowledge of the Tenryu canyon area gained during previous submersible programs (Kawamura et al. 2009). We focus exclusively on the mesoscale (outcrop) structure to make a very simple point: that folds in the turbiditic strata indicate a strong component of trench-parallel shortening. In so doing we also present some new observations of the Tokai thrust zone and distribution of stratigraphic units.

3 Outcrop Geology of Tenryu Canyon from SHINKAI 6500

SHINKAI 6500 dives 1056, 1057, and 1058 each conducted transects within Tenryu canyon that were approximately one kilometer long at depths from roughly 2,000 to 3,000 mbsl (Fig. 3). Because most of the sedimentary units exposed in the Tenryu canyon walls are well-bedded alternating layers of sand and mud, the strike and dip of these strata can be estimated from the yaw and pitch of the external video camera and the bearing of the submarine. These estimates obviously yield *apparent* strikes and dips, but by traversing the area of dipping strata we were able to avoid observing strata at extremely high-angles to strike.

We do not truly quantify the uncertainty associated with our strike-and-dip estimates here, but point out that such estimates can be considered at the very least semi-quantitative. One of the largest sources of uncertainty in any strike and dip measurement is the angle between the true dip (TD) and apparent dip (AD), where α is the angle between TD and AD directions:

$$TD = \tan^{-1}\left(\frac{\tan AD}{\cos \alpha}\right)$$

We suggest that our views (α) were typically within ~10–20° of strike, thereby providing true dip estimates with an error of less than ±4°. However, this error estimate is probably overly optimistic considering that there is no systematic way to circumnavigate every structural feature, many features were in cliff-faces, and the horizontal is difficult to control in the vehicle. Nonetheless, we suspect that our estimates are within perhaps 10° of TD (See Table 1 for a full list of strike and dip measurements for the three dives of interest).

The three dives of interest here traversed sequences of predominantly well-bedded silt and mud that locally contain interbedded tuff deposits. Silt and sand

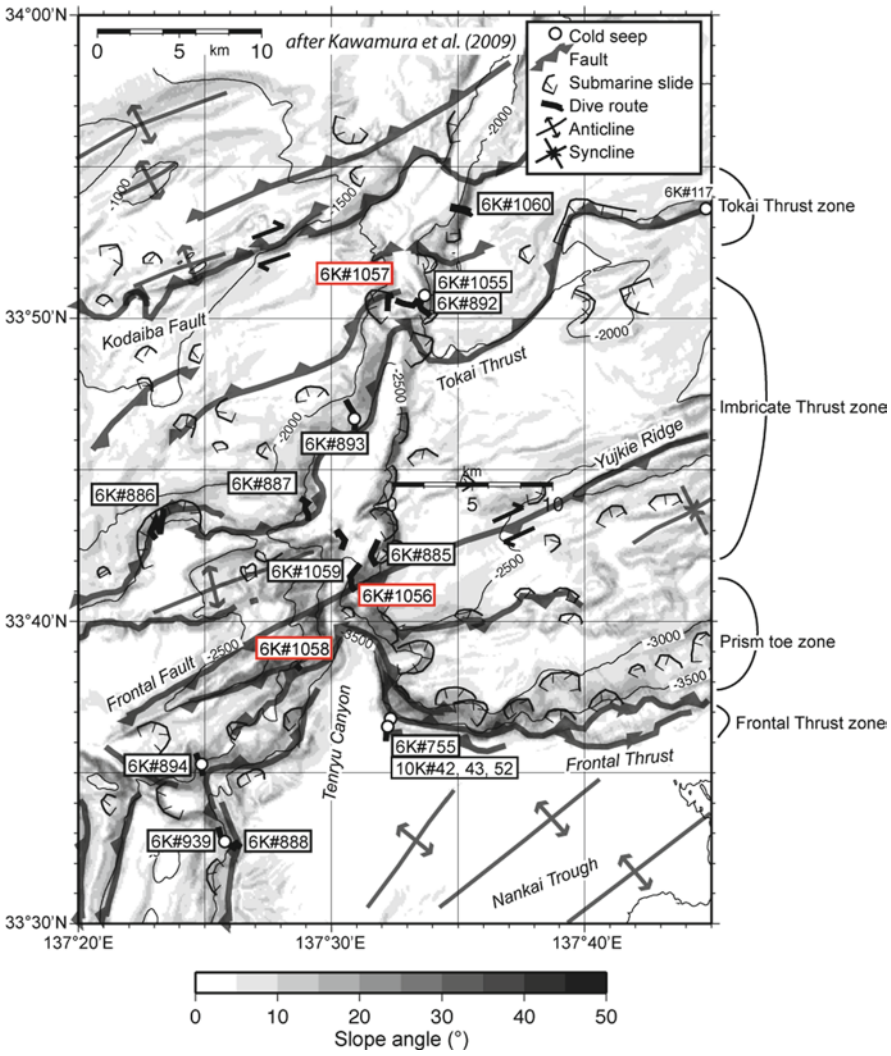

Fig. 3 Dive locations and major structural features of Tenryu canyon. Dives 1056, 1057, and 1058 are the focus of this effort and their locations are outlined in *red* (Basemap and structural interpretations from Soh and Tokuyama (2002) and Kawamura et al. (2009))

layers average approximately 20 cm thick, while mud layers average roughly 10 cm thick (Fig. 4). These strata were likely deposited as turbidite flows associated with the transport of sediment into the trench from Tenryu canyon and other areas to the east-northeast, as is the case for other areas of the Nankai trough (Pickering et al. 1992; Underwood and Pickering 1996). Therefore we can assume an original horizontality for the bedding, or at least a depositional dip of <~5°.

We estimate that the samples collected during dives 1056 and 1057 have roughly the same biostratigraphic ages as those collected during the Kawamura et al. (2009)

Table 1 Structural data from cruse YK08-E04 dives 1056, 1057, and 1058

Dive	Strike	Dip	Dip direction	Type
Dive 1056	45	35	S	Bedding
	70	60	N	Bedding
	30	30	N	Bedding
	90	40	N	Bedding
	40	45	N	Bedding
	0	20	W	Bedding
	100	90	–	Bedding
	0	0	–	Bedding
	25	45	W	Bedding
	42	30	N	Bedding
	50	30	N	Bedding
	54	45	N	Bedding
	160	45	E	Bedding
	64	35	N	Bedding
	134	60	E	Bedding
	64	40	N	Bedding
	87	40	W	Bedding
	80	45	W	Bedding
	80	30	S	Bedding
	80	30	S	Bedding
	65	30	W	Bedding
	39	25	W	Bedding
Dive 1057	225	60	NW	Bedding
	170	60	SW	Bedding
	180	50	W	Bedding
	200	40	NW	Bedding
	20	80	SE	Bedding
	160	60	SW	Bedding
	220	45	NW	Bedding
	0	45	E	Bedding
	180	40	W	Bedding
	240	70	NW	Bedding
	190	45	W	Bedding
	20	70	SE	Bedding
	225	70	NW	Bedding
	245	70	NW	Bedding
	10	60	E	Bedding
	350	70	E	Bedding
	250	50	NW	Bedding
	350	70	E	Bedding
	345	60	NE	Bedding
	210	45	NW	Bedding
	210	45	NW	Bedding
	210	45	NW	Bedding
	10	45	E	Bedding

(continued)

Table 1 (continued)

Dive	Strike	Dip	Dip direction	Type
	0	60	E	Bedding
	330	45	E	Bedding
	232	60	NW	Bedding
	20	70	E	Bedding
	245	70	NW	Bedding
Dive 1058	285	10	NE	Bedding
	315	10	NE	Bedding
	285	15	NNE	Bedding
	315	15	E	Bedding
	300	10	N	Bedding
	330	30	NE	Bedding
	255	20	N	Bedding
	20	10	E	Bedding
	290	10	N	Bedding
	260	15	N	Bedding
	325	20	N	Bedding
	0	20	E	Bedding
	290	20	N	Bedding
	270	10	N	Bedding
	270	5	N	Bedding
	250	15	N	Bedding
	30	15	E	Bedding
	340	20	E	Bedding
	270	15	N	Bedding
	45	15	E	Bedding
	124	70	W	Joint
	35	70	E	Joint
	145	80	N	Joint
	280	90	–	Joint
	330	90	–	Joint
	150	60	W	Joint
	320	90	–	Joint
	200	90	–	Joint
	290	90	–	Joint
	200	80	W	Joint
	120	20	S	Fault
	325	90	–	Fault
	15	90	–	Fault
	310	90	–	Fault
	330	90	–	Fault

dives 886 and 892, respectively, and therefore were deposited in Early to Middle Pleistocene. Age constraints on sediments observed on Dive 1058 are not readily available, but range from Early Pliocene and could be as young as <0.18 Ma, based on biostratigraphic ages of the sediments near the frontal thrust (Kawamura et al. 2009).

Shipboard uniaxial compression strength measurements show that the samples collected on Dives 1056, 1057, and 1058 are relatively weak, poorly consolidated

and unmetamorphosed materials (e.g. <5 MPa) (see Kawamura et al. 2009), and are unlike the relatively strong (i.e. ~20 MPa) phyllites from the Tokai thrust described in Kawamura et al. (2009) and Kawamura et al. (2011). Dive 1055, also of the 2008 cruise, collected samples including a cemented and slightly foliated mudstone cut by thin carbonate veins. Interestingly, samples collected from within the Tokai thrust zone during dive 1057 did not include similar diagenetic material, though some of the 1057 samples have slip lineations on some parting planes.

Outcrops observed from *SHINKAI 6500* during the 2008 cruise contain abundant structural relationships, including dipping strata (Fig. 4a, b), joint sets that are roughly axial planar to the folds (Fig. 4c), outcrop-scale tight folds (Fig. 4d). A variety of

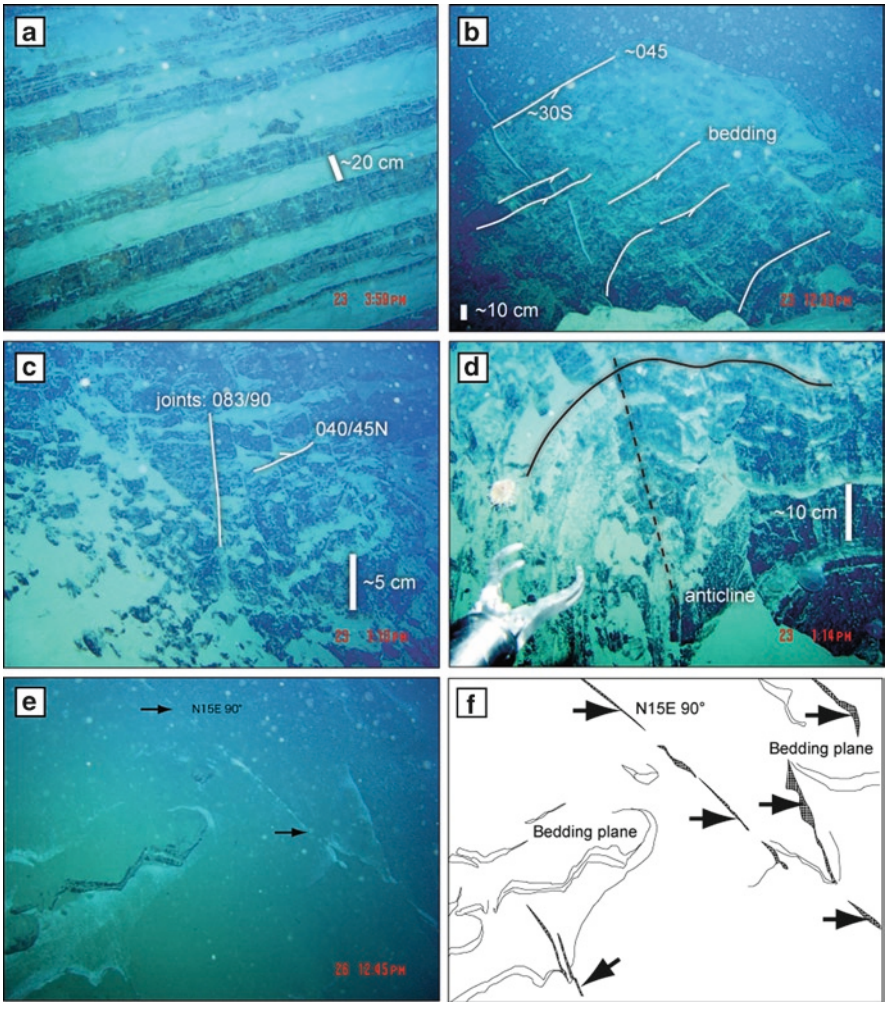

Fig. 4 Shinkai 6500 images of Tenryu canyon outcrops: (**a**) dipping stratigraphic sequence of mud, silt, and fine sand layers; (**b**) dipping strata; (**c**) axial planar jointing and dipping strata; (**d**) anticline; (**e**) bedding plane offset in the distance by minor strike-slip faulting; (**f**) sketch of photograph in '(**e**)'

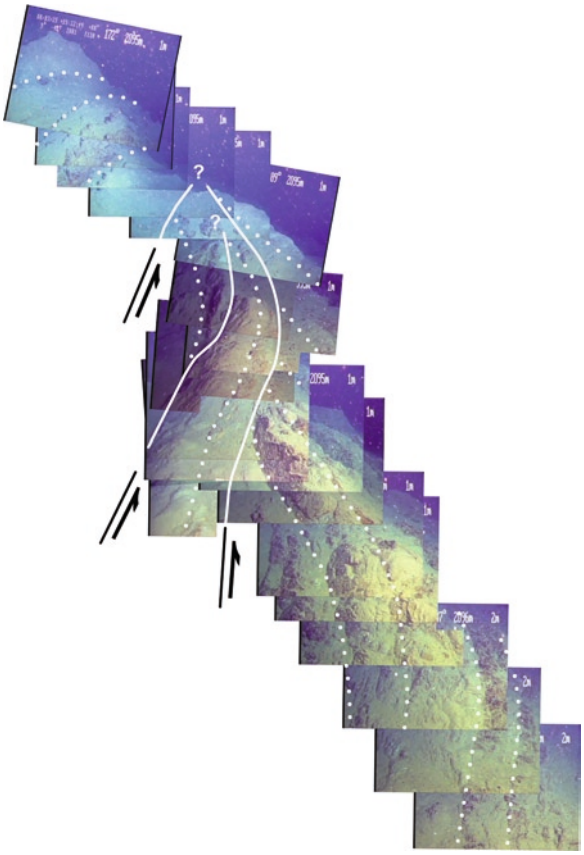

Fig. 5 Oblique, southerly view south of overturned antiformal stack within the Tokai thrust zone from Dive 1057 (see text and Fig. 7 for details). Bedding is approximately 20 cm thick

outcrop-scale faulting relationships were observed, including thrust faults and syndepositional and post-depositional normal faults. A few outcrops on Dive 1058 contained strike-slip faults (Fig. 4e, f). The most complex outcrop-scale structures occur in the imbricate zone of the Tokai thrust imaged during Dive 1057. These exposures include an overturned antiformal stack of gently folded, fault-bound imbricates that provides an unparalleled potential window into the structural style of the region (Fig. 5). In the following section, we draw on these and other outcrop observations to document map-scale evidence for trench-parallel shortening.

4 Dive-Transect Maps

By systematically measuring strikes and dips from dive video collected along the dive tracks, we were able to construct two structural maps that illustrate the attitude of bedding, joints, and faults. Dive 1056 encountered a largely homoclinal sequence

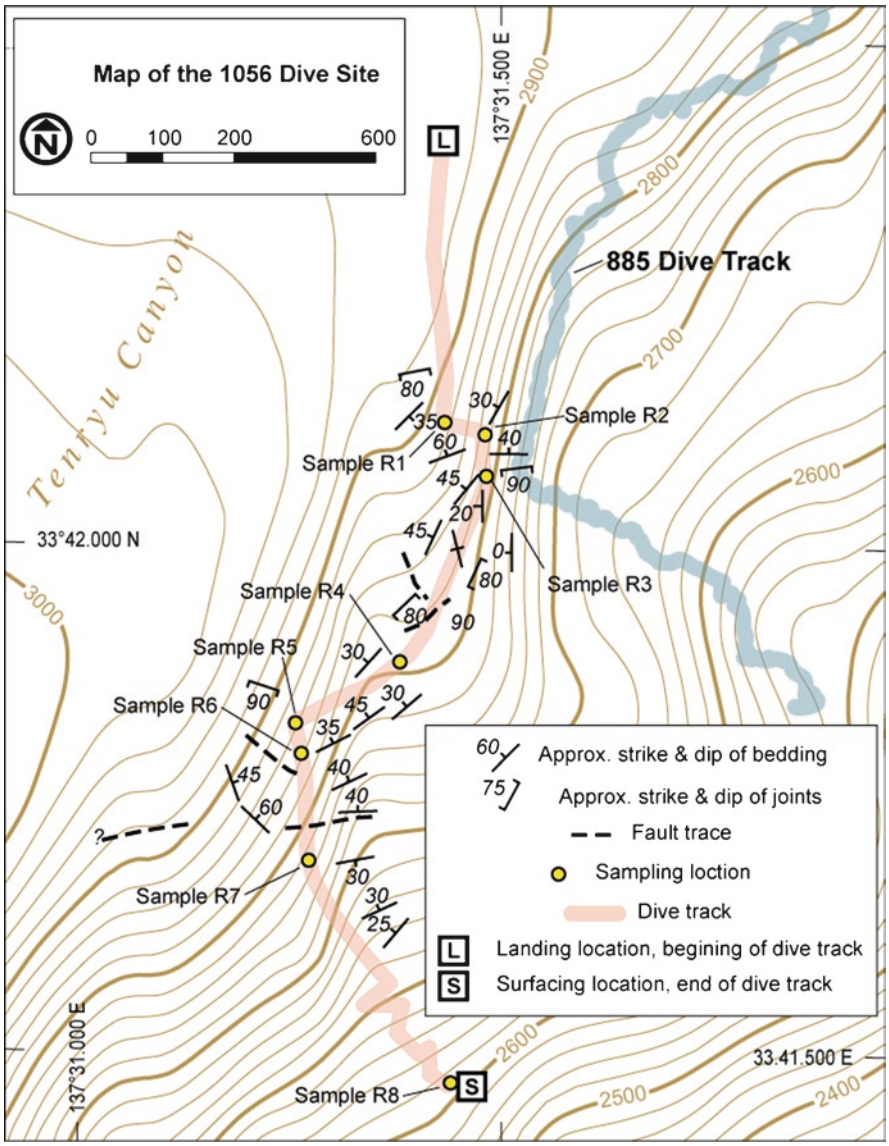

Fig. 6 Structural map of Shinkai 6500 Dive 1056. Note changes in bedding direction near sample site R7 and R2, as well as variation in amount and orientation of jointing

of strata that dip moderately (30–40°) northwest (Fig. 6). These strata are cut by east-west striking faults and locally involved in east-west trending folds (e.g. Fig. 6 just south of sample site R7). In contrast with the overall trench-parallel, north-dipping sequence of strata at the 1056 dive locality, outcrops east of the main dive track strike northerly (perpendicular to the trench) and expose the limb of a tight fold (Fig. 4d). North of the dive track bedding is broadly folded, as indicated by the

map-view trajectory of bedding orientation (Fig. 6). A distinctive jointing (Fig. 4) is well developed in these areas of folding, and oriented roughly axial planar to the folds.

In contrast with Dive 1056, Dive 1057 transected the hinge area of a synformal fold during most of the southern portion of its dive-track, with strata to the east and west of the track dipping towards one another (Fig. 7, south of sample sites 1R1 and 2R2). Within the central portion of the dive track containing the overturned, imbricate thrust sheets discussed above, bedding is oriented in a more east-westerly

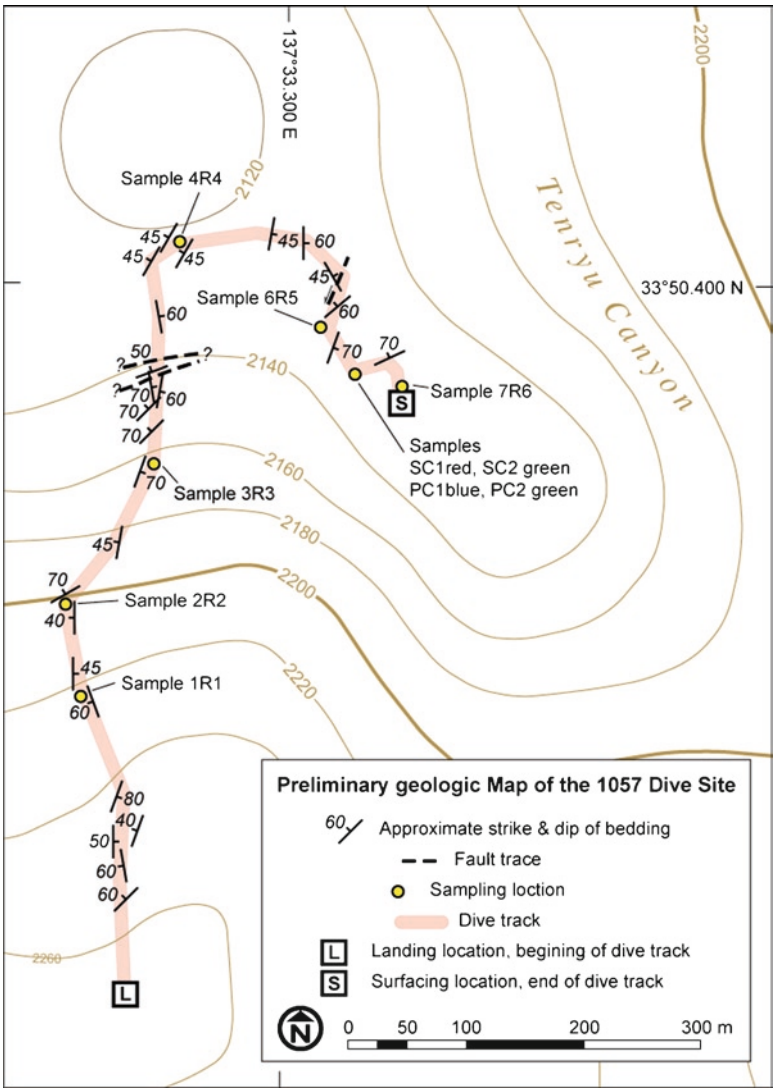

Fig. 7 Structural map of Shinkai 6500 Dive 1057. Note changes in bedding orientation both at the map scale in the north, and at the outcrop scale near sample sites 2R2 and 1R1

orientation as the result of tight folding associated with slip along the Tokai thrust. The northern portion of the 1057 dive track crossed the nose of a broad antiformal fold, with strata dipping away from the dive track on both sides. Thus, the 1057 dive track crossed a broad synform-antiform pair within a broad Tokai thrust zone. By comparison, Dive 1058 crossed very simple geology, with persistently northeast and shallowly dipping strata.

A revelatory observation comes from plotting the strike and dip data from the three dives (Table 1) on lower-hemisphere, equal area stereographic projections (Fig. 8). The poles to bedding measurements from Dive 1056 plot as a crudely

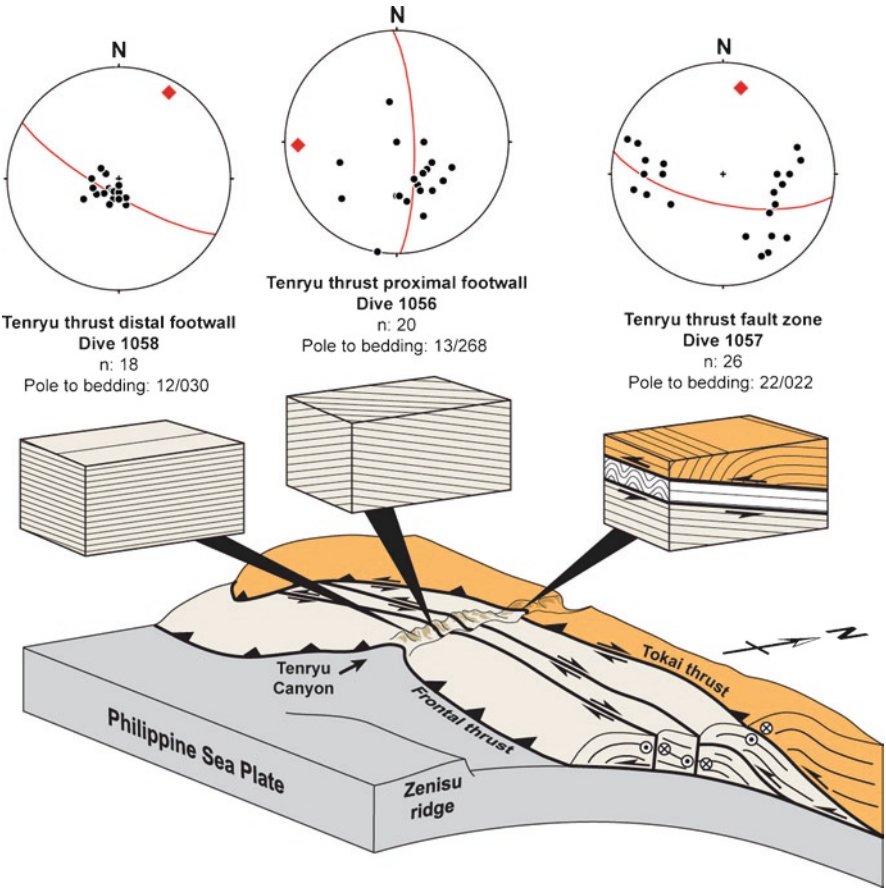

Fig. 8 Stereoplots of poles to bedding (*black dots*) and p-axis (*red square*) for structural data collected during dives 1056, 1057, and 1058 in Tenryu Canyon. These data are presented within the context of a series of schematic, *block diagrams* highlighting inferred structural trends. Strata observed during dive #1058 are generally flat lying. Bedding data collected during Dives #1056 and #1057 define regional folds. Poles to bedding from Drive #1056 track a girdle distribution around a great circle, whereas poles to bedding from Dive #1507 plot on opposite sides of the stereonet. Note the difference in orientation of the p-axis between all three dives

defined great circle with a "pole-to-poles (π-axis)" that plunges west. Therefore, bedding within the 1056 dive is folded about a roughly cylindrically, east-west trending fold. This average of bedding orientations does not, of course, include the smaller, tight, north trending folds observed locally in outcrop. In contrast, the poles to bedding planes from Dive 1057 define separate east and west dipping populations that have a pole-to-planes that plunges gently to the northeast. Not surprisingly, the poles to bedding from Dive 1058 define a relatively flat-lying sequence. However, structural observations made during Dive 1058 described in the previous section include young, high-angle faults with strike-slip indicators. We bring together these field observations in a conceptual structural model linking east-west shortening to the Tokai thrust in the following discussion.

5 Discussion

In a strictly break-forward thrust system, where strain is accommodated within a nearly cross-sectional plane, the mechanics of an accretionary prism are governed solely by slip on the basal décollement relative to the overriding wedge and incoming trench sediment (e.g. Boyer and Elliot 1982). To date the NanTroSEIZE area off the Kii peninsula has provided rich observations bearing on important exceptions to this simple model for accretionary prisms. Two noteworthy observations are (*i*) significant out-of-sequence thrusting (Park et al. 2002; Moore et al. 2007), and (*ii*) a pattern of offset reflectors in the NanTroSEIZE 3D seismic volume that can be explained by strike-slip faulting in the hanging wall immediately adjacent to the megasplay (Martin et al. 2010). Such large-scale observations set the stage for interpreting *in situ* measurements of spatially heterogeneous principal stress orientations (Lin et al. 2010), and Integrated Ocean Drilling Program (IODP) cores from the prism, which contain strike-slip and normal faults as well as thrusts (Lewis et al. 2008; Hayman et al. 2009). If the amount of oblique deformation along the Nankai margin is significant, it would bear on both the geological evolution and seismic behavior of the prism. Among other things, oblique deformation can enhance exhumation of deep-seated rocks (e.g. Karig 1980) and should affect the spatial/temporal distribution and focal mechanisms of earthquakes (e.g. McCaffrey et al. 2000).

In contrast with the NanTroSEIZE area, the sinuous bathymetry and sharp scarps of the Tenryu canyon area have long been interpreted as potential indicators of transpressional deformation in the eastern Nankai accretionary prism (Le Pichon 1987a, b; Soh and Tokuyama 2002) (Fig. 3). However, similar to the NanTroSEIZE area, there are few clear markers in seismic reflection data that can be used to demonstrate trench-parallel, strike-slip faulting. Additionally, there is no simple way to evaluate displacements on the Tokai thrust because—similar to the NanTroSEIZE megasplay—the fault roots below the Plio-Pleistocene section of the accretionary wedge that is not exposed and is difficult to interpret in seismic data. This disconnect in scales of observation is, in essence, where the advantage of using submersible technology in a setting such as the Nankai trough lies. Submersible surveys

provide the mesoscale observations needed to connect the regional view provided by seismic reflection work with the fine-scale details of drilling data.

In order to bridge the gap between local observations in drill holes and cores and the regional seismic reflection data, we now summarize our new observations made using *SHINKAI 6500* submersible. We mapped and sampled a turbiditic sequence of Plio-Pleistocene (mostly Pleistocene based on the results of Kawamura et al. 2009) mud, silt, and fine-grained sand. Higher metamorphic grade rocks associated with the Tokai thrust (as documented by Kawamura et al. 2009) were observed locally (on Dive 1055, for example), but were not widespread. Rather, samples were generally relatively weak, unconsolidated sediments, even within the Tokai thrust zone.

The first order structure of the accretionary prism in the vicinity of Tenryu canyon comprises east-west trending folds that are associated with slip along an underlying array of thrust faults. However, we observed a number of second order structures that trend at a high angle to the trench. Second order structures include both tight outcrop-scale folds and broad map-scale folds with north plunging hinges. These structures appear to be associated with transpressional deformation that appears to intensify in the vicinity of the Tokai thrust. Where observed, the Tokai thrust zone appears to comprise folded strata and overturned imbricate thrust slices, which reflect some degree of along-strike displacement history.

In order to tie our observations together, we present a simple geometric, conceptual model for the evolution of this part of the Nankai accretionary prism (Fig. 8). In this model we rely on a seamount or a proto-Zenisu ridge to impose deviations from plane strain, though there are alternative hypotheses described in the following paragraph. The subduction of a seamount or ridge imparts a map-scale, indenter-controlled curve in the trends of first order structures within the accretionary prism (c.f., Marshak 2004) and causes trench-parallel shortening, which manifest as second order folds with north plunging hinges such as observed on Dives 1056 and 1057.

In our model, ultimately this east-west shortening gave way to strike-slip faulting. Evidence for this strike-slip faulting includes small-scale strike-slip faults observed during Dive 1058, and the slivers within the duplex structure in the Tokai imbricate zone appear to have undergone some strike-slip offset. Such mesoscale evidence reinforces inferences from bathymetry (Le Pichon et al. 1987a, b) and seismic reflection data (Takahashi et al. 2002) for strike-slip deformation. Such strike-slip faulting also offers a possible mechanism for exhumation of deeper prism materials; transpressive deformation typically has a strong component of uplift (Karig 1980).

There are alternative hypotheses for the causes of trench-parallel shortening and strike-slip faulting. It is possible that out-of-plane deformation is necessary to accommodate plate-convergence and accretion near the triple junction of the Nankai and Sagama troughs and the Izu-Bonin arc. Indeed, velocity models indicate that the top of the subducting Philippine Sea plate is dipping toward the northwest in this part of the prism (Nakanishi et al. 2002a, b). A subset of this hypothesis is that transpressional deformation is related to the plate-boundary reorganization in the early Pliocene that gave rise to the current plate-boundary geometry (Hirono 2003).

Lastly, there is a roughly 15° obliquity in Philippine Sea-Eurasian plate convergence. Strain partitioning due to this obliquity was proposed to cause strike-slip faulting in the NanTroSEIZE area (Martin et al. 2010). Of the alternatives, we prefer the hypothesis that a subducted seamount or proto-Zenisu ridge causes the oblique deformation in the Tenryu canyon area simply because this deformation appears to be most pronounced adjacent to the bathymetric high over a geophysically imaged subducted basement object. Without a subducted ridge, we suspect that the obliquity of the plate boundary would not produce such localized folds, nor would it cause strike-slip faulting in strata detached from the basement.

In closing, we note the relevance of the newly recognized trench-perpendicular fold axes and potential strike-slip faults to seismic hazards of the Nankai margin, and by extension accretionary subduction zones worldwide. Firstly, if these are indeed associated with strike-slip faulting, we should expect some seismic strain release to have a strike-slip component, or at the very least P-T axes rotated from coaxiality with the trench front. Secondly, the amount of elastic strain in the form of folding must be somewhat larger than expected from existing interpretations of the Nankai trough since these estimates have not to-date incorporated folding parallel to the trench. Either of these two aspects of the Tenryu canyon structure has implications for the total moment release expected from seismogenic zone earthquakes and ground-shaking dynamics that will result.

Lastly, we note that many of the sharp scarps on the surface of the Nankai prism likely postdate most of the folding (i.e. they cut the folds). Since the folds are in mostly Pleistocene strata, the relationship between folding and faulting could potentially be exploited as a paleoseismological indicator of geologic rates of new rupture development and fault-reactivation.

6 Conclusions

Bedding orientation estimates collected during a 2008 SHINKAI 6500 survey indicate that Plio-Pleistocene turbiditic strata exposed within Tenryu canyon area are involved in both trench-parallel and trench-perpendicular folds. While trench parallel folds are expected within the structural architecture of accretionary prisms, trench-perpendicular folds indicate trench-parallel, oblique or transpressional shortening. Based upon observations of mesoscale strike-slip faults and overturned thrust imbricates, we suggest this oblique deformation also includes strike-slip faults, previously proposed solely on the basis of bathymetric interpretations and seismic reflection work. The oblique deformation appears to be associated partly with the Tokai thrust, a potentially seismogenic and tsunamigenic thrust and approximately equivalent to the NanTroSEIZE megasplay. We suggest this oblique deformation may reflect the accommodation of a subducted seamount or proto-Zenisu ridge. Furthermore, we suggest that the estimates of past seismicity, and future seismic moment and earthquake focal mechanisms may be affected by this transpressional strain.

Acknowledgements We thank two anonymous reviewers and editor Yujiro Ogawa for valuable reviews. Hayman thanks the Institute for Geophysics and Jackson School of Geoscience at University of Texas, and the Consortium for Ocean Leadership (for participation in NanTroSEIZE Expedition 319) for support. This is UTIG contribution 2278.

References

Ando M (1975) Source mechanisms and tectonic significance of historical earthquakes along Nankai trough, Japan. Tectonophysics 27:119–140

Bangs NLB, Gulick SPS, Shipley TH (2006) Seamount subduction erosion in the Nankai trough and its potential impact on the seismogenic zone. Geology 34(8):701–704

Bilek SL (2007) Influence of subducting topography on earthquake rupture. In: Dixon T, Moore JC (eds) The seismogenic zone of subduction thrust faults. Columbia University Press, New York

Boyer SE, Elliot D (1982) Thrust systems. AAPG Bull 66:1196–1230

Byrne TB, Lin W, Tstsumi A, Yamamoto Y, Lewis JC, Kanagawa K, Kitamura Y, Yamaguchi A, Kimura G (2009) Anelastic strain recovery reveals extension across SW Japan subduction zone. Geophys Res Lett 36:6

Dominguez S, Lallemand SE, Malavieille J, Von Huene R (1998) Upper plate deformation associated with seamount subduction. Tectonophysics 293:207–224

Hayman NW et al (2009) Structural geology of cuttings and cores recovered from below the Kumano forearc basin, Nankai accretionary margin of Japan: expedition 319 of the Integrated Ocean Drilling Program (IODP). Eos Trans Am Geophys Union 90: NH31A-1100

Hirono T (2003) Strain partitioning between the Suruga Trough and the Zenisu Thrust: Neogene to present tectonic evolution in the onland and offshore Tokai district, Japan. Tectonophysics 361:205–214

Hyndman RD, Wang K, Yamano M (1995) Thermal constraints on the seismogenic portion of the southwestern Japan subduction thrust. J Geophys Res Solid Earth 100:15373–15392

Karig D (1980) Material transport within accretionary prisms and the "Knocker" problem. J Geol 88:27–39

Kawamura K, Ogawa Y, Anma R, Yokoyama S, Kawakami S, Dilek Y, Moore GF, Hirano S, Yamaguchi A, Sasaki T, YK05-08 Leg 2 and YK06-02 Shipboard Scientific Parties et al (2009) Structural architecture and active deformation of the Nankai accretionary prism, Japan: submersible survey results from the Tenryu submarine canyon. Geol Soc Am Bull 121:1629–1646

Kawamura K, Ogawa Y, Hara H, Anma R, Dilek Y, Kawakami S, Moore GF, Chiyonobu S, Mukoyoshi H, Hirano S, Motoyama I (2011) Rapid exhumation of subducted sediments along an out-of-sequence thrust due to seamount subduction followed by gravitational collapse in the active eastern Nankai accretionary prism. In: Ogawa Y, Anma R, Dilek Y (eds) Accretionary prisms and convergent margin tectonics in the Northwest Pacific Basin (Modern approaches in solid earth sciences 8). Springer, Dordrecht, pp 215–227

Kodaira S, Takahashi N, Park JO, Mochizuki K, Shinohara M, Kimura S (2000) Western Nankai trough seismogenic zone: results from a wide-angle ocean bottom seismic survey. J Geophys Res Solid Earth 105:5887–5905

Le Pichon X et al (1987a) Nankai trough and Zenisu Ridge: a deep-sea submersible survey. Earth Planet Sci Lett 83:285–299

Le Pichon X et al (1987b) Nankai trough and the fossil Shikoku ridge – results of Box-6 Kaiko survey. Earth Planet Sci Lett 83:186–198

Lewis J, Kanagawa K, Byrne T, Famin V, Berhmann J, Kanamatsu T, Pares J, 314/315/316 Scientists IE (2008) Subhorizontal extension of the upper plate at NanTroSEIZE Sites C0001 and C0002. Eos Trans. AGU, 89(53), Fall Meet. Suppl., T31B-2005

Lin W, Doan ML, Moore JC, Byrne TB, Ita T, Saffer D, Conin M, Kinoshita M, Sanada Y, Moe KT, Araki E, Tobin H, Boutt D, Kano Y, Hayman NW, Flemings P, Huftile GJ, Cukur D, Buret C, Schleicher AM, Efimenko N, Kawabata K, Buchs DM, Jiang S, Kameo K, Horiguchi K, Wiersberg T, Kopf A, Kitada K, Eguchi N, Toczko S, Takahashi K, Kido Y (2010) Present-day principal horizontal stress orientations in the Kumano forearc basin of the southwest Japan subduction zone determined from IODP NanTroSEIZE drilling Site C0009. Geophys Res Lett 37:L13303. doi:10.1029/2010GL043158

Marshak S (2004) Salients, recesses, arcs, oroclines, and syntaxes – a review of ideas concerning the formation of map-view curves in fold-thrust belts. In: McClay KR (ed) Thrust tectonics and hydrocarbon systems. Am Assoc Petrol Geol Mem 82:131–156

Martin KM, Gulick SPS, Bangs NL, Moore GF, Ashi J, Park J-O, Kuramoto S, Taira A (2010) Possible strain partitioning structure between the Kumano Forearc Basin and the slope of the Nankai trough accretionary prism. Geochem Geophys Geosyst. doi:10.1029/2009GC002668

McCaffrey R, Zwick PC Bock Y, Prawirodirdjo L, Genrich JF, Stevens CW, Puntodewo SSO, Subarya C (2000) Strain partitioning during oblique plate convergence in northern Sumatra: geodetic and seismologic constraints and numerical modeling. J Geophys Res 105(B12):28363–28376. doi:10.1029/1999JB900362

Mogi K (2004) Two grave issues concerning the expected Tokai earthquake. Earth Planet Space 56:1–16

Moore JC, Karig DE (1976) Sedimentology, structural geology, and tectonics of Shikoku subduction zone, southwestern Japan. Geol Soc Am Bull 87:1259–1268

Moore GF, Bangs NL, Taira A, Kuramoto S, Pangborn E, Tobin HJ (2007) Three-dimensional splay fault geometry and implications for tsunami generation. Science 318:1128–1131

Nakanishi A et al (2002a) Deep crustal structure of the eastern Nankai trough and Zenisu ridge by dense airgun-OBS seismic profiling. Mar Geol 187:47–62

Nakanishi A et al (2002b) Crustal structure across the coseismic rupture zone of the 1944 Tonankai earthquake, the central Nankai trough seismogenic zone. J Geophys Res Solid Earth 107:21

Park JO, Tsuru T, Kodaira S, Cummins PR, Kaneda Y (2002) Splay fault branching along the Nankai subduction zone. Science 297:1157–1160

Pickering KT, Underwood MB, Taira A (1992) Open-ocean to trench turbidity-current flow in the Nankai trough – flow collapse and reflection. Geology 20:1099–1102

Seno T (1977) Instantaneous rotation vector of Philippine Sea plate relative to Eurasian plate. Tectonophysics 42:209–226

Seno T, Sakurai T, Stein S (1996) Can the Okhotsk plate be discriminated from the North American plate? J Geophys Res Solid Earth 101:11305–11315

Soh W, Tokuyama H (2002) Rejuvenation of submarine canyon associated with ridge subduction, Tenryu Canyon, off Tokai, central Japan. Mar Geol 187:203–220

Takahashi N, Amano H, Hirata K, Kinoshita H, Lallemant S, Tokuyama H, Yamamoto Y, Taira A, Suyehiro K (2002) Faults configuration around the eastern Nankai trough deduced by multichannel seismic profiling. Mar Geol 187:31–46

Tobin HJ, Kinoshita M (2006) NanTroSEIZE: the IODP Nankai trough seismogenic zone experiment. Sci Drill 2:23–27

Underwood MB, Pickering KT (1996) Clay-mineral provenance, sediment dispersal patterns, and mudrock diagenesis in the Nankai accretionary prism, southwest Japan. Clays Clay Mineral 44:339–356

Rapid Exhumation of Subducted Sediments Along an Out-of-Sequence Thrust in the Modern Eastern Nankai Accretionary Prism

Kiichiro Kawamura, Yujiro Ogawa, Hidetoshi Hara, Ryo Anma, Yildirim Dilek, Shunsuke Kawakami, Shun Chiyonobu, Hideki Mukoyoshi, Satoshi Hirano, and Isao Motoyama

Abstract A foliated mudstone with illite crystallization was recovered at an outcrop during dive surveys of manned submersible *SHINKAI 6500* to the bottom of the Tenryu Submarine Canyon near the Tokai Thrust, which is one of the largest out-of-sequence thrusts within the Nankai accretionary prism (NAP) off Southwest Japan. The mudstone contains a strong preferred orientation of illite flakes that define two foliations (S_1 and S_2): both are schistosity-like texture defined by shape and crystallographic preferred orientation. The S_2 foliation is subparallel to a later

K. Kawamura (✉)
Fukada Geological Institute, 2-13-12 Hon-Komagome, Bunkyo, Tokyo 113-0021, Japan
e-mail: kichiro@fgi.or.jp

Y. Ogawa
The University of Tsukuba, 1-127-2-C-740 Yokodai, Tsukubamirai 300-2358, Japan (home)
e-mail: fyogawa45@yahoo.co.jp

H. Hara
Geological survey of Japan, AIST Tsukuba Central 7, Tsukuba 305-8567, Japan
e-mail: hara-hide@aist.co.jp

R. Anma
Graduate School of Life and Environmental Sciences, University of Tsukuba,
Ten-nodai 1-1-1, Tsukuba, Ibaraki 305-8572, Japan
e-mail: ranma@sakura.cc.tsukuba.ac.jp

Y. Dilek
Department of Geology, Miami University, 114 Shider Hall, Oxford, OH 45056, USA
e-mail: dileky@muohio.edu

S. Kawakami
Earth-Appraisal Co. Ltd., Chiyoda, Tokyo 101-0063, Japan
e-mail: kawakami@earth-app.co.jp

S. Chiyonobu
Research Institute of Innovative Technology for the Earth, CO_2 Storage Research Group,
9-2 Kizugawadai, Kizugawa-shi, Kyoto 619-0292, Japan
e-mail: chiyonob@rite.or.jp

Y. Ogawa et al. (eds.), *Accretionary Prisms and Convergent Margin Tectonics in the Northwest Pacific Basin*, Modern Approaches in Solid Earth Sciences 8,
DOI 10.1007/978-90-481-8885-7_10, © Springer Science+Business Media B.V. 2011

tension fracture (S_3). The illite flakes within the foliated mudstone clearly formed from diagenetic recrystallization rather than being detrital in origin. The peak metamorphic temperature for the mudstone samples was estimated to be ~200–230°C on the basis of illite crystallinity. Based on the representative thermal gradients within the NAP at present (~50°C/km), the rock was exhumed from 4 to 5 km in depth, corresponding to the depth of the seismogenic zone. Nannofossils in the foliated mudstone indicate a depositional age older than 3.8 Ma. Radiolarians inserted within the tension fractures of the sample indicate <0.42 Ma, suggesting the sediments subducted and then returned to the surface <0.42 Ma ago. The present sample site is located ca. 30 km from the leading edge of the trough. Present subduction rate of the Philippine Sea plate (4.0–7.0 cm/year) gives estimates for the rate of lateral transportation of sediments. These results indicate that the mudstone along the out-of-sequence thrust were rapidly exhumed from the seismogenic zone.

Keywords *SHINKAI 6500* • Submarine landslide • OOST • Phyllite • Illite crystallinity

1 Introduction

Understanding the processes and mechanisms of large seismogenic and tsunamigenic faults that occur at active subduction zones is one of the fundamental targets of the Integrated Ocean Drilling Program (IODP) (Tobin and Kinoshita 2006). The up-dip limit of fault slip locking depth in the Nankai seismogenic zone is controlled by various factors (Hyndman 2004), including the transition from smectite to illite at temperatures between 100°C and 150°C as shown by Vrolijk (1990). Below depths where large earthquakes occur, interseismic slips occur along the décollement zones that are the subduction plate boundaries (Park et al. 2002; Kodaira et al. 2003, 2004). The Nankai Trough is a plate convergent margin where the Philippine Sea plate (hereafter PHP) subducts below the Eurasia (Amur) plate at Southwest Japan (Moore et al. 2007; Seno et al. 1993). The convergence rate between these plates is estimated as 4–5 cm/year (Seno et al. 1993) or 6–7 cm/year (Miyazaki and Heki 2001) (Fig. 1a). The pelagic/hemipelagic sediments and trench-fill turbidites on the PHP are successively accreted to Southwest Japan to form the Nankai accretionary prism (NAP), as a result of repeated occurrences of thrust-anticlines (Taira et al. 1991; Shipboard Scientific Party 2001). In the eastern NAP, collision/subduction of seamount chains, namely paleo-Zenisu ridges, occurred at least twice

H. Mukoyoshi and S. Hirano
Marine Works Japan, Showa-machi 3175-25, Kanazawa, Yokohama 236-0001, Japan
e-mail: mukoyoshih@jamstec.go.jp; hiranos@nwj.co.jp

I. Motoyama
Department of Earth and Environmental Sciences, Graduate School of Science Department, Yamagata University, Yamagata 990-8560, Japan
e-mail: i-motoyama@sci.kj.yamagata-u.ac.jp

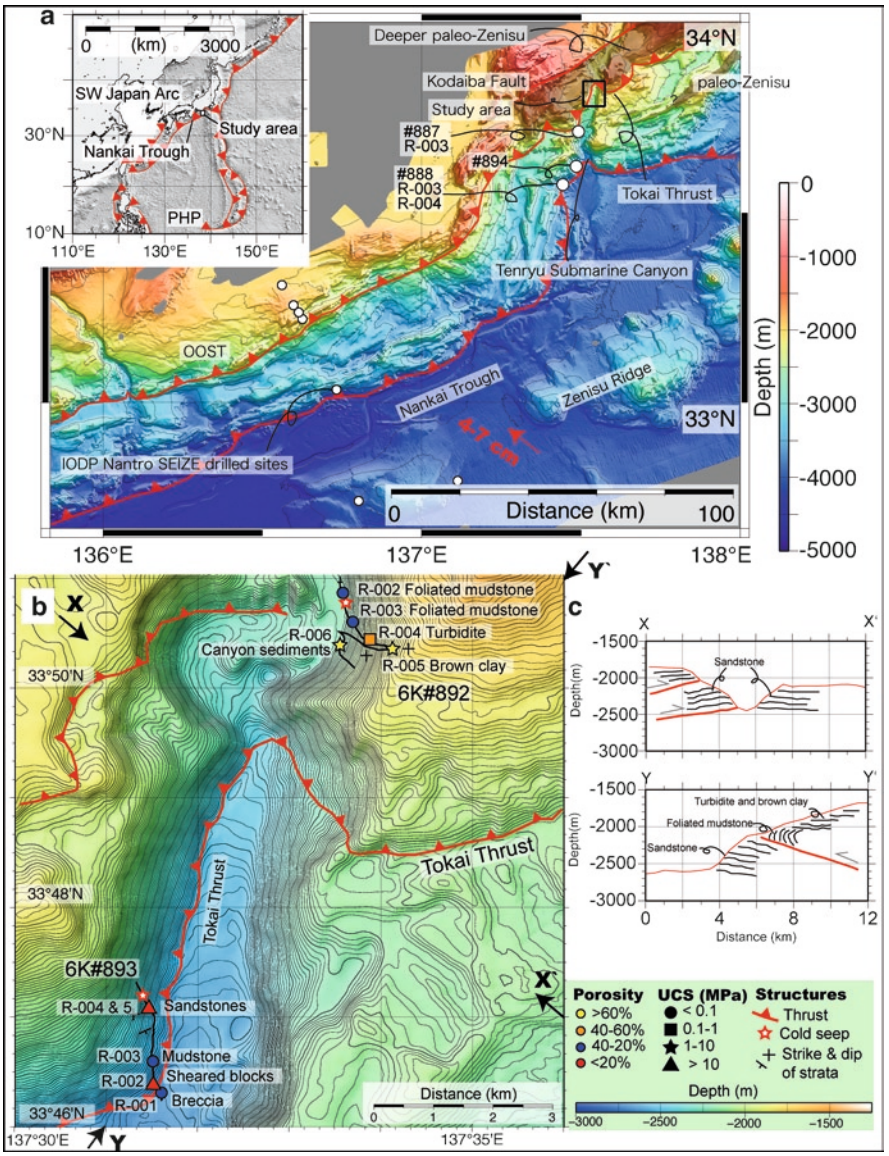

Fig. 1 (**a**) Bathymetric map of the Nankai accretionary prism (NAP) showing the major tectonic elements in the region and the location of our dive survey. Inset map depicts the plate boundaries and the Nankai Trough. The Philippine Sea Plate (PSP) moves to the NNW at 4–7 cm/year. Sediments on the PSP are off-scraped and accreted to the edge of the Southwest Japan Arc to form the NAP. Bathymetric contour interval is 500 m. (**b**) Locations of dive sites visited by the manned submersible *SHINKAI 6500* as part of dives 6K#892 and 6K#893. These surveys targeted the hanging wall of the Tokai Thrust, which is one of the largest out-of-sequence thrust faults within the NAP. The submersible surveyed the sidewalls of the Tenryu Submarine Canyon, which down-cuts through ~1 km of the NAP strata. In the lower slope of the sidewall, down to ca. 300 m from the bottom of the canyon, the strata are steeply dipping and characterized by foliated mudstone and sandstone, whereas in the upper slope the strata are composed mainly of horizontal turbidites. Bathymetric contour interval is 10 m. (**c**) Topographic profiles and schematic structural sections along X–X′ and Y–Y′ in b, based on the results of our dive surveys and the seismic profiles by Mazzotti et al. (2002) and Kuramoto et al. (1999)

(Soh and Tokuyama 2002; Lallemand et al. 1992; Le Pichon et al. 1996; Kodaira et al. 2003; 2004) deforming the repetition of the thrust-anticline architecture.

We have recently performed seafloor geological mappings along the Tenryu Submarine Canyon in the eastern part of the NAP (Fig. 1b) in four separate cruises using the manned submersible *SHINKAI 6500* (hereafter referred to as 6K) operated by the Japan Agency of Marine Science and Technology (JAMSTEC) (Fig. 1a). Because of the deep incision of the Tenryu Canyon ~1 km down into the NAP (Fig. 1b), the deeper parts of the accretionary prism are exposed allowing us to collect rock samples from the outcrops without drilling. The submersible surveys recovered low-grade metamorphic and foliated rocks (foliated mudstone and sandstone) from the Tokai Thrust, which is one of the largest out-of-sequence thrusts (OOSTs) within the prism.

The recovered foliated rocks provide clues to the deformation processes and mechanisms, particularly the exhumation process in the active accretionary prism. In this study, the peak temperatures of the recovered foliated rocks are determined on the basis of illite crystallinity and vitrinite reflectance. Detailed descriptions of the deformation textures, depositional ages estimated from micro- and nannofossils, and physical and mechanical properties of the rocks are provided to enable the reconstruction of the exhumation processes that brought these rocks to the surface. We conclude that the rocks have been rapidly exhumed, later than 0.42 Ma. The processes and mechanisms are discussed in association with the subduction of a ridge or a seamount chain below the eastern NAP. The rapid rate of exhumation can be explained in terms of dual effects of thrusting along the OOST during the paleo-Zenisu ridge collision/subduction, and normal faulting as a result of collapse just behind the passing ridge.

2 Deformed Rocks of the Tenryu Canyon

During the dive survey 6K#892, a sample of foliated mudstone (sample number 6K#892R-002) was collected from the bottom of the Tenryu Canyon (Fig. 1b); the sampling site is located in the hanging wall of the Tokai Thrust. The outcrop of the sample site is approximately 10 m wide and 100 m long, and extends in a N–S direction. Another sample of foliated mudstone (6K#892 R-003) was collected from the lower slope of the eastern sidewall of the canyon (Fig. 1b). The foliation within these rocks strikes N–S and dips ca. 60° to the west (Figs. 1b and 2a, b). Horizontal turbidite (6K#892 R-004) and brown clay (6K#892 R-005) overlie the foliated mudstones (Fig. 1c).

The following three stages of deformation are recognized within the foliated mudstone samples. First, sedimentary layers S_0 are folded tightly by D_1 event to form an axial planar cleavage (S_1 in Fig. 2c, g). Second, flattening deformation (D_2) led to the alignment of recrystallized illite flakes along the slaty cleavage (S_2), developed oblique to the S_1. Third, a release of overburden pressure (D_3) led to the formation of numerous tension fractures (S_3) of several millimeters in spacing subparallel to S_2 (Fig. 2d, h).

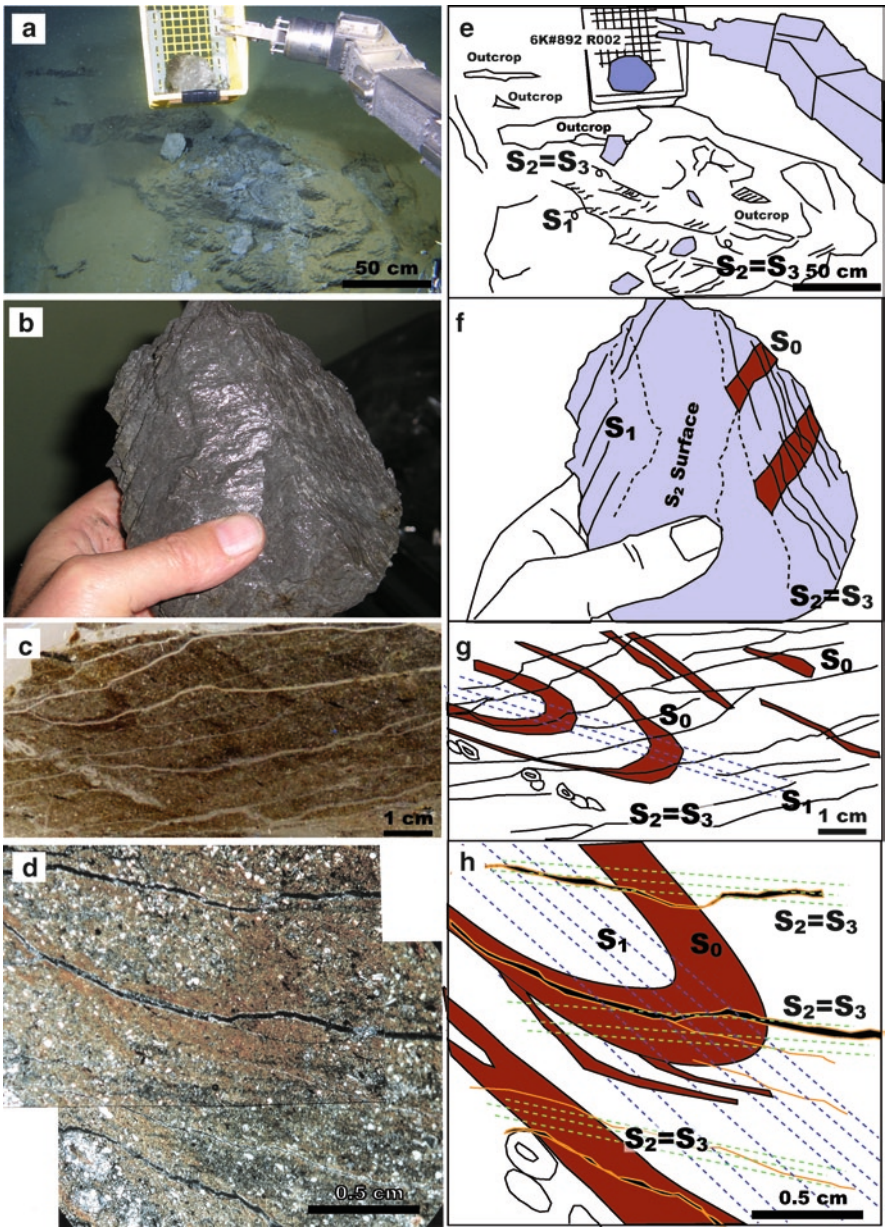

Fig. 2 Deformation structures and textures in analyzed foliated rocks. (**a**) Sea-floor outcrop from which sample 6K#892 R-002 was recovered. (**b**) Slickensides upon tension fracture surfaces in sample 6K#892 R-002. (**c**) Photomicrograph of folded sedimentary layers (S_0) and tension fracture (S_2) in sample 6K#892 R-002. Plane polarized light. (**d**) Photomicrograph of folded sedimentary layers (S_0), alignment of recrystallized illite flakes (S_1), and tension fractures (S_2) in sample 6K#892 R-002. Plane polarized light. Sketches of the photographs (**a**)–(**d**) are shown in (**e**)–(**h**), respectively

During the dive survey 6K#893, sheared blocks that are composed of calcareous silt and fine- to medium-grained sandstones (6K#893 R-002) and massive fine- to medium-grained sandstones (6K#893 R-004 and R-005) were recovered from the middle slope of a western sidewall of the canyon, close to the Tokai Thrust (Fig. 1b). These rocks contain fragments of pumice and plant fossils, and are cut by bifurcating network of faults demarcated by concentration of clay minerals that are strongly aligned parallel to the fault planes. Mudstone (6K#893 R-003) and breccia (6K#893 R-001) (Fig. 1b) in shear zones were also recovered during this dive survey.

During the dive surveys 6K#887 and 6K#888, turbidite samples (sample numbers 6K#887 R-003, and 6K#888 R-003 and R-004) were recovered from the lower slopes of the western walls of the Tenryu Canyon (Fig. 1a). These samples are not well consolidated and have high porosities and low strengths.

3 Ages of Recovered Rocks

We extracted radiolarian microfossils from the foliated mudstone samples 6K#892 R-002. They preserved details of the tests and are characterized by assemblage of rare to moderately abundant radiolarian tests of *Didymocyrtis tetrathalamus, Cycladophora davisiana davisiana, Theocorythium trachelium trachelium, Botryostrobus aquilonaris, Amphirhopalum ypsilon, Thecosphaera dedoensis* and *Collosphaera tuberosa.* On the basis of the obtained radiolarian assemblage, we concluded that the sediments have the *Collosphaera tuberosa* Zone assemblage, ranging in age from 0.42 to 0.18 Ma (middle Pleistocene) according to the timescale by Sanfilippo and Nigrini (1998). The upper limit of the *Collosphaera tuberosa* Zone is defined by the first appearance of *Buccinosphaera inveginata*, that is rather rare in recent sediments. Thus, estimation of radiolarian zone age may extend from 0.42 Ma to recent. The sample 6K#892 R-002 was barren in calcareous nannofossils.

The sample 6K#892R-003 yields calcareous nannofossils characterized by a rare occurrence of *Reticulofenestra Pseudoumbilicus* and *Sphenolithus abies* (identified by the smear slide method), indicating older than the NN15 zone (Martini 1971) as >3.8 Ma (early Pliocene) (Cande and Kent 1995). The calcareous nannofossils in sample 6K#893 R-002 are characterized by *Reticulofenestra* spp. and *Discoaster bergenii*, representing the NN11A zone (Martini 1971) ranging in age from 8.6 to 6.5 Ma (late Miocene) (Cande and Kent 1995). However, no reliable radiolarian ages were obtained from these samples.

A large gap was recognized between the radiolarian zone age obtained from the Sample 6K#892R-002 sample and the nannofossil zone age estimated from the Sample 6K#892R-003, collected just above the former sample. Furthermore, no radiolarian fossil was confirmed in a thin section from the Sample 6K#892R-002. We confirmed the existence of some radiolarian tests along the fractures, indicating that the radiolarian microfossils were not in Sample 6K#892R-002, but were

rather present along the tension fractures (S_3). We further considered that they may have derived from the seafloor during the exhumation by suction during volume expansion due to decompression and/or fault activities. Although we have consumed all 6K#892 R-002 sample for different analyses and there is no way to test our hypothesis.

4 Illite Crystallinity and Vitrinite Reflectance

We measured the illite crystallinity (IC) of the recovered foliated rocks (6K#892 R-002, R-003, and 6K#893 R-003) and other rocks sampled from the seaward parts of the same canyon (6K#887 R-003, 6K#888 R-003, and 6K#892 R-004; see Fig. 1a). The illite crystallinity (IC) value is a useful geothermal indicator for mudstone samples subjected to very low-grade metamorphic conditions (Blenkinsop 1988). The IC value is represented by the Kübler Index (Kübler 1968), which is the half-width (=2θ) of the 10 Å peak of illite (001). The Kübler Index decreases with increasing illite recrystallization because of the thermal dehydration of smectite (Blenkinsop 1988). We used the conversion equations between the obtained IC value (=2θ) and the peak temperatures, which were previously proposed for the Cretaceous–Tertiary Shimanto accretionary prism (Underwood et al. 1993; Mukoyoshi et al. 2009) underlying the present-day NAP (Taira et al. 1988).

$$\mathrm{IC} = 1.197 - (0.0029 \times \mathrm{T}) \quad \text{(Underwood et al. 1993)}$$

$$\mathrm{IC} = 1.7136 - (0.00485 \times \mathrm{T}) \quad \text{(Mukoyoshi et al. 2009)}$$

$$\mathrm{T}: \text{temperature in } ^{\circ}\mathrm{C}$$

The obtained XRD spectra revealed the occurrence of smectite within the analyzed samples, except for sample 6K#892 R-002 (Fig. 3a). We therefore considered that any smectite within sample 6K#892 R-002 were fully recrystallized to illite. This inference is supported by the strong alignment of illite flakes in sample #892 R-002 (Fig. 2d). In contrast, the IC values for the other samples reflect the crystallinity of detrital illite, because most smectite were not converted to illite in the same specimens. The IC value for sample #892 R-002 is 0.62 (Fig. 3a); using conversion equations (see appendix) we estimated the corresponding peak temperatures to be ~200–230°C.

We also assessed the vitrinite reflectance of sample 6K#893 R-004, as this is a useful geothermal indicator for samples that contain organic matter by measurements of mean random reflectance (Rm) of vitrinites (Middleton 1982; Laughland and Underwood 1993). We used the equation by Sweeney and Burnham (1990) for a 1 Ma heating period to estimate the peak metamorphic temperatures as follows:

$$\mathrm{T}(^{\circ}\mathrm{C}) = 174 + \left(93\left[\ln \text{ percentage Rm}\right]\right)$$

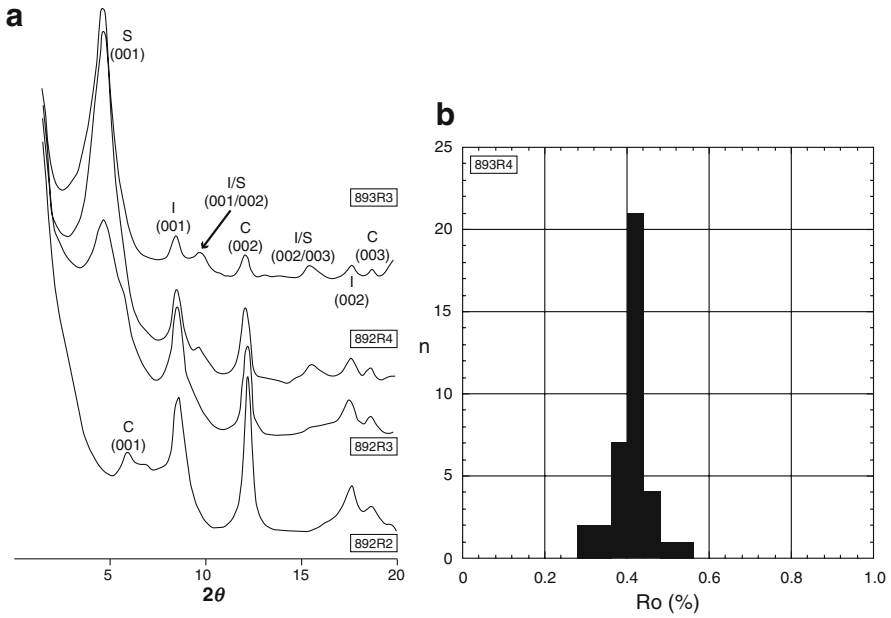

Fig. 3 (**a**) XRD spectra for samples #892 R-002, #892 R-003, #892 R-004, and #893 R-003. Sample #892 R-002 is illite (*I*)-rich and devoid of smectite (*S*) and illite–smectite mixed layers (*I/S*), whereas the other samples contain smectite, chlorite (*C*), and illite–smectite mixed layers. Illite crystallinity value for samples #892 R-002 is 0.62. The peak temperatures recorded by these rocks are estimated to be ~200–230°C. (**b**) Vitrinite reflectance values for the sandstone, sample 6K#893 R-004. The mean and mode for Rm are both 0.4%; this corresponds to peak temperatures of ~90°C. See text for the details

The error associated with Rm–temperature correlations for the Cretaceous–Tertiary Shimanto accretionary prism has been reported as ±30°C (Laughland and Underwood 1993). We obtained an Rm value of 0.4% for 38 analyzed fragments (Fig. 3b); based on conversion equation (see appendix), this value represents a peak temperature of 90°C ± 30°C.

5 Physical-Mechanical Properties of Recovered Rocks

The physical properties of these rocks are summarized in Kawamura et al. (2009). The porosities of samples 6K#892 R-002 and R003 are 25–30%, whereas those of the sandstones (6K#893 R-001, -002 and -004) range from 13% to 30%. In contrast, rocks within undeformed accretionary prisms commonly have porosities around 43–61%. The uniaxial compression strength (hereafter UCS) of the mudstone sample 6K#892 R-003 is measured ca. 5.0 MPa, whereas those of the recovered sandstones are mostly >10 MPa. The strengths of our sandstone samples are

much higher than those of typical prism rocks that range from 1.06 to 1.54 MPa (from 6K#888 R-004 to 6K#887 R-003).

6 Processes of Tectonic Burial and Rapid Exhumation in the NAP

6.1 Burial Conditions

The recovered foliated mudstone and sandstone samples were distributed along the out-of-sequence Tokai Thrust within the eastern NAP. The porosity of these rocks is <30%, and the UCS is >10 MPa. Bray and Karig (1985) estimated the porosity distributions within the western NAP to be >30% based on their measurements of drilled core samples from DSDP Sites 582 and 583. The porosity of <30% in foliated mudstone and sandstone corresponds to a burial depth of > ~0.5 km. The data obtained from drill cores recently recovered at ODP Sites 1175 and 1178 within the western NAP enabled the measurement of a porosity curve with burial depth (Shipboard Scientific Party 2001).

Using this curve and the porosity values for our foliated rocks, we estimated the burial depths of these rocks to be >0.7 km in the NAP. The peak temperatures calculated for our foliated mudstone (sample 6K#892 R-002) and sandstone (sample 6K#893 R-004) are ~200–230°C and 60–120°C, respectively. In the western NAP, the geothermal temperature gradients at the DSDP and ODP Sites were ~50°C/km (Kinoshita and Yamano 1986; Shipboard Scientific Party 2001). Shallow-level geothermal gradients calculated from the depths of methane-hydrate reflectors were ranging from 41 to 66°C/km (Kinoshita and Yamano 1986; Ashi and Taira 1993). Thus, we assumed an average geothermal gradient in the eastern NAP to be 50°C/km, and then estimated the maximum burial depth of the sampled foliated mudstone (6K#892 R-002) to be ~4–5 km, whereas that of the sandstone sample (6K#893 R-004) is ~2 km. These depths are not inconsistent with the maximum burial depths estimated on the basis of the physical properties of the samples. The IC value of the foliated mudstone indicates that it was buried deeper than the up-dip limit of the seismogenic zone (see Hyndman 2004). Such deep burial conditions imply that the sediments deposited at >3.8 Ma were buried to 4 km-deep and then returned to the seafloor against the oceanic plate subducting obliquely at a rate over 40 km/Ma.

6.2 Processes and Mechanism of Rapid Exhumation

Interpretations of a seismic profile (Kodaira et al. 2003) suggest that two separate chains of the E-W trending paleo-Zenisu ridges were subducted beneath the eastern NAP (Fig. 1). The earlier subducted paleo-Zenisu body has been inferred to be

currently located between the Tokai Thrust and the Kodaiba Fault (Soh and Tokuyama 2002; Le Pichon et al. 1996; Kodaira et al. 2003) and ca. 30 km landward of the frontal thrust (Fig. 1b), close to the site from which the present foliated rocks were collected. Thus, we consider that the rapid exhumation documented above is closely associated with collision/subduction of the paleo-Zenisu ridges, as shown by Lallemand et al. (1992), Le Pichon et al. (1996) and Kodaira et al. (2003).

Based on a plausible relative subduction rate for the PHP of 4.0–5.0 cm/year (Seno et al. 1993) or 6.0–7.0 cm/year (Miyazaki and Heki 2001), we infer that the landward limit of the deeper paleo-Zenisu body started to subduct beneath the accretionary prism by 0.75–0.42 Ma as shown in Fig. 4T1. The protolith of the sampled foliated rocks must have been deposited in the Shikoku basin in front of the subducting deeper paleo-Zenisu body at 3.8 Ma. It was subsequently brough to considerable depth (4–5 km) and was then rapidly exhumed from the seismogenic zone. Given this scenario, the vertical exhumation rate might well have been >1.0 cm/year.

Dominguez et al. (2000) conducted sandbox experiments to investigate the effect of seamount collision/subduction on the evolving patterns of accretionary prisms. In the experiment, the accretionary prism body that formed in front of the proceeding seamount was thrust over completely during collision/subduction of the seamount, and was then collapsed onto the trench floor. Although most of the cover sediments above the seamount were sliced and underplated as the décollement zone migrated outboard of the seamount, some of the cover sediments and/or sediments deposited in front of the advancing seamount were subducted more deeply (Fig. 4T2). During the subsequent seamount collision/subduction of the seamount, the frontal sediments were exhumed along the décollement zone with significant shear deformation (Fig. 4T3). After that, normal faulting (landsliding) occurred by large-scale subsidence and uplifting associated with seamount subduction (Fig. 4T4).

The downward slip along the normal fault may have been due to gravitational collapse and could further push the uplifted sediments much faster toward the trench along the OOST, as shown in Fig. 4T4. During dive surveys of 6K#887 and 6K#894, numerous normal faults were observed at the base of the sidewalls of the Tenryu Canyon. Those observations suggest that normal faulting occurred frequently in this region, and might have accelerated the exhumation of the metamorphosed sediments along the OOST.

Deformational textures of the sampled foliated rocks are the best clues to understand the emplacement processes that occurred during accretion and exhumation. The deformation textures within the foliated mudstones record an early phase of ductile deformation (D_1), flattening (D_2), release of confining pressure (D_3), and simple shear deformation features (slickenside on S_3). The ductile deformation (D_1 folds) represent lateral shortening under the unconsolidated state. The S_1 and S_2 foliations (Fig. 2c) indicate low-grade metamorphism and illite recrystallization, and S_3 (Fig. 2d) represents exhumation. The occurrence of lateral shortening, flattening and simple shearing represent progressive deformation and low-grade metamorphism within the NAP (e.g., a décollement zone or an OOST). The tension fractures (S_3; Fig. 2c, d) imply expansion sub-parallel to S_2 during rapid exhumation of the foliated mudstones.

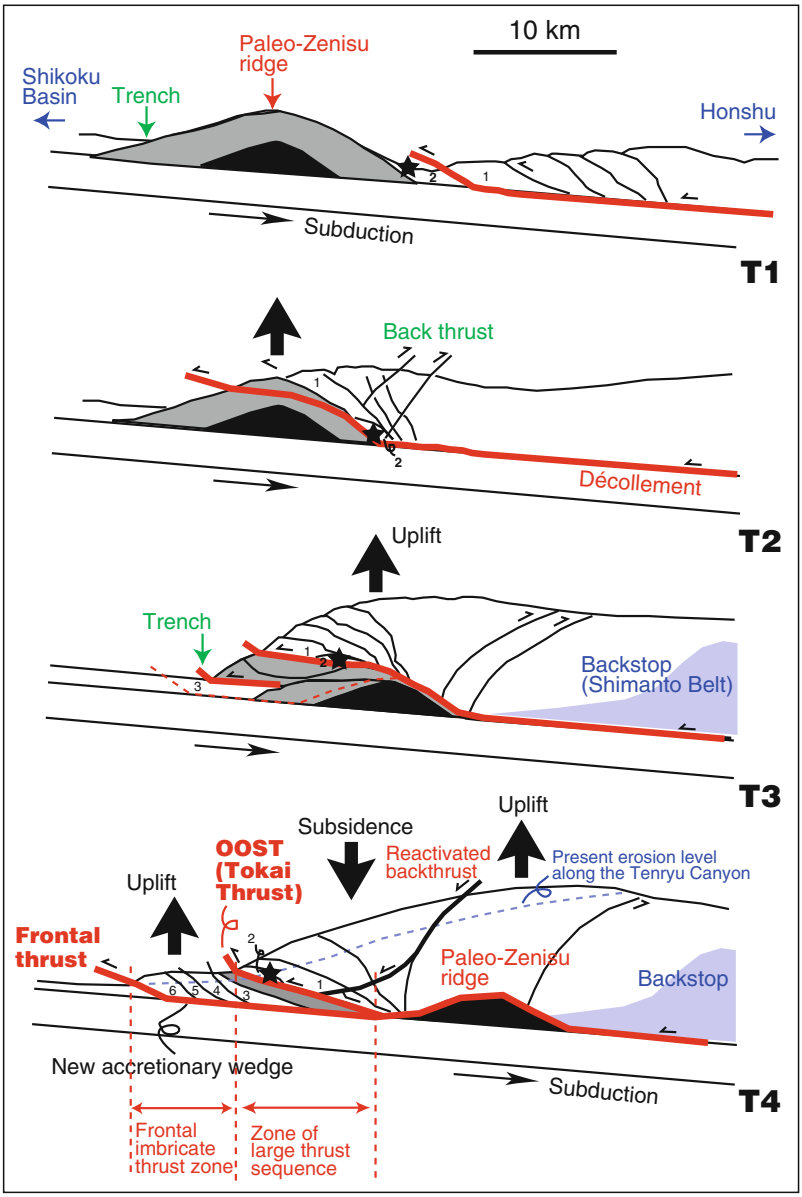

Fig. 4 Tectonic model to explain mechanisms from burial to exhumation through time (Modified after Dominguez et al. 2000) in the eastern Nankai Accretionary Prism. *Solid stars* show location of the protolith of the foliated rocks. (**T1**) The protolith of the foliated rocks was buried into the Nankai prism following the paleo-Zenisu ridge subduction. (**T2**) The buried protolith was accreted to the Nankai prism after the décollement zone was jumped (*broken red line*). (**T3**) The protolith was uplifted by OOST motion. (**T4**) Normal faulting was accelerated the OOST motion

Acknowledgments We gratefully acknowledge the assistance of the captain and his crew of R/V *Yokosuka,* and operation team aboard the submersible *SHINKAI 6500* during YK05-08 Leg. 2. Ms Keiko Fujino provided much help with the heat flow measurement data. Professor Tadashi Sato reviewed an early draft of the manuscript. Part of this study was supported by a Grant-in-Aid from the Ministry of Education, Culture, Sports, Science and Technology of Japan (B-14740295). Critical but constructive and thorough reviews of an earlier version of this paper for GEOLOGY by Tim Byrne, Mike Underwood and John Wakabayashi helped us with our interpretations and improved both the science and organization of work.

References

Ashi J, Taira A (1993) Thermal structure of the Nankai accretionary prism as inferred from the distribution of gas hydrate BSRs. Geol Soc Am Spec Pap 273:137–149

Blenkinsop TG (1988) Definition of low-grade metamorphic zones using illite crystallinity. J Metamorph Geol 6:623–636

Bray CJ, Karig DE (1985) Porosity of sediments in accretionary prisms and some implications for dewatering processes. J Geophys Res 90:768–778

Cande SC, Kent DV (1995) Revised calibration of the geomagnetic polarity timescale for the Late Cretaceous and Cenozoic. J Geophys Res 100:6093–6095

Dominguez S, Malavieille J, Lallemand SE (2000) Deformation of accretionary wedges in response to seamount subduction: insights from sandbox experiments. Tectonics 19:182–196

Hyndman RD (2004) Controls on subduction thrust earthquakes: Downdip changes in composition and state. In: Karner GD, Taylor B, Driscoll NW, Kohlstedt DL (eds) Rheology and deformation of the lithosphere at continental margins. Columbia University Press, New York, pp 166–178

Kinoshita M, Yamano M (1986) The heat flow anomaly in the Nankai trough area. In: Kagami H, Karig DE, Coulbourn WT (eds) Initial reports of the deep sea drilling project 87. U.S. Government Printing Office, Washington, DC, pp 737–743

Kodaira S, Nakanishi A, Park JO, Ito A, Tsuru T (2003) Cyclic ridge subduction at an interpolate locked zone off central Japan. Geophys Res Lett 30:1139. doi:10.1029/2002GL016595

Kodaira S, Hidaka T, Kato A, Park JD, Iwasaki T, Kaneda Y (2004) High pore fluid pressure may cause silent slip in the Nankai trough. Science 304:1295–1298

Kübler B (1968) Evaluation quantitative du metamorphism par la cristallinite de I'llite. Bull Centre Rech Pau-SNPA 2:385–397

Kuramoto S, Okamura Y, Arai K, Murakami F (1999) High resolution multichannel seismic survey in off Tokai area. Geol Surv Jpn Cruise Rep 24:33–50

Lallemand SE, Malavieille J, Calassou S (1992) Effects of oceanic ridge subduction on accretionary wedges: experimental modeling and marine observation. Tectonics 11:1301–1313

Laughland MM, Underwood MB (1993) Vitrinite reflectance and estimates of paleotemperature within the Upper Shikoku Group, Muroto Peninsula, Shikoku, Japan. Geol Soc Am Spec Pap 273:25–43

Le Pichon X, Lallemant S, Tokuyama H, Thoue F, Huchon P, Henry P (1996) Structure and evolution of the backstop in the eastern Nankai trough area (Japan): implications for the soontocome Tokai earthquake. Isl Arc 5:440–454

Martini E (1971) Standard tertiary and quaternary calcareous nannoplankton zo-nation. In: Farinacci A (ed) Proceedings of 2nd planktonic conference, Rome, 1970, Proceedings 2. Tecnoscienza, Rome, pp 738–785

Mazzotti S, Lallemant SJ, Henry P, Le Pichon X, Tokuyama H, Takahashi N (2002) Intraplate shortening and underthrusting of a large basement ridge in the eastern Nankai subduction zone. Mar Geol 187:63–68

Middleton MF (1982) Tectonic history from virtinite reflectance. J Geophys Res 87:121–132

Miyazaki S, Heki K (2001) Crustal velocity field of southwest Japan: subduction and arc-arc collision. J Geophys Res 106:4305–4326

Moore GF, Bangs NL, Taira A, Kuramoto S, Pnagborn E, Tobin HJ (2007) Three-dimensional splay fault geometry and implications for tsunami generation. Science 318:1128–1131

Mukoyoshi H, Hirono T, Hara H, Sekine K, Tsuchiya N, Sakaguchi A, Soh W (2009) Style of fluid flow and deformation in and around an ancient out-of-sequence thrust: an example from the Nobeoka Tectonic Line in the Shimanto accretionary complex, Southwest Japan. Formation of chaotic rock units during primary accretion processes. Isl Arc 18:333–351

Park JO, Tsuru T, Kodaira S, Phil RC, Kaneda Y (2002) Splay fault branching along the Nankai subduction zone. Science 297:1157–1160

Sanfilippo A, Nigrini C (1998) Code numbers for Cenozoic low-latitude radio-larian biostratigraphic zones and GPTS conversion tables. Mar Micropaleontol 33:109–156

Seno T, Stein S, Gripp AE (1993) A model for the motion of the Philippine Sea Plate consistent with Nuvel I and geological data. J Geophys Res 98:941–948

Shipboard Scientific Party (2001) Deformation and fluid flow processes in the Nankai Trough accretionary prism. In: Moore GF, Taira A, Klaus A (eds) Proceedings of the Ocean Drilling Program, scientific results, Leg 190 summary. Ocean Drilling Program, College Station

Soh W, Tokuyama H (2002) Rejuvenation of submarine canyon associated with ridge subduction, Tenryu Canyon, off Tokai, central Japan. Mar Geol 187:203–220

Sweeney JJ, Burnham AK (1990) Evaluation of a sample model of vitrinite reflectance based on chemical kinetics. Am Assoc Petrol Geol Bull 74:1559–1570

Taira A, Katto J, Tashiro M, Okamura M, Kodama K (1988) The Shimanto belt in Shikoku, Japan – Cretaceous to Miocene accretionary prism. Mod Geol 12:5–46

Taira A, Hill IA, Firth J, Party SS (1991) Proceedings of the Ocean Drilling Program, Initial reports, vol 131. Ocean Drilling Program, College Station, 434 pp

Tobin HJ, Kinoshita M (2006) NanTroSEIZE: the IODP Nankai trough seismogenic zone experiment. Sci Drill 2:23–27

Underwood MB, Laughland MM, Kang SM (1993) A comparison among organic and inorganic indicators of diagenesis and low-temperature metamorphism, Tertiary Shimanto belt, Shikoku, Japan. Geol Soc Am Spec Pap 273:45–61

Vrolijk P (1990) On the mechanical role of smectite in subduction zones. Geology 30:155–158

Dark Bands in the Submarine Nankai Accretionary Prism – Comparisons with Miocene–Pliocene Onshore Examples from Boso Peninsula

Yoko Michiguchi and Yujiro Ogawa

Abstract Unique planar structures made of thin, dark bands in host siltstones were described at microscopic scale in samples collected from the Tenryu Canyon in the eastern Nankai accretionary prism. Their mechanisms of formation and tectonic relationships were compared with similar onshore examples from the unmetamorphosed Miocene–Pliocene Miura–Boso accretionary prism. Four modes of occurrences that had been identified previously in onshore rocks were recognized in the submarine rock samples. The dark bands were formed at different stages. Two formed during sedimentation and subsequent burial (i.e., gravity origin), and the other two formed during accretion (i.e., tectonic origin).

Keywords Dark bands • The Nankai accretionary prism • The Miura–Boso accretionary prism • Gravity origin • Tectonic origin

1 Introduction

The Nankai accretionary prism, off Southwest Japan, is regarded as a natural laboratory for studying subduction processes. The eastern Nankai accretionary prism is formed by the subduction of the Philippine Sea plate beneath Southwest Japan and is characterized by active fault zones developed in highly fractured and folded sedimentary rocks,

Y. Michiguchi (✉)
Doctoral Program in Earth Evolution Sciences, University of Tsukuba,
Tsukuba 305-8572, Japan
Current address:
Japan Nuclear Energy Safety Organization, Toranomon 4-3-20, Tokyo 105-0001, Japan
e-mail: y-michi@hotmail.co.jp

Y. Ogawa
The University of Tsukuba, 1-127-2-C-740 Yokodai, Tsukubamirai 300-2358, Japan (home)
e-mail: fyogawa45@yahoo.co.jp

Y. Ogawa et al. (eds.), *Accretionary Prisms and Convergent Margin Tectonics in the Northwest Pacific Basin*, Modern Approaches in Solid Earth Sciences 8,
DOI 10.1007/978-90-481-8885-7_11,

numerous calcite veins, and cold seeps inhabited by chemosynthetic biocommunities (Moore et al. 2007; Kawamura et al. 2008, 2009). Cochonat et al. (2002) and Kawamura et al. (2009) suggested that the Tokai margin of the Eurasian plate was formed by slope failure and mass movements, followed by tectonic accumulation to form the accretionary prism. Thus, it is thought that both tectonic forces and gravitational instability have influenced this region.

During cruises YK05-08 Leg 2 and YK08-E04 of the manned submersible vessel *Shinkai 6500* (hereafter 6K) of JAMSTEC (Japan Agency for Marine Science and Technology), rock specimens were collected from the accretionary prism area along the Tenryu Submarine Canyon, which dissects the eastern Nankai Trough (Figs. 1 and 2). The rock specimens contain dark planar bands, 1 to 10 mm in width, that are oblique or subparallel to bedding planes (Fig. 3). Similar structures have been reported from cores obtained from accretionary prisms during cruises of deepsea drilling, where they were called shear bands or deformation bands. In the Nankai accretionary prism, Lundberg and Moore (1986) described these bands as kink bands. Maltman (1993) reported that they may reflect an early response to bulk prism shortening. Ujiie et al. (2004) interpreted them as compactive shear bands developed under plate convergence stresses.

In the unmetamorphosed Miocene–Pliocene accretionary prism of the southern Boso Peninsula, central Japan (the Miura–Boso accretionary prism), dark bands have been interpreted as healed faults (Ishimaru and Miyata 1991) or as layer-parallel faults formed during accretion (Hanamura and Ogawa 1993; Yamamoto et al. 2000). Michiguchi and Ogawa (2011) classified various dark bands developed in the Miura–Boso accretionary prism into four major types on the basis of distribution, crosscutting relations, and internal texture. As is discussed in more detail later, they suggested that the bands were formed at various stages and in different settings (Figs. 4 and 5); some are of pre-accretion gravitational origin and some formed during accretion (Fig. 6). Such dark bands have been reported only at plate convergent margins and are thought to be tectonic structures, but the mechanism by which the dark bands are formed remains poorly understood.

During the dive survey of 6K, many rock samples containing dark bands of various origins were collected. These structures are common, and it is important to understand the roles they play in the deformational development of the accretionary prism. Aiming to understand their origin, we described the various dark bands from the Nankai prism in detail and compared them with similar onshore structures described by Michiguchi and Ogawa (2011). Based on our classification, we considered possible formation mechanisms and their implications for each dark band sampled from the eastern Nankai accretionary prism.

2 Geological Setting of the Study Area

The Tenryu Submarine Canyon is in the eastern part of the Nankai accretionary prism off central Japan (Fig. 1). The eastern part of the Nankai prism is strongly affected by the Izu–Bonin and Honshu arc–arc collision (Le Pichon et al. 1987;

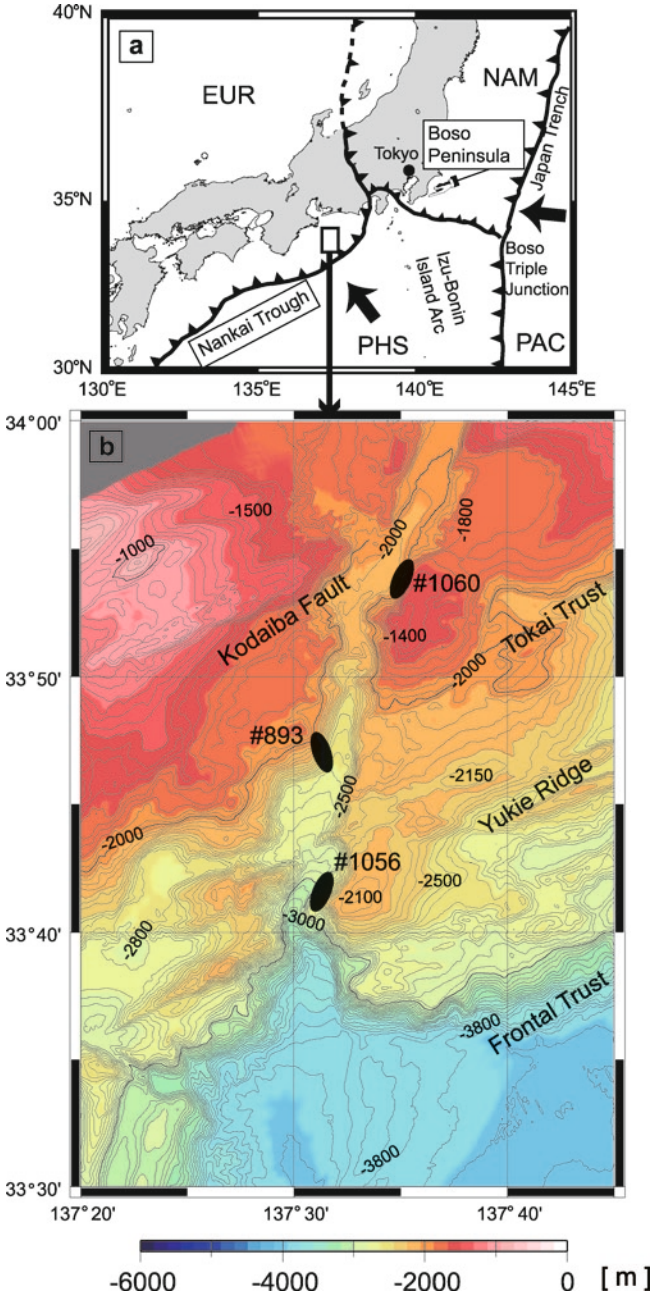

Fig. 1 (**a**) Plate tectonic setting of the Japan region. The Nankai accretionary prism lies along the boundary between the Eurasian and Philippine Sea plates, off the southwestern coast of Japan. (**b**) Bathymetric map of the Tenryu Canyon region overlying the Nankai accretionary prism. *Solid ovals* indicate dive sites

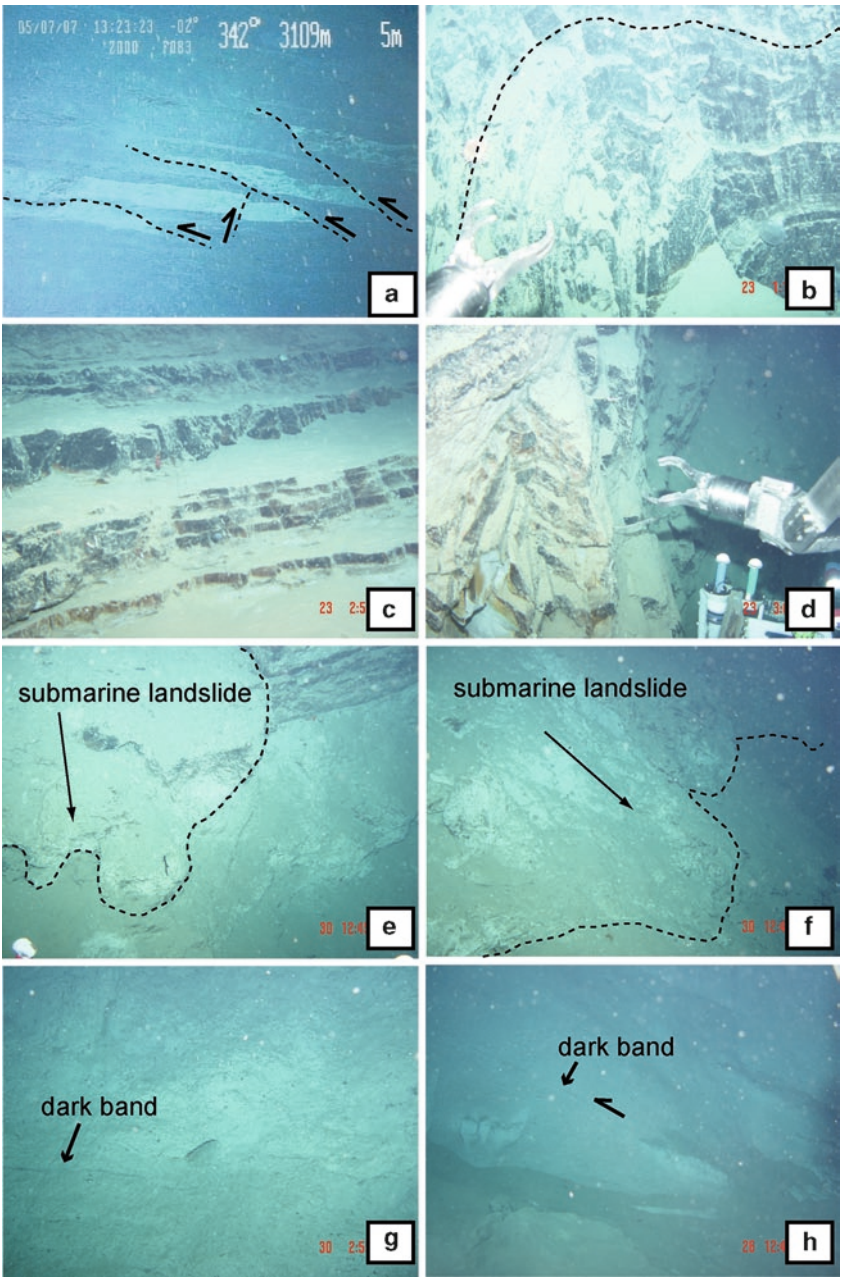

Fig. 2 Photographs of subsea outcrops along the Tenryu Canyon. (**a**) Turbidite layers cut by thrusts (6K#894). *White layers* are tuffaceous siltstone. (**b**) Anticline in a mud-rich tuffaceous siltstone (6K#1056). (**c**, **d**) Subhorizontal turbidite layers (6K#1056). 6K#1056R-6 samples were collected at this location. (**e**, **f**) Submarine landslide deposits partly covering a sandy layer (6K#1060). 6K#1060R-2 samples were collected at this location. (**g**) Dark band developed parallel to bedding planes (6K# 1060). (**h**) Dark band developed along a thrust fault (6K#1058)

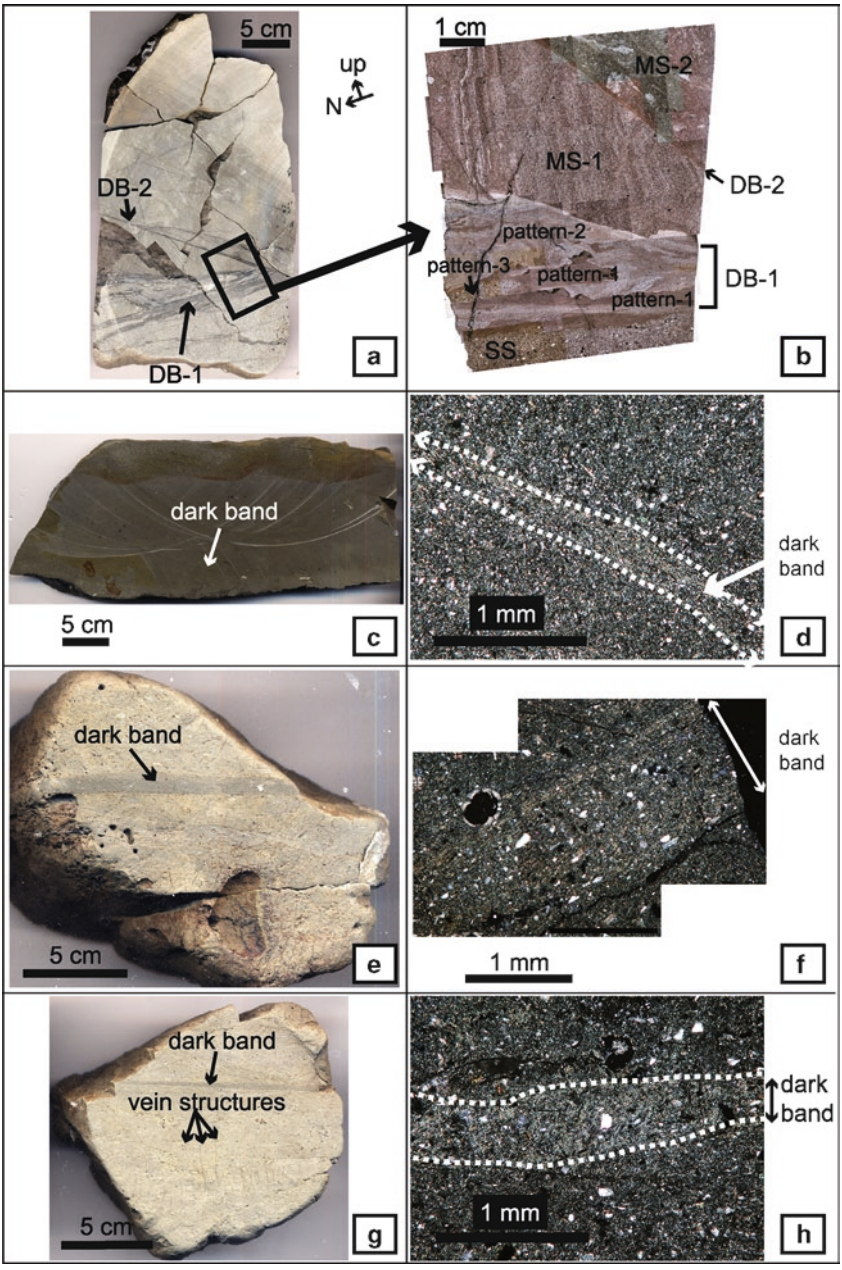

Fig. 3 Sample photos and photomicrographs showing dark bands in samples from the Nankai accretionary prism. The bands are thin (a few to tens of millimeters thick), planar and dark. (**a**, **b**) YK05-08 Leg 2, 6K#893 R-3. (**c**, **d**) YK08-E04, 6K#1056 R6-2. (**e**, **f**) YK08-E04, 6K#1060 R2-1. (**g**, **h**) YK08-E04, 6K#1060 R2-2. YK08-E04 6K#1060 samples also include vein structures

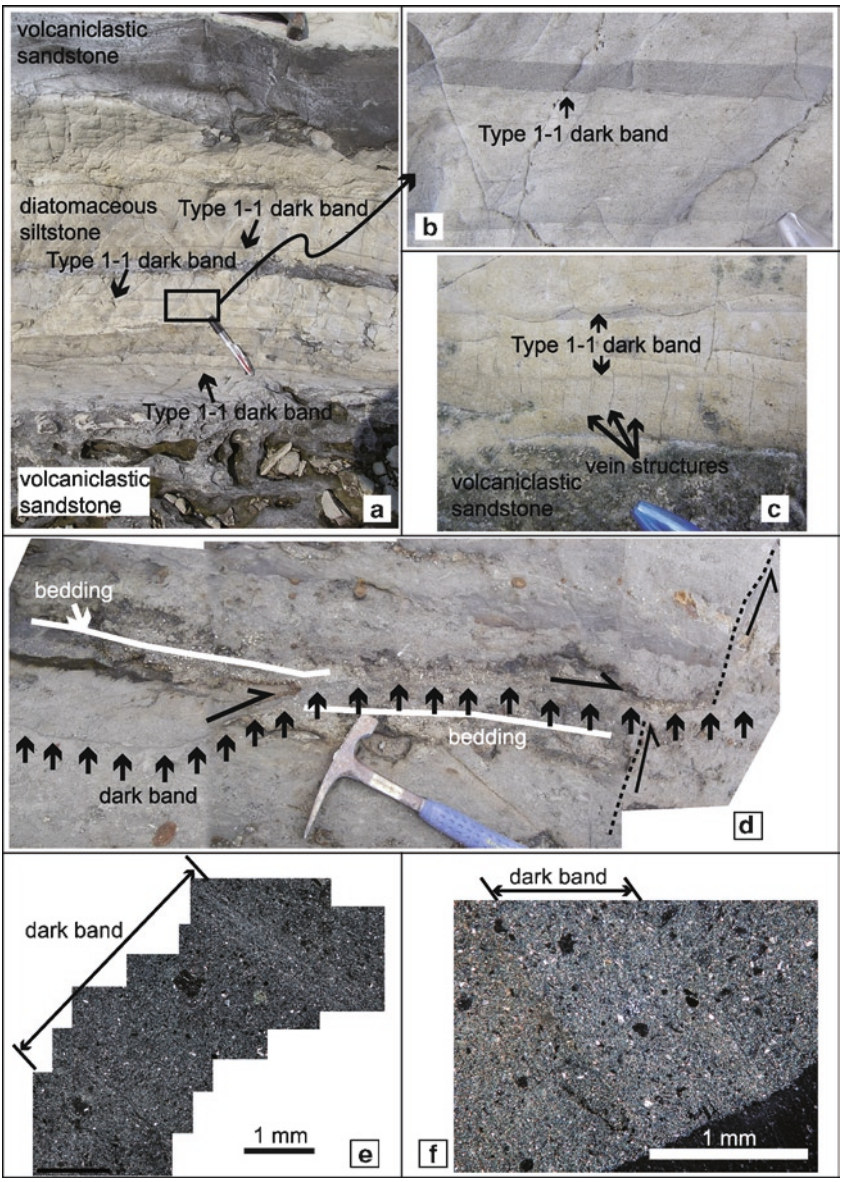

Fig. 4 Outcrop photos and photomicrographs of type 1–1 and 1–2 dark bands from the Boso Peninsula. (**a**–**c**) Outcrop photos of type 1–1: the dark bands are parallel to bedding. Some type 1–1 bands cut vein structures, others are cut by vein structures. (**d**) Outcrop photo of type 1–2: the dark band is subparallel to bedding. Some type 1–2 bands cut across bedding planes. (**e**) Photomicrograph of type 1–1: clay flakes are concentrated and rearranged to form the preferred orientation, in particular, along the boundary between type 1–1 bands and the host rock. (**f**) Photomicrograph of type 1–2: grain alignment in the dark band cuts obliquely across that of the host rock (Modified from Michiguchi and Ogawa (2011))

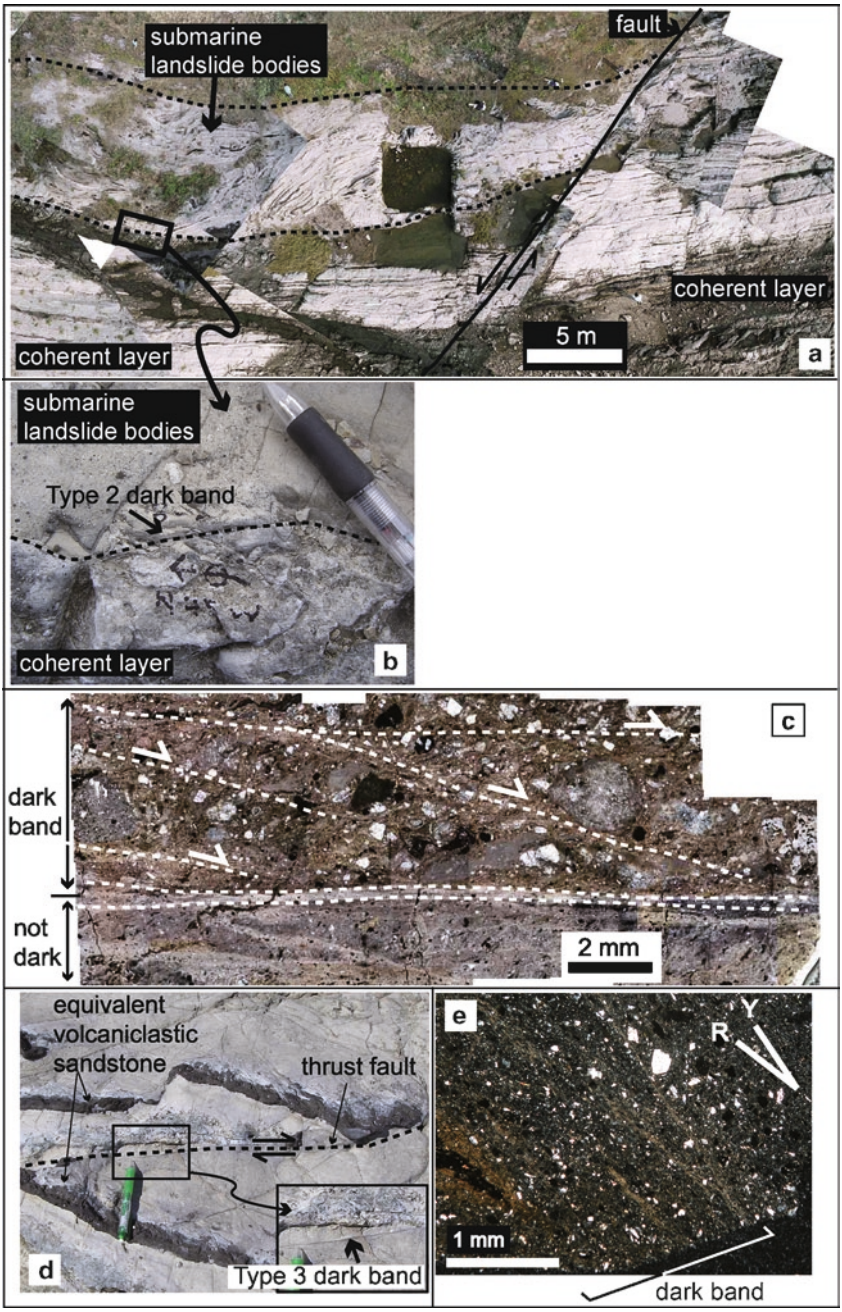

Fig. 5 Outcrop photos and photomicrographs of type 2 and 3 dark bands from Boso Peninsula. (**a**) Aerial photograph showing submarine landslide bodies: type 2 is observed just beneath the submarine landslide body. (**b**) Outcrop photo of type 2: the dark band is in a landslide slide plane. (**c**) Photomicrograph of type 2: the ductile deformation of grains indicates an S-C structure. (**d**) Outcrop photos of type 3: the dark band lies along an accretion thrust (Yamamoto et al. 2000). (**e**) Photomicrograph of type 3: cataclastic grains are observed. Y and R are dominant shear and Riedel shear, respectively (Modified from Michiguchi and Ogawa (2011))

	character	cause	deformation style
Type 1-1	• layer-parallel to bedding • no deformed and crushed grains • flakes of clay minerals are concentrated along the boundary	increase of pore-fluid pressure by burial	independent particulate flow
Type 1-2	• oblique to bedding • no deformed and crushed grains • flakes of clay minerals are distributed pervasively in the dark bands	horizontal tectonic compression during accretion	flexural-slip faults (thrust sense)
Type 2	• under submarine landslide • ductile deformation similar to an S-C' structure	submarine landslides	slide planes of submarine landslides
Type 3	• dislocation bedding • inside grains are strongly sheared	horizontal tectonic compression during accretion	thrust faults with Riedel shears

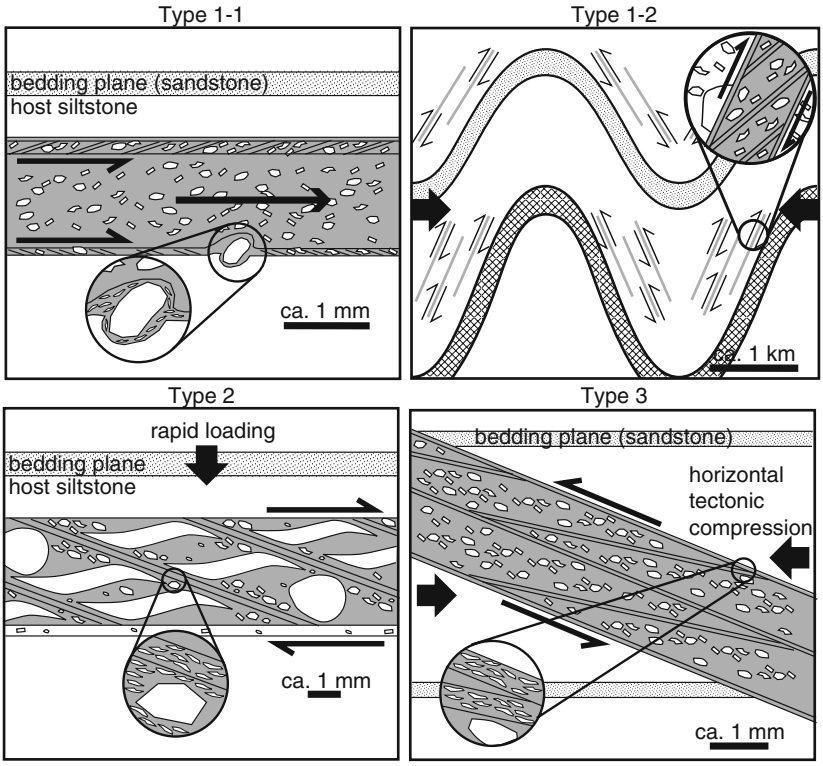

Fig. 6 Classification and formation mechanisms of the dark bands on Boso Peninsula (After Michiguchi and Ogawa (2011)). Type 1–1 was formed by an increase of pore pressure resulting from low permeability or liquefaction caused by earthquake shaking during deposition. This causes independent particulate flow. Type 1–2 corresponds to a flexural-slip fault where, under the extreme compression of accretion, frictional sliding on the fault is replaced by cataclastic deformation. Type 2 is formed under normal consolidation conditions in the slip plane of a submarine landslide. Type 3 occurs when, under the extreme compression associated with accretion, the frictional sliding on a thrust fault is converted to cataclastic deformation

Cochonat et al. 2002; Mazzotti et al. 2002). It is characterized by multiple intraplate shortenings and by recurrent earthquakes (Le Pichon et al. 1987). The Tokai Thrust (Fig. 1) is one of the largest subhorizontal out-of-sequence thrusts within the Nankai prism (Ashi et al. 2002; Mazzotti et al. 2002; Kawamura et al. 2009). In addition, the eastern Nankai prism is characterized by a steeper slope than the Kumano region which is just on the study area (Cochonat et al. 2002). In the eastern Nankai prism, large-scale gravitational sliding is common, particularly between the Kodaiba Fault and the Tokai Thrust (Cochonat et al. 2002; Kawamura et al. 2009, 2011 Chapter 10). The Tenryu Submarine Canyon cuts the geologic architecture between the Kodaiba Fault and the Tokai Thrust (Figs. 1 and 2). Therefore, the side walls of the Tenryu Canyon show the vertical and lateral changes in intraprism geologic architecture (Kawamura et al. 2009, 2011 Chapter 10).

3 Occurrence of Samples and Dark Bands

The samples described in this study were collected by the 6K from three sites in the Tenryu Canyon during cruises YK05-08 Leg 2 and YK08-E04 (Fig. 1). Several representative samples are described below.

3.1 6K#893 R-3

During cruise YK05-08 Leg 2, sample 6K#893 R-3 was collected from the Tokai Thrust zone (Fig. 1). This sample includes dark bands in two zones: DB-1 and DB-2 (Fig. 3a). The sample is composed of sandstone (SS), mudstone-1 (MS-1), and mudstone-2 (MS-2; Fig. 3b). DB-1 is a boundary between SS and MS-1, and DB-2 is between MS-1 and MS-2. MS-1 and MS-2 have similar lithofacies and include similar fine elongate grains and radiolarian fossils (Fig. 3b). However, the attitudes of the DB-1 and DB-2 bedding planes are different.

DB-1 is about 10 mm wide, whereas DB-2 is only a few mm wide. DB-1 and DB-2 are parallel to the SS and MS-2 bedding planes, respectively. Both bands are oblique to the bedding plane of MS-1 (Fig. 3a, b). The upper and lower surfaces of DB-2 are sharply defined and straight, whereas DB-1 has an undulating upper surface. Because DB-2 cuts DB-1, DB-1 was formed before DB-2.

3.2 6K#1056 R6-2, 6K#1060 R2-1 and R2-2

During YK08-E04, three samples including dark bands were collected: 6K# 1056 R6-2 (Fig. 3c), 6K#1060 R2-1 (Fig. 3e), and 6K#1060 R2-2 (Fig. 3g). Dive 6K#1056 was on the eastern wall of the Tenryu Canyon, south of the Tokai Thrust and west of the Yukie Ridge (Kawamura et al. 2008; Fig. 1). There is a broad

syncline in this area, which may have formed in response to the combined effects of accretionary processes and seamount subduction or collision (Kawamura et al. 2008). 6K#1056 R6-2 was collected from the southern limb of the syncline. The dark bands in the sample are a few mm thick.

Dive 6K#1060 was over the hanging wall of the Tokai Thrust (Fig. 1), where there are several small-scale cliffs about 10 m high on a gentle slope (Kawamura et al. 2008). 6K#1060 R2-1 and −2 were collected from step-like outcrops of bedded siltstone layers that continue from 1,800 to 1,600 m water depth (Kawamura et al. 2008). The bands in both samples are up to 5 mm thick, and both samples include vein structures (Fig. 3g).

4 Internal Structure of the Dark Bands

In this section, the dark bands are described on the basis of observations by polarized and scanning electron microscopes (SEM).

4.1 DB-1 in 6K#893 R-3

The alignment and size distribution of silt-size grains (hereafter grains) and micaceous clay mineral flakes (hereafter clay flakes) within DB-1 (Fig. 7a) of this sample show three distinct patterns (Figs. 3b and 7). Pattern 1 is a homogeneous structure without grains. Pattern 2 contains grains of <0.1 mm that are aligned subparallel to the general direction of the DB-1 bands. Pattern 3 is only observed in SS and is characterized by various grain types (quartz and feldspar) and glass shards of >0.2 mm in random fabric.

Pattern 1 in DB-1 (Fig. 7b) is characterized by several planar structures composed of aggregated clay flakes. These structures are observed along the boundary between DB-1 and SS. The clay flakes have two preferred orientations, one parallel to and the other oblique to the direction of DB-1 (Fig. 7d–g), the latter being correspondent to a Riedel shear.

The grain and clay flake arrangement of Pattern 2 is indicative of fluid flow (Fig. 7b). The constituent minerals are the same as those in the host SS, although the grains and clay flakes are smaller than those in the host rock. There is no evidence of cataclastic or plastic deformation of the constituent grains. The clay flakes are concentrated along the boundaries between the two lithofacies (Fig. 7d–g).

X-ray diffraction (XRD) analysis for SS, DB-1, and MS-1 indicated that SS, DB-1, and MS-1 have similar mineral compositions (Fig. 8e), with strong quartz peaks. Only MS-1 has weak peaks for calcite, which indicates that MS-1 has undergone a small amount of calcite cementation. The clay flakes are composed mainly of smectite, illite, and chlorite. Smectite is richer in DB-1 than in the other two

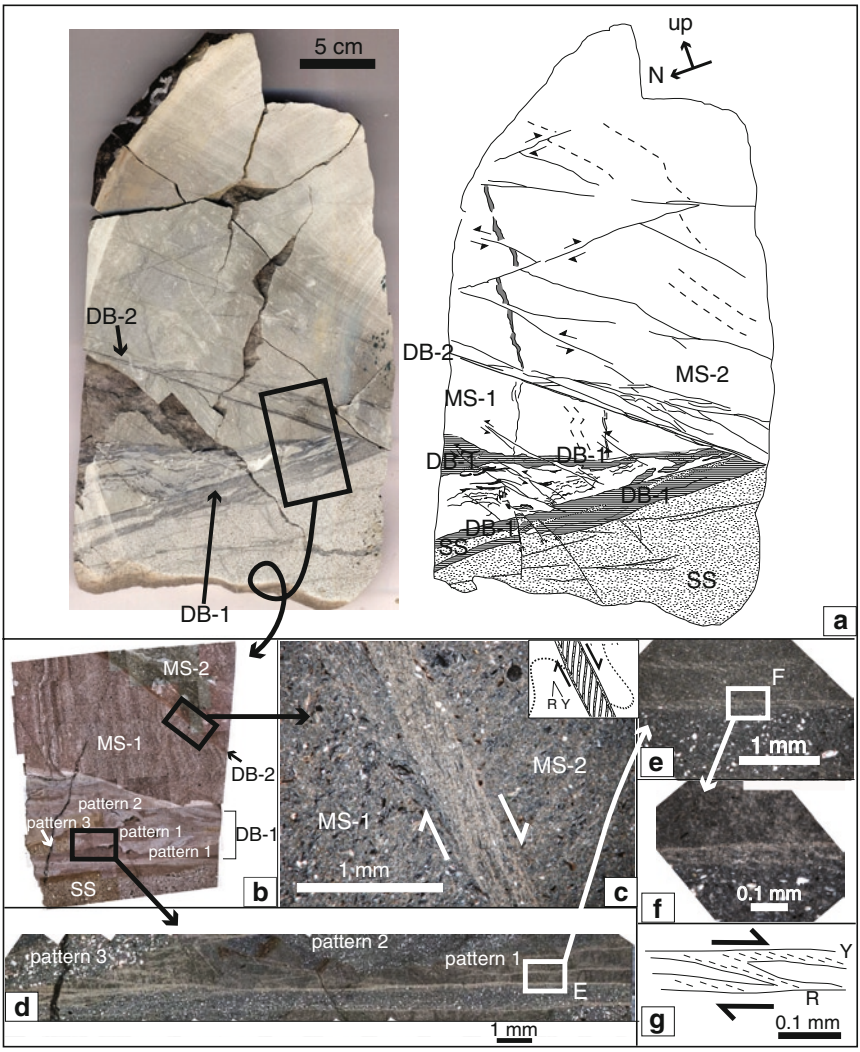

Fig. 7 (**a**) Cut-section photo and sketch of the 6K#893 R-3 sample. In the sketch, the *arrow* shows slip direction and the dotted lines are bedding planes. (**b**) Photomicrograph around DB-1 and DB-2 (open nicols). DB-1 is at the boundary between SS and MS-1, and is divided into three patterns (see text). DB-2 is between MS-1 and MS-2. MS-1 and MS-2 are the same lithofacies, but the attitudes of the bedding planes are different. (**c**) Photomicrograph around DB-2 (crossed nicols). MS-1 and MS-2 show drag at the DB-2 boundaries. Additionally, Riedel shear is observed in DB-2. (**d**) Photomicrograph around DB-1 (crossed nicols) in which shear planes are developed. (**e**, **f**) Photomicrographs of the boundary between DB-1 and SS: particles are arrayed in two directions, indicating right-lateral displacement, as shown in (**g**)

samples (Fig. 8e). The boundaries between DB-1 and SS or MS-1 are sharp at mesoscopic scale, but they are obscured at the microscopic scale of the SEM (Fig. 8a, b). Scaly clay flakes were observed in places on the boundary between SS and DBN-1 and in DB-1.

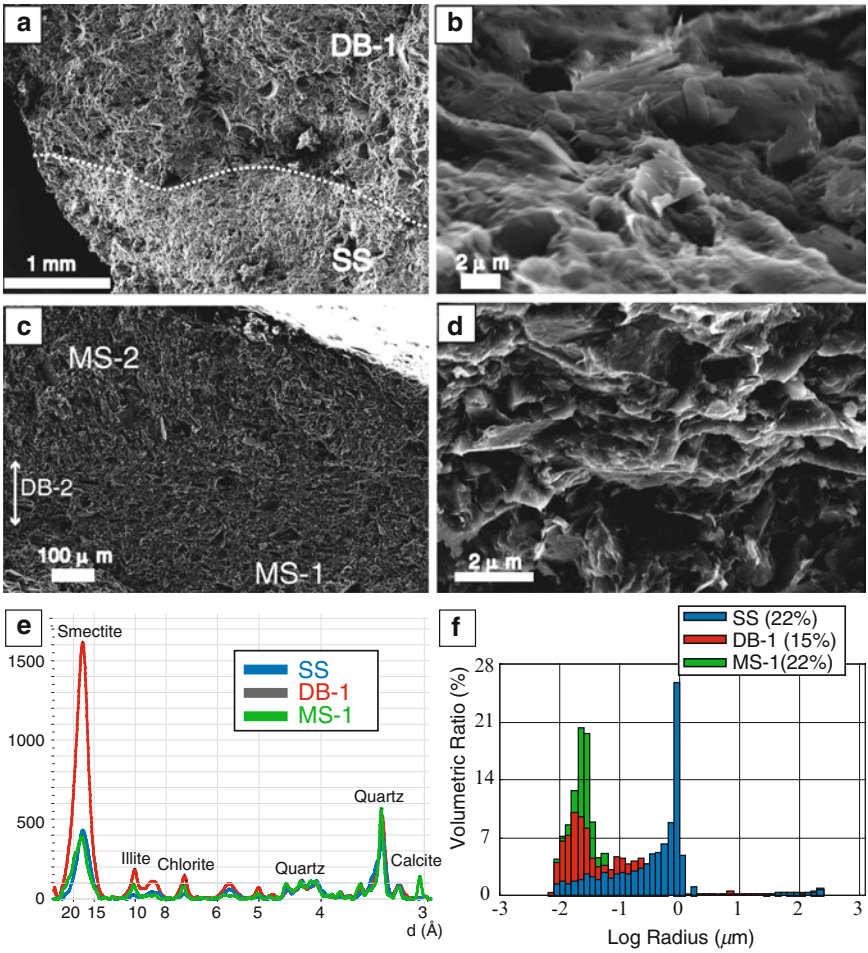

Fig. 8 (**a**–**d**) SEM images of dark bands from sample 6K#893 R-3. (**a**) Based on grain size differences, we can differentiate DB-1 and SS. DB-1 is less granular than SS. (**b**) Scaly particles (probably smectite) are observed at the margin between DB-1 and SS. (**c**) A difference in particle arrangement in DB-2 and MS-1 or −2 is observed around DB-2. (**d**) Deformed clay particles at the boundary between DB-2 and MS-2. Based on XRD analysis, the clay particles are smectite. (**e**) XRD analysis of clay minerals in MS-1, DB-1, and SS after ethylene-glycol treatment. (**f**) Porosity and pore size distributions of MS-1, DB-1, and SS (measured by mercury intrusion porosimeter)

The porosities of SS and MS-1 in the sample are all about 22%, whereas the porosity of DB-1 is about 7% lower (Fig. 8f). Computer tomography (CT) images also show that the density of DB-1 is higher than that of the host rocks. A porosity reduction such as this can be caused by dehydration and/or compression because the void space collapses as clay flakes assume the preferred orientation (Hirono 2005).

4.2 DB-2 in 6K#893 R-3

DB-2 in 6K#893 R-3 is developed between MS-1 and MS-2 (Fig. 7a). The SEM images show that clay-size minerals are also concentrated in DB-2 (Fig. 8d). The alignment pattern of clay flakes in DB-2 indicates Riedel shear (Fig. 7c). Furthermore, foliation in MS-1 and MS-2 is dragged along the DB-2 boundaries. These results clearly show that DB-2 is a shear band of right-lateral displacement at the band surfaces (Fig. 7c). DB-1 has two or three shear planes within the dark band, but DB-2 represents a single shear plane. SEM images show that the constituent grains have undergone ductile deformation, with the long axes oblique to the foliation of both MS-1 and MS-2 (Fig. 8c, d), suggesting Riedel shear.

4.3 6K #1056 R6-2

In thin sections, alignment of the constituent grains in this dark band is oblique to that in the host rock, although clay flakes are arranged in a preferred orientation subparallel to the bedding plane (Fig. 3d). Under crossed nicols, clay flakes are developed pervasively in the band. SEM images indicate that the constituent grains, including smectite, along the boundary between the host rock and the dark band are sheared. The above observation supports the interpretation that the dark band was formed by dehydration or compression similar to that shown by DB-1 in 6K#893 R-3. CT images show that the density inside the dark band is higher than that of the host rocks.

4.4 6K#1060 R2-1

In thin sections, the grain size inside the band of this sample is almost the same as the host rock (Fig. 3f). Various grains and radiolarian microfossils in the dark band are undeformed. Clay flakes are strongly aligned parallel to the band boundaries. SEM images show scaly flakes of clay similar to those in DB-1 in 6K#893 R-3.

4.5 6K#1060 R2-2

Thin section analysis under crossed nicols shows that pervasive clay flakes have been newly formed in the dark band (Fig. 3h). SEM images show that the constituent grains along the band boundaries are sheared. Clay flakes (probably smectite) are observed along the boundary.

5 Comparison with the Miura–Boso Accretionary Prism and Formation Processes and Mechanisms of the Dark Bands

5.1 Characteristics of the Dark Bands of the Miura–Boso Accretionary Prism

We previously classified the dark bands in the rocks of the Miura–Boso accretionary prism into four major types on the basis of distribution, crosscutting relations, and internal texture: 1–1 (independent particulate flow; Figs. 4 and 6), 1–2 (flexural-slip faults; Figs. 4 and 6), 2 (sliding planes caused by submarine landslides; Figs. 5 and 6), and 3 (thrust faults; Figs. 5 and 6). The occurrence, internal structure, and formation mechanism of each type were explained in detail by Michiguchi and Ogawa (2011) (Fig. 9). They are briefly described below.

Type 1–1 dark bands developed parallel to bedding planes (Figs. 4a–e) without any crushed or deformed grains within the bands (Fig. 4e). They are not original sedimentary structures, unlike the sedimentary laminae. Instead, they show evidence of independent particulate flow caused by the generation of excess pore-fluid pressure, which occurred within the bed just after sedimentation (Fig. 6). Type 1–2 developed parallel to bedding planes, but the constituent grains in the band are aligned oblique to those in the host rock (Fig. 4d, f). Many bands of types 1–2 are found in fold limbs and in sheared strata exhibiting thrust-sense dislocation. These indicate flexural-slip faults formed during folding (Fig. 6).

Type 2 is distributed immediately beneath a submarine landslide body and includes ductilely deformed grains (Fig. 5a), which are similar to those of an S-C′ structure (Fig. 5b, c). Type 2 bands are observed in the slide planes of submarine landslides (Fig. 9). Type 3 is characterized by cataclastic grains (Fig. 5d, f) and is developed along thrust faults formed during accretion (Fig. 9).

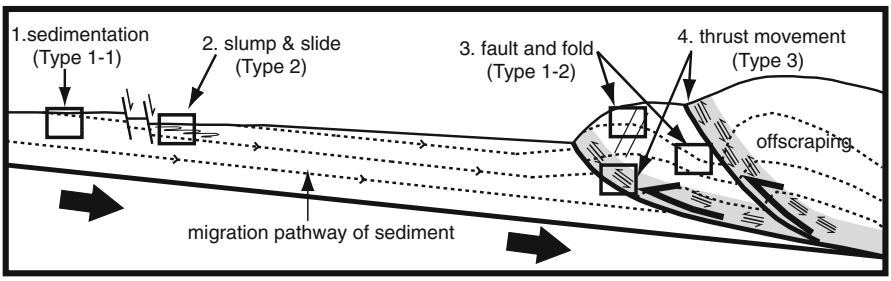

Fig. 9 Four stages of formation of the dark bands (Modified from Michiguchi and Ogawa (2011)). Type 1–1 shows evidence of independent particulate flow caused by high pore-fluid pressures that occurred during sedimentation (stage 1). Type 1–2 shows flexural-slip faults formed during folding in the accretionary prism (stage 3). Type 2 shows slide planes formed during submarine landslides (stage 2). Type 3 shows thrust faults formed during accretion (stage 4)

All of the dark bands represent shear bands or slip planes that formed after sedimentation and possibly during accretion, although the amount of dislocation varies for the different types of band. The physical properties of the dark bands (e.g., permeability and degree of consolidation) reflect the deformation processes and the magnitude of stress during their formation. In the following sections, we use the above classification system to categorize dark bands in the Nankai samples.

5.2 DB-1 in 6K#893 R-3

MS-1 and MS-2 are characterized by many radiolarian microfossils and by calcite cementation (Fig. 8), but SS hardly included calcite. Thus, the boundary between MS-1 and SS appears to post-date calcite cementation.

DB-1, the boundary between SS and MS-1, is divided into three patterns based on the differences in grain alignment and grain size (Fig. 7b). Pattern 1 abuts SS with some shear zones in which Riedel shears are developed. This internal structure is similar to type 2 of the Miura–Boso accretionary prism (Fig. 4). Flakes of smectite are concentrated along and within the shear zones.

Pattern 2 is found at the boundary between DB-1 and MS-1, but this boundary is not sharp in thin section. There is flow deformation along the boundary, and the constituent grains are not strongly crushed and deformed (Fig. 7d). This deformation mode indicates independent particulate flow without shearing of grains (Borradaile 1981; Rawling and Goodwin 2002), implying that DB-1 was formed under unlithified or semi-lithified conditions.

Michiguchi (2008) proposed that the slide plane of the submarine landslide corresponds to the type 2 dark band because the internal structures are similar to those of type 2. Cochonat et al. (2002) reported that submarine sliding occurred in the hanging wall of the Tokai Thrust at the dive site of 6K#893. We suggest that DB-1 conforms to this theory because submarine landslides are common along Tenryu Canyon. The sliding direction is from N to S, as determined from the Riedel shear pattern, indicating that the submarine landslide occurred on the landward slope (Fig. 1). These results suggest that gravitational collapses occurred progressively in the hanging wall of the thrust.

5.3 DB-2 in 6K#893 R-3

DB-2 is characterized by Riedel shears (Fig. 6c). Foliations along DB-2 are dragged, and DB-2 cuts DB-1, indicating that DB-2 was formed after DB-1. Internal structures within DB-2 are very similar to those in the type 3 bands of the southern Boso Peninsula (Fig. 6). SEM images show that the constituent grains of DB-2 are strongly deformed and obliquely aligned to the strain alignment in the

host rock (Fig. 8). Based on the tectonostratigraphic relationships, we interpret that DB-2 formed as a result of compressive stresses, such as those associated with thrusting.

5.4 6K#1056 R6-2

The clay flakes in this dark band are dominantly in two preferred orientations. Grains and clay flakes are oblique to the bedding place trace. Thus, in addition to the SEM observation that the constituent grains along the boundary of the dark band were sheared, it is suggested that this boundary is attributable to faulting. Additionally, CT images show that the density of the dark band is higher than that of the host rocks. These properties correspond to the type 1–2 and 3 bands from the southern Boso Peninsula.

In the area of dive 6K #1056 there is a broad syncline, whose formation was attributed by Kawamura et al. (2009, 2011) to the combined effects of accretionary processes and seamount subduction or collision. Thus, the dark band in 6K#1056 R6-2 may be related to the formation of this syncline and it may have been subjected to similar flexural-slip movement to that of the type 1–2 band (Fig. 6).

5.5 6K#1060 R2-1

For this sample: (1) the grain size in the dark band is almost the same as in the host rock, (2) the constituent grains have a preferred sub-horizontal orientation, (3) the dark bands include many undeformed grains and radiolarians, and (4) clay flakes are concentrated near the boundaries of the bands (Fig. 3f). These dark bands result from independent particulate flow. Therefore, the characteristics of the dark bands in 6K#1060 R2-1 are similar to those of the type 1–1 band of the Boso Peninsula (Fig. 6) and are interpreted to be of gravity origin.

5.6 6K#1060 R2-2

The dark band in 6K#1060 R2-2 is characterized by sheared grains and the alignment of clay flakes (Fig. 3h). It is similar to the type 1–2 and 3 bands of the Boso Peninsula.

Although this sample was collected from a location close to 6K#1060 R2-1 (for which the bands were formed by gravitational processes), the dark band in 6K#1060 R2-2 was formed by tectonic processes. Thus, the sediments in the accretionary prism in the region of this site have been affected by both gravitational and tectonic forces.

6 Summary and Conclusions

We investigated dark bands in fine-grained sedimentary rocks in the Nankai accretionary prism and compared them to similar bands in rocks from the Boso Peninsula. Dark bands found on the Boso Peninsula had previously been classified into four types: 1–1 (independent particulate flow), 1–2 (flexural-slip faults), 2 (slide planes of submarine landslides), and 3 (thrust faults). We confirmed that types 1–1, 1–2, 2, and 3 are also present in the Nankai accretionary prism. Before this study, the dark bands from the Nankai accretionary prism were attributed only to the tectonic effects of accretionary processes. However, the results presented here clearly show that some of those dark bands were formed by gravitational forces, such as submarine landslides (Fig. 9).

Several deformation structures in the Miura–Boso and Nankai accretionary prisms were found to have similar permeabilities and degrees of consolidation, and to have been subjected to stresses of similar magnitudes during their formation.

Our detailed study of the outcrops and textures in rocks from these two accretionary prisms has improved our understanding of the geologic forces that have formed the two regions.

Acknowledgments We thank Dr. Kiichiro Kawamura, chief scientist on board submersible vessel *Shinkai 6500* during cruises YK05-08 Leg 2 and YK08-E04, for his help and support. Sincere gratitude is also extended to Captains Sadao Ishida (YK05-08 Leg 2) and Shinya Ryono (YK08-E04) and their crews. Reviews by Drs. Kohtaro Ujiie and Ryo Anma are greatly appreciated.

References

Ashi J, Kuramoto S, Morita S, Tsunogai U, Goto S, Kojima S, Okamoto T, Ishimura T, Ijiri A, Toki T, Kudo S, Asai S (2002) Structural and cold seep of the Nankai accretionary prism off Kumano – outline of the off Kumano survey during YK01-04 Leg 2 Cruise. JAMSTEC J Deep Sea Res 20:1–8

Borradaile GJ (1981) Particulate flow of rock and the formation of cleavage. Tectonophysics 72:305–321

Cochonat P, Cadet JP, Lallemant JS, Mazzotti S, Nouze H, Fouchet C, Foucher PJ (2002) Slope instabilities and gravity processes in fluid migration and tectonically active environment in the eastern Nankai accretionary wedge (KAIKO-Tokai'96 cruise). Mar Geol 187:193–202

Hanamura Y, Ogawa Y (1993) Layer-parallel faults, duplexes, imbricate thrust and vein structures of the Miura Group: key to understanding the Izu fore-arc sediment accretion to the Honshu forearc. Isl Arc 3:126–141

Hirono T (2005) The role of dewatering in the progressive deformation of a sandy accretionary wedge: constraints from direct imagings of fluid flow and void structure. Tectonophysics 397:261–280

Ishimaru K, Miyata Y (1991) Morphology of shear planes in soft sediments – effects of compaction load and sediment composition. J Geol Soc Jpn 97:713–727

Kawamura K, Anma R, Nakamura A, Maruoka T, Burmeister CK, Heyman WN, Yamada Y, Michiguchi Y, Muraoka S, Suzuki T, Shimizu T, Miyakawa A, Yamada K, Minamizawa S (2008) On board report of YK08-E04. YOKOSUKA cruise report YK08-E04: 126 p

Kawamura K, Ogawa Y, Anma R, Yokoyama S, Kawakami S, Dilek Y, Moore G, Hirano S, Yamaguchi A, Sasaki T, YK05–08 Leg 2 and YK06–02 Shipboard Scientific Parties (2009) Ongoing formation of the Nankai accretionary prism: direct observations via a submersible survey along the Tenryu Submarine Canyon. Geol Soc Am Bull 121:1629–1646

Kawamura K, Ogawa Y, Hara H, Anma R, Dilek Y, Kawakami S, Chiyonobu S, Mukoyoshi H, Hirano S, Motoyama I (2011) Rapid exhumation of subducted sediments along an out-of-sequence thrust due to seamount subduction followed by gravitational collapse in the active eastern Nankai accretionary prism. Accretionary Prisms and Convergent Margin Tectonics in the Northwest Pacific Basin. In: Ogawa Y et al. (ed), Modern Approaches in Solid Earth Sciences 8, Springer Science+Business Media B.V. doi:10.1007/978-90-481-8885-7_10

Le Pichon X, Iiyama T, Boulegue J, Chavet J, Faure M, Kano K, Lallement S, Okada H, Rangin C, Taira A, Urabe T, Uyeda S (1987) Nankai Trough and Zenisu Ridge: a deep-sea submersible survey. Earth Planet Sci Lett 83:285–299

Lundberg N, Moore JC (1986) Macroscopic structural features in Deep Sea Drilling Project cores from forearcs. Geol Soc Am Mem 166:13–44

Maltman AJ (ed) (1993) The geological deformation of sediments. Chapman and Hall, London, 362 p

Mazzotti S, Lallemant SJ, Henry P, Le Pichon X, Tokuyama H, Takahashi N (2002) Intraplate shortening and underthrusting of a large basement ridge in the eastern Nankai subduction zone. Mar Geol 187:63–88

Michiguchi Y (2008) Formation process and mechanism of chaotic blocks in the Nishizaki formation of the southern Boso Peninsula. J Geol Soc Jpn 114:461–473

Michiguchi Y, Ogawa Y (2011) Implication of dark bands in Miocene–Pliocene accretionary prism, Boso Peninsula, central Japan. Geol Soc Am Spec Pap 480: (in press)

Moore GF, Bangs NL, Taira A, Kuramoto S, Pangborn E, Tobin HJ (2007) Three-dimensional splay fault geometry and implications for tsunami generation. Science 318:1128–1131

Rawling GC, Goodwin LB (2002) Cataclasis and particulate flow in faulted, poorly lithified sediments. J Struct Geol 25:317–331

Ujiie K, Maltman AJ, Sanchez-Gomez M (2004) Origin of deformation bands in argillaceous sediments at the toe of the Nankai accretionary prism, southwest Japan. J Struct Geol 26:221–231

Yamamoto Y, Ohta Y, Ogawa Y (2000) Implication for the two-stage layer-parallel faults in the context of Izu forearc collision zone – examples from the Miura accretionary prism, central Japan. Tectonophysics 325:133–144

Gas Chemistry of Pore Fluids from Oomine Ridge on the Nankai Accretionary Prism

Tomohiro Toki, Kenji Maegawa, Urumu Tsunogai, Shinsuke Kawagucci, Naoto Takahata, Yuji Sano, Juichiro Ashi, Masataka Kinoshita, and Toshitaka Gamo

Abstract Pore fluids were sampled from a sediment core acquired at a seepage site at Oomine Ridge in the Nankai accretionary prism, and dissolved gases in the pore fluids were concurrently extracted with an onboard vacuum system. Gas concentrations of gas samples were higher than those of fluid samples, suggesting the gas

T. Toki (✉)
Department of Chemistry, Biology and Marine Science, Faculty of Science, University of the Ryukyus, 1, Senbaru, Nishihara, Okinawa 903-0213, Japan
e-mail: toki@sci.u-ryukyu.ac.jp

K. Maegawa and U. Tsunogai
Earth and Planetary System Science, Faculty of Science, Hokkaido University, N10 W8, Kita-ku, Sapporo 060-0810, Japan
e-mail: maegawa@mail.sci.hokudai.ac.jp; urumu@mail.sci.hokudai.ac.jp

S. Kawagucci
Precambrian Ecosystem Laboratory (PEL), Japan Agency for Marine-Earth Science and Technology (JAMSTEC), 2-15 Natsushima, Yokosuka 237-0061, Japan
e-mail: kawagucci@jamstec.go.jp

N. Takahata and Y. Sano
Atmospheric and Marine Analytical Chemistry Group, Department of Chemical Oceanography, Atmosphere and Ocean Research Institute, The University of Tokyo, 5-1-5, Kashiwanoha, Kashiwa, Chiba 277-8564, Japan
e-mail: ntaka@aori.u-tokyo.ac.jp; ysano@aori.u-tokyo.ac.jp

J. Ashi
Department of Ocean Floor Geoscience, Atmosphere and Ocean Research Institute, The University of Tokyo, 5-1-5, Kashiwanoha, Kashiwa, Chiba 277-8568, Japan
e-mail: ashi@aori.u-tokyo.ac.jp

M. Kinoshita
Institute for Research on Earth Evolution (IFREE), Japan Agency for Marine-Earth Science and Technology (JAMSTEC), 2-15, Natsushima, Yokosuka 237-0061, Japan
e-mail: masa@jamstec.go.jp

T. Gamo
Marine Inorganic Chemistry Group, Department of Chemical Oceanography, Atmosphere and Ocean Research Institute, The University of Tokyo, 5-1-5, Kashiwanoha, Kashiwa, Chiba 277-8564, Japan
e-mail: gamo@aori.u-tokyo.ac.jp

Y. Ogawa et al. (eds.), *Accretionary Prisms and Convergent Margin Tectonics in the Northwest Pacific Basin*, Modern Approaches in Solid Earth Sciences 8,
DOI 10.1007/978-90-481-8885-7_12, © Springer Science+Business Media B.V. 2011

sampling greatly reduced the effect of degassing. Air contamination was assessed using noble gases and was negligible. Profiles of isotopic compositions of CH_4 and ΣCO_2 were strongly consistent between fluid and gas samples, suggesting that the vacuum extraction procedure was successful. Distribution of δD_{H2} values was consistent with control of hydrogen by fermentation and oxidation of sulfate and carbonate. The relationship of $^3He/^4He$ and $^4He/^{20}Ne$ ratios suggested that He composition can be explained by simple mixing of primordial mantle He, radiogenic crustal He, and atmospheric He. When corrected for the atmospheric He component, the helium in the samples is almost entirely of radiogenic origin. The samples represent fluids discharged through a splay fault from the plate boundary, but the contribution of mantle He was very low. It is clear that crustal He pervasively mixed into the fluids from sediment and crust surrounding the pathway of the discharging fluid.

Keywords Seepage • Pore fluid • Nankai Trough • Oomine Ridge • Gas chemistry • Hydrogen • Helium

1 Introduction

Pore fluids in surface sediments of the deep seafloor originate from seawater prior to burial. Early diagenesis takes place in the surface sediments, causing reactive components to migrate to the pore fluids from sediments. Particularly at seepage areas, advective fluids bear chemical components with different compositions from those of the pore fluids in the surface sediments. We investigated the distribution of chemical components in the surface sediments from a seepage site at Oomine Ridge in the Nankai accretionary prism and inferred the origin and pathway of the advective fluids.

H_2, one of the most reactive of these components, plays an important role in microbial diagenesis in anoxic sediments (e.g., ZoBell 1947). However, quantifying its concentration is difficult because of its great reducing power and high diffusivity. With conventional procedures, hydrogen in sediment samples escapes through degassing and air contamination occurs during sampling and storage. Moreover, hydrogen must be reliably sampled to acquire information from its isotopic composition. We succeeded in extracting hydrogen and other gases dissolved in pore fluids by squeezing sediments with the newly designed vacuum extraction.

We used chemical and isotopic compositions of CH_4 and H_2 in pore water to consider the origin, diagenesis, and transport of pore fluids, and used compositions of noble gases in pore water to investigate the origin and nature of the pathway of seeping fluid. In this way, we demonstrated that gas chemistry of extracted pore water, combined with conventional pore-water chemistry, sheds light on the reductive/oxidative conditions of the in situ environment and its transition with increasing depth to provide information on in situ geochemical processes of biochemical and tectonic relevance.

2 Sampling

Oomine Ridge is on the Nankai accretionary prism, which is constructed by accretion of sediment from the subducting Philippine Sea plate (Fig. 1a). On Oomine Ridge, deep-sea chemoautosynthesis-based faunal communities, consisting of tube worms and bacterial mats, have been observed by several explorations at a depth of 2,530 m. They indicate the existence of seeping fluid containing H_2S or CH_4, and they support prolific benthic communities. Chemical analyses of pore water have led to the postulation that lateral input of groundwater is the source of these fluids (Toki et al. 2004).

During the KY04-11 cruise (5 Sept to 2 Oct 2004) of R/V *Kaiyo* (JAMSTEC), a sediment sample was obtained with a piston corer (4 m length) at the seepage site (PC08: 33°7.32′N, 136°28.75′E), as shown in Fig. 1b. The piston corer was deployed on a Navigable Sampling System (NSS) belonging to the Ocean Research Institute, University of Tokyo. The NSS consists of a transponder, four thrusters, a TV camera, and a trigger for a corer and is controlled from the tender ship. The recovered length of the sediment in the core of PC08 was 268.5 cm. The core was composed of homogeneous sandy silt containing layers of gravelly sand. The lowest part of the core, about 265 cm below the seafloor (cmbsf), contained a carbonate clast about 5 cm in diameter.

Subsamples of sediments for gas extraction were taken as quickly as possible after recovery (to avoid degassing and air contamination) using an onboard vacuum system illustrated schematically in Fig. 2. First, 3.4-cm holes were drilled in the side of the inner tube at 30, 80, 130, and 180 cm from the core bottom. A 50-mL stainless steel cylinder was inserted through the holes into the core sediment, then the sediment in the cylinder was transferred into a stainless steel syringe with filter for squeezing. A plunger was held fixed in the syringe with a double O-ring seal, and the nozzle of the syringe was sealed by a check valve (Swegelok, SS-4H) with no headspace. The check valve was connected to a stainless steel line, through which pore water was transferred to a 54-cm^3 evacuated stainless steel container with amide sulfuric acid and $HgCl_2$ by compressing the sediment sample in the syringe with a stainless steel vice (Manheim 1968). The retrieved pore water in the container was degassed by ultrasonication and reaction with amide sulfuric acid to convert all dissolved carbonates to CO_2 gas and then reacted with $HgCl_2$ to deposit H_2S as HgS. The gas phase in the container was transferred to an evacuated stainless steel vessel of 50-mL capacity, where it was stored for analysis on shore. The liquid phase was filtered and sampled into a 50-cm^3 polypropylene bottle for measurement of gas concentrations in pore water, which is calculated on the assumption that gas is dissolved in the liquid phase of pore water.

Pore water from other sediment samples was retrieved into sample bottles by standard handling described by Tsunogai et al. (2002) and using procedures and equipment described by Manheim (1968). About 2 cm^3 of the retrieved pore water was immediately transferred to a 3-cm^3 vial with amide sulfuric acid and $HgCl_2$ as a preservative against microbial activity, and the vial was capped with a butyl rubber

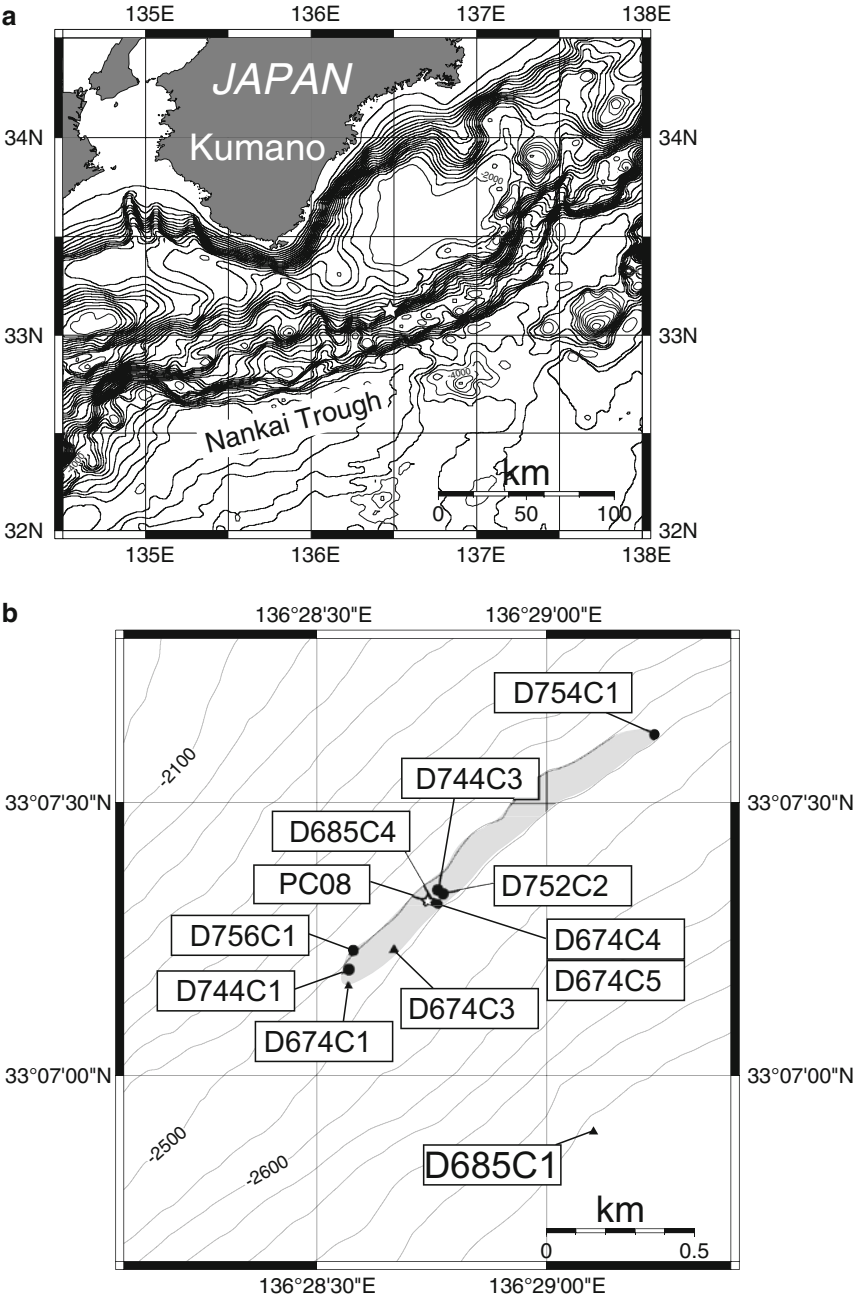

Fig. 1 (**a**) Map showing Oomine Ridge in the Nankai Trough. Oomine Ridge (*star*) is located at 33°7.32′N, 136°28.75′E. (**b**) Map showing the sites of cores from Oomine Ridge used in this study, together with the sampling sites of Toki et al. (2004). Contour interval is 50 m. *Shaded area* represents the area where we observed many bacterial mats scattered at intervals of several hundred meters at water depths ranging from 2,500 to 2,550 m. *Star* show the position where the core sample was taken in the present study (PC08). *Circles* denote the positions where core samples include low-Cl fluids in the sediments, but not triangles, as described in detail in Toki et al. (2004)

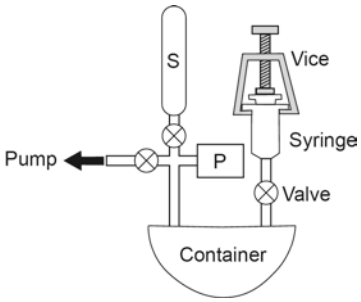

Fig. 2 Schematic diagram of onboard gas-extraction system showing pressure gauge (*P*) and sample bottle (*S*)

septum for subsequent shore-based analysis of dissolved CH_4 and total carbon dioxide (ΣCO_2) for reference of gas samples. The remaining fluid was preserved in a polypropylene bottle for measurements of major cations and anions as well as isotopic analyses of pore water. All samples were refrigerated in the dark and kept at 4°C until analysis.

3 Analysis

Immediately after collection, the pore-water samples in the polypropylene bottles were analyzed for silica, ammonium, and alkalinity (Gieskes et al. 1991). For the silica determination, the samples were diluted fivefold and analyzed by the silicomolybdate colorimetric method (Strickland and Parsons 1968). Ammonium content was determined by spectrophotometry of phenol blue (Solorzano 1969). Alkalinity was measured by potentiometric titration (Dyrssen and Sillen 1967; Edmond 1970).

Concentrations of major elements including cations (Na, Mg, and Ca) and anions (Cl and SO_4) were measured with an ion chromatograph after appropriate dilutions at Hokkaido University (Tsunogai and Wakita 1995). Isotope analyses of carbon were made on a Finnigan MAT-252 mass spectrometer at Hokkaido University. For measurements of isotopic composition and concentration of CH_4, the samples were prepared by cryogenic removal of CO_2 and oxidation of CH_4 with cupric oxide at 960°C, then introduced into the mass spectrometer (Tsunogai et al. 2002). Analytical precision was 6.5% for concentration and 0.3‰ for isotopic determinations.

Hydrogen concentration was measured with a reduction gas analyzer at Hokkaido University (Konno et al. 2006). Hydrogen isotopic composition of H_2 was determined using a continuous flow isotope ratio mass spectrometer system at the Ocean Research Institute, University of Tokyo (Kawagucci et al. 2010). Gas samples were injected into the analytical system through a pre-evacuated stainless steel line and carried by ultrapure He through gas chromatograph columns. H_2 in the injected gas was separated from the other gas species and introduced into the isotope ratio mass spectrometer (Thermo Finnigan, DELTA^{XP}). Analytical precision was estimated to be 5‰.

The oxygen isotopic ratio of water was measured on an aliquot of 100 μl, which was equilibrated with 0.5 mg reagent $NaHCO_3$ for 12 h at 25°C, and a headspace gas of 15 μl was injected into a mass spectrometer (Ijiri et al. 2003). All samples were measured at least twice, and analytical precision was 0.1‰. Hydrogen isotopic composition of water was measured using an aliquot of 2 μl, which was reduced to H_2 on zinc pellets at 470°C. The reduced H_2 was desorbed and its isotopic composition was measured by a mass spectrometer (Coleman et al. 1982). Analytical precision was 1‰. Isotope compositions are reported as δ values relative to the PDB standard for carbon and oxygen (Craig 1957) and the SMOW standard for hydrogen (Craig 1961), where

$$\delta = \left(R_{\text{sample}} / R_{\text{standard}} - 1\right) \times 1{,}000‰, \quad (1)$$

with R being the respective isotope ratios $^{13}C/^{12}C$, $^{18}O/^{16}O$, and D/H.

$^3He/^4He$ ratios were measured with a high-precision mass spectrometer (VG5400) at the Ocean Research Institute following the procedure described by Sano et al. (2006). About 0.5 cm^3 STP of gas sample was introduced into a metallic high-vacuum line. He and Ne were purified using hot Ti-Zr getters and activated charcoal traps held at 77 K. Abundance ratios of $^4He/^{20}Ne$ were determined by a quadrupole mass spectrometer installed in the purification line. Then, He was separated from Ne using a cryogenic charcoal trap held at 40 K, and the $^3He/^4He$ ratios were measured statically with a branch tube mass spectrometer. Resolving power of about 550 at 5% peak height was attained for complete separation of the ^3He beam from the H_3 and HD beams. Observed $^3He/^4He$ ratios were calibrated using the atmospheric He standard. The standard deviation of the $^3He/^4He$ ratio was less than 1%, and that of the $^4He/^{20}Ne$ ratio was estimated to be about 10%.

4 Results and Discussion

4.1 Quality of Extracted Gas

The analytical results are shown in Figs. 3 and 4. The novelty in this study is gas extraction from pore water by an onboard vacuum system. Gas concentrations in gas samples were higher than those in fluid samples (Fig. 4a, b), suggesting that the gas sampling could minimize degassing. Figure 4d, e show that profiles of isotopic composition of CH_4 and ΣCO_2 in pore water are reasonably congruent with those of the fluid and gas samples. It suggests that the degassing process does not critically affect isotopic compositions, and the vacuum extraction procedure adopted in this study yields results that are compatible with conventional methods.

Air contamination can be assessed by using compositions of noble gases (Fig. 5). The isotopic ratio of upper mantle-derived He and Ne, $(^4He/^{20}Ne)_m$, is 1×10^3 (Lupton

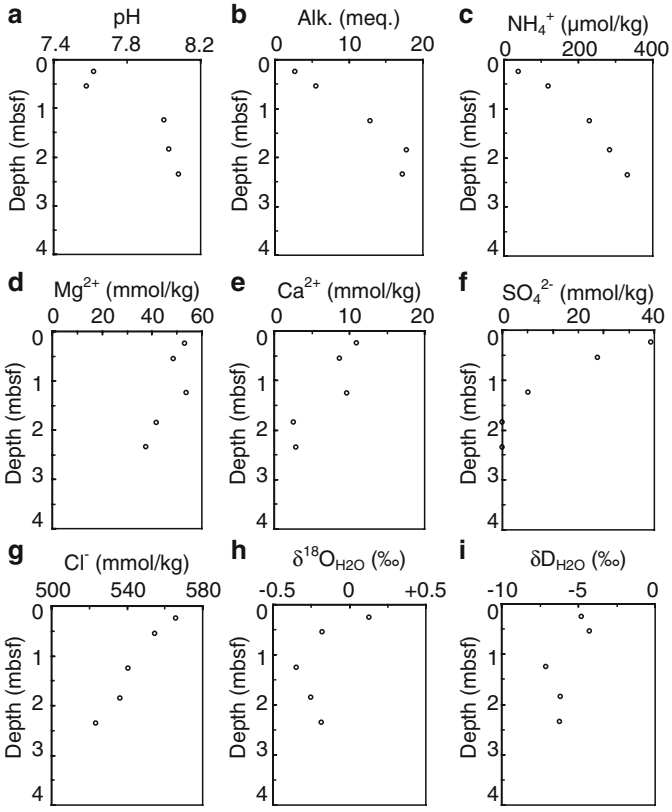

Fig. 3 Chemical and isotopic compositions of pore water from Oomine Ridge

and Craig 1975; Craig and Lupton 1976; Rison 1980), as is the radiogenic crustal ratio, $(^4He/^{20}Ne)_c$ (Morrison and Pine 1955). The atmospheric ratio, $(^4He/^{20}Ne)_a$, is 0.25. Because the $^4He/^{20}Ne$ ratios of radiogenic and mantle He are much larger than that of atmospheric He dissolved in seawater, it is possible to correct atmospheric He components as follows (Craig et al. 1978):

$$r = (^4He / {}^{20}Ne)_a / (^4He / {}^{20}Ne)_{obs}, \quad (2)$$

where $(^4He/^{20}Ne)_{obs}$ is the observed $^4He/^{20}Ne$ ratio. The r value is useful to evaluate the air contamination, and in our samples we obtained r values from 0.011 to 0.052, indicating negligible contamination, corresponding to 1.1% and 5.2%.

Therefore, the data for gas samples are sufficiently reliable and closely reflect in situ chemical composition, thanks to our effort to avoid degassing. We rely on the data from gas samples in discussing concentrations and isotopic data from fluid samples as complementary information.

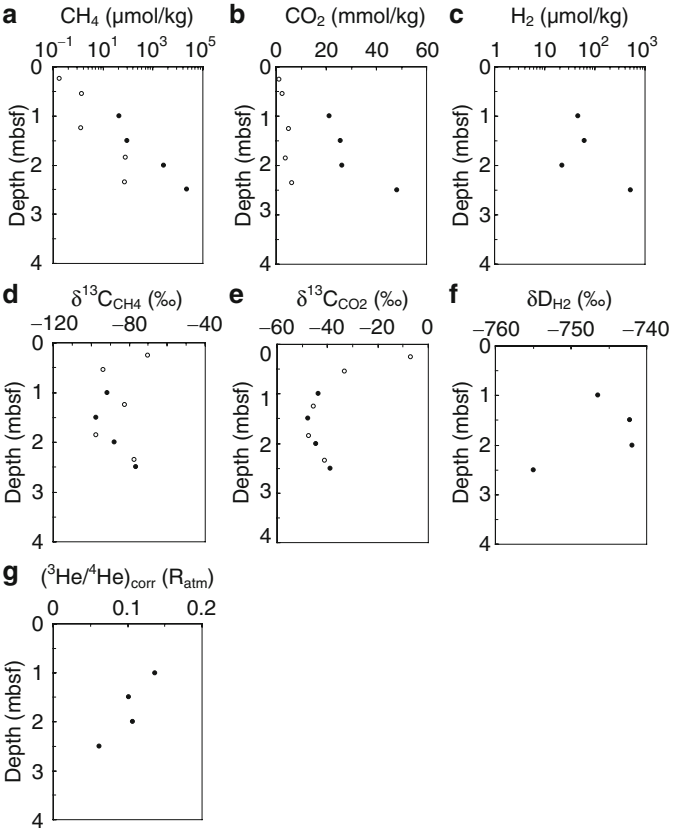

Fig. 4 Chemical and isotopic compositions of dissolved gases in pore water from Oomine Ridge. *Open symbols* denote water samples and *solid symbols* denote gas samples

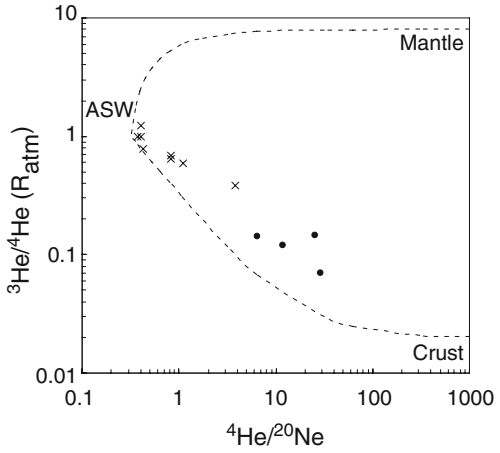

Fig. 5 Plot of $^{3}He/^{4}He$ and $^{4}He/^{20}Ne$ ratios of gas samples from Oomine Ridge of this study (*dots*) and those of Nankai Trough (*crosses*) from Sano and Wakita (1987). *Dashed lines* are mixing lines between mantle-derived He and air-saturated seawater at 0°C (ASW) and between crustal radiogenic He and ASW

4.2 Pore-Water Chemistry

Figure 3g shows that chloride ion (Cl^-) concentrations at the seepage site on Oomine Ridge decreased with depth, as mentioned by Toki et al. (2004). Because chloride is a nonreactive component, the Cl profile cannot be explained by the normal interaction of seawater and sediment in hemipelagic environments, instead suggesting low-Cl fluid moving upward from deeper in the sediment. The pore water at this site was influenced by seeping fluid characterized as Cl-depleted (Toki et al. 2004). Likewise, stable-isotope profiles of pore water ($\delta^{18}O$ and δD) showed depletion with depth (Fig. 3h, i), suggesting that the seeping fluid was $\delta^{18}O$- and δD-depleted. These results are consistent with a previous study in this area (Toki et al. 2004), which proposed ground water input as the cause of the chemical and isotopic features.

The convex-upward Cl concentration profile observed in the Oomine Ridge core can be fitted with a steady-state kinetic model (Martens and Berner 1977) incorporating diffusion and pore-water velocity:

$$D_s \partial^2 C / \partial x^2 + v \partial C / \partial x = 0, \tag{3}$$

where

x = depth below the sediment–water interface measured positively downward (cm).
C = Cl concentration in pore water (mmol/kg);
D_s = whole-sediment diffusion coefficient for Cl, 160 cm^2/year (Li and Gregory 1974); and
v = advection rate (cm/year).

This yields the solution

$$C = (C_\infty - C_0)(1 - \exp(-\alpha x)) + C_0, \tag{4}$$

where $C = C_0$ at $x = 0$ and $C \to C_\infty$ as $x \to \infty$, $\alpha = v/D_s$ (cm^{-1}).

The core data are well fitted using α of 3×10^{-3} cm^{-1}, C_0 of 560 mmol/kg, and C_∞ of 490 mmol/kg. The α value corresponds to an advection rate of 3 mm/year. A previous estimate of the rate based on a 30-cm core from Oomine Ridge was 0.4–2.0 m/year and referred to seepage as a localized phenomenon (Toki et al. 2004). The advection rate determined in this study is considerably lower than the previously reported values and supports the inhomogeneity of seepage. In this case, the nearly linear gradient of the Cl profile shows that the transport of pore water is dominantly controlled by diffusion and very weak advection in the sediment column.

Sulfate (SO_4^{2-}) concentrations rapidly decreased to zero within 2 m of the sediment surface and remained there below 2 m (Fig. 3f), indicating either that sulfate reduction occurred in the surface sediments or that sulfate-free fluid flowing

upward had already undergone sulfate reduction by some organic carbon sources, including sedimentary organic carbon (Eq. 5) and methane (Eq. 6):

$$\begin{aligned}&(CH_2O)_{106}(NH_3)_{16}(H_3PO_4)+55SO_4^{2-}\\&\quad\rightarrow 106CO_2+16NH_3+55S^{2-}+H_3PO_4+106H_2O\end{aligned}\tag{5}$$

$$CH_4+SO_4^{2-}\rightarrow HS^-+HCO_3^-+H_2O\tag{6}$$

However, the latter interpretation (sulfate-free fluid flowing upward) contradicts with the interpretation for Cl profile (very slow advection rate). It is clear that in situ sulfate reduction plays substantially important role to control SO_4^{2-} profile and fluid ascent affects negligibly the SO_4^{2-} profile.

Sulfate reduction by sedimentary organic carbon occurs widely in sediments and produces ammonium (NH_4^+), as described in Eq. 5, but sulfate reduction by methane generates no NH_4^+ at all (Eq. 6). NH_4^+ concentrations increased even below the depth at which sulfate was completely reduced (Fig. 3c), which indicates that there are processes of organic matter decomposition, such as fermentation, producing ammonium even where sulfate is thoroughly depleted:

$$\begin{aligned}&(CH_2O)_{106}(NH_3)_{16}(H_3PO_4)+106H_2O\\&\quad\rightarrow 106CO_2+212H_2+16NH_3+H_3PO_4\end{aligned}\tag{7}$$

Mg and Ca concentrations showed decreases below 1 m that represent consumption by carbonate precipitation, as is frequently observed in seepage areas (e.g., Kulm et al. 1986). Anaerobic oxidation of methane results in an alkalinity increase, favoring precipitation of calcium carbonate.

Such pore-water chemistry profiles have been reported in numerous seepage fields (see references in Reeburgh 2007). Reductive fluids, methane-rich or sulfate-free, rise to surface sediments of seepage fields and reduce the depth at which early diagenesis occurs, including microbial anaerobic methane oxidation consuming sulfate.

4.3 Gas Chemistry of Reactive Components

CH_4 concentrations showed a concave-up depth profile (Fig. 4a), and the carbon isotopic composition of ΣCO_2 was considerably lighter than normal sedimentary organic matter (Fig. 4e), both of which are consistent with concurrent microbially mediated oxidation of sedimentary organic matter (Eq. 5) and isotopically light methane (Eq. 6) (Barnes and Goldberg 1976; Martens and Berner 1977; Reeburgh 1976; Reeburgh and Heggie 1977). Such isotopically light methane shows definitively that the methane is derived from microbial production in sediment by carbonate reduction (Schoell 1983):

$$CO_2+4H_2\rightarrow CH_4+2H_2O\tag{8}$$

Concentrations of H_2 in our pore water samples were low above 2 mbsf and reached a peak of about 500 μmol/kg at 2.5 mbsf (Fig. 4c). Hydrogen is an intermediate product during fermentation (Conrad 1999). As mentioned above in the interpretation of the ammonium profile, fermentation occurred at all depths in the core sediment and can be considered the origin of the hydrogen in pore water (Dolfing 1988). Sulfate reducers take up H_2 in the sulfate reduction zone above 1.5 mbsf:

$$4H_2 + SO_4^{2-} + H^+ \rightarrow HS^- + 4H_2O \tag{9}$$

Below 2 mbsf, in the methane production zone, H_2 would be utilized by methanogens through carbonate reduction as shown in Eq. 8. Sulfate reducers utilize hydrogen more effectively than methanogens, leading to the peak of H_2 concentration (Lovley and Goodwin 1988). Distribution of dissolved H_2 in the pore water was controlled by production via fermentation and consumption by oxidants such as sulfate and carbonate.

As for the isotopic composition of hydrogen, δD_{H2} values were around −745‰ above 2 mbsf and as light as −755‰ at 2.5 mbsf (Fig. 4f). δD_{H2} in natural environments is considered to be related to isotopic equilibrium with ambient H_2O at in situ temperature, promoted by microbial metabolisms (Romanek et al. 2003; Valentine et al. 2004). Given this tendency, δD_{H2} can be calculated as follows (Horibe and Craig 1995):

$$\left(D/H\right)_{H_2O} / \left(D/H\right)_{H_2} = 1.05 + 2.01\times10^5 / T^2 + 2.06\times10^9 / T^4 + 1.80\times10^{14} / T^6, \tag{10}$$

where T is temperature (K). The observed δD_{H2} value has been shown to be useful for estimating the equilibrium temperature, which has strong correlations with measured temperatures of hydrothermal samples (Proskurowski et al. 2006; Kawagucci et al. 2010). If the observed δD_{H2} were controlled by equilibrium between H_2 and H_2O, the observed value of −742‰ above 2 mbsf corresponds to 23°C, and the value of −755‰ at 2.5 mbsf corresponds to 16°C using Eq. 10.

The temperature of the bottom seawater was recorded as 1.674 ± 0.004°C by the temperature sensor attached to the NSS during core sampling. Heat flow values were previously reported to be 120 mW/m^2 at the outside of bacterial mats and 200 mW/m^2 at the inside of the mats on Oomine Ridge (Goto et al. 2003). These values are much higher than the reference value of about 50 mW/m^2 for the outer ridge of the Nankai accretionary prism. Such a high heat flow would result from seepage. Seepage must be highly variable from place to place to yield a heat-flow range from 50 to 200 mW/m^2. The thermal conductivity of the sediment sample, measured onboard, was around 1 W/m/K. Taking this value into account, the corresponding temperature gradient is 50–200 K/km. Given such a thermal gradient in this area, the in situ temperature several meters below the seafloor can be estimated to be about 2°C, which is not consistent with the estimated temperatures of 16°C and 23°C using δD_{H2} values.

The estimated temperature using δD_{H2} values suggests that hydrogen reached equilibrium with water at depths below the seafloor ranging from 70 to 400 m, given the thermal gradient in the sediment. At the advection rate we estimated from

the Cl profile of the samples, 3 mm/year, the hydrogen in the surface pore fluid must have equilibrated with H_2O at 70–400 mbsf 20–140 ky ago and then migrated up through the sediment column for 20–140 ky. It may seem strange that isotopic equilibrium has not been achieved in contemporary sediments after 20–140 ky, because the isotopic exchange by sulfate reduction bacteria requires about 40 days (Campbell et al. 2009).

We were afraid the gases equilibrated with coexistent pore water during its sampling and storage. Our sampling procedure, however, conducted extracting the gases from pore waters within a day of storage in a refrigerator after sampling the sediment from the seafloor. Isotopic equilibrium is reached slowly in low-temperature conditions or without catalysis (Koehler et al. 2000). The gas extraction interrupted the contact between H_2 and H_2O and the involvement of microbes living in sediment, and it is unlikely that the hydrogen and water isotopically reached equilibrium at a room temperature.

As stated above, the observed δD_{H2} cannot be explained by isotopic equilibrium with H_2O at reasonable temperature, and it would be the net value of hydrogen that is produced through fermentation occurring throughout the core as suggested by the NH_4^+ profile (Eq. 7), and consumed by sulfate and carbonate reduction above 2 mbsf (Eqs. 9 and 8, respectively). The δD_{H2} values show a heavier shift to −745‰ by sulfate and carbonate reduction, as microbes preferentially utilize ^1H during their metabolism (Landmeyer et al. 2000). The explanation of the δD_{H2} distribution is consistent with that of the hydrogen distribution described above.

We succeeded in retrieving dissolved gases from pore water and measured the concentrations and isotopic ratios of trace gases. The reactive components of these gases provide useful information about early diagenesis in surface sediment, which involves biochemical reactions. In the next section, the conservative components of these gases provide information on their origin and pathways, which is one of the important geochemical subjects.

4.4 Gas Chemistry of Nonreactive Components

Figure 4g shows ^{4}He-richer fluids distribute at deeper sediments, suggesting ^{4}He-rich fluids diffuse upward into the surface sediment. Figure 5 shows a correlation diagram between the observed ^{3}He/^{4}He and ^{4}He/^{20}Ne ratios. The ^{3}He/^{4}He ratios are normalized to R_{atm}, the atmospheric ^{3}He/^{4}He ratio of 1.393×10^{-6} (Davidson and Emerson 1990). The samples in the diagram lie in a mixing field of three end-members: primordial He derived from the mantle beneath the Nankai accretionary prism, radiogenic He produced from U and Th in crustal rocks, and atmospheric He dissolved in seawater (ASW). This distribution suggests that He in our sample is well explained by simple mixing of the three sources (Sano and Wakita 1985). We can correct for atmospheric He using the r value (Eq. 2) (Craig et al. 1978):

$$\left(^3\mathrm{He}/^4\mathrm{He}\right)_{cor} = \left[\left(^3\mathrm{He}/^4\mathrm{He}\right)_{obs} - \left(^3\mathrm{He}/^4\mathrm{He}\right)_a \times r\right]/(1-r), \tag{11}$$

where $(^3He/^4He)_{cor}$ and $(^3He/^4He)_{obs}$ denote the corrected and observed $^3He/^4He$ ratios, respectively, and $(^3He/^4He)_a$ is the atmospheric ratio 1.393×10^{-6} (R_{atm}). The mixing ratio of the mantle and crustal components of the corrected $^3He/^4He$ ratio can be estimated from the isotopic ratio of mantle He, $(^3He/^4He)_m$, which is 8 R_{atm} (Lupton and Craig 1975; Craig and Lupton 1976; Rison 1980), and the radiogenic crustal $(^3He/^4He)_c$ ratio, which is 0.02 R_{atm} (Morrison and Pine 1955). The resulting equation for helium composed of crustal (C) and upper mantle (M) components is

$$(^3\mathrm{He}/^4\mathrm{He})_{cor} = (^3\mathrm{He}/^4\mathrm{He})_m \times \mathrm{M} + (^3\mathrm{He}/^4\mathrm{He})_c \times \mathrm{C} \quad (12)$$

where M + C = 1.

The calculated mixing ratios for all of the samples show that the apparent contribution of radiogenic crust-derived He is as large as 95%. Crustal He can be a mixture of in situ radiogenic He and trapped He from the degassing of the basement rock beneath the sediments, equivalent to those observed in subduction zones (Gerling et al. 1971; Sano and Wakita 1987). The measured samples were collected at a seepage field, which could reflect discharge of fluid through a splay fault from the plate boundary (Park et al. 2002). However, the small contribution of mantle He in these samples more likely reflects mixing of crustal He from sediment and crust surrounding the pathway of the discharging fluid.

The sampling procedure employed here has been shown to be useful for trace gas chemistry in pore water in sediment, as it can distinguish between mantle and crustal contributions. It is important to estimate the contribution of components from magma (abiotic origin) to assess the contribution of sediment and microbes (biotic origin), particularly in sediment-rich hydrothermal fields. The trace gases in pore water provide important information on its origin and modification by hydrothermal processes; hence, this new technique extends the horizons of studies of rock–water interactions.

5 Conclusions

1. New techniques were employed for gas sampling, extraction, and measurement. The results showed that the gas concentrations of the gas samples were higher than those of fluid ones, suggesting that the effect of degassing on gas samples during sampling is reduced by rapid gas extraction on board ship. Assessment of the air contamination by using compositions of noble gases showed that contamination was negligible. Profiles of isotopic compositions of CH_4 and ΣCO_2 showed congruity between fluid and gas samples, suggesting that degassing did not significantly affect isotopic composition and that the extraction procedure using the vacuum system worked well.
2. Profiles of Cl, $\delta^{18}O$, and δD in pore water showed depletion with depth, suggesting that pore water was affected by seeping fluids depleted in Cl, $\delta^{18}O$, and δD. The convex-upward Cl concentration profile indicates an advection rate of 3 mm/

year, showing seepage to be a localized phenomenon. The estimated rate is low enough for the pore water to be dominantly controlled by diffusion rather than advection in sediment.

3. As a benefit of gas extraction, δD_{H2} values were successfully determined. Above 2 mbsf, hydrogen was oxidized by sulfate and carbonate, and the heavier shift to −745‰ could reflect oxidation by microbes (Eqs. 8 and 9), as ^{1}H is preferentially utilized by methanogens for carbonate reduction.
4. The strong correlation between the $^{3}He/^{4}He$ and $^{4}He/^{20}Ne$ ratios suggests that the He composition can be explained by a simple mixing of primordial He, radiogenic He, and atmospheric He. Correction for atmospheric He shows the predominant contribution of radiogenic He. Although the samples were collected from a seepage field in the discharge zone of fluid through a splay fault from the plate boundary, the crustal He component from sediment and crust surrounding the pathway of the discharging fluid was pervasively mixed in the fluids.

Acknowledgments We thank the NSS operation team (University of Tokyo), K. Ikehara (AIST), M. Murayama (Kochi University), M. Komure (Kyushu University), K. Fujino (Nihon University), W. Tanikawa (Kyoto University), S. Suganuma (Kochi University), and Marine Works Japan for their support of sampling, and we thank the captain and crew of R/V *Kaiyo* during the KY04-11 cruise for their continued dedication.

References

Barnes RO, Goldberg ED (1976) Methane production and consumption in anoxic marine sediments. Geology 4:297–300

Campbell BJ, Li C, Sessions AL, Valentine DL (2009) Hydrogen isotopic fractionation in lipid biosynthesis by H_2-consuming *Desulfobacterium autotrophicum*. Geochim Cosmochim Acta 73:2744–2757

Coleman ML, Shepard TJ, Durham JJ, Rouse JE, Moore GR (1982) Reduction of water with zinc for hydrogen isotope analysis. Anal Chem 54:993–995

Conrad R (1999) Contribution of hydrogen to methane production and control of hydrogen concentrations in methanogenic soils and sediments. FEMS Microbiol Ecol 28:193–202

Craig H (1957) Isotopic standards for carbon and oxygen and correction factors for mass-spectrometric analysis of carbon dioxide. Geochim Cosmochim Acta 12:133–149

Craig H (1961) Standard for reporting concentrations of deuterium and oxygen-18 in natural waters. Science 133:1833–1834

Craig H, Lupton JE (1976) Primodal neon, helium and hydrogen in oceanic basalts. Earth Planet Sci Lett 31:369–385

Craig H, Lupton JE, Horibe Y (1978) A mantle helium component in Circum-Pacific volcanic gases: Hakone, the Marianas. and Mt. Lassen. In: Alexander EC, Ozima M (eds) Terrestrial rare gases. Japan Scientific Society Press, Tokyo, pp 3–16

Davidson TA, Emerson DE (1990) Direct determinaton of helium-3 content of atmospheric air by mass spectrometer. J Geophys Res 95:3563–3568

Dolfing J (1988) Acetogenesis. In: Zehnder AJB (ed) Biology of anaerobic microorganisms. Wiley, New York

Dyrssen D, Sillen LG (1967) Alkalinity and total carbonate in sea water: a plea for p-T-independent data. Tellus 19:113–121

Edmond JM (1970) High precision determination of titration alkalinity and total carbon dioxide content of sea water by potentiometric titration. Deep Sea Res 17:737–750

Gerling EK, Mamyrin BA, Tolstikhin IN, Yakovleva SS (1971) Helium isotope composition in some rocks. Geochem Int (Geokhimiya) 8:755–761

Gieskes JM, Gamo T, Brumsack H (1991) Chemical methods for interstitial water analysis aboard Joides resolution, Technical note, edited. Texas A&M University, College Station

Goto S, Kuramoto S, Ashi J, Yamano M (2003) Heat and fluid fluxes at a biological community site on the Nankai accretionary prism off Kii peninsula. International Union of Geodesy and Geophysics, Sapporo, A198

Horibe Y, Craig H (1995) D/H fractionation in the system methane-hydrogen-water. Geochim Cosmochim Acta 59:5209–5217

Ijiri A, Tsunogai U, Gamo T (2003) A simple method for oxygen-18 determination of milligram quantities of water using $NaHCO_3$. Rapid Commun Mass Spectrom 17(13):1472–1478

Kawagucci S, Toki T, Ishibashi J, Takai K, Ito M, Oomori T, Gamo T (2010) Isotopic variation of molecular hydrogen in 20°–375°C hydrothermal fluids as detected by a new analytical method. J Geophys Res 115:G03021

Koehler G, Wassenaar L, Hendry J (2000) An automated technique for measuring δD and $\delta^{18}O$ values of pore water by direct CO_2 and H_2 equilibration. Anal Chem 72:5659–5664

Konno U, Tsunogai U, Nakagawa F, Nakaseama M, Ishibashi J, Nunoura T, Nakamura K (2006) Liquid CO_2 venting on seafloor: Yonaguni IV Knoll hydrothermal system, Okinawa Trough. Geophys Res Lett 33:L16607

Kulm LD, Suess E, Moore JC, Carson B, Lewis BT, Ritger SD, Kadko DC, Thornburg TM, Embley RW, Rugh WD, Massoth GJ, Langseth MG, Cochrane GR, Scamman RL (1986) Oregon subduction zone: venting, fauna, and carbonates. Science 231:561–566

Landmeyer JE, Chapelle FH, Bradley PM (2000) Microbial H_2 cycling does not affect δ^2H values of ground water. Ground Water 38:376–380

Li Y-H, Gregory S (1974) Diffusion of ions in sea water and in deep-sea sediments. Geochim Cosmochim Acta 38:703–714

Lovley DR, Goodwin S (1988) Hydrogen concentrations as an indicator of the predominant terminal electron-accepting reactions in aquatic sediments. Geochim Cosmochim Acta 52:2993–3003

Lupton JE, Craig H (1975) Excess ^3He in oceanic basalts: evidence for terrestrial primodal helium. Earth Planet Sci Lett 26:133–139

Manheim FT (1968) Disposable syringe techniques for obtaining small quantities of pore water from unconsolidated sediments. J Sedment Petrol 38:666–668

Martens CS, Berner RA (1977) Interstitial water chemistry of anoxic Long Island Sound sediments. 1. Dissolved gases. Limnol Oceanogr 22:10–25

Morrison P, Pine J (1955) Radiogenic origin of the helium isotopes in rock. Ann NY Acad Sci 62:69–92

Park J-O, Tsuru T, Kodaira S, Cummins PR, Kaneda Y (2002) Splay fault branching along the Nankai subduction zone. Science 297:1157–1160

Proskurowski G, Lilley MD, Kelley DS, Olson EJ (2006) Low temperature volatile production at the Lost City Hydrothermal Field, evidence from a hydrogen stable isotope geothermometer. Chem Geol 229:331–343

Reeburgh WS (1976) Methane consumption in Cariaco Trench waters and sediments. Earth Planet Sci Lett 28:337–344

Reeburgh WS (2007) Oceanic methane biogeochemistry. Chem Rev 107:486–513

Reeburgh WS, Heggie DT (1977) Microbial methane consumption reactions and their effect on methane distributions in freshwater and marine environments. Limnol Oceanogr 22:1–9

Rison W (1980) Isotopic studies of the rare gases in igneous rocks. Implications for the mantle and atmosphere. University of California, Berkeley

Romanek CS, Zhang CL, Li Y, Horita J, Vali H, Cole DR, Phelps TJ (2003) Carbon and hydrogen isotope fractionations associated with dissimilatory iron-reducing bacteria. Chem Geol 195:5–16

Sano Y, Wakita H (1985) Geographical distribution of $^{3}He/^{4}He$ ratios in Japan: implications for arc tectonics and incipient magmatism. J Geophys Res 90:8729–8741

Sano Y, Wakita H (1987) Helium isotopes and heat flow on the ocean floor. Chem Geol (Isotope Geosci Sect) 66:217–226

Sano Y, Takahata N, Seno T (2006) Geographical distribution of $^{3}He/^{4}He$ ratios in the Chugoku district, southwestern Japan. Pure Appl Geophys 163:745–757

Schoell M (1983) Genetic characterization of natural gases. AAPG Bull 67:2225–2238

Solorzano L (1969) Determination of ammonia in natural waters by phenol-hypochlorite method. Limnol Oceanogr 14:799–801

Strickland JDH, Parsons TR (1968) A practical handbook of sea water analysis, Bulletin 167. Fisheries Research Board of Canada, Ottawa, 311 pp

Toki T, Tsunogai U, Gamo T, Kuramoto S, Ashi J (2004) Detection of low-chloride fluids beneath a cold seep field on the Nankai accretionary wedge off Kumano, south of Japan. Earth Planet Sci Lett 228:37–47

Tsunogai U, Wakita H (1995) Precursory chemical-changes in-ground water – Kobe earthquake, Japan. Science 269:61–63

Tsunogai U, Yoshida N, Gamo T (2002) Carbon isotopic evidence of methane oxidation through sulfate reduction in sediment beneath cold seep vents on the seafloor at Nankai trough. Mar Geol 187:145–160

Valentine DL, Sessions AL, Tyler SC, Chidthaisong A (2004) Hydrogen isotope fractionation during H_2/CO_2 acetogenesis: hydrogen utilization efficiency and the origin of lipid-bound hydrogen. Geobiology 2:179–188

ZoBell CE (1947) Microbial transformation of molecular hydrogen in marine sediments, with particular reference to petroleum. AAPG Bull 31:1709–1751

Long-Term Stability of Acoustic Benchmarks Deployed on Thick Sediment for GPS/Acoustic Seafloor Positioning

Hiromi Fujimoto, Motoyuki Kido, Yukihito Osada, Keiichi Tadokoro, Takashi Okuda, Yoshihiro Matsumoto, and Kozue Kurihara

Abstract GPS/Acoustic seafloor positioning has become an indispensable geodetic observation for the monitoring of crustal activities in subduction zones. There remain, however, some key problems to be settled. Among them is long-term stability of acoustic benchmarks deployed on the seafloor: long-term attitude stability, especially against ground motions of earthquakes, and their electrical/mechanical durability for long-term geodetic observation. M7-class earthquakes occurred in 2004 off Kii Peninsula, Central Japan, and then coseismic seafloor crustal movements were detected by using the GPS/Acoustic (GPS/A) observations. This event gave us a unique opportunity to test the stability. We carried out diving surveys in 2006 and visually inspected the benchmarks that detected the crustal movements. All of them stood stably on the flat sediment. No effects of the earthquakes were observed. In case that the slight tilts of the instruments were caused by the earthquakes, the effect on the observed crustal movements is estimated to be within 1 cm. One of old benchmarks deployed 6 years before was recovered and inspected. There was no problem on the battery, and no damages on the outer frame of the instrument.

H. Fujimoto (✉), M. Kido, and Y. Osada
Graduate School of Science, Tohoku University, Aza Aoba 6-6, Aramaki, Aoba-ku, Sendai 980-8578, Japan
e-mail: fujimoto@aob.gp.tohoku.ac.jp; kido@aob.gp.tohoku.ac.jp; osada@aob.gp.tohoku.ac.jp

K. Tadokoro
Graduate School of Environmental Studies, Nagoya University, Furo-cho, Chikusa-ku, Nagoya 464-8602, Japan
e-mail: tad@seis.nagoya-u.ac.jp

T. Okuda
Technical Center of Nagoya University, Furo-cho, Chikusa-ku, Nagoya 464-8602, Japan
e-mail: okuda@seis.nagoya-u.ac.jp

Y. Matsumoto
Hydrographic and Oceanographic Department, Japan Coast Guard, Tsukiji 5-3-1, Chuo-ku, Tokyo 104-0045, Japan

K. Kurihara
Japan Marine Enterprise, Ltd., Natsushima-cho 2-15, Yokosuka 237-0061, Japan

Y. Ogawa et al. (eds.), *Accretionary Prisms and Convergent Margin Tectonics in the Northwest Pacific Basin*, Modern Approaches in Solid Earth Sciences 8,
DOI 10.1007/978-90-481-8885-7_13,

The diving surveys have settled a basic problem in seafloor geodesy and paved the way for long-term geodetic monitoring on the seafloor.

Keywords Seafloor benchmark • Long-term stability • GPS/Acoustic • Seafloor geodesy

1 Introduction

Most of large earthquakes occur in subduction zones under deep oceans. Owing to progresses in the analysis of geodetic data as well as extensive GPS networks, like the GEONET over the Japanese Islands, we can now roughly estimate lateral variation in the coupling and slip-deficit rate on the plate boundaries (e.g. Hashimoto et al. 2009). GPS is not, however, directly available on the seafloor. That is why the GPS/Acoustic (GPS/A) technique was developed for seafloor geodesy, combining kinematic GPS sea surface positioning and acoustic ranging between a sea surface unit and PXPs (precision acoustic transponders) on the seafloor (Spiess 1985). Since a steady plate motion was observed on the ocean bottom for the first time by Spiess et al. (1998), many important results have been reported: continuous plate motion at mid-ocean ridge 25 km from the spreading axis (Chadwell and Spiess 2008), strong seismic coupling on the subducting plate boundary in the Peru-Chile trench (Gagnon et al. 2005) and in the Japan trench (Fujita et al. 2006), co-seismic crustal movements in the Nankai trough (Kido et al. 2006; Tadokoro et al. 2006) and in the Japan trench (Matsumoto et al. 2006), and so on.

The PXP is a geodetic benchmark like a triangulation station on land. While benchmarks on land are firmly set up on the ground, PXPs are deployed from the sea surface on the ocean bottom covered with thick sediment. Long-term attitude stability of them is one of key problems underlying the GPS/A seafloor positioning. Repeated observations in a long time scale are crucial for geodetic monitoring, and electrical/mechanical durability of the acoustic benchmarks is another key problem.

Although seismicity is generally low along the Nankai trough off southwestern Japan, three large earthquakes with magnitude 7.4 or less occurred in September 2004 near Kumano-nada, where every historic Tonankai earthquake initiated the rupture. Three research groups, Nagoya University, Tohoku University, and JHOD (Hydrographic and Oceanographic Department, Japan Coast Guard) collaborating with IIS (Institute of Industrial Science, University of Tokyo), independently had deployed several GPS/A seafloor stations in the Kumano-nada region. They carried out geodetic observations before and after the earthquakes, and detected horizontal displacements larger than 20 cm (Kido et al. 2006; Tadokoro et al. 2006). It was the first co-seismic crustal movement that was detected by seafloor geodetic observations. Since the stations are located close to one of the estimated faults, the observed results provided good constraint on the fault model (Fig. 1).

It was suspected, however, that strong ground motions of the earthquakes might have tilted the seafloor benchmarks deployed on thick sediment. An acoustic transducer stands on the top of each PXP, which is about 0.6 m high. If a PXP

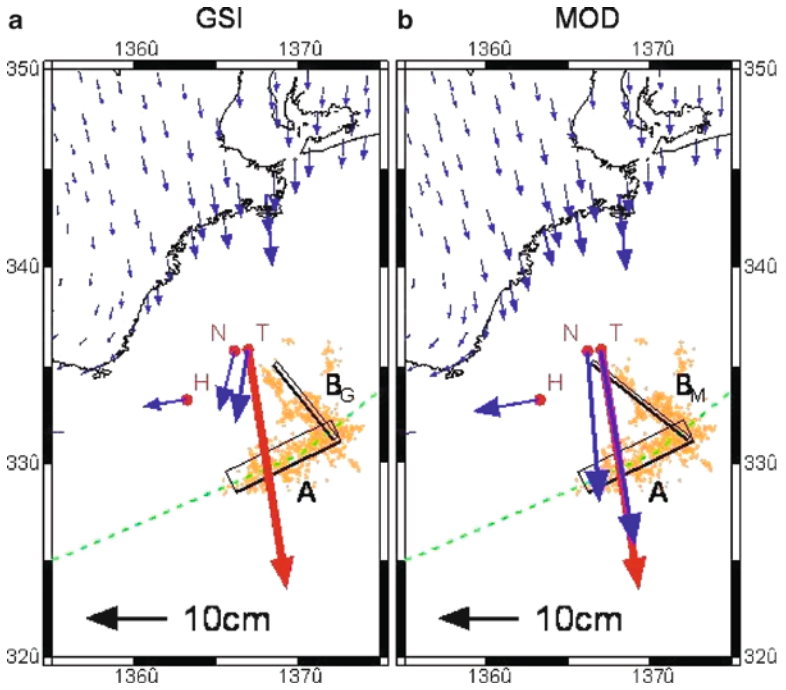

Fig. 1 Crustal movements detected by repeated GPS/Acoustic seafloor positioning (Kido et al. 2006). The *red arrow* shows the average of the observed seafloor displacements, and *blue arrows* are calculated displacement vectors for fault models (**a**) from GPS observation on land (GSI 2004) and (**b**) from observation on land and seafloor. *T*, *N*, and H indicate seafloor stations of Tohoku University, Nagoya University, and JHOD, respectively. *Orange dots* show aftershock activities. *Green dashed line* indicates the trench axis

is tilted by 10°, for example, horizontal position of the transducer shifts by some 10 cm; tilting of a benchmark results in an apparent crustal movement. This is a serious problem underlying seafloor geodesy. It is so difficult to carry out a laboratory experiment to test the stability of PXPs above soft sediments. The big earthquakes occurred in 2004 near the seafloor arrays gave us a rare opportunity to investigate the problem.

2 Diving Surveys

Three research groups had deployed 12 PXPs at three sites in Kumano-nada as shown in Fig. 2. We carried out visual inspection of ten of them in April 2006 during the NT06-07 cruise of the JAMSTEC R/V Natsushima and the ROV (remotely operated vehicle) *Hyper-dolphin*. This was the first diving survey to observe seafloor benchmarks that experienced strong ground motion of earthquakes. Photographs of all the instruments are shown below, because all of them are necessary to estimate the stability of their attitude.

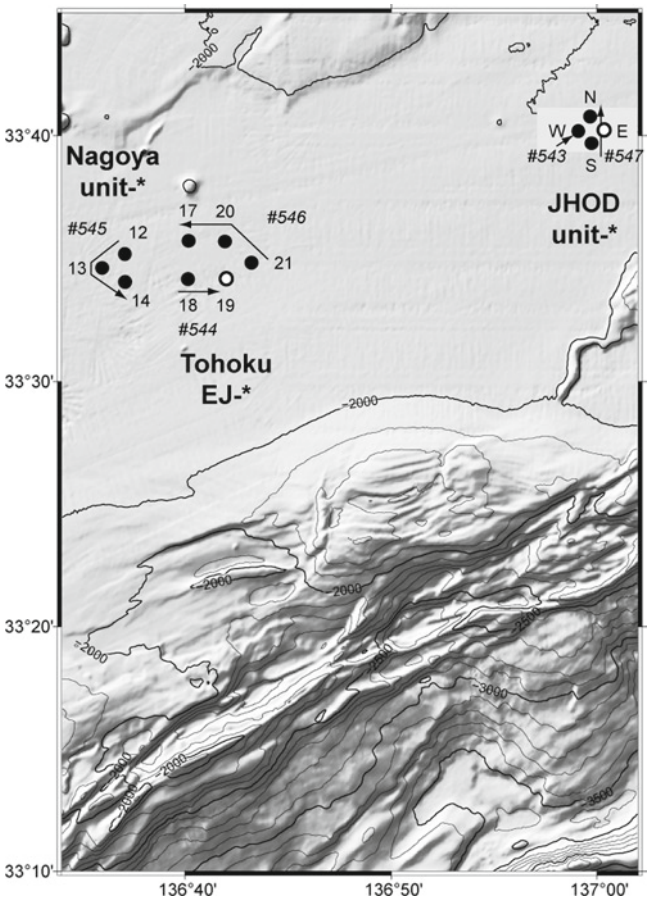

Fig. 2 PXP locations with their site names indicated. Nagoya and Tohoku sites correspond to N and T in Fig. 1. *Solid circles* are surveyed PXPs during this diving cruise, while *open circles* are not. Dive courses are schematically shown by *arrows* with dive numbers

Three PXPs at the westernmost site deployed by the Nagoya University group contributed to the detection of a co-seismic crustal movement (Tadokoro et al. 2006). Figure 3a–c show photographs of them on the seafloor. Figure 3d shows an instrument before deployment. The reddish hard hut contains a glass-sphere pressure vessel of 0.3 m in diameter, and the black unit on the top is an acoustic transducer. The bottom frame supporting the hard hut is buried in the sediment. Each instrument stands almost vertical on the bottom, and there was nothing indicating an effect of the earthquakes.

The ROV visited four of the five PXPs in the central array of the Tohoku University group, which also detected the co-seismic movement (Kido et al. 2006). As is shown in Fig. 4, they sat stably on the floor. The yellow hard hut contains a glass sphere of 0.4 m in diameter. The white bottom frame, 1 m in diameter, stably holds the hard hut.

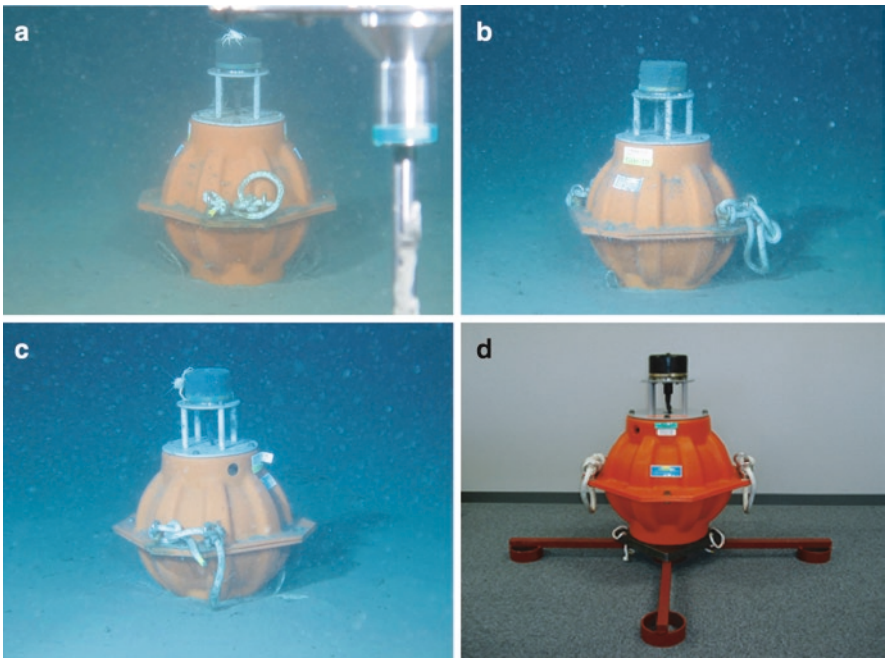

Fig. 3 PXPs of Nagoya University. (**a**) Unit 12, (**b**) Unit 13, and (**c**) Unit 14. Location of seafloor position of each PXP is shown in Fig. 2. (**d**) A unit before deployment

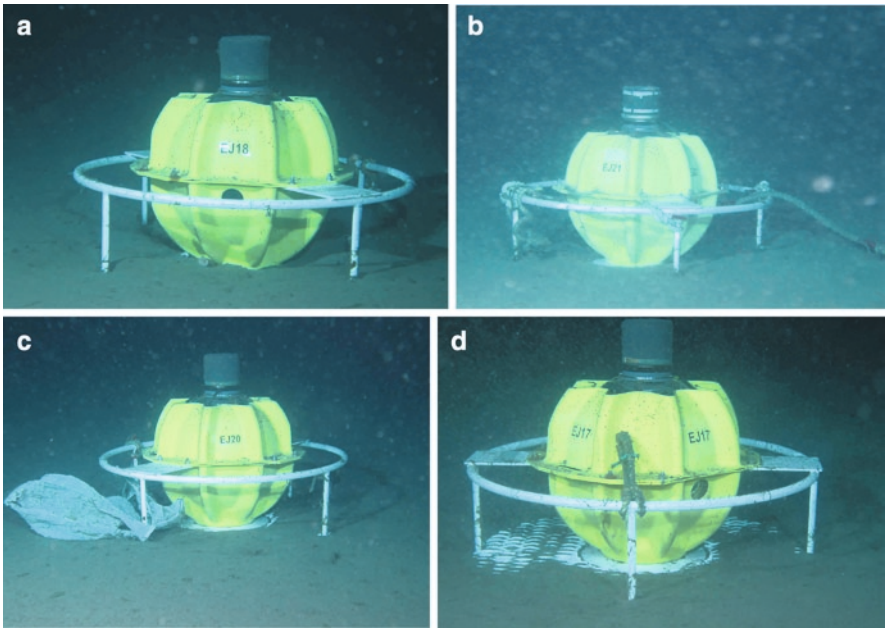

Fig. 4 PXPs of Tohoku University. (**a**) EJ18, (**b**) EJ21, (**c**) EJ20, and (**d**) EJ17. Location of seafloor position of each PXP is shown in Fig. 2. Bottom part of the frame is partly shown in (**d**)

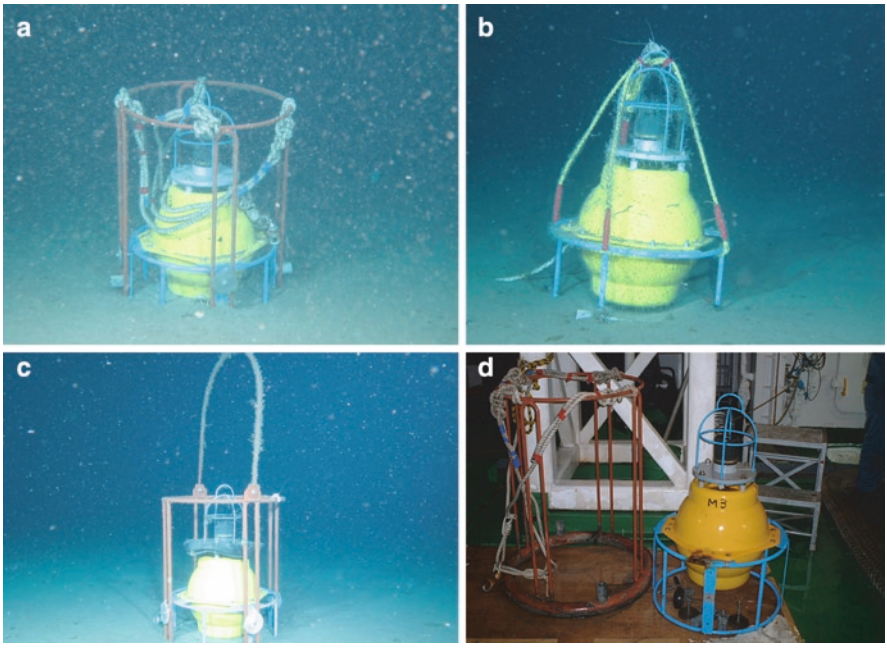

Fig. 5 PXPs of JHOD. (**a**) Unit W, (**b**) Unit S, (**c**) Unit N. Location of seafloor position of each PXP is shown in Fig. 2. (**d**) PXP Unit W after recovery

Although the JHOD group was maintaining an observation site for GPS/A observation some 50 km southwest of the study area (Site H in Fig. 1), a set of four PXPs shown in the eastern part of Fig. 2 was selected as the target of the diving survey. The PXPs deployed in 2000 were the first seafloor benchmarks for GPS/Acoustic seafloor positioning around Japan. The three instruments in Fig. 5a–c show the condition after a stay for about 6 years on the ocean bottom. Variety of design was adopted for the first generation of the instruments. The PXP in Fig. 5b was tilted by 6°, but there was no indication of disturbances of the sediment around it. This suggests that it was slightly tilted at the time of landing on the seafloor after a free-fall.

As the JHOD group planned to renew the PXP array, we recovered one of them to check the health of the instrument. The ROV recovered the one shown in Fig. 5a with a rope as is shown in Fig. 6a. The Fig 5d shows the instrument on the deck after the recovery. It was impressive that the outside of the frame was almost free from corrosion or marine lives.

Because most of benchmarks for seafloor geodetic observation in the subduction zones are deployed on the sediment, stiffness of the surface portion of the sediment is an important factor for the attitude stability of an instrument on the seafloor. In each dive one or two core samples were obtained from each dive using a push corer into the sediment nearly vertically with a manipulator of the ROV, and the top part of the sediment was sampled. As is shown in Fig. 7, the sediment was composed mostly of mud. Upper 4–5 cm of the surface layer is quite soft, and is

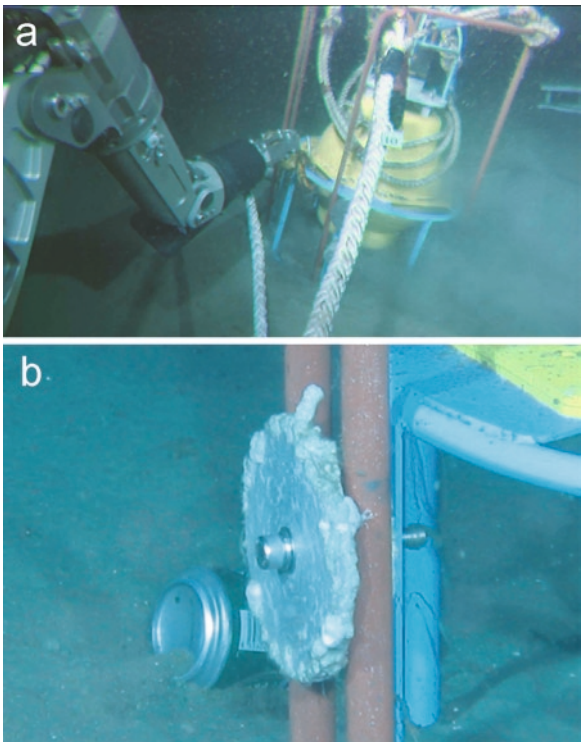

Fig. 6 (**a**) A snap shot showing the recovering operation of the JHOD PXP Unit W with the ROV. (**b**) A photograph showing an anti-erosion metal made of Zn on the JHOD PXP Unit N. Owing to the metal, the frame of the PXP was almost free from erosion by the sea water

visually different from the deeper layer. The size of the corer was 4.8 cm in outer diameter, and 30 cm in length. The sediment except the topmost part was stiff enough to stop the push-coring halfway.

3 Discussions

Geodetic observation by GPS on land is precise to an order of 1 mm, and a benchmark for the GPS positioning is founded firmly on the ground. Seafloor positioning is now aiming at precision of 1 cm. Then the position of sensor part of a benchmark should be stable within 1 cm relative to the seafloor. One of approaches to such problems is to visually observe how the benchmarks stand on the sediment after a strong earthquake occurred nearby. The 2004 M7-class earthquakes off Kii Peninsula gave us a unique chance to investigate the problem. Visual observation of ten acoustic benchmarks deployed on thick sediment showed that all of them stood on the flat sediment as if there had been no earthquakes. There was no disturbance on the surface of the sediment around the instruments.

Fig. 7 A sample of a push core with good penetration. The size of the corer is 4.8 cm in diameter and 30 cm in length. Some 5 cm of the topmost part of the sediment is quite soft and the color is different from the lower part

The benchmarks were dropped from the sea surface, fell in the sea water, and landed on the sediment. It sank partly into the sediment due to the shock of the landing. Judging from the photographs shown above, the sediment was stiff enough to stop the penetration within 10–20 cm. The average density of the instrument is only slightly higher than the sea water in order to reduce the shock at the landing. The density of the unconsolidated sediment is not so different from the sea water. The instrument is designed to keep the attitude vertical during the free-fall in the sea water. Therefore, there is little force for it to further sink into the sediment or tilt.

Considering that the bottom part of each benchmark is partly buried in the sediment, the problem is not a horizontal movement but a tilt. Tilting of an instrument on the seafloor may probably result from its sinking into the sediment. Stiffness of the surface layer of the sediment can be estimated from the above-mentioned penetration at the landing on the sediment. It was also estimated from push-coring. The coring showed that the sediment was very soft in the top 4–5 cm, became gradually stiff with the depth, and stopped push-coring at 15–25 cm penetration. Because the size of the bottom part of a PXP is much larger than the diameter of the push-corer (4.8 cm), attitude of each benchmark is stable on the sediment with a large resistance against sinking.

The bottom frame shown in Fig. 4d is meshed in order to keep the instrument vertical during a free-fall from the sea surface. Stable attitude of the instrument during a free-fall in the sea had been confirmed during an experiment using an ROV. The visual observation shows that the large diameter and the meshed bottom of the frame worked well to stably support a benchmark on the sediment.

Another important point is the motion of seafloor instruments associated with ground motion caused by an earthquake. Because P wave velocity in unconsolidated sediment is much the same with that in sea water, top part of the sediment must move much the same way with the sea water in case of an earthquake. Then a seafloor instrument on the sediment will move with the outside, and there will be little motion relative to the sediment. This is a merit of submarine observation, and must be why a broad-band ocean bottom seismometer can measure seismic waves on the sediment.

Visual observation suggests that the slight tilts of the benchmarks show the condition after the landing on the sediment. Supposing that the tilts were the effects of the earthquakes, however, a maximum possible effect of the tilts on the results shown in Fig. 1 was estimated. Tilts of the benchmarks shown in Figs. 3 and 4 were roughly measured by using the picture. They were the benchmarks that detected the seafloor crustal movement shown in Fig. 1. The tilt in degree is as follows: Fig. 3 (a) 1°, (b) 0°, (c) 2°, and Fig. 4 (a) 2°, (b) 1°, (c) 0°, (d) 1°. Altitude of the acoustic transducers is some 60 cm from the bottom, and so a tilt of 2° corresponds to a horizontal shift of 2 cm of the acoustic sensor. The results shown in Fig. 1 are obtained by using an array of 3–4 acoustic benchmarks. Because the possible error of each unit is 0–2 cm, a possible error in the position of the array is about 1 cm.

One of the PXPs that JHOD deployed in 2000 was recovered to check the degree of degradation. The battery was still alive as was expected. Although some parts of the outer frame made of Al were slightly stained, corrosion of the metal part or damage by marine lives was quite limited. Anti-corrosion metal made of Zn equipped on each PXP as is shown in Fig. 6b might have protected the frame effectively against the sea water. Degradation of the instrument was limited enough to confirm that the present seafloor instrumentation is basically appropriate and to encourage much longer-term observation on the ocean bottom.

4 Summary

Diving surveys were carried out to visually inspect benchmarks deployed for GPS/Acoustic precise seafloor positioning that had been deployed near the focal area of 2004 M7-class earthquakes off Kii Peninsula, Central Japan. The observation confirmed stable attitude of the benchmarks used for detection of the coseismic crustal movements larger than 20 cm. In case that the slight tilts of the instruments were caused by the earthquakes, the effect on the observed crustal movements is estimated to be within 1 cm.

We estimate that the following points are important for the stable attitude of the benchmarks. (1) The average density of them is not so different from that of the

sediment in order to reduce the shock at the landing after a free-fall in the sea water. (2) Judging from the penetration at the landing and at push-coring, the sediment is stiff enough to support them stably. (3) They have large resistance against sinking into the sediment owing to the size of the bottom part that is much larger than the diameter of the push-corer. (4) Because P wave velocity in unconsolidated sediment is much the same with that in sea water, top part of the sediment and a seafloor instrument must move much the same way with the sea water in case of an earthquake.

One of old benchmarks was recovered after a long stay on the ocean bottom for about 6 years. Outside of the recovered instrument was healthy enough to encourage longer-term observation: there was no corrosion on the instrument by the sea water nor damages by marine lives. Diving survey have provided us many important suggestions, which should be utilized in seafloor instrumentation in the future.

Aknowledgements The authors thank Captain Y. Iwasaki, crew of the R/V Natsushima, Commander K. Chiba, and team of the ROV Hyper-Dolphin for efficient operations during the diving surveys. This study was supported by the Deep-sea Research Program of JAMSTEC, and was partly supported by the program of Dense Oceanfloor Network System for Earthquakes and Tsunamis (DONET) of JAMSTEC and MEXT, Japan.

References

Chadwell CD, Spiess FN (2008) Plate motion at the ridge-transform boundary of the south Cleft segment of the Juan de Fuca Ridge from GPS-Acoustic data. Geophys Res Lett 113:B04415. doi:10.1029/2007JB004936

Fujita M, Ishikawa T, Mochizuki M, Sato M, Toyama S, Katayama M, Kawai K, Matsumoto Y, Yabuki T, Asada A, Colombo OL (2006) GPS/Acoustic seafloor geodetic observation: method of data analysis and its application. Earth Planet Space 58:265–275

Gagnon K, Chadwell CD, Norabuena E (2005) Measuring the onset of locking in the Peru-Chile trench with GPS and acoustic measuring. Nature 434:205–208

Geographical Survey Institute (GSI) (2004) The earthquake SE off Kii peninsula on September 5. In: the Summary of the 159 Meeting of the Coordinating Committee for Earthquake Prediction. http://cais.gsi.go.jp/YOCHIREN/JIS/159/index159.html

Hashimoto C, Noda A, Sagiya T, Matsu'ura M (2009) Interplate seismogenic zones along the Kuril – Japan trench inferred from GPS data inversion. Nat Geosci 2:141–144

Kido M, Fujimoto H, Miura S, Osada Y, Tsuka K, Tabei T (2006) Seafloor displacement at Kumano-nada caused by the 2004 off Kii Peninsula earthquake, detected through repeated GPS/Acoustic surveys. Earth Planet Space 58:911–915

Matsumoto Y, Fujita M, Ishikawa T, Mochizuki M, Yabuki T, Asada A (2006) Undersea co-seismic crustal movements associated with the 2005 Off Miyagi Prefecture Earthquake detected by GPS/acoustic seafloor geodetic observation. Earth Planet Space 58:1573–1576

Spiess FN (1985) Analysis of a possible seafloor strain measurement system. Mar Geod 9:385–398

Spiess FN, Chadwell CD, Hildebrand JA, Young LE, Purcell GH Jr, Dragert H (1998) Precise GPS/Acoustic positioning of seafloor reference points for tectonic studies. Phys Earth Planet Inter 108:101–112

Tadokoro K, Ando M, Ikuta R, Okuda T, Besana GM, Sugimoto S, Kuno M (2006) Observation of coseismic seafloor crustal deformation due to M7 class offshore earthquakes. Geophys Res Lett 33. doi:10.1029/2006GL026742

Index

Y. Ogawa et al. (eds.), *Accretionary Prisms and Convergent Margin Tectonics in the Northwest Pacific Basin*, Modern Approaches in Solid Earth Sciences 8,
DOI 10.1007/978-90-481-8885-7, © Springer Science+Business Media B.V. 2011